

Transactions of the ASME®

Editor
LEE S. LANGSTON (2006)
Assistant to the Editor
LIZ LANGSTON
Associate Editors
Fuels and Combustion Technologies
S. GOLLAHALLI (2004)
Internal Combustion Engines
D. ASSANIS (2005)
Nuclear
R. DUFFY (2004)
International Gas Turbine Institute
IGTI Review Chair
R. NATOLE (2001)
E. BENVENUTI (2002)
H. R. SIMMONS (2003)
Combustion and Fuels
P. MALTE (2003)
Structures and Dynamics
N. ARAKERE (2004)
M. MIGNOLET (2005)

BOARD ON COMMUNICATIONS
Chair and Vice-President
OZDEN OCHOA

OFFICERS OF THE ASME
President, **REGINALD VACHON**
Executive Director, **V. R. CARTER**
Treasurer, **R. E. NICKELL**

PUBLISHING STAFF
Managing Director, Engineering
THOMAS G. LOUGHLIN

Director, Technical Publishing
PHILIP DI VIETRO

Managing Editor, Technical Publishing
CYNTHIA B. CLARK

Manager, Journals
JOAN MERANZE

Production Coordinator
JUDITH SIERANT

Production Assistant
MARISOL ANDINO

Transactions of the ASME, Journal of Engineering for Gas Turbines and Power (ISSN 0742-4795) is published quarterly (Jan., April, July, Oct.) by The American Society of Mechanical Engineers, Three Park Avenue, New York, NY 10016. Periodicals postage paid at New York, NY and additional mailing offices. POSTMASTER: Send address changes to Transactions of the ASME, Journal of Engineering for Gas Turbines and Power, c/o THE AMERICAN SOCIETY OF MECHANICAL ENGINEERS, 22 Law Drive, Box 2300, Fairfield, NJ 07007-2300.

CHANGES OF ADDRESS must be received at Society headquarters seven weeks before they are to be effective. Please send old label and new address.

STATEMENT from By-Laws. The Society shall not be responsible for statements or opinions advanced in papers or ... printed in its publications (B7.1, par. 3).

COPYRIGHT © 2003 by the American Society of Mechanical Engineers. For authorization to photocopy material for internal or personal use under circumstances not falling within the fair use provisions of the Copyright Act, contact the Copyright Clearance Center (CCC), 222 Rosewood Drive, Danvers, MA 01923, Tel: 978-750-8400, www.copyright.com.

INDEXED by Applied Mechanics Reviews and Engineering Information, Inc. Canadian Goods & Services Tax Registration #126148048

Journal of Engineering for Gas Turbines and Power

Published Quarterly by The American Society of Mechanical Engineers

VOLUME 125 • NUMBER 4 • OCTOBER 2003

TECHNICAL PAPERS

Gas Turbines: Combustion and Fuels

- 861 **Low NO_x Combustion for Liquid Fuels: Atmospheric Pressure Experiments Using a Staged Prevaporizer-Premixer (2001-GT-0081)**
J. C. Y. Lee, P. C. Malte, and M. A. Benjamin
- 872 **Investigation of the Response of an Air Blast Atomizer Combustion Chamber Configuration on Forced Modulation of Air Feed at Realistic Operating Conditions (2000-GT-30059)**
C. Hassa, J. Heinze, and K. Stursberg
- 879 **Advanced Catalytic Pilot for Low NO_x Industrial Gas Turbines (2002-GT-30083)**
H. Karim, K. Lyle, S. Etemad, L. L. Smith, W. C. Pfefferle, P. Dutta, and K. Smith
- 885 **Combustion System Development for the Ramgen Engine (2002-GT-30084)**
D. W. Kendrick, B. C. Chenevert, B. Trueblood, J. Tonouchi, S. P. Lawlor, and R. Steele
- 895 **The Premixed Conditional Moment Closure Method Applied to Idealized Lean Premixed Gas Turbine Combustors (2002-GT-30094)**
S. M. Martin, J. C. Kramlich, G. Kosály, and J. J. Riley
- 901 **Liquid Fuel Placement and Mixing of Genetic Aeroengine Premix Module at Different Operating Conditions (2002-GT-30102)**
J. Becker and C. Hassa

Gas Turbines: Controls, Diagnostics & Instrumentation

- 909 **Fuzzy Fuel Flow Selection Logic for a Real Time Embedded Full Authority Digital Engine Control (2000-GT-0046)**
A. Martucci and A. J. Volponi
- 917 **The Use of Kalman Filter and Neural Network Methodologies in Gas Turbine Performance Diagnostics: A Comparative Study (2000-GT-0547)**
A. J. Volponi, H. DePold, R. Ganguli, and C. Daguang
- 925 **Active Combustion Instability Control With Spinning Valve Actuator (2002-GT-30042)**
P. Barooah, T. J. Anderson, and J. M. Cohen

Gas Turbines: Cycle Innovations

- 933 **The Recuperative-Auto Thermal Reforming and the Recuperative-Reforming Gas Turbine Power Cycles With CO₂ Removal—Part I: The Recuperative-Auto Thermal Reforming Cycle (2002-GT-30116)**
D. Fiaschi, L. Lombardi, and L. Tapinassi
- 940 **Thermodynamic Performance Analysis of New Gas Turbine Combined Cycles With No Emissions of Carbon Dioxide (2002-GT-30117)**
R. Gabbriellini and R. Singh
- 947 **Thermoeconomic Analysis of Gas Turbine Plants With Fuel Decarbonization and Carbon Dioxide Sequestration (2002-GT-30120)**
M. Bozzolo, M. Brandani, A. Traverso, and A. F. Massardo

(Contents continued on inside back cover)

This journal is printed on acid-free paper, which exceeds the ANSI Z39.48-1992 specification for permanence of paper and library materials. ©™
♻️ 85% recycled content, including 10% post-consumer fibers.

- 954 Comparative Analysis of Off-Design Performance Characteristics of Single and Two-Shaft Industrial Gas Turbines (2002-GT-30132)
J. H. Kim, T. S. Kim, J. L. Sohn, and S. T. Ro
- 961 Steady and Dynamic Performance and Emissions of a Variable Geometry Combustor in a Gas Turbine Engine (2002-GT-30135)
Y. G. Li and R. L. Hales
- 972 A New Generalized Carbon Exergy Tax: An Effective Rule to Control Global Warming (2002-GT-30139)
A. Traverso, A. F. Massardo, M. Santarelli, and M. Cali
- 979 A New Scaling Method for Component Maps of Gas Turbine Using System Identification (2002-GT-30150)
C. Kong, J. Ki, and M. Kang
- Gas Turbines: Cycle Innovations, and Marine*
- 986 Off-Design Performance Analysis of a Hybrid System Based on an Existing Molten Fuel Cell Stack (2002-GT-30115)
P. Bedont, O. Grillo, and A. F. Massardo
- Gas Turbines: Heat Transfer*
- 994 Experimental and Numerical Study of Heat Transfer in a Gas Turbine Combustor Liner (2002-GT-30183)
J. C. Bailey, J. Intile, T. F. Fric, A. K. Tolpadi, N. V. Nirmalan, and R. S. Bunker
- Gas Turbines: Heat Transfer, and Turbomachinery*
- 1003 Disintegration of Oil Jets Emerging From Axial Passages at the Face of a Rotating Cylinder (2001-GT-0201)
A. Glahn, M. F. Blair, K. L. Allard, S. Busam, O. Schäfer, and S. Wittig
- 1011 Disintegration of Oil Films Emerging From Radial Holes in a Rotating Cylinder (2001-GT-0202)
A. Glahn, M. F. Blair, K. L. Allard, S. Busam, O. Schäfer, and S. Wittig
- Gas Turbines: Manufacturing, Materials & Metallurgy*
- 1021 Mechanical Surface Treatment Technologies for Gas Turbine Engine Components
W. Zhuang and B. Wicks
- Gas Turbines: Structures and Dynamics*
- 1026 Imbalance Response of a Rotor Supported on Flexure Pivot Tilting Pad Journal Bearings in Series With Integral Squeeze Film Dampers (2001-GT-0257)
L. San Andrés and O. De Santiago
- 1033 Contact Stresses in Dovetail Attachments: Alleviation via Precision Crowning (2001-GT-0550)
G. B. Sinclair and N. G. Cormier
- Gas Turbines: Structures and Dynamics and Aircraft Engines*
- 1042 Computation of the Optimal Normal Load of a Friction Damper Under Different Types of Excitation (99-GT-0413)
D. Cha and A. Sinha
- Internal Combustion Engines*
- 1050 Engine Torque Nonuniformity Evaluation Using Instantaneous Crankshaft Speed Signal
N. Cavina and F. Ponti
- 1059 Numerical Study of Lean-Direct Injection Combustor With Discrete-Jet Swirlers Using Reynolds Stress Model
S. L. Yang, Y. K. Siow, C. Y. Teo, R. R. Tacina, A. C. Iannetti, and P. F. Penko
- 1066 Development of an Exhaust Recirculation Distribution Prediction Method Using Three-Dimensional Flow Analysis and Its Application
K. Yoshizawa, K. Mori, Y. Matayoshi, and S. Kimura
- 1075 Energy and Exergy Analyses of the Pulse Detonation Engine
T. E. Hutchins and M. Metghalchi
- 1081 Numerical Investigation of the Effects of Axial Cylinder Bore Profiles on Piston Ring Radial Dynamics
Y. Piao and S. D. Gulwadi

ERRATUM

- 1090 "Effect of Biodiesel Utilization of Wear of Vital Parts in Compression Ignition Engine"
A. K. Agarwal, J. Bijwe, and L. M. Das
- 1091 Author Index

ANNOUNCEMENTS AND SPECIAL NOTES

1098 2004 Heat Transfer/Fluids Engineering Summer Conference—Announcement

1100 Information for Authors

The ASME Journal of Engineering for Gas Turbines and Power is abstracted and indexed in the following:

AESIS (Australia's Geoscience, Minerals, & Petroleum Database), Applied Science & Technology Index, AMR Abstracts Database, Aquatic Sciences and Fisheries Abstracts, Civil Engineering Abstracts, Compendex (The electronic equivalent of Engineering Index), Computer & Information Systems Abstracts, Corrosion Abstracts, Current Contents, Engineered Materials Abstracts, Engineering Index, Enviroline (The electronic equivalent of Environment Abstracts), Environment Abstracts, Environmental Science and Pollution Management, Fluidex, INSPEC, Mechanical & Transportation Engineering Abstracts, Mechanical Engineering Abstracts, METADEX (The electronic equivalent of Metals Abstracts and Alloys Index), Pollution Abstracts, Referativnyi Zhurnal, Science Citation Index, SciSearch (The electronic equivalent of Science Citation Index), Shock and Vibration Digest

Low NO_x Combustion for Liquid Fuels: Atmospheric Pressure Experiments Using a Staged Prevaporizer-Premixer

J. C. Y. Lee¹

P. C. Malte

Department of Mechanical Engineering,
University of Washington,
Box 352600,
Seattle, WA 98195-2600

M. A. Benjamin

Gas Turbine Fuel System Division,
Parker Hannifin Corporation,
9200 Tyler Boulevard,
Mentor, OH 44060

Low emissions of NO_x are obtained for a wide range of liquid fuels by using a staged prevaporizing-premixing injector. The injector relies on two stages of air temperature and fires into a laboratory jet-stirred reactor operated at atmospheric pressure and nominal ϕ of 0.6. The liquid fuels burned are methanol, normal alkanes from pentane to hexadecane, benzene, toluene, two grades of light naphtha, and four grades of No. 2 diesel fuel. Additionally, natural gas, ethane, and industrial propane are burned. For experiments conducted for 1790 K combustion temperature and 2.3 ± 0.1 ms combustion residence time, the NO_x (adjusted to 15% O₂ dry) varies from a low of 3.5 ppmv for methanol to a high of 11.5 ppmv for No. 2 diesel fuel. For the most part, the NO_x and CO are positively correlated with the fuel carbon to hydrogen ratio (C/H). Chemical kinetic modeling suggests the increase in NO_x with C/H ratio is caused in significant part by the increasing superequilibrium concentrations of O-atom created by the increasing levels of CO burning in the jet-stirred reactor. Fuel bound nitrogen also contributes NO_x for the burning of the diesel fuel. This paper describes the staged prevaporizing-premixing injector, the examination of the injector, and the NO_x and CO measurements and their interpretation. Optical measurements, using beams of He-Ne laser radiation passed across the outlet stream of the injector, indicate complete vaporization and a small variation in the cross-stream averaged fuel/air ratio. The latter is determined by measuring the standard deviation and mean of the transmission of the laser beam passed through the stream. Additional measurements and inspections indicate no pressure oscillations within the injector and no gum and carbon deposition. Thus, the NO_x and CO measurements are obtained for fully vaporized, well premixed conditions devoid of preflame reactions within the injector. [DOI: 10.1115/1.1584476]

Introduction

Lean-premixed combustion of natural gas is widely practiced in gas turbine engines applied to electrical generation and mechanical drive. Most of the engines emit NO_x less than 25 ppmv (at 15% O₂ dry), though for some engines in the field, the NO_x emission is less than 10 ppmv (at 15% O₂ dry). In general, lean premixed (LP) combustors are sensitive to fuel composition. For example, natural gas high in non-methane hydrocarbon content (NMHC), when premixed with the high temperature compressor discharge air, may experience autoignition and flashback. Further, for many dual fuel engines, the combustor is switched to diffusion flame mode for liquid fuel firing and uses water or steam injection for NO_x control. A preferred alternative is dry low NO_x (DLN) combustion for all fuels, since elimination of the water/steam injection generally improves the engine economics and efficiency. The prevaporizing-premixing injector used should be designed to minimize preflame fuel oxidation (e.g., coking and autoignition) and should not be prone to flashback. Further, it is important to understand the NO_x behavior of the combustor fitted with the prevaporizing-premixing injector.

The present study involves the application of the staged prevaporizing-premixing injector, [1], for lean premixed combustion of liquid fuels. The staging is accomplished by using two

stages of air temperature, including a relatively low temperature air to accomplish as much of the vaporization and mixing as possible and a high temperature air to bring the injector outlet stream to the desired combustor inlet temperature without causing preflame reaction and autoignition. The inside of the staged prevaporizer-premixer (SPP) is monitored and inspected to confirm the absence of reaction within the SPP. The outlet stream of the SPP is optically examined for completeness of vaporization and degree of mixedness between the fuel vapor and air. The objective of the study is to show DLN combustion for a wide range of fuels burned in a high-intensity combustor fed by the reactants from the SPP injector. Most significantly, the study provides a database of NO_x as a function of fuel type for lean, fully vaporized, well premixed combustion. The combustor is an atmospheric pressure jet-stirred reactor (JSR) operated at combustor inlet temperatures (up to 773 K) and flame temperature (normally 1790 K) typical of LP combustion turbines. The gaseous fuels burned are natural gas, ethane, and industrial propane. The liquid fuels burned are methanol, normal alkanes of C₅ to C₁₆, benzene, toluene, two grades of light naphtha, and four grades of No. 2 diesel fuel (DF2). The DF2s contains small amounts of fuel bound nitrogen (FBN), about 50 to 100 ppm by weight. One of the pure liquid fuels (n-dodecane) was previously burned, [2], with and without a FBN dopant (n-ethylethylenediamine). The experiments, conducted under conditions very close to those of the present study, indicated complete conversion of small levels of FBN to NO_x.

The paper contains the following sections:

- description of the SPP injector and JSR combustor,

¹Currently with Solar Turbines Incorporated.

Contributed by the International Gas Turbine Institute (IGTI) of THE AMERICAN SOCIETY OF MECHANICAL ENGINEERS for publication in the ASME JOURNAL OF ENGINEERING FOR GAS TURBINES AND POWER. Paper presented at the International Gas Turbine and Aeroengine Congress and Exhibition, New Orleans, LA, June 4–7, 2001; Paper 2001-GT-0081. Manuscript received by IGTI, Dec. 2000, final revision, Mar. 2001. Associate Editor: R. Natole.

- description of the optical method used to evaluate the mixedness of the SPP outlet stream,
- data and analysis on the mixedness of the SPP outlet stream,
- experimental data of NO_x and CO as a function of fuel type,
- analysis of the NO_x and CO data by chemical kinetic modeling, and
- conclusions and recommendations.

Stage Prevaporizer-Premixer (SPP) Injector and Diagnostics

The experimental setup of the SPP injector with the JSR combustor is schematically depicted in Fig. 1.

SPP Injector. The SPP injector is shown in the lower three-fourths of Fig. 1. First stage air, of relatively low temperature, enters at the bottom, i.e., upstream end of the SPP. The first stage air is accelerated through jets located at the upstream end of the film atomizer that is coaxial with the fuel nozzle. Two streams of the jetted first stage air are obtained, separated by the thin annular splitter plate constituting the film atomizer. Second stage air enters through a manifold near the top, i.e., downstream end of the SPP. This air is mixed into the internal flow of the SPP through several staggered jets. These jets enter the SPP at an angle of 45 deg to the axial direction and do not have a tangential velocity component. The total air flow rate of the SPP as used for atmospheric pressure firing is 4.7 kg/hr. In the first stage of the SPP, the light ends and middle boiling compounds of a blended fuel are vaporized, while in the second stage, the vaporization process is completed. As the temperature of the second stage air is increased, the residence time of the gases in the second stage can be decreased to small values to prevent reaction within the SPP.

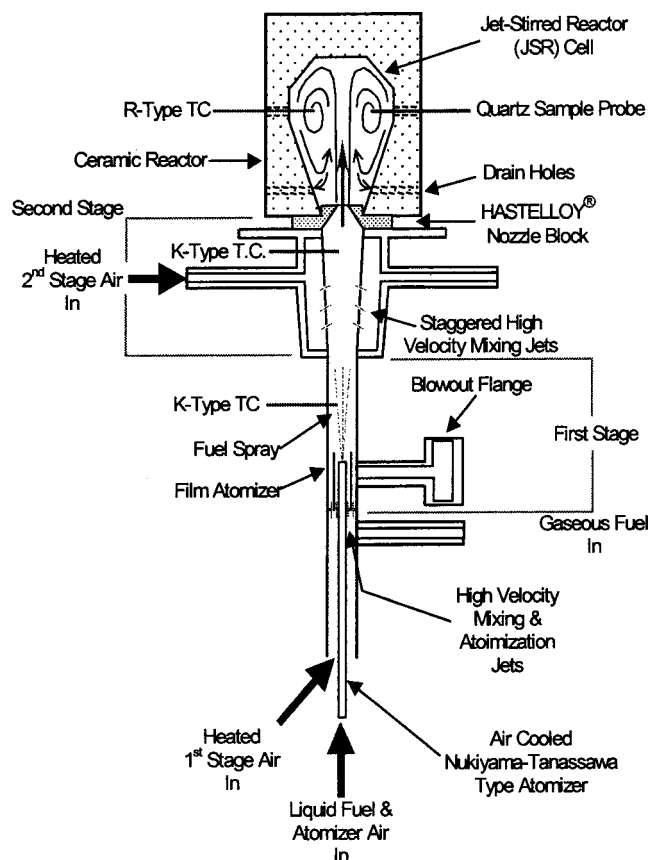


Fig. 1 Schematic drawing of the atmospheric pressure JSR, of 15.8 cm³ volume, with the staged prevaporizing-premixing injector

Gaseous fuel is injected through a single port into the first stage air. As noted in Fig. 1, this port is located slightly upstream of the film atomizer. Liquid fuel is atomized by a Nukiyama-Tanasawa type, plain-jet, air-blast atomizer custom built for this application and located on the centerline of the first stage. The Nukiyama-Tanasawa type atomizer is described by Lefebvre [3]. The previous embodiment of this atomizer for research at the University of Washington is discussed by Lee et al. [4]. Within the Nukiyama-Tanasawa type nozzle, pressure atomization occurs first, followed by air-assist atomization and spray cone angle adjustment.

The Nukiyama-Tanasawa type nozzle provides good atomization and spray quality for the low fuel flow rates associated with the atmospheric pressure firing of this study. The nominal flow rate of the fuel is 0.2 kg/hr and that of the unheated atomizing air is 0.4 kg/hr. The atomizer nozzle flow is choked and the calculated SMD of the spray is about 10 μm . However, for high pressure industrial applications, with significantly greater flow rates of fuel, a commercial air blast, pressure swirl or macrolaminated, [5], atomizer will be used for the SPP.

For the present study, the first stage temperature is varied from 293 to 623 K and that of the second stage, which is also the total temperature of the outlet stream, is varied from 293 to 773 K (though the data shown are limited to 723 K). The outlet nozzle of the SPP, which couples the SPP to the jet stirred reactor, is 4 mm in diameter. Nominal pressure within the SPP, downstream of the film atomizer, is 1.15 atm. The nominal nozzle exit velocity (from 293 to 773 K) is 85 to 230 m/s. The ratio of the first stage to second stage air mass flow rates is set at 0.5, 1.0, and 2.0. Some variation in the performance of the SPP is obtained with respect to this air split, however, as shown in the results section, the variation is relatively small. For use in gas turbine engines, a low ratio of first stage to second stage air is preferable, since this would require the least amount of modification to the engine cycle for cooling the compressor discharge air to the desired first step temperature of the SPP.

In the present work, the nominal residence time of the first stage of the SPP is 12 ms and that of the second stage is either 5 or 12 ms, depending on whether the short or long version of the second stage is installed. These nominal values correspond to an airflow ratio of 1.0 and a temperature of 623 K in each stage.

Absence of preflame reactions in the liquid fueled SPP is confirmed by the absence of C_1 and C_2 hydrocarbons, by the absence of wall deposits of gum and carbon and by the absence of pressure oscillations. The absence of the C_1 and C_2 hydrocarbons is determined by probe sampling of the internal flow of the SPP, followed by GC analysis of the gas samples. The absence of pressure oscillations is determined by continuous monitoring of the SPP via a pressure probe and transducer. In earlier work [4], with a single-stage prevaporizer-premixer of about 100 ms residence time and 2–3 atm pressure, several preflame reaction indicators (i.e., gum deposits and pressure oscillations) were observed when the temperature was approximately 100°C above the normal boiling point of the fuel.

The supporting components of the SPP system are the following:

- electrical air preheaters,
- cascade-type temperature controller for setting and maintaining air preheating and SPP temperature levels, and
- air and fuel control: The mass flow rates of the air and gaseous fuels are controlled and measured by electronic mass flow controllers. The mass flow rates of the liquid fuels are controlled by placing the liquid fuels under nitrogen pressure and pushing the fuels through a control valve. The liquid flow rates are measured with a calibrated rotameter.

Laser Diagnostics. Two laser-based methods are used for examining the outlet stream of the SPP. (1) Completeness of vaporization is confirmed by observing the absence of droplet and aerosol scattering from a 5 mW, 0.63 μm He-Ne laser beam passed

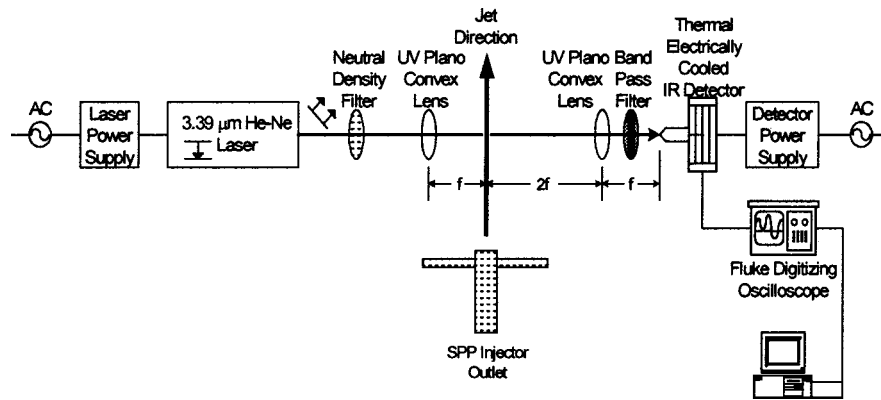


Fig. 2 Schematic diagram of the laser absorption system

through the outlet stream of the SPP. (2) A separate laser absorption system is used to investigate the mixedness of the fuel vapor-air stream as it departs the SPP injector. The laser absorption system is a relatively simple diagnostic tool based on the absorption of electromagnetic radiation of $3.39 \mu\text{m}$ wavelength by hydrocarbons, [6]. The major components of the system were provided by the University of California at Berkeley, [7]. Mongia [8], in his Ph.D. thesis, describes the technique and its application to pre-mixer outlet streams.

Figure 2 is a schematic drawing of the laser absorption setup used. The major components are the 50 mW, $3.39 \mu\text{m}$ He-Ne laser with power supply and the infrared (IR) detector that is thermal electrically cooled and maintained at 5°C temperature. The neutral density filter shown is used to attenuate the laser beam, since the power laser is too great for the IR detector. The plano-convex focusing lenses are required in order to minimize the effects of beam steering caused by differences in index of refraction as the laser beam passes through the heated outlet stream of the SPP. The narrow bandwidth IR band pass filter is used to remove any thermal radiation emitted from the metal surfaces of the SPP. Signal display and processing are accomplished with the digitizing oscilloscope.

Temporal fluctuations spatially averaged over the line-of-sight path length are measured with the laser absorption system. The line-of-sight measurements are made along a 12.7-mm diametric path through the SPP outlet stream at a location 2 mm above the SPP outlet. The SPP outlet nozzle and JSR are removed.

By the Beer-Lambert law:

$$\frac{I}{I_o} = e^{-kPL} \quad (1)$$

where I is the beam intensity (or the transmission signal) leaving the absorbing medium, I_o is the beam intensity entering the absorbing medium (or the signal in the absence of the absorbing species), k ($\text{cm}^{-1}\text{atm}^{-1}$) is the absorption coefficient at the given wavelength, P (atm) is partial pressure of the absorbing species (fuel), and L (cm) is the path length. Perrin and Hartmann [9] determined the absorption coefficient for the $3.39 \mu\text{m}$ laser wavelength for methane diluted in nitrogen at temperatures of 293 to 787 K and 1 atm total pressure. Their data may be expressed as follows:

$$k = 22.89e^{-0.0030337T} \quad (2)$$

Yoshiyama et al. [10] examined absorption at the $3.39 \mu\text{m}$ wavelength by methane and propane. Their results are expressed in terms of an extinction coefficient, ϵ (cm^2/gmol). The definition of ϵ and its expression for CH_4 are given as follows:

$$\epsilon = \frac{\log_{10} \frac{I_o}{I}}{C \cdot L} = \frac{110,000}{P_T^{0.302}} \quad (3)$$

where C (gmol/cm^3) is the concentration of the absorbing species and P_T (atm) is the total pressure.

Equation (1) is rearranged for the case of fluctuations in the absorbing medium and laser/detector system. This is done as follows:

- I_o , I , and kPL are assumed to have time-mean ($_m$) and time-fluctuating ($'$) components: $I_o = I_{om} + I_o'$, $I = I_m + I'$ and $kPL = (kPL)_m + (kPL)'$.
- It is assumed that $(kPL)' \ll 1$. Thus, $e^{-kPL'} \cong 1 - (kPL)'$.
- The fluctuations in I_o (i.e., the signal without absorbing species present) and kPL (i.e., the absorbing medium) are assumed uncorrelated. Thus, the mean value of the product $I_o'(kPL)'$ is zero. Also, terms of order higher than two in the fluctuations are assumed negligible.

Substitution into Eq. (1) and rearrangement gives the following equation linking the standard deviation ($_{sd}$) over the mean ($_m$) of the variables:

$$\frac{I_{sd}}{I_m} = \sqrt{\left[\frac{(kPL)_{sd}}{(kPL)_m} \cdot \ln \left(\frac{I_{om}}{I_m} \right) \right]^2 + \left(\frac{I_{osd}}{I_{om}} \right)^2} \quad (4)$$

The transmission data (I) are collected with the digitizing oscilloscope over a period of 50 ms at a rate of 10 samples per millisecond for a total of 500 samples. For each case of 500 samples, the mean (I_m) and standard deviation (I_{sd}) are determined. The noise base is determined in the absence of fuel flow with only the flow of air. The measurements indicate the base noise inherent in the laser/electronic system is independent of the inlet temperature (from 293 to 773 K) and is constant with a value of $I_{osd}/I_{om} = 0.023$. In the results section, I_{sd}/I_m is plotted as a function of I_m/I_{om} for different values of $(kPL)_{sd}/(kPL)_m$ and the measurements with the fuel present are superimposed, thereby permitting $(kPL)_{sd}/(kPL)_m$ to be determined.

Fluctuations in kPL can arise in at least three ways: (1) the absorption coefficient (k) can fluctuate through variations in temperature, (2) the partial pressure of the fuel (P) can fluctuate through variations in the fuel/air ratio (F/A), and (3) the path length (L) can fluctuate through fluctuations in the thickness of the mixing layer along the outer edge of the stream. Additionally, for the case of a blended fuel, differential diffusion of the fuel components could cause kPL to vary. Fluctuations in the transmission signal would also occur in the case of incomplete vapor-

ization, though, as stated above, the evidence from the laser scattering tests indicates this effect is absent from the present experiments.

With increasing temperature, the absorption decreases, note Eq. (2). Thus, I_m approaches I_{om} and the effect of the kPL fluctuations on I_{sd}/I_m decreases as the temperature increases. This effect is illustrated in the results section.

Jet-Stirred Reactor (JSR), JSR Operating Conditions, Diagnostics, and Fuels

Jet-Stirred Reactor. The jet-stirred reactor used in this study is described by Lee et al. [4] and detailed in the Ph.D. thesis of Lee [11]. The internal dimensions of the JSR are identical to the JSR used by Steele et al. [12]. The JSR is depicted in the upper part of Fig. 1. The internal volume is 15.8 cm^3 , the internal height is 45 mm, and the internal diameter (at the widest point) is 25 mm. The JSR is fed by reactants and stirred by the outlet stream of the SPP accelerated through a 4-mm diameter nozzle. The nozzle is located in the Hastelloy® nozzle block. Exhaust gases leave the JSR through four drain holes located 90 deg apart near the bottom of the reactor. Temperature measurements, gas sampling, and viewing of the JSR cavity are conducted at 2/3rd reactor height. There are four ports located at this height, 90 deg apart. Two of these are blocked during operation. One of the remaining open ports accepts the thermocouple probe and the other accepts the gas sample probe.

JSR Operating Conditions. The JSR operating conditions are listed as follows:

- The combustion temperature (i.e., the measured, corrected temperature of the recirculation zone) is normally maintained at 1790 K.
- The air mass flow rate (given above) is maintained at 4.7 kg/hr.

- The mean residence time of the JSR is 2.3 ± 0.1 ms, based on the air and fuel mass flow rates, the combustion temperature of 1790 K, the molecular weight of the combustion gases and the JSR volume.
- The inlet total temperature of the JSR is the second stage temperature of the SPP. For the combustion experiments shown, it is varied from 423 to 723 K. An inlet total temperature of 623 K is used for the experiments of NO_x as a function of fuel type.
- The fuel-air equivalence ratio (ϕ) is adjusted to maintain the constant combustion temperature. For the experiments run at 1790 K combustion temperature and 623 K inlet total temperature, this results in $\phi = 0.61 \pm 0.02$ for most of the fuels. The exceptions are natural gas ($\phi = 0.65$), benzene ($\phi = 0.57$), and toluene ($\phi = 0.58$).

JSR Characterization. Calculations of the Damköhler number (Da) and the turbulence Reynolds number (Re_T) are performed for the JSR operated with the 623 K inlet temperature. With methane selected as the example fuel, the laminar flame speed (S_L) is estimated using the method of Göttgens et al. [13]. The laminar flame speed leads to the characteristic chemical time (τ_L), assuming $\tau_L \cong D_L / S_L^2$. The laminar diffusivity (D_L) is estimated based on the inlet temperature [14], using the air value for thermal diffusivity. The result is $\tau_L \approx 0.15$ ms. The characteristic mixing time (τ_T) is evaluated assuming $\tau_T \cong d / u'$, where d is taken to be the inlet jet diameter (4 mm) and the RMS turbulence velocity (u') is assumed to be 10% of the inlet jet velocity. This gives the characteristic mixing time as 0.2 ms. Hence, $Da = \tau_T / \tau_L \approx 1.3$. The turbulence Reynolds number ($u'd/\nu$) is 1350, where the kinematic viscosity (ν) is based on air at the jet inlet temperature.

Under these conditions, the JSR operates as a two-zone reactor. Studies by Rutar et al. [15] indicate the Damköhler number must be reduced to about 0.15 before the JSR can operate as a single-zone, well-stirred reactor. In the present experiments, the flame

Table 1 List of fuels used in experiments (FBS: fuel bound sulfur, FBN: fuel bound nitrogen)

| Fuel | Purity | Chemical Formula | FBS (ppmw) | FBN (ppmw) |
|---------------------------------------|--------|----------------------------------|----------------|------------|
| natural gas | ... | 93% CH_4 | negligible | negligible |
| industrial propane | ... | 95% C_3H_8 | negligible | negligible |
| methanol | 99% | CH_3OH | 0 | 0 |
| ethane | 99% | C_2H_6 | 0 | 0 |
| propane | 99% | C_3H_8 | 0 | 0 |
| n-pentane | 99% | C_5H_{12} | 0 | 0 |
| n-hexane | 99% | C_6H_{14} | 0 | 0 |
| n-heptane | 99% | C_7H_{16} | 0 | 0 |
| n-dodecane | 99% | $\text{C}_{12}\text{H}_{26}$ | 0 | 0 |
| n-hexadecane | 99% | $\text{C}_{16}\text{H}_{34}$ | 0 | 0 |
| benzene | 99% | C_6H_6 | 0 | 0 |
| toluene | 99% | C_7H_8 | 0 | 0 |
| light naphtha (K-LN) | ... | $\text{C}_{5.9}\text{H}_{12.5}$ | negligible | <1 |
| supplied by K light naphtha (U-LN) | ... | $\text{C}_{5.9}\text{H}_{13.4}$ | negligible | <3 |
| supplied by U low sulfur DF2 (C-LSD) | ... | $\text{C}_{13.8}\text{H}_{26.3}$ | ≈ 200 | 46 |
| supplied by C low sulfur DF2 (T-LSD) | ... | $\text{C}_{13.8}\text{H}_{24.2}$ | ≈ 200 | 91 |
| supplied by T high sulfur DF2 (T-HSD) | ... | $\text{C}_{13.8}\text{H}_{23.7}$ | ≈ 3000 | 84 |
| supplied by T low sulfur DF2 (U-LSD) | ... | $\text{C}_{13.8}\text{H}_{24.2}$ | ≈ 200 | 49 |
| supplied by U | | | | |

zone is wrapped around the inlet jets and represents about 5–10% of the reactor volume. The large recirculation zone serves as the post-flame zone. Because of the stirring within the recirculation zone, combined with the relatively short residence time (2.3 ms) and relatively low pressure (1 atm), free radical and intermediate species, in particular O, H, OH, H₂, and CO, remain at relatively large concentrations throughout the reactor. Both zones contribute NO_x as discussed in the “modeling and interpretation” section below.

Combustion Temperature and Species Concentration Measurements. For the work reported herein, all probe measurements of temperature and species concentrations are obtained in the recirculation zone of the JSR. This zone comprises the bulk of the JSR and exhibits nearly uniform temperature and composition.

Combustion temperature is measured with a 0.127-mm type-R thermocouple coated with a ceramic compound (to prevent oxidation of CO, H₂, and hydrocarbons at the thermocouple surface) and corrected for radiation losses (typically, a +40° correction).

Gas composition is measured by drawing combustion gas through a small, water-cooled, quartz sampling probe and routing the gas through water removal impingers and into a bank of gas analyzers for CO, CO₂, O₂, NO, and NO_x determination. A metal bellows sample pump is located between the impingers and the bank of gas analyzers. In order to minimize the disturbance of the JSR flow field as well as to minimize internal probe reactions, the uncooled tip of the probe is made as small in diameter and as short as practical, i.e., 3-mm O.D. by 30-mm length. The I.D. of the probe is maintained constant, that is, the entry is not restricted. The remainder of the probe, which sits outside the JSR cavity, is jacketed with water flow. The water is made sufficiently warm to prevent condensation within the probe sample. The overall length of the sample probe is 300 mm. A 6-mm O.D. Teflon tube, also maintained warm, connects the sample probe outlet to the impingers. By the sampling technique used, most of the NO_x measured is NO, indicating conversion of NO to NO₂ in the sample probe is small. Hence, loss of NO_x by absorption of NO₂ in water is taken to be a minor-to-negligible effect in the present work. Gasdynamic calculations indicate the residence time of the sampled gas within the hot uncooled tip of the probe is approximately 0.1 ms. Although this time is small, some loss of CO by oxidation and a relatively small production of NO within the hot uncooled tip of the probe cannot be ruled out. That is, the hot

uncooled tip of the sample probe is an extension of the JSR. From time to time, gas chromatography is employed to check for light hydrocarbon gases in the JSR. Typically, total measured hydrocarbon for the JSR recirculation zone is small (i.e., less than 100 ppmv C₁ basis).

Fuels. The fuels used in this study are listed in Table 1. The empirical chemical formulas listed for the naphtha and diesel fuels are based on elemental analyses performed at commercial fuel analysis laboratories. Compound information obtained with the analyses indicates the light naphtha fuels are composed of n-alkanes (50%), iso-alkanes (30%), naphthenes (15%), and aromatics (5%), all in the C₅–C₆ range.

Experimental Results

Laser Absorption Measurements. Percent mean transmission ($I_m/I_{om} \times 100$) as a function of the temperature for the outlet stream of the SPP is plotted in Fig. 3. Comparison to the literature, that is, to Eqs. (2) and (3) applied to the present experimental conditions, is also plotted. The fuels are natural gas and industrial propane, each at a mole fraction of 0.0277 in the stream. The corresponding fuel-air equivalence ratios are 0.27 for natural gas and 0.68 for industrial propane. The figure clearly shows the increase in transmission with increasing temperature. The figure also indicates a good agreement between the measurements for natural gas and Eq. (2). On the other hand, Eq. (3) predicts lower transmission than measured, though the trend with respect to temperature is consistent with the other results.

Percent standard deviation in transmission ($(I_{sd}/I_m) \times 100$) is plotted versus the temperature of the outlet stream of the SPP in Figs. 4 and 5. The fuels are natural gas (Fig. 4) and No. 2 diesel fuel (Fig. 5). For all data, $\phi=0.68$. The legend of each figure indicates the ratio of the first and second stage airflow rates and the first stage temperature of the SPP. The measurements for methane exhibit a falloff in the percent standard deviation as the temperature of the SPP outlet stream is increased. Also seen is a decrease in the percent standard deviation as the airflow rate of the first stage of the SPP is increased relative to the airflow rate of the second stage. All of the diesel fuel measurements (Fig. 5) lie close to the noise base of the experiment.

Analysis of the transmission signals of these measurements in the frequency domain indicates no predominant frequencies.

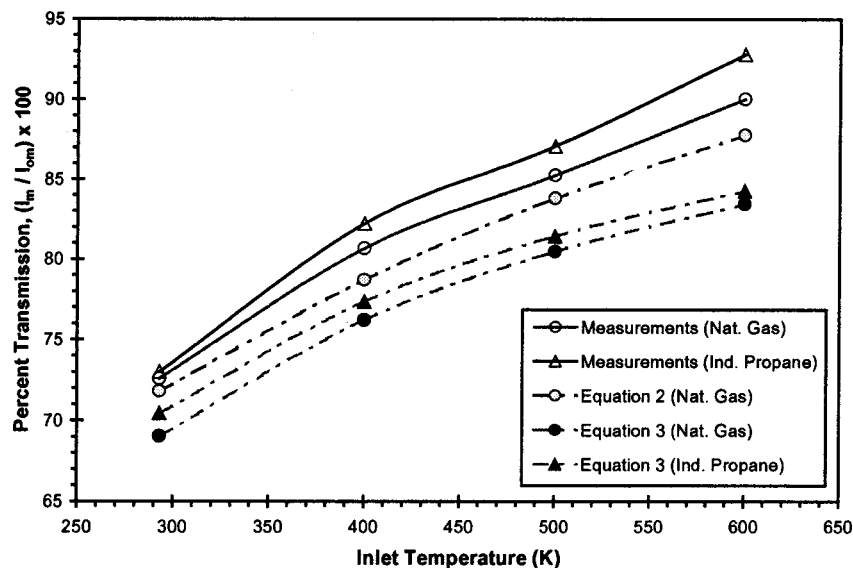


Fig. 3 Effect of temperature on the transmission of the 3.39 μm He-Ne laser for methane/air and propane/air mixtures at 1 Atm

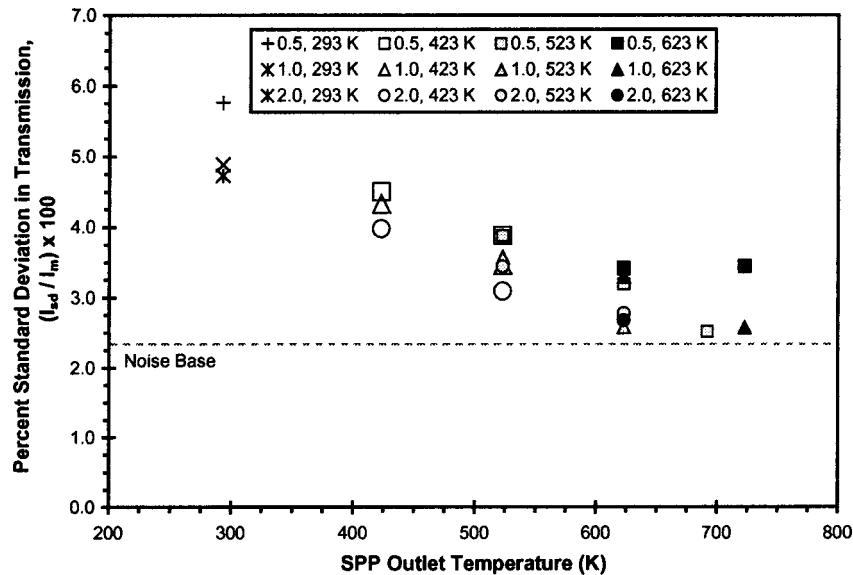


Fig. 4 Effect of temperature and air split on the percent standard deviation in the laser transmission for the outlet stream of the SPP with natural gas-air mixture at $\phi=0.68$. Legend: First stage airflow rate divided by the second stage airflow rate, and nominal first stage temperature in Kelvin. Long second stage used.

In Fig. 6, results from the laser absorption experiments are displayed on the basis of Eq. (4). The fuel-air equivalence ratio is $\phi=0.68$, and the first to second stage ratio of the SPP airflow rates is 1 and 2. Plotted as the dependent variable is I_{sd}/I_m . The independent variable is I_m/I_{om} . The parameter is the ratio of the standard deviation of kPL divided by the mean of the term. The curves are calculated from Eq. (4). The measurements are superimposed on the curves. The asymptotic value of I_{sd}/I_m is 0.023, the noise of the laser/detector system.

From left to right in Fig. 6, the temperature of the outlet stream of the SPP increases and, thus, the transmission increases. The

standard deviation over mean of the laser transmission changes by two effects: (1) temperature and (2) fluctuations in kPL .

With natural gas as fuel, Fig. 6 shows the percent mean transmission increase from 46% (corresponding to the stream temperature of 293 K) to 89% (corresponding to 723 K). The measurements at 293 K have the highest sensitivity of the experiment and indicate a percent standard deviation in kPL (i.e., $(kPL)_{sd}/(kPL)_m \times 100$) of 5 to 6%. Because of the 293 K temperature, there is temperature uniformity, and thus, negligible variation in k . The standard deviation in kPL represents the variation in the fuel partial pressure (or fuel/air ratio) integrated over

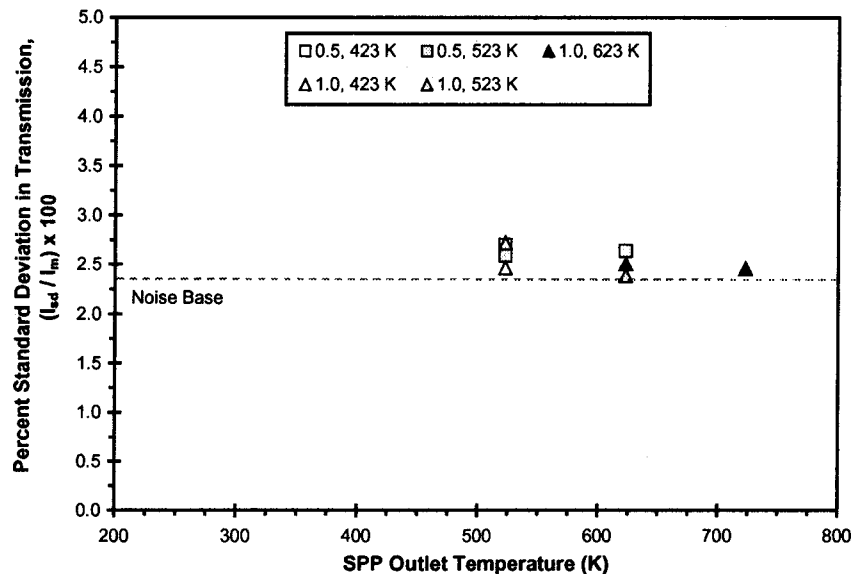


Fig. 5 Effect of temperature and air split on the percent standard deviation in the laser transmission for the outlet stream of the SPP with No. 2 low sulfur diesel fuel-air mixture at $\phi=0.68$. Legend: First stage airflow rate divided by the second stage airflow rate, and nominal first stage temperature in Kelvin. Long second stage used.

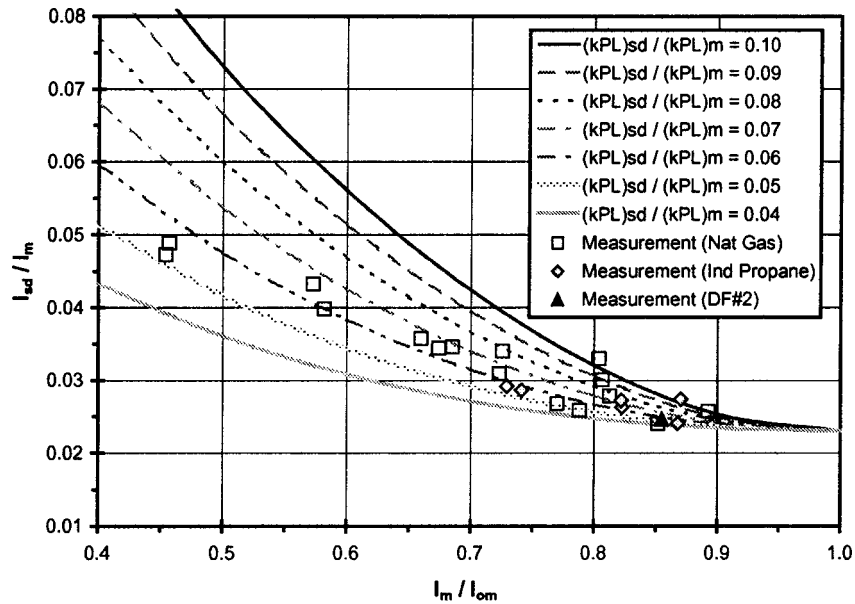


Fig. 6 Standard deviation in transmission versus mean transmission. Long second stage for the SPP.

the width of the stream. The 5–6% standard deviation indicates a small variation in the cross-stream averaged fuel/air leaving the SPP.

With increasing temperature, I_m/I_{om} increases and I_{sd}/I_m decreases. The I_{sd}/I_m measurement becomes less sensitive to the variation in kPL , and thus, there is more uncertainty in the values of $(kPL)_{sd}/(kPL)_m$ inferred from the experiment. The maximum percent standard deviation in kPL is about 10%, or double that of the 293 K data.

With the industrial propane, the mean transmission increases, since fewer fuel molecules are present with ϕ maintained constant. The temperature range is 293 to 623 K, corresponding to an increase in percent mean transmission from 73 to 87%. The maximum value of the percent standard deviation in kPL is again about 10%.

With diesel fuel, a further increase in mean transmission occurs. One measurement point is shown in Fig. 6. This indicates a percent mean transmission of about 85% and a value of no more than about 5% in the percent standard deviation in kPL .

Measurements with a multiple-pass reflected laser beam or at greater total pressure would be useful for both improving the sensitivity of the experiment and permitting enhanced spatial resolution. Nonetheless, the measurements indicate the standard deviation of the cross-stream averaged fuel-air ratio of the outlet stream of the SPP is no more than about 10% of the mean fuel-air ratio.

NO_x as a Function of the Outlet Temperature of the SPP.

The amount of NO_x formed in the jet-stirred reactor is first examined as a function of the outlet temperature of the SPP. In order to

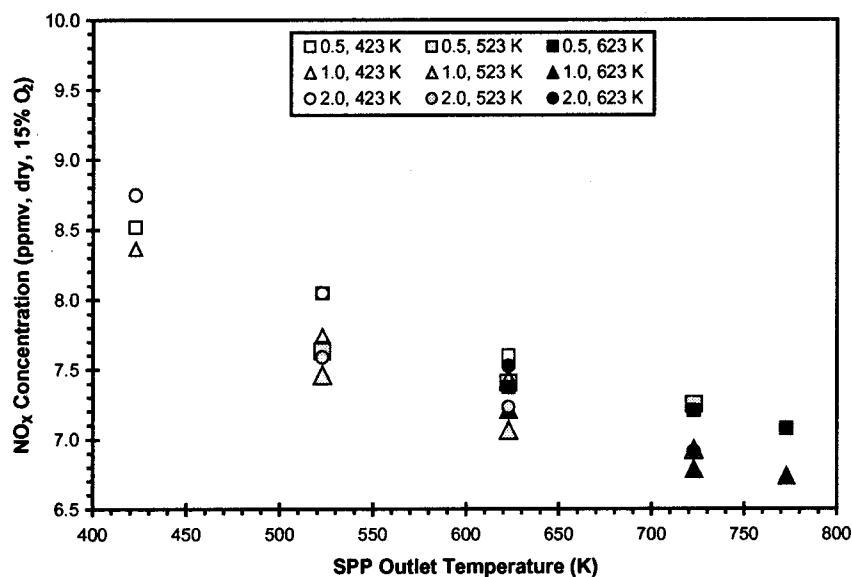


Fig. 7 Effect of SPP temperatures and air split on NO_x for natural gas-firing of the JSR. Legend: First stage airflow rate divided by the second stage airflow rate and nominal first stage temperature in Kelvin. Long second stage used.

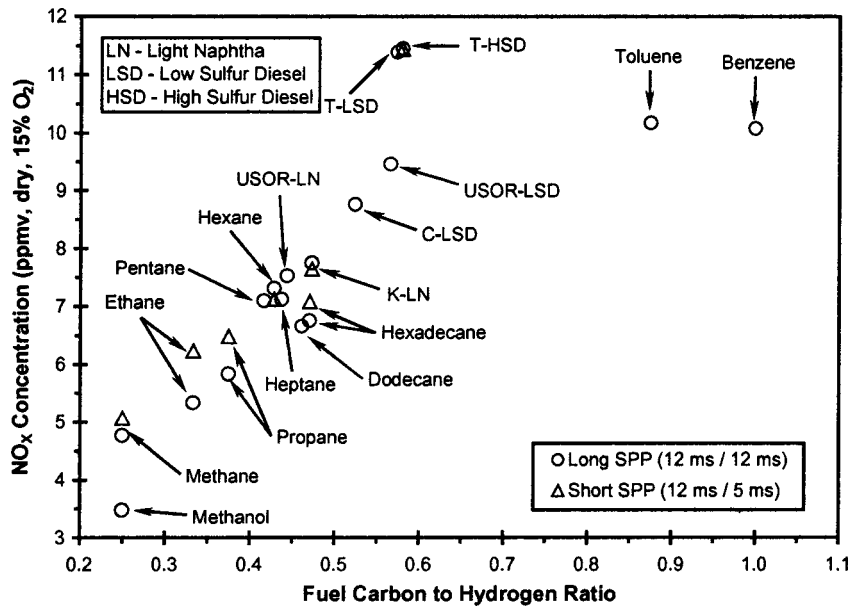


Fig. 8 Effect of fuel type on NO_x JSR combustion temperature of 1790 K and residence time of 2.3 ± 0.1 ms. The SPP conditions are outlet temperature of 623 K, and first to second stage airflow ratio of 1.

maintain a constant combustion temperature in the JSR, the fuel-air equivalence ratio is decreased as the outlet temperature of the SPP is increased.

Results for natural gas are shown in Fig. 7. (These experiments were run at a combustion temperature of about 1850 K, rather than the normal value of 1790 K for this study.) Two trends are noted in the figure. (1) A mild decrease in NO_x , from about 8.5 to 7.0 ppmv, occurs as the outlet temperature increases from 423 to 773 K and (2) a slight decrease in NO_x is noted when the SPP is adjusted to give equal airflow rates for the first and second stages.

Results for ethane and industrial propane also indicate minimum NO_x with the SPP set for the equal first and second stage airflow rates. Interestingly, however, these fuels do not exhibit a dependence of NO_x on the SPP outlet temperature.

The decrease in NO_x with increasing outlet temperature is probably caused mainly by a decrease in Fenimore prompt NO_x as the mixture is leaned. This behavior is suggested in the work of Rutar et al. [16], in which a high-pressure jet-stirred reactor was operated for both preheated and unheated inlet streams. For running at short residence times, the NO_x dropped when the reactor was leaned upon preheating the inlet stream of premixed methane and air. Chemical kinetic calculations of the CH radical showed a significant decrease upon preheating, indicating a decrease in the formation of prompt NO_x . Improvement in fuel-air mixedness could in principle also explain the trend in NO_x . However, the measurements in Fig. 6 do not support this hypothesis, since the ratio $(kPL)_{sd}/(kPL)_m$ does not decrease with increasing SPP outlet temperature.

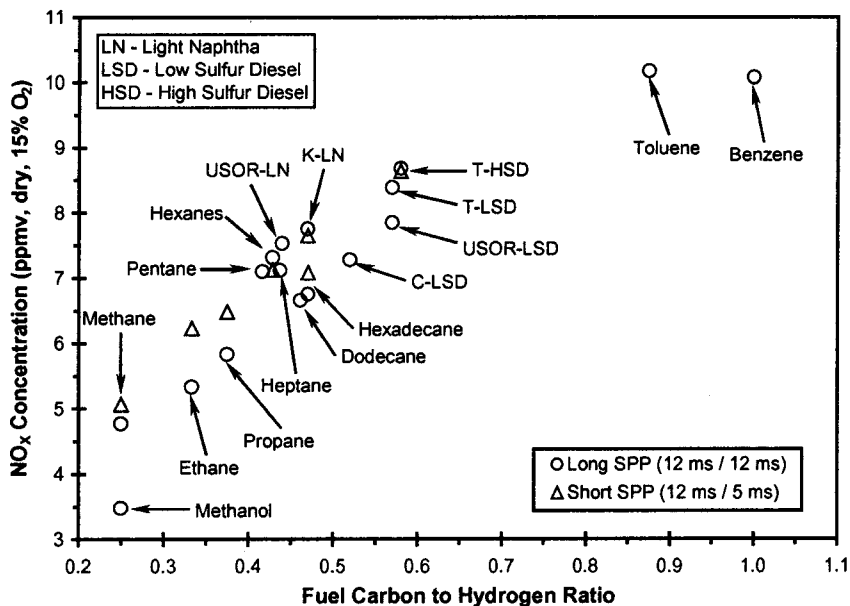


Fig. 9 Same conditions as Fig. 8, except the fuel NO_x formed through 100% conversion of FBN is deducted for the diesel fuels

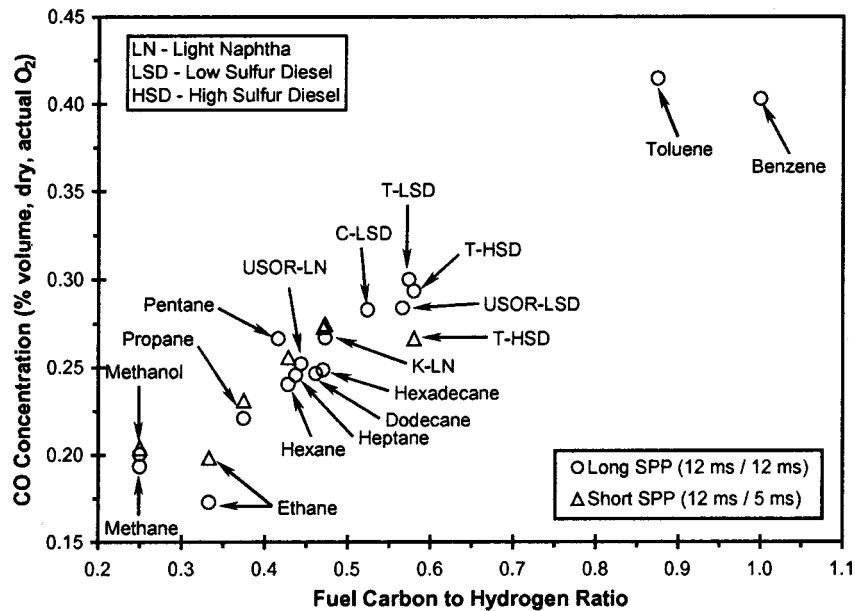


Fig. 10 Effect of fuel type on CO for JSR combustion temperature of 1790 K and residence time of 2.3 ± 0.1 ms. The SPP conditions are outlet temperature of 623 K, and first to second stage airflow ratio of 1.

NO_x and CO as a Function of Fuel Type. The measurement of NO_x for the full range of the fuels used in this study is plotted in Fig. 8. In this case, the SPP outlet temperature is 623 K and the ratio of the first to second stage SPP airflow rates is 1.0. The combustion temperature of the JSR is 1790 K. The residence times are: SPP first stage: 12 ms, SPP second stage: 5 or 12 ms and JSR: 2.3 ± 0.1 ms. Lowest NO_x (3.5 ppmv) is measured for methanol, while highest NO_x (11.4 ppmv) is found for the diesel fuels containing 84–91 ppmw FBN. These measurements of NO_x, obtained in the recirculation zone of the JSR, closely represent exhaust emissions, since the recirculation zone is nearly uniform in NO_x and the exhaust leaves the JSR from the recirculation zone.

In Fig. 9, the NO_x data are adjusted by subtracting the contribution of the FBN for the diesel fuels. This is done assuming complete conversion of the FBN to NO_x. Noted now is a relatively well-behaved increase in NO_x with increasing molar carbon-to-hydrogen ratio of the fuels from methane through the diesel fuels. Over this range of fuels, it appears possible to reasonably predict the NO_x emission (from fixation of the air-nitrogen) based on the fuel carbon-to-hydrogen ratio. The blended fuels, i.e., the naphthas and diesel fuels, are essentially indistinguishable from the pure alkanes tested on the basis of NO_x as a function of C/H ratio. However, methanol exhibits unique NO_x behavior. This is most likely the result of very little Fenimore prompt NO_x formed by the combustion of methanol.

The carbon monoxide (CO) measurements obtained for the recirculation zone of the JSR also exhibit a significant dependence on the fuel carbon-to-hydrogen ratio (see Fig. 10). A relatively well-behaved increase in CO with C/H ratio is noted for ethane through the diesel fuels. Methane (i.e., natural gas) and methanol, being relatively slow burning fuels, exhibit more CO than indicated by the extrapolation of data for ethane-to-diesel. The CO measurements for the recirculation zone of the JSR are 80 to 90% lower than the peak CO levels measured in the flame zone of the reactor that surrounds the inlet jet of the JSR. Nonetheless, the CO concentrations for the recirculation zone are significantly higher than exit plane emissions acceptable for a commercial combustor. This is caused because the JSR does not have a plug flow burnout zone for CO.

Modeling and Interpretation of NO_x

Reactor modeling is conducted to help explain the increase in NO_x with increasing C/H ratio. Chemical kinetic modeling is performed using simple, though realistic, chemical reactor arrangements to simulate the JSR. Thus, as a first step, the structure and behavior of the JSR is examined.

The combustion field of the atmospheric pressure jet-stirred reactor consists of a turbulent flame zone on and near the jet-centerline of the reactor, surrounded by the recirculating post-flame zone, which accounts for the bulk of the reactor. The flame zone volume is about 5–10% of the JSR volume, contains significant energy release and exhibits peak concentrations of CO (of about 1–2% by mole). These points are known from sampling measurements for CO, CO₂, and O₂ on a path across the reactor and through the centerline (see [4]). Because the oxidation of CO is relatively slow at 1 atm pressure and because the back-mixing delays CO burnoff, the CO levels of the recirculating post-flame zone only fall to about 0.15 to 0.4% by mole. These data are plotted in Fig. 10. On the other hand, equilibrium levels for CO for the temperature and stoichiometry conditions of the recirculating post-flame zone are much lower—about 0.005 to 0.007% by mole. Recombination of the active species O, H, and OH is also relatively slow in the 1 atm reactor. The estimated chemical time for O-atom recombination under the present conditions is 10–20 ms, [17]. This is significantly longer than the 2.3 ms residence time of the JSR. Thus, the O-atom remains at super-equilibrium levels throughout the reactor. This indicates significant formation of NO by O-atom attack on N₂ for most points in the reactor. The mechanisms at work are the nitrous oxide and Zeldovich mechanisms.

The CH radical, on the other hand, is short lived, resides mainly in the flame zone and does not survive into the post-flame zone. Thus, prompt NO formation caused by the attack of the CH radical on N₂ mainly occurs in the flame zone.

Studies by Steel et al. [18], Bengtsson et al. [19], and Rutar et al. [15] used a model of two perfectly stirred reactors (PSRs) in series to chemical kinetically study JSRs. This is the 2-PSR model. The first PSR simulates the flame zone, that is, the region of rapid oxidation and maximum free radical concentrations,

Table 2 Results for NO_x from the 2-PSR modeling

| Fuel | % Difference in NO _x of Model to Measurement | % NO _x by Zone PSR1:PSR2 | % of NO _x as Prompt NO _x |
|----------|---|-------------------------------------|--|
| Methanol | -33% | 20%:80% | 5% |
| Methane | +12 to +21% | 60%:40% | 34% |
| Ethane | -6 to -19% | 50%:50% | 30% |

while the second PSR simulates the recirculating post-flame zone. In Rutar et al. [15], two independent methods are used to determine the fraction of the reactor that is the flame zone. In one method, the thickness of the turbulent flame zone is estimated from the literature results for premixed turbulent flame speed, while in the second method, the modeled values of both NO_x and CO are matched to the experimental values by adjusting the relative sizes of the two PSRs. The two methods show agreement. For the Damköhler number of 1.3 of the present research, the results of Rutar et al. [15] indicate a flame zone size of about 10% of the reactor volume.

The chemical kinetic mechanism used for the present modeling of the methane, methanol, ethane, and propane flames is GRI 3.0, [20]. The computations are performed for the measured fuel and air flow rates of the experimental reactor. The first PSR is assumed adiabatic, since the rate of chemical energy release is large relative to the rate of heat loss for this zone. The second PSR is assigned the corrected measured temperature of 1790 K for the recirculation zone. Results from the 2-PSR modeling of NO_x are listed in Table 2. In this modeling, the first PSR has 5% of the reactor total residence time, and the second PSR has 95%.

The results in Table 2 indicate reasonable agreement of the modeled to the measured NO_x. The modeling shows the distinct difference between NO_x formation for methanol and methane-ethane. Little prompt NO_x is formed during the combustion of methanol. This is responsible for the relatively small percentage of NO_x formed in the methanol flame zone. On the other hand, the modeling for methane and ethane shows about a 50:50 division in the NO_x formed in the flame and post-flame zones. Also, prompt NO_x (formed exclusively in PSR1) accounts for about 1/3rd of the total NO_x modeled.

In subsequent modeling, the first PSR is split into two zones—an initial PSR operating at incipient blowout, followed by a second PSR. The initial PSR is meant to simulate the thin flame fronts, while the second PSR is meant to simulate reaction in the balance of the flame zone. The concluding PSR is the recirculating post-flame zone, as above. The initial PSR is assumed to be adiabatic, while the second and third PSRs are assigned the measured temperature of 1790 K. The initial PSR has a very short residence time. The second PSR is assigned 10% of the reactor residence time, while the third PSR is assigned the balance of the residence (i.e., almost 90%).

The three PSRs in series model shows good agreement to the measurements and simulates the increase in NO_x from methanol to methane and with increasing C/H ratio. The results are shown in Table 3.

The GRI 3.0 mechanism does not consider hydrocarbon fuels of order greater than C₃. For the C₅ to C₁₆ alkanes, toluene, benzene,

Table 3 Comparison of NO_x by the 3-PSR model to the measured NO_x (all NO_x expressed as ppmv (15% O₂ dry))

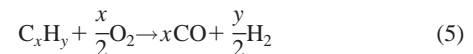
| Fuel | Modeled | Measured |
|----------|---------|----------|
| Methanol | 2.8 | 3.3 |
| Methane | 5.2 | 4.7–5.1 |
| Ethane | 5.2 | 5.3–6.2 |
| Propane | 5.9 | 5.8–6.5 |

Table 4 Modeling of NO_x as a function of CO/H₂ ratio; also listed are the NO_x measurements of this study (all NO_x expressed as ppmv (15% of O₂ dry))

| Fuel | C/H=2CO/H ₂ | 2-PSR NO _x | 3-PSR NO _x | Measured NO _x |
|--------------|------------------------|-----------------------|-----------------------|--------------------------|
| Methane | 0.25 | 3.0 | 3.7 | 4.7–5.1 |
| n-Hexadecane | 0.47 | 4.2 | 4.7 | 6.8–7.1 |
| Benzene | 1.00 | 6.4 | 6.5 | 10.2 |

and the blended fuels studied, no satisfactory chemical kinetic mechanism for fuel oxidation with nitric oxide formation has been identified (though some have been tested) in the present work.

In order to chemically kinetically model the full range of fuels tested, fast oxidative pyrolysis is assumed. That is, CO and H₂ are the fuels fed into the models and the O₂ input is debited, per the following chemical equation:



The first PSR of the two and three PSR models is assigned the average temperature found in the methanol, methane, ethane, and propane computations above and the second and third PSRs are again assigned the experimental temperature of 1790 K. The mechanism used is that due to Miller and Bowman [21]. This mechanism is used so that the NO_x resulting from the attack of O-atom on N₂ may be exclusively studied. Prompt NO_x is not a factor, since no hydrocarbon material is injected into the model reactor. Additionally, NO_x formed from NNH, which is a factor in the GRI 3.0 mechanism, is not present in the Miller-Bowman mechanism. The only mechanisms forming NO_x are the Zeldovich and nitrous oxide mechanisms.

The results are shown in Table 4 below. The modeling replicates the trend of the measurements, i.e., the increase in NO_x with increasing C/H ratio. The modeling shows an approximate doubling in the NO_x from methane to benzene. The doubling is also seen in the experiment.

The results provide evidence for the finding that NO_x increases with C/H ratio, because of increasing attack of O-atom on N₂ leading to increasing amounts of NO_x formed by the Zeldovich and nitrous oxide mechanisms.

The increasing amounts of O-atom result from the increasing amounts of CO oxidized. Key reactions are



The impact of O-atom on NO formation by the Zeldovich and nitrous oxide mechanism is contained in the following reactions:



In the case of the experiment, complex hydrocarbon-nitrogen chemistry, leading to variable prompt NO formation is also occurring. How prompt NO_x changes with increasing C/H ratio under lean premixed combustion is unclear and must await chemical mechanism developments for large fuel molecules.

Conclusions and Recommendations

The major findings of this study are as follows:

- 1 Low NO_x emissions are obtained for pure and practical blended liquid fuels burned under lean, fully vaporized, well premixed, high intensity combustion conditions. The NO_x

emission for No. 2 diesel fuel is about double that of natural gas, given the same combustion temperature and residence time.

- 2 The staged prevaporizing-premixing injector, that relies on two stages of air temperature, is described and used to obtain the fuel-air stream fed into the combustor. The operating conditions of the injector as used in the present research are discussed. Measurements and inspection of the injector indicate the NO_x measurements were obtained for a fully prevaporized, well premixed inlet stream devoid of pre-flame reaction of the mixture.

Recommendations for future work on the staged prevaporizing-premixing injector are the following:

- 1 Operation for significantly reduced residence times within the injector. (Preliminary testing at double the flow rate of the present paper has already been conducted. This showed no significant increase in NO_x , indicating little if any degradation in the fuel vaporization and fuel-air mixing within the injector.)
- 2 Testing of the injector at elevated pressure, beginning at about 10 atm and ultimately approaching 30 atm.

Acknowledgments

The research has been made possible through a Graduate Fellowship from the Parker Hannifin Corporation, through equipment donation from the John Fluke Corporation and through the loan of laser system components from the University of California, Berkeley.

References

- [1] Lee, J. C. Y., and Malte, P. C., 2000, "Staged Prevaporizer-Premixer," U.S. Patent No. 6,174,160B1, Jan. 16, 2001.
- [2] Capehart, S. A., Lee, J. C. Y., Williams, J. T., and Malte, P. C., 1997, "Effect of Fuel Composition on NO_x Formation in Lean Premixed Prevaporized Combustion," ASME Paper No. 97-GT-336.
- [3] Lefebvre, A. H., 1989, *Atomization and Sprays*, Taylor & Francis, Bristol, PA.
- [4] Lee, J. C. Y., Malte, P. C., and Nicol, D. G., 1999, " NO_x as a Function of Fuel Type: C_1 -to- C_{16} Hydrocarbons and Methanol," ASME Paper No. 99-GT-270.
- [5] Mansour, A., Benjamin, M. A., Straub, D. L., and Richards, G. A., 2000, "Application of Macrolamination Technology to Lean, Premix Combustion," ASME Paper No. 2000-GT-0115.
- [6] Tsuboi, T., Inomata, K., Tsunoda, Y., Isobe, A., and Nagaya, K., 1985, "Light

Absorption by Hydrocarbon Molecules at 3.392 μm of He-Ne Laser," Jpn. J. Appl. Phys., **24**, No. 1, pp. 8–13.

- [7] Dibble, R. W., 1999, personal communication, University of California, Berkeley, CA.
- [8] Mongia, R. K., 1998, "Optical Probe for Measuring the Extent of Air and Fuel Mixing in Lean Premixed Combustors and the Effect of Air and Fuel Mixing on Combustor Performance," Ph.D. dissertation, University of California-Berkeley, Berkeley, CA.
- [9] Perrin, M. Y., and Hartmann, J. M., 1989, "High Temperature Absorption of the 3.39 μm He-Ne Laser Line by Methane," J. Quant. Spectrosc. Radiat. Transf., **42**(6), pp. 459–464.
- [10] Yoshiyama, S., Hamamoto, Y., Tomita, E., and Minami, K., 1996, "Measurement of Hydrocarbon Fuel Concentration by Means of Infrared Absorption Technique with 3.39 μm He-Ne Laser," JSAE Review, **17**, pp. 339–345.
- [11] Lee, J. C. Y., 2000, "Reduction of NO_x Emission for Lean Prevaporized-Premixed Combustors," Ph.D. dissertation, University of Washington, Seattle, WA.
- [12] Steele, R. C., Malte, P. C., Nicol, D. G., and Kramlich, J. C., 1995, " NO_x and N_2O in Lean-Premixed Jet-Stirred Flames," Combust. Flame, **100**(3), pp. 440–449.
- [13] Götgens, J., Mauss, F., and Peters, N., 1992, "Analytical Approximations of Burning Velocities and Flame Thicknesses of Lean Hydrogen, Methane, Ethylene, Ethane, Acetylene and Propane Flames," *Twenty-Fourth Symposium (International) on Combustion*, The Combustion Institute, Pittsburgh, PA, pp. 129–135.
- [14] Abraham, J., Williams, F. A., and Bracco, F. V., 1985, "A Discussion of Turbulent Flame Structure in Premixed Charges," *Engine Combustion Analysis: New Approaches*, P-156, SAE, Warrendale, PA, pp. 27–43.
- [15] Rutar, T., Malte, P. C., and Kramlich, J. C., 2000, "Investigation of NO_x and CO Formation in Lean Premixed, Methane-Air, High-Intensity, Confined Flames at Elevated Pressures," *Twenty-Eighth Symposium (International) on Combustion*, The Combustion Institute, Pittsburgh, PA.
- [16] Rutar, T., and Malte, P. C., 2001, " NO_x Formation in High-Pressure Jet-Stirred Reactors With Significance to Lean-Premixed Combustion Turbines," paper submitted to ASME Turbo Expo 2001.
- [17] Nicol, D. G., 1995, "A Chemical Kinetic and Numerical Study of NO_x and Pollutant Formation in Low-Emission Combustion," Ph.D. dissertation, University of Washington, Seattle, WA.
- [18] Steele, R. C., Tonouchi, J. H., Nicol, D. G., Horning, D. C., Malte, P. C., and Pratt, D. T., 1998, "Characterization of NO_x , N_2O , and CO for Lean-Premixed Combustion in a High-Pressure Jet-Stirred Reactor," ASME J. Eng. Gas Turbines Power, **120**, pp. 303–310.
- [19] Bengtsson, K. U. M., Benz, P., Schaeren, R., and Frouzakis, C. E., 1998, "NyOx Formation in Lean Premixed Combustion of Methane in a High-Pressure Jet-Stirred Reactor," Proc. Combust. Inst., **27**, pp. 1393–1401.
- [20] Smith, G. P., Golden, D. M., Frenklach, M., Moriarty, N. W., Eiteneer, B., Goldenberg, M., Bowman, C. T., Hanson, R., Song, S., Gardiner, W. C. Jr., Lissianski, V., and Qin, Z., 1999, GRI-Mechanism 3.0, http://www.me.berkeley.edu/gri_mech.
- [21] Miller, J. A., and Bowman, C. T., 1989, "Mechanism and Modeling of Nitrogen Chemistry in Combustion," Prog. Energy Combust. Sci., **15**, pp. 287–338.

Investigation of the Response of an Air Blast Atomizer Combustion Chamber Configuration on Forced Modulation of Air Feed at Realistic Operating Conditions

C. Hassa

e-mail: Christoph.Hassa@dlr.de

J. Heinze

K. Stursberg

Institute of Propulsion Technology,
German Aerospace Center,
Linder Höhe
51147 Köln, Germany

DLR investigated forced combustion oscillations of two liquid fuel burners in a research combustion chamber at elevated pressures simulating idle conditions of aircraft engine combustors. The work was performed in collaboration with MTU Munich. An existing combustion chamber with optical access, capable to operate up to 20 bar, was upgraded with an air flow pulsator, that bypasses air from the combustor plenum to the exhaust with a sinusoidal massflow variation up to 700 Hz. Pressure transducers in the plenum and the flame tube monitored the forced disturbances. A photomultiplier recorded the OH chemiluminescence of the flame. For the agreed operating conditions frequency scans of these values were registered. Additionally images of the OH* chemiluminescence were taken at selected frequencies and evaluated in a statistical manner, to separate turbulent and periodic behavior. From the analysis of the pressure data, it can be concluded, that serious thermoacoustic feedback was not observed for both burners. However, burner 2 with the flame detached from the wall exhibited a higher fluctuation level as burner 1 with the wall attached flame. A resonant behavior was observed near the characteristic frequency of the sound room comprised of plenum, flame tube, and burner nozzle as connecting passage. The chemiluminescence images show different modes of spatial fluctuation for the burners and for burner 2 they also vary with the operating condition.*

[DOI: 10.1115/1.1584478]

Introduction

In the ACIACOC project, European manufacturers of industrial gas turbines and aeroengines have been working together with research establishments and universities towards the understanding of combustion instabilities and their reduction by active control (CORDIS RTD [1]). In power generation, lean premixed combustion is widely implemented in gas turbines fueled by natural gas. However, many of these engines experience potentially fatal combustion instabilities, those are difficult to predict and limit the power output or a further reduction of unwanted emissions. Hence active control is desirable (Berenbrink and Hoffmann [2]). For future generations of aeroengines implementation of lean premixed prevaporized (LPP) combustion is also considered as a means to reduce NO_x emission (IPCC Report [3]). Aviation, having higher safety standards, must therefore develop solutions for combustor oscillations concurrently with LPP development to avoid problems from day one of service. Therefore comparatively more work has to be invested in the analysis of the problems also including the effect of the liquid fuel. In part load conditions, combustor oscillations are sometimes also observed for the diffusion burners in use today (Konrad et al. [4]). Hence it seems worthwhile to gain understanding of the influence of burner design parameters on combustion oscillations of diffusion burners whose steady-state behavior is well understood. This is especially true for the higher lean blowout limits needed for future engines with increased inlet pressures and turbine inlet temperatures.

Contributed by the International Gas Turbine Institute (IGTI) of the THE AMERICAN SOCIETY OF MECHANICAL ENGINEERS for publication in the ASME JOURNAL OF ENGINEERING FOR GAS TURBINES AND POWER. Paper presented at the International Gas Turbine and Aeroengine Congress and Exhibition, Amsterdam, The Netherlands, June 3–6, 2002; Paper No. 2002-GT-30059. Manuscript received by IGTI, Dec. 2001, final revision Mar. 2002. Associate Editor: E. Benvenuti.

In the European project, DLR had the task to investigate the response of a generic aeroengine combustor on forced modulation of the air feed to practical airblast atomizer nozzles furnished by MTU at realistic operating conditions. The response of the spray combustion was to be studied by monitoring flame tube pressure and total OH* emission in their dependence on the applied forcing frequency versus the steady state. Having found frequency ranges of interest, further two-dimensional imaging of OH* was to be performed with conditional averaging through the cycle to acquire the time response of the combusting system and to understand the influence of the most important geometric and thermodynamic parameters.

Experimental Set-up

To meet the requirements of the experimental program, the single sector combustor (SSC test rig) was chosen for the experiments, because of its operating range and its excellent optical access for laser diagnostics. The test rig is shown in Fig. 1 as schematic representation. Electrically preheated air enters the combustor plenum via a choked nozzle. It is then fed to the flame tube through the atomizer and the heat shield of the combustor head plate from where it is issued as cooling film along the quartz windows in the primary zone. 20% of the primary air is bypassed through the pulsator, a rotating valve with a controllable frequency range between 0 and 700 Hz, that creates a sinusoidal modulation of the combustion air.

The investigated airblast atomizers are shown in Fig. 2. Liquid kerosene is sprayed from the central pressure atomizer onto the atomizer lip and is atomized between the two co-swirling air streams of the nozzle. The only geometrical difference between the two atomizers consists in the contour of the outer swirl channel, which plays a decisive role for the flame shape and flame

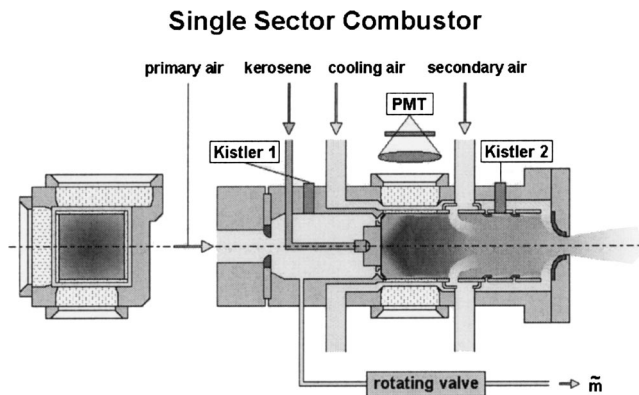


Fig. 1 Schematic representation of the single sector combustor

position within the combustor. The diffuser formed as quarter-circle (MTU 1) causes a strong opening of the flow field and a flame burning near the combustor entrance plane, while the cylindrically ending swirl channel (MTU 2) positions a slim flame more downstream.

Ignition is achieved with a hydrogen pilot flame which in turn is ignited by a spark igniter. The primary zone recirculation is closed by a row of opposed, preheated secondary air jets. Air at ambient temperature is used to convectively cool the flame tube and control the combustor pressure via the choked nozzle at the combustor exit. Optical access to the primary zone is achieved by three quartz windows in the side walls of the pressure casing and four quartz windows in the flame tube.

Diagnostics and Data Analysis

Characteristic pressures, temperatures, air mass flow rates, air fuel ratio, cooling water mass flow rates and modulation frequency are continuously recorded. The operating parameters

- air preheat temperature,
- pressure loss of the atomizer,
- combustion chamber pressure,
- air fuel ratio, and
- modulation frequency

are controlled and varied by a computer program. The global view of the flame is recorded with a video camera.

FFT-Analysis of Pressure and OH* Chemiluminescence Oscillations. As indicated in Fig. 1 two transient wall pressures are detected by water cooled quartz pressure sensors with small dimensions: the plenum pressure (Kistler 1) and the flame tube pressure (Kistler 2). The OH* chemiluminescence intensity fluctuation of the fluctuating part of the flame is synchronously recorded by a photo multiplier tube (PMT).

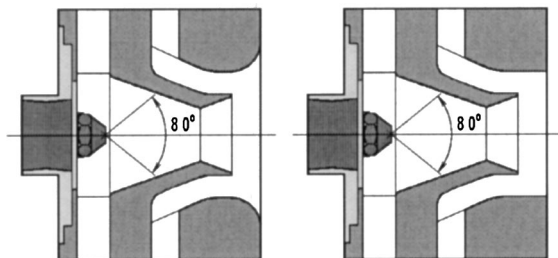


Fig. 2 Airblast atomizers; on the left: MTU 1 (for wall attached flames); on the right: MTU 2 (for lifted flames)

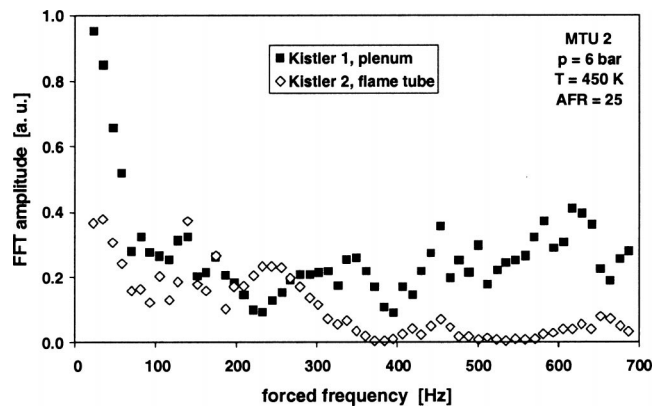


Fig. 3 FFT peak amplitudes at forced frequencies of plenum and flame tube pressure

The signals continuously produced by the sensors are sampled with an AD converter card on a PC and processed by "Flex Pro Control," a software for data recording, analysis and graphic representation. At constant flow conditions eight batches of each of these signals are taken in a time interval of 4 s. Each batch comprises 4000 individual samples with a time between samples of 0.125 ms, resulting in a frequency resolution of 1 Hz in the Fourier transform. Its maximum amplitude is usually situated at the forcing frequency.

The variation of modulation frequency results in a variation of the FFT amplitudes at forced frequency. Figure 3 presents these peak values. The amplitude of the plenum pressure response decreases rapidly with increasing modulation frequency at low frequencies, reaches in this case a minimum at 232 Hz and increases with a moderate slope, strongly fluctuating at higher frequencies. The flame tube pressure shows a similar behavior, but with less fluctuations at higher frequencies and with a relative maximum at 232 Hz. The PMT signal not shown here exhibits a strong maximum at the same frequency.

To show the response of the flame tube pressure and combustion intensity on the plenum pressure modulation more clearly, the ratio of the flame tube pressure and PMT signal to the plenum pressure at the forcing frequency are used for the evaluation of the experimental data. The amplitude ratios are shown in Fig. 4; both plots result in the same resonance frequency of 232.8 Hz.

During the frequency variation the following parameters were kept constant:

- combustion air preheat temperature,
- flame tube pressure,
- pressure loss of the airblast atomizer, and
- fuel flow rate.

It was assumed that the air inflow into the plenum via critical nozzles is not influenced by pressure oscillations in the combustor. But this assumption was slightly wrong. The flame tube pressure p , the air preheat temperature T , and the fuel flow rate m_F vary during the test duration of 20 minutes by less than 1% of the nominal value. Only the deviation from nominal value of the pressure loss $\Delta p/p$ of the airblast atomizer is more pronounced: up to 5%.

In spite of the constant pressure and temperature in front of the airblast atomizer and the constant pressure loss of the atomizer during frequency variation, the air mass flow rate is not constant (Fig. 5). The measured air flow rate (foxboro vortex flowmeter) and the mass flow rate calculated from measured pressure and temperature in front of the critical nozzles show the same characteristic decrease with increasing frequency. It is assumed, that the oscillating velocity portion increases the pressure loss of the airblast atomizer with increasing frequency in a nonlinear manner.

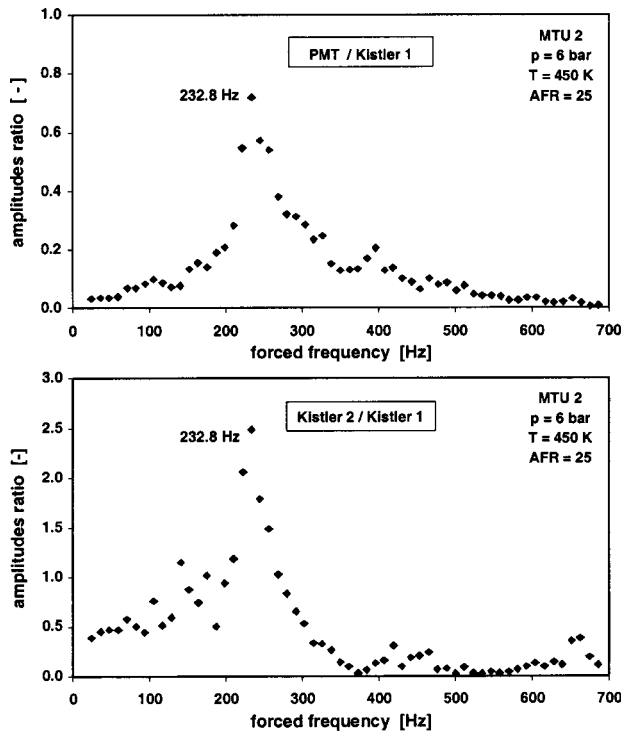


Fig. 4 FFT amplitudes ratio of OH* emission (top) and flame tube pressure (bottom) related to plenum pressure

Two-Dimensional OH* Chemiluminescence Imaging. For the indication of the reaction zone the radiation of electronically excited hydroxyl radicals OH* at 312 ± 7 nm was used (Haber et al. [5]). From a measurement of the OH* chemiluminescence only the volumetric information of the heat release can be deduced. The intensity of an OH* image is always the integral of all contributions towards the camera view.

On the additional assumption of axial symmetry it is possible to deconvolute the OH* image to deduce the spatially resolved heat release (Dasch [6]). To illustrate the difference, Fig. 6 shows the measured and deconvoluted OH* distributions of highly axially symmetric wall attached and detached flames.

For time resolved measurements of the combustion oscillations a representative area of the flame of about 3 cm is imaged on the photocathode of the PMT. Figure 7 shows these areas marked by a circle for the MTU1 air blast injector. The Fourier analysis of the

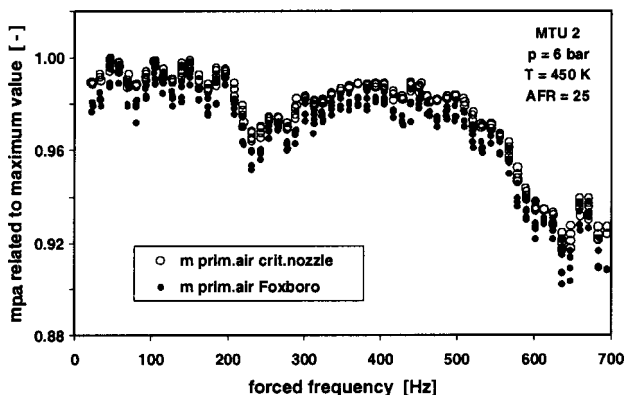


Fig. 5 Measured primary air flow rate as function of forcing frequency

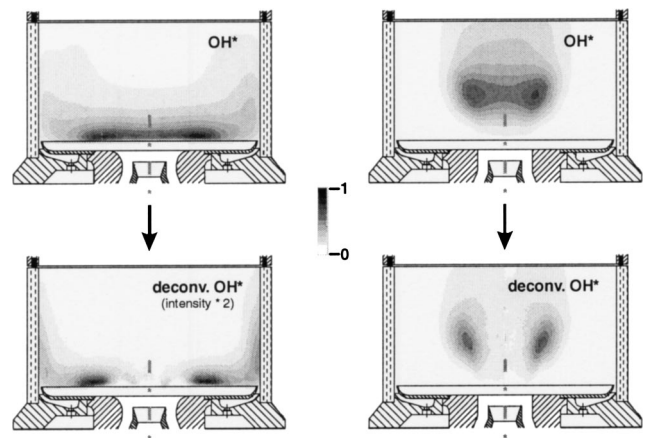


Fig. 6 Measured volumetric OH* distributions (top) and deconvoluted spatially resolved OH* distributions (bottom) of a wall attached flame (left) and of a lifted flame (right) at $T_{preheat}=700$ K, AFR=25 and $p=9$ bar

PMT signal shows significant contributions only at the fundamental frequency and the harmonics of the forced combustion oscillation.

For the spatially resolved OH* imaging an intensified CCD camera is used. The integration time of 5μ s for a single image is sufficiently short to freeze the motion of all movements. Because of the highly turbulent fluctuations of the combustion normally only phase averaged images are digitized and stored on a PC for further image processing. To enable the synchronization with the combustion oscillation and to define the phase angle, the modulator of the primary air flow is equipped with an optical switch. This switch generates a trigger pulse at fully opened by pass valve (minimal combustion air flow rate) which defines the phase angle of 0 deg. In general, a combustion oscillation is monitored by a series of nine subsequent phase averaged images taken with an equidistant phase angle increment of 45 deg. The periodic fluctuation of the phase averaged images is generally small, two to three times smaller than the turbulent fluctuations of single images. Creating a short movie of the phase averaged images the periodic motion of the OH* chemiluminescence of the reaction zone during the combustion oscillation can be visualized in an instructive way.

For a fixed operating condition (nozzle type, pressure, AFR, air preheating), phase averaged images averaged over the oscillation period are equal to within 5% with respect to their integral intensity for all examined forced oscillation frequencies from 22 Hz up to 696 Hz. But the periodic fluctuations are quite different for these frequencies. To enable a systematic overview of the periodic OH* fluctuations of the different oscillation frequencies, the periodic fluctuations of the oscillation frequencies from 72 Hz to 696 Hz together with the phase averaged OH* distribution averaged

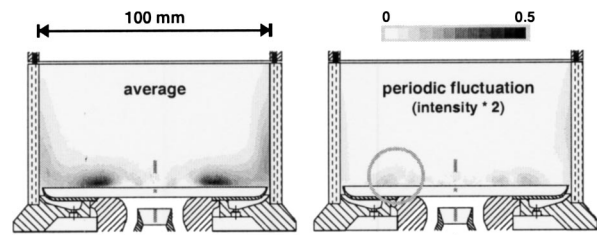


Fig. 7 OH* chemiluminescence of a forced combustion oscillation at 295 Hz of the wall attached flame at 9 bar. The average and the periodic fluctuation of all phase resolved images are shown.

Table 1 ACIACOC test conditions

| | |
|-------------------------|---|
| Test objects | MTU–Burner 1 (for wall attached flames) MTU–Burner 2 (for lifted flames) |
| Flametube pressure | 3 bar, 6 bar, 9 bar |
| Air preheat temperature | 450 K, 700 K |
| Burner pressure loss | 3% |
| Air/fuel ratio | 25 and near lean extinction |

over the oscillation period are shown. To separate the periodic fluctuation from the influence of the turbulent fluctuation, the periodic fluctuations are deduced from phase averaged images comprising 600 single shots. This means, that 4.800 phase resolved images are used for the determination of *each* periodic fluctuation image.

Operating Conditions

As previously expressed, the industrial interest focused on the frequency range of 0 to 700 Hz at idle conditions. A fluctuation of 20% RMS was seen as the maximum value necessary to cover oscillations induced by compressor instabilities. MTU was specifically interested to see behavioral differences between the two air blast nozzle designs that are respectively used in different applications. Thermodynamic parameters were to be varied around a typical idle condition in order to understand their influence on the oscillatory behavior of the combustor. Thus after consultation of partners MTU and University of Karlsruhe, the following mutually agreed test conditions were determined (Table 1).

Pressure was varied between 3 and 9 bar, covering idle pressures for small and large engines, preheat temperature between 450 K being below and 700 K being above the final boiling point of the fuel, to see the eventual influence of prevaporization of the liquid fuel and AFR between 25 and near lean blow out to register the influence of eventual partial extinction during the modulation period on combustion oscillation.

Experimental Results

FFT-Analysis of Pressure and OH* Chemiluminescence Oscillations. At all test conditions the pulsation frequency was varied between 0 and 700 Hz in steps of 12 Hz. After a short period for adjustment, the signal samples were taken at every frequency stop. All recorded data were analyzed as indicated above.

Each frequency scan results in spectral amplitude distributions resembling qualitatively Fig. 4. The forcing frequencies of the spectral peaks of the scans are considered as resonance frequencies of the system. These frequencies and the FFT amplitudes of the PMT signal at these spectral positions (in arbitrary, but always the same units) for all test conditions are plotted in Fig. 8. With respect to frequency, the data exhibit the following trends (note that there is a small difference between peak frequency in the absolute and in the relative spectral amplitude distributions):

- all measured resonance frequencies are found in the frequency range 256–326 Hz (because of the frequency steps of 12 Hz the uncertainty amounts to +/- 6 Hz),
- the frequencies at low preheat temperature (450 K) tend to the lower limit and at high preheat temperature (700 K) to the upper limit,
- the ratio between the limiting frequencies (1.27) is equal to the root extracted from the preheat temperature ratio (1.25), and
- there is no distinct difference in the resonance frequencies for both test objects.

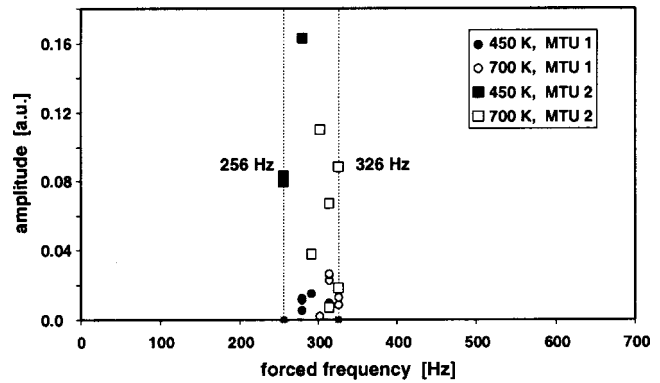


Fig. 8 Resonance frequencies according to PMT signal for all operating conditions; marked are the different injectors and preheat temperatures

From these results and the identity of the swirlers within the tested airblast atomizers it can be concluded:

- there is no influence of the airblast atomizer’s diffuser shape on the examined resonance frequency of the system,
- there is no distinguishable influence of the flame shape and the thermal conditions within the flame tube on the examined resonance frequency, and
- at a constant geometry of the test section the resonance frequency depends only on air preheat temperature.

Therefore the plenum/flame-tube combination can be treated as a sound room, consisting of two hollow spaces and a connecting passage (airblast atomizer). The condition, that all dimensions of the sound room are smaller than $\lambda/4$ of the stimulating oscillation, is fulfilled.

The resonance frequency of the system f_0 can then be calculated by the equation deduced from (Veit [7])

$$f_0 = c / (2\pi) * \sqrt{2 * \sqrt{A_{eff} / \pi} * (V_1 + V_2) / (V_1 * V_2)}$$

with

- c = speed of sound of the medium within the passage
- A_{eff} = cross-section of the connecting passage
- V_1 = plenum volume
- V_2 = flame tube volume.

The oscillating gas volume within the connecting passage—driven by the changing plenum pressure—is the deciding factor in the acoustic coupling. The gas in the passage (atomizer) has always preheat temperature; no hot gas is passing upstream. Thus only the preheat temperature influences the resonance frequency; there is no influence of the backside temperature. In this case the analogue model results in a remarkably good agreement with the above given experimental findings:

$$T = 450 \text{ K} \rightarrow f_0 = 259.9 \text{ Hz}$$

$$T = 700 \text{ K} \rightarrow f_0 = 324.2 \text{ Hz}$$

Nearly the same result as with the PMT signal (Fig. 8) is obtained, if the ratio of flame tube pressure/plenum pressure is examined (Fig. 9).

The chemiluminescence images were evaluated for the periodic fluctuation of the intensity in the phase-averaged images in the resonant frequency band at 295 Hz. The experimental results show the influence of the nozzle configuration, pressure, tempera-

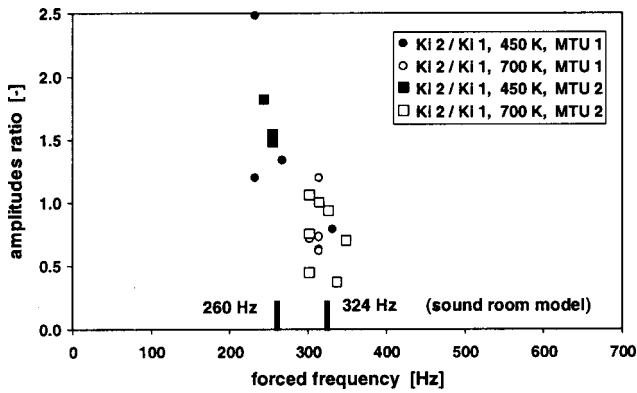


Fig. 9 Resonance frequencies according to ratio $p_{\text{flame tube}}/p_{\text{plenum}}$ for all operating conditions; marked are the different preheat temperatures

ture and AFR on the flame tube and flame response. Their sequence in decreasing order of importance turns out to be

- burner geometry,
- preheat temperature,
- pressure, and
- AFR.

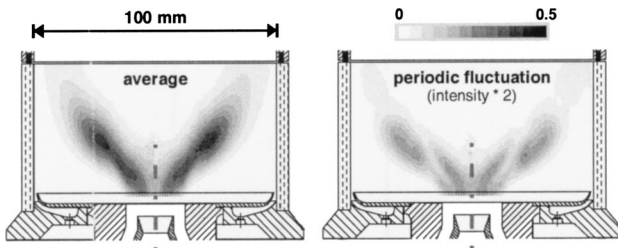


Fig. 10 Averaged OH^* chemiluminescence of the detached flame at 9 bar, AFR 25, and 450 K preheat temperature

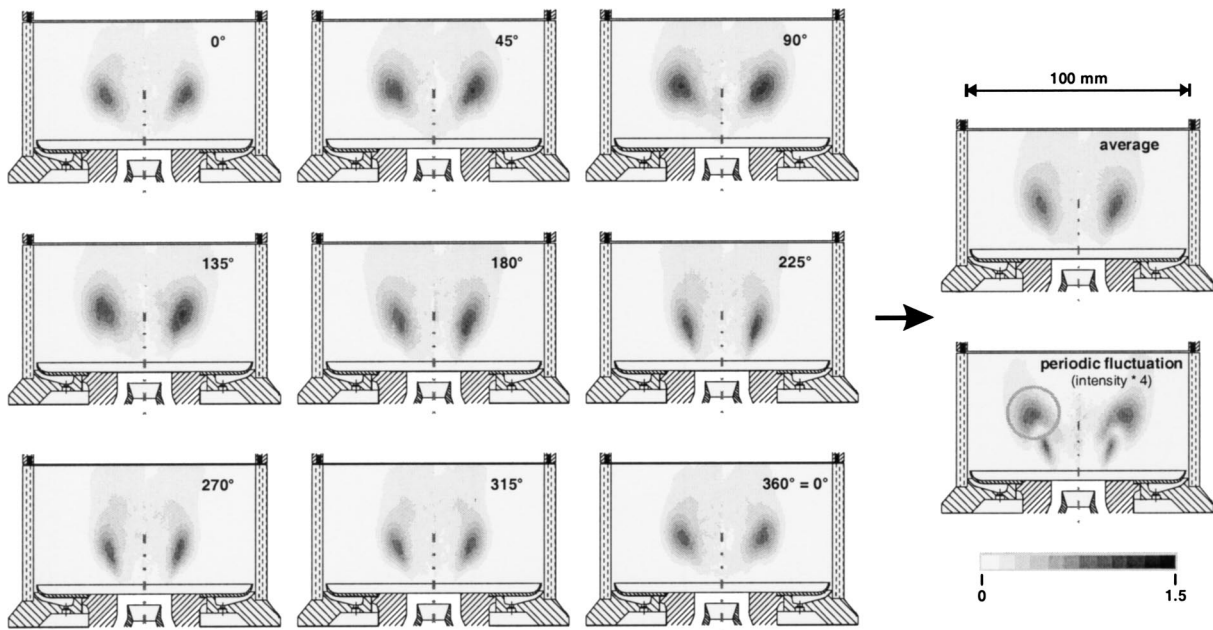


Fig. 11 Phase resolved OH^* chemiluminescence of a forced combustion oscillation at 295 Hz of a detached flame at 9 bar (AFR 25, 700 K air preheat temperature) and averaged over 600 single images

The burner geometry is by far the most sensible factor, with configuration 2 producing about twice as much pressure and chemiluminescence fluctuation as configuration 1. The geometry effect was expected by the industrial partner, however since acoustic feedback was not registered and fluctuating pressure amplitudes remained small in this combustor, there does not seem to be cause for serious concern.

The preheat temperature has a different influence on pressure and rate of heat release. The lower temperature gives slightly higher heat release fluctuations but roughly a twofold increase in relative pressure fluctuation. This is explained with the help of Fig. 10. It represents the deconvoluted image of the average chemiluminescence and its periodic fluctuation at resonance for the lower preheat. The fluctuation shows two different burning zones, which we believe to be connected to flame stabilization by inner and outer recirculation. Whereas the photomultiplier registers luminescence irrespective of its origin, the pressure sensor will more likely be influenced by the change of the location of heat release.

With rising pressure, the amplitudes of the flame tube pressure fluctuation normalized with the plenum fluctuation remain rather constant, whereas the chemiluminescence increases less than proportional with pressure due to the more important quenching at higher pressure. The two facts suggest that the oscillation is proportional to the gas density or the number of molecules taking part in the combustion.

The differences with respect to air/fuel ratio are also small with a slightly higher fluctuation for the richer AFR 25 case. Here, the higher reaction rate seems to outweigh the influence of partial extinction for the AFR near blowoff. This is probably a feature which is specific to the nozzle design and method of fuel preparation. During the lean blowoff trials preceding the choice of the lean AFR, it was noted that the nozzle exhibits a rather sharp extinction with good circumferential homogeneity close to blowoff.

Summarizing the influence of the operating conditions, the parameters leading to a more compact reaction zone, higher pressure, temperature and equivalence ratio, display lower fluctuation levels.

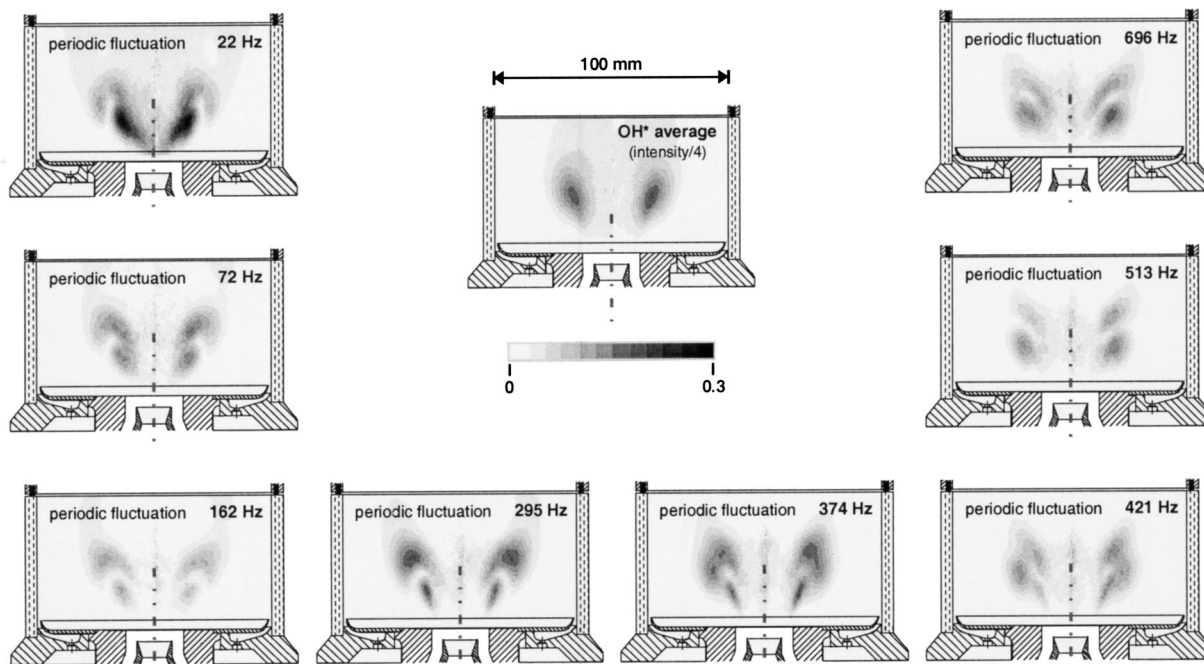


Fig. 12 Periodic fluctuations of the OH* chemiluminescence for a detached flame at 9 bar for the different oscillation frequencies of 22 Hz–696 Hz. The detached flame (MTU 2 nozzle) burns at an AFR of 25 and an air preheating of 700 K.

Two-Dimensional OH* Chemiluminescence Imaging.

Compared to the wall attached flame (MTU 1 nozzle, Fig. 6 and Fig. 7) the wall detached flames generated by the MTU 2 nozzle (Fig. 10) show a higher sensitivity to forced combustion oscillations. Both the integral intensity and the spatial distribution of OH* vary significantly during a combustion oscillation. For 3 bar, 700 K, and AFR 25 the flame exhibits a periodic lifting from and reattachment to the burner mouth. Figure 11 shows for an example the strong flame zone variation of the combustion oscillation at 295 Hz of the detached flame at 9 bar. The picture with the periodic fluctuations brings out, that they are most intensive at the root of the flame and in the burn out zone. However comparison with the average shows the flame burning rather stable in the region of maximum heat release. Since the location and fluctuation intensity of the region of maximum heat release is most important for the thermo-acoustic oscillation, the comparison of mean and fluctuating parts shows a favorable behavior even in the resonance frequency of the sound room.

Figure 12 shows the systematic overview of the periodic oscillations of the wall detached flame at 9 bar. Because the intensities averaged over a period are equal within 5% for all frequencies, only once the OH* distribution averaged over all phase angles and frequencies (“OH* average”) is shown. For the lowest frequencies (≤ 72 Hz) the combustion oscillations of the detached flame are very intense, but the increase with respect to decreasing frequencies is less pronounced as it is for the wall attached flame. The integral value of the periodic combustion fluctuation of the detached flame is about three times higher for frequencies excluding the lowest modulation frequency of 22 Hz. At that frequency the highest variation of the expansion of the hot flow, probably connected to the highest AFR fluctuation, with the ensuing radial displacement of the reaction zone is observed.

At frequencies above 162 Hz, the periodic fluctuations often show two separate zones of high periodic fluctuation. In the video sequences the frequencies above 295 Hz create a “waving” motion of the chemiluminescence distribution as opposed to the “breathing” motion of the lower frequencies. While the “breathing” behavior can be understood as the quasi-steady response of chemistry and flow having short time scales compared to the pe-

riodicity of the induced mass flow or AFR variation this is not the case for the “waving” motion. Most probably, it is connected to a residence time effect.

On the basis of a calculation of the isothermal flow field and a Lagrangian particle tracking routine, the residence time of a fluid volume in the luminescent part of the images can be estimated between 1 and 2 ms. Hence, exchange of the charge of the heat release zone between two successive phase averaged images can be expected for frequencies above 162 Hz. Since the wave effect becomes apparent in the phase averaged images, it must be a periodic effect, not connected to a time or length scale of statistical turbulence.

Different mechanisms could be responsible for the formation of that movement of the chemiluminescent zone:

- AFR variations, caused by periodic accumulation of liquid at the atomizer lip could also lead to a periodic variation of the dispersion of the fuel,
- periodic vortex detachment could be triggered by the forced modulation of the airflow (Büchner [8]), and
- periodic disturbances of the nozzle through flow could lead to a loss of self similarity for the gas flow. Such an effect was recently observed in an isothermal investigation of a sinusoidally modulated air blast nozzle (Giuliani et al. [9]).

For the investigation of these effects, different diagnostics would be needed. The Schlieren technique was tried to detect coherent vortices but failed due to the three-dimensional nature of the flow and strong thermal boundary layers from the window cooling.

Conclusion

From the analysis of the pressure data, it can be concluded that serious thermoacoustic feedback was not observed for both burners. The separation of turbulent and periodic fluctuations by phase averaging of chemiluminescence showed the turbulent fluctuation to be higher than the periodic part.

Burner 2 with the flame detached from the wall exhibited a higher fluctuation level as burner 1 with the wall attached flame.

A resonant behavior was observed near the characteristic frequency of the sound room comprised of plenum, flame tube, and burner nozzle as connecting passage.

The importance of the varied parameters in decreasing order was: burner geometry, preheat temperature, pressure and AFR.

The chemiluminescence images show different modes of spatial fluctuation for the burners. Burner 2 exhibits a “breathing” motion of the heat release zone at lower frequencies and a “waving” motion at frequencies above 295 Hz.

Outlook

In a follow-up project with MTU we will investigate more specifically the role of the liquid fuel, since this is the missing link between the forced airflow and the heat release. It is planned to observe simultaneously the Mie scattering and the chemiluminescence to clarify the extent of AFR variations with forced oscillation frequency and the influence of the fuel contained in the fuel film prior to atomization.

Acknowledgments

Financial support of the ACIACOC Project by the European Commission, BE 97 4324 BRPR CT97 0506 is gratefully acknowledged.

The authors thank K. Katheder of MTU Munich for the use of the data of his isothermal flowfield calculation and T. Behrendt for the use of his deconvolution algorithm.

References

- [1] CORDIS RTD-PROJECTS/© European Communities, 2000, “Active Control of Instabilities in Advanced Combustion Chambers,” <http://dbs.cordis.lu>.
- [2] Berenbrink, S., and Hoffmann, S., 2000, “Suppression of Dynamic Combustion Instabilities by Passive and Active Means,” *ASME-2000-GT-0079*.
- [3] IPCC Special Report, 1999, *Aviation and the Global Atmosphere*, Cambridge University Press, Cambridge, UK.
- [4] Konrad, W., et al., 1998, “Combustion Instability Investigations on the BR 710 Jet Engine,” *ASME J. Eng. Gas Turbines Power*, **120**, pp. 34–40.
- [5] Haber, L., Vandsburger, U., Saunders, W., Khanna, V., 2000, “An Examination of the Relationship Between Chemiluminescent Light Emissions and Heat Release Rate Under Non Adiabatic Conditions”, 2000-GT-0121.
- [6] Dasch, C. J., 1992, “One-dimensional Tomography: A Comparison of Abel, Onion-Peeling, and Filtered Backprojection Methods,” *Appl. Opt.*, **31**(8), 1146–1152.
- [7] Veit, I., 1974, *Technische Akustik*, Kamprath-Reihe kurz und bündig, Vogel-Verlag, Würzburg.
- [8] Büchner, H., 1992, “Experimentelle und theoretische Untersuchungen der Entstehungsmechanismen selbsterregter Druckschwingungen in technischen Vormisch-Verbrennungssystemen,” *Diss.*, Univ. Karlsruhe, Shaker-Verlag Aachen.
- [9] Giuliani, F., Diers, O., Gajan, P., and Ledoux, M., 2002, “Characterization of an Air-Blast Injection Device With Forced Periodic Entries,” *Proceedings of the IUTAM Symposium on Turbulent Mixing and Combustion*, Pollard and Candel, eds., Kluwer, Dordrecht, The Netherlands.

Advanced Catalytic Pilot for Low NO_x Industrial Gas Turbines

H. Karim

K. Lyle¹

S. Etemad

L. L. Smith

W. C. Pfefferle

Precision Combustion, Inc.,
410 Sackett Point Road,
North Haven, CT 06473

P. Dutta

K. Smith

Solar Turbines, Inc.,
2200 Pacific Highway,
San Diego, CA 92186

This paper describes the design and testing of a catalytically stabilized pilot burner for current and advanced Dry Low NO_x (DLN) gas turbine combustors. In this paper, application of the catalytic pilot technology to industrial engines is described using Solar Turbines' Taurus 70 engine. The objective of the work described is to develop the catalytic pilot technology and document the emission benefits of catalytic pilot technology when compared to higher, NO_x producing pilots. The catalytic pilot was designed to replace the existing pilot in the existing DLN injector without major modification to the injector. During high-pressure testing, the catalytic pilot showed no incidence of flashback or autoignition while operating over wide range of combustion temperatures. The catalytic reactor lit off at a temperature of approximately 598 K (325°C/617°F) and operated at simulated 100% and 50% load conditions without a preburner. At high pressure, the maximum catalyst surface temperature was similar to that observed during atmospheric pressure testing and considerably lower than the surface temperature expected in lean-burn catalytic devices. In single-injector rig testing, the integrated assembly of the catalytic pilot and Taurus 70 injector demonstrated NO_x and CO emission less than 5 ppm @ 15% O_2 for 100% and 50% load conditions along with low acoustics. The results demonstrate that a catalytic pilot burner replacing a diffusion flame or partially premixed pilot in an otherwise DLN combustor can enable operation at conditions with substantially reduced NO_x emissions. [DOI: 10.1115/1.1586313]

Introduction

Government regulations are forcing both industrial and utility gas turbine manufacturers to improve engine designs for achieving lower possible CO and NO_x emissions, [1,2]. In this quest to achieve lower emissions, lean-premixed combustion technology is preferred by both the industrial and utility engine manufacturers. Lean-premixed combustion technology has demonstrated the ability to achieve NO_x concentrations as low as 9 ppm corrected to 15% O_2 , during operation on natural gas, [1,3].

At low- NO_x operating conditions, however, flame temperatures are reduced and flame stability issues arise. In addition, combustion of uniform, premixed fuel/air mixtures, with little additional combustor air, can lead to combustion-induced pressure oscillations (noise). To mitigate these combustion instability issues with lean-premixed flames, gas turbine manufacturers frequently use higher temperature pilot flames to impart stability to the main combustion process. One such technique is the use of either a diffusion flame pilot or a partially premixed pilot, [3–5]. Traditionally the pilot is another fuel injector in which a small portion of the fuel is combusted in a diffusion flame or partially premixed mode. The rest of the fuel is combusted in a lean-premixed flame while the pilot maintains the stability of this main flame. In addition to providing stability at baseload, the pilot also provides combustion stability during engine startup, load ramping, transients, and fuel transfer operation.

Depending on the design of the combustor, 2–10% of the fuel can be used for the piloting at baseload. If more fuel is used for piloting, more NO_x is produced due to the higher temperatures associated with pilot flame. Thus with such conventional pilots, dry low NO_x (DLN) combustors can operate close to the overall

lean limit and achieve 9–25 ppm NO_x . Nevertheless the reliance on a high NO_x pilot can be a barrier to further NO_x reductions.

Catalytic Combustion/Catalytic Pilot

Catalytic combustion has been known to provide combustion stability to very lean fuel air mixtures [6–8]. Catalytically stabilized combustion was first demonstrated by Pfefferle [6] and was shown to be an efficient method for burning fuels in lean fuel air mixtures without significant formation of pollutants. Dalla Betta [7] demonstrated $\text{NO}_x < 3$ ppm from a small-scale staged catalytic combustion system operated at outlet temperatures from 1225°C to 1500°C and pressure from 12 to 20 atmosphere. Current development status and design challenges for application of full catalytic combustion that have been addressed by Siemens Westinghouse Power Corp for large utility engines and Solar Turbine for smaller industrial engines are discussed in the reference by Fant [9]. Dalla Betta [10] discusses application of full catalytic combustion for a 1.5 MW engine.

This paper presents an alternative concept to a full catalytic combustion system. Instead of replacing the entire DLN combustor with catalytic combustion, the catalytic combustion technology discussed in this paper only replaces the diffusion flame pilot. Thus the catalytic pilot concept focuses on replacing the highest temperature portion of DLN combustor with catalytic combustion technology. This makes the catalytic pilot a good candidate for both new engines and retrofit applications without major modification and cost. The concept uses the best features of catalytic combustion (increased stability through prereaction) and conventional (proven) aerodynamically stabilized combustion technology.

The motivation of using a catalytic pilot is that the catalytic prereaction in the pilot will provide enhanced reactivity to the gas mixture exiting the pilot and thereby obviate the need to use high temperature flames to stabilize the combustion of the primary fuel air mixture exiting the swirler.

This paper discusses the application and results from integration of a catalytic pilot with a lean-premixed fuel injector from a DLN gas-turbine combustor. Figure 1 shows a sketch of the catalytic pilot concept and how it integrates within a main injector

¹Currently Research Assistant at the Department of Mechanical Engineering, Stanford University, Building 520, Stanford, CA 94305.

Contributed by the International Gas Turbine Institute (IGTI) of THE AMERICAN SOCIETY OF MECHANICAL ENGINEERS for publication in the ASME JOURNAL OF ENGINEERING FOR GAS TURBINES AND POWER. Paper presented at the International Gas Turbine and Aeroengine Congress and Exhibition, Amsterdam, The Netherlands, June 3–6, 2002; Paper No. 2002-GT-30083. Manuscript received by IGTI, December 2001, final revision, March 2002. Associate Editor: E. Benvenuti.

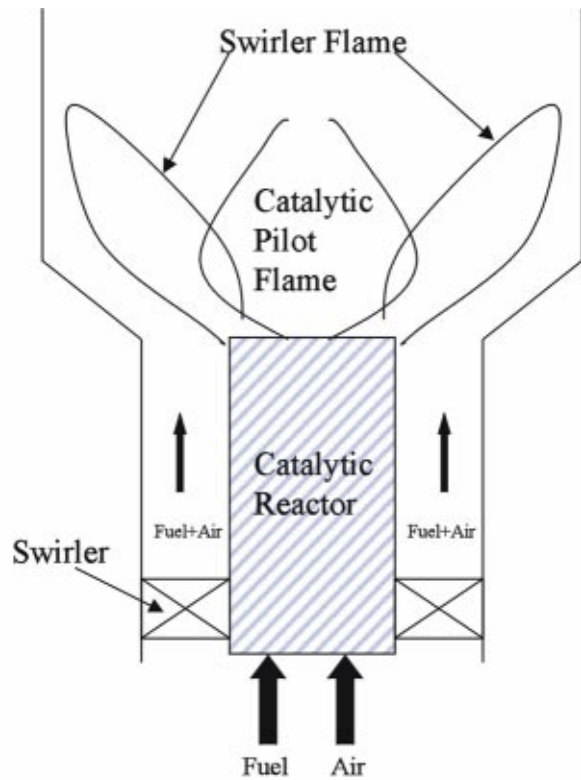


Fig. 1 Sketch of the catalytic pilot concept within a lean pre-mixed injector (swirler+pilot)

(injector consist of an annular swirler and a pilot in the center of it) for a lean pre-mixed combustion system. The figure shows that a portion of the fuel air/mixture passes through the catalytic pilot and prereacts within the catalytic reactor before a pilot flame is stabilized downstream of the reactor. The rest of the fuel and air passes through the swirler portion of the injector and the catalytic pilot flame anchors a swirl-stabilized flame.

At low equivalence ratios, which are required for low NO_x operation of the combustor, the main swirler flame depends on the catalytic pilot flame for its stability and the pilot's flame depends on the catalytic prereaction for its stability. Depending on design and load condition of the engine, the equivalence ratios of the main swirler flame and the pilot flame can be different.

Catalytic Reactor Design

As shown in Fig. 1, a catalytic pilot consists of a catalytic reactor and a downstream homogeneous combustion zone. There are several approaches currently practiced in design of a catalytic reactor for the gas turbine and example of these approaches can be found in the literature, [11–13]. In the subject approach, the temperature rise in the catalytic reactor is limited by limiting the extent of fuel oxidation that occurs within the catalyst itself. Figure 2 shows a sketch of the catalytic reactor concept.

The catalytic reactor of Precision Combustion Inc.'s (PCI) pilot utilizes fuel-rich partial oxidation to limit the extent of reaction in the reactor. As shown schematically in Fig. 2, all of the pilot fuel and a fraction of the pilot air are mixed before contacting a catalyst under fuel-rich conditions. The balance of the pilot air provides catalyst cooling. The cooling air and catalyzed fuel/air mixture are subsequently rapidly mixed after the catalyst section to produce a fuel-lean, reactive mixture. The mixing is complete before the mixture exits the pilot and comes in contact with the fuel/air mixture from the swirler. Thus even though the catalyst section of the reactor uses fuel-rich combustion, overall the reactor for the pilot operates fuel lean. Ignition and combustion of the

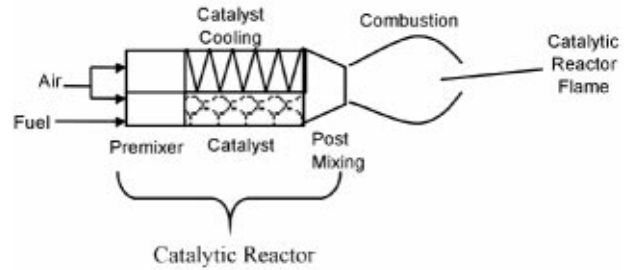


Fig. 2 Sketch of the catalytic reactor for the pilot

now-lean reactive mixture are then achieved in the downstream combustion section to produce the pilot flame. This is called "Rich Catalytic/Lean-burn," or RCL™ combustion. This approach avoids both soot formation as discussed in literature, [14,15], and the high temperatures, which in noncatalytic RQL (rich-burn/quench/lean-burn) designs lead to high NO_x formation. In the RCL™ system, fuel-rich reaction occurs at moderate temperatures on the catalyst surface. The catalyst also allows fuel-rich reaction outside the gas-phase flammability limits in the temperature range of 700–900°C (973 K/1533°F–1173 K/1652°F). Thus, the high temperatures present in the fuel-rich stage of noncatalytic systems (e.g., RQL) are simply not present in the RCL device. As a result, of long autoignition delay time, which is shown in Fig. 3, for mixing catalytically reacted natural-gas with air after the catalytic reactor, mixing can be completed without autoignition. Subsequent to mixing, a low temperature lean premixed pilot flame can be stabilized and as a result this combustion approach yields low NO_x .

In Fig. 3, the autoignition delay time is shown as calculated for a representative gas-mixture (in the post-mix region after the catalytic section) as a function of mixed gas temperature and it can be observed that at 973 K (700°C/1292°F), the autoignition delay time is approximately 0.045 seconds, which is sufficiently long to permit mixing.

This reactor design approach can provide several advantages over fuel lean catalytic reactor design and these are

- *Low temperature lightoff:* Significantly lower temperature lightoff (as discussed in the results section) than can be achieved in fuel-lean catalysis.
- *No preignition or flashback danger in the catalytic reactor:* Unlike fuel-lean catalyst systems, there is no fuel in the cooling air stream to ignite. At the same time, reaction of the

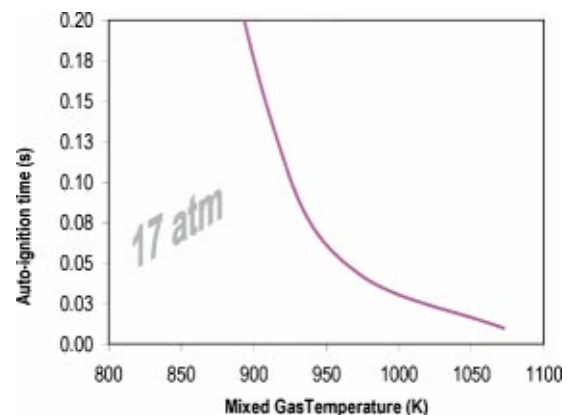


Fig. 3 Prediction of autoignition delay

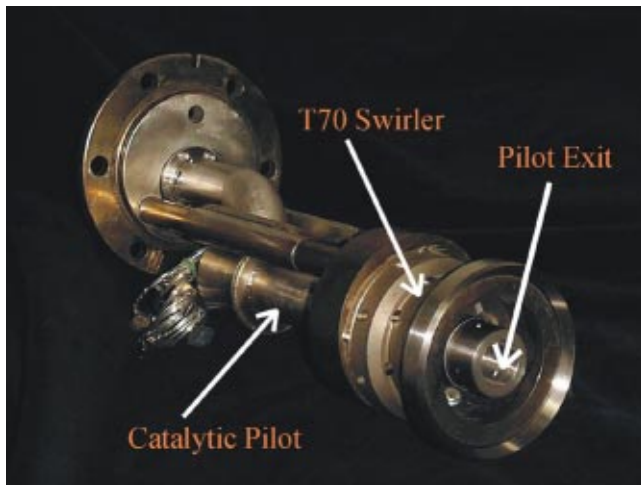


Fig. 4 Photograph of modified Solar Taurus 70 premixed fuel/air injector hardware, with PCI's catalytic pilot

fuel-rich mixture in contact with the catalyst is oxygen-limited, and gas-phase combustion within the catalyst bed poses no problem.

- *Tolerant to fuel/air unmixedness:* In addition to reducing the potential for flashback/preignition, the fuel rich catalyst design reduces the sensitivity of catalyst temperature to fuel/air ratio, allowing safe operation with up to $\pm 10\%$ uniformity (compared to the required $\pm 2\%$ as reported in Yee [16]).
- *Improved catalyst durability:* Fuel-rich operation reduces catalyst volatilization and substrate oxidation, enhancing catalyst life relative to lean burn systems.

Single-Injector Catalytic Pilot

To verify and demonstrate the low NO_x potential of the catalytic pilot for industrial engines, a pilot was fabricated for a single injector that is used in Solar Turbines' Taurus 70 turbine. The Taurus 70 is an industrial engine with a design rating of 7.2 MW @ 1394 K (1121°C/2050°F) turbine rotor inlet temperature, [17]. The engine has 12 injectors (swirler+pilot) arranged circumferentially around an annular combustor liner.

Figure 4 shows a hardware picture of the catalytic pilot integrated inside a Taurus 70 injector. The catalytic pilot replaced the existing partial premixed pilot without modification to the surrounding injector geometry.

As shown in Fig. 4 the catalytic pilot is installed on the injector centerline within the swirler hub. The orientation of the injector in the photograph shows the mounting flange at upper left, and swirler and catalytic reactor exits at lower right. All the testing reported in this paper was conducted with the modified Taurus 70 injector shown in Fig. 4.

The modified Taurus 70 injector assembly was integrated with an augmented backside cooled (ABC) combustor liner, [18]. Approximately 50% of the combustion system airflow enters the liner through the catalytic pilot and injectors. The remaining 50% of the air is used to cool the liner and enters the combustion zone (liner) either through the dome cooling holes in the liner at the front or through dilution holes in the post-primary combustion zone.

Test Facilities

Two different test facilities were used during the evaluation of the catalytic pilot performance.

Atmospheric Pressure Testing Facility at PCI. The integrated assembly of the modified T-70 injector and the ABC liner

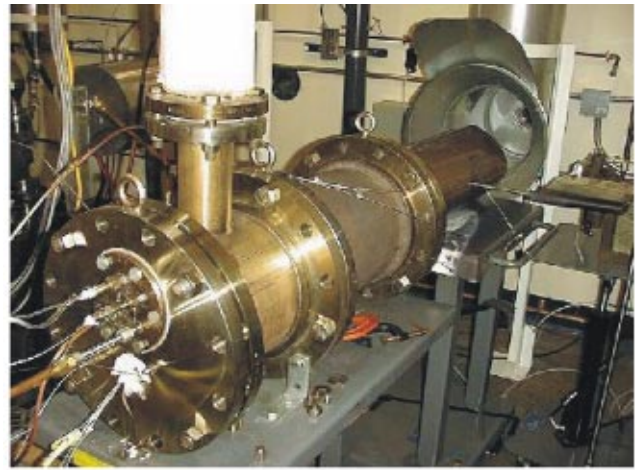


Fig. 5 Top panel: single-injector atmospheric pressure test facility at PCI. bottom panel: single-injector high-pressure test facility at Solar Turbine.

configuration was first tested at PCI, in an atmospheric pressure rig, a photograph of which is shown in the top panel of Fig. 5.

Testing was conducted both for the catalytic reactor only and for the catalytic pilot and injector together. These tests were conducted at the simulated baseload condition of T-70 engine. This implies that the pilot and injector were run at the same flow velocities in the atmospheric pressure rig as they would at baseload condition in an engine. The velocities through the component were identical to their values at baseload when the inlet temperature used at atmospheric condition was same as that of the baseload.

High-Pressure Testing Facility at Solar Turbines. After completion of testing at atmospheric pressure conditions, the modified injector assembly was tested at Solar's high-pressure single-injector test facility; a photograph of the facility is shown above in the bottom panel of Fig. 5. The test facility permitted independent control of the airflow, natural gas (CH_4 : 95.82%, C_2H_6 : 1.8%, C_3H_8 : 0.32%, C_4H_{10} : 0.13%, CO_2 : 0.89%, N_2 : 1.0) flows to the catalytic pilot and swirler, and total pressure of the system. At this facility, the modified injector was tested at close to full load (limited by available air flow) and half-load conditions, which are shown in Table 1.

During the several days of operation at Solar's high-pressure facility no autoignition or flashback in the catalytic pilot was observed.

Table 1 Nominal Taurus 70 full-load combustor operating conditions

| | |
|-----------------------------|---------------------|
| Baseload inlet temperature | 705 K (432°C/810°F) |
| Baseload inlet pressure | 1.7 Mpa (250 psia) |
| Baseload pressure drop | 4.0% |
| Half-load inlet temperature | 636 K (363°C/687°F) |
| Half-load inlet pressure | 1.02 Mpa (153 psia) |
| Half-load pressure drop | 3.5% |

Discussion of Results

Results have been obtained for both atmospheric pressure and a pressure of 15 atm. operation. Only high pressure results will be discussed as these are more relevant to the Taurus 70 engine.

Catalyst Lightoff. The lightoff characteristics of the catalytic reactor at 15 atm. are shown in Fig. 6. A heater was used to heat the air to the rig. The abscissa shows the inlet air temperature and the ordinate shows both the catalyst surface temperature, and the temperature of the fuel-lean gas exiting the catalytic reactor. As expected, prior to lightoff, the catalyst temperature and the temperature of the gas exiting the reactor were both the same as that of the inlet air temperature. It can be observed from Fig. 6 that lightoff of the reactor occurred when the inlet air temperature reached a temperature of approximately 325°C (598 K/617°F). Lightoff is indicated by the separation of the catalyst temperature and the exit gas temperature, and also by the difference of these two temperatures from that of the inlet air. As the catalyst lights off, it becomes sufficiently active that fuel was oxidized and heat release occurred on the surface. The gas in the catalytic reactor was heated by the convection of heat from the catalyst surface. Due to resistances in heat transfer mechanisms, the exit gas temperature was less than the maximum surface temperature.

The measured lightoff temperature of 325°C (598 K/617°F) is substantially lower than the 450°C (723 K/842°F) lightoff temperature reported in the literature for catalytic combustion of natural gas using fuel lean catalysis, [19]. This lower lightoff temperature is a direct consequence of using fuel rich oxidation in the catalytic reactor and has shown no dependence on pressure. Figure 6 also shows that the lightoff temperature is lower than the compressor outlet temperatures both at 100% and 50% load conditions of the Taurus 70 machine. Thus the catalytic reactor of the pilot does not need a preburner for operation from 50% load to 100% load.

During startup, the catalytic pilot can be used as a noncatalytic fuel stage to provide 50% to 60% of the fuel for the combustor thereby creating a rich primary zone. Since compressor exit air temperature will be lower than the lightoff temperature for the

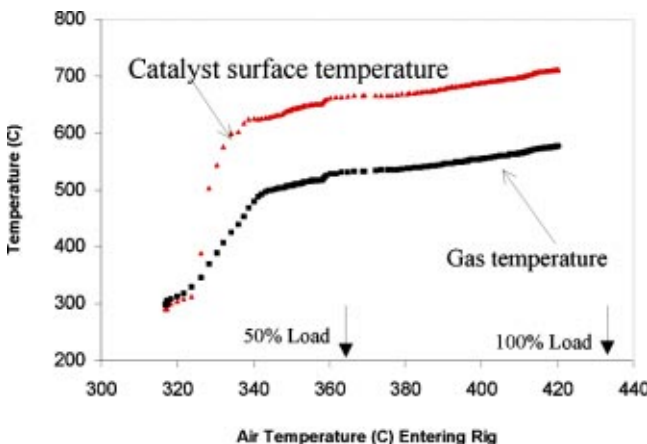


Fig. 6 Lightoff for the catalytic reactor at a pressure of 15 atm

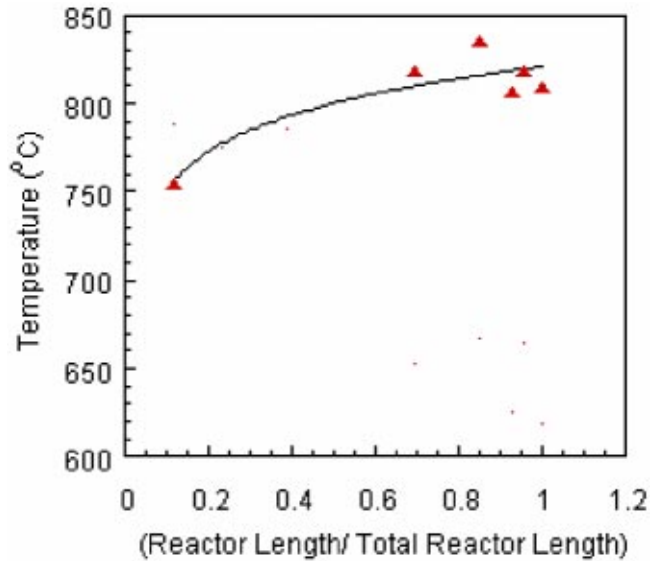


Fig. 7 Catalyst surface temperatures at a pressure of 15 atm

reactor, no reaction will occur inside the catalytic reactor. The unreacted fuel air mixture exiting the catalyst will then be combusted in the downstream liner (combustor) section along with the fuel/air mixture from the swirler albeit with higher emissions. Once the combustor ramps up and the compressor discharge temperature reaches the lightoff temperature of the reactor, fuel oxidation in the reactor starts to occur. This catalytic reaction provides further stability to the overall combustion process. The higher fuel-rich equivalence ratios which will result from such a fuel split are within the safe operating range of the reactor, since higher fuel rich equivalence ratios produce less heat. When 50% load is reached, fuel flow to the pilot is readjusted for operating in the low NO_x regime

Surface Temperature of the Catalyst. Figure 7 shows catalyst surface temperatures at a pressure of 15 atmospheres as function of nondimensional reactor length. The maximum catalyst surface temperature was below 850°C, a temperature much lower than the reported maximum surface temperature for fuel lean catalytic combustion by (Dalla Betta, [20]). This reduced temperature operation decreases catalyst volatilization, and sintering, which are factors judged potentially life limiting for catalytic combustors and permits the use of metal for catalyst substrate.

The maximum catalyst surface temperature was similar to the maximum surface temperature during atmospheric operation. As a consequence of this, catalytic reactor operation at atmospheric pressure gives a good estimate to the maximum temperature at high pressure.

Emission Results. Due to air flow limitation in the high pressure rig, emission data were collected at 15 atm. instead of 17 atm, which is the baseload pressure for Taurus 70 engine. As discussed earlier in the “single-injector catalytic pilot” section, the modified Taurus 70 injector was integrated with an ABC liner and installed in the high-pressure rig. As shown in Table 2, the

Table 2 Air splits in the combustor

| | Catalytic Pilot Configuration | | Standard Pilot Configuration | |
|------------------------|-------------------------------|------------------------|------------------------------|--|
| Catalytic pilot | 12.2% | Pilot | 3.3% | |
| Swirler | 40.6% | Swirler | 45.0% | |
| Liner (dome cooling) | 12.2% | Liner (dome cool.) | 13.4% | |
| Liner (dilution holes) | 35.0% | Liner (dilution holes) | 38.3% | |

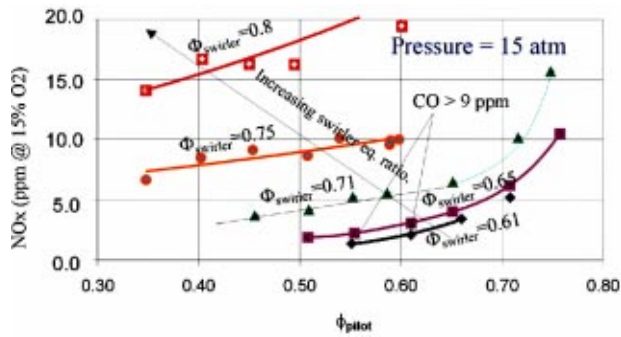


Fig. 8 NO_x emission dependence on catalytic pilot equivalence ratios

replacement of the standard diffusion pilot with the catalytic pilot increased the air split to the pilot to 12.2% from 3.3%.

All emission results will be discussed in terms of pilot and swirler equivalence ratios and front end adiabatic flame temperatures (calculated based on pilot and swirler air and fuel flow) rather than primary zone flame temperatures, which are difficult to measure because of entrainment of dome cooling air and liner dilution air.

Figure 8 shows the sensitivity of NO_x emission to catalytic pilot equivalence ratios at a pressure of 15 atm. The symbols show the experimental data obtained after correction to 15% O₂ in a dry sample, and the lines represent trend lines drawn through the data points with constant swirler equivalence ratio. For a constant swirler equivalence ratio ($\phi_{swirler}$), emission data were first collected with the highest pilot equivalence ratio (NO_x < 20). Then gradually the pilot equivalence ratio (ϕ_{pilot}) was dropped until blowoff occurred or CO exceeded 20 ppm. CO exceeded 10 ppm in only the first two data points (ϕ_{pilot} = 0.55, 0.61) from the lowest swirler equivalence ($\phi_{swirler}$ = 0.61) ratio series shown in Fig. 8. CO was lower than 10 ppm at all other data points shown in Fig. 8.

We observe from this figure that for higher swirler equivalence ratio less piloting is necessary and blowoff occurred at lower pilot equivalence ratio. This is expected and the increased stability is achieved at the expense of higher NO_x emission. Below ϕ of 0.65, NO_x dependence on the pilot equivalence ratio was linear.

Figure 8 also shows that the best NO_x emission (NO_x < 5 ppm) can be obtained for this configuration of modified Taurus 70 injector and ABC liner when the swirler equivalence ratio is between 0.5 to 0.65 and the pilot equivalence ratio is between 0.55 to 0.65. Thus the modified injector showed a wide operability range. If the fuel to the catalytic pilot was shut-off while operating at these low swirler equivalence ratios (0.5–0.65), blowoff would occur. This indicated that the catalytic pilot provided stability to the main flame.

Figure 9 shows the same emission data (CO and NO_x) of Fig. 8 when plotted as a function of front end temperature of the combustor. The front-end temperature was calculated based on the air flows to the pilot, and injector, and fuel flows to the swirler and pilot. Note that the calculated front end temperature does not take into account any reverse flow dilution air (liner cooling) or dome cooling that may participate in the combustion process occurring in the primary zone of the combustor. As such, the temperature shown in the x-axis is not the primary zone temperature during combustion. Comparison of these data with data from lean-premixed combustion of Kendric [4] and Snyder [3] suggest that the primary zone temperatures may be 200 K lower than the calculated front-end temperature shown in the abscissa of Fig. 9.

The symbols represent measured emission data (closed symbols represent NO_x data and open symbols represent CO data) after correction and the solid line is an exponential trend line drawn

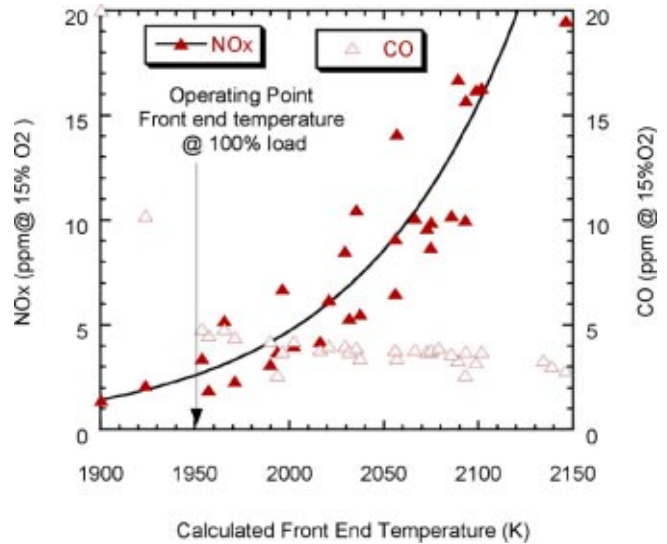


Fig. 9 Measured NO_x and CO emission for the modified Taurus 70 injector at close to 100% load condition

through the NO_x data set. Figure 9 also shows the operating temperature for this modified configuration at 100% load to be around 1950 K (1677°C/3050°F).

We observe that with this modified configuration less than 5 ppm NO_x was achieved for the operating condition. Also, less than 5 ppm NO_x was also achieved in the front end temperature range of 1900–2000 K (1627–1732°C/3000–3150°F). In diffusion flame pilot tests with a similar (same effective area) swirler, NO_x emission of 15 ppm resulted for an operating front end temperature of approximately 2140 K (1868°C/3394°F). Clearly, the use of larger air split for the catalytic pilot (can be observed from flow-splits shown in Table 2) has permitted operating at lower front end operating temperature and thereby decreased NO_x.

Figure 9 also shows that at a front end temperature of 1960 K (1687°C/3070°F), measured NO_x values of 1.9 ppm and 5.2 ppm were observed. This discrepancy in NO_x data is due to the use of very different pilot and swirler equivalence ratios for the two cases. If these data are compared to the data of Fig. 8, it can be

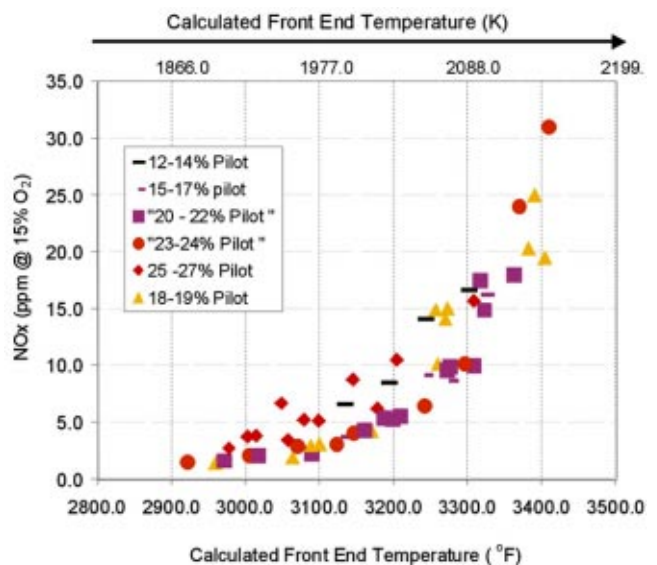


Fig. 10 NO_x emission (100% load) as function of front end temperature with percent pilot as parameter

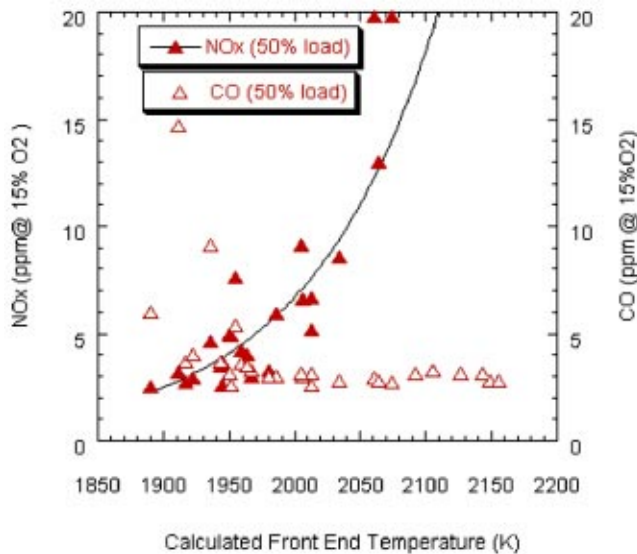


Fig. 11 Measured NO_x and CO emission for the modified Taurus 70 injector at 50% load condition

observed that a NO_x level of 1.9 ppm was observed for swirler and pilot equivalence ratios of 0.66 and 0.51, respectively, whereas for the higher NO_x case ϕ_{swirler} and ϕ_{pilot} were 0.61 and 0.71, respectively. The use of a higher pilot equivalence ratio was responsible for the increase in NO_x. Thus there is an optimum percent of pilot fuel flow above which increasing the percentage has detrimental effect on NO_x emission. This can be observed in Fig. 10, which shows the emission data plotted as function of front end temperature with percent pilot as a parameter. The data shows that 18–20% pilot to be the optimum percentage for lowest NO_x emission. It can also be observed from Fig. 10 that for a lower percent pilot of 12%, blowoff occurred at a higher front end flame temperature of approximately 3100°F.

In addition to the testing at close to 100% load condition, emission data were also obtained at 50% load condition. The 50% load condition is shown in Table 1. The catalytic reactor of the pilot was active even when the inlet temperature was dropped to the 50% load inlet temperature of 636 K (363°C/687°F).

The pressure of the system was also brought down to a pressure of 153 psia, which is the inlet pressure for Taurus 70 engine at 50% load condition. Figure 11 shows data similar to Fig. 9 but for 50% load condition. In an effort to control emission over the entire operating range, lean-premixed combustion systems are frequently designed to maintain constant flame temperature as the engine changes power level. Thus for an operating point of 1950 K, which is the same as that of the 100% load condition, it can be observed from Fig. 10, that emissions less than 5 ppm are achievable.

Combustion Noise. During the testing of the modified Taurus 70 injector at Solar's facility, pressure fluctuations in the combustor were recorded. The magnitude of the pressure fluctuations never exceeded 0.5 psi (rms) during testing including 100% and 50% load conditions.

Conclusions

A prototype catalytic pilot was fitted into an existing Taurus 70 injector without major modifications to the lean premixed portion of the injector. Testing of a single Taurus 70 modified injector (representative of the 12 injectors in an engine) has been completed. The catalytic pilot operated robustly without any flashback or autoignition even with wide variation of fuel/air ratio. No pre-burner was required for the operation of catalytic pilot from 50%

load to 100% load condition. High-pressure testing for catalytic pilot has demonstrated single digit (<5 ppm) NO_x and CO emissions along with low acoustics at 50% and 100% load conditions for Solar Turbines Taurus 70 engine.

Acknowledgments

Precision Combustion Inc. gratefully acknowledges the support of the U.S. Department of Energy SBIR program and Energy Efficiency & Renewable Energy program. DOE SBIR and DOE EREN/Office of Power Technologies funding supported development of the catalytic reactor technology. In particular we want to recognize Mr. Stephen Waslo and Ms. Patricia Hoffman from the DOE OPT program for supporting the development of the catalytic reactor technology, and Dr. Richard Johnson and Ms. Abbie Layne from the National Energy Technology Laboratory, NETL, for supporting the catalytic pilot application. PCI also gratefully acknowledges the facilities, equipments, support, and technical discussions provided by Solar Turbines.

References

- [1] Vandervort, C. L., 2000, "9 PPM NO_x/CO Combustion System for "F" Class Industrial Gas Turbines," ASME Paper No. 2000-GT-0086.
- [2] Davis, L. B., and Black, S. H., 2000, "Dry Low NO_x Combustion Systems for GE Heavy-Duty Gas Turbines," General Electric Technical Report, GER-3568G, GE Power Systems, Schenectady, NY.
- [3] Snyder, T. S., Rosfjord, T. J., Mcvey, J. B., Hu, A. S., and Schlein, B. C., 1996, "Emission and Performance of a Lean-Premixed Gas Fuel Injection System for Aero-derivative Gas Turbine Engines," *Trans. ASME*, **118**, pp. 38–45.
- [4] Kendrick, D. W., Bhargava, A., Colket, M. B., and Sowa, W. A., 2000, "NO_x Scaling Characteristics for Industrial Gas Turbine Fuel Injectors," ASME Paper No. 2000-GT-1998.
- [5] Prade, B., Streb, H., Berenbrink, P., Schetter, B., and Pyka, G., 1996, "Development of an Improved Hybrid Burner—Initial Operating Experience in a Gas Turbine," *Proceedings from the 41st ASME IGTA Congress and Exhibition*, Birmingham, UK.
- [6] Pfefferle, W., 1978, "The Catalytic Combustor: An Approach to Cleaner Combustion," *J. Energy*, **2**, pp. 142–146.
- [7] Dalla Betta, R. A., 1997, "Catalytic Combustion Gas Turbine Systems: The Preferred Technology for Low Emissions Electric Power Production and Co-generation," *Catalysis Today*, **35**, pp. 129–135.
- [8] Kraemer, G., Strickland, T. R., Pfefferle, W. C., and Ritter, J., 1998, "A Compact Catalytic Combustor System for Small Turbogenerators," *Proceeding of the Joint Power Generation Conference*, EC-Vol. 5, ASME New York.
- [9] Fant, D. B., Jackson, G. S., Karim, H., Newbury, D. M., Dutta, P., Smith, K. O., and Dibble, R. W., 2000, "Status of Catalytic Combustion R&D for the Department of Energy Advanced Turbine Systems Program," *ASME J. Eng. Gas Turbines Power*, **122**, pp. 293–300.
- [10] Dalla Betta, R. A., and Rostrup-Nielsen, T., 1999, "Application of Catalytic Combustion to a 1.5 MW industrial Gas Turbine" *Catalysis Today*, **47**, pp. 369–375.
- [11] Sadamori, H., Tanioka, T., and Matsuhisa, T., 1994, "Development of a High Temperature Combustion Catalyst System and Prototype Catalytic Combustor Turbine Test Results," *Proc. of 1st Workshop on Catalytic Combustion*, H. Arai, ed., The Research Association for Catalytic Combustion of Catalysis Society of Japan, Tokyo, pp. 18–20.
- [12] Ozawa Y., Tochiyama, Y., Mori, N., Yuri, I., Kanazawa, T., and Sagimori, K., 1998, "High Pressure Test Results of Catalytically Assisted Ceramic Combustor for a Gas Turbine," ASME Paper No. 98-GT-381.
- [13] Furuya, T., Sasaki, K., Hanakata, Y., Mitsuya, K., Yamada, M., Tsuchiya, T., and Furuse, Y., 1995, "Development of a Hybrid Catalytic Combustor for a 1300 Class Gas Turbine," *Catal. Today*, **26**, pp. 345–350.
- [14] Rollbuhler, J. R., 1989, "Fuel-Rich Catalytic Reaction Experimental Results," AIAA/SAE/ASME/ASEE, 27th Joint Propulsion Conference, Sacramento, CA.
- [15] Brabbs, T. A., and Olson, S. L., 1985, "A Soot Free Technique for In Situ Hydrogen-Like Enrichment," NASA Technical Paper #2498.
- [16] Yee, D., Lundberg, K., and Weakley, C. K., 2000, "Field Demonstration of a 1.5 MW Industrial Gas Turbine With a Low Emission Catalytic Combustion System," ASME Paper No. 2000-GT-088.
- [17] Hoshizaki, J. A., 1997, "Operating Experience of the First Solar Taurus 70S Mechanical Drive Installation," ASME Paper No. 97-GT-354.
- [18] Smith, K., and Fahme, A., 1999, "Back Side-Cooled Combustor Liner for Lean-Premixed Combustion," ASME Paper No. 99-GT-239.
- [19] Beebe, K. W., Cutrone, M. B., Matthews, R. N., Dalla Betta, R. A., Schlatter, J. C., Furuse, Y., and Tsuchiya, T., 1995, "Design and Test of a Catalytic Combustor for a Heavy Duty Industrial Gas Turbine," ASME Paper No. 95-GT-137.
- [20] Dalla Betta, R. A., Schlatter, J. C., Nickolas, S. G., Razdan, M. K., and Smith, D. A., 1995, "Application of Catalytic Combustion Technology to Industrial Gas Turbines for Ultra-Low NO_x Emissions," ASME Paper No. 95-GT-65.

Combustion System Development for the Ramgen Engine

D. W. Kendrick¹

B. C. Chenevert

B. Trueblood

J. Tonouchi

S. P. Lawlor

R. Steele

Ramgen Power Systems,
Bellevue, WA 98005

The research and development of a unique combustion engine is presented. The engine converts the thrust from ramjet modules located on the rim of a disk into shaft torque, which in turn can be used for electrical power generation or mechanical drive applications. A test program was undertaken that included evaluation of the pre-prototype engine and incorporation of improvements to the thrust modules and supporting systems. Fuel mixing studies with vortex generators and bluff-body flame holders demonstrated the importance of increasing the shear-layer area and spreading angle to augment flame volume. Evaluation of flame-holding configurations (with variable fuel injection methods) concluded that the heat release zone, and therefore combustion efficiency, could be manipulated by judicious selection of bluff-body geometry, and is less influenced by fuel injection distribution. Finally, successful operation of novel fuel and cooling air delivery systems have resolved issues of gas (fuel and air) delivery to the individual rotor segments. The lessons learned from the pre-prototype engine are currently being applied to the development of a 2.8MW engine. [DOI: 10.1115/1.1586314]

Introduction

The paper presents the design and development of a fundamentally new kind of power generation device known as the Ramgen engine. These efforts have been aided by the Department of Energy, as part of an initiative to bring viable and innovative energy technologies to market.

The design of the pre-prototype engine represents the application of well-established ramjet principles to power generation. Instead of using a ramjet to provide thrust for a supersonic aircraft or missile, the engine converts the linear thrust from a ramjet into shaft torque, which in turn drives a generator which provides electricity or shaft power for a mechanical drive applications. At maturity, the production engine will have a thermal efficiency rivaling and surpassing conventional gas turbines, with highly competitive CO and NO_x emissions through its operation in a lean premixed mode. The unique engine design also permits the use of waste fuels, including landfill gas and coal bed methane as well as synthetic ("Syn Gas") and biomass fuels, for energy production. Such atypical gaseous fuels cannot be currently utilized in conventional gas turbine systems due to the risks of autoignition, flashback, engine wear and inability to ingest atmospheric fuels directly.

The pre-prototype engine was fully assembled in Tacoma, WA in July 1998. Tests occurring in 1999 validated ignition and flame holding at idle rotor speeds, the mechanical integrity of the rotor at supersonic tip speeds, and overall system integrity. Development work conducted between late 1999 to September 2000 focused on improving combustion stability, fuel delivery methods, and air film cooling systems. These efforts resulted in substantial progress toward operation at full rotor speeds (4300 rpm, Mach 1.1 inflow conditions).

¹Corresponding author, Technology Leader Aero-Thermal. E-mail: kendriw@aol.com.

Contributed by the International Gas Turbine Institute (IGTI) of THE AMERICAN SOCIETY OF MECHANICAL ENGINEERS for publication in the ASME JOURNAL OF ENGINEERING FOR GAS TURBINES AND POWER. Paper presented at the International Gas Turbine and Aeroengine Congress and Exhibition, Amsterdam, The Netherlands, June 3–6, 2002; Paper No. 2002-GT-30084. Manuscript received by IGTI, December 2001, final revision, March 2002. Associate Editor: E. Benvenuti.

Theory of Operation: The Ramgen Engine

Ramjet Technology. The engine is based on ramjet technology which produces propulsive force by increasing the momentum of the working fluid via combustion and expansion through a supersonic nozzle, [1]. In contrast to other air-breathing engines, the working cycle of the ramjet engine is not accompanied by mechanical compression of the working fluid but rather through a shock system located within the inlet portion of the engine. This makes the ramjet engine the simplest mechanical air-breathing engine to date through its minimal use of moving parts. Figure 1 illustrates the working cycle of the ramjet engine and demonstrates the four fundamental processes: ingestion, compression, heat release, and expansion. Flame stabilization is typically achieved from a simple flame holder (V-Gutter or equivalent) located at the end of the inlet passage or dump plane and sized for the appropriate flow velocities. The air-fuel mixture entering the combustion chamber is ignited by recirculating hot combustion products comprising the recirculation zone. The flow within the combustor is subsonic; hence, an initial contraction of the flow area (throat) is necessary to both reduce the internal pressure and accelerate the flow to sonic conditions, [2]. After attaining sonic velocities, the flow encounters a diverging passage to continue the acceleration process. The addition of the nozzle allows the flow to continue to expand to supersonic exit velocities, until ambient pressure is attained—"ideal expansion."

The Ramgen Engine. The essential concept of the engine is the incorporation of one or more ramjets onto the rim of a rotor such that the thrust from the ramjets acts tangentially, causing it to rotate at supersonic rim speeds. In this way, the thrust from the ramjets is converted into shaft torque. Figure 2 is an isometric illustration of the high-speed rotor and the stationary main engine case from the pre-prototype engine. The figure illustrates how the two ramjet flow-paths are incorporated into the rim of the high-speed rotor. As shown, the two-dimensional ramjet flowpaths are open on their exterior, or radially outermost, surface. Closure of the ramjet flowpath is facilitated by the stationary surface of the main engine case. The combination of a ramjet flowpath where one of the ramjet surfaces is moving relative to the other is analogous to the moving projectile and stationary barrel wall of the ram-accelerator, [3–6]. The ramjet flow-paths are mounted on the rim of the rotor as intertwined helixes at an optimized angle to

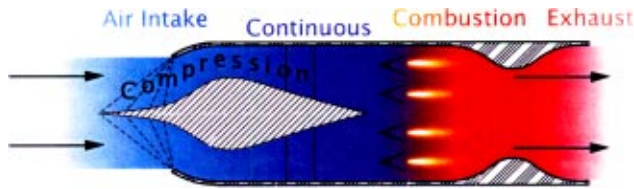


Fig. 1 Ramjet engine working cycle

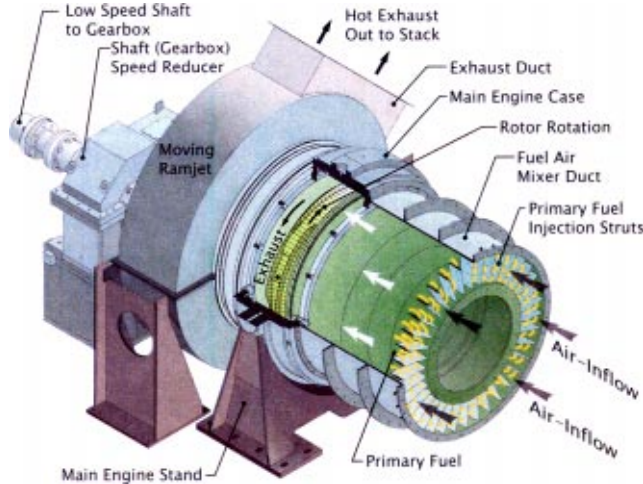


Fig. 2 The pre-prototype ramjet engine

ensure sufficient inlet length, combustor velocities, residence times and optimized thrust vectors. Combustion products from one ramjet are not ingested into its neighbor due to a mechanical separation known as a strake which wraps around the rotor's periphery (Fig. 2). Note that the helix/strake angle dictates the inlet, diffuser, combustor, and nozzle lengths, which in turn dictates the combustor velocity, residence time, and thrust vectors.

The shallow strake angle has a number of implications. First, despite the supersonic rim speeds, the axial velocity of the premix ingested is very low. As a result, the inflow can be delivered to the ramjets with minimal pressure and viscous losses, facilitating a simple premixer system. As a consequence, the engine is capable of burning a wide variety of low pressure and subquality fuels, including coal-bed methane, low-BTU natural gas, biomass fuels, and hydrogen. Secondly, the "auguring" nature of the rotor en-

ables the engine to be self-pumping, drawing in the required flow as determined by the effective flow area of the inlet system.

Figure 3 is a cut-away view depicting the flow path including the supersonic inlet, diffuser, combustor and exit nozzle for the pre-prototype engine. As shown in the figure, supersonic inflow (Station 0) meets the compression surface of the inlet. Through a series of Mach waves and strongly reflected shock, the required inlet compression is achieved. The gas is then diffused through a two dimensional diffuser whereby the static pressure rises to attain required combustor inflow conditions. A simple rearward-facing step flameholder is employed as the baseline flameholder to anchor the combustion activity. Standard diffusion piloting schemes (to be discussed) serve to anchor the flame and ensure acceptable combustion efficiency and acoustic levels. The hot combustion gases are then accelerated to supersonic velocities in the nozzle.

Experimental Results: The Pre-Prototype Engine

Experimental Setup

Engine Layout. Figure 2 illustrates the layout of the pre-prototype engine. The primary fuel employed was industrial grade methane (NG), supplied at a line pressure of two atmospheres and ambient temperature. The fuel system was manifolded and accurately measured by Worcester Model 20-755X I/P valves and Sponsler Model SP1-1/2-CB-PH7-8-4RFX turbine meters. This base fuel was supplemented with pure hydrogen to assess alterations in the ignition delay times and flame speeds on combustor performance. Hydrogen was supplied by a 1200 m³ tube trailer, with an initial supply pressure of 136 atmospheres. Consistent with the methane supply, the hydrogen was regulated and controlled via I/P control valves and turbine meters. Downstream of the metering systems, the hydrogen and methane lines were joined and routed to the main engine fuel line. To eliminate any hydrogen backflow into the lower pressure methane line, a check valve was installed in the methane line.

Three fuel systems were installed in the engine. The first or primary fuel system was via radial fuel struts located inside the inlet air annulus (see Fig. 2). Due to their upstream location, fuel delivery struts induced a high level of mixedness by the time the mixture reached the rotor. The second or tertiary fuel system was via a series of porous metal plates circumferentially arranged around the inlet, downstream of the primary fuel struts. This also achieved a high degree of mixedness due to its upstream location. Both of the fuel systems supply the bulk of the gaseous fuel to the system and required only slightly above atmospheric pressures to operate effectively. The third or pilot fuel system supplied pure fuel to the flame stabilization device (to be discussed) and paral-

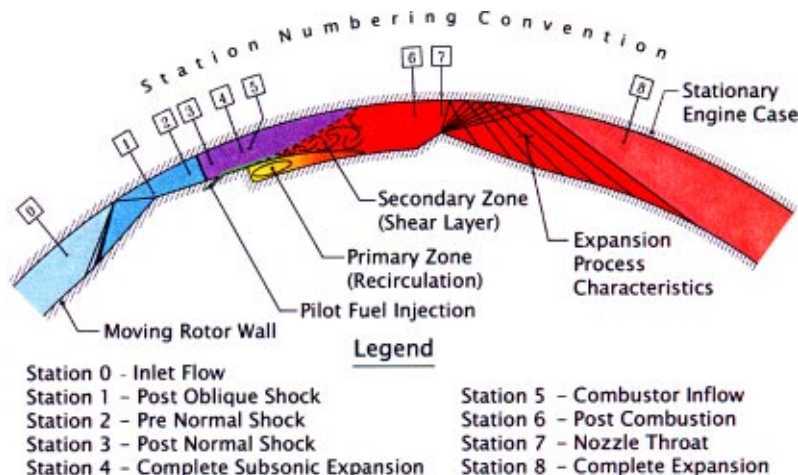


Fig. 3 Ramjet engine flow details

led similar diffusion piloting schemes, [7,8]. Injection of the pilot fuel was either through film-type slots located 1 cm upstream of the dump plane (interfacial plane dividing the end of the diffuser with the front of the combustor) and/or through the bluff-body flame stabilizer itself. For all of the reported tests, only the diffusion piloting system was employed.

As with typical combustion systems, the engine was outfitted with a variety of instrumentation and diagnostic features to maximize output data from each combustion run. Combustor dynamic pressures and floor temperatures were measured using PCB Model 112A04 piezoelectric pressure transducers and a Land Infrared IR Thermometer Model X0144IRT, respectively. The IR detector viewed the combustor through a 1 cm diameter quartz window and had a spectral range from 700–2000 nm to accurately measure the liner floor temperature without significant contamination from such combustion byproducts as CO₂ and H₂O, [9]. Two additional IR detectors were mounted on the engine inlet and exhaust, and aligned with the axis of engine rotation, to monitor the combustor and nozzle strake wall temperatures. A 3 cm diameter quartz port was also added to the exhaust duct in order to view the broadband chemiluminescence via color video cameras.

Instrumentation interfaced with the System Control and Data Acquisition System (SCADA), and included emergency shutoff control logic where appropriate. All low-speed data (gas flow rates, static pressures and temperatures) were monitored via RS-View (Allen-Bradley), while control logic was managed by RSLogics software (Allen-Bradley). All high-speed data (dynamic combustor pressures and liner temperatures) were similarly monitored in real time via a PC running a National Instruments WaveView7 system sampling up to 100 kHz per channel. Post processing was facilitated via in-house Excel macros and documented in Excel workbooks.

Table 1 details the range of flow conditions for a standard run. The “AFC” depicts the level of air film cooling (liner cooling) required to maintain acceptable combustor floor temperatures and hence mechanical system integrity. Engine starting and ramp up to

Table 1 Engine conditions (per ramjet)

| Mair (kg/s) | Mfuel (kg/s) | Pilot (% by volume) | Fuel - | H ₂ (% by volume) | AFC (% mass total flow) |
|-------------|--------------|---------------------|-------------------|------------------------------|-------------------------|
| 4 | ≤.095 | 0–100% | NG/H ₂ | 0–70% | 10% |

design point speeds was accomplished with a 447 kW AC starter motor connected to a regenerative variable frequency drive unit (VFD). The VFD also compensates for ramjet thrust generation. The starting motor is required to “start,” [5], the inlet shock system to initiate positive thrust generation. Combustion was initiated at low rotor speeds via a pulse discharged igniter timed appropriately to the location of the dump plane via magnetic pickups.

Flame Stabilizers. Three flame stabilizers were employed in this investigation (Figs. 4 and 5). The first is a 2.5 cm high, rearward-facing step flameholder built into the engine’s floor. The second builds from the first in that it employs vortex generators (“VG”s) 1 cm upstream of the step. This configuration was chosen to enhance mixing of the pilot fuel and core airflow and encourage a radial growth in combustion activity. Four sizes were investigated: 1, 1.3, 1.91, and 3.81 cm high. The final flame holder concept, “pylon,” was again an adaptation of the rearward facing step and was chosen to increase flame surface area through creation of multiple shear layers issuing from the dump plane.

Experimental Results. A timed spark from the pulsed discharge ignitors resulted in the simultaneous ignition of the combustor once pilot fuel had been initiated and engine speed had been stabilized at 800 rpm. The fuel/oxidizer mixture ratio, ignition timing and AFC flow rates were optimized for greater than 95% ignition effectiveness irrespective of the flame stabilizer employed. Ignition was verified by monitoring the high speed data

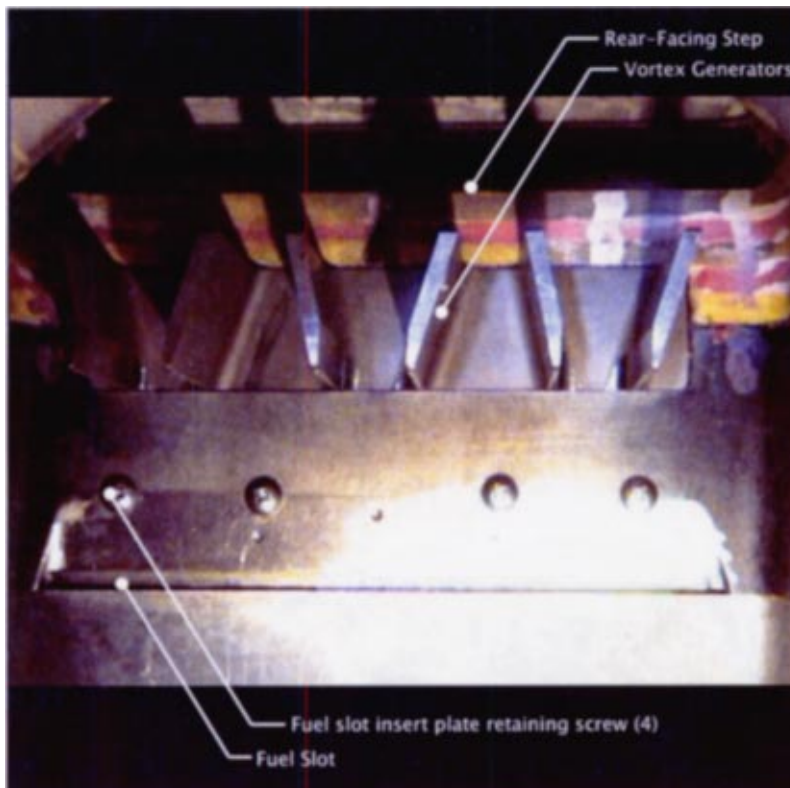


Fig. 4 Vortex generator flameholder

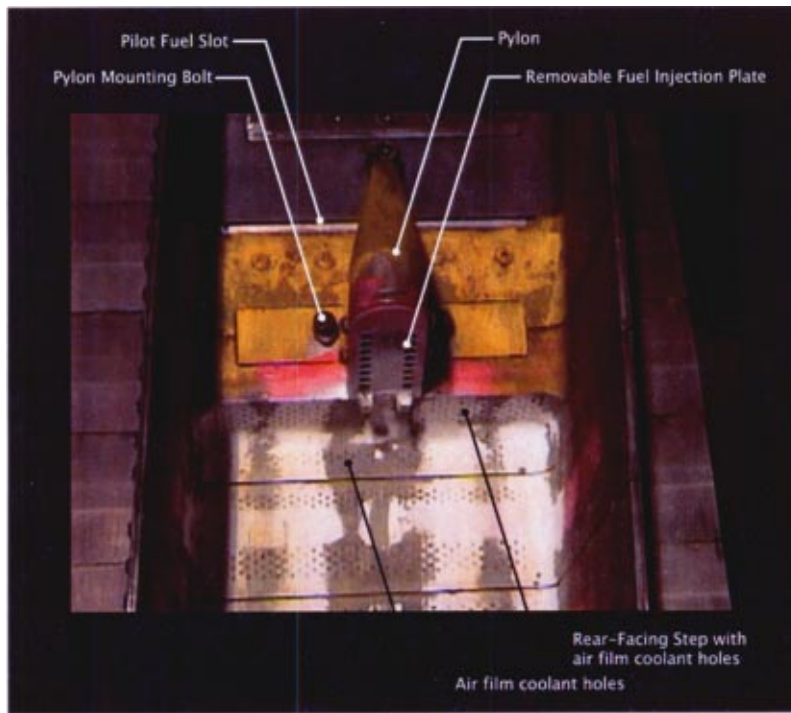


Fig. 5 Pylon and rearward-facing step

acquisition system and ensuring that both combustors revealed typical floor temperature traces as shown in Fig. 6 below. This particular test was conducted with the 1.9 cm tall VGs in place, located between the pilot fuel slot and the dump plane. Both combustors were lit as noted by the successive temperature pulses seen in the plot (top curve). It should be noted that due to the single location of the IR detector at the 12 o'clock position on the engine case, adjacent pulses denote opposite combustors. Due to the sampling rate of the detector, the trace gives an accurate measure of the floor temperature as the rotor moves relative to the fixed position of the Land IR. In fact, taking into consideration the rotor's speed and sampling rate, the rotor travels approximately 3 mm between successive samples at the design speed (4300 rpm). Also noted in the figure is the location of the beginning and end of the 33 cm long combustor as determined by magnetic pickups in the stationary engine case—see the square pulse (dump plane) and the triangle pulse (throat—middle curve). Also shown is the combustor pressure versus rotor position (bottom curve).

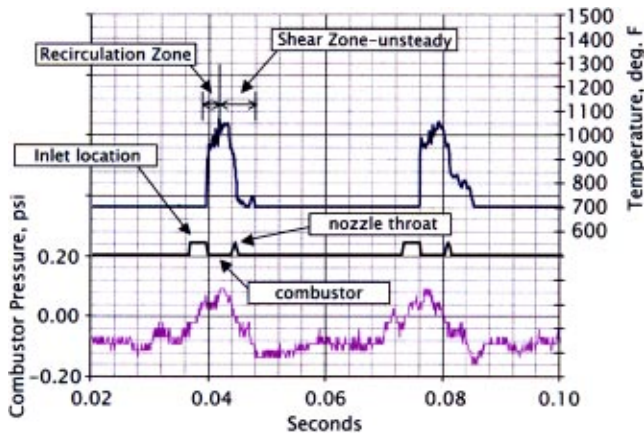


Fig. 6 Single rotor rotation showing combustor floor temperature and pressure traces

Evident is that the first half of the combustion chamber encompasses the recirculation zone and furthermore, that the location of the shear layer reattachment point is located approximately 20 cm downstream of the step (note the location of the maximum floor temperature). A relatively stationary thermal trace develops in the forward half of the combustor, fluctuating within 27 K from trace to trace. The latter half of the combustor, however, appears dominated by more incomplete combustion zones as evident by substantially greater temperature fluctuations (± 120 K) between successive cycles.

After stabilization at 800 rpm for two minutes, an automated fuel, AFC and rotor ramp schedule was initiated via the Allen-Bradley control logic (RSLogics) to attain the desired rim Mach number of approximately 1.1 (4300 rpm). This inlet Mach number permits the exit nozzle to choke, and maximizes available thrust. In practice, the ramp is broken down into three separate ramps, which are individually optimized for adequate pilot fuel, AFC and rotor acceleration: 800–2000 rpm, 2000–3000 rpm, and 3000–4300 rpm. The main issue of using a single ramp for all the quantities was evident from the video and temperature traces during the ramping process. The fluid dynamics and combustion clearly alter as inlet/rotor speeds increase—most likely the combined effects of the nonuniform boundary conditions, increasing flow velocities, centrifugal effects and stratification with increasing centrifugal loadings. The AFC flow rates were found to be critical in ensuring a sufficiently robust flame during the ramping process. If not incremented correctly, it would eventually quench the entire combustion process.

Above 2000 rpm, flame stabilization was generally restricted to the recirculation zone. The shear layer combustion, as indicated by the IR traces whose peaks move progressively upstream, was reduced as the overall combustor residence time dropped. Simple reactor modeling of the combustion zone (to be discussed) revealed that above 2000 rpm, combustion is only possible in the recirculation zone where local residence times are conducive to methane oxidation. It appears, therefore, that there is a critical rotor speed above which the shear layer combustion is replaced by combustion within the recirculation zone.

The VFD is shown to hold the rotor at 4300 rpm after some

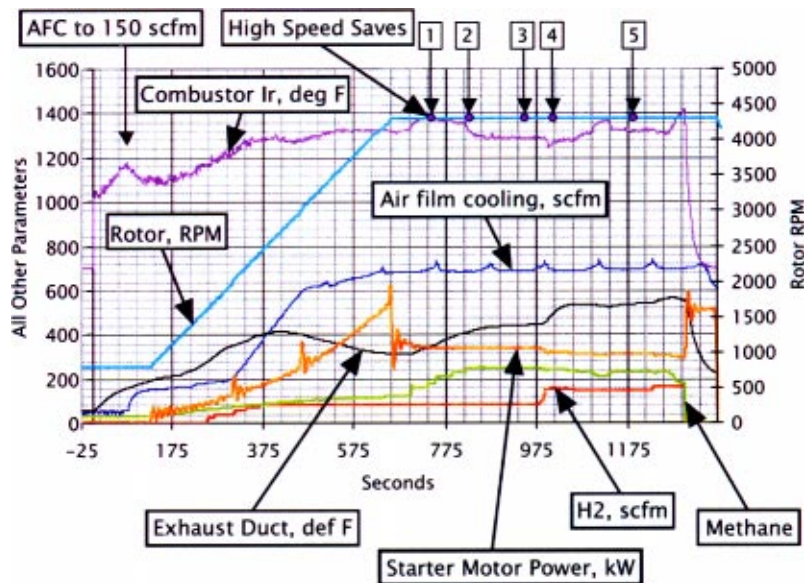


Fig. 7 NG and H₂ addition test plan with 1.3 cm VGs

perturbations at the top of the ramp (Fig. 7). This transient is due to imbalance in required motor power transitioning from ramping to steady-state operation. The power output required to maintain the engine's speed is a critical factor in the overall performance of the two thrust modules (combustor/nozzle systems). A typical test matrix (varying fuel loading between the three fuel circuits, H₂ addition, etc.) is effectuated after the rotor speed and drive stabilizes.

Typical Test Sequence. Depicted in Table 2 is a sample test run whereby the methane flow rate was incrementally ramped to a prescribed point, whereafter the hydrogen level was then incremented. Also included on the table is the VFD power required to stabilize the engine rpm at 4300 rpm. Decreases in the required VFD level is a direct measure of the effectiveness of the thrust modules and hence system efficiency. Points labeled 1 through 5 on the table refer to low-speed data points (see Fig. 7) at prescribed operating conditions. Shown in Fig. 7 is a marked drop in the combustor floor temperature between points 1 and 3. If it is assumed that the floor temperature is linked to the bulk average flame temperature, it would seem reasonable that the combustion zone is leaning out with this increase in NG flow rate and hence has passed through the stoichiometric fuel-air ratio. The argument can be extended through all points at a constant rotor speed of 4300 rpm. Figure 8 depicts the indicated combustor floor temperature versus local equivalence ratio based on an estimate of the entrained airflow rate into the recirculation zone per the rationale above. The baseline air entrainment rate was determined by assuming that the maximum combustor temperature was coincident

with stoichiometric conditions. The figure was then generated assuming the entrainment rate was preserved throughout the exercise.

Also shown in the figure are three curves estimating the floor temperature based on a simple, one dimensional model which includes the heat transfer from the gas to the floor, [10], and equilibrium calculations (STANJAN) of flame temperatures for each fuel mixture. As demonstrated by the model, it is evident that the local equivalence ratio is a significant factor in determining the gas temperature.

Details of the above combustor are further explored through chemical reactor modeling of the events depicted in Fig. 7. It should be noted that at each of the denoted points, high-speed data (IR and combustor pressure traces) were taken. A five-element reactor network was used and is shown in Fig. 9. Two reactor blocks (#1 and 2) were employed to model the shear layer which communicated with the recirculation zone (#5). The shear layer half-angle was assumed to be 5°, [11], and extended five duct heights downstream, [12]. The shear layer entrainment rate (as discussed above) was maintained at 3% and all the fuel was assumed to enter element 1 to simulate the thin layer of fuel issuing from the fuel slot. The recirculation zone element received fuel through entrainment from neighboring elements 1 and 2. The GRI-MECH 2.12 was used to model the chemical kinetics mechanism for NG/H₂ oxidation. It will be shown that the model accurately predicted the observed trends of Fig. 7.

Figure 10 shows the high speed data trace at point 1 for one rotation of the rotor. The top curve depicts the temperature while the bottom is the combustor pressure. Apparent is the forward location of the peak heat release within the combustor. A rapid drop ensues in the IR trace as the gas is unable to sustain combustion outside the recirculation zone.

Figure 11 depicts the modeling results corresponding to point 1. It reveals the predicted reactor temperatures based on the assumed flow rates and residence times determined experimentally. The highest temperature is seen to occupy reactor element 2 (2908°F) which corresponds to the shear layer near the middle and end of the recirculation zone, consistent with the high-speed trace (Fig. 10). The recirculation zone (element 5) predicts a lower temperature (1303°F), most likely attributed to the reduced fuel-air ratio and increased wall heat transfer at this location. Element 1 appears to be insensitive to local equivalence ratio and behaves more as a mixing element since its residence time is below the required

Table 2 1.3 cm tall VGs test plan

| Pt. | NG (Kg/s) | H ₂ (Kg/s) | VFD (KW) | AFC (kg/s) | T (K) |
|------|-----------|-----------------------|----------|------------|-------|
| 1 | 0.041 | 0.0034 | 361 | 0.41 | 991 |
| | 0.054 | 0.0034 | 345 | 0.41 | 1020 |
| | 0.061 | 0.0034 | 342 | 0.41 | 1020 |
| | 0.071 | 0.0034 | 335 | 0.41 | 1014 |
| | 0.078 | 0.0034 | 335 | 0.41 | 1009 |
| 2, 3 | 0.084 | 0.0034 | 335 | 0.41 | 969 |
| 4 | 0.081 | 0.0066 | 320 | 0.41 | 964 |
| | 0.071 | 0.0061 | 310 | 0.41 | 1011 |
| 5 | 0.078 | 0.0061 | 310 | 0.41 | 989 |

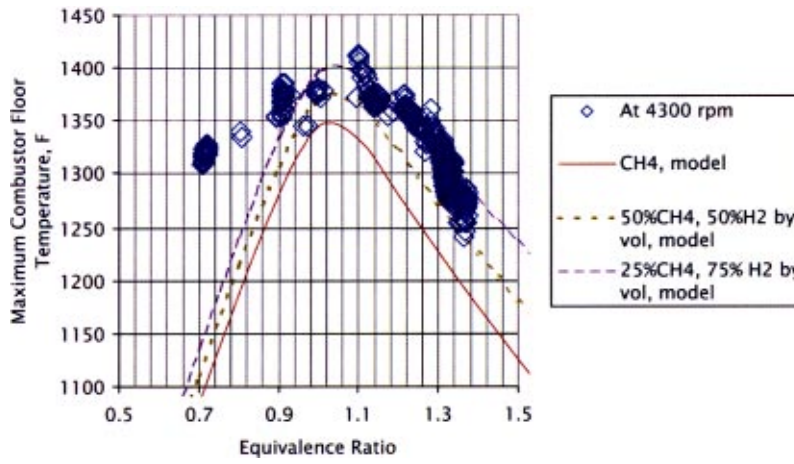
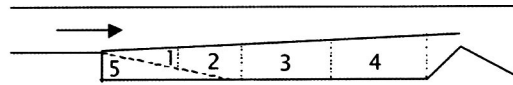


Fig. 8 Combustor floor temperatures versus equivalence ratio (data and model predictions)



- Assumptions:
1. Shear Layer half angle - 5 degrees
 2. Recirc air entrainment = 3% total air mdot
 3. All fuel enters element #1 (simulate thin layer off step)
 4. GRI-Mech 2.12 mechanism
 5. Reactor volumes fixed for each run

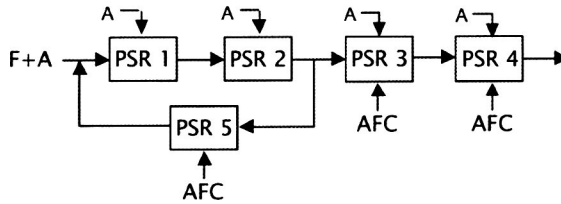


Fig. 9 Chemical reactor modeling network

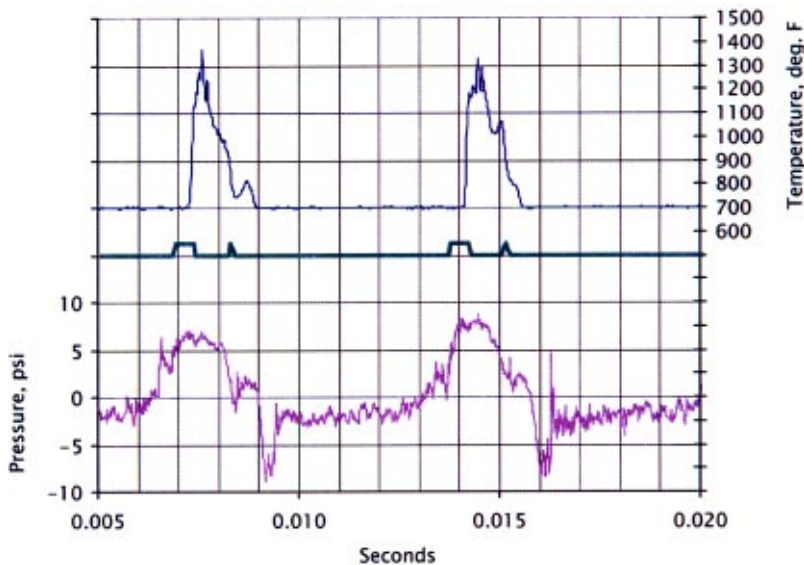


Fig. 10 High-speed data trace for point 1

blowoff residence time for its equivalence ratio ($\Phi = 1.65$). The temperature in the combustor is shown to drop off after the centrally located peak, most likely attributed to entrainment of the large, unreacted core flow and AFC flows with the products of combustion.

A similar analysis is made at point 2. The high speed data trace and reactor network modeling results are shown in Figs. 12 and 13, respectively. As evidenced in both figures, there is a downstream migration in the peak heat release location. The model results show that the fuel addition has quenched most combustion activity in the recirculation zone and shear layer and shifted it downstream. Residence times in the upstream elements (1, 2, and 5) are below the required blowout times required to sustain combustion. The high-speed data traces confirm these modeling results as evidenced by the combustion activity near the nozzle. Contrary to the model results is the reduced participation of the recirculation zone in the high-speed data. This is most likely due to the model's overprediction of fuel entering the recirculation zone.

At the termination of the experiment, the maximum combustor floor temperature is 1413°F. Combustion modeling results for this condition appear in Fig. 14 below. It appears that the recirculation zone residence times are adequate to sustain combustion with the hydrogen addition (compare Figs. 13 and 14) and such predictions are aligned with the temperature rise at the end of the test (Fig. 7).

Comparisons in Flame Stabilization Configurations. As noted previously, three flame stabilization devices were tested: a baseline, rearward-facing step, a rearward-facing step and VGs, and a rearward-facing step and pylon. The mechanism for fuel-air mixing and flame stabilization with the baseline rearward facing step flameholder is conventional shear layer mixing and creation of a recirculation zone, [13]. The combustion is sustained by the steady entrainment of the combustion byproducts into the shear

layer, which ignites the incoming cold charge. The success of this flameholder, therefore, depends on the spreading rate of the shear layer, which must extend to the opposite wall to ensure high combustion efficiency. The inflow shear spreading half-angle is approximately 5°, [11]. This angle (ϕ) can be augmented though combustion, [14], by the following relation, where S_T is the turbulent flame speed and U is the approach velocity:

$$\phi = \sin^{-1} \left(\frac{S_T}{U} \right). \quad (1)$$

Recognizing that the spreading angle can be augmented with a fuel with a higher turbulent flame speed, hydrogen was blended with the baseline methane fuel. Note that hydrogen's turbulent flame speed is up to four times methane's flame speed, [14]. Tests with the baseline rearward-facing step revealed poor mixing between the pilot fuel and mainstream airflow. As such, most of the pilot fuel directly entered the recirculation zone, resulting in over-rich conditions. These disadvantageous situations resulted in significant quenching of the combustion directly behind the step, and often shifted the combustion zone towards the center of the combustion chamber. Efforts were focused on enhancing the mixing of the pilot fuel stream with the main core flow with the implementation of the VGs.

Vortex generators of various heights were examined with the intention of creating sufficient streamwise vorticity to enhance mixing of the pilot and core air flows to radially extend the combustion zone. Throughout the series of tests, it was found that there was a delicate balance between increased mixing (taller VGs) and reduced combustion stability. The larger the VGs, the less stable the combustion zone, most likely due to the increased turbulence and quenching activity promoted by the larger struts, [15]. A sample high speed trace is shown in Fig. 15 for the optimal VG configuration (1 cm long).

Figure 15 shows that there is a greater streamwise distribution in temperature relative to the baseline step and secondly, the combustor pressure is more uniform. This is important since it is this pressure which forces the exhaust nozzle to choke, maximizing system performance.

The VGs provided some improvement with regards to heat release distribution and fuel-air mixing but failed to demonstrate a dramatic decrease in VFD power over the baseline configuration with fuel loading variations. The next series of tests investigated the Pylon design with various configurations in fuel injection (Fig. 5). This concept provides the greatest flexibility in fuel placement,

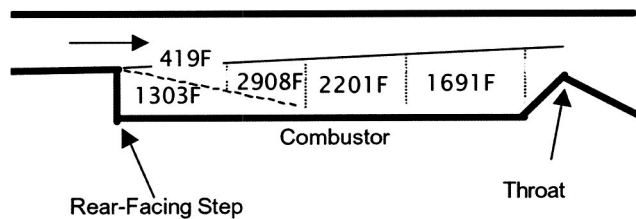


Fig. 11 Gas temperature modeling results for point 1

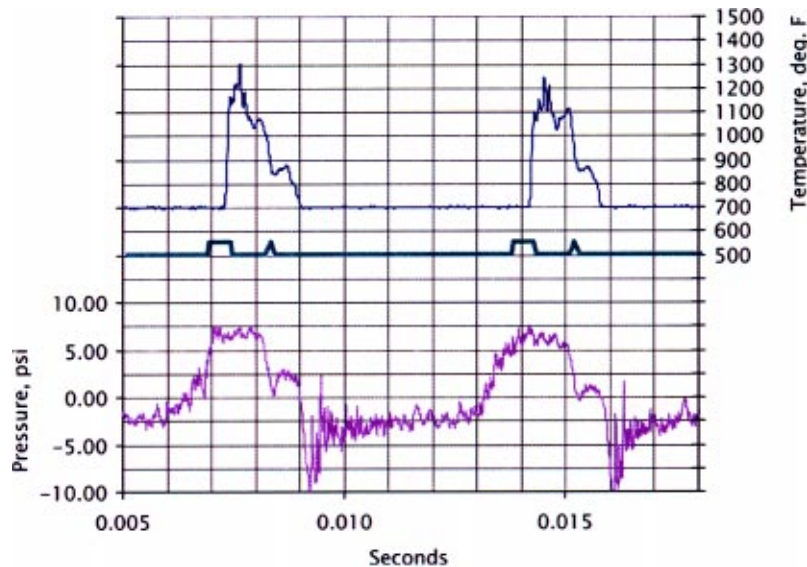


Fig. 12 High-speed data trace for point 2

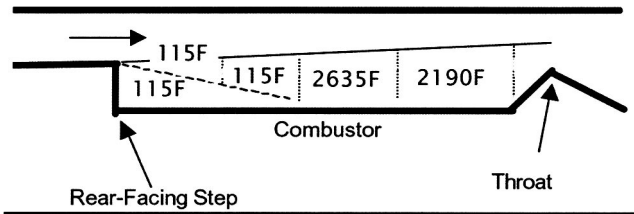


Fig. 13 Gas temperature modeling results for point 2

affords the combustor with the largest possible combustion volume to maximize heat release and provides the largest flame surface area. Such attributes favor an increase in overall combustion efficiency.

Preliminary CFD simulations using Star-CD showed encouraging results (Fig. 16). The pressure based solver was employed using the standard $k-\epsilon$ turbulence model and included the effects of rotation. The figure depicts total temperature contours through various axial slices of the combustor. Apparent is the radial growth in combustion activity near the center line due to the presence of the pylon. Unfortunately, due to the insufficient blockage afforded by the pylon and the high momentum of the approach flow, it was ineffective in extending combustion in the axial direction. The design did, however, provide a more homogenous temperature distribution relative to the proceeding designs, irrespective of the fuel injection configuration (Fig. 17). This test was conducted with pilot fuel issuing from a single, 32 mm diameter hole from the pylon's faceplate and from the fuel slot along the

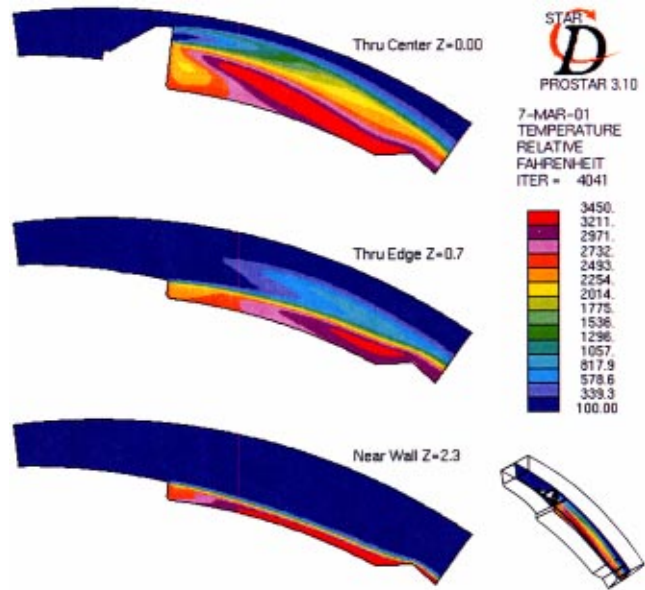


Fig. 16 Temperature contours from a CFD simulation of the pylon flame stabilizer

floor. Due to this more uniform and elevated temperature distribution, combustion intensity and pressures were increased.

An overall comparison between VG and pylon test data is made by comparing corresponding fuel loadings (BTUs of fuel) to VFD power for a rotor speed of 4300 rpm. Lower VFD levels for the same fuel (BTU) loading would therefore signify higher system effectiveness. A summary plot appears in Fig. 18. All VG tests are denoted by square symbols while their pylon counterparts are denoted by diamonds. Apparent is the more compact grouping of the pylon data. The dotted box, which captures all such runs, further illustrates the fact that increasing fuel loading (expressed in BTU/s) lowers required VFD power. The greater slope and compactness of the pylon data illustrates that it is more effective in flame holding, providing increased flame surface area and hence higher burner pressures through increased combustion activity. The net effect is higher ramjet thrust and overall cycle efficiency.

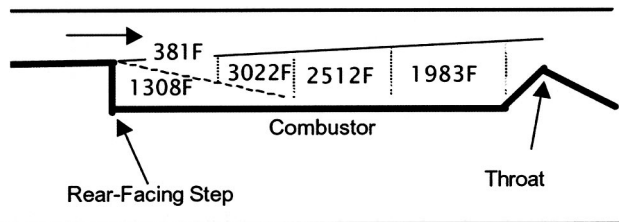


Fig. 14 Gas temperature modeling results for gas off

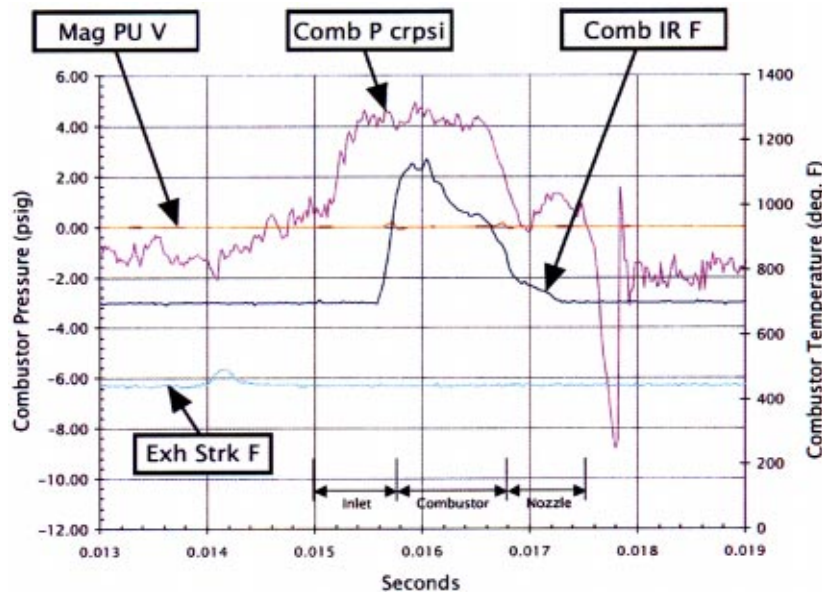


Fig. 15 High-speed trace for the 1 cm tall VGs

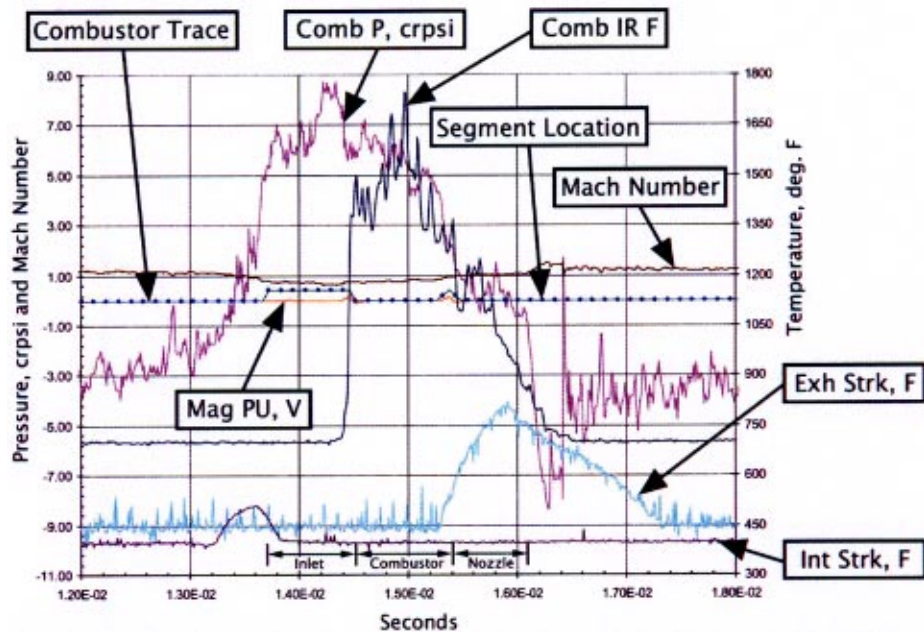


Fig. 17 High-speed trace for the pylon flame stabilizer with 32 mm fuel hole

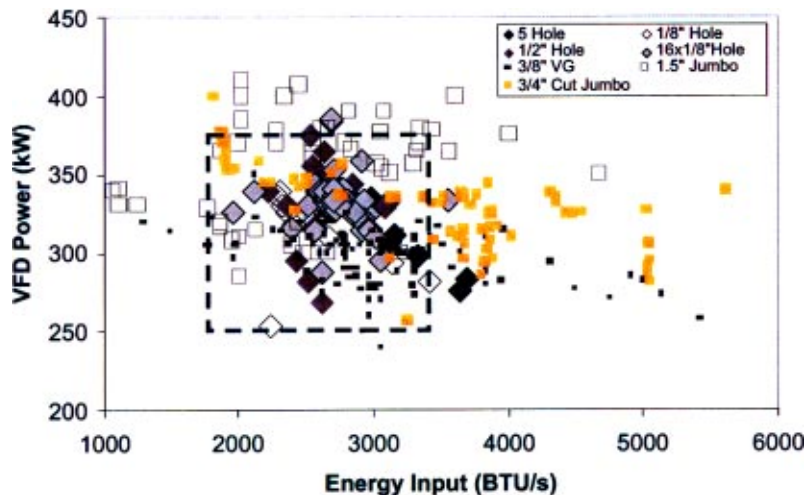


Fig. 18 VFD comparisons between all VG and pylon runs

Conclusions

The preliminary results from a pre-prototype engine are presented. Initial combustion tests reveal the importance of flame volume and surface area for increased combustion efficiency, irrespective of fuel injection schemes. Chemical kinetic modeling was shown to accurately depict the essential flow features of a sample test matrix whereby stepwise increases in NG and hydrogen flow rates were separately investigated. The results confirm the visual observations that dramatic flow field variations occur both during ramp up and pilot fuel excursions due to the nature of the engine.

Acknowledgments

This effort was funded in part by the Department of Energy under the cooperative agreement #DE-FC26-00NT40, awarded between the period of Sept. 29, 2000 and Aug. 31, 2001. The computational support (Star CD) was provided by Combustion Science and Engineering (Columbia, MD).

References

- [1] Heiser, W. H., and Pratt, D. T., 1994, *Hypersonic Airbreathing Propulsion* (AIAA Ed. Series), AIAA, Washington, DC.
- [2] Oates, G. C., 1997, *Aerothermodynamics of Gas Turbine and Rocket Propulsion* (AIAA Ed. Series) AIAA, Washington, DC.
- [3] Bogdanoff, D. W., 1992, "Ram Accelerator Direct Space Launch System: New Concepts," *J. Propul. Power*, **8**(2), pp. 481–490.
- [4] Harsha, P. T., and Edelman, R. B., 1981, "Assessment of a Modular Ramjet Combustion Model," *J. Spacecraft*, **19**(3), pp. 430–436.
- [5] Hertzberg, A., Bruckner, A. P., and Bogdanoff, D. W., 1988, "Ram Accelerator: A New Chemical Method for Accelerating Projectiles to Ultrahigh Velocities," *AIAA J.*, **26**(2), pp. 195–203.
- [6] Yungster, S., Eberhardt, S., and Bruckner, A. P., 1991, "Numerical Simulation of Hypervelocity Projectiles in Detonable Gases," *AIAA J.*, **29**(2), pp. 187–193.
- [7] Kendrick, D. W., Anderson, T. J., Sowa, W. A., and Snyder, T. S., 1999, "Acoustic Sensitivities of Lean-Premixed Fuel Injectors in a Single Nozzle Rig," *ASME J. Eng. Gas Turbines Power*, **121**, pp. 429–436.
- [8] Snyder, T. S., Rosfjord, T. J., McVey, J., Hu, A., and Schlein, B., 1994, "Emissions and Performance of a Lean-Premixed GasFuel Injection System for Aeroderivative Gas Turbine Engines," *ASME Paper No. 94-GT-234*.
- [9] Eckbreth, A. C., 1988, *Laser Diagnostics for Combustion Temperature and Species*, Turnbridge Wells, Kent, UK.

- [10] Kreith, F., and Bohn, M. S., 1986, *The Principals of Heat Transfer*, Harper and Row, Cambridge, UK.
- [11] Schlichting, H., 1979, *Boundary-Layer Theory*, McGraw-Hill, New York.
- [12] Ozawa, R. I., 1981, "Survey of Basic Data on Flame Stabilization and Propagation for High Speed Combustion Systems," Paper No. AFAPL-TR-70-81.
- [13] Zukoski, E. E., 1978, "Afterburners," *The Aerothermodynamics of Aircraft Gas Turbine Engines*, Gordon C. Oates, ed., Air Force Propulsion Laboratory, AFAPL-TR-78-52, Chap. 21.
- [14] Glassman, I., 1987, *Combustion*, Academic Press, San Diego, CA.
- [15] Lefebvre, A. H., 1983, *Gas Turbine Combustion*, Hemisphere, Washington, DC.

S. M. Martin

17136 Bak Road,
Belleville, MI 48111-3525
e-mail: smmartin7@netscape.net

J. C. Kramlich

e-mail: kramlich@me.washington.edu

G. Kosály

e-mail: kosaly@me.washington.edu

J. J. Riley

e-mail: riley@me.washington.edu

Department of Mechanical Engineering,
University of Washington,
Box 352600,
Seattle, WA 98195-2600

The Premixed Conditional Moment Closure Method Applied to Idealized Lean Premixed Gas Turbine Combustors

This paper presents the premixed conditional moment closure (CMC) method as a new tool for modeling turbulent premixed combustion with detailed chemistry. By using conditional averages the CMC method can more accurately model the effects of the turbulent fluctuations of the temperature on the reaction rates. This provides an improved means of solving a major problem with traditional turbulent reacting flow models, namely how to close the reaction rate source term. Combined with a commercial CFD code this model provides insight into the emission formation pathways with reasonable runtimes. Results using the full GRI2.11 methane kinetic mechanism are compared to experimental data for a backward-facing step burning premixed methane. This model holds promise as a design tool for lean premixed gas turbine combustors. [DOI: 10.1115/1.1587740]

Introduction

The premixed conditional moment closure (CMC) method is developed and coupled to a commercial CFD program to model an idealized lean premixed (LMP) gas turbine (GT) combustor, a two-dimensional backward-facing step burning premixed methane at an equivalence ratio of 0.9. Using the full GRI2.11 kinetic mechanism, temperature, velocity, and major species are compared to data with good agreement. Intermediate species that contribute to the three NO_x formation pathways are calculated, but are not presented here. The CMC method is a new theory that has been applied to nonpremixed combustion with good success (Klimenko and Bilger [1] and Smith [2]). The application of the CMC method to premixed systems has been proposed, but has not yet been done. The premixed CMC method replaces the species mass fractions as independent variables with species mass fractions that are conditioned on a reaction progress variable (RPV). Conservation equations for these new variables are then derived and solved. The general idea behind the premixed CMC method is that the behavior of the chemical species is closely coupled to the reaction progress variable (Klimenko and Bilger [1]). Thus, species conservation equations that are conditioned on the RPV will have terms involving the fluctuation quantities that are much more likely to be negligible, hence improving the accuracy of the chemical kinetic rates. In essence, knowledge of the statistics of the RPV contains most of the information needed to calculate species mass fractions. In return for this better conditioned problem, an increase in dimensionality occurs and a new conservation equation (for the RPV) must be solved, along with a conservation equation for the variance of the RPV. The CMC method accounts for the interaction between scalar dissipation (micromixing) and the chemical kinetics, while decoupling the kinetics from the bulk flow (macromixing). The RPV and its variance are used to generate an assumed shape beta function PDF that is used to integrate the conditioned mass fractions to obtain the species mass fractions in physical space. In certain cases the conditioned mass fractions are uniform over the computational domain, reducing the dimensionality of the problem. It will be shown that lean premixed gas

turbine combustors fall into this regime. The premixed CMC method had runtimes approximately twice as long as a three-step global mechanism using the same CFD program, while providing a better match of the data and details of the intermediate species. The goal of this research is to develop the model and validate it against a simplified reactor that has many of the same features as a LPM GT combustor. Further research will enhance the model and validate it against LPM GT combustor data.

Formulation

For a turbulent premixed combustion model to accurately predict the emissions from a LPM GT combustor it must account for the effects of temperature fluctuations on the reaction rates, model the effects of micromixing on the chemical kinetics and allow detailed chemistry. Most premixed turbulent combustion models used to date have been based on chemical reactor modeling or the eddy breakup model, mainly because of their relatively short runtimes. Chemical reactor models break the flow into a series of perfectly stirred reactors and plug flow reactors, which allow full kinetic mechanisms, but are limited to the infinite mixing and no mixing regimes, respectively. The eddy breakup (EBU) model and its variant, the eddy dissipation model assume the reaction rates are mixing limited and base the reaction rates on ad hoc mixing models. While these models are popular for their runtimes, they do not model the interaction between the small scale mixing and the chemical kinetics, so they are limited in their capability to predict the emissions of LPM GT combustors. Recently PDF methods have been used to model LPM GT combustors. These models account for the temperature fluctuation in the reaction rates and allow larger kinetic models, but require a model for the micromixing. So far a universally accepted micromixing model has not been developed and it is still open to debate whether the improved accuracy over earlier models justifies the longer runtimes. The flamelet and g-equation models are only valid for flames in the wrinkled and corrugated flamelet regimes and are not valid for the high intensity mixing of a LPM GT combustor.

The CMC method was independently developed by Klimenko [3] and Bilger [4,5] from first principles as a model for turbulent non-premixed flames. Rather than using conventional averages, the reactive scalars are conditionally averaged on the mixture fraction. Klimenko [3] has emphasized that turbulent diffusion in mixture fraction space can be modeled more rigorously than in physical space. Bilger [4,5] observed that most fluctuations in

Contributed by the International Gas Turbine Institute (IGTI) of THE AMERICAN SOCIETY OF MECHANICAL ENGINEERS for publication in the ASME JOURNAL OF ENGINEERING FOR GAS TURBINES AND POWER. Paper presented at the International Gas Turbine and Aeroengine Congress and Exhibition, Amsterdam, The Netherlands, June 3–6, 2002; Paper No. 2002-GT-30094. Manuscript received by IGTI, Dec. 2001, final revision Mar. 2002. Associate Editor: E. Benvenuti.

mass fraction were associated with fluctuations of the mixture fraction. Rather than considering flame surface statistics and the laminar reactive-diffusive structure attached to the flame surface as in the flamelet model, the CMC model is based on conditional moments at a fixed location and time within the flow field.

A conditional average is an average taken with only those members of the whole ensemble that meet a specified condition (Bilger [4]). For the non-premixed method the conditioning variable is normally the mixture fraction and the conditional average is taken with the mixture fraction within an infinitesimal range of a set value. For the premixed CMC method the conditioning variable is the reaction progress variable (RPV), defined later. A conditioned variable is not only a function of position in space (and time in unsteady problems) but also of the mixture fraction (or RPV). The dimension of the problem is increased and experimental data must be recorded over the additional dimensions (Bilger [4]). However, experiments have shown that for some problems the conditioned variables are nearly constant in some coordinates, so the spatial derivatives can be ignored. Crocco [6] was the first to use a normally dependent variable as an independent variable in boundary layer theory. A simplification of the conservation equations for the remaining dependent variables results when they are transformed into the new coordinate system (Bilger [4]).

Before developing the premixed CMC equations it is useful to define a unconditional and conditional averaged variable. An unconditional average is defined as follows (also termed ensemble average):

$$\langle Y(x,t) \rangle = \frac{1}{N} \sum_i^N Y^i(x,t). \quad (1)$$

The $\langle \rangle$ brackets denote an averaged value. The instantaneous values are defined as follows:

$$Y(x,t) = \langle Y(x,t) \rangle + y(x,t) \quad (2)$$

where Y is the instantaneous value at a given location and time, $\langle Y \rangle$ is the unconditioned average, and y is the fluctuating (deviatoric) term. The governing conservation equations are usually based on the unconditional average values (due to Reynolds or Favre averaging) and require closure models for the fluctuating terms. Normally first-order closure models are used, which are based on the average values. If the fluctuating terms are large relative to the average values the model will be inaccurate. This is one problem with traditional CFD combustion modeling. A conditioned average is defined as follows (Bilger [4]):

$$\langle Y(x,t) | x = x_a \rangle = \frac{1}{N} \sum_i^N Y^i(x,t) \delta(x^i - x_a). \quad (3)$$

Only values of Y are averaged that meet a given condition, in this case $x = x_a$. A shorthand notation for the conditional average is $\langle Y | x_a \rangle$. The vertical bar means that only those values that meet the conditions to the right of the bar are used in the averaging. For every value of the conditioning variable, x_a , there will be a different average value $\langle Y | x_a \rangle$, thus increasing the dimensionality of the problem. The instantaneous value is similar to the unconditional form.

$$Y^i(x,t) = \langle Y | x_a \rangle + y_x^i(x,t) \quad (4)$$

With the correct choice of conditioning variable the fluctuating term in Eq. (4) will be smaller than in Eq. (2). In essence, by increasing the dimensionality of the problem, the fluctuating terms are reduced, which should allow more accurate prediction of the average species mass fractions. Additional conditioning constraints can be added to further reduce the fluctuating terms.

The conditioning variable should be selected to describe the instantaneous degree of reactedness, so scatter caused by variations in the reactedness is eliminated from the conditionally aver-

aged statistics. The conditioning variable used here is the reaction progress variable (RPV) based on the sensible enthalpy defined in Eq. (10).

The premixed CMC equations using Smith's [2] derivation (which follows Klimenko [3]) starts from the conservation of species mass fraction equation given below. Bilger's [4,5] derivation uses different equations and assumptions than Klimenko, but develops the same equations.

$$\rho \frac{\partial Y_i}{\partial t} + \rho \mathbf{u} \cdot \nabla Y_i = \nabla \cdot (\rho D_i \nabla Y_i) + \rho \omega_i \quad (5)$$

Here ρ is the density, Y_i is the species mass fraction, \mathbf{u} is the velocity vector, D_i is the species diffusivity, ω_i is the production rate (1/s) of species Y_i , and $i = 1, ns$ where ns is the number of species.

The enthalpy conservation equation is given as follows:

$$\rho \frac{\partial h}{\partial t} + \rho \mathbf{u} \cdot \nabla h = \nabla \cdot (\rho D_h \nabla h) - \rho W_R + \frac{\partial P}{\partial t}. \quad (6)$$

Here h is enthalpy, D_h is the enthalpy diffusivity, ρW_R is the heat loss due to radiation (it is positive for heat loss), and P is the pressure. Klimenko and Bilger [1] and Bilger [7] assume that $Le = 1$, so all the diffusivities are equal. Below is the sensible enthalpy equation, which is derived in Martin [8].

$$\rho \frac{\partial h^s}{\partial t} + \rho \mathbf{u} \cdot \nabla h^s = \nabla \cdot (\rho D_h \nabla h^s) - \rho W_R + \frac{\partial P}{\partial t} - \rho \sum_i \omega_i h_{f,i} \quad (7)$$

where h^s is the sensible enthalpy and $h_{f,i}$ is the species heat of formation, defined as follows:

$$h = h^s + \sum_i^{ns} h_{f,i} Y_i \quad (8)$$

$$h^s = \sum_i^{ns} \int_{T_0}^T Y_i C_{p,i} dT. \quad (9)$$

The reaction progress variable (RPV) is defined as

$$c(\mathbf{x},t) \equiv \frac{h^s - h_u^s}{\Delta h_{ad-u}^s}. \quad (10)$$

The u subscript signifies the unburned state. The denominator is the difference in sensible enthalpy between the adiabatic equilibrium and unburned states, which is fixed for a given mechanism and initial conditions. C will have values between 0.0 and 1.0. The conservation equation for c is derived in Martin [8] and is shown as follows:

$$\begin{aligned} \frac{\partial \bar{\rho} \bar{c}}{\partial t} + \nabla \cdot [\bar{\rho} \bar{u} \bar{c}] &= \nabla \cdot \left(\frac{\mu_t}{\sigma_c} \nabla \bar{c} \right) + \frac{[\bar{\rho} W_R] - \left[\sum_i \bar{\rho} \bar{\omega}_i h_{f,i} \right]}{\Delta h_{ad-u}^s} \\ &\equiv \nabla \cdot (\bar{\rho} D_h \nabla \bar{c}) + \bar{\rho} \bar{S}_c. \end{aligned} \quad (11)$$

Equation (11) is essentially a nondimensional energy (enthalpy) equation.

The premixed CMC equation is derived in Martin [8] using the above relations to give

$$\begin{aligned} \langle \rho | \zeta \rangle \frac{\partial Q_i}{\partial t} + \langle \rho u | \zeta \rangle \cdot \nabla Q_i &= \langle \rho \omega_i | \zeta \rangle + \langle \rho D (\nabla c)^2 | \zeta \rangle \frac{\partial^2 Q_i}{\partial \zeta^2} \\ &\quad - \langle \rho S_c | \zeta \rangle \frac{\partial Q_i}{\partial \zeta} + \langle e_y | \zeta \rangle + \langle e_Q | \zeta \rangle \end{aligned} \quad (12a)$$

$$\langle e_y | \xi \rangle \equiv \frac{1}{P_\xi} \left\{ 2 \left[\langle \rho D(\nabla c \cdot \nabla y_i) | \xi \rangle \frac{\partial P_\xi}{\partial \xi} \right] - \frac{\partial}{\partial \xi} [\langle \rho D(\nabla c)^2 y_i | \xi \rangle P_\xi] - \nabla \cdot (\langle \rho u y_i | \xi \rangle P_\xi) \right\} - (\langle \rho S_{c y_i} | \xi \rangle) \quad (12b)$$

$$\langle e_Q | \xi \rangle \equiv [\langle \rho(\nabla c \cdot \nabla Q_i) | \xi \rangle] + \nabla \cdot (\langle \rho D | \xi \rangle \nabla(Q_i P_\xi)) \quad (12c)$$

where e_y and e_Q are error terms that require models to close. The terms in Eq. (12a) are the time rate of change of Q , the convection in physical space, the production due to reactions, turbulent diffusion in c space and convection in c space. This equation describes the conditional averages of the species as a function of space and c . It would nominally be solved as a coupled system with equations for momentum, turbulence model and c (mean and variance). Q is defined as the value of the species mass fraction or enthalpy conditioned on the RPV (ξ) being equal to a given value η , Bilger [4].

$$Q \equiv \langle Y(x, t) | \xi = \eta \rangle \quad (13)$$

One of the main differences between the premixed and non-premixed CMC methods is that the premixed version is based on a nonconserved scalar, which adds an additional term to the equations (the third term on the RHS of Eq. 12(a)). This extra term makes the equations more difficult to solve as explained below. The only known attempt to solve the premixed CMC equations was by Smith [2], who was not able to obtain a converged solution.

Non-premixed jet flame data have suggested that the spatial derivatives in Eq. (12a) can often be neglected (Klimenko and Bilger [1], Smith [2], and Bilger [9]). This is particularly true for the radial dependence in jet flames, but it is often also true for the axial dependence in jet flames with fast chemistry (e.g., hydrogen flames). Note that this does not imply that unconditional mean species mass fractions are independent of axial or radial position. Instead, it implies that the conditional mass fractions are independent of spatial location, while the PDF depends on spatial location through the RPV and its variance. If the spatial dependence can indeed be neglected, a substantial reduction in computational complexity can be obtained. Specifically, the behavior of the conditioned variables depend only on the conditioning variable (mixture fraction or c) and its scalar dissipation, which will vary with position. Thus, the calculation of the conditioned variables can be decoupled from the flow field calculation, since the only interlinkage will be through c and its scalar dissipation. This opens the possibility of doing a detailed chemistry calculation off line and using a lookup table to feed information back to the fluid dynamics calculation.

For premixed problems with high mixing intensities (i.e., in the distributed reaction regime) the conditioned species may be sufficiently uniform within the reactor to allow the equations to be simplified by neglecting spatial derivatives (Smith [2]). This is along the lines of a partially stirred reactor, which has strong back mixing giving nearly uniform properties throughout the reactor. This is a generalization of a perfectly stirred reactor, and is similar to a LPM GT combustor. Here this hypothesis will be used and the validity of this assumption will be discussed in the next section. With this assumption the equations are volume averaged over the entire reactor volume to give (see Martin [8] for the derivation).

$$\{ \{ \langle \rho \omega_i | \xi \rangle \} \} - \{ \{ \langle \rho S_{c i} | \xi \rangle \} \} \frac{\partial Q_i}{\partial \xi} + \{ \{ \langle \rho D(\nabla c)^2 | \xi \rangle \} \} \frac{\partial^2 Q_i}{\partial \xi^2} = 0 \quad (14)$$

The double curly brackets, $\{ \{ \} \}$, signify volume averaging. The volume averaging will cause the error terms in Eq. (12a) to be negligible. Besides the advantage of removing spatial dependence from the equation, the other advantage of volume averaging is that it also eliminates the conditioned velocity term, which is difficult

to model. This leaves just three terms in Eq. (14), which are the production, diffusion and convection in c space, respectively.

Equation (14) is a set of $ns + 1$ (ns is the number of species) second order ordinary differential equations in c space. Here only adiabatic problems were investigated, so the conditional enthalpy equation is not needed. For a given chemical kinetic mechanism the only inputs are the initial conditions and the scalar dissipation (micromixing frequency) given as follows:

$$\{ \{ \langle N | \xi \rangle \} \} \equiv \{ \{ \langle \rho D(\nabla c)^2 | \xi \rangle \} \} \approx \{ \{ \langle \rho D(\nabla c)^2 \rangle \} \} \quad (15)$$

N is calculated from the flow field and used in the table lookup to obtain the conditioned species and temperature. The sensitivity of the scalar dissipation on the solution will be explored in the next section. The conditioned reaction rate is approximated as

$$\langle \rho \omega | \eta \rangle \approx \omega(Q_1, Q_2, \dots, Q_{ns}, Q_h). \quad (16)$$

The fluctuating components of the species and enthalpy are much smaller in conditioned space, so this will give a much better approximation of the reaction rate than in normal unconditioned methods. This set of equations was solved over a range of N and used as a table lookup for the results discussed in the next section. Equation (16) is also used to calculate S_c in Eq. (14).

To convert the conditioned data to unconditioned data an assumed shape beta function PDF is used based on the RPV from Eq. (11) and its variance calculated from the following equation.

$$\frac{\partial \bar{\rho} \bar{c}^{n2}}{\partial t} + \nabla \cdot [\bar{\rho} \bar{u} \bar{c}^{n2}] - \nabla \cdot \left[\frac{\mu_t}{\sigma_c} \nabla \bar{c}^{n2} \right] = C_{c1} \mu_t (\nabla \bar{c})^2 - C_{c2} \bar{\rho} \frac{\bar{\epsilon}}{\bar{K}} \bar{c}^{n2} - 2 \frac{\left[\bar{\rho} \sum_i \bar{c}'' \bar{\omega}'' h_{f,i} \right]}{\Delta h_{ad-u}^s} \quad (17)$$

The last term is modeled with the following relationship, see Martin [8] for the derivation.

$$\sum_i^{NS} \frac{\bar{c}'' \bar{\omega}'' h_{f,i}}{h_{ad-u}^s} = 100 \frac{\bar{c}^{n2}}{\bar{T}(\bar{c} + 0.167)} \sum_i^{NS} \left\{ \frac{\bar{\omega}_i h_{f,i}}{h_{ad-u}^s} \right\} \quad (18)$$

Results and Discussions

The test problem used to validate the model was an experiment by El Bahawy et al. [10] that consists of a flame stabilized by a backward-facing step. Premixed natural gas (94% CH₄) and air are flowed across the backward-facing step, which establishes a recirculation zone that stabilizes the flame. A flame sheet is anchored to the lip of the step, from which it progresses across the free portion of the duct. The flame sheet touches the wall at a specific axial location, and matching this "touching distance" is a challenging test of the various modeling approaches. The Reynolds number based on step height was approximately 13,500 and the airflow rate was 125 kg/hr giving an inlet velocity of 10.5 m/sec at 300 K. Velocity measurements of nonreacting (not shown in their paper) and reacting flows were measured with a laser-Doppler anemometer. Both mean and RMS axial velocities are reported. Temperature measurements were taken with a bare thermocouple and have an error of up to 40 K due to radiative heat transfer between the thermocouple and the cold walls. The instruments included a flame ionization detector for unburned hydrocarbons (UHC), infrared detectors for CO and CO₂ and a paramagnetic analyzer for O₂. CO, CO₂ and O₂ samples had the UHC and H₂O removed before being measured. The UHC samples retained the H₂O. This test case was chosen because it has many of the characteristics of LPM GT combustors, which have lean, premixed fuel and air burning in a flame that is stabilized by a recirculation zone. This is generally easier to model than an actual burner, which has a complex three-dimensional, swirl induced recirculation zone and normally burns natural gas. The purpose of

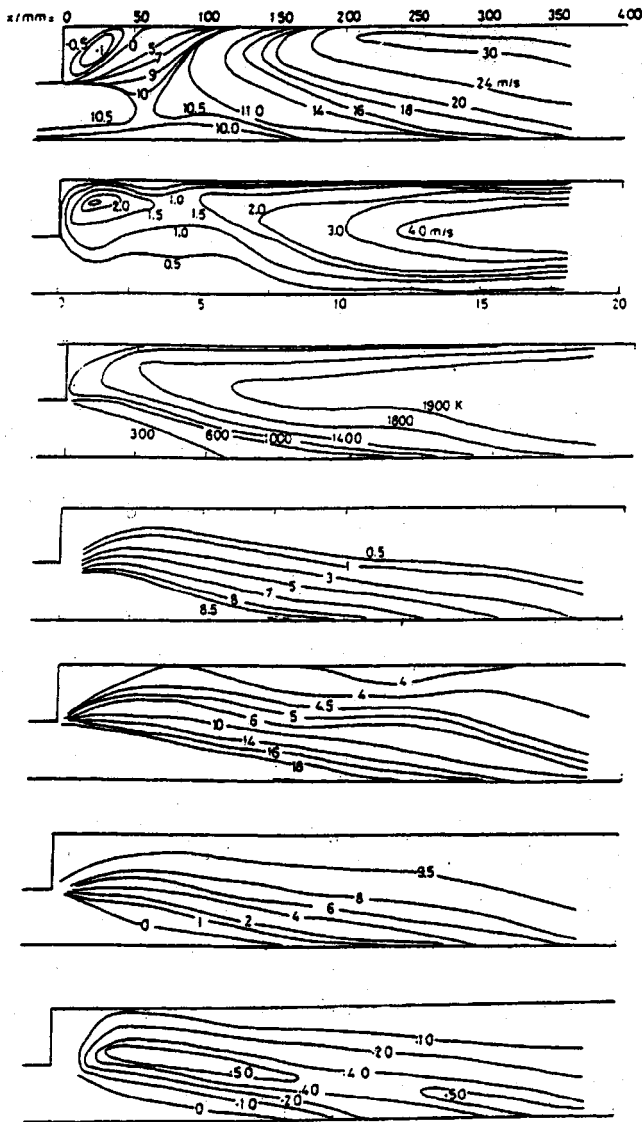


Fig. 1 El Banhawy et al. [10] data, equivalence ratio=0.9, axial velocity m/sec, axial velocity rms, temperature K, unburned hydrocarbons-wet, O₂-dry, CO₂-dry, and CO-dry, species are mole percentages (O₂, CO₂, and CO have the UHC removed). Reprinted by permission of Elsevier Science from *Premixed, Turbulent Combustion of a Sudden-Expansion Flow*, by Y. El Banhawy et al., *Combustion & Flame*, 50, pp. 153–165, copyright 1983 by The Combustion Institute.

this research was to show the potential of the premixed CMC combustion model for modeling LPM GT combustors, so simplifications of the fluid mechanics that do not greatly affect the combustion are desirable. These simplifications will reduce the errors caused by the turbulence model and reduce runtimes. The fuel was modeled as pure methane instead of natural gas.

The volume averaged premixed CMC equations, which were described in the previous section, were added to the Fluent CFD program (Fluent [11]) with the Reynolds stress turbulence model (RSM) and the nonequilibrium wall boundary conditions. The full GRI2.11 kinetic mechanism (Bowman et al. [12]) was used over a range of scalar dissipation values. The current formulation of the premixed CMC method assumes adiabatic walls, while the data had water cooled walls, so there will be some errors in the model near the walls.

Figure 1 shows contour plots of axial velocity m/sec, the axial velocity rms m/sec, temperature K, unburned hydrocarbons

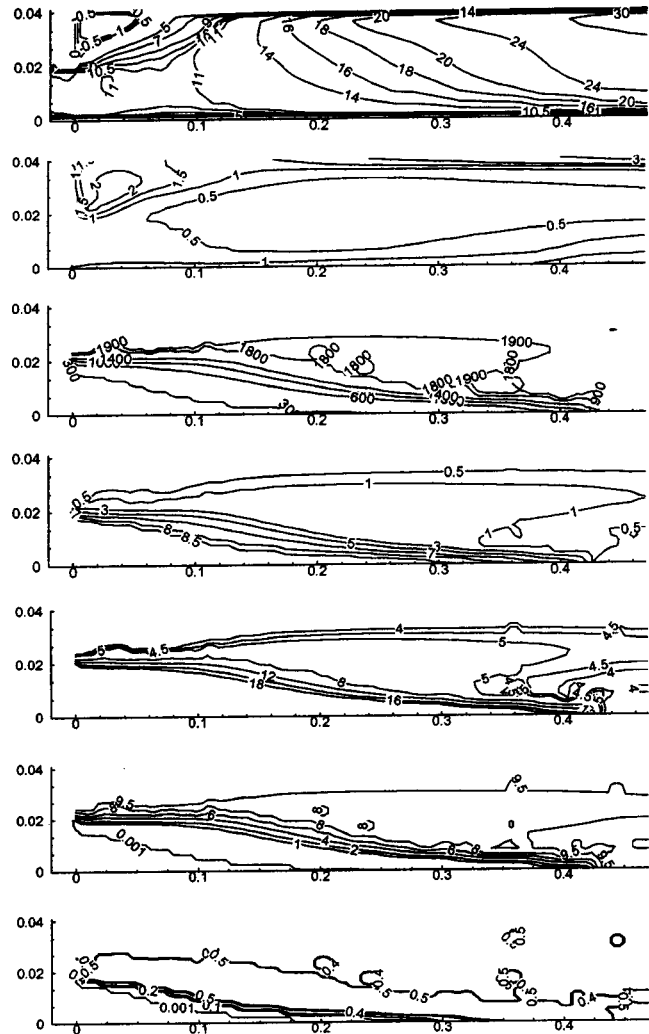


Fig. 2 Fluent and CMC with GRI2.11 $N=1$, RSM turbulence model, equivalence ratio=0.9 axial velocity (m/sec), axial velocity rms (m/sec), temperature K, CH₄-wet, O₂-dry, CO₂-dry, and CO-dry, species are mole percentages, (O₂, CO₂, and CO have the UHC removed)

(UHC) as mole percentage-wet, O₂ as mole percentage-dry, CO₂ as mole percentage-dry, and CO as mole percentage-dry (the O₂, CO and CO₂ also had the UHC removed) from El Banhawy et al. [10] for an equivalence ratio of 0.9 and a step height of 0.02 m (giving an expansion ratio of 2.0). Figure 2 shows the same variables calculated from the volume-averaged premixed CMC method using the full GRI2.11 kinetic mechanism with a scalar dissipation (N) of 1.0 1/sec. This value was found by trial and error by solving the equations with a guessed value of N and using Eq. (15) to calculate a new value of N . This was continued until both values agreed. It was found that N could be varied by an order of magnitude from this value with minimal affect on the flow field and major species solution, so small errors in calculating the scalar dissipation will not adversely affect the solution. The intermediate species and radicals do vary with changes in scalar dissipation. As N is increased from a value of unity there is less intermediates species, such as C₂H₄, CH₂O, C₂H₆, H₂, H₂O₂, and CH₂. As N increases the mixing becomes more intense, decreasing the Damköhler number and eventually becoming a perfectly stirred reactor. The free radicals are relatively constant with small changes in scalar dissipation around a value of unity, but the NO increases as N increases at larger values of c . It is seen from the temperature and species plots that the flame starts at about the same location and initially burns at about the same rate.

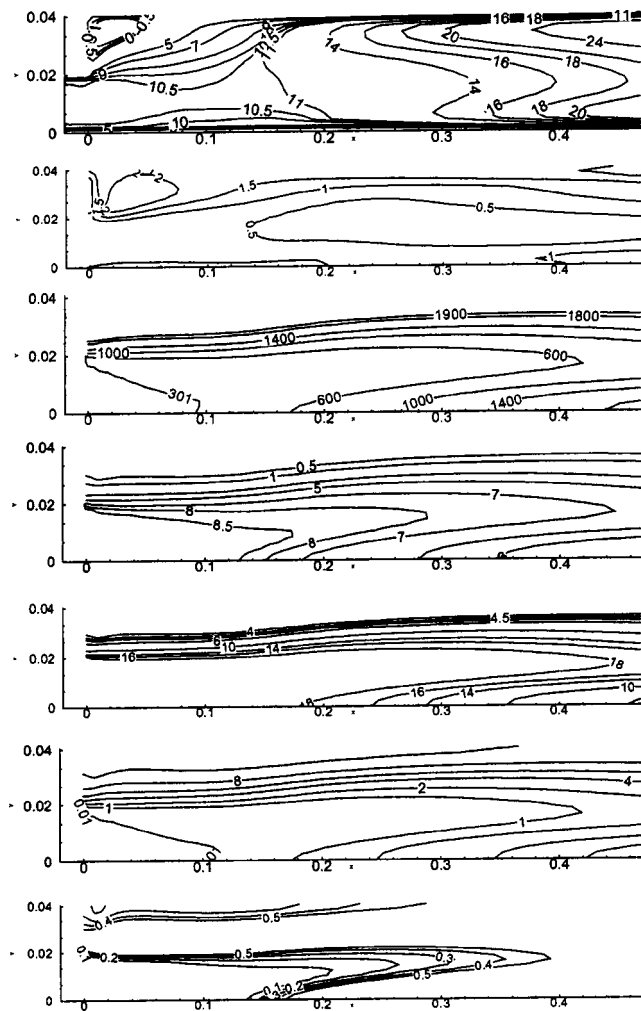


Fig. 3 Fluent three-step EDM, Reynolds stress model equivalence ratio=0.9 axial velocity (m/sec), axial velocity rms (m/sec), temperature K, CH₄-wet, O₂-dry, CO₂-dry, and CO-dry, species are mole percentages, (O₂, CO₂, and CO have the CH₄ removed)

Approximately two thirds of the way through the flame the modeled results appear to burn slightly slower than the data. From the velocity contours it is seen that the reattachment point of the recirculation zone is close to the data, but the peak velocity is farther downstream. The turbulence intensity in the recirculation zone closely matches the data, but downstream it is much lower, the reason for this will be discussed later. The peak temperature is about 200 K higher than the data, which has heat loss through the walls. In previous runs using Fluent's built in three-step EDM mechanism with adiabatic and nonadiabatic walls (not shown here) it was seen that the nonadiabatic walls reduced the peak temperature by about 200 K. Based on this the temperature is a good match. The UHC (plotted here as CH₄), O₂, and CO₂ match the data very well, except for the slower burning rate late in the flame. The CO gradients are in the correct location, but the magnitude is high in the modeled results. The experimental data has a peak CO concentration of about 0.50%, while the calculated peak is about 4.3%.

Figure 3 shows the same conditions as the previous figure calculated using the built in three-step kinetic mechanism and EDM model in Fluent instead of the CMC method. Here the flame starts to burn slightly earlier than the data, but burns much slower with a large amount of unburned fuel exiting the burner. Overall this gave a poor match. No attempt was made to adjust the parameters of the EDM model to improve the match, because this defeats the purpose of a predictive model.

Figures 2 and 3 show that both combustion models predict the turbulence intensity of the recirculation zone (shown as the axial velocity rms) well, but through the flame zone the match is poor. Both combustion models (using the same turbulence model) predict a nearly constant turbulence intensity, while the data shows an order of magnitude increase through the flame. One explanation for this is that there is no direct link from the reactions to the turbulence generation. The CMC model provides a direct link for the turbulence (small-scale turbulence) to feed into the reaction rates, but there is not a source term in the turbulent kinetic energy equation for the reactions to generate turbulence, which seems physically possible as the flow accelerates through the reactor. This is a short-coming of all turbulence models, since they were developed for incompressible flows. Improving this aspect of turbulence models is beyond the scope of this work.

The premixed CMC method had runtimes approximately twice as long as the three-step global EDM CH₄ mechanism using the same CFD program, while providing a much better match of the data and details of the intermediate species. The runtimes were about two hours using an 800MHz Intel PC with the Linux operating system. Using a previous solution as the initial conditions reduced the runtimes to about half an hour. A structured 110 by 20 cell grid was used. To generate the CMC table lookup database required 10 seconds to 5 minutes for each value of N . The smaller values of N gave a stiffer system, which required longer to solve.

These initial results from the premixed CMC gave a good match of the experimental data for the backward-facing step problem. To fully validate the model, more test cases will need to be run over a range of problem types. Additional runs will also help determine the range of validity of the volume averaged CMC method. When measurements of conditioned species in premixed flames becomes available in the future, they can also be used to determine the range of validity of the model. Since LPM GT combustors have more intense mixing than the backward facing step used here, this method should be applicable for that class of problems. More detailed experimental data will also help estimate the size of the error terms that were neglected in the derivation of the volume-averaged equations.

Earlier it was stated that for a turbulent premixed combustion model to accurately predict the emissions of a LPM GT combustor it needed three features, namely it must account for the effects of temperature fluctuations on the reaction rates, model the effects of micromixing on the chemical kinetics and allow detailed chemistry. The CMC method has all three features. By doing conditional averages the temperature fluctuations are accounted for, the scalar dissipation models the small scale mixing and full kinetic mechanisms can be used with reasonable runtimes.

Conclusions

It was shown that the premixed CMC method in its volume-averaged form gave a good match to the experimental data and also provided details of the intermediate species that are very difficult to measure. The results were much closer to the data than the three-step global mechanism that is similar to the ones used in most industrial reacting CFD work with only a small increase in runtimes. The premixed CMC method shows good promise as a future design tool for lean premixed gas turbine combustors.

More work will need to be done to determine the size of the error terms that were neglected in Eq. (14) and to determine the limits of applicability of the volume averaged formulation of the premixed CMC method.

Nomenclature

- c = reaction progress variable
- C_p = specific heat at constant pressure
- D = diffusivity
- e_Y = error term
- e_O = error term
- h = enthalpy

N = scalar dissipation (micromixing frequency)
 N = total number of values to be averaged
 ns = number of species
 P = probability density function
 P = pressure
 Q_i = conditioned mass fraction or enthalpy
 Sc = source term for c equation
 t = time
 u = velocity
 W_R = radiation heat loss
 x = space dimension
 x = conditioning variable
 Y = species mass fraction
 y = fluctuating species mass fraction

Greek Letters

ζ = conditioning variable
 η = value of conditioning variable
 ρ = density
 ω = reaction rate

Subscripts

a = conditioning variable
 $ad-u$ = difference between adiabatic and unburned
 f = heat of formation
 h = enthalpy
 i = species number
 ns = number of species
 u = unburned state

Superscripts

i = species number
 s = denotes sensible enthalpy

References

- [1] Klimenko, A. Y., and Bilger, R. W., 1999, "Conditional Moment Closure for Turbulent Combustion," *Prog. Energy Combust. Sci.*, **25**, pp. 595–687.
- [2] Smith N. S. A., 1994, "Development of the Conditional Moment Closure Method for Modeling Turbulent Combustion," Ph.D. thesis, University of Sydney.
- [3] Klimenko, A. Y., 1990, "Multicomponent Diffusion of Various Admixtures in Turbulent Flow," *Fluid Dyn.*, **25**, pp. 327–334.
- [4] Bilger, R. W., 1991, "Conditional Moment Methods for Turbulent Reacting Flow Using Crocco Variable Conditions," Charles Kolling Report, Department of Mechanical Engineering, the University of Sydney, TN F-99.
- [5] Bilger, R. W., 1993, "Conditional Moment Closure for Turbulent Reacting Flow," *Phys. Fluids A*, **A5**(2), pg. 436–444.
- [6] Crocco, 1948, "Lo Stato Limite Laminare Neigas," Monographie Scientifique di Aeronautica No. 3, Rome, 1946, Translated as Report No. AL684 Aerophys Lab, North American Aviation Inc., Los Angeles, CA.
- [7] Bilger, R. W., 1993, "Conditional Moment Closure Modeling and Advanced Laser Measurements," *Turbulence and Molecular Processes in Combustion*, T. Takeno, ed., The 6th Toyota Conference, Elsevier, New York, pp. 267–285.
- [8] Martin, S. M., 2003, "The Conditional Moment Closure Method for Lean Premixed Turbulent Combustion," Ph.D. thesis, University of Washington, to be published.
- [9] Bilger, R. W., 2000, "Future Progress in Turbulent Combustion Research," *Prog. Energy Combust. Sci.*, **26**, pp. 367–380.
- [10] El Banhawy, Y., Sivasegaram, S., and Whitelaw, J. H., 1983, "Premixed, Turbulent Combustion of a Sudden-Expansion Flow," *Combust. Flame*, **50**, pp. 153–165.
- [11] Fluent, 2001, www.fluent.com.
- [12] Bowman, C. T., Hanson, R. K., Davidson, D. F., Gardiner, Jr., W. C., Lissianski, V., Smith, G. P., Golden, D. M., Frenklach, M. and Goldenberg, M., 1998, [www.me.berkeley.edu/gri_mech/GRI 2.11](http://www.me.berkeley.edu/gri_mech/GRI_2.11).

Liquid Fuel Placement and Mixing of Generic Aeroengine Premix Module at Different Operating Conditions

J. Becker

C. Hassa

DLR—German Aerospace Center,
Institute of Propulsion Technology,
51170 Cologne, Germany

Fuel placement and air-fuel mixing in a generic aeroengine premix module employing plain jet liquid fuel injection into a counter-swirling double-annular crossflow were investigated at different values of air inlet pressure (6 bar, 700 K and 12 bar, 700 K) and liquid-to-air momentum flux ratio, both parameters being a function of engine power. Kerosene Jet A-1 was used as liquid fuel. Measurement techniques included LDA for investigation of the airflow and Mie-scattering laser light sheets and PDA for investigation of the two-phase flow. Measurements were taken at various axial distances from the fuel nozzle equivalent to mean residence times of up to 0.47 ms. It was found that the initial fuel placement reacts very sensitively to a variation of liquid-to-air momentum flux ratio. Susceptibility of the spray to dispersion due to centrifugal forces and to turbulent mixing is primarily a function of the fuel droplet diameters, which in turn depend on operating pressure. The data are interpreted by evaluation of the corresponding Stokes numbers. [DOI: 10.1115/1.1587741]

Introduction

The injection of kerosene fuel through plain jet nozzles into an annular crossflow is one of several possible concepts of a premix module for lean premixed prevaporized (LPP) combustion for aviation gas turbines, [1]. The motivation for LPP technology, [2], is the fact that under typical aeroengine combustion conditions, harmful oxides of nitrogen (NO_x) are primarily formed according to the thermal or Zeldovich mechanism, which is characterized by an exponential dependence of the NO formation rates on temperature. Since the chemical reaction of NO formation remains far from its thermodynamic equilibrium during typical combustor residence times on the order of 5 ms, NO_x emissions can be effectively reduced by lowering the rate of NO formation. This is achieved by feeding the combustor with an air-fuel mixture of lean composition, i.e., by using a significant amount of excess air which acts as thermal ballast and hence keeps the combustion temperature low. In order to provide this mixture, premix modules, which are mounted at the combustor inlet, must be optimized concerning their mixing performance, keeping in mind that the parameters that affect mixing performance can change significantly over an engine flight cycle and that the risk of autoignition limits the acceptable residence time to less than 1 ms. The benefits of the above-mentioned premix module concept employing radial plain jet fuel injection into an annular swirling airflow are thermal management considerations and the fact that the very fuel rich core associated with axial fuel injection through pressure swirl atomizers at high air inlet pressure is avoided.

The objective of the present work is the investigation of the process of air-fuel mixing inside a generic premix module of this type as a function of those operating parameters whose variation over a flight cycle have the greatest effect on air-fuel mixing performance. These are (1) air density, typically varying by a factor between 3 and 4, which has a pronounced effect on liquid fuel atomization and fuel spray dispersion, and (2) liquid fuel mass

flow, changing by about the same factor as air density, which profoundly affects fuel jet penetration and hence the initial fuel placement.

Measurement techniques employed included laser-Doppler anemometry (LDA) for an investigation of the airflow, in the absence of the liquid fuel, concerning the mean and rms values of the three velocity components. Furthermore, additional high data rate LDA measurements were analyzed by fast Fourier transformation (FFT), which allowed the estimation of the turbulence length scale. In the presence of the liquid fuel flow, Mie-scattering laser light sheets were employed for visualization of the dense spray in the vicinity of the fuel nozzle and phase-Doppler anemometry (PDA) was applied for a detailed investigation of the fuel spray, particularly the spatial distribution of the liquid fuel flux and the representative droplet diameters, such as the SMD.

Experiment

Generic Premix Module. Figure 1 shows the generic premix module investigated in this work, consisting of a cylindrical center body, an outer cylinder, and an annulus with two concentric axial swirlers in between. Looking upstream, the airflow passing through the inner swirler rotates in the clockwise direction, whereas the airflow passing through the outer swirler rotates in the counterclockwise direction. Both swirlers are designed to generate a swirl angle of 30 deg. During operation, fuel is injected out of the center body in the radial direction through small plain jet nozzles into the counter-swirling double-annular airflow. A supplementary airflow passes through the center body for cooling of the fuel lines. Whereas in regular operation, several fuel nozzles equispaced about the circumference of the center body would be used, measurements were made with only one active fuel nozzle. The single-nozzle data was later extrapolated to more than one fuel nozzle by means of a superposition algorithm. However, the premix module was equipped with identical fuel nozzles at various axial stations, all of them oriented as shown in Fig. 1. Hence by taking measurements at a fixed location 1 mm downstream from the outlet of the premix module and switching from one fuel nozzle to another, different downstream distances of the measurement planes were realized. The swirler kit could be moved in the axial direction, so that the axial distance between the

Contributed by the International Gas Turbine Institute (IGTI) of THE AMERICAN SOCIETY OF MECHANICAL ENGINEERS for publication in the ASME JOURNAL OF ENGINEERING FOR GAS TURBINES AND POWER. Paper presented at the International Gas Turbine and Aeroengine Congress and Exhibition, Amsterdam, The Netherlands, June 3–6, 2002; Paper No. 2002-GT-30102. Manuscript received by IGTI, Dec. 2001, final revision, Mar. 2002. Associate Editor: E. Benvenuti.

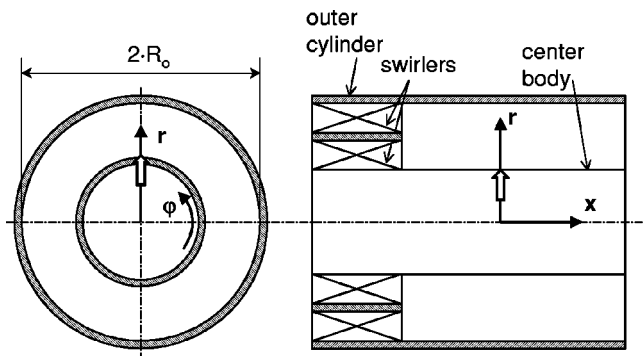


Fig. 1 Schematic of premix module (not to scale). White arrow indicates active fuel nozzle.

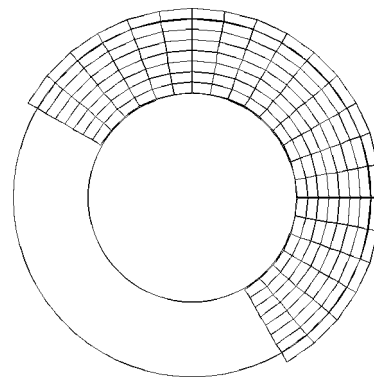


Fig. 2 PDA measurement grid

swirler outlet plane and the active fuel nozzle was kept constant. Reference measurements by PDA at ambient temperature, hence precluding evaporation, but elevated pressure for realistic atomization behavior, showed that the difference in SMD of the fuel spray droplets generated by any two fuel nozzles was between 6% and 11% of the mean of all fuel nozzles, so that for engineering purposes, the fuel nozzles can be considered to be identical.

Test Conditions. The primary goal of the present work was to elucidate how the considerable variations of inlet air density and of fuel mass flow that are characteristic of a flight cycle of an aviation gas turbine affect the mixing performance of the present generic premix module. Air inlet conditions were chosen to be 6 bar, 700 K, resulting in actual values of density and kinematic viscosity of $\rho_{\text{air}} = 3.0 \text{ kg/m}^3$, $\nu_{\text{air}} = 1.1 \cdot 10^{-5} \text{ m}^2/\text{s}$, and 12 bar, 700 K, resulting in $\rho_{\text{air}} = 6.0 \text{ kg/m}^3$, $\nu_{\text{air}} = 5.6 \cdot 10^{-6} \text{ m}^2/\text{s}$. The total velocity of the swirling airflow was kept constant. Kerosene Jet A-1 with a density of 795 kg/m^3 was used as liquid fuel, so that the effect of realistic evaporation behavior on spray dispersion is taken into account. Since previous research has shown that the jet penetration and hence the initial fuel placement of a liquid jet in cross-flow is governed by the liquid-to-air momentum flux ratio $q = (\rho_{\text{liq}} \cdot u_{\text{liq}}^2) / (\rho_{\text{air}} \cdot u_{\text{air}}^2)$, [3–6], this parameter will be used throughout this work instead of the fuel mass flow. The air velocity is calculated from the volumetric airflow at the inlet of the premix module and the cross-sectional area of the annulus, and the fuel velocity is calculated from the volumetric fuel flow and the cross-sectional area of the fuel nozzle orifice.

Measurement Techniques. In a first step, the initial fuel placement was visualized by laser light sheets. The beam of a continuous wave 400 mW Nd:YAG laser ($\lambda = 532 \text{ nm}$) was formed into a sheet by means of a set of lenses. The sheet had a nominal height (i.e., based on the Gaussian beam diameter) of about 48 mm, of which only the central 30 mm were used, so that the illumination intensity at the edge of the sheet was still 68% of the peak value in the center. The nominal thickness of the waist of the light sheet was $110 \mu\text{m}$. The Mie-scattering image of the spray illuminated by the laser light sheet was recorded by an intensifying CCD camera equipped with an interference filter using a gate time (effectively an exposure time) of $2 \mu\text{s}$. Due to restrictions of optical access, the camera could not be positioned perpendicular to the light sheet. The resulting distortions were corrected for by the camera control software after calibration with reference grid positioned in the light sheet plane. Each measurement consisted of the acquisition of 100 single images and subsequent averaging.

PDA measurements were conducted focusing on the spatial distribution of liquid fuel flux and representative droplet diameters. A Dantec 2-D PDA system was used to measure the axial and the vertical droplet velocities and the droplet diameters. The receiving optics were positioned at an off-axis angle of 50° , where light scattered by first-order refraction is about 150 times stronger than

light scattered by reflection, hence satisfying the requirement of clear dominance of one single scattering mechanism. In order to be able to access the full plane just 1 mm downstream of the outlet of the premix module, the beam separation at the 310 mm front lens of the transmitting optics was set to just 18 mm. The resulting small number of fringes in the measurement volume was accounted for by setting a SNR requirement of +3dB for burst validation. For good dense-spray performance, the measurement volume had rather small dimensions of about $70 \mu\text{m}$ in diameter and $100 \mu\text{m}$ in length due to a slit in the receiving optics. The measurement grid consisting of 198 positions is shown together with the contour of the annulus in Fig. 2. At each node, the measurement was stopped after acquisition of 20000 validated samples or after 10 seconds, whichever came first. If fewer than 200 validated samples were recorded in 10 seconds, the measurement was discarded altogether and the measured liquid flux was set to zero. Otherwise, the raw data was processed using an in-house algorithm, [7]. The uncertainty of the SMD measurements is about $\pm 5\%$, which is the aggregate error due to possible optical misalignment, changes of droplet refractive index during heat-up, and photomultiplier voltage setting. The uncertainty of the representative diameters D10% and D50%, where, e.g., D10% is the droplet diameter such that 10% of the total liquid volume of the spray is present in droplets below this diameter, is estimated to be on a similar level. The measurement of the D90%, which can react very sensitively to just a few very large droplets, is less reliable.

For the investigation of the airflow by LDA in the absence of the fuel, the air was seeded with submicron particles of a mixture of ethanol and glycerin, necessitating tests at ambient temperature. Since the Reynolds number of the airflow at 6 bar and 700 K, using the hydraulic diameter of the annulus, is already $0.9 \cdot 10^5$, so that the region of Reynolds number invariance has basically been reached, the test conditions were scaled to 1 bar, 280 K at constant air velocity, resulting again in a Reynolds number of about $0.9 \cdot 10^5$. The LDA system consisted of the two-dimensional PDA transmitting optics mentioned above, an in-house high sensitivity, wide aperture receiving optics positioned at an off-axis angle of 15° for maximum data rates, and a Dantec Burst Spectrum Analyzer. The uncertainty of the velocity measurements is estimated to be less than $\pm 2\%$.

If LDA data rates are sufficiently high and if the sample size is sufficiently large, then the turbulence time scale can be derived by spectral analysis, [8]. Application of the Taylor hypothesis then leads to the turbulence length scale L_t . In the present case, data rates of 120 kHz to 240 kHz were achieved by using three particle seeders in parallel. Based on these data rates, the density of the particles of about 800 kg/m^3 and the upper bound of the particle size of $1 \mu\text{m}$, which is ensured by an impactor at the outlet of the particle generators, a mass loading ratio of approximately $1 \cdot 10^{-4}$ is calculated, so that feedback of the seeding on the flow itself is

Table 1 Measurement planes

| Measurement Techniques | Mean Residence Times Corresponding to Measurement Planes (ms) |
|------------------------|---|
| Laser light sheets | 0.09; 0.16; 0.35 |
| PDA | 0.27; (0.35); 0.47 |
| LDA | (0.07); 0.27 |

negligible. The required sample size was increased from 10,000 to 100,000 validated events. By variation of the signal gain, it was usually possible to ensure that the velocity, i.e., turbulence, spectrum was not significantly corrupted by the noise spectrum. The uncertainty of the results amounts to a factor of about 2, so that the true value of L_r is estimated to be between approximately 1/2 and 2 times the measured value. Details of the measurements are given by Becker and Hassa [9]. Similar measurements are reported by Hassa et al. [10].

Measurements were conducted at various axial distances from the fuel nozzle corresponding to mean residence times of up to 0.47 ms. This value is sufficiently low to offer acceptable safety margins regarding autoignition even at high power operating conditions. According to the correlation for autoignition times in pre-mix modules derived by Guin [11], the autoignition time expected for 35 bar and 850 K is 1.1 ms, implying a safety factor of greater than 2 if the most downstream measurement plane is taken as the exit plane of the premix module. Table 1 lists the measurement planes for each measurement technique. The data of the measurement planes put in parentheses is not discussed explicitly in this paper.

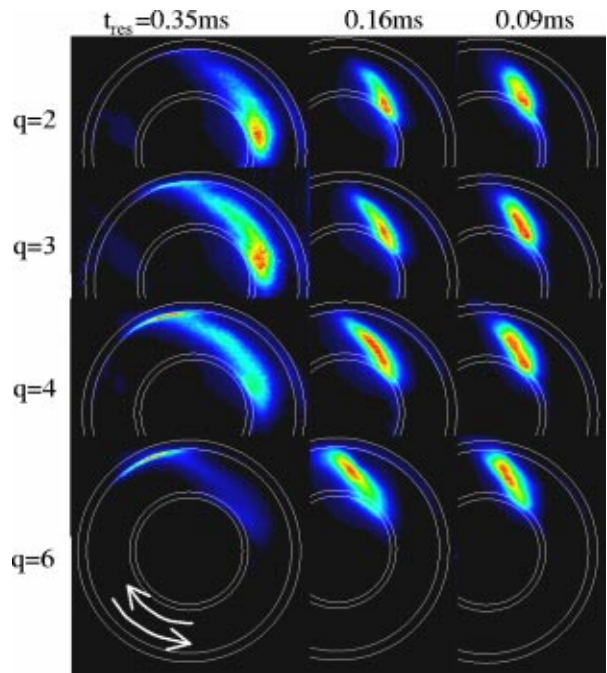
Results

Laser Light Sheet Images. Different values of the liquid-to-air momentum flux ratio q between $q=2$ and $q=6$ were realized, because liquid fuel penetration at a fixed location is primarily a function of q and the fuel nozzle diameter, [3–6]. Particularly at elevated air density and q up to $q=12$, it had been found that the outer contour of the liquid fuel jet can be described by the correlation

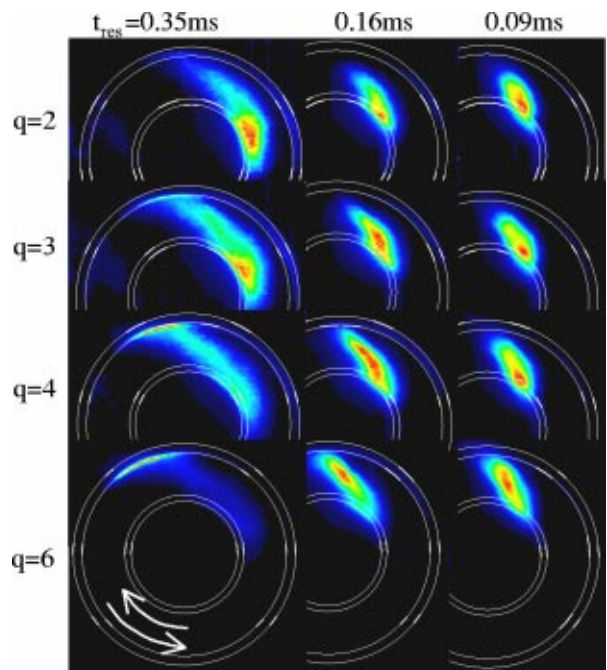
$$\frac{z}{D} = 1.57 \cdot q^{0.36} \cdot \ln\left(1 + 3.81 \cdot \frac{x}{D}\right) \quad (1)$$

between $x/D=2$ and $x/D=22$, where x is the streamwise distance, z is the penetration depth, and D is the diameter of the fuel nozzle, [6]. Fuel film formation on the center body or the inner surface of the outer cylinder was to be avoided in order to control the risk of autoignition due to possibly very long residence times of the fuel contained in the film and also to avoid coke and gum formation by thermal decomposition of the fuel. Film formation on the center body is a consequence of insufficiently high values of q , whereas exceedingly high values of q (relative to the width of the annulus) lead to equally undesirable impingement of the fuel jet on the outer cylinder. Film formation on the outer cylinder can also be brought about by strong centrifugal forces acting on the fuel spray.

The Mie-scattering laser light sheet images are presented in Figs. 3 and 4. The intensity of the images has been normalized so that the highest pixel count in each image corresponds to the brightest shade of red. Analysis of the results revealed that film formation is difficult to avoid completely in the present geometry. Since the premix module had to be scaled to fit into the pressure housing of an existing test rig, the annular width is rather small, resulting in a narrow allowable range of q . Greater annular widths will be able to accommodate a wider range of q without the occurrence of unacceptable fuel film formation on either surface. The effect of q on the initial fuel placement can be seen clearly in Figs. 3 and 4. The effect of air density seems to be small, but the

**Fig. 3 Laser light sheet images at 6 bar**

core of the spray cloud is found to remain slightly closer to the center body at 12 bar. For the subsequent detailed investigation of the spray development in the counter-swirling annular airflow by combined analysis of the LDA data of the airflow and the PDA data of the fuel spray, a constant value of $q=3$ was considered to offer the best compromise. Test conditions with $q>3$ were ruled out due to significant impingement of the liquid fuel on the outer cylinder at $t_{res}=0.35$ ms. At $q=2$, on the other hand, the bulk of the spray remains close to the center body, resulting in poor interaction with the shear layer and even partial film formation on the

**Fig. 4 Laser light sheet images at 12 bar**

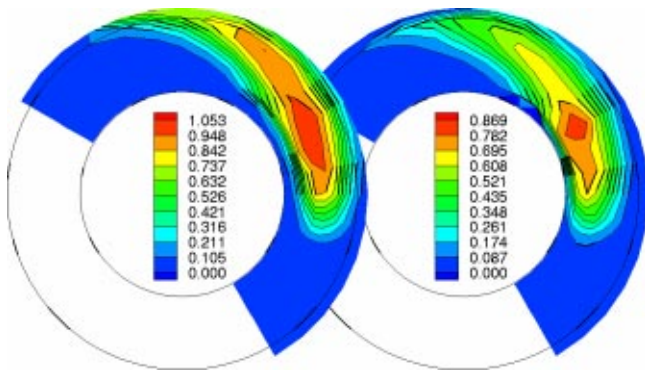


Fig. 5 Measured fuel flux ($\text{cm}^3/\text{cm}^2\cdot\text{s}$) at $t_{\text{res}}=0.47$ ms, $q=3$, left: 6 bar; right: 12 bar

center body. Film formation was not observed at $q=3$. The fuel mass flow rates at $q=3$ based on a single nozzle were 1.38 g/s at 6 bar, 700 K and 1.95 g/s at 12 bar, 700 K.

If the premix module is to be operated at constant AFR throughout the flight cycle, then this implies that q is proportional to the air density. If AFR decreases as engine power is increased, then the variation of q becomes even greater. The narrow range of acceptable variation of q in the present geometry hence can probably only be achieved by internal circumferential staging of the fuel nozzles or external staging of the premix modules, or a combination of both.

Phase-Doppler Anemometry (PDA) Data (Single Nozzle).

Results, all of which have been obtained at $q=3$, are presented in Figs. 5 and 6. Figure 5 consists of the contour plots of the measured liquid fuel flux at 6 bar and 12 bar at the measurement plane corresponding to 0.47 ms. The color map is adjusted to the maximum measured value at each test condition and consists of ten colors. Hence the deepest red represents fuel flux values between 90% and 100% of the maximum, orange represents values between 80% and 90% of the maximum et cetera. At 6 bar, the core of the spray cloud is found almost exactly in the center of the annulus, enabling close interaction of the spray with the shear layer. As a consequence, a significant portion of the spray has been displaced from the core in the counterclockwise direction by the swirl component of the flow in the outer part of the annulus, while the core itself was still under the influence of the clockwise swirl in the inner part of the annulus. At 12 bar, the spray is located closer to the center body and its interaction with the shear layer has been somewhat poorer. The fuel flux in the outer part of the annulus is noticeably lower than in the inner part.

Contour plots of the measured SMD at 6 bar and 12 bar are given in Fig. 6. The color map is identical for both plots. Whereas

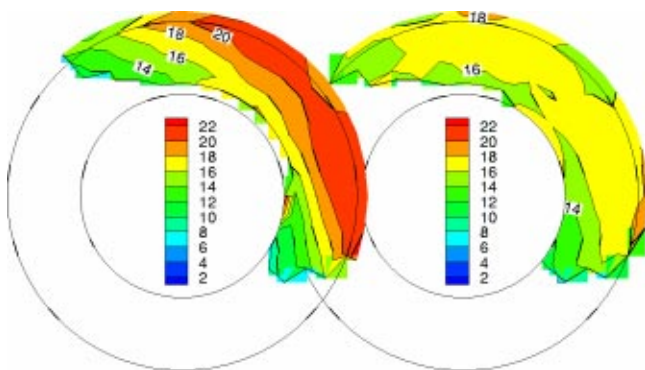


Fig. 6 Measured SMD (μm) at $t_{\text{res}}=0.47$ ms, $q=3$, left: 6 bar; right: 12 bar

Table 2 Representative droplet diameters

| Test Condition | Meas. Plane | SMD (μm) | D10% (μm) | D50% (μm) | D90% (μm) |
|----------------|-------------|-----------------------|------------------------|------------------------|------------------------|
| 6 bar, 700 K, | 0.27 ms | 18.2 | 11.4 | 18.7 | 37.4 |
| | $q=3$ | 0.47 ms | 19.2 | 11.9 | 20.0 |
| 12 bar, 700 K, | 0.27 ms | 16.2 | 10.1 | 16.4 | 34.8 |
| | $q=3$ | 0.47 ms | 16.0 | 10.2 | 16.3 |

the spatial distribution of SMD at 12 bar is very homogeneous, a layered structure is found at 6 bar, where larger droplets are found at greater radii. This suggests that at 12 bar, the spray is subjected to a stochastic mixing process due to turbulence. At 6 bar, on the other hand, the spray dispersion appears to be governed by inertial forces resulting from the initial radial velocity of the liquid fuel and centrifugal forces resulting from the tangential velocity imparted on the fuel by the airflow. These effects will be discussed in more detail below. Table 2 summarizes the measured representative diameters of the spray at two different PDA measurement planes. The values for the downstream measurement plane given in the table have been computed by weighting the representative diameter considered at each node of the grid with the measured liquid fuel flux at the same node. At the more upstream measurement plane, the spray was extremely dense, yielding raw data rates above 150 kHz and validation rates below 50% in the spray core. Under these adverse conditions, the fuel flux cannot be reliably determined, so that the local representative diameters had to be weighted with the raw data rate instead.

As is to be expected, the airblast atomization of the liquid fuel jet yields smaller droplets if the air density is increased. At 12 bar, the representative diameters remain approximately constant, but at 6 bar, an increase is observed as the smallest droplets present in the upstream measurement plane have disappeared so quickly due to evaporation that shrinking of slightly larger droplets could not compensate the loss by the time the spray reaches the downstream measurement plane.

Laser-Doppler Anemometry (LDA) Data. In order to obtain the full velocity information including rms values of all three velocity components using a two-dimensional LDA system, radial velocity profiles were recorded at three different tangential positions. Exploratory measurements had indicated wakes resulting from the swirler vanes. Hence, in each measurement plane, tangential profiles of the axial velocity were obtained first in order to identify the locations of the wakes. Then, for a comprehensive characterization of the airflow, measurements were taken in a wake as well as in the region between two adjacent wakes, resulting in the need to record six profiles each in the inner and outer part of the annulus.

Figures 7 and 8 show these data after transposition into the cylindrical coordinate system. In the measurement plane corresponding to 0.27 ms, the peak tangential velocity has already decayed considerably from its values further upstream, and the wakes and passages have largely disappeared. The rms-values of all three velocity components are around 15 m/s, with slightly higher values in the center of the annulus where the shear layer of the counter-rotating swirling flow is located.

Results of measurements of L_t in the plane corresponding to 0.27 ms are given in Fig. 9. The data pertaining to the direction perpendicular to the axial direction was not decomposed into the radial and tangential component due to the high uncertainty of the measurement. Clearly, the turbulence length scale in the axial direction is much larger than the length scale in the perpendicular direction, which can be attributed to the ratio of length to hydraulic diameter of the passages of the axial swirlers of approximately three.

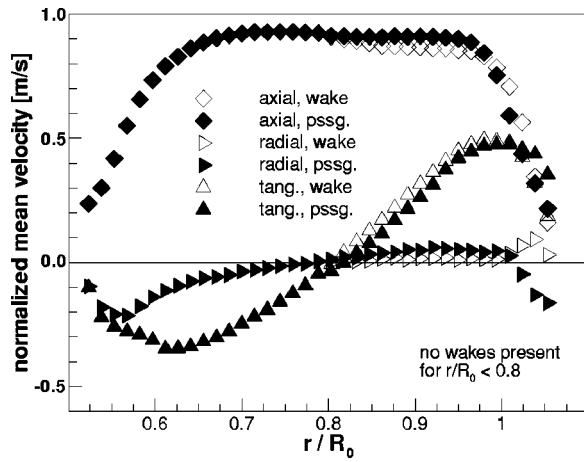


Fig. 7 Radial profiles of mean velocity components at $t_{res} = 0.27$ ms, normalized with nominal total velocity

Analysis

In order to understand the fuel spray dispersion and hence the air-fuel mixing, the PDA data was analyzed together with the LDA data of the airflow, with the laser light sheet images providing information concerning the initial fuel placement. Primarily, the observed differences between the results obtained at 6 bar and 12 bar concerning liquid fuel placement and spatial distribution of SMD will be analyzed.

Liquid fuel placement is the aggregate result of three contributions: (1) penetration of the liquid jet, (2) the stop distance of the individual droplets after breakup of the liquid jet, and (3) radial displacement of the spray due to centrifugal forces.

The penetration of the liquid jet until breakup can be estimated from the equation for the time required for completion of breakup, [5], which was originally derived for the secondary breakup of droplets

$$t_b = C \cdot D_0 \cdot \sqrt{\frac{\rho_{liq}}{\rho_{air}}} \cdot \frac{1}{u_{air}} \quad (2)$$

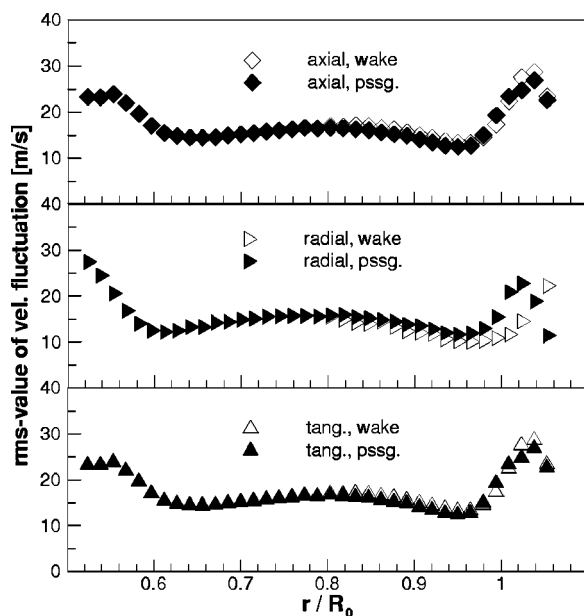


Fig. 8 Radial profiles of velocity fluctuation at $t_{res} = 0.27$ ms

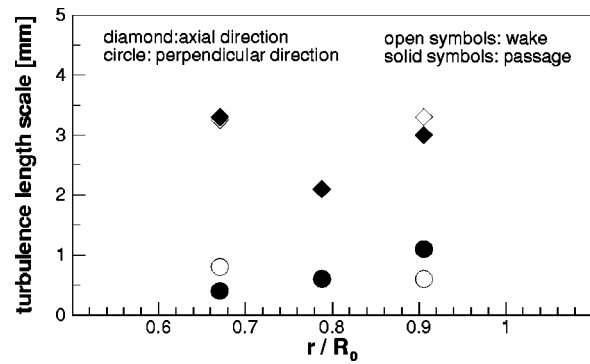


Fig. 9 Radial profiles of turbulence length scale at $t_{res} = 0.27$ ms

and the assumption that the liquid jet maintains its exit velocity u_{liq} until breakup. If q is held constant, then $u_{liq} \propto \rho_{air}^{0.5}$, so that the penetration depth of the liquid jet $u_{liq} \cdot t_b$ is not a function of air density.

The stop distance s_{stop} in this case is the distance covered by a droplet until its velocity relative to the surrounding air has vanished. s_{stop} is the product of the initial droplet velocity and the velocity relaxation or response time of the droplet, given by [6]:

$$\tau_{relax} = \frac{4}{3} \cdot \frac{\rho_{liq}}{\rho_{air}} \cdot \frac{D_p^2}{c_D \cdot Re_p \cdot \nu_{air}} \quad (3)$$

$$c_D = \frac{24}{Re_p} \cdot (1 + 0.15 \cdot Re_p^{0.687}) \quad (4)$$

$$Re_p = \frac{|\mathbf{u}_{air} - \mathbf{u}_p| \cdot D_p}{\nu_{air}} \quad (5)$$

For creeping flow ($Re_p < 1$) only, Eqs. (3)–(5) reduce to the better known form $\tau_{relax} = \rho_{liq} D_p^2 / 18 \mu_{air}$ and τ_{relax} is the time constant of the differential equation describing droplet motion. In a noncreeping flow, as is the case in the present investigation, τ_{relax} depends on the relative droplet velocity, so that the concept of τ_{relax} as a constant is—strictly speaking—invalidated and a comparison of τ_{relax} of droplets with different relative velocities leads to unphysical results. Therefore, the creeping flow equation for τ_{relax} is often found in the literature even if $Re_p > 1$. Numerically, the error thus incurred is often not large. However, the effect of air density on droplet motion, which is non-negligible in the present context, can only be taken into consideration if the more cumbersome Eqs. (3)–(5) are used, but care must be taken not to evaluate the effect of different values of relative velocity on the relaxation time. Returning now to the task of evaluating the stop distance and assuming that the initial droplet velocity is identical to the velocity of the liquid jet u_{liq} , Eqs. (3)–(5) applied to the D50% of the two different test conditions yield $s_{stop} = 0.9$ mm at 6 bar and 0.8 mm at 12 bar. This small difference could not have been detected based on the PDA measurement grid. Hence neither liquid jet penetration nor the stop distance can explain the differences in fuel placement between 6 bar and 12 bar, which must therefore be due to the effect of centrifugal forces acting on the spray.

Susceptibility to radial displacement due to centrifugal forces is represented by the value of the swirl Stokes number, [12]. The definition of the Stokes number in general is [13]:

$$St = \frac{\tau_{relax}}{\tau_{flow}} \quad (6)$$

τ_{flow} is the time scale of the feature of the flow that is to be considered. In the context of the swirl Stokes number, $\tau_{flow} = r/u_{tan}(r)$. The value of the swirl Stokes number indicates whether droplet movement in the swirling airflow is dominated by

Table 3 Stokes numbers at $t_{res}=0.27$ ms

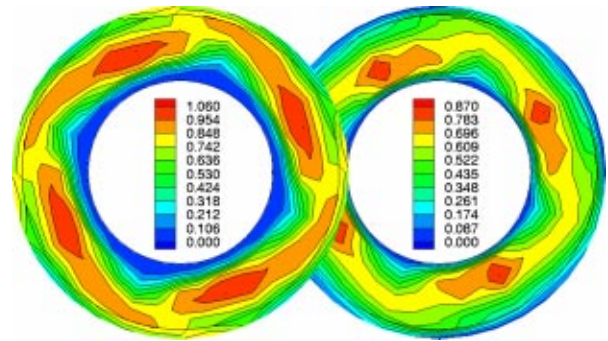
| Test Cond. | Repr. Droplet | D (μm) | St_{swirl} | St_{turb} |
|------------|---------------|-----------------------|--------------|-------------|
| 6 bar, | D10% | 11.4 | 0.2 | 1.1 |
| 700 K, | D50% | 18.7 | 0.4 | 2.5 |
| $q=3$ | D90% | 37.4 | 1.1 | 7.0 |
| 12 bar, | D10% | 10.1 | 0.1 | 0.7 |
| 700 K, | D50% | 16.4 | 0.2 | 1.4 |
| $q=3$ | D90% | 34.8 | 0.7 | 4.3 |

centrifugal forces, resulting in radial displacement of the droplet, or whether it is dominated by the drag force, causing the droplet to faithfully follow the streamlines of the airflow. This latter case is expected for $St < 0.1$. If $St > 0.1$, then the drag force is not clearly dominant and the droplet will be centrifuged out of the swirling flow sooner or later. In the range $0.1 < St < 1$, even small variations of St can lead to markedly different droplet trajectories. If the swirl Stokes number is very large, i.e., $St > 10$, then the droplet will hardly follow the curved streamlines of the airflow to begin with [12].

Correspondingly, the turbulence Stokes number, for which $St_{flow} = L_t / u'$, indicates to which degree the motion of a given droplet can be affected by the large turbulent eddies of the airflow. While large droplets may be too heavy to interact with a turbulent eddy over the eddy's lifetime, as indicated by a large value of the turbulence Stokes number, smaller droplets may be subjected to intense turbulent mixing due to their shorter relaxation times and correspondingly small Stokes numbers.

For both test conditions, the swirl Stokes number and the turbulence Stokes number were calculated for the three representative diameters D10%, D50%, and D90% in the measurement plane $t_{res} = 0.27$ ms. The Stokes numbers were evaluated for the inner part of the annulus, where almost all of the liquid fuel is located in this measurement plane (see Figs. 2 and 3). The liquid density of the droplets was estimated to be around 650 kg/m^3 , based on a CFD analysis of a similar test case, [7]. A representative relative droplet velocity of 28 m/s was derived from a comparison of the velocity information of the PDA data and the air velocity data of Fig. 7. The turbulence data used for St_{turb} was $u' = 15 \text{ m/s}$, $L_t = 0.75 \text{ mm}$ (see Figs. 8 and 9). Results are given in Table 3. Based on the assessment of experimental errors given above and the fact that the liquid density of the droplets is not known exactly, the uncertainty of the swirl Stokes number is about $\pm 20\%$. The uncertainty of the turbulence Stokes number, which due to the uncertainty of the turbulence length scale measurement alone amounts to a factor of about 2, is hence increased to a factor of roughly 2.5.

Since the Stokes number in general depends on the droplet response or droplet velocity relaxation time and hence on the square of the droplet diameter, the values of both Stokes numbers considered here are noticeably lower for the 12 bar test case than for the 6 bar test case. The higher air density *per se* at 12 bar also lowers the Stokes number, but to a lesser degree than the droplet diameters. Based on the data in Table 3, about half of the liquid fuel of the spray at 12 bar is contained in droplets that are expected to be subject to only very slow radial displacement due to centrifugal forces, whereas at 6 bar, significantly faster radial displacement is expected. This is in agreement with the spatial distribution of the liquid fuel flux shown in Fig. 5. In this context it should be noted that in the center of the annulus, the tangential velocity of the airflow vanishes, which is an inherent feature of a counter-swirling flow field. This constitutes a barrier for small droplets in the inner part of the annulus that may drift in the radial direction due to centrifugal forces, but then lose their tangential momentum—and hence the centrifugal forces acting on them—during their slow drift through the zone of negligible tangential air velocity. These droplets hence become trapped in the inner annulus. In order to overcome this trapping effect, which is expected to

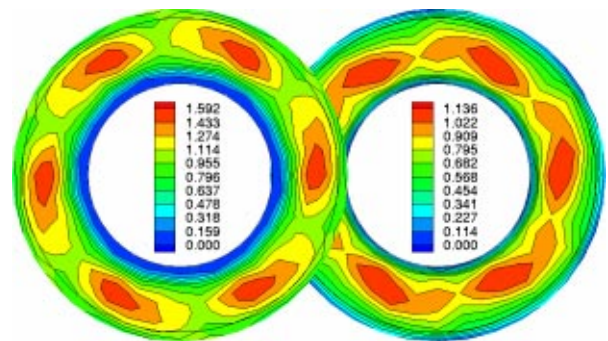
**Fig. 10 Fuel flux ($\text{cm}^3/\text{cm}^2 \cdot \text{s}$) at $t_{res}=0.47$ ms, $q=3$, extrapolated to four fuel nozzles, left: 6 bar; right: 12 bar**

become serious at high pressure, initial fuel placement at high power conditions should be such that swirl-induced radial displacement of the spray is not needed to transport liquid fuel into the outer part of the annulus.

Regarding the values of the turbulence Stokes number, almost all of the liquid fuel at 6 bar is contained in droplets that are too heavy to react to the turbulent eddies of the airflow, because the droplet response time is significantly longer than the large eddy lifetime. At 12 bar, however, interaction with turbulent eddies should still be possible for the D50%, so that about half of the liquid fuel is subject to turbulent mixing. These trends are borne out by the spatial distributions of SMD presented in Fig. 6. Turbulent mixing is not fast enough, though, to move the bulk of the spray due the brevity of the residence time of the premix module.

Extrapolation to N Fuel Nozzles

Extrapolation of the fuel flux data to more than one fuel nozzle was accomplished by copying, rotating and superpositioning the spatially resolved single-nozzle fuel flux data recorded in the most downstream PDA measurement plane. The results presented in Figs. 10–12 show that for eight equispaced fuel nozzles, the circumferential homogeneity of the fuel spray has basically reached its asymptotic value, as the maximum fuel flux varies by less than 10% in the circumferential direction. However, this value of the recommended number of fuel nozzles is not necessarily applicable to other premix modules, as it probably depends on the circumferential length as well as on the swirl angle. It is interesting to note that the particular, highly asymmetric shape of the spatial fuel flux distribution at 6 bar involving a long, one-sided tail actually causes a decrease in fuel spray homogeneity as the number of fuel nozzles is increased from 4 to 6.

**Fig. 11 Fuel flux ($\text{cm}^3/\text{cm}^2 \cdot \text{s}$) at $t_{res}=0.47$ ms, $q=3$, extrapolated to six fuel nozzles, left: 6 bar; right: 12 bar**

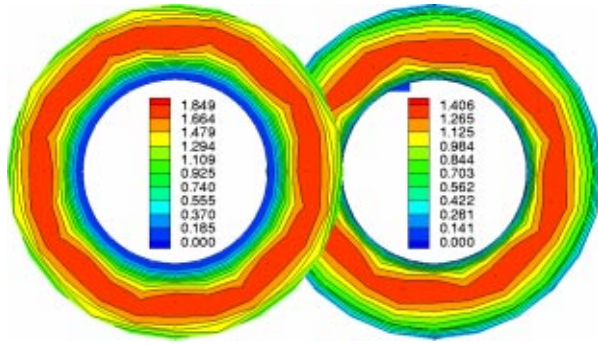


Fig. 12 Fuel flux ($\text{cm}^3/\text{cm}^2 \cdot \text{s}$) at $t_{\text{res}}=0.47$ ms, $q=3$, extrapolated to eight fuel nozzles, left: 6 bar; right: 12 bar

Conclusions

Considering the practical implications of this research, it appears to be important to carefully match, by way of the number of fuel nozzles, the maximum value of q occurring during a flight cycle to the width of the annulus of the pre-mixer. Usually, q will reach its maximum value at the highest power setting. Based on correlations for the droplet sizes resulting from atomization of a plain liquid jet in crossflow at elevated pressure, [6,14,15], and the swirl Stokes number analysis performed in the present work, the very small droplets generated at a typical takeoff condition will be highly able to follow the spiral path of the airflow, so that no radial displacement of the spray is expected. Therefore, q can, and should, be selected so that initial fuel placement makes use of nearly the entire width of the annulus at the highest power setting. At lower power operating conditions, q will also be lower and thus initial fuel placement will be disproportionately in the inner part of the annulus. However, the larger droplets generated due to the lower air density associated with lower power conditions will have larger swirl Stokes numbers and hence be susceptible to centrifugal forces. Hence the spray will be distributed across the width of the annulus as it travels through the pre-mix module.

Obviously, a Stokes number analysis requires a considerable amount of input data and therefore mainly serves to increase understanding of data already acquired. A detailed predictive calculation of the spray dispersion appears to be possible only by CFD simulation. This in turn requires accurate spray initial conditions, which usually have to be acquired by time-consuming PDA measurements. Recently, however, a comprehensive model of the atomization of a plain liquid jet in crossflow has been developed by Rachner et al. [16]. The results of the present investigation may serve as input data for a design optimization by CFD, in the course of which the inner and outer diameters of the annulus, the swirl angles, and the number of fuel nozzles could be varied as far as the boundary conditions set by the engine as a whole permit. In order to accommodate the wide variation of q occurring in an engine cycle without resorting to staging, it appears promising to increase the number of concentric axial swirlers from 2 to 3 and include a concentric filmer surface between the outer two swirlers. This would avoid impingement of the fuel jet on the outer cylinder at all values of q and simultaneously ensure that the spray is exposed to the highly beneficial shear layer generated by the inner two swirlers.

Acknowledgments

The authors wish to thank Sebastian Cordes for his design work related to this investigation and Dr. Ralf von der Bank of Rolls-Royce Deutschland for his comments and cooperation.

Nomenclature

| | |
|-------|---|
| c_D | = drag coefficient |
| D | = diameter |
| L_t | = turbulence length scale |
| p | = pressure |
| q | = fuel-to-air momentum flux ratio ($= (\rho_{\text{liq}} \cdot u_{\text{liq}}^2) / (\rho_{\text{air}} \cdot u_{\text{air}}^2)$) |
| r | = radial coordinate |
| Re | = Reynolds number |
| s | = distance |
| St | = Stokes number |
| t | = time |
| T | = temperature |
| u | = velocity |
| u' | = rms-value of velocity fluctuation |

Greek Letters

| | |
|--------|-----------------------|
| ν | = kinematic viscosity |
| ρ | = density |
| τ | = time scale |

Subscripts

| | |
|-----|---|
| 0 | = initial value |
| b | = breakup |
| res | = residence |
| p | = particle (used synonymously with droplet) |

Abbreviations

| | |
|-----|-------------------------------|
| AFR | = air-to-fuel ratio (by mass) |
| LDA | = laser doppler anemometry |
| PDA | = phase doppler anemometry |
| rms | = root mean square |
| SMD | = Sauter mean diameter |

References

- [1] Bittlinger, G., and Brehm, N., 1999, "High Pressure Combustion Test of LPP Modules in an Axially Staged Combustor Using a Multisector Rig," 14th International Symp. on Airbreathing Engines (ISABE), Florence, Italy, paper IS-007.
- [2] Lefebvre, A. H., 1998, *Gas Turbine Combustion*, 2nd Ed., Taylor & Francis, Philadelphia, PA, Chap. 9.
- [3] Inamura, T., Nagai, N., Hirai, T., and Asano, H., 1991, "Disintegration Phenomena of Metalized Slurry Fuel Jets in High Speed Air Stream," *Proceedings, 5th Int'l Conference on Liquid Atomization and Spray Systems (ICLASS-91)*, National Institute of Standards and Technology, Gaithersburg, MD, pp. 839–846.
- [4] Chen T. H., Smith, C. R., Schommer, D. G., and Nejad, A. S., 1993, "Multi-zone Behavior of Transverse Liquid Jet in High-Speed Flow," AIAA Paper No. 93-0453.
- [5] Wu, P. K., Kirkendall, K. A., Fuller, R. P., and Nejad, A. S., 1997, "Breakup Processes of Liquid Jets in Subsonic Crossflows," *J. Propul. Power*, **13**, pp. 64–73.
- [6] Becker, J., and Hassa, C., 2002, "Breakup and Atomization of a Kerosene Jet in Crossflow at Elevated Pressure," *Atomization Sprays*, **12**, pp. 49–67.
- [7] Brandt, M., Schmitz, G., and Rachner, M., 1998, "An Experimental and Numerical Study of Kerosene Spray Evaporation in a Premix Duct for Gas Turbine Combustors at High Pressure," *Combust. Sci. Technol.*, **138**, pp. 313–348.
- [8] Adrian, R. J., and Yao, C. S., 1987, "Power Spectra of Fluid Velocities Measured by Laser Doppler Velocimetry," *Exp. Fluids*, **5**, pp. 17–29.
- [9] Becker, J., and Hassa, C., 2001, "Messung des turbulenten Längenmaßes in einem generischen Vormischmodul für Flugtriebwerke," *Proceedings, 9, GALA Fachtagung, Winterthur, Switzerland, paper 25 (in German)*.
- [10] Hassa, C., Blümcke, E., and Eickhoff, H., 1990, "Measurements of Eulerian Macro Timescales in Highly Swirling Flows and Comparison With Computational Model," *Proceedings, 5th Int'l Symp. on Application of Laser Techniques to Fluid Mechanics, Lisbon, Portugal, paper 10.1*.

- [11] Guin, C., 1998, "Characterization of Autoignition and Flashback in Premixed-Injection Systems," *RTO Meeting Proceedings 14, Gas Turbine Engine Combustion, Emissions and Alternative Fuels*, NATO Research and Technology Organization (RTO), Neuilly-sur-Seine, France, pp. 30/11–30/19.
- [12] Dring, R. P., and Suo, M., 1978, "Particle Trajectories in Swirling Flows," *J. Energy*, **2**, pp. 232–237.
- [13] Chung, J. N., and Troutt, T. R., 1987, "Simulation of Particle Dispersion in an Axisymmetric Jet," *J. Fluid Mech.*, **186**, pp. 199–222.
- [14] Jasuja, A. K., 1982, "Plain-Jet Airblast Atomization of Alternative Liquid Petroleum Fuels Under High Ambient Pressure Conditions," ASME Paper No. 82-GT-32.
- [15] Hautman, D. J., and Rosfjord, T. J., 1990, "Transverse Liquid Injection Studies," AIAA Paper No. 90-1965.
- [16] Rachner, M., Becker, J., Hassa, C., and Doerr, T., 2002, "Modelling of the Atomization of a Plain Liquid Jet in Crossflow at Gas Turbine Conditions," *Aerospace Science and Technology*, **6**, pp. 495–506.

Fuzzy Fuel Flow Selection Logic for a Real Time Embedded Full Authority Digital Engine Control

A. Martucci
Senior Design Engineer

A. J. Volponi
Fellow

Pratt & Whitney,
400 Main Street,
East Hartford, CT 06108

The control logic of the modern full authority digital engine control is comprised of many control loops, each of which has a specific purpose. Typical control loops include (but are not limited to) a high or low rotor speed governor, an acceleration and deceleration loop, and various limiting loops for temperature, speed, fuel flow, and rate of change of fuel flow. The logic that determines which of these loops is "in control" at any particular time has a history of being very simplistic. This selection logic is usually nothing more than a cascade of minimum and maximum selection logic gates. Since this logic is so simplistic, the control engineer often has to "fine-tune" the compensator design for each loop, in order to achieve proper performance. [DOI: 10.1115/1.1365396]

Introduction

The purpose of this paper is to present a means of achieving a selection logic design based on fuzzy logic principles. Hereafter, this shall be referred to as a fuzzy fuel flow selector. The paper provides a brief overview of the most typical architecture for real time embedded full authority digital engine control (FADEC) control logic, rule development for the fuzzy fuel flow selector, and a realistic implementation of the fuzzy fuel flow selector. Also provided is a typical application that is used to contrast the performance between traditional selection logic and the fuzzy fuel flow selector. An overview of the fuzzy logic process is also included for completeness.

It is certainly an understatement to say that it is difficult to design the control logic for the modern FADEC. After all, it is not like the control designers have only one control loop to worry about. On the contrary, many control loops need to be designed in order to meet the overall system requirements. Naturally, each loop has its own particular function and unique set of requirements.

For reasons of simplicity, the control design engineers typically design and optimize all control loops as stand-alone systems using piecewise linear models. Many control loops are designed conservatively. Typically, loops that maintain a fixed set point (so-called governor loops) are among these. Some loops need to be designed more aggressively. Loops, which cause the engine to transition from one power setting to another, are good examples of aggressively designed control loops.

The logic that decides which of these loops control at any one time is referred to as fuel flow selection logic (hereafter called selection logic). Historically, selection logic is simplistic, comprised of cascades of *select min* and *select max* logic gates. Interesting things begin to happen when all of these individually designed (and optimized) control loops are connected to the selection logic. It is very common, for example, for the selection logic to transfer control prematurely from an aggressively designed loop to a conservatively designed loop. The end result is performance that is not quite as good as it could have been had the selection logic allowed the aggressive loop to control a little longer. In order to avoid such situations, the control designers will "fine-tune" the individual loops to achieve the desired performance. This fine tuning usually involves adjusting the loop gain of

the conservative loop to keep it from being selected under certain circumstances. This, of course, changes the stability design of the previously optimized conservative loop.

This paper provides an alternate means to "fine-tune" the control. The means of fine tuning, however, will not affect the control loops that the control engineers went through such trouble to optimize. Instead, fuzzy logic principles will be applied to the selection logic. The end result will be referred to as fuzzy fuel flow selection logic and will minimize the common control design problems from loop interaction, while maximizing performance for flight maneuvers that require maximum performance.

This paper is organized as follows:

1. A brief overview of *the fuzzy logic process* will be provided.
2. The *typical control loop architecture*, used in a modern FADEC, will be described (including the traditional fuel flow selection logic). This architecture will be the basis for the design of the fuzzy fuel flow selection logic.
3. The details of the *fuzzy fuel flow selection logic* will be developed and explained.
4. An *example implementation* will be provided. The system performance using the traditional fuel flow selection logic, and the fuzzy fuel flow selection logic, will be compared.
5. The issue of fuzzy fuel flow selection and control loop *stability* will be discussed.

The Fuzzy Logic Process

The notion of a fuzzy set was introduced in 1965 by Lotfi Zadeh [1], who was then a professor of Electrical Engineering at the University of California at Berkeley. His idea was to expand upon the general definition of a set in order to allow for the treatment of uncertainty in the classification of objects. A fuzzy set is a collection of objects whose membership, *unlike* those in a *crisp* set, is a matter of degree. This is expressed in terms of a membership function that assigns a number between 0 and 1 to each object, where 1 denotes absolute membership in the set and 0 denotes exclusion from the set. An object assigned a value somewhere in between 0.6 is said to belong to the set with degree (or membership) 0.6. This also implies that it is excluded from the set with degree $1 - 0.6 = 0.4$. Thus, by virtue of this fuzzy classification, it is possible to deal with sets which are not (mathematically) well defined, but rather, have been defined in linguistic terms, such as the set of numbers that are *approximately equal to π* , or the set of jet engines exhibiting *low* exhaust gas temperature margin.

Inasmuch as ordinary set theory serves as a foundation for classical logic, *fuzzy* set theory has likewise aided the development of *fuzzy* logic ([2]). Fuzzy logic combines notions from ordinary Ar-

Contributed by the International Gas Turbine Institute (IGTI) of THE AMERICAN SOCIETY OF MECHANICAL ENGINEERS for publication in the ASME JOURNAL OF ENGINEERING FOR GAS TURBINES AND POWER. Paper presented at the International Gas Turbine and Aeroengine Congress and Exhibition, Munich, Germany, May 8–11, 2000; Paper 2000-GT-0046. Manuscript received by IGTI October 1999; final revision received by ASME Headquarters October 2000. Associate Editor: D. Wisler.

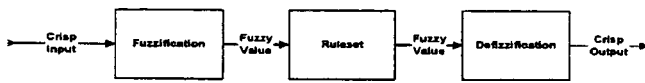


Fig. 1 Fuzzy logic processes

istotelian logic and fuzzy set theory, in that the truth of a given proposition (like a fuzzy set) can be something between 0 (representing false) and 1 (representing true). Logical operations and rules of inference have also been defined, which allows for the description (and analysis) of complex systems in a natural language setting. This process mimics the way humans convey and process information, and thus provides a mathematical vehicle for the representation of imprecise rules and heuristics. It wasn't long after Zadeh's introduction of fuzzy logic that applications arose in the area of dynamic control. Mandami [3] demonstrated its utility by successfully constructing a fuzzy logic control system for a steam engine. This first application heralded a new era for fuzzy logic as a control paradigm, with what seems an innumerable number of applications to follow, ranging from focus systems in camcorders to automated control of railway cars.

Generally speaking, there are three major processes common to all fuzzy control systems: *fuzzification*, *rulebase inference*, and *defuzzification* (Fig. 1).

1. *Fuzzification* is the process that converts a crisp input value to fuzzy set values, thereby forming the interface between the real world and the fuzzy inference process.

2. *Rulebase inference* is the application of a series of rules given in terms of fuzzy set values and producing for output variable(s), fuzzy set values for each rule fired. These rules usually take the form IF (X_1 is big) AND (X_2 is small), THEN (Y is medium).

3. *Defuzzification* converts the fuzzy set values [of the output variable(s)] back to a crisp value so that it may be utilized in the control.

The process of *fuzzification* consists of assigning linguistic labels (e.g. *large*, *small*, etc.) to a crisp input variable and determining the level of belief for that label for each point in the domain of the input. Unlike traditional logic, we may have levels of belief that range somewhere between 0 (false) and 1 (true). Figure 2, for example, illustrates three linguistic labels (*small*, *medium*, and *large*) being applied to the crisp variable X , which takes on values from 0 to 1000. The membership curves depicted for *small*, *medium*, and *large* provide the level of belief (or truth level) that the variable X falls in these three categories (or classifications) at each value of X throughout its domain. For example, at the value of 325, X is considered *small* with belief w_{small} and is considered to be *medium* with belief w_{medium} . Since the value 325 intersects *large* at an ordinate value of zero, its level of belief is 0, i.e., $X = 325$ is definitely NOT *large*.

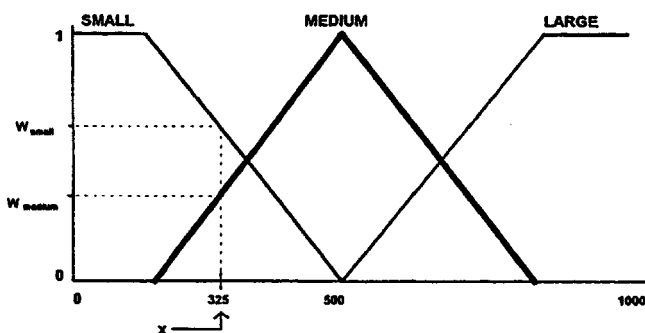


Fig. 2 Example membership curves

Table 1 Min/Max and Bayesian methods

| Operation | Min/Max Method | Bayesian Method |
|-----------------|------------------|-------------------------|
| X_1 AND X_2 | $\min(W_1, W_2)$ | $W_1 * W_2$ |
| X_1 OR X_2 | $\max(W_1, W_2)$ | $W_1 + W_2 - W_1 * W_2$ |
| NOT X_1 | $1 - W_1$ | $1 - W_1$ |

This process is carried out for each input variable X_i and their respective beliefs are forwarded to the rulebase for evaluation. A typical rule may, for example, take the form:

IF (X_1 is small) AND (X_2 is medium) THEN (Y is positive).

The first step in evaluating this rule is to determine the belief value of the rule which is, by definition, the belief value of the antecedent (the IF part). This can be accomplished in many ways. The two most popular methods are referred to as the Min/Max method and the Bayesian method. The former method takes the Min belief of the arguments that are combined by AND and the Max belief of arguments that are combined by an OR. In a similar fashion, the Bayesian method uses product and generalized sum to accomplish these operations. These relations are summarized in Table 1, where w_1 and w_2 are the beliefs assigned to antecedent variables X_1 and X_2 , respectively.

The second step is to transfer this composite belief to the consequent variable (in this case Y). This *transfer* can also be accomplished in many ways. Once again there are three methods which are in popular use: the *Mandami* method, the *Larsen* method, and the *Sugeno* method. The first two of these methods essentially reconfigure the membership sets associated with the output variable(s). In our example above, if we assume that X_1 is *small* and X_2 is *medium* has belief 0.6 and 0.7 respectively, then if we were using the Min/Max method, the rule would assign a belief of 0.6 to the classification Y is *positive* (it would be 0.42 if we used the Bayesian method). Figure 3 illustrates the effect of the *Mandami* and *Larsen* methods in this example.

The bold lines indicate how the membership of *positive* is changed using both methods. The *Mandami* method uses the *Min* of the incoming belief level (0.6) and the membership curve and the *Larsen* method uses the *product* of the incoming belief and the membership curve.

In the *Sugeno* method, the output is not a fuzzy set but rather a crisp numerical value. For example, a rule in this type of system would have the form

IF(X_1 is small) AND (X_2 is medum) THEN ($Y=0.75$).

Since the output parameter (Y) is given an exact numerical value as a result of *satisfying* the rule, there is no need for assigning membership functions to this variable.

The last step in the general process is to *defuzzify* the results of each rule to form a crisp value and to aggregate all of these crisp results to form a single crisp output to pass to the control. Since the *Sugeno* systems already accomplish this directly, this step is not required for such systems. Once again, there are many methods available to accomplish this. We will describe only two,

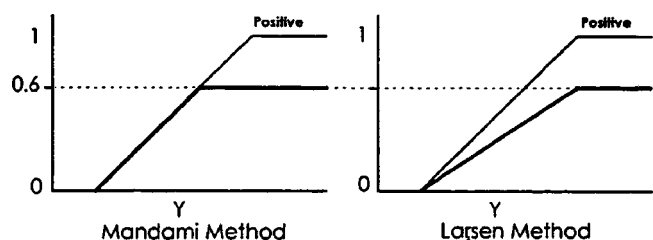


Fig. 3 Mandami and Larsen methods

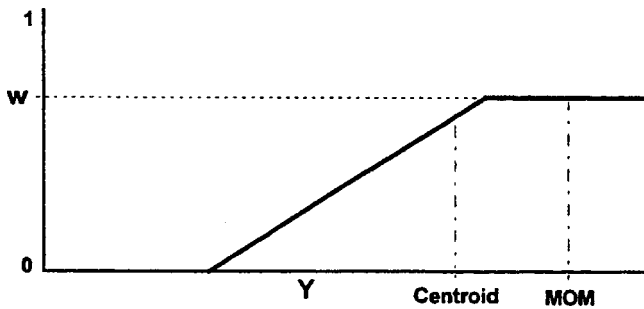


Fig. 4 Centroid and mean of max methods

namely the *Centroid* and *Mean of Max* (MOM) methods. The centroid method takes the adjusted membership (bold line) and computes the centroid or first moment. This involves computing $\int xf(x)dx$, where $f(x)$ denotes the membership function in question. This will produce a crisp value on the horizontal axis that geometrically represents the *balancing* point for that membership area. The MOM method picks those abscissa values which admit maximum belief points on the adjusted membership and then computes the mean of these points (see Fig. 4). Because of the computational complexity of the centroid method, the MOM method is typically used in real time applications.

The final step is to aggregate these crisp values to form a single crisp output value. The method which we will employ is to take a weighted average where the weights will be equal to the level of belief in the corresponding rules (Tuskamoto's method). Thus, if we had n rules R_1, R_2, \dots, R_n with respective beliefs w_1, w_2, \dots, w_n yielding crisp values (after defuzzification) y_1, y_2, \dots, y_n , then the final output would be

$$y = \frac{\sum_{i=1}^n w_i y_i}{\sum_{i=1}^n w_i}$$

It should be evident from the above descriptions that once the membership curves are defined and fixed and the rulebase specified, then the fuzzy system defines a deterministic mapping between the input variables and the output variable(s), and that this relationship is neither capricious nor random. It will, like any mathematical relationship, *yield the same output for the same input*. The utility of this approach is that we have employed only natural language rules and have taken advantage of the imprecision in the classification of the input/output variables to arrive at a quantifiable (and easily modifiable) algorithm. In the fuel flow selection logic described in the sequel, we will employ the *Sugeno* method because of its effectiveness in real-time applications.

Typical Control Loop Architecture

A high level overview of typical FADEC control law architecture is provided in Fig. 5. Inspection of Fig. 5 shows *three categories of control loops, selection logic, and a common integrator*. The reader should note that the output of each control loop is a rate of change of fuel flow (hereafter called Wfdot) which, when integrated, will produce the fuel flow required to meet the performance criterion demanded by the engine operating condition.

Control Loops. The three categories of Control loops are as follows.

The *rotor speed governing loops* are designed to hold a particular engine rotor speed ($N1$ or $N2$) at a particular operating point. Since the only function of these loops is to maintain an operating point, they are traditionally designed very conservatively (i.e., 2–3 rad crossover), and to have hardly any overshoot. It is com-

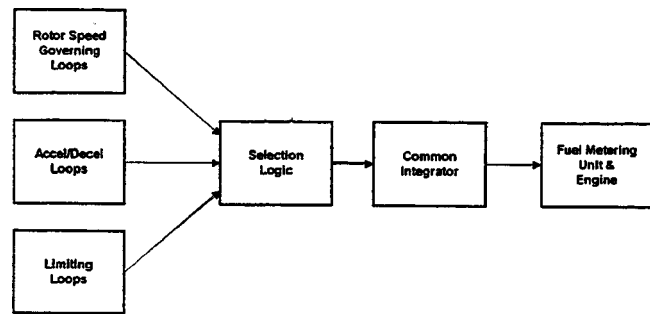


Fig. 5 Typical control law architecture

mon practice to govern on one rotor speed for “above idle” conditions (usually $N1$) and to idle govern on the $N2$ rotor speed. The idle governor can be thought of as a limiting loop that will not let the engine drop below the minimum speed required to maintain the idle operating point. Since the engine W_f to rotor speed transfer function can usually be reduced to a first order lag with a gain, the typical compensation method for the rotor speed governor is a lead lag compensator. Once again, the output of the rotor speed governor is a rate of change of fuel flow.

The *acceleration loop* (accel loop for short) and *deceleration loop* (decel) are both designed to transition the engine from one operating point to another as quickly as possible and not exceed any physical engine operating parameters. As such, these loops are designed to be as aggressive as possible (i.e., 4–5 rad crossover). It is common practice that the accel and decel loops control on the rate of change of $N2$ ($N2$ dot). Since the calculation of $N2$ dot involves the use of some sort of derivative lag, the typical compensation method, for the accel or decel loops, is a proportional plus integral compensator.

The limiting loops act as bounds on the Wfdot to the common integrator. They represent either physical engine and/or actuator limitations of the real engine hardware, or safety limits to avoid flameout or surge. It is common practice for a FADEC to contain the following limiting loops.

$N2$ and $N1$ redline loops: These loops place limitations on how fast the high and low rotor spools are allowed to rotate. These loops represent allowable maximums. The compensation for these loops is typically the same as for any other speed control loop.

Temperature limit loop: This loop limits the temperature of the parameter in question, usually exhaust gas temperature (EGT). This loop represents an allowable maximum. Since the engine W_f to temperature transfer function can usually be reduced to a single pole and zero, the typical compensation method for the temperature limiter is a lead lag compensator.

Ratio unit limit loop: This loop limits the $W_f/P3$ ratio units, and represents both maximum and minimum allowable limits. This loop contains no compensation in the classic sense. Rather, max and min ratio units are calculated as a function of corrected $N2$, multiplied by burner pressure, and compared to the actual fuel flow through a gain.

Wfdot limits: The Wfdot limits are not really control loops. They represent scheduled physical limits on the rate of change of fuel flow to the engine. They represent both maximum and minimum allowable limits, and are usually scheduled as a function of corrected $N2$.

The reader should note that care must be taken to ensure that a loop's compensator does not “wind up” when it is not being selected by the selection logic. There are various techniques to accomplish this, but these methods are not the subject of this paper and, as such, will not be presented.

Selection Logic. This section will discuss the traditional selection logic used in a typical FADEC. In order to facilitate this discussion, a simplified FADEC control law architecture will be defined with the following loops:

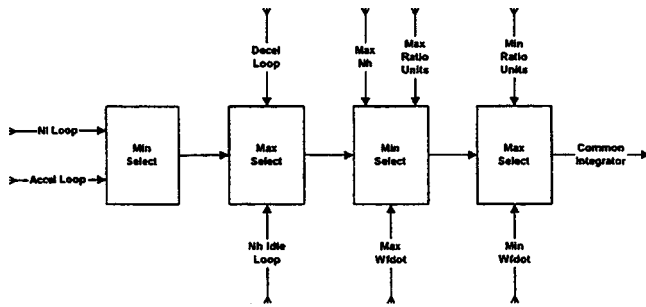


Fig. 6 Traditional selection logic

- An $N2$ Idle Governing Loop
- An $N1$ Governing Loop
- Acceleration and Deceleration Loops
- An $N2$ Red Line Limiting Loop
- A Wfdot Limiting Loop
- A Ratio Units Limiting Loop

The simplified architecture defined above also will be used as the basis for the design of the fuzzy selection logic. This design will be presented in the next section.

The traditional selection logic is a simplistic cascade of min select and max select logic gates. This is illustrated in Fig. 6, with explanations to follow. Figure 6 is provided to show the selection in *functional* form. The intent here is to facilitate better understanding. The actual implementation may be different to optimize code.

Selection begins with a min select between the calculated Wfdots from the $N1$ governor loop and the accel loop. This is more easily explained if we consider the situation at steady state. At steady state the $N1$ request and the actual $N1$ are equal. The $N1$ loop error is zero and the Wfdot from the $N1$ loop is also zero. The accel loop error, however, is very large since an accel reference is being calculated, but the rate of change of $N2$ is zero. In this situation the $N1$ loop will be chosen by the min select and, barring any limit exceedence, the $N1$ governing loop will be in control.

A different situation will occur if a transient to full power is suddenly requested. In this situation the $N1$ loop error, and the Wfdot from the $N1$ loop, will become very large. When the Wfdot from the $N1$ loop becomes larger than the Wfdot from the accel loop, the accel loop will win the min select and assume control. The accel loop will remain in control until the actual $N1$ gets close enough to the $N1$ reference such that the Wfdot from the $N1$ loop drops below the Wfdot from the accel loop.

The output from the first min select is sent to a max select with Wfdots from the $N2$ idle loop and the decel loop. The $N2$ idle loop acts to ensure that the minimum Wfdot required to keep the engine at idle is satisfied. This max select will not let the Wfdot to the common integrator fall below this minimum idle limit. The reasoning for the max select with the decel loop is similar to that of the min select with the accel loop, but for transients in the reverse direction.

The remaining min select and max select gates are utilized to protect against physical limit exceedence. The winning Wfdot, from the first two selections, is min selected with the maximum allowable Wfdots from the $N2$, Wfdot, and ratio units loops. The winner of that selection is max selected with the minimum allowable Wfdots from the Wfdot, and ratio units loops.

Common Integrator. The purpose of the common integrator is to integrate the winning Wfdot from the selection logic into the Wf fuel flow command to the engine. This integrator is very often implemented as a limited integrator to eliminate the possibility of integrator windup.

Fuzzy Fuel Flow Selection Logic

The selection logic, in the present FADEC designs, grants absolute authority to the selected control loop. One and only one loop is in control at any given moment. The approach taken in the fuzzy fuel flow selector is a departure from this classical paradigm. In this design, each loop has a *level of authority* (LA) which is computed in terms of fuzzy rules and membership functions. The sum of the LAs over all loops is unity. Thus, at any given moment, several loops may be in control to differing levels of authority. This approach provides a smoother transition between loops competing for control with an attendant increase in system performance.

The fuzzy selector will be designed to perform loop selection for the performance loops of the FADEC. These include the $N1$ speed governing loop, the accel loop, and the decel loop. Limiting loops such as $N2$ redline and min/max fuel flow rates of change limiting are best performed as crisp limiters (i.e., the simplistic cascade of min and max select gates), and are not included in this design. A simplified block diagram is provided in Fig. 7.

The fuzzy selector is segmented into two stages. The first computes a *degree* of authority for each control loop under consideration. These values will be numbers between 0 and 1. The second stage computes a rate of change of fuel (Wfdot) which combines all of the control loop outputs in accordance to their computed degree of authority.

The fuzzy selector inputs will consist of the loop errors and the Wfdots for each of the loops in question. Dividing each of the loop errors by the max error for that loop will normalize these errors. This will provide a non-dimensional loop error in the range of $[-1, 1]$. A similar method is used for the Wfdots.

The inputs are passed through the fuzzy rulebase, a sample of which is depicted in Table 2. This table is a succinct (though functional) representation of the rules. The qualifiers are chosen as follows: large positive (LP), small positive (SP), zero (ZE), small negative (SN), large negative (LN), positive (POS), and negative (NEG).

The rulebase is a combination of two sets of rules. The first set (rules 1 through 3) mimics the rules from the traditional selector, but with the aid of the fuzzy qualifiers. For example, rule 1 states:

If the loop error from the $N1$ Governor is SN or ZE or SP and...

...The difference between the Wfdots from the $N1$ Governor Loop and the Accel Loop is ZE or NEG (the $N1$ Governor Wfdot is smaller than the Accel Wfdot) and...

...The difference between the Wfdots from the $N1$ Governor Loop and the Decel Loop is ZE or POS (the $N1$ Governor Wfdot is larger than the Decel Wfdot), then...

...The Level of Authority for the $N1$ Governor Loop is 1, and the Level of Authority for the Accel and Decel Loops is 0.

This rule (longwinded though it may sound) would be exactly the same as choosing the $N1$ governor loop through the min select with accel and the max select with decel, if the qualifiers were crisp.

The second set (rules 4 through 7) defines rules which are designed to enhance performance. For example, rule 4 states:

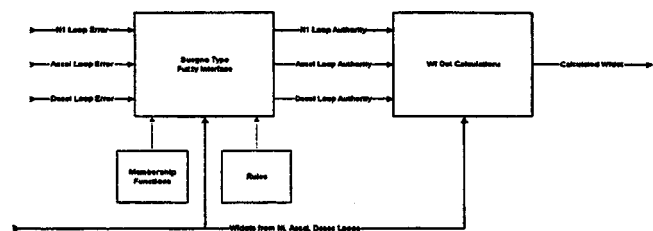


Fig. 7 Overview of fuzzy selector

Table 2 Fuzzy selector rule base

| Rule # | Loop errors | | | WfDot errors | | Loop LA=1 |
|--------|----------------|----------------------|-------|--------------|-----------|-----------|
| | N1 | Accel | Decel | N1-Accel | N1-Decel | |
| 1 | SN or ZE or SP | | | ZE or NEG | ZE or POS | N1 Gov |
| 2 | SN or ZE or SP | | | POS | | Accel |
| 3 | SN or ZE or SP | | | | NEG | Decel |
| 4 | LP | SN or ZE or SP or LP | | | | Accel |
| 5 | LP | LN | | | | Decel |
| 6 | LN | LN or SN or ZE or SP | | | | Decel |
| 7 | LN | LP | | | | Accel |

If the loop error from the N1 Governor is LP and...

The loop error from Accel is LN or SN or ZE or SP then...

The Level of Authority for the Accel Loop is 1, and the Level of Authority for the N1 governor and Decel Loops is 0.

This rule effectively keeps the control on the accel loop when the N1 governor position loop error is considered to be large positive (according to the fuzzy definition of a large positive error). The accel loop is allowed to do its job as long as this rule is satisfied.

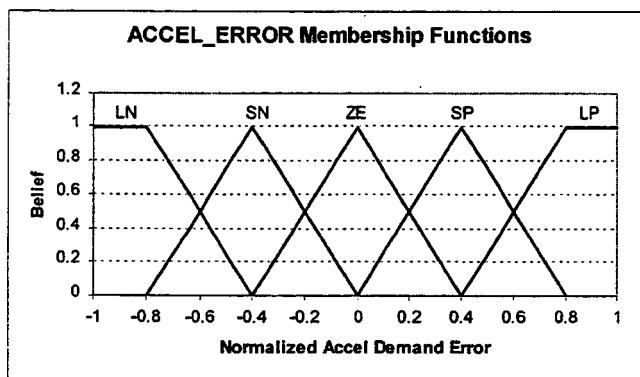
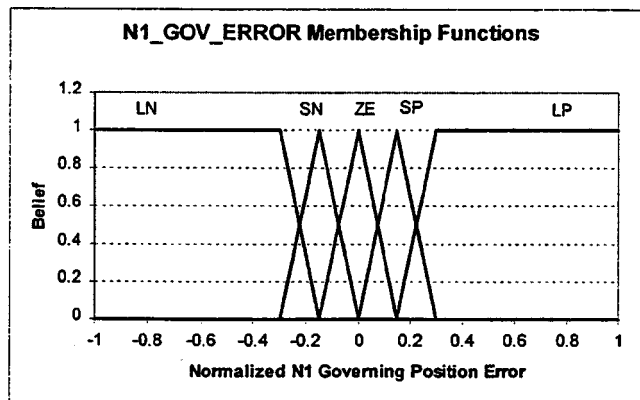


Fig. 8 (a) N1 governor error membership functions; (b) accel (decel) error membership functions.

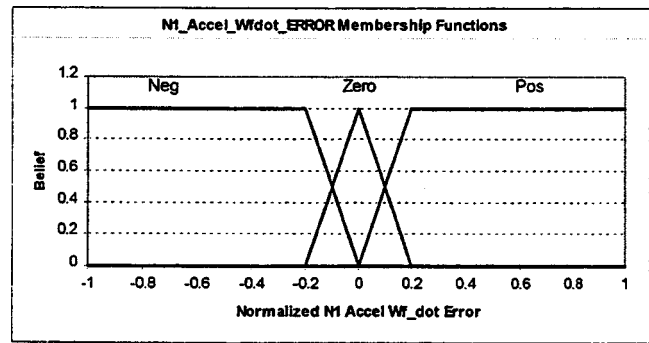


Fig. 9 N1-accel (decel) Wfdot membership functions

The qualifiers LN, SN, ZE, SP, LP, POS, and NEG are defined by means of membership functions for each loop. The membership functions for the N1 governor, and accel loops, are provided in Figs. 8(a) and 8(b), respectively. The membership function for decel is identical to that of accel. The membership functions for the N1-accel Wfdot is provided in Fig. 9. The membership functions for the N1-decel is identical to that of N1-accel.

The performance of the fuzzy selector will be demonstrated with an example implementation.

An Example Implementation

The performance of the fuzzy fuel flow selection logic will be compared to that of the traditional selection logic. This will be accomplished by using a non-real-time simulation model of a small engine control system of Hamilton Sundstrand manufacture. This model uses a three state, state variable engine model (SVM) as the representation of the plant. The simulation of the FADEC contains all of the control loops already presented in the sections on selection logic. The simulation was implemented using an industry standard simulation tool.

A loop indicator is included in the simulation. This loop indicator will indicate which loop is currently being chosen by the selection logic. Table 3 is provided to define the loop indicator.

A series of test cases will provide the means of comparison of the two selection methods. The test cases shall be limited to sea level static, standard day conditions for brevity.

First and foremost is the case that represents a snap accel from idle to max take-off conditions. Figures 10 and 11 show the time response of the N1 spool speed, and the loop indicator, when TLA is moved from the idle detent to the max take off detent in 1 sec. The solid line represents the response when the traditional selector is used, and the dashed line represents the response when the fuzzy selector is used. The reader will note the performance increase when the fuzzy selector is used. The typical specification for a 1-sec acceleration from idle to max take off, at sea level static standard day conditions, is 5 sec to reach 98 percent of the N1 reference. When considered against this specification, the per-

Table 3 Control loop indicator definition

| Loop indicator # | Loop in control |
|------------------|----------------------|
| 1 | N1 Governor |
| 2 | Acceleration |
| 3 | Deceleration |
| 4 | Not used |
| 5 | N2 idle governor |
| 6 | N2 red line |
| 7 | Not used |
| 8 | Max Wfdot limit |
| 9 | Min Wfdot limit |
| 10 | Max ratio unit limit |
| 11 | Min ratio unit limit |

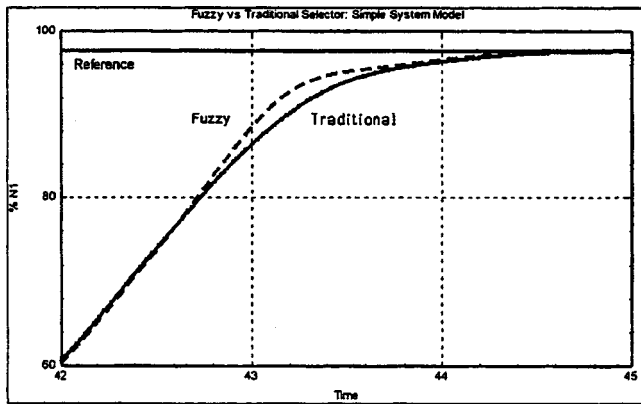


Fig. 10 $N1$ time response for idle/MTO snap accel

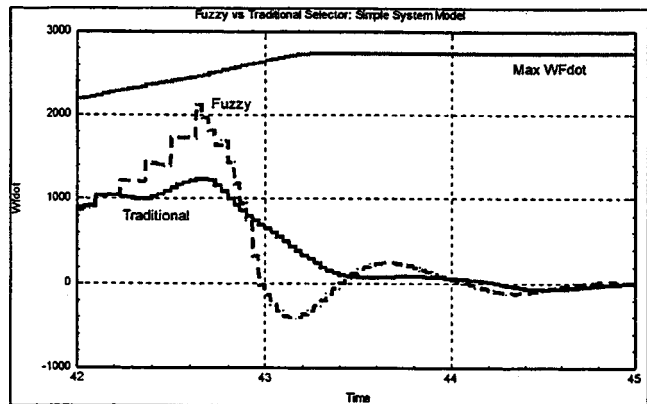


Fig. 13 Wfdot and limits for idle/MTO snap accel

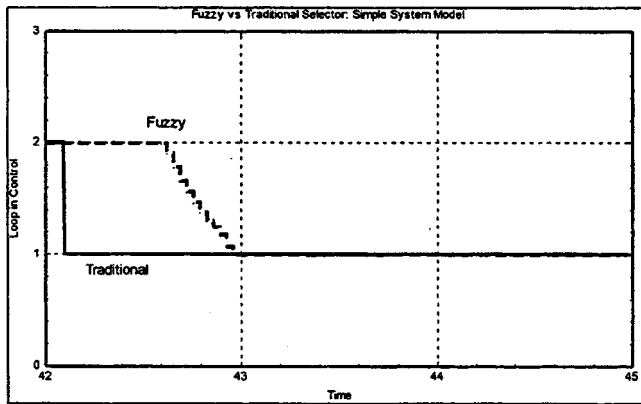


Fig. 11 Loop indicator for idle/MTO snap accel

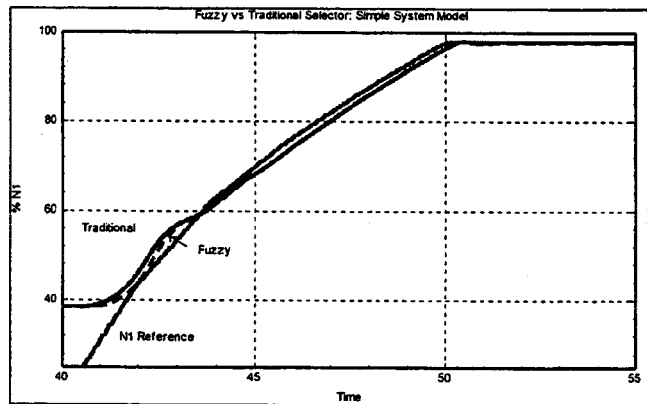


Fig. 14 $N1$ time response for idle/MTO slow accel

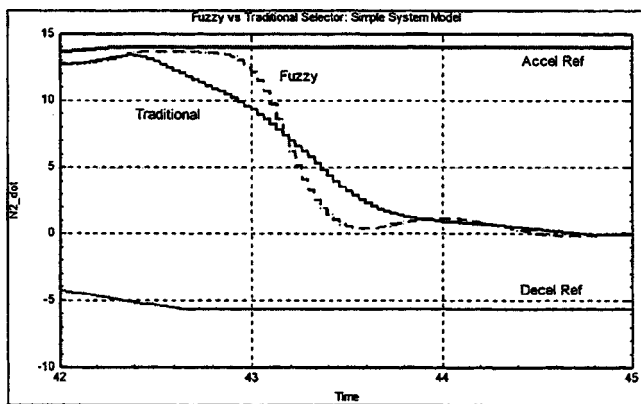


Fig. 12 $N2$ dot and accel reference for idle/MTO snap accel

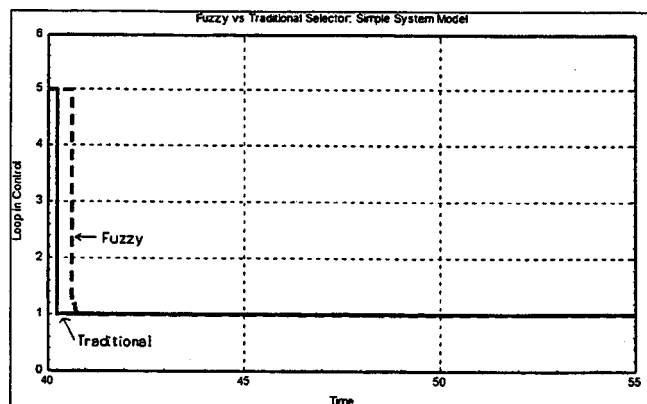


Fig. 15 Loop indicator for idle/MTO slow accel

formance increase is slightly greater than 2 percent. This is a modest increase, but is considered promising given the simplicity of the rulebase.

The performance increase is realized because the control stays on the accel loop longer, and smoothly transitions from the accel loop to the $N1$ governor loop according to the fuzzy ruleset. This is in sharp contrast to the abrupt (and premature) change dictated by the traditional selection logic. Figure 12 provides the time response of the rate of change of $N2$ dot and the accel reference. The reader will note that no potentially harmful overshoot of the accel reference is observed.

A word needs to be said about the modest performance in-

crease. Figure 13 provides the winning Wfdot plotted alongside the max Wfdot limit. The reader will note that the fuzzy selector causes the winning Wfdot to come closer to the Wfdot max limit than the traditional selector. Indeed, this higher Wfdot is the reason any performance increase was realized at all. If the allowable maximum Wfdot (the physical limitations) were higher, it would have been possible to tune the fuzzy selector to realize an even greater performance increase.

The same test case can be run, but this time a 10-sec transient will be used. Examination of Figs. 14, 15, and 16 (analogous to Figs. 10, 11, and 12) shows virtually identical results between the traditional selector and the fuzzy selector.

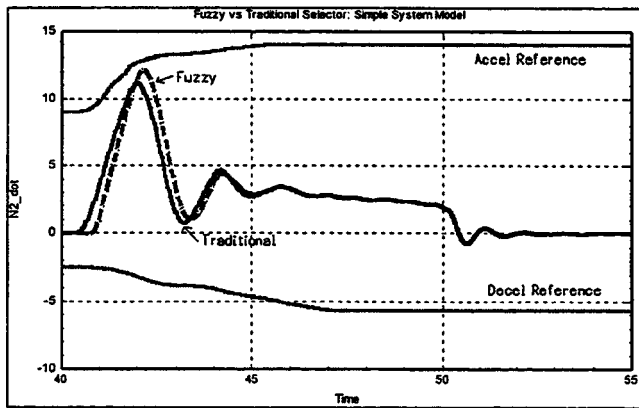


Fig. 16 N2 dot and accel reference for idle/MTO slow accel

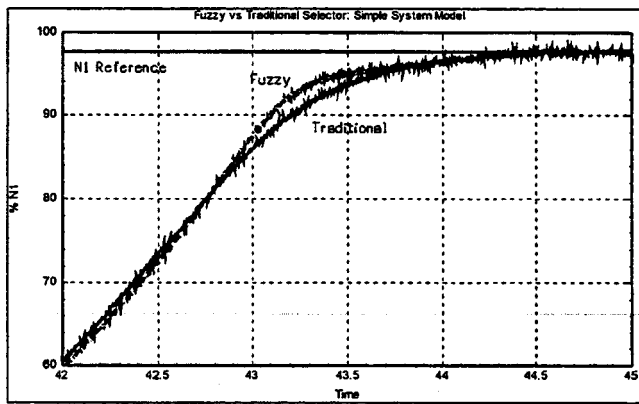


Fig. 17 N1 time response for idle/MTO snap accel w/noise

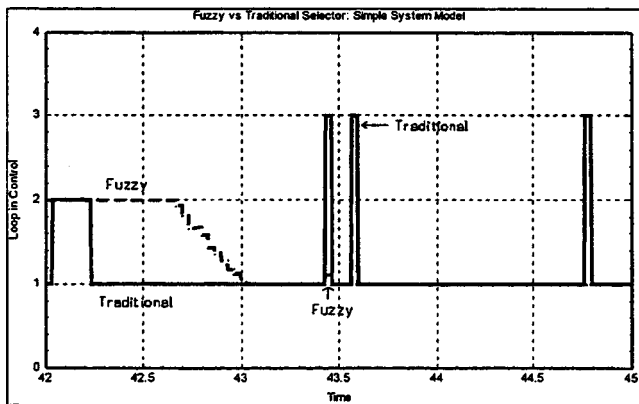


Fig. 18 Loop indicator for idle/MTO snap accel w/noise

The reason the results are so similar is that, for this particular case, the error in the $N1$ governor loop never gets sufficiently large to trigger the performance enhancement rules of the fuzzy selector. Therefore, the fuzzy selector exhibits behavior very similar to that of the traditional selector.

The fuzzy selector seems to be more tolerant to system noise than the traditional selector. Figures 17 and 18 show the time response of the $N1$ spool speed, and the loop indicator, when the same 1-sec transient, outlined above, is run with white noise applied to the $N1$ speed signal.

Examination of Fig. 18 shows that while the traditional selector has a tendency to momentarily jump onto the decel loop in the

Table 4 Additional test cases for fuzzy selector

| Test case(s) | Expected results |
|---|--|
| Wfdot max (and min) limits exceeded | Both selectors choose Wfdot max (or min) limiting loop |
| $N2$ red line limit exceeded | Both selectors choose $N2$ red line limiting loop |
| Ratio units max (and min) limits exceeded | Both selectors choose ratio units max (or min) limiting loop |

presence of white noise, the fuzzy selector has a tendency to stay on the $N1$ governor. This additional noise immunity is gained because the fuzzy selector is based on a series of weighted rules, rather than simplistic max and min logic select gates.

Additional test cases were run whose results will not be presented here. A description of the additional test cases, and the expected results, are tabulated in Table 4. All expected results were realized.

The reader will note that, in all test cases, the transient began at the same $N2$ idle governing point.

Stability

The stability of a control loop is usually specified in terms of its relative stability characteristics. The most classic of these is the gain margin (GM) and the phase margin (PM). These relative stability measures are obtained from frequency response plots of the loop while it is in a steady-state operating condition. It is possible, for example, to determine the relative stability of the $N1$ governing loop, stand alone, when it is in steady state. The relative stability for each of the control loops of the example system presented in this paper is well known and considered sufficient.

It is not possible, however, to determine the relative stability characteristics of the fuzzy selector system while it is transitioning from one control loop to another since, during the transition, the system is not in steady state. The authors have chosen a very simple test, however, to determine the stability of the entire system at discrete transition points. A simulation of an impulse was input into the $N1$ governing loop and the accel loop at three transition points during a 1-sec accel from idle to maximum take off. The transition points were chosen as 25 percent $N1$ governing (i.e., LA for the $N1$ governor is 0.25)–75 percent accel, 50 percent $N1$ governing–50 percent accel, and 75 percent $N1$ governing–25 percent accel. The resulting impulse responses demonstrate stability at all three transition points. Figure 19 provides the $N1$ time response for idle/MTO snap accel when an impulse is input to accel loop at the 25 percent $N1$ governing–75

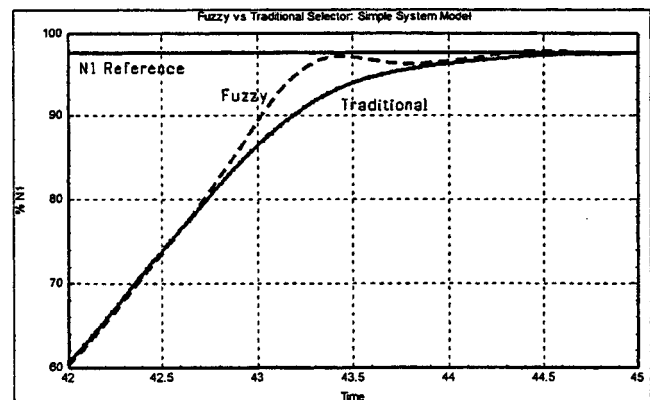


Fig. 19 N1 impulse Response for idle/MTO snap accel

percent accel transition point (42.66 sec). The conclusion from Fig. 19, and the other responses not provided, is that the fuzzy selector is stable.

The reader should note that the approximation of the impulse function that was used for this demonstration was 10,000 percent $N1$ (or 10,000 percent/sec $N2$ dot) for one update of the $N1$ governing and accel control logic (33 millisecc).

Future Considerations

The authors intend to pursue the following three areas regarding the fuzzy fuel flow selector:

1. The example implementation used in this paper was simplistic. Its purpose was to demonstrate the feasibility of the fuzzy fuel flow selector. Future work will integrate the fuzzy fuel flow selector into a simulation that represents the complete implementation of a typical FADEC. Since this will require the fuzzy fuel flow selector to work in the presence of additional control loops, there is little doubt the rulebase will need to be expanded.

2. The amount of program memory required in implementing the fuzzy fuel flow selector, and the program execution time, requires investigation.

3. The authors would like to establish a technique whereby the relative stability of the fuzzy fuel flow selector, during transitions, may be established.

Nomenclature

Accel = acceleration control loop
Decel = deceleration control loop
EGT = exhaust gas temperature
FADEC = full authority digital engine control
GM = gain margin

LA = level of authority
LN = large negative
LP = large positive
MTO = max take off power
NEG = Negative
N2 = high rotor spool speed
N2dot = rate of change of N2
N1 = low rotor spool speed
N1Gov = N1 governor control loop
POS = positive
PM = phase margin
P3 = burner pressure
SN = small negative
SP = small positive
SVM = state variable engine model
TLA = throttle lever angle
Wf = gas generator fuel flow
Wfdot = rate of change of Wf
ZE = zero

References

- [1] Zadeh, L. A., 1965, *Fuzzy sets*, Inform. Control Vol. 8.
- [2] Zadeh, L. A., 1973, *Outline of a New Approach to the Analysis of Complex Systems and Decision Processes*, IEEE Transactions on Systems, Man, and Cybernetics, SMC-3,(1)(1973).
- [3] Mandami, E. H., 1974, *Applications of Fuzzy Algorithms for Simple Dynamic Plant*, Proc. IEEE, Vol. 121, No. 12.
- [4] Ross, Timothy J., 1995, *Fuzzy Logic with Engineering Applications*, McGraw-Hill, Inc., ISBN 0-07-053917-0
- [5] Volponi, Allan J. and Solomonides, Jason B., 1994, *Advanced Engine Control Development Utilizing Fuzzy Logic and Rapid Prototyping*, Royal Aeronautical Society Proceedings ISBN 1 85768 021 9, November 1994.

The Use of Kalman Filter and Neural Network Methodologies in Gas Turbine Performance Diagnostics: A Comparative Study

A. J. Volponi
H. DePold
R. Ganguli

Pratt & Whitney,
400 Main Street,
East Hartford, CT 06108

C. Daguang
Beijing University of Aeronautics
and Astronautics,
Beijing, China

The goal of gas turbine performance diagnostics is to accurately detect, isolate, and assess the changes in engine module performance, engine system malfunctions and instrumentation problems from knowledge of measured parameters taken along the engine's gas path. The method has been applied to a wide variety of commercial and military engines in the three decades since its inception as a diagnostic tool and has enjoyed a reasonable degree of success. During that time many methodologies and implementations of the basic concept have been investigated ranging from the statistically based methods to those employing elements from the field of artificial intelligence. The two most publicized methods involve the use of either Kalman filters or artificial neural networks (ANN) as the primary vehicle for the fault isolation process. The present paper makes a comparison of these two techniques. [DOI: 10.1115/1.1419016]

Introduction

The goal of gas turbine performance diagnostics is to accurately detect, isolate, and assess the changes in engine module performance, engine system malfunctions, and instrumentation problems from knowledge of measured parameters taken along the engine's gas path. Discernable shifts in engine speeds, temperatures, pressures, fuel flow, etc., provide the requisite information for determining the underlying shift in engine operation from a presumed nominal state. Historically, this type of analysis was performed through the use of a Kalman filter or one of its derivatives to simultaneously estimate a plurality of engine faults. In the past decade, artificial neural networks (ANN) have been employed as a pattern recognition device to accomplish the same task. Both methods have enjoyed a reasonable success.

The purpose of this paper is to outline the two methodologies, discuss their relative merits and weaknesses, and provide a direct comparison of the two techniques via a controlled computer simulation study. In the sequel, we will provide a brief general description of both the Kalman filter and ANN as applied to the diagnostic problem. For the purpose of conducting a comparison, we will limit the framework of the diagnostic system to the problem of isolating a single fault to the component level. The single faults under consideration will be comprised of engine module, engine system, and instrumentation faults.

Kalman Filter Approach

Kalman filter methods were introduced as a fault isolation and assessment technique for relative engine performance diagnostics in the late 1970s and early 1980s ([1–3]). The success enjoyed in these early programs promoted the use of these techniques in subsequent years to become the central methodology utilized in many current engine performance analysis programs. In the sequel we

will briefly describe this procedure, however, for a more detailed discussion we refer the reader to the following sources: [4–13].

The general approach taken for engine fault diagnostics typically involves the use of a linearized model approximation evaluated at a selected engine operating point. This provides a matrix relationship between changes in engine component performance (independent parameters) and the attendant changes in typically measured engine parameters such as spool speeds, internal temperatures and pressures, fuel flow, etc. (dependent parameters). This relationship may be succinctly represented as

$$\mathbf{z} = \mathbf{H}\mathbf{x} + \theta \quad (1)$$

where \mathbf{z} is a vector of measured parameter deltas, \mathbf{x} is a vector of fault deltas, \mathbf{H} is a matrix of fault influence coefficients, and θ is a random vector representing the uncertainties inherent in the measurement process. In addition to the precision of the individual sensors, it has been customary to address the potential for sensor bias and drift. Consequently, the fault vector given in the model above is often configured to contain components directly related to sensor error in addition to engine fault deltas.

The fault vector x given in the model can be thought of as the concatenation of an engine fault vector (x_e) and a sensor (error) fault vector x_s , i.e., $x = [x_e; x_s]^T$ where

$$x_e = \begin{bmatrix} \Delta \eta_{\text{FAN}} \\ \Delta \Gamma_{\text{FAN}} \\ \Delta \eta_{\text{CH}} \\ \vdots \\ \Delta A_5 \end{bmatrix} \text{ and } x_s = \begin{bmatrix} \Delta N1_{\text{err}} \\ \Delta P3_{\text{err}} \\ \Delta Wf_{\text{err}} \\ \vdots \\ \Delta T49_{\text{err}} \end{bmatrix}. \quad (2)$$

We may rewrite Eq. (1) as

$$z = H_e x_e + H_s x_s + \theta = [H_e \quad \vdots \quad H_s] \begin{bmatrix} x_e \\ \cdots \\ x_s \end{bmatrix} + \theta = Hx + \theta. \quad (3)$$

The matrix H has been partitioned into two parts; a matrix of engine fault influence coefficients (H_e) and a matrix of sensor fault influence coefficients (H_s). The generation of these matrices

Contributed by the International Gas Turbine Institute (IGTI) of THE AMERICAN SOCIETY OF MECHANICAL ENGINEERS for publication in the ASME JOURNAL OF ENGINEERING FOR GAS TURBINES AND POWER. Paper presented at the International Gas Turbine and Aeroengine Congress and Exhibition, Munich, Germany, May 8–11, 2000; Paper 2000-GT-0547. Manuscript received by IGTI November 1999; final revision received by ASME Headquarters February 2000. Associate Editor: D. Wisler.

Table 1 Sample root cause influences

| | T49C2 °C | WF percent | N2C2 percent | N1C2 percent | P25Q2 percent | T25C2 °C | T3C2 °C | P3Q2 percent |
|-----------|-------------|---------------|-----------------|-----------------|------------------|-------------|------------|-----------------|
| FAN | 3.86 | 0.70 | 0.30 | -0.68 | -2.00 | -1.95 | -1.58 | -0.03 |
| LPC | -4.54 | -0.66 | -0.29 | -0.14 | 1.18 | 0.11 | -2.62 | 0.01 |
| HPC | -6.80 | -0.80 | 0.06 | -0.05 | -0.83 | -0.71 | -3.66 | 0.17 |
| HPT | -10.88 | -1.29 | 0.57 | -0.08 | -1.29 | -1.14 | 4.03 | 1.26 |
| LPT | -1.19 | 0.96 | -0.63 | 0.98 | 3.40 | 3.45 | -1.42 | 0.11 |
| 2.5 BLD | -3.07 | -0.49 | -0.16 | 0.00 | 1.04 | 0.85 | -0.86 | 0.00 |
| FP14 | 1.22 | 0.21 | 0.07 | -0.24 | -0.67 | -0.73 | 0.15 | -0.01 |
| FP8 | -0.61 | -1.39 | -0.17 | -0.64 | -1.06 | -1.31 | -2.62 | -1.09 |
| 2.9 BLD | -4.22 | -1.06 | -0.29 | -0.06 | 0.68 | 0.63 | 0.60 | 0.02 |
| TCC | 17.75 | 2.10 | -0.90 | 0.12 | 2.14 | 1.86 | -4.38 | -1.11 |
| HPCSV M | -0.95 | -0.11 | 0.39 | 0.00 | -0.08 | -0.09 | 0.34 | 0.09 |
| P49 Error | -0.33 | -1.70 | -0.25 | -0.46 | -0.55 | 0.63 | -0.21 | -1.22 |

and their interpretation have been discussed in great detail in [4,14] and elsewhere in the literature and will not be pursued in this paper.

The model, as configured above, has often been used for the purpose of tracking slowly occurring changes in engine performance from revenue flight data, through the use of a Kalman filter-based methodology. An estimate for these performance shifts, \hat{x} , would be given by

$$\begin{bmatrix} \hat{x}_e \\ \dots \\ \hat{x}_s \end{bmatrix} = \hat{x} = \bar{x} + D(z - H\bar{x}) = \begin{bmatrix} \bar{x}_e \\ \dots \\ \bar{x}_s \end{bmatrix} + \begin{bmatrix} D_e \\ \dots \\ D_s \end{bmatrix} \left(z - [H_e; H_s] \begin{bmatrix} \bar{x}_e \\ \dots \\ \bar{x}_s \end{bmatrix} \right)$$

$$\hat{x} = \text{prediction} + \text{GAIN}(\text{residual}) = \text{prediction} + \text{correction} \quad (4)$$

where \bar{x} represents an a priori estimate of the engine/sensor fault deltas and D is the (Kalman) gain matrix referred to as the *diagnostic matrix*. The diagnostic matrix is computed as a function of several quantities; the engine/sensor influence coefficients H , the measurement covariance matrix R , and a positive semidefinite weighting matrix P_0 . The diagnostic matrix is computed as

$$D = \begin{bmatrix} D_e \\ \dots \\ D_s \end{bmatrix} = P_0 H^T (H P_0 H^T + R)^{-1} = \begin{bmatrix} P_0^e H_e^T (H_e P_0^e H_e^T + R)^{-1} \\ \dots \\ P_0^s H_s^T (H_s P_0^s H_s^T + R)^{-1} \end{bmatrix} \quad (5)$$

where P_0^e and P_0^s are weighting submatrices for the engine and sensor fault estimation, respectively. An in-depth report on the generation of the P_0 and R matrices can be found in references [4,5].

The use of the predictor/corrector methods like the Kalman filter to estimate sensor error has made possible a more reliable and consistent gas turbine module performance analysis. The procedure outlined above can be applied in a snapshot analysis or as a continuing recursive analysis as new engine data are made available over time. In either scenario, the simultaneous determination of both engine faults and measurement errors by this methodology has been successfully applied to a large number of commercial and military families of engines with varying instrumentation suites for two decades.

In the sequel, we shall alter our emphasis to consider the problem of fault isolation, given the premise that a fault event has been detected. The problem of detection becomes one of recognizing a step or rate change in a gas path parameter or a collection of parameters. The problems associated with fault detection and the mechanisms which can be applied to accomplish this task have been reported by [15]. The types of faults that will be considered in this discussion include engine performance faults, engine system faults, and instrumentation faults.

Single Fault Isolation. The Kalman filter can be configured to emulate a *single fault isolator (SFI)*. This is a snapshot type of analysis in the sense that it operates on a set of measurement deltas without any a priori information or pre-history. The object of the analysis is to flag a root cause on the basis of a single measurement delta set. Root causes are *single fault* occurrences and are pre-defined for the system. They consist of coupled faults within the major modules of the engine, certain system faults such as handling and ECS bleed leaks and failures, variable stator vane malfunctions, TCC malfunctions as well as certain instrumentation faults. These faults are assumed to occur in isolation, i.e., there will be one and only one root cause occurrence at any given time. The purpose of the single fault isolator is to identify the correct root cause once a trend shift is detected.

Root Causes. Root Causes can be thought of as state variables, x_1, x_2, \dots, x_n . They are represented within this system as vectors of measurement deltas, $z_1^*, z_2^*, \dots, z_n^*$, which are calculated by applying influence coefficients. As an illustration, we can consider the following 12 root causes. These root causes may exist at varying levels. The state representation of the root cause will be in the form of a one percent cause to be consistent with other influences.

- | | | |
|-----|-----------|--|
| 1. | FAN | coupled FAN (-1 percent η , -1.25 percent FC) |
| 2. | LPC | coupled LPC (-1 percent η , -1.10 percent FC) |
| 3. | HPC | coupled HPC (-1 percent η , -0.80 percent FC) |
| 4. | HPT | coupled HPT (-1 percent η , +0.75 percent FP4) |
| 5. | LPT | coupled LPT (-1 percent η , +1.65 percent FP45) |
| 6. | 2.5 BLD | stability bleed leak (one percent) |
| 7. | 2.9 BLD | start bleed (one percent) |
| 8. | FP14 | fan discharge area (one percent) |
| 9. | FP8 | core discharge area (one percent) |
| 10. | TCC | turbine case cooling (on) |
| 11. | HPCSV M | HPC stator vane misrigging |
| 12. | P49 Error | P49 indication problem (two percent) |

An example of the influences for these root causes is depicted in Table 1.

The actual root cause may appear as some multiple of the influences represented in Table 1. For instance, a 2.5 bleed root cause may manifest itself as a stuck open bleed (≈ 15 percent 2.5 bleed fault) or a partial bleed leak, say two percent 2.5 bleed fault. These two faults will be treated as the same by the Kalman estimator. The difference between the two faults is one of magnitude. The magnitude is estimated by the Kalman filter. Its ability to estimate correctly will depend on the signal to noise ratio for the given fault. In this particular case, a two percent 2.5 bleed is sometimes confused with an LPC fault or a 2.9 Bleed fault. On the other hand, a stuck 2.5 Bleed (14.77 percent) has a significantly higher S/N ratio and is estimated correctly. Another factor which impacts accuracy of the estimator is the number of measured parameters. We will consider systems that have between four and eight measurements in flight.

Given the definitions above for root cause influences (one percent), a typical set of possible *single faults* may be constructed. For purposes of this study, we will consider the following single fault definitions, depicted in Table 2.

If we represent these 11 faults as, x_1, x_2, \dots, x_{11} , and the matrix of influences by H^* , $(9 \times 8)^1$ matrix depicted above then a set of expected measurement delta vectors, $z_1^*, z_2^*, \dots, z_{11}^*$, would be calculated by

$$z_i^* = (H^*)^T x_i \quad \text{for } i=1,2,\dots,11. \quad (6)$$

Each z_i^* would be an 8×1 vector of measurement deltas.

The general form of the discrete Kalman filter estimator at time $k+1$ is as follows:

State extrapolation:

$$\hat{x}(k+1|k) = \Phi(k+1)\hat{x}_k.$$

Covariance extrapolation:

$$P(k+1|k) = \Phi(k+1)P_k\Phi^T(k+1) + Q_{k+1}.$$

Kalman gain:

$$D_{k+1} = P(k+1|k)H_{k+1}^T(H_{k+1}P(k+1|k)H_{k+1}^T + R_{k+1})^{-1}.$$

State update:

$$\hat{x}_{k+1} = \hat{x}(k+1|k) + D_{k+1}[z_{k+1} - H_{k+1}\hat{x}(k+1|k)]$$

Covariance update:

$$P_{k+1} = [I - D_{k+1}H_{k+1}]P(k+1|k).$$

For the single fault isolator we make the following adjustments:

$$\Phi_{k+1} = I$$

$$Q_{k+1} = 0$$

$$H_{k+1} = M_c(H^*)^T$$

M_c = measurement configuration vector = $\text{diag}(m_1, m_2, \dots, m_8)$

(diagonal matrix assuming eight potential measurements)

$$\text{where } m_j = \begin{cases} 1 & \text{if } j\text{th measurement is available} \\ 0 & \text{otherwise.} \end{cases}$$

The effect of the measurement configuration matrix is to zero the rows of the root cause influence matrix corresponding to the measurements that are NOT available. The resulting matrix of influences is 8×9 for this example.

The single fault isolation is obtained by processing the general Kalman equations iteratively to provide a snapshot analysis for each of the root causes under consideration (11 in this example). Each "call" to the Kalman filter will be made with a different P_0 matrix chosen to accentuate the k th root cause. Since these are snapshot analyses, the covariance update calculation is not required. The a priori state estimate is also assumed to be zero. An SFI analysis is performed typically after a trend shift has been detected in the measurement deltas at some discrete time, say, between time k and $k+1$. The "delta-delta" ($Z_{k+1} - Z_k$) constitutes the input measurement delta, Z , to the SFI.

The SFI is evaluated iteratively for each single fault (11 in the above example). This process will yield estimates for each single fault under consideration. It is necessary to rank each of these estimates and determine the top two or three single faults. The measure used to compare estimates for this purpose of ranking is a normalized measurement error norm which we will describe below. The single fault admitting the minimum error is deemed the most likely, the second smallest error, the next likely, and so forth.

¹The row dimension of H^* is 9 (and not 11) since the BLD25 and BLD29 root causes are used to model the two different magnitude faults being considered.

Table 2 Single fault problem set

| Fault | percent |
|------------------------|----------------|
| FAN | -2 |
| LPC | -2 |
| HPC | -2 |
| HPT | -2 |
| LPT | -2 |
| 2.5 BLD (low and high) | 2 and 14.77 |
| 2.9 BLD (low and high) | 6.74 and 15.45 |
| HPCSVM | -6 |
| P49 Error | 2 |

As mentioned above, the normalized measurement error will take into consideration the measurement nonrepeatabilities of the system. It is assumed that these are known a priori or computed from data during initialization of the diagnostic system. However the values are obtained, they are assumed to be known and are passed to the Kalman filter in the form of a positive definite matrix R . The diagonal elements of this matrix represent the *variances* of the measurement deltas (*corrected* quantities). Thus, if we represent the measurement delta-delta vector (between time k and $k+1$, assuming that a trend shift has been detected during this time period) by $Z = [z_1, z_2, \dots, z_8]$, then the $\text{diag}(R) = [\sigma_1^2, \sigma_2^2, \dots, \sigma_8^2]$, represents the individual variances. For definiteness, assume we have calculated the n th single fault estimate. The associated normalized measurement error norm, e_n , is calculated as follows: \hat{x}_n = SFI estimate for the n th root cause

$$e_n = \left[\frac{\sum_{k=1}^8 \left(\frac{z_k - z_k^*}{\sigma_k} \right)^2}{\sum_{k=1}^8 z_k^2} \right]^{1/2} \quad (7)$$

z_k^* = k th element of the vector $M_c(H^*)^T \hat{x}_n$.

It is possible for the estimated values for some single faults to be *opposite* in polarity than what would be reasonably expected.² For example, an HPT SF of magnitude -2 percent might yield an estimated value of +0.5 percent for an LPC SFI. Given that a sudden shift in observed gas path parameters has taken place during engine operation, it is not likely that the condition of any given module has improved and thus a positive shift in performance would not be given serious consideration. Thus, some pre-processing is mandated before the error ranking is performed. This takes the form of perusing each of the SFI estimates and considering only those which admit a reasonable polarity. Ordering the errors from min to max we obtain

$$e_{i_1} \leq e_{i_2} \leq \dots \leq e_{i_n} \quad (8)$$

corresponding to the single fault estimates

$$\hat{x}_{i_1} \leq \hat{x}_{i_2} \leq \dots \leq \hat{x}_{i_n} \quad (9)$$

in order of likelihood. In most cases, the first of these ranked single faults is deemed to be the underlying fault and is reported to the user. In some instances, however, it may be prudent to report the first and second SFs, since there exists the possibility for an erroneous fault identification, especially if the associated error norms are "close."

Depending on the circumstances, the SFI may experience a confusion between two single faults. The aliasing of SFs depends on the single faults themselves, their relative magnitude with respect to the nonrepeatability of the measurements and the number of measurements available for the analysis. All of these factors can contribute to a confounding of the underlying SF with another

²Although this is not a common occurrence, it is possible for an SF estimate indicating an improvement in performance to admit the minimum measurement error norm and hence *win* the isolation selection.

Table 3 SFI accuracy: Kalman filter, 8 measurements

| 8 Measurement Set | | | |
|-------------------|-------|-------|-------|
| FAULT | 1st | Top 2 | Top 3 |
| FAN | 100% | 100% | 100% |
| LPC | 90% | 100% | 100% |
| HPC | 100% | 100% | 100% |
| HPT | 100% | 100% | 100% |
| LPT | 100% | 100% | 100% |
| 2.5 BLD | 85% | 100% | 100% |
| 2.9 BLD | 96.7% | 100% | 100% |
| HPCSV M | 100% | 100% | 100% |
| P49err | 100% | 100% | 100% |
| Total | 96.9% | 100% | 100% |

Table 4 SFI accuracy: Kalman filter, 4 measurements

| 4 Measurement Set | | | |
|-------------------|-------|--------|-------|
| FAULT | 1st | Top 2 | Top 3 |
| FAN | 100% | 100% | 100% |
| LPC | 90% | 90% | 100% |
| HPC | 100% | 100% | 100% |
| HPT | 100% | 100% | 100% |
| LPT | 100% | 100% | 100% |
| 2.5 BLD | 50% | 75% | 95% |
| 2.9 BLD | 80.0% | 100.0% | 100% |
| HPCSV M | 100% | 100% | 100% |
| P49err | 100% | 100% | 100% |
| Total | 91.1% | 96.1% | 99.4% |

SF. To mitigate the possibility of a false identification, some post-processing of the SFI results may be required. This will improve the overall accuracy of the system. The rules to be applied would be empirically motivated and would be suggested by computer simulation test cases. For the problem set considered in this study (Table 2), it was not necessary to undergo this type of post-processing.

Computer Simulation Results. Using Equation (1), we can generate a set of hypothetical “noisy” measurements for each of the 11 single faults under consideration ($x_i, i = 1, 2, \dots, 11$). These noisy measurement vectors (z_k) are then passed through the SFI process, the results ranked and tabulated for first, second, and third ranked faults. These results appear in Table 3 and 4 for eight and four measurement set³ systems, respectively, where the four bleed leak faults have been combined into two faults. The

³The four measurements set used in this study consisted of the flight required parameters ($T49, Wf, N1$ and $N2$).

entries indicate the percentage of time the implanted fault is correctly announced as first, second, and third choice.

The results demonstrate a 96.9 percent and 91.1 percent accuracy for the first choice fault isolation for eight and four measurement systems, respectively. If we weaken the accuracy criteria to that of being correct within the top two choices, the relative precision of the isolation increases to 100 percent and 96.1 percent. In either case, the isolation accuracy is quite good.

The fact that we can obtain a 91 percent *hit rate* with only four measurements raises the question as to why one would ever consider adding more instrumentation. There are several answers to this question, one being that a *multiple* fault performance assessment would not perform as well with fewer measurements. But even within the constraints of this study (i.e., single fault annunciation), the “*more the better*” argument still holds if we consider the robustness of the system. One measure of robustness would be to vary the module couplings (flow capacity versus efficiency, hard coupled relationship) in the implanted faults beyond that which is assumed in the numerical model (i.e., the influences coefficients H^*). Figures 1 and 2 depict the impact on first choice accuracy for eight and four measurement systems, respectively, when the coupling factor for the compression modules (FAN, LPC, HPC) are randomly varied.⁴

The LPC and HPC clearly exhibit greater robustness to modeling assumptions in the 8 measurement system.

In the sequel, we will briefly discuss artificial neural networks (ANNs), and their usage in engine performance diagnostics. The discussion will be intentionally brief since there already exists ample documentation of this methodology in the literature, and the reader is directed to the references for additional detail. For the purpose of making a direct comparison with the Kalman filter methodology, we will confine much of the discussion to the single fault isolation problem introduced in the prelude. The identical computer simulation test will be used as the vehicle for the evaluation.

Artificial Neural Network Approach

The fault isolation problem can be considered to be a pattern classification problem. N -dimensional vectors in an N -dimensional space represent the system response. The system response for different faults tends to be partitioned into different regions of this space and can be regarded as patterns. Pattern recognition involves learning these partitions, from simulated or real data, so that a given system response can be classified as a particular fault. Neural networks represent a powerful pattern recognition technique, and have been applied for fault detection of

⁴The turbine modules’ (HPT and LPT) isolation accuracy was essentially unaffected and hence were not plotted.

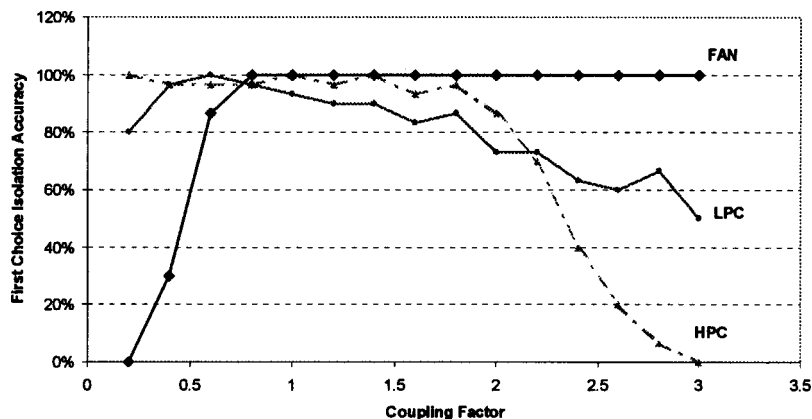


Fig. 1 Coupling factor impact on 8 measurement system

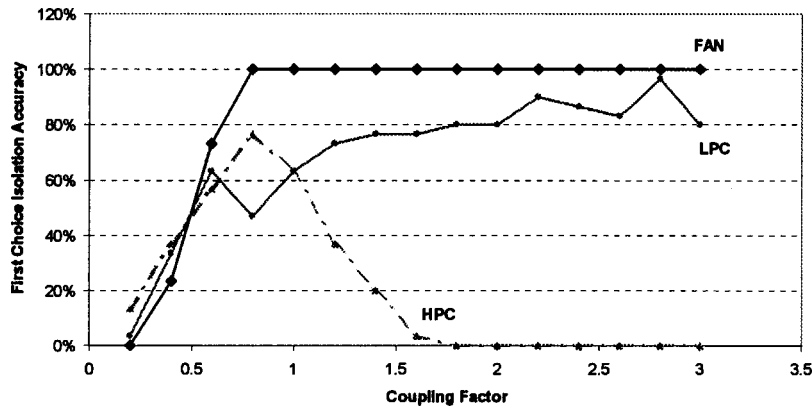


Fig. 2 Coupling factor impact on 4 measurement system

complex systems such as aerospace vehicles ([16]), nuclear power plants ([17]), and chemical process facilities ([18]) among others. A key advantage of neural networks over other methods is their ability to recognize relationships between patterns despite the presence of noise contamination and/or partial information ([19]).

Most applications of ANN to fault diagnostics follow a common process. The ANN is trained off-line on fault signatures relating the changes in system measurements from a “good” baseline to system faults. Typically, faults are embedded into the computer simulations, or real fault data is used, or a combination of both. In case simulated data is used, noise must be added to make the simulations realistic. Such a training process where the ANN is presented input and output data by the system designer is known as supervised learning. Once the ANN has been properly trained using this process of supervised learning, it can analyze data that are different from those it was originally exposed to during the training sessions. When the trained ANN is placed on-line, it recognizes a similar response from the actual system.

The discussion below involves the use of two types of neural networks for engine fault diagnostics, a feed forward ANN trained using back-propagation (BP) algorithm and a hybrid neural network.

Back-Propagation (BP) Algorithm. While there are several types of neural networks, multilayer feedforward networks trained using the backpropagation algorithm have emerged as the most widely used. Figure 3 illustrates the schematic of a feedforward neural network, which consists of an input layer, an output layer, and one or more hidden layers. The number of neurons in the input and output layers is determined by the number of input measurements and output parameters. The number of hidden layer nodes is selected based on convergence criterion and the characteristic of the input-output mapping relationship.

A three-layer feedforward network is used for the present work, as shown in Fig. 1. The feedforward network is trained using supervised learning, which involves presenting input-output pairs to the ANN and then using the BP algorithm to learn the relationships between the inputs and outputs by minimizing the following error measure:

$$E = \sum_{k=1}^N E_k \quad (10)$$

in which E_k represents the root mean square error associated with the k th training sample and where N represents the number of samples that are used for training the network. The BP algorithm uses a gradient search to perform the nonlinear optimization needed to minimize the error. Further details about the BP algorithm are outlined in standard texts on neural networks ([20]).

To improve the ANN’s ability to deal with data scatter, the input data were normalized using the following formula:

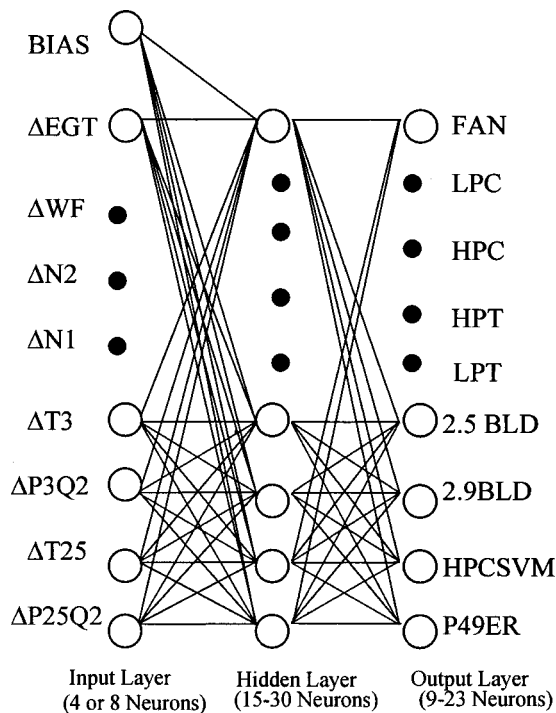


Fig. 3 Architecture of three layer feedforward ANN

Table 5 SFI accuracy: ANN, 8 measurements

| 8 Measurement Set | | | |
|-------------------|-------|-------|-------|
| FAULT | 1st | Top 2 | Top 3 |
| FAN | 100% | 100% | 100% |
| LPC | 60% | 80% | 90% |
| HPC | 100% | 100% | 100% |
| HPT | 100% | 100% | 100% |
| LPT | 100% | 100% | 100% |
| 2.5 BLD | 80% | 85% | 85% |
| 2.9 BLD | 86.7% | 86.7% | 86.7% |
| HPCSVM | 90% | 100% | 100% |
| P49err | 100% | 100% | 100% |
| Total | 90.7% | 94.6% | 95.7% |

Table 6 SFI accuracy: ANN, 4 measurements

| 4 Measurement Set | | | |
|-------------------|-------|-------|-------|
| FAULT | 1st | Top 2 | Top 3 |
| FAN | 100% | 100% | 100% |
| LPC | 90% | 90% | 90% |
| HPC | 90% | 100% | 100% |
| HPT | 100% | 100% | 100% |
| LPT | 100% | 100% | 100% |
| 2.5 BLD | 75% | 75% | 75% |
| 2.9 BLD | 86.7% | 86.7% | 86.7% |
| HPCSVM | 100% | 100% | 100% |
| P49err | 100% | 100% | 100% |
| Total | 93.5% | 94.6% | 94.6% |

$$Y_{in} = Y_{im} / (Y_{i \max} \cdot \sigma_i)$$

where Y_i is the i th monitoring parameter; n , m , and \max are the normalized, measured, and maximum possible value, respectively; σ_i is the standard deviation of the i th monitoring parameter.

The standard deviations and the influence coefficients used for the ANN testing are the same as those used for the Kalman filter described previously. For comparison of fault isolation results with four inputs and eight inputs, 20 training cases and 50 testing cases were generated. The training cases were used for the BP algorithm to train the neural network. Once the neural network was trained, the test cases were used to evaluate the performance of the neural network. Data used for training was not used for testing the neural network. The diagnostic results were considered for the three highest outputs, which represent the three most likely faults.

The test results for eight and four measurements using the BP ANN are shown in Table 5 and Table 6, respectively. For both the eight and four measurement cases, the Kalman SFI results shown in Tables 5 and 6 are better than the BP ANN results. For the eight measurements case, the Kalman SFI has a 100 percent accuracy in fault isolation among the top three choices, compared to 95.7 percent for the BP ANN. For the four measurements case, the Kalman SFI has an accuracy of 99.4 percent in fault isolation among the top three choices, compared to 94.6 percent for the BP ANN.

Hybrid Neural Network Algorithm. The BP ANN is handicapped relative to the Kalman SFI in some ways. For example, while the Kalman SFI uses influence coefficients in the form of the H matrix to define the model, the BP ANN uses data generated from influence coefficients to “learn” the model.

A Hybrid NN is a network architecture where one or more ANN functions are replaced by an algorithm that includes domain knowledge ([21]). The objective is to substitute features in the neural network architecture that are already analytically understood. This avoids the need for training the ANN to learn information which is already known. For example, instead of using

Table 7 SFI accuracy: hybrid NN, 8 measurements

| 8 Measurement Set | | | |
|-------------------|-------|-------|-------|
| FAULT | 1st | Top 2 | Top 3 |
| FAN | 100% | 100% | 100% |
| LPC | 90% | 100% | 100% |
| HPC | 100% | 100% | 100% |
| HPT | 100% | 100% | 100% |
| LPT | 100% | 100% | 100% |
| 2.5 BLD | 90% | 100% | 100% |
| 2.9 BLD | 100% | 100% | 100% |
| HPCSVM | 100% | 100% | 100% |
| P49err | 100% | 100% | 100% |
| Total | 97.8% | 100% | 100% |

Table 8 SFI accuracy: hybrid NN, 4 measurements

| 4 Measurement Set | | | |
|-------------------|-------|-------|-------|
| FAULT | 1st | Top 2 | Top 3 |
| FAN | 90% | 100% | 100% |
| LPC | 90% | 90% | 100% |
| HPC | 100% | 100% | 100% |
| HPT | 100% | 100% | 100% |
| LPT | 100% | 100% | 100% |
| 2.5 BLD | 70% | 90% | 100% |
| 2.9 BLD | 86.7% | 86.7% | 86.7% |
| HPCSVM | 70% | 100% | 100% |
| P49err | 100% | 100% | 100% |
| Total | 91.1% | 97.8% | 100% |

training data based on influence coefficients, the Hybrid ANN uses the influence coefficients as part of the network model.

A Gaussian nearest neighbor function was substituted for the ANN feature identification function and the fault mapping function was ignored for this Hybrid NN algorithm. The output of the network was the root-sum-of-the-squares number of standard deviations from a perfect match of the fault pattern. The output of the network was used directly to rank the faults.

A test was made to determine if the neural network mapping to the faults could also be optimized. Up to 72 weightings were available between the eight measurement features and the nine faults. Thirty-six weightings were available with four measurements. While it was demonstrated that the weightings could be optimized, the tests were run with all the weightings set to unity.

The results from the Hybrid neural net are shown in Tables 7 and 8, for eight and four measurements, respectively. The accuracy of the Hybrid neural network compares favorably with the Kalman SFI. For the eight measurements case, both the Kalman SFI and the Hybrid ANN show a fault isolation accuracy among the top three choices of 100 percent. For the four measurement case, the Kalman SFI shows a fault isolation accuracy among the top three choices of 99.4 percent compared to 100 percent for the Hybrid ANN.

In general, the Hybrid ANN gives better results than the BP ANN. This may be because the hybrid uses the influence coefficients for each fault within the network, whereas the BP ANN has to learn the influence coefficients from the training data.

Kalman Filter and Neural Network Methods

Feedforward neural networks are typically made of interconnected nonlinear neurons and are particularly useful where the input-output relationship is nonlinear. The Kalman filter and the Hybrid neural network assume a linearized model of the system. In the present application, the linear model takes the form of influence coefficients. For a feedforward ANN, BP learning for linear problems in engine fault diagnostics will generally result in poorer performance compared to a Kalman filter or hybrid ANN approach.

Learning in neural networks involves mapping an input to an output. The input and outputs can be generated from models, from real data, or a combination of both. ANNs can therefore also be model-free estimators, a quality that is very useful if modeling information such as influence coefficients are not available. Kalman filters, on the other hand, are model-based estimators, and are suitable for problems in engine performance diagnostics where influence coefficients are available as the model.

Neural networks are not limited to multilayer neurons with BP training. Self-organizing maps based on competitive learning ([22]), simulated annealing based on statistical thermodynamics ([23]), Boltzmann learning ([24]) and radial basis functions ([25]) are some of the other developments in ANN which may be applicable to engine diagnostics. Combining the Kalman filter ap-

proach with some of the ANN methods may yield superior results for the engine diagnostic problem, than those obtainable within either methodology acting alone.

Concluding Remarks

Test results have suggested that the back-propagation neural network, the hybrid neural network, and the Kalman filter method are highly accurate for isolating single gas turbine fault symptoms. Furthermore, the results also indicate that these methodologies compare favorably in terms of accuracy, with a very slight advantage going to the Kalman filter approach.

Each method has its own advantages and disadvantages.

The ANN is inherently nonlinear and can be used in applications where model information is scarce or lacking altogether. The ANNs are, however, data driven and therefore must be trained. The training is typically performed offline in a supervised fashion, meaning that the input-output relationship is known. In the present application this means that the underlying fault(s) in the training data are already known. This could be a drawback if real engine data was used for training, since the precise disposition of the fault may or may not be known. If the engine configuration and/or instrumentation noise levels change, the ANN approach would require that a re-training be performed. Once trained, the ANN architecture provides a numerically simple, and hence fast diagnostic operator suitable for real-time application.

The Kalman filter is a linear model-based estimator and is suitable in those instances where a linear model is available and is known to be a reasonably accurate representation of the input-output relationship. In the engine performance diagnostics application, influence coefficients have, historically, been fairly accurate and robust linear models. The Kalman filter approach utilizes all model information available (a priori estimate information, measurement noise information, etc.) and can be easily configured to operate with different measurement suites, and fault configurations: single fault (as in this present study) or multiple fault isolation systems. Adaptive measures are also available to allow real-time reconfiguration of the Kalman filter to changing measurement noise levels.

The hybrid neural network, like the Kalman filter, is a model-based method utilizing influence coefficients as the primary linear model in a neural network architecture framework. For the single-fault isolation problem referenced in this study, the hybrid NN closely resembles a weighted least squares solution. This explains the close agreement between the hybrid NN and Kalman filter in the single-fault isolation computer simulation study.

Acknowledgment

The authors wish to thank Zhang Jin, Zhang Mingchuan, and Zhu Zhili of the Department of Jet Propulsion and Power at the Beijing University of Aeronautics and Astronautics as well as Lu Pong-jeu and Hsu Tzu-cheng of the Institute of Aeronautics and Astronautics, National Cheng Kung University in Taiwan for their work in developing the ANN Fault Analysis Application under contract with Pratt & Whitney.

Nomenclature

| | | |
|---------|---|---------------------------|
| ANN | = | artificial neural network |
| FAN | = | fan module |
| LPC | = | low pressure compressor |
| HPC | = | high pressure compressor |
| HPT | = | high pressure turbine |
| LPT | = | low pressure turbine |
| 2.5 BLD | = | stability bleed |
| 2.9 BLD | = | start bleed |
| TCC | = | turbine case cooling |
| N1 | = | low spool speed |
| N2 | = | high spool speed |
| T49 | = | exhaust gas temperature |

| | | |
|----------|---|-------------------------------|
| P3 | = | HPC exit pressure |
| P49 | = | exhaust pressure |
| HPCSV | = | variable stator vane |
| SFI | = | single fault isolator |
| H | = | influence coefficient matrix |
| D | = | Kalman gain matrix |
| R | = | measurement covariance matrix |
| P | = | state covariance matrix |
| Φ | = | state transition matrix |
| x | = | state Δ vector |
| z | = | measurement Δ vector |
| η | = | efficiency Δ |
| Γ | = | flow capacity Δ |
| FC | = | flow capacity |
| A | = | turbine nozzle area Δ |

Subscripts

| | | |
|-----|---|-------------------------------|
| e | = | relating to engine parameters |
| s | = | relating to sensor parameters |
| 0 | = | initial condition |
| k | = | discrete time k |

Superscripts

| | | |
|------|---|------------------|
| T | = | matrix transpose |
| -1 | = | matrix inverse |

References

- [1] Urban, L. A., 1974, "Parameter Selection for Multiple Fault Diagnostics of Gas Turbine Engines," *AGARD Conference Proceedings*, No. 165, NATO, Neuilly-sur-Seine, France.
- [2] Urban, L. A., 1972, "Gas Path Analysis Applied to Turbine Engine Condition Monitoring," AIAA/SAE Paper 72-1082.
- [3] Volponi, A., 1983, "Gas Path Analysis: An Approach to Engine Diagnostics," *Time-Dependent Failure Mechanisms and Assessment Methodologies*, Cambridge University Press, Cambridge, UK.
- [4] Volponi, A. J., and Urban, L. A., 1992, "Mathematical Methods of Relative Engine Performance Diagnostics," SAE Trans., **101**; Journal of Aerospace, Technical Paper 922048.
- [5] Doel, D. L., 1992, "TEMPER—A Gas Path Analysis Tool for Commercial Jet Engines," ASME Paper 92-GT-315.
- [6] Doel, D. L., 1993, "An Assessment of Weighted-Least-Squares Based Gas Path Analysis," ASME Paper 93-GT-119.
- [7] Stamatias, A. et al., 1991, "Jet Engine Fault Detection With Discrete Operating Points Gas Path Analysis," J. Propul. Power, **7**, No. 6.
- [8] Merrington, G. L., 1993, "Fault Diagnosis in Gas Turbines Using a Model Based Technique," ASME Paper 93-GT-13.
- [9] Glenn, D. E., 1988, "Gas Path Analysis and Engine Performance Monitoring In A Chinook Helicopter," AGARD: Engine Condition Monitoring, NATO, Neuilly-sur-Seine, France.
- [10] Winston, H., et al., 1991, "Integrating Numeric and Symbolic Processing For Gas Path Maintenance," AIAA Paper 91-0501.
- [11] Luppold, R. H., et al., 1989, "Estimating In-Flight Engine performance Variations Using Kalman Filter Concepts," AIAA Paper 89-2584.
- [12] Gallops, G. W., et al., 1992, "In-Flight Performance Diagnostic Capability Of An Adaptive Engine Model," AIAA Paper 92-3746.
- [13] Kerr, L. J., et al., 1991, "Real-Time Estimation of Gas Turbine Engine Damage Using a Control Based Kalman Filter Algorithm," ASME Paper 91-GT-216.
- [14] "Sensor Error Compensation in Engine Performance Diagnostics," 1994, ASME Paper No. 94-GT-058.
- [15] DePold, H., and Gass, F. D., 1998, "The Application of Expert Systems and Neural Networks to Gas Turbine Prognostics and Diagnostics," ASME Paper 98-GT-101.
- [16] McDuff, R. J., and Simpson, P. K., 1990, "An Investigation of Neural Network for F-16 Fault Diagnosis," *Proceedings of the SPIE Technical Symposium on Intelligent Information Systems*, The International Society for Optical Engineering, Bellingham, WA.
- [17] Guo, Z., and Uhrrig, R. E., 1992, "Using Modular Neural Networks to Monitor Accident Conditions in Nuclear Power Plants," *Proceedings of the SPIE Technical Symposium on Intelligent Information Systems*, The International Society for Optical Engineering, Bellingham, WA.

- [18] Wantanabe, K. et al., 1989, "Incipient Fault Diagnosis of Chemical Processes via Artificial Neural Network," *AIChE J.*, **35**, No. 11.
- [19] Holmstrom, L., and Koistinen, P., 1992, "Using Additive Noise in Back Propagation Training," *IEEE Trans. Neural Netw.*, **3**, No. 1.
- [20] Haykin, S., 1994, *Neural Networks—A Comprehensive Foundation*, Macmillian, New York.
- [21] Dasarathy, B. V., 1991, *Nearest Neighbor (NN) Norms: NN Pattern Classification Techniques*, IEEE Computer Society Press, New York.
- [22] Kohonen, T., 1990, "The Self-Organizing Map," *Proc. IEEE*, **78**, IEEE, New York.
- [23] Kirkpatrick, S., 1984, "Optimization by Simulated Annealing: Quantitative Studies," *J. Stat. Phys.*, **34**.
- [24] Ackley, D. H., Hinton, G. E., and Sejnowski, T. J., 1985, "A Learning Algorithm for Boltzmann Machines," *Cognitive Science*, Vol. 9, Cognitive Science Society, Cincinnati, OH.
- [25] Broomhead, D. S., and Lowe, D., 1988, "Multivariate Function Interpolation and Adaptive Networks," *Complex Systems*, Vol. 2, Complex Systems Publications, Champaign, IL.
- [26] Cybenko, G., 1989, "Approximations of Superposition of a Sigmoidal Function," *Mathematics of Control, Signals and Systems*, Vol. 2.

Active Combustion Instability Control With Spinning Valve Actuator

P. Barooah¹

T. J. Anderson²

J. M. Cohen³

United Technologies Research Center,
East Hartford, CT 06108

Active combustion control has been accomplished in many laboratory and real-world combustion systems by fuel modulation as the control input. The modulation is commonly achieved using reciprocating flow control devices. These demonstrations have been successful because the instabilities have been at relatively low frequencies (~200 Hz) or the scale of demonstration has been small enough to require very small levels of modulation. A number of real-world instabilities in gas turbine engines involve higher frequencies (200–500 Hz) and attenuation requires the modulation of large fractions of the engine fuel flow rate (hundreds of pounds per hour). A spinning drum valve was built to modulate fuel for these applications. Tests showed that this device provided more than 30% flow modulation up to 800 Hz for liquid fuel flows of greater than 400 lbm/hr. This paper describes the performance of the valve in flow bench tests, open-loop forcing, and closed-loop instability control tests. The closed-loop tests were done on a single-nozzle combustor rig which exhibited a limit-cycling instability at a frequency of ~280 Hz with an amplitude of ~7 psi. It also encounters an instability at 575 Hz under a different set up of the rig, though active control on that instability has not been investigated so far. The test results show that the spinning valve could be effectively used for active instability control, though the control algorithms need to be developed which will deal with or account for actuator phase drift/error. [DOI: 10.1115/1.1582495]

1 Introduction

As the environmental pressures to further reduce NO_x, CO and smoke continue, combustion chambers in gas turbines have become more susceptible to combustion instabilities. The traditional design methodology for suppressing combustion instabilities is proving inadequate; therefore new techniques, such as active control approaches are sought.

Combustion instabilities are caused by the coupling of acoustic velocity/pressure fluctuations with unsteady heat release, [1]. One method of active control that has been widely used in recent times is modulation of fuel supply to the combustor. If the heat release fluctuation due to the modulating fuel supply is in opposite phase to the natural instability driven heat release fluctuation, the two will cancel each other out and the instability will be suppressed. The simplest implementation of this method is the phase shifting controller, in which the fuel supply is modulated at a certain phase shift from the main harmonic of the pressure oscillations inside the combustor.

One impediment to the successful application of such active control schemes is the lack of actuators capable of providing large modulation levels at frequencies in the range of these instabilities, i.e., in the 250–1000 Hz range. A rotary fuel modulation device, or “spinning valve” was developed which could modulate fuel with an amplitude of more than 30% of mean flow rate up to 1 kHz. The valve was used for active combustion control in a NASA program in which the goal was the suppression of high-frequency longitudinal modes, which exist in higher-volumetric

heat release aeroengines. Two different instabilities are observed under different rig setups. One is a limit cycling instability at around 280 Hz and the other is a resonant peak at around 575 Hz. So far the spinning valve has been used in active control of only the 280 Hz instability, though it was developed with instabilities at higher frequencies in mind.

This paper reports active control work for the 280 Hz instability using the spinning valve as the fuel modulation actuator. Section 1.2 describes the experimental facility set up for combustion instability control. Section 2 describes the operating principles of the spinning valve and the results of fuel modulation tests done in a cold-flow test loop. Section 3 briefly describes the phase shifting control algorithm, as it was applied in combustion control tests. A valve controller was employed to make the spinning valve modulate fuel in phase with a controller command. Section 4 describes the valve controller development work. The results of active control tests with the spinning valve in the single nozzle combustor rig are described in Section 5 and finally, Section 6 summarizes the lessons learned from the exercise.

1.2 Single-Nozzle Combustor. As part of a NASA-sponsored active instability control program, a single-nozzle combustor rig was constructed to replicate combustion instabilities seen in full-scale aeroengines, [2]. The active combustion control tests with the spinning valve were conducted using this combustor. Figure 1 shows a schematic of the combustor test section assembly. Jet-A fuel was supplied to the injector by a high-pressure fuel supply. The fuel injector was a prefilming, high-shear airblast injector that was traceable to full-scale engine hardware. The combustor operated at realistic engine conditions and produced ~4 MW at peak power. All the active control tests described in this paper were done at the operating conditions shown in Table 1. These values are for a mid-power condition.

Dynamic measurements of the unsteady component of pressure were made at a number of locations within the combustor. The sensor labeled “PLA1C1” in Fig. 1 is used within this paper as a

¹Current address: Department of Electrical and Computer Engineering, University of California, Santa Barbara, CA.

²Current address: Institute for Defense Analyses, Alexandria, VA.

³Corresponding author. Current address: Pratt & Whitney, 411 Main Street, MS 163-03, East Hartford, CT 06108.

Contributed by the International Gas Turbine Institute (IGTI) of THE AMERICAN SOCIETY OF MECHANICAL ENGINEERS for publication in the ASME JOURNAL OF ENGINEERING FOR GAS TURBINES AND POWER. Paper presented at the International Gas Turbine and Aeroengine Congress and Exhibition, Amsterdam, The Netherlands, June 3–6, 2002; Paper No. 2002-GT-30042. Manuscript received by IGTI, Dec. 2001, final revision, Mar. 2002. Associate Editor: E. Benvenuti.

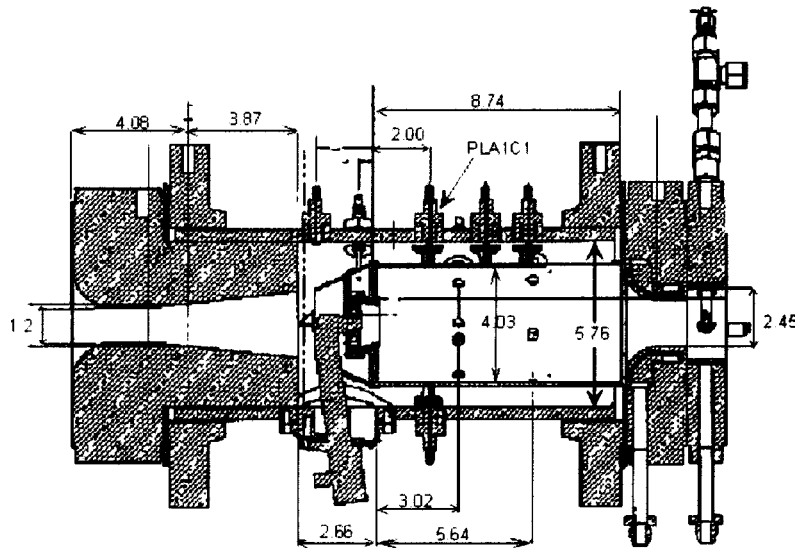


Fig. 1 Single-nozzle combustor assembly, showing choked inlet (left) and outlet (right) boundaries, fuel injector and combustor liner. Unsteady pressure measurement (PLA1C1) located at 1.865 in. downstream of combustor bulkhead. Dimensions shown are in inches.

pressure representative of the unsteady combustor pressure. This sensor was mounted on the liner at 1.865 in. downstream of the combustor bulkhead. Data were acquired with a dSpace data acquisition system typically sampling at 5 kHz. Low-pass (2 kHz) anti-aliasing filters were installed on all channels. Fast response pressure measurements were also made in the fuel line downstream and upstream of the fuel modulating valve to measure modulation levels and check steadiness of the fuel supply pres-

sure, respectively. The fuel flow rate was modulated with the spinning valve, which was controlled by a PC-based DSP (dSpace data acquisition/ control system, ds1003 processor board) through a Moog T200 motor controller.

2 Spinning Valve Actuator

The spinning valve design was based on a rotary concept rather than a conventional reciprocating-spool configuration in order to generate the maximum frequency response (Fig. 2). The concept used a rotating drum with 12 regularly spaced holes around the circumference, which aligned with holes in the surrounding housing to pass flow. By minimizing the clearance between the housing and the drum, leakage was reduced when the holes in the drum and housing were misaligned. Exit holes in the housing were radially opposed to balance pressure and minimize transverse loads. A design with two exit holes was chosen for this application to balance radial pressure loads on the shaft and provide sufficient flow capacity in a reasonably sized package.

It should be noted that additional exit holes could have been built into the housing, reducing the valve size for a given flow capacity in exchange for added plumbing complexity. Additional

Table 1 Combustor operating conditions and uncontrolled instability characteristics for 300 Hz instability

| Test Variable | Mean Value |
|--|------------|
| Inlet air pressure, P_3 (psia) | 110 |
| Inlet air temperature, T_3 ($^{\circ}$ F) | 610 |
| Fuel flow rate, W_f (lbm/hr) | 207 |
| Air flow rate, W_a (lbm/sec) | 2.55 |
| Unsteady pressure | 6.5 |
| Amplitude, P'_{comb} (psi) | |
| Mean fuel/air ratio | 0.022 |
| Instability frequency (Hz) | 280 |

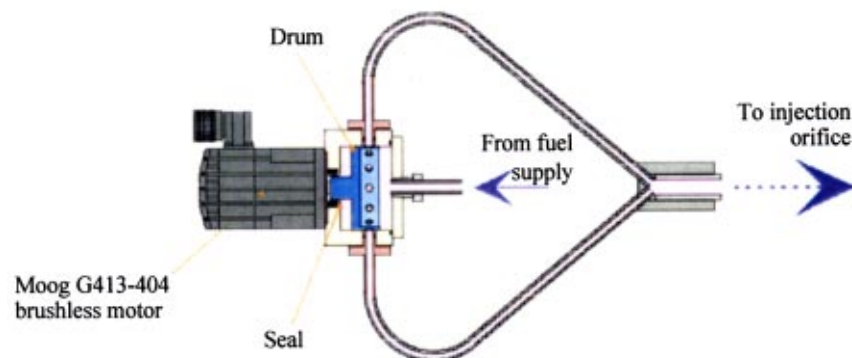


Fig. 2 Schematic of the spinning valve concept, using a rotating drum with multiple holes, which align with exit holes in the case. A close tolerance was maintained to produce the maximum level of modulation and to minimize leakage. An even number of exit holes provided a pressure balance.

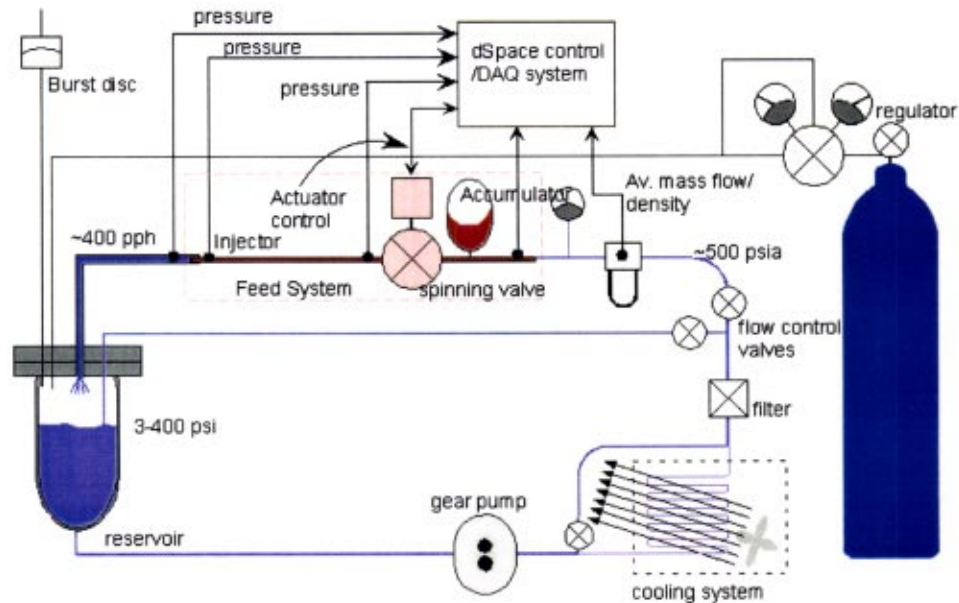


Fig. 3 Schematic of the cold flow test facility. A cooling system maintained a constant temperature despite heat added from pump work at high-pressure differentials. A high-pressure nitrogen system was used to pressurize the fuel system to realistic operating pressures.

manifold complexity can, however, introduce unexpected systems response characteristics due to the acoustics of the plumbing system.

Unlike a reciprocating device, the upper frequency limit of the spinning valve was not due to the spool inertia or power required to accelerate it. A relatively low power was required to run this device at all frequencies to overcome motor losses, shaft seal friction and limited fluid friction in the valve chamber.

The valve built for this program used a Moog G413-404 motor, a readily available motor capable of meeting the speed, acceleration, and precision requirements. Runout and radial clearance tolerances were better than 0.001 in., making it possible to design for clearances that minimized leakage when the valve is closed. Twelve holes around the spool circumference allowed a fuel modulation frequency of 1 kHz to be reached at 5000 rpm, well within the capability of this motor.

2.1 Fuel Flow Rate Modulation Authority. The valve system and its associated plumbing were tested in a small Jet-A flow loop with a capacity similar to that required for the single nozzle combustor tests (~500 lbm/hr). The flow-loop facility configuration is shown in Fig. 3. The valve was tested with a downstream orifice with a flow capacity equal to that of the fuel nozzle. A bypass line upstream of the test valve could be opened to set the upstream supply pressure. An accumulator or pulse damper was installed upstream of the spinning valve to reduce pressure oscillations at the inlet. This device was pressurized to approximately 60% of the operating pressure at the valve inlet and, in lower modulation levels, could damp out almost all upstream oscillations. However, the modulation levels achieved using the spinning valve were so large that the pulse damper was less effective with this valve. The fuel reservoir could be pressurized with nitrogen to simulate operation at elevated fuel system pressures (such as would be encountered during combustion tests).

The modulating valve must have a flow capacity approximately equal to or greater than the injector flow capacity when open, and substantially lower (or almost zero) than the orifice flow capacity when closed, to allow the device to effectively modulate the flow. The valve was required to have sufficient response at the frequencies expected in aeroengine instabilities, so it was designed to

operate at frequencies up to at least 1 kHz. It was designed to provide on/off flow modulation. The level of modulation could be reduced, if necessary, with the installation of a valve bypass line.

The performance metric used to evaluate this valve system was its ability to modulate the fuel flow at the point of injection: the fuel nozzle. It was difficult to directly make high-response mass flow rate measurements and, as such, the results presented here infer flow modulation from fluctuations in pressure differential, which were easier to measure. With up and downstream measurements close-coupled to the simulated injector, a reasonably accurate measure of flow modulation could be made. The three fuel pressure sensors (upstream of valve, downstream of valve, and downstream of the orifice) showed that fluctuations downstream of the injector were negligible and could be ignored and that fluctuations upstream of the valve were negligible for small levels of modulations. However, these did not hold for large levels of modulations and so mass flow calculations done for the high modulation cases have some error. Figure 4 shows a sample time trace from a pressure transducer downstream of the valve when it was running at 500 Hz. Flow modulation was inferred from pressure oscillations by a simple analysis based on the momentum equation for incompressible mass flow through an orifice in terms of the pressure differential. From these basic equations, it can be shown that

$$\frac{\partial W_f}{W_f} = \frac{1}{2} \cdot \frac{\partial(\Delta P)}{\Delta P} \quad (1)$$

This equation assumes that ΔP remains approximately constant ($\delta(\Delta P) \ll \Delta P$) which was not always the case for the modulation levels associated with this valve. Nonetheless, this equation was used to evaluate modulation and the results compared with other methods of measurement. Despite this discrepancy, the use of pressure measurements and this correlation seem to provide reasonably accurate results, based on the results shown by Anderson [3].

Forced-response sine-sweep experiments were done from which pressure amplitude modulation levels were determined as a function of frequency. These were used to compute mass flow

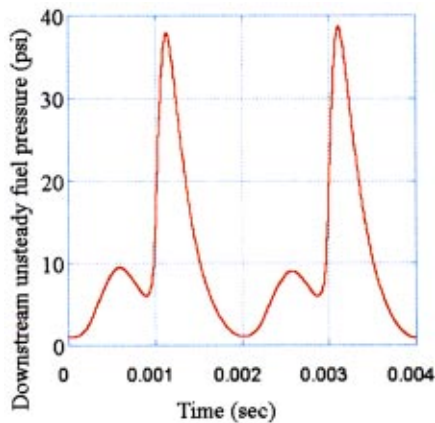


Fig. 4 Time traces showing response of fuel pressure (measured downstream of the valve and upstream of fuel nozzle orifice) to 500 Hz flow modulation command (cold flow test) to the spinning valve

modulation with Eq. (1). Figure 5 shows a sample mass-flow frequency-response curve based on pressure data for the spinning valve over a range of 20 Hz to 800 Hz.

Figure 5 plots the amplitude of fuel modulation normalized with the mean flow rate as a function of frequency. Several characteristics stand out in this response curve. The first is that the modulation levels are about 60% of mean fuel flow or more up to 400 Hz. However, they did decay at the higher frequencies. Also, a repeatable dip occurred at 500 Hz; which might be due to fuel manifold acoustics. Lengthening of the line between the valve and accumulator did show a reduction in the resonant dip frequency, but because of the configuration of the accumulator plumbing, it was difficult to determine the exact line length associated with this problem. When the system was operated at higher pressures, the frequency and level of attenuation were reduced. Figure 6 shows modulated fuel mass flow response curves (amplitude versus frequency) as the base pressure was changed. It was observed that elevated base pressures improved the modulation level and shifted the 500-Hz resonant dip to a lower frequency. It is not known why the response changes with base pressure. Note that Fig. 6 shows only the modulation pressure amplitude measured downstream of the valve and not the mass flow rate amplitudes. From these open-

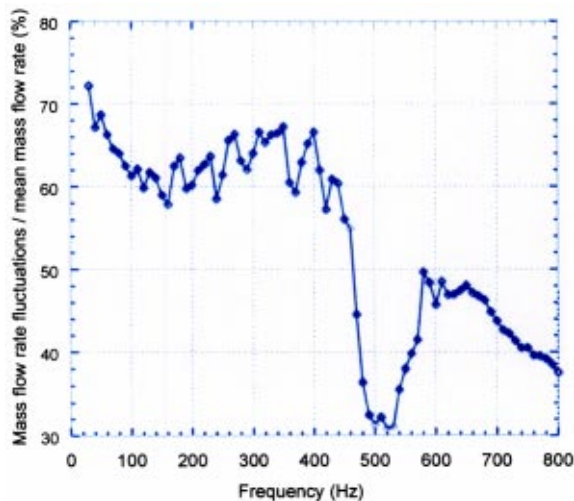


Fig. 5 Valve flow modulation capacity as a function of frequency

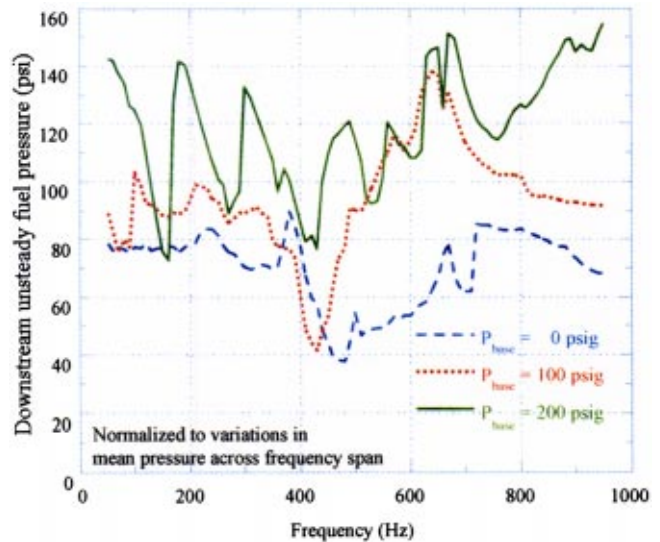


Fig. 6 Modulated fuel pressure response curves for the spinning valve as the base pressure was changed between atmospheric and combustor pressure (flow bench tests)

loop tests at cold flow facility it was seen that the spinning valve has considerable mass flow modulation capacity up to 1 kHz.

3 Phase-Shifting Instability Control Algorithm

The control algorithm used to suppress instability in this program was of a phase-shifting type. This is one of the simplest control algorithms that can be used to suppress instabilities and has been successfully used in the past for this purpose, [4].

In this scheme, the main harmonic of the combustor pressure signal near the instability frequency (~ 280 Hz) was extracted with a filter, scaled by a control gain, and shifted by a control phase which was then sent to the secondary fuel modulation actuator as the driving control signal. A modified form of an extended Kalman filter (EKF) based frequency tracking algorithm proposed by LaScala [5] was used to construct the phase-shifted control signal.

A disadvantage of both a fixed-gain observer-based and delay-based phase-shifting controllers is that the bandpass filters involved in these implementations are nominally fixed. If the frequency of the pressure oscillations varies over a large interval for a narrow bandpass filter, the filtered signal will be significantly attenuated and the control signal will be dominated by noise. Widening the filter bandwidth prevents attenuation of the pressure signal, but more noise is accepted. More dynamical modes can then affect the actuator action, and destabilization of these modes is possible.

The advantage of the frequency tracking EKF observer was that even if the main mode frequency of the oscillations changed from its nominal value, so long as the rate of change was slow, the observer kept track of the main mode frequency and the signal to noise ratio of the filtered signal was maintained. It was observed that the maximum rate of change in the peak frequency the observer could track was about 5 Hz/s.

4 Spinning Valve Controller Development

The spinning valve presented a unique challenge in adapting it to closed-loop control. The shaft position had to be controlled such that it followed a certain trajectory yielding the fuel modulation with a desired frequency and phase. This was done by running the motor in the “torque mode” where the command to the T200 motor controller controlled the motor armature current. That command was determined by a PID controller. Figure 7 shows the block diagram of the spinning valve control system. V_c (command

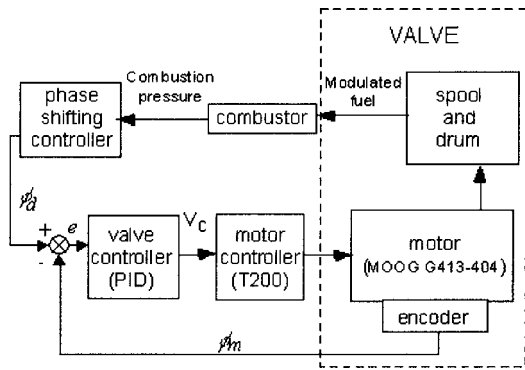


Fig. 7 Block diagram of the spinning valve controller

to the T200 motor controller) was the control input and ϕ_m shaft position was the output. ϕ_m was measured with an encoder and had to follow a desired trajectory, which was determined from the phase of the combustor pressure (described below).

Determining the Desired Trajectory. The phase of the fuel modulation and the phase of the motor shaft were therefore related by a factor of N_H (number of holes on the drum, namely 12). If the phase of the motor shaft was, say, ϕ_m , and the location of the hole nearest the 0 point of the shaft in the direction of rotation was ϕ_h , the phase of the fuel modulation measured immediately downstream of the valve would be $12\phi_m + \phi_h$. Due to the feed line and injector dynamics, the phase of the fuel modulation into the combustor was not the same as that at the outlet of the valve. If the phase difference introduced by the feed line and injector was ϕ_f , then the phase of fuel modulation into the combustor would be $12\phi_m + \phi_h + \phi_f$. For positive voltage command, the shaft always rotated in a CW direction looking from the shaft end. The direction of rotation was kept always the same by allowing only positive commands. If ϕ_c was the phase of the combustion pressure at any time, and γ was the control phase shift, the desired fuel pressure phase was $\phi_c + \gamma$. Hence the problem reduced to making $12\phi_m + \phi_h + \phi_f$ follow $\phi_c + \gamma$ as closely as possible.

This was simplified to a tracking problem of ϕ_m following $(\phi_c + \gamma)/12$ as closely as possible. This simplification was possible since all the other phases are constant with time and was taken care of by the control phase γ . The phase $(\phi_c + \gamma)/12$ was the desired motor shaft phase, ϕ_d .

Another issue that had to be resolved was that since the measured phase was between 0 and 2π , at any point it was also to be decided which ramp was to be tracked (Fig. 8). To get around this problem, the phase angles were added to create a single phase ramp instead of a saw-tooth phase trajectory. However, since the phases cannot be stacked infinitely due to finite floating point number sizes, after a while the value had to be reduced by an integral multiple of 2π so as to make it small again. Some book-keeping had to be done at this point to ensure all variables were modified uniformly (especially the derivative of error, etc.). The result was that the desired phase trajectory was a saw-tooth function with period much larger than 2π , but an integral multiple of it (Fig. 9).

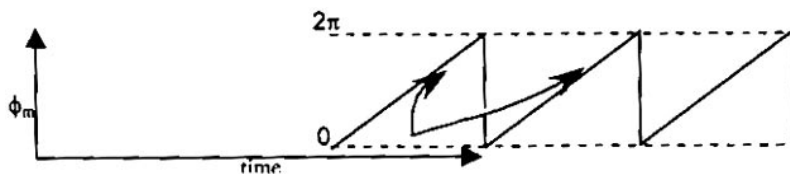


Fig. 8 Schematic of change of shaft position during several cycles of rotation. This behavior led to an ambiguity in deciding which branch to track.

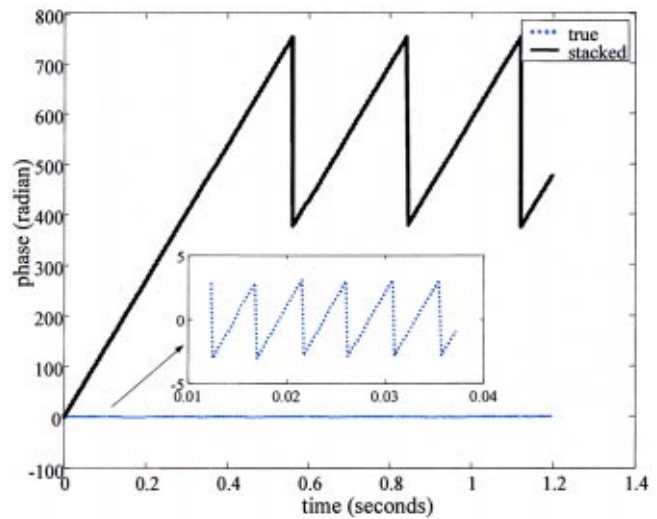


Fig. 9 Stacking of combustor pressure phase to create a single trajectory for the spinning valve motor shaft to follow

Measuring the Motor Shaft Position. An incremental three-channel encoder measured the position of the motor shaft. The encoder used was a HP HEDS 6540 three-channel encoder with a resolution of 1024 counts per revolution. The output of the circuit was the measured motor shaft position in volts (-9.89 V for 0 to 9.86 V for 0 to 2π). The encoder's two quadrature outputs were used to produce the incremental position advance measurement, and the absolute position information was inferred with the help of the third index channel, which produced a high signal once per revolution—always at the same position of the codewheel.

Valve Control Algorithm. A PID controller was used to control the motor shaft angle by commanding the required command input V_c to the spinning valve motor. Figure 7 shows the block diagram of the control system. It should be noted that part of the loop, from the motor shaft rotation to the fuel modulation into the combustor, was run open loop. The motor shaft position was not controlled to produce minimum error between the phase of modulated fuel in the combustor and the phase of combustion pressure, but to minimize error between the motor shaft position and a calculated desired position which was expected to yield a fuel modulation that follows the phase of the combustion pressure. The tracking error was defined as the desired minus the actual shaft position.

$$e = \phi_d - \phi_m$$

The control command was computed as a combination of the error, the derivative error and the integral of the error

$$V_c = K_p e + K_I \int_{t_0}^t e dt + K_D \frac{de}{dt}$$

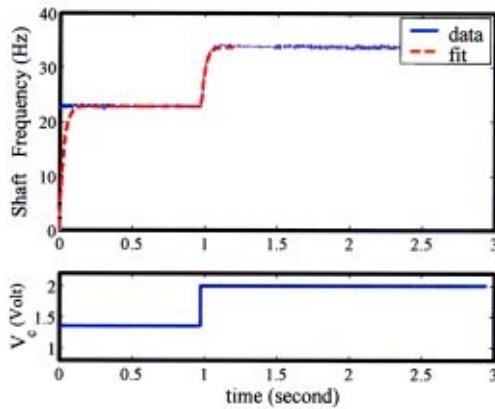


Fig. 10 Response of the spinning valve in a step-input test

where the parameters K_p , K_I , and K_D are to be determined appropriately to make the shaft position ϕ_m follow the desired phase ϕ_d as closely as possible.

4.1 System Identification and Control Design. To design an effective PID controller, an accurate model of the spinning valve was needed. For a DC motor, the relation between motor armature current I_m and shaft position ϕ_m (in radian) is given by a first-order transfer function. Since the valve is a combination of a DC motor and a spool rotating on a fluid film, its overall dynamics can be expected to be more complicated than that of just the motor.

Step input tests were done with the spinning valve where step inputs of voltage were supplied to the motor in the “torque mode” and resulting shaft rotation was examined to identify the transfer function of the valve. Tests were done in the cold flow bench under various operating conditions (i.e., different fuel system base pressures and different levels of step inputs) to investigate if there were nonlinearities in the system, and if any, how strong those effects were.

Figure 10 shows the result of such a test (step in $V_c = +0.65$ V). The best-fit second-order system to match the response of the valve (with a sampling rate of 4 kHz) was

$$G_{v2f} = \frac{0.156(z + 0.687)}{(z + 0.823)(z - 0.991)} \quad (2)$$

Step input tests with different command steps yielded very similar results when it was a positive step. For negative steps, i.e., when the voltage command was reduced, the valve responses were considerably different from those for positive steps. The best fit transfer function for a step input test (step in $V_c = -0.6$ V) was

$$G_{v2f} = \frac{0.053(z - 0.835)}{(z - 0.941)(z - 0.991)} \quad (3)$$

(4 kHz sampling rate), which was considerably different from the transfer function in Eq. (2).

The system transfer function depended on the direction of control input (command V_c); hence a controller designed on the basis of one such identified model would not work well under different circumstances. Hence it was decided to tune the PID gains for a nominal model to get a good phase margin with the required bandwidth; and use those values as initial guesses in real application. The PID gains were tuned during debugging of the control system by commanding the fuel modulation to track a sinusoidal signal from an analyzer. The choice of a PID controller can itself be questioned for such a nonlinear plant. PID was chosen over other more sophisticated techniques due to its ease of implementation.

Figure 11 shows the Bode plot of the loop transfer function of the plant and controller, the plant was the spinning valve as

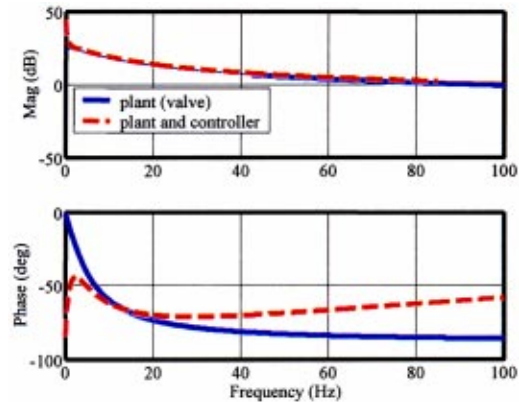


Fig. 11 Bode plot (magnitude and phase) of the identified valve transfer function and loop transfer function (product of valve and controller transfer functions $G_{loop} = G_v * G_c$)

identified from the step response test described earlier (Eq. (2)) and the controller was the one designed according to the above procedure with a gain crossover set to 100 Hz. The PID gains were $K_p = 1.1$, $K_I = 6.8$, and $K_D = 0.001$. Since the fuel modulation frequency was 12 times that of the motor, the bandwidth of the system was 1200 Hz, well beyond the nominal operating point of 280 Hz for this program. The phase margin was about 120 deg.

Since the identified valve models were recognized as not very useful in representing the system, evaluating the controller’s performance in simulation using these models was not useful. One point should be noted here that since the fuel modulation produced by the valve is 12 times the motor shaft frequency; small errors in the shaft position results in large errors between the commanded and actual fuel pressure phase.

5 Active Instability Control Test Results

The spinning valve was used for closed-loop combustion control of the single nozzle combustor. The combustor was operated at the conditions shown in Table 1. The nominal operating point was established first by setting the air inlet temperature, fuel flow rate, and air flow rate. Baseline, uncontrolled measurements of the instability were acquired. Figure 12 shows a short time trace, the amplitude spectrum (amplitude as a function of frequency) and PDF (probability density function) of fluctuating combustion pressure, P'_{comb} (measurement from transducer PLA1C1). The shape of the PDF shows this to be a limit-cycling instability according to

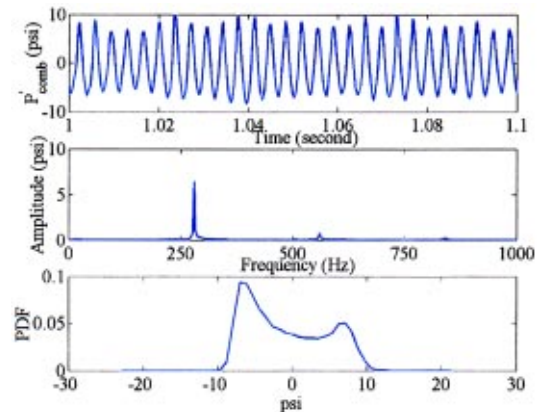


Fig. 12 Time trace, amplitude spectrum and PDF of fluctuating combustor pressure in the 280 Hz instability condition (mid-power)

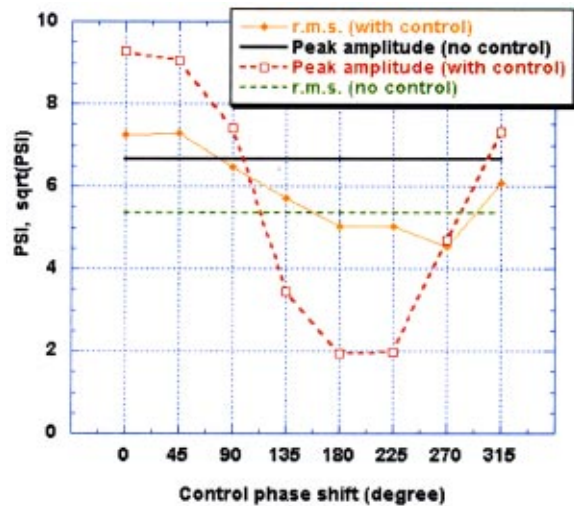


Fig. 13 Peak amplitude near 280 Hz and r.m.s. value of combustor pressure as a function of control phase, showing discrepancy between amplitude and r.m.s. attenuation

criteria given by Banaszuk et al. [6]. The amplitude spectrum is computed by computing the power spectrum with Welch's averaged periodogram method (using Matlab's PSD function) and then using the following scaling formula to compute amplitude as a function of frequency

$$A_p(f) = 2 * \sqrt{\text{PSD}(p') \frac{\|w\|^2}{(\sum w)^2}} \quad (4)$$

where $A_p(f)$ is the amplitude, p' is the fluctuating combustion pressure and w is a hanning window of length equal to the number of fft points chosen. The number of fft points was 4096, yielding a frequency resolution of 1.2 Hz for the 5 kHz sampling rate used in data acquisition.

Closed-loop control was applied by modulating the fuel flow rate and varying the phase shift of the control signal through a complete cycle of 360 deg with 30 deg increments and measuring combustor pressure response at those points. Inlet temperature, fuel flow rate, and air flow rate were held constant through the test. The PID gains for the valve controller were $K_p=2$, $K_I=1$, and $K_D=0.005$. These were empirically determined by trial and error. Figure 13 shows the peak amplitude of combustor pressure near 280 Hz and also the r.m.s. of P'_{comb} as a function of control phase shift. The largest suppression of the peak amplitude (~3 times) was achieved at a control phase shift of 180 deg. The attenuation of r.m.s. value was smaller (~15%), and occurred at a phase shift of about 270 deg. Note that the r.m.s. value was computed from the time trace data directly and the peak amplitude near 280 Hz was extracted from the amplitude spectrum calculation as explained previously.

Figure 14 shows the comparison of uncontrolled and controlled amplitude spectra of the fluctuating combustor pressure for the point where best attenuation was achieved. The amplitude at the instability frequency (280 Hz) was brought down by a factor of 10. The time traces show that, during control, although the amplitude of oscillations near the instability frequency was low, the oscillations were not uniformly low over time. A "peak-splitting" phenomenon and excitation of low-frequency modes, as evident in Fig. 14, contributed to this. Peak splitting was the primary reason why attenuation of the r.m.s. was considerably less than for the tonal peak. Peak splitting has been observed in other demonstrations with other types of actuators, [6]. As explained by Banaszuk et al. [6] peak splitting is primarily due to large time delays in the combustor and actuation systems. In order to be effective, the

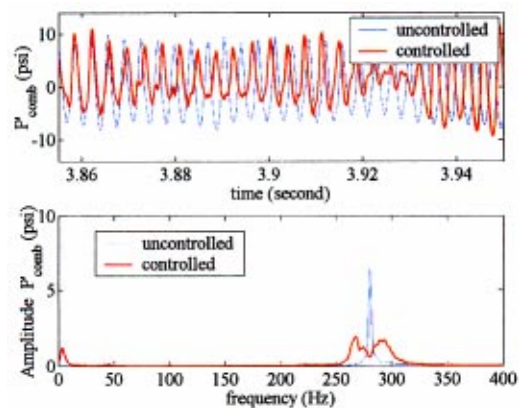


Fig. 14 Comparison of combustion pressure amplitude spectra for uncontrolled and the best controlled point

control algorithm must ameliorate the adverse effect of time delay and noise in the plant. The control algorithm used in this demonstration was not sufficiently sophisticated to account for these effects.

5.1 Spinning Valve Performance. Control authority may also have been affected by the tracking performance of the spinning valve. Figure 15 shows the difference between the instantaneous phases of the combustion pressure and the fuel pressure (measured downstream of the valve) for the best-controlled case. The commanded control phase shift was constant, so the valve should modulate fuel with a constant phase difference from the combustor pressure. However, Fig. 15 shows that the valve periodically lost tracking by as much as 250 deg.

It was found that this periodic change in the phase difference between combustor and fuel line pressures was due to the loss of tracking by the spinning valve motor. Since the spinning valve drum had 12 holes, the fuel modulation frequency was 12 times the motor shaft frequency. Therefore, the difference between fuel pressure phase and $12\phi_m$ should be constant.

Figure 16 shows the difference between the fuel line pressure (downstream of valve) and $12\phi_m$. The phase difference was not constant, but was slowly drifting in one direction. This could have been caused by one of two things: either the encoder codewheel was slipping on the motor shaft, or the encoder electronics were

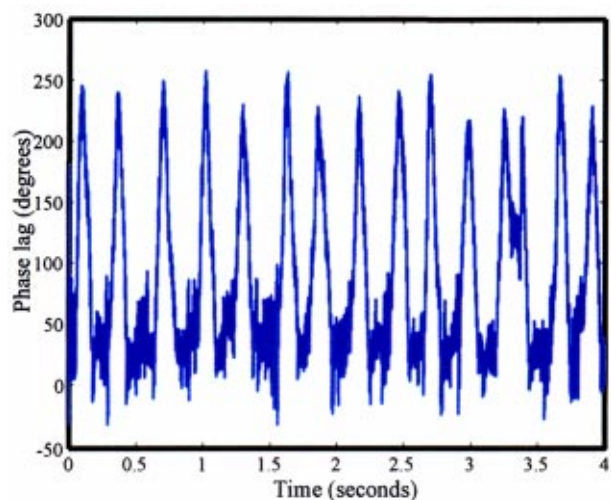


Fig. 15 Instantaneous phase difference between P_{fuel} and P'_{comb} during closed-loop control

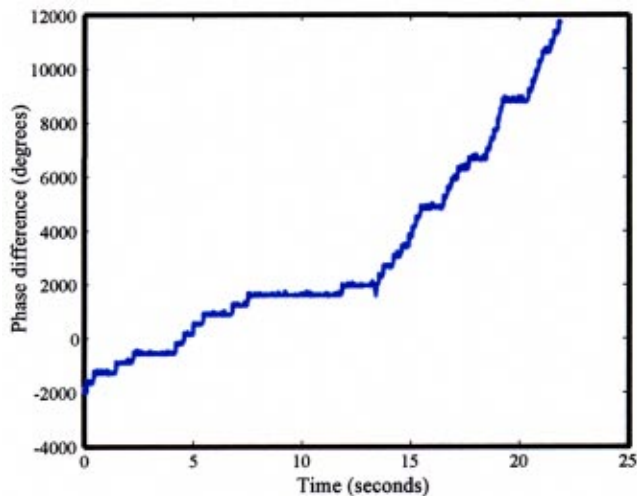


Fig. 16 Instantaneous difference between the phase of fuel pressure and 12^* (motor shaft position) from during closed-loop control, showing “phase drift” of spinning valve control

not measuring the position accurately. Unfortunately, none of these hypotheses can be checked with available data, more experiments will have to be done. This “phase drift” contributed to the poor control performance. Future work will have to address this issue.

6 Summary

The spinning valve was capable of modulating fuel flow rate (at least 30% of mean fuel flow up to 1 kHz) at high frequencies and was used for closed-loop control of combustion instabilities. The spinning valve’s modulation capability depended on the feed line configurations and operating pressures. These features may be exploited to design the feed line plumbing so that the valve has maximum authority in the frequency range of interest.

This valve was used to control a ~ 280 -Hz combustion instability in a 4 MW single-nozzle combustor with realistic engine hardware. A three times reduction of maximum pressure amplitude was achieved. However, reduction of r.m.s. pressure was small ($\sim 15\%$), due to side-band amplification (“peak splitting”) and phase drift of the spinning valve controller.

The drift of the spinning valve phase relative to the control phase may be addressed through investigating and improving the ability of this system to track a fixed command over time. The phase-ramping strategy, illustrated in Fig. 9, may have resulted in an accumulation of some fixed error, leading to this phase drift.

Avoidance of side-band amplification or “peak splitting” may require the application of more sophisticated control techniques, such as LQG-LTR controllers, [7], or evolution algorithms, [8].

Acknowledgments

This work was funded by the NASA Glenn Research Center. The NASA Glenn Program Manager was Mr. John DeLaat. The contributions of Messrs. Daniel Paxson and Clarence Chang, also of NASA Glenn, were notable. Dr. Jeffery Lovett was the Pratt and Whitney Program Manager. At UTRC, Messrs. William Proscia, Scott Bortoff, Joseph Haley, and John Miano made significant contributions that affected the outcome of this work.

Nomenclature

| | |
|--------------------|--------------------------------------|
| P_3 | = inlet air pressure |
| T_3 | = inlet air temperature |
| W_f | = fuel flow rate |
| W_a | = air flow rate |
| P' | = unsteady pressure |
| P'_{comb} | = unsteady combustor pressure |
| f | = frequency |
| ϕ_m | = motor shaft phase |
| ϕ_d | = desired motor shaft phase |
| ϕ_c | = combustion pressure phase |
| γ | = control phase shift |
| ϕ_f | = feed line phase shift |
| V_c | = command to valve |
| e | = shaft position error |
| K_P, K_I, K_D | = PID controller gains |
| G_v | = motor transfer function |
| G_c | = valve controller transfer function |

References

- [1] Kiel, B., 2001, “Review of Advances in Combustion Control, Actuation, Sensing, Modeling and Related Technologies for Air Breathing Gas Turbines,” AIAA Paper No. AIAA 2001-0481.
- [2] Cohen, J. M. et al., 2000, “Longitudinal-Mode Combustion Instabilities: Modeling and Experiments,” presented at the “NATO RTO Symposium on Active Control Technology for Enhanced Performance Operational Capabilities of Military Aircraft, Land Vehicles and Sea Vehicles,” Braunschweig, Germany, May 8–11.
- [3] Anderson, T. J., Proscia, W., and Cohen, J. M., 2001, “Control of a Liquid-Fuel Jet in an Unsteady Cross-Flow,” ASME Paper No. 2001-GT-0048.
- [4] Cohen, J. M., Rey, N. M., Jacobson, C. A., and Anderson, T., 1998, “Active Control of Combustion Instability in a Liquid Fueled Low- NO_x Combustor,” *ASME/IGTI Gas Turbine Expo and Congress*, Stockholm, June.
- [5] LaScala, B., 1994, “Approaches to Frequency Tracking and Vibration Control,” *Ph.D. Thesis*, Department of Systems Engineering, The Australian National University, Dec.
- [6] Banaszuk, A., Mehta, P., Jacobson, C. A., and Khibnik, A., 2003, “Limits of Achievable Performance of Controlled Combustion Processes,” *IEEE Trans. Autom. Control*, submitted for publication.
- [7] Muruguppan, S., Park, S., Annaswamy, A. M., Ghoniem, A. F., Acharya, S., and Allgood, D. C., 2001, “Optimal Control of a Swirl Stabilized Spray Combustor Using System Identification Approach,” Paper No. AIAA 2001-0779.
- [8] Paschereit, C. O., Schuermans, B., and Campos-Delgado, D., 2001, “Active Combustion Control Using an Evolution Algorithm,” Paper No. AIAA 2001-0783.

The Recuperative-Auto Thermal Reforming and the Recuperative-Reforming Gas Turbine Power Cycles With CO₂ Removal—Part I: The Recuperative-Auto Thermal Reforming Cycle

D. Fiaschi

e-mail: danif@de.unifi.it

L. Lombardi

L. Tapinassi

Dipartimento di Energetica "Sergio Stecco,"
University of Florence,
Via Santa Marta, 3,
50139 Firenze, Italy

The relatively innovative gas turbine based power cycles R-ATR and R-REF (Recuperative-Auto Thermal Reforming GT cycle and Recuperative-Reforming GT cycle) here proposed are mainly aimed to allow the upstream CO₂ removal by the way of natural gas fuel reforming. The power unit is a gas turbine (GT), fueled with reformed and CO₂ cleaned syngas produced by adding some basic sections to the simple GT cycle:

- auto thermal reforming (ATR) for the R-ATR solution, where the natural gas is reformed into CO, H₂, CO₂, H₂O, and CH₄; this endothermic process is completely sustained by the heat released from the reactions between the primary fuel (CH₄), exhausts and steam.
- water gas shift reactor (WGSR), where the reformed fuel is, as far as possible, shifted into CO₂ and H₂ by the addition of water.
- water condensation, in order to remove a great part of the fuel gas humidity content (this water is totally reintegrated into the WGSR).
- CO₂ removal unit for the CO₂ capture from the reformed fuel. Among these main components, several heat recovery units are inserted, together with GT cycle recuperator, compressor intercooler, and steam injection in combustion chamber. The CO₂ removal potential is close to 90% with chemical scrubbing using an accurate choice of amine solution blend: the heat demand is completely provided by the power cycle itself. The possibility of applying steam blade cooling by partially using the water released from the dehumidifier downstream the WGSR has been investigated: in these conditions, the R-ATR has shown an efficiency range of 44–46%. High specific work levels have also been observed (around 450–550 kJ/kg). These efficiency values are satisfactory, especially if compared with ATR combined cycles with CO₂ removal, more complex due to the steam power section. If regarded as an improvement to the simple GT cycle, R-ATR shows an interesting potential if directly applied to a current GT model; however, partial redesign with respect to the commercially available version is required. Finally, the effects of the reformed fuel gas composition and conditions on the amine CO₂ absorption system have been investigated, showing the beneficial effects of increasing pressure (i.e., pressure ratio) on the thermal load per kg of removed CO₂. [DOI: 10.1115/1.1587743]

Introduction

During the last ten years, special attention was devoted by research boards and industry to the study and development of power cycles with low CO₂ emissions. The activities in this field registered an important increase during the last five years, due to Kyoto Protocol, subscribed by many industrialized countries.

Many of the proposals for new-concept environmentally friendly plants involved GT-based power cycles. Two basic solutions seem to be practicable in short-medium term:

1. semi-closed GT cycles with downstream CO₂ removal from the CO₂ enriched exhausts, [1–10];
2. GT-based power cycles with upstream CO₂ removal, obtained by the fuel decarbonization amount of the combustion chamber, [10–12].

Contributed by the International Gas Turbine Institute (IGTI) of THE AMERICAN SOCIETY OF MECHANICAL ENGINEERS for publication in the ASME JOURNAL OF ENGINEERING FOR GAS TURBINES AND POWER. Paper presented at the International Gas Turbine and Aeroengine Congress and Exhibition, Amsterdam, The Netherlands, June 3–6, 2002; Paper No. 2002-GT-30116. Manuscript received by IGTI, Dec. 2001, final revision, Mar. 2002. Associate Editor: E. Benvenuti.

The power plants proposed in both parts of the present work belong to the second category, consisting in two GT power cycles with integrated fuel decarbonization and subsequent CO₂ capture.

The CO₂ removal from the fuel is an increasingly investigated opportunity: the general approaches are those linked with CRGT (chemically recuperated gas turbine) and POGT (partial oxidation gas turbine) cycles, [11,13]. In the CRGT, the original methane fuel is converted into a mixture of H₂, CO₂, CO and steam by the steam reforming: The heat due to the related endothermic reactions can be provided by thermal recuperation from the exhausts [10,11] and/or by a partial combustion into the reformer itself (auto thermal reforming, ATR, [12]). The recently studied CRGTs represent an attractive alternative to the classic GT recuperative cycles, resulting in higher levels of heat recovery, thanks to chemical enhancement, [14]. When considering its application in the field of power plants with low CO₂ emissions, a high level of methane fuel conversion into H₂ becomes mandatory. To this aim, the operating temperature and pressure of the reformer play a key role: temperatures of 800–1000°C allow a conversion level of about 60 to 95%, increasing with the steam/methane ratio and with lowering reformer pressure, [11].

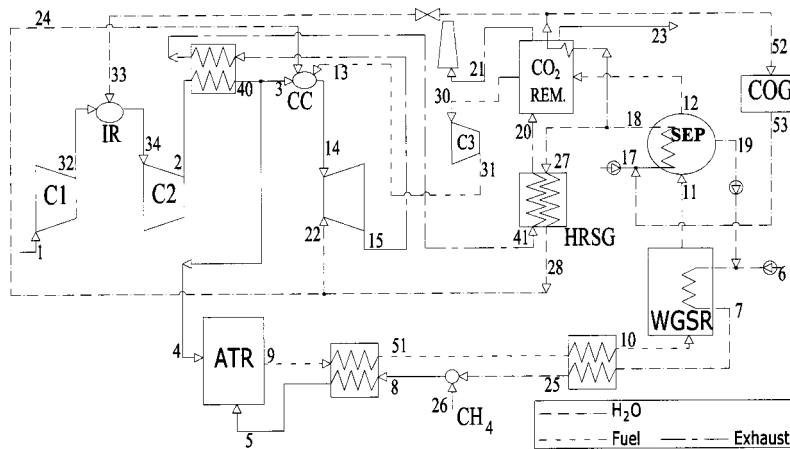


Fig. 1 Schematic of the steam cooled R-ATR cycle

Since GT exhaust temperatures range between 500 and 600°C, it is impossible to achieve high levels of conversion by simple reforming. This is the reason for adding the water gas shift reactor (WGSR) downstream the reformer, which allows the conversion of the reformed gas into a CO₂ and H₂ rich mixture, ready to be treated by the CO₂ removal sections.

The upstream CO₂ removal allows a notable size reduction of the CO₂ separation equipment with respect to the downstream option, due to the very different mass flow rates. Chemical CO₂ separation is here investigated and discussed. Physical separation by membranes is a continuously evolving alternative technology and has reached commercial levels, even if the presence of the hydrogen is not, at present, well studied; the separation efficiency is, however, much lower than in chemical scrubbing, [15]. Moreover, the membranes require high pressure levels, which reduce the methane conversion in the reforming process. Consequently, chemical CO₂ separation by solution of ethanolamines was selected as more promising, also in the field of upstream CO₂ capture, [1,2].

Chemical absorption has been selected for a number of reasons:

1. information about properties of physical solvents for CO₂, such as Selexol, Rectisol, etc., is proprietary and reliability of the data available is disputable.

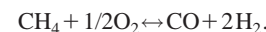
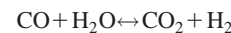
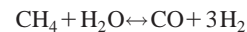
2. n/desorption of physical solvents by pressure swinging is theoretically effective, but in practice a system including as many as six small turbine/generator sets to recover the energy of the expansion, [16], must be considered. In such conditions the power expenditure for CO₂ capture exceeds the values of 4 MJ/kg of captured CO₂ which is considered the good practice for MEA/DEA chemical systems, [1]. With more optimized solutions of amines in water (as were assumed in the present work), values as low as 1.8–2 MJ/kg CO₂ have been calculated.

3. Use of amine solutions in chemical industry is very common (e.g., CLAUS processes for H₂S; LPG purification, ammonia processes) so the know-how is widespread and there are no proprietary rights, so that the documentation about thermochemical data is wide. The typical range of heat consumption in modern chemical absorption processes for ammonia production is 0.7–1.4 MJ/kg CO₂. The physical absorption processes may be designed for zero heat consumption, but for comparison with the chemical processes, the mechanical energy requirements have also to be considered, [17,18].

Description of the R-ATR Power Cycle

The R-ATR cycle (recuperated auto thermal reforming) is schematically represented in Fig. 1: The heat demand due to the methane fuel reforming is provided by the partial combustion reactions of compressed air and methane into the ATR. The primary CH₄

fuel is premixed with steam produced by thermal recuperation from the hot reformed fuel at the ATR exit (streams 51–10). The following reactions take place into the ATR:



The gas composition downstream the ATR can be considered, with a satisfactory approximation, to be that resulting from chemical equilibrium if the correct catalyzers are used, [12], and an adequate reactor catalyst bed volume, with a heat exchanger of three to four tube rows per cold side pass is adopted, [14,19,20]. The partial combustion reaction of methane can be, in practice, considered completely at equilibrium.

On the whole, the ATR input and output parameters can be summarized as shown in Table 1. The nine output parameters are determined by the overall energy and mass balances, the chemical species balances, and the chemical equilibrium of the three considered reactions. If the flow rate of the oxygen input corresponds to the stoichiometric amount, there is no oxygen left at the ATR exit.

The reformed fuel is then sent, after having provided the necessary heat to produce the steam needed by the reforming process, to the water gas shift reactor (WGSR), where the main shift reac-

Table 1 Summary of ATR inputs and outputs

| Input Parameters | | Output Parameters | |
|----------------------------|---|----------------------------|--------------------------|
| Variable | Description | Variable | Description |
| p | Reformer pressure | m_9 | ATR exit gas mass flow |
| m_4 | Air Flow rate | T_9 | ATR exit gas temperature |
| T_4 | Inlet air temperature | $x_{\text{CH}_4,9}$ | ATR exit gas composition |
| $x_{\text{N}_2,4}$ | Inlet air composition | $x_{\text{CO},9}$ | |
| $x_{\text{O}_2,4}$ | | $x_{\text{CO}_2,9}$ | |
| $x_{\text{CO}_2,4}$ | | $x_{\text{H}_2,9}$ | |
| $x_{\text{H}_2\text{O},4}$ | | $x_{\text{H}_2\text{O},9}$ | |
| m_5 | H ₂ O-CH ₄ mixture mass flow rate | $x_{\text{N}_2,9}$ | |
| $x_{\text{CH}_4,5}$ | CH ₄ mass fraction at point 5 | $x_{\text{O}_2,9}$ | |
| T_5 | H ₂ O-CH ₄ mixture temperature | | |

Table 2 Main R-ATR cycle operating data

| β_1 | First Compressor Pressure Ratio | $\sqrt{\beta}$ |
|-------------------|---|----------------|
| m_{comp} (kg/s) | Compressor mass flow | 100 |
| T_{max} (K) | Maximum cycle temperature | 1500 |
| T_b (K) | Turbine blade metal temperature | 1100 |
| ϵ_H | Turbine blade cooling effectiveness | 0.4 |
| e_f | Turbine film cooling effectiveness | 0.2 |
| η_{sc} | Compressor isentropic efficiency | 0.89 |
| η_{sc} | Turbine isentropic efficiency | 0.91 |
| Lp_{CC} | Combustion chamber pressure loss $\Delta p/p$ | 3% |
| Lp_{RIG} | Recuperator pressure loss $\Delta p/p$ | 5% |
| Lp_{ATR} | ATR pressure loss $\Delta p/p$ | 10% |
| DT_{RIG} (K) | Recuperator approach temperature difference | 30 |
| η_{CO_2} | CO ₂ removal efficiency of the chemical absorber | 90% |

tion $CO + H_2O = CO_2 + H_2$ takes place. In this component, the concentration of CO₂ and H₂ in the fuel gas is enhanced, in order to facilitate their separation. The WGSR reaction is slightly exothermic, with surplus heat used to preheat the external water entering at point 5. The fuel coming out from the WGSR (point 11) has a relevant concentration in H₂ and CO₂, but a consistent fraction of water vapor is still present: This is removed by the subsequent condensation in the condensing heat exchanger (point 12, SEP). Part of the condensed water (stream 19) is recovered and integrated with the external input stream 6, and directed to the ATR section. The heat of condensation released by the SEP process is used to preheat the external water (point 17), before producing steam for the turbine blade cooling. The fraction of water/steam eventually exceeding the amount due to blade cooling is sent to the compressor intercooler (point 33), after having provided part of its sensible heat to the CO₂ removal section, and/or to the combustion chamber steam injection (downstream the HRSG).

Subsequently, the dehumidified fuel coming from SEP is sent to the amine CO₂ removal section (CO₂ REM, Fig. 1), where the 90% of CO₂ is separated and prepared for storage and disposal (point 23). The decarbonized fuel is sent to the combustion chamber (point 13). The heat content of the exhausts is used for GT cycle recuperation (points 31–41), for the production of the steam eventually due to blade cooling (HRSG, points 41–20) and, finally, to sustain the amine regeneration of the CO₂ removal section upstream the stack, [1]. The air due to the ATR is taken in point 40, downstream the GT recuperator.

The remaining heat can cover some cogeneration utilities (points 52–53). The small compressor C3 is needed to move the clean fuel gas to the GT combustor, against the friction losses encountered along the ATR, WGSR, CO₂ removal and the other heat exchangers.

The basic cycle operating data on which the whole analysis is carried out are reported in Table 2.

Performance Analysis of the R-ATR Cycle

The R-ATR power cycle has been simulated using a dedicated program, developed by the authors using EES. The adopted blade cooling model has been recently developed and tested on some current production GTs, [21]. Since the GT cycle is the core of the proposed powerplant and the exhaust temperature is a strong function of pressure ratio, an extensive analysis of the performance and CO₂ removal potential versus pressure ratio β has been carried out. The effects of maximum cycle temperature T_{max} have not been discussed, because an increase of this parameter enhances the performance of both gas cycle and reforming process, leading to lower CO₂ emissions.

The performance map exploited by the R-ATR power cycle (primary fuel LHV efficiency η_{GT} versus specific power W_{sp}) with variable β is represented in Fig. 2, for air and steam blade cooling. The efficiency levels are interesting, showing a consistent margin of improvement with the adoption of blade steam cooling. Significantly different optimizing pressure ratios can be observed: 9 for steam cooling and 17 for air cooling. In the case of steam

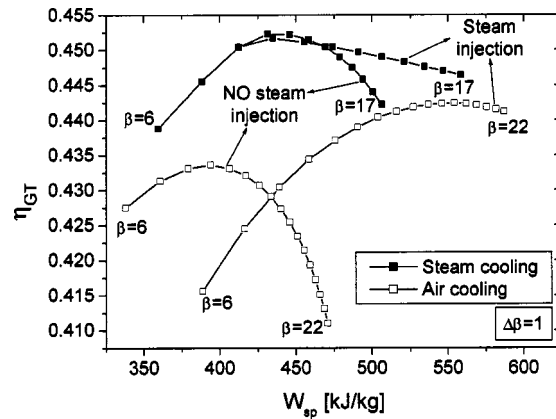


Fig. 2 Performance maps of R-ATR cycle

cooling, two fundamental effects influence the efficiency: the recuperation and the steam injection in combustion chamber. At low pressure ratios, high levels of recuperation can be applied, which leads to lower T_{41} temperature (Fig. 3) and then to lower steam production (Fig. 4), that is almost entirely due to blade cooling. With increasing pressure ratio, the lower recuperation brings to higher T_{41} ; under such conditions, an amount of steam exceeding that necessary for blade cooling is produced and the steam injection in combustion chamber can be applied. Above $\beta=8$, the penalization due to lower recuperation is dominant and the efficiency drops. The steam injection has, however, positive effects on the specific work W_{sp} , which is further increased after the best

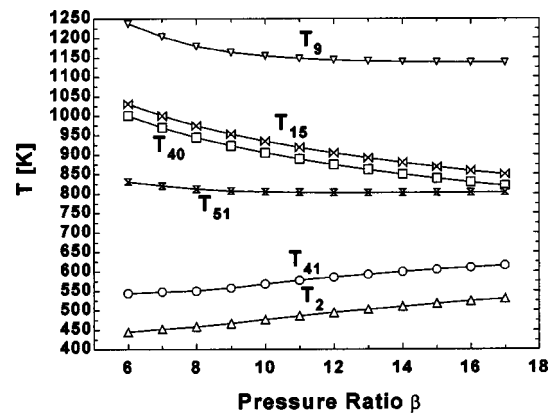


Fig. 3 Recuperator end temperatures versus β for the steam cooled R-ATR

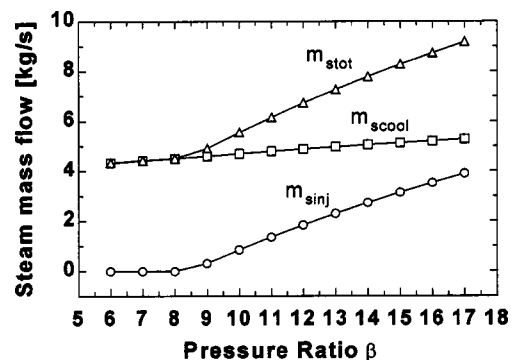


Fig. 4 Steam production versus β for the steam cooled R-ATR

efficiency point. On the whole, the variation in efficiency is limited to about 1 point on the whole inquired field for the steam-cooled case.

In the air cooled R-ATR, a more than double flow rate of coolant has to be supplied to the turbine with respect to the steam cooling case, [21], which entails the displayed negative effects on the efficiency.

The amount of steam production is at the same level of the steam cooled R-ATR. The specific work is higher, due to the larger amount of allowable steam injection in combustion chamber (Fig. 4) which cancels the negative effect of the increased compressor work for extensive air cooling. The compressor intercooling levels are very similar at pressure ratios higher than the optimizing value, since the spray injected water $m_{w,s}$ is set to be the saturating amount. At β lower than the η_{GT} optimizing value, the amount of intercooling water for the steam-cooled cycle is not the saturating one, but the maximum possible to allow the production of the necessary steam for blade cooling. Some beneficial effects of pressure ratio on performance are due also to the reduced heat demand of CO₂ sequestration unit, with increasing absorber operating pressure, [15,22], as will be remarked in the section dedicated to the CO₂ removal system.

The sharpened shape of the performance and steam production curves related to the steam cooling cases around the optimization point is directly linked with the intercooler mass flow rate: This is set to be the saturating amount only starting from pressure ratios that allow the production of the necessary steam for blade cooling. At very low β s, the recuperation level of the cycles is limited by the reduction of the spray intercooling and the subsequent increase of T_{41} to allow the production of the required steam mass flow due to blade cooling. Two different operating regimes are thus present for β lower and higher than the optimizing value. In other words, the efficiency of the steam cooled configurations is optimized when $m_{w,s}$ is a little higher than the amount required for blade cooling.

The Reforming Section: Parametric Analysis of the R-ATR Power Cycle

The fuel gas composition from the ATR to the combustion chamber is shown in Table 3 for the η_{GT} optimizing β . One of the main parameters influencing the ATR performance is the K_{steam} ratio, defined as $K_{steam} = m_{s,s} / m_{pf}$ (symbols are referred to the cycle points of Fig. 1). Its allowable range is limited by the temperature T_7 at the WGSR exit (cooling water side) plus an approach $DT = 10$ to 30 K, since the steam directed to the ATR is produced in recuperative way by cooling of the reformed fuel. This influences both the cycle efficiency (especially at low and high β s, Fig. 5) and CO₂ capture potential (Fig. 6). A rather important effect on W_{sp} has been observed, due to the decreasing steam production with increasing K_{steam} . It can be explained by observing that the reduction of T_{10} entails the decay of T_{11} and then T_{18} (Fig. 7), which leads to the subsequent drop in HRSG steam production. The lower bound of K_{steam} , is about 1.5, to avoid the formation of solid carbon in the ATR, [10]. The pressure

Table 3 Fuel gas composition at the main exits of the R-ATR deCO₂ chain devices

| SPECIE | Composition [%] (Mass/Volume) | | | |
|------------------|-------------------------------|--------------------------|---------------------------|---|
| | ATR exit $T = 1154$ K | WGSR exit $T = 489$ K | SEP exit $T = 395.6$ K | deCO ₂ exit $T = 316.7$ K |
| H ₂ | 4.09/35.6 | 5.17/44.5 | 5.96/51.1 | 9.67/60.2 |
| H ₂ O | 23.8/21.7 | 14.2/13.7 | 0.97/0.94 | 1.40/0.975 |
| CO | 15.4/9.99 | 0.44/0.27 | 0.51/0.31 | 0.82/0.37 |
| CO ₂ | 13.3/5.10 | 36.8/14.5 | 42.5/16.7 | 6.90/1.97 |
| CH ₄ | 0.18/0.21 | 0.18/0.19 | 0.20/0.22 | 0.30/0.23 |
| N ₂ | 43.2/27.3 | 43.2/26.8 | 49.9/30.8 | 80.9/36.2 |
| O ₂ | 0/0 | 0/0 | 0/0 | 0/0 |

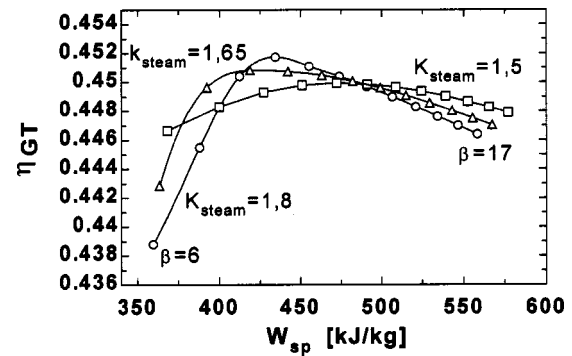


Fig. 5 CO₂ removal and cycle efficiency versus K_{steam}

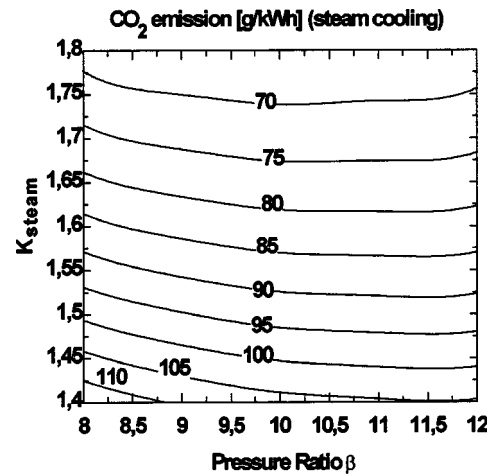


Fig. 6 R-ATR Specific CO₂ emission versus β and K_{steam}

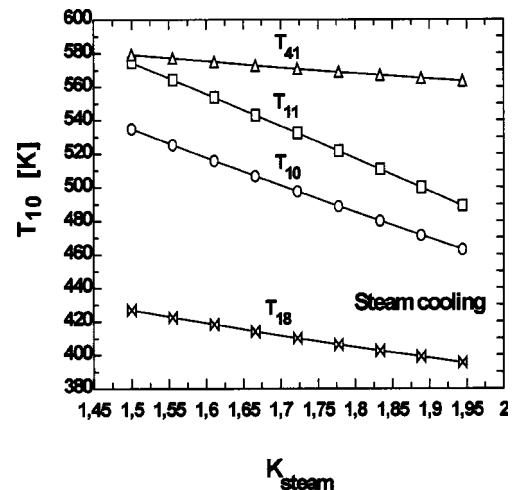


Fig. 7 Influence of K_{steam} on the main fuel reforming and deCO₂ chain components

ratio has a marginal influence on the CO₂ removal but determines the upper limit for K_{steam} in order to satisfy the condition $T_{10} > T_7$.

The specific CO₂ emission of R-ATR versus β (around the optimizing values) and K_{steam} is shown in Fig. 6: A low sensitivity to β is confirmed, whereas the K_{steam} ratio plays a key role in this way. In particular, it must be kept at the maximum allowable values, in order to maintain the lowest possible CO₂ emission level.

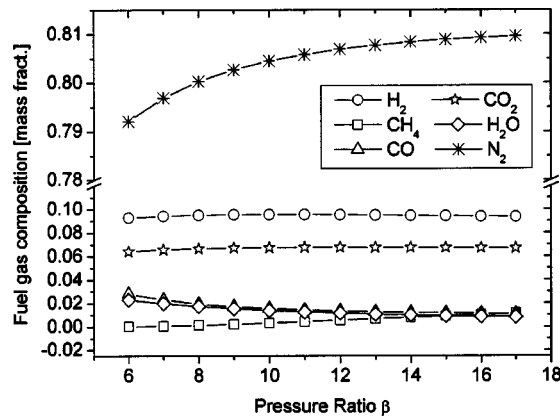


Fig. 8 CO₂ Clean fuel gas composition at the combustor inlet

The reformed CO₂ clean fuel gas composition at the combustion chamber inlet of GT versus pressure ratio (related to the steam cooling configuration at fixed $K_{\text{steam}}=1.8$) is reported in Fig. 8: The species H₂, CO₂, and CH₄ are practically unchanged with increasing β , whereas the N₂ increases due to the decrement of the H₂O and CO. This suggests, coupled with the results shown in Fig. 8, a wide margin for the operative range of R-ATR in terms of CO₂ emissions, and consequently a wide adaptability to many different GT models.

The temperature range of the hot side (9–51) of the steam/CH₄ superheater, shown in Fig. 3 versus β , can bring to metal dusting conditions, a well-known phenomena involved in reforming processes. An alloy is likely to be carburised if the carbon activity of the environment is higher than that of metal, [23]. The carbon activity depends on C, CO, CO₂, CH₄, and H₂O partial pressures. Referring to the average composition of the reformed fuel at the ATR exit (Table 3), the following values have been calculated:

$$p_{\text{CO}}p_{\text{H}_2}/p_{\text{H}_2\text{O}}=1.80$$

$$p_{\text{CO}}^2/p_{\text{CO}_2}=2.15$$

$$p_{\text{CH}_4}/p_{\text{H}_2}^2=0.0015.$$

Referring to the graphs of carbon activity as a function of gas composition and temperature (originally from [24] and reported on [23]), the operating field of the 9–51/8–5 heat exchanger falls in a dangerous zone, where, depending on the alloy used, metal dusting is likely to proceed, especially into the 500–700°C range.

Practical experience from various reforming plants around the world appears to be contradictory concerning the success or failure of specific materials in resisting metal dusting attack. Exposure trials of various highly alloyed metals in the Moss gas reforming plant have consistently demonstrated that high Cr containing materials (50/50 Cr-Ni alloy) appeared to be totally immune to metal dusting after 17 months [23,25]. The experience on these chemical plants can be effectively extended to the reforming sections of the R-ATR.

Detailed Evaluation of CO₂ Absorption Section Heat Demand

The carbon dioxide removal section consists substantially in an absorption unit and a regeneration unit (a schematic of this section, which is common to many absorption/desorption applications, can be found in [4]). The CO₂ rich stream enters the absorber from the bottom and is scrubbed by the descending solution of amines. Here, CO₂ passes into liquid phase and reacts with the amines forming new compounds that subtract CO₂ from liquid phase, enhancing thus its further transfer from gaseous to liquid phase.

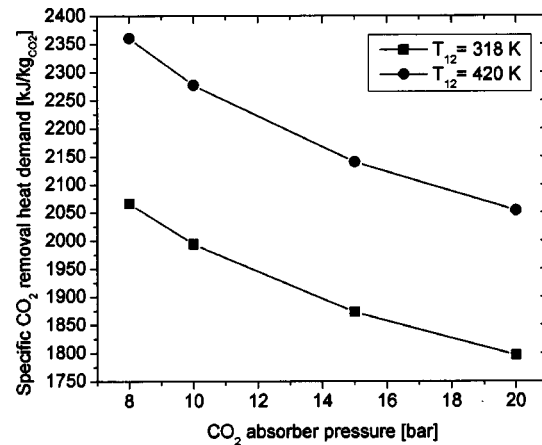


Fig. 9 CO₂ Amine absorption system heat demand for the R-ATR cycle

The purified gas leaves the column at the top and the solution—loaded with CO₂—leaves at the bottom. This liquid stream is thermally regenerated in the stripper, the previous formed CO₂ compounds are broken and gaseous CO₂ is produced. The heat requirement for the thermal regeneration is the energetic price to pay for the reduction of CO₂. The CO₂ amine absorption system has been simulated by the ASPEN+ code, [26].

The stream exiting from the top of the stripper, hence, contains essentially carbon dioxide and it needs compression up to at least 80 bars for transportation and final storage. In calculation of the powerplant efficiency, the energetic expense for CO₂ compression (which can be estimated in about 355 kJ/kgCO₂ from [22]) has not been directly accounted as it can depend on several variables (type of disposal, transportation system, etc.).

Including this reference value, and considering that, in the optimized case 4.94 kg/s of CO₂ are separated for the R-ATR cycle, the efficiency changes from 45.0% to 43.4%.

The same kind of system was studied for removal of CO₂ from the exhaust of power cycles such as natural gas combined cycle (NGCC) or semi-closed gas turbine combined cycle (SCGT/CC, [22]). However, in the present application there are relevant differences in design and performance.

The first difference lays in the operating pressure of the absorption unit: While in this case one must work at a high pressure level depending on the pressure ratio, in the case of flue gas treatment the operating pressure is atmospheric. Moreover, the mass flow rate to be processed is definitely less than exhausts from a gas turbine: in the R-ATR case the mass flow rate to be treated is 14.9 kg/s with reference to a compressor inlet flow rate of 100 kg/s, while, with the same reference, in a conventional gas turbine it would be about 102 kg/s. Absorption of CO₂ is favored by increasing pressure, as the mass transfer from gaseous to liquid phase grows with pressure, allowing a better removal efficiency at constant solution mass flow rate or, vice versa, constant efficiency with reduced mass flow rate. As a direct consequence, working at higher pressure allows a reduction of the specific thermal request for the regeneration of amine solution.

The specific thermal request of the CO₂ removal on the R-ATR cycle—reported in Fig. 9 versus pressure ratio and for different temperature levels of the inlet gas to the absorber—ranges between 1700 and 2300 kJ/kg. Considering an SCGT/CC with CO₂ amine chemical absorption from the exhaust, the minimal specific thermal request is about 3590 kJ/kg, [22]. The comparison is, of course, favorable to the present system, considering that the specific emission factors are almost comparable: between 70 and 100 gCO₂/kWh for the present type of cycle and about 60–70 gCO₂/kWh for the SCGT/CC.

The better removal efficiency and the consequent specific ther-

Table 4 Main operating results for using ALSTOM cyclone GT in R-ATR cycle

| CYCLE | | | | | | | | | | | | CO ₂ | Fuel |
|-----------------------------|-----------------|---------|------------------|----------------------|-----------------------|------------------|---------------------|--------------------|------------------|---------------------|-------------------|-----------------|------|
| ALSTOM Cyclone | m_c [kg/s] | β | T_{max} [K] | m_{cool} [kg/s] | $m_{s inj}$ [kg/s] | W_{GT} [kW] | W_{sp} [kJ/kg] | η_{GT} [%] | T_{exh} [K] | m_{exh} [kg/s] | Emiss. [g/kWh] | LHV [kJ/kg] | |
| Standard GT | 38.66 | 16.23 | 1602 | 8.29 | 0 | 13124 | 339 | 35.9 | 827 | 39.4 | 695 | 50009 | |
| R-ATR (steam cooling) | 38.66 | 16.23 | 1602 | 4.86 | 3.42 | 22181 | 574 | 39.1 | 890 | 46.6 | 150 | 11201 | |

mal request reduction are also due to the more favorable composition of the gas to be treated. In fact, a higher concentration of CO₂ enhances the gas-liquid CO₂ transfer. In this type of cycle the CO₂ mass concentration reaches the 42.5% in the case of the R-ATR, while in the SCGT/CC case the CO₂ mass concentration is only 14.5%—already about three times that of a conventional GT—and the nitrogen is up to 77%, [22].

From the above considerations, it is possible to state that the substantial reduction of the specific thermal request, with respect to the SCGT/CC case, is due to the combined effects of increased operating pressure and CO₂ concentration.

From Fig. 9 it is also evident that when the temperature of the gas at absorber inlet increases, the specific thermal request increases as well, due to the lower efficiency in the gas-liquid CO₂ transfer.

One problem that could affect the gas turbine of the R-ATR is that linked with the eventual entrainment of traces of amine (DEA and MDEA) in the clean fuel, that are likely to be corrosive for blades, combustor and so on. From the calculation carried out with ASPEN+, the possible presence of residual amine in the cleaned fuel is marginal (pollutant level), having estimated DEA and MDEA mass fractions of $2.19 \cdot 10^{-7}$ and $2.18 \cdot 10^{-5}$, respectively. Literature data about the corrosive effects of amine solutions is lacking when such low concentration are encountered, being mainly focused on the analysis of specific chemical plants where the concentrations are much higher, [27]. Then, here it is to be supposed that these effects are negligible, or, anyway, they should be evaluated by dedicated test campaigns.

Finally, the gas leaving CO₂ absorption system is saturated in DEA and MEA solutions, that could bring to the eventual carry-over of amine droplets, having an high damaging potential for the GT parts (particularly blades and combustor). The prevention of this phenomena requires an adequate design of the amine droplets separation system, also considering that the CO₂ absorber is pressurized and the effect of gravimetric contribution (in cyclone systems, for example) is relatively reduced.

Test Case of the R-ATR Cycle on a Current Production GT Model

As stated in the previous sections of this work, the performance levels of the proposed R-ATR power cycle are interesting, especially considering that there is no coupling with a steam bottoming cycle. On the whole, the cycles efficiency levels under optimized conditions are only 1–2% lower than other proposed chemically recuperated GT cycles with CO₂ removal, involving a steam bottomer cycle, [11,13].

In this section, the test on a current production GT model (ALSTOM CYCLONE) has been performed to have a preliminary verification of the adaptability of the proposed cycle to the current production technology: in this way, a preliminary evaluation of the short-term applicability chances of the R-ATR can be given.

The basic data used for the simulation and tuning of the ALSTOM Cyclone gas turbine model with the manufacturer catalog data have been applied to the R-ATR cycle. Since the existing machine does not include the possibility of compressor intercooling, this last has been canceled with respect to the previously proposed configuration (Fig. 1). This leads to a consistent loss in performance, but the aim of this section is just to give an idea of

the actual potential of the selected machine with very limited adaptation to the proposed cycle. Even if the inquired GT model works with air blade cooling, the configurations with steam cooling have been inquired too, in order to limit the change in design inlet turbine mass flow and maintaining the steam injection. The blade cooling system should undergo some off design level by changing the coolant, which was not evaluated in this work. The main modifications (common for example to biomass-fueled applications) are required for the combustion chamber, that should manage a low heating value fuel (highly diluted with nitrogen).

The main results are reported in Table 4. They show that a relatively limited efficiency improvement can be obtained, whereas a large increase in specific power is possible, especially due to the steam injection. The relatively low heating value per unit mass of reformed fuel implies the need of much higher amounts of fuel at combustion chamber inlet and a higher flow rate in the turbine with respect to design levels: this leads to a consistent degree of off design, that could bring to additional losses in performance. The absence of intercooled compression brings to consistently lower efficiency values with respect to those reported in Fig. 2.

Conclusions

A relatively innovative GT-based power cycle has been proposed, with CO₂ removal upstream of combustion chamber (R-ATR): The proposed cycle involves the use of auto-thermal reforming (ATR), with a recuperative GT. Downstream, further heat recovery from the exhaust proceeds into the fuel reforming—cleaning chain. The proposed solution makes extensive use of compressor spray intercooling and steam injection into the combustion chamber. Moreover, the possibility of adopting steam blade cooling has been examined. The cycle does not involve any steam bottoming cycle, ensuring thus a more limited complexity of the powerplant layout in comparison to reforming combined cycles with CO₂ removal and allowing the possibility to refer to a wide range of power sizes.

The performance potential in terms of efficiency and CO₂ removal have been inquired versus the typical parameters of chemically recuperated GTs. In particular, the influence of GT pressure ratio has been investigated, since the gas turbine is the core of the entire cycle layout. For the proposed configurations, the GT pressure ratio heavily influences the cycle performance, showing generally low values for the efficiency optimization. The best performance has been obtained with the adoption of steam blade cooling, even if interesting values are shown also by air cooling.

The inquired R-ATR solutions provide interesting performance levels (around 45.5% with steam cooling and 44% with air cooling), together with low values of CO₂ emissions (70–80 g/kWh) if the highest possible K_{steam} values are used.

The analysis of the CO₂ removal section shows that the particularly favorable fuel gas composition allows very low thermal requests, due to the high concentration and pressure of CO₂. Moreover, the higher the operating pressure (i.e., GT pressure ratio) the lower the CO₂ removal heat demand.

A test of the adaptability of the R-ATR with a current production gas turbine model has been performed, showing the possibility of increasing efficiency and specific power, as well as a consistent reduction in specific CO₂ emissions. The main problem is

surely linked to the higher turbine and combustion chamber mass flow rates with respect to the design values, due to the lower reformed fuel heating value and to the addition of steam for blade cooling and combustor. On the whole, the applicability of existing machines to the proposed cycle brings to a moderate increase in efficiency, but guarantees a consistent reduction potential of CO₂ emissions. However, some dedicated studies for off design operation are deserved in future works.

Nomenclature

DT = temperature difference
 K_{steam} = steam-fuel mass ratio at reformer inlet
 Lp = pressure loss
 m = mass flow
 T = temperature
 W = power

Subscripts

ATR = related to the ATR
 CC = combustion chamber
 CO₂ = related to CO₂ removal
 comp = compressor inlet
 exh = related to gas turbine exhaust
 GT = related to gas turbine cycle
 inj = injected
 max = maximum in cycle
 pc = post combustion
 pf = primary fuel
 RIG = recuperator
 s5 = steam added to the REF or ATR at point 5
 sat = water-steam saturation
 scool = coolant steam
 sinj = injected steam
 s tot = total steam
 ws = spray water

Greeks

β = GT cycle pressure ratio
 η = Efficiency

References

- [1] Corti, A., Failli, L., Fiaschi, D., and Manfrida, G., 1998, "Exergy Analysis of Two Second-Generation SCGT Plant Proposals," Proceedings of ASME IGTI 43rd Gas Turbine and Aeroengine Congress and Exhibition, Stockholm, Sweden, June.
- [2] Corti, A., Lombardi, L., and Manfrida, G., 1998, "Absorption of CO₂ With Amines in a Semi-Closed GT Cycle: Plant Performance and Operating Costs," Proceedings of ASME IGTI 43rd Gas Turbine and Aeroengine Congress and Exhibition, Stockholm, Sweden, June.
- [3] Corti, A., and Manfrida, G., 1998, "Economic Analysis of a Semi-Closed Gas Turbine/Combined Cycle (SCGT/CC) With CO₂ Removal by Amines Absorption," GHGT-4, 4th International Conference on Greenhouse Gas Control Technologies, InterLaken, Switzerland, Aug. 30–Sept. 2.
- [4] Corti, A., Fiaschi, D., and Manfrida, G., 1999, "Thermo-Economic Evaluation of the SCGT Cycle," *Energy Convers. Manage.*, **40**, pp. 1917–1929.
- [5] Facchini, B., Fiaschi, D., and Manfrida, G., 1996, "Semi-Closed Gas Turbine/Combined Cycle With Water Recovery," ASME Paper No. 96-GT-317.
- [6] Facchini, B., Fiaschi, D., and Manfrida, G., 1997, "SCGT/CC: An Innovative Cycle With Advanced Environmental and Peakload Shaving Features," *Energy Convers. Manage.*, **38(15–17)**, pp. 1647–1653.
- [7] Fiaschi, D., and Manfrida, G., 1999, "A New Semi-Closed Gas Turbine Cycle With CO₂ Separation," *Energy Convers. Manage.*, **40**, pp. 1669–1678.
- [8] Mathieu, Ph., Dechamps, P., and Distelmans, M., 1994, "Concepts and Applications of CO₂ Gas Turbines," *Power-Gen Europe '94*, Cologne.
- [9] Mathieu, Ph., Chefneux, E., and Dechamps, P., 1995, "Energy and Exergy Analysis of CO₂ Based Combined Cycle Plants," *Proceedings of the Second Law Analysis of Energy Systems: Towards the 21st Century*, Roma.
- [10] Cau, G., and Cocco, D., 2000, "Performance Assessment of Semi-Closed Chemically Recuperated Gas Turbine Systems," Proceedings of ASME Turbo Expo, May 8–11, Munich, Germany.
- [11] Lozza, G., and Chiesa, P., 2000, "Natural Gas Decarbonization to Reduce CO₂ Emission From Combined Cycles. Part B: Steam-Methane Reforming," ASME Paper No 2000-GT-0164.
- [12] Andersen, T., Kvamsdal, M., and Bolland, O., 2000, "Gas Turbine Combined Cycle With CO₂-Capture Using Auto-Thermal Reforming of Natural Gas," Proceedings of ASME Turbo Expo, May 8–11, Munich, Germany.
- [13] Lozza, G., and Chiesa, P., 2000, "Natural Gas Decarbonization to Reduce CO₂ Emission From Combined Cycles. Part A: Partial Oxidation," ASME Paper 2000-GT-0163.
- [14] Carcasci, C., and Harvey, S., 1998, "Design Issues for the Methane-Steam Reformer of a Chemically Recuperated Gas Turbine Cycle," ASME IGTI International Gas Turbine Congress, Stockholm.
- [15] Tapinassi, L., 2001, "Studio di impianti di potenza innovativi con turbina a gas integrati con sistemi di rimozione della CO₂ tramite conversione del metano in combustibile ad alto contenuto di idrogeno," Graduation thesis, Environmental Engineering Faculty, Università degli Studi di Firenze, Italy (in Italian).
- [16] Chiesa, P., and Consonni, S., 1999, "Shift Reactors and Physical Absorption for Low-CO₂ Emission IGCCs," *ASME J. Eng. Gas Turbines and Power*, **121**, pp. 295–305.
- [17] EFMA, 1995, "Best Available Techniques for Pollution Prevention and Control in the European Fertilizer Industry," Booklet No. 1 of 8: "PRODUCTION OF AMMONIA", copyright 1995—EFMA, European Fertilizer Manufacturers' Association.
- [18] IEA, 2000, "Carbon Dioxide Capture and Storage," Report from Department of Trade and Industry, Sept. on www.dti.gov.uk/cct.
- [19] Adelman, S. T., Hoffman, M. A., and Baughn, J. W., 1995, "A Methane-Steam Reformer for a Basic Chemically Recuperated Gas Turbine," *ASME J. Eng. Gas Turbines and Power*, **117**, pp. 16–23.
- [20] Carcasci, C., Facchini, B., and Harvey, S., 1998, "Design Issues and Performance of a Chemically Recuperated Aero-derivative Gas Turbine," *Proc Instn Mech Engrs*, **212**, Part A.
- [21] Fiaschi, D., and Lombardi, L., 2001, "Cellular Thermodynamic Model for Gas Turbine Blade Cooling," Proceedings of ECOS 2001 Conference, July 4–6.
- [22] Lombardi, L., 2000, "LCA Comparison of Technical Solutions for CO₂ Emissions Reduction in Power Generation," Ph.D. thesis, Dipartimento di Energetica "Sergio Stecco," Università degli Studi di Firenze, Italy.
- [23] Holland, M. L., and De Bruyn, H. J., 1996, "Metal Dusting Failures in Methane Reforming Plant," *Int. J. Pressure Vessels Piping*, **66**, pp. 125–133.
- [24] Lai, G. Y., 1990, *High Temperature Corrosion of Engineering Alloys*, ASM International, Materials Park, OH, pp. 47–72.
- [25] Holland, M. L., 2000, "Practical Experience With Countering Metal Dusting in a Methane Reforming Unit," Mossgas (PTY) Ltd., Mossel Bay, South Africa, on <http://www.mossgas.com/research/nace2000a.pdf>.
- [26] Aspen+, 2000, v. 10 *User Manual*, AspenTech TM.
- [27] Kohl, A. L., and Riesenfeld, F. C., 1985, *Gas Purification*, 4th Ed., Gulf Publishing, Houston, TX.

Thermodynamic Performance Analysis of New Gas Turbine Combined Cycles With No Emissions of Carbon Dioxide

R. Gabbrielli

Università di Pisa,
Dipartimento di Energetica,
via Diotisalvi 2,
Pisa 56126, Italy
e-mail: r.gabbrielli@ing.unipi.it

R. Singh

School of Mechanical Engineering,
Cranfield University,
Cranfield,
Bedfordshire MK43, OAL, UK
e-mail: r.singh@cranfield.ac.uk

In the context of the reduction of the carbon dioxide (CO_2) emissions as prescribed by the Kyoto protocol, this paper describes a thermodynamic performance analysis of new gas turbine combined cycles with no emissions of CO_2 and nitrogen oxides. Three new similar cycles belonging to the same typology are proposed. These cycles use water/steam as working fluid, which is compressed in liquid and vapor phase, and the internal combustion process, which takes place between syngas and pure oxygen. The top Brayton cycle and the bottom Rankine cycle are integrated together. The syngas is produced by steam-natural gas reforming with internal chemical heat recovery. The CO_2 produced in the combustion is captured simply by water condensation from the exhaust gas and liquefied to be stored. A simulation analysis has been performed to evaluate the net efficiency and the net specific work of the cycles. Varying the most important operative variables and using the least-square regression and 2^k factorial design techniques, a very large sensitivity analysis has permitted the highlighting of performance behavior of the cycles. Including the energy penalty due to the liquefaction of CO_2 and to the oxygen production and adopting standard operative conditions, the LHV-based net efficiency and the net specific work may exceed 50% and 1000 kJ/kg, respectively. [DOI: 10.1115/1.1610017]

Introduction

In the last hundreds of years, the content of some greenhouse gases (CO_2 , CH_4 , N_2O , CFC, HFC, and PFC) in the atmosphere has grown markedly. With a wide agreement in the scientific sector, this fact seems to have caused a continuous increase of the Earth surface temperature with consequent alteration of the global climate.

In 1997, the Kyoto Protocol defined the goal of global greenhouse gas emission reduction of about 5% within the years 2008–2012 in comparison with the emission level of 1990. Although the CO_2 is the least aggressive greenhouse gas, the overall amount released into the atmosphere from the human activities is so high in comparison with all other gases that the CO_2 is responsible for about 60% of the greenhouse effect due to the increase of greenhouse gas content in the atmosphere. The fossil fuel fired power generation sector produces about 16% of the overall anthropogenic CO_2 emissions.

A wide variety of techniques could be adopted to obtain the CO_2 emission reduction, as the Kyoto Protocol commitments. The more attractive possibilities are: reduction of the overall energy consumption, by increasing the thermodynamic efficiency of energy conversion and utilization, for example converting the old steam power plants to new more efficient natural gas fired combined cycles; use of lower carbon content fuels, for example natural gas instead of coal; enhancement of the natural sinks for CO_2 , such as forests and oceans, which naturally capture CO_2 from the atmosphere; use of power sources with intrinsically very low CO_2 emissions, as renewable (for example, biomass) or nuclear energy; deep modifications of standard fossil fuel fired power plants introducing the capture and storage of CO_2 . In this context, a large

interest in the design and development of new power generation technologies based on fossil fuels with lower CO_2 emissions has grown in the energy sector.

In particular, many modifications to standard gas turbine power generation technologies have been proposed in these last years with the purpose of reducing or eliminating the CO_2 emissions from the fossil fuel combustion. The proposals may be catalogued essentially in the following well-known typologies:

- CO_2 as working fluid and internal combustion with pure oxygen, [1–6],
- water/steam as working fluid and internal combustion with pure oxygen, [7–10],
- air gas turbine combined cycles with post-combustion CO_2 capture, [10–13],
- chemical looping combustion, [14,15],
- air gas turbine combined cycles with fossil fuel pre-combustion decarbonization to produce a hydrogen enriched fuel without carbon content, [16–20], and
- water/steam working fluid gas turbine combined cycles with fossil fuel pre-combustion decarbonization to produce pure hydrogen, [21–23].

In the present paper, three new similar gas turbine combined cycles with no CO_2 emissions belonging to the second typology are proposed. The four main literature proposals of steam/ CH_4 gas turbine combined cycles cited above have the following common features: (1) the working fluid is water/steam; (2) the compression is executed by a pump in liquid phase with low energy consumption; (3) the combustion takes place between natural gas and pure oxygen in atmosphere of steam, which mitigates the combustion temperature (recent interesting studies about the technological feasibility of new combustors for the combustion of natural gas with pure oxygen in steam atmosphere may be found in [24]); (4) steam or saturated water is produced recovering internally the exhaust gas heat; (5) the exhaust gas, whose components are steam and CO_2 , is cooled down to nearly ambient temperature with water condensation and consequent separation and capture of

Contributed by the International Gas Turbine Institute (IGTI) of THE AMERICAN SOCIETY OF MECHANICAL ENGINEERS for publication in the ASME JOURNAL OF ENGINEERING FOR GAS TURBINES AND POWER. Paper presented at the International Gas Turbine and Aeroengine Congress and Exhibition, Amsterdam, The Netherlands, June 3–6, 2002; Paper No. 2002-GT-30117. Manuscript received by IGTI, Dec. 2001, final revision, Mar. 2002. Associate Editor: E. Benvenuti.

the combustion CO_2 without emissions into the atmosphere. Practically, in these combined cycles, a top steam Brayton cycle is integrated with a bottom steam Rankine cycle, where the heat is provided by the top one.

The cycles here proposed have the following peculiarities in comparison with the other steam/ CH_4 gas turbine cycles: (1) the working fluid is compressed in both liquid and vapor phase, adopting a pump and an intercooled multistage compressor, where the intercoolings are executed down to saturation conditions with steam production; (2) the exhaust gas is partially recirculated and mixed with the working fluid; (3) the fuel is syngas (H_2 , CO , CO_2 , H_2O , and CH_4), which is produced via steam–natural gas reforming with internal chemical heat recovery from the exhaust gas, [25].

In this paper, first the features of the proposed cycles are described. Then, the results of thermodynamic simulations, in terms of thermodynamic efficiency (η) and net specific work (sw), are reported. Finally, with the regression and 2^k factorial design techniques, the operative performance behavior of a possible power plant based on the thermodynamic processes here proposed are highlighted.

Cycle Configurations

The process flow diagram of each cycle here proposed, referenced, respectively, as A, B, and C, is reported together with the qualitative temperature-specific entropy plane in Fig. 1. First of all, the thermodynamic transformations of the cycle A are described in the following using the number references of Fig. 1:

- 1–2: the water is compressed in a pump from the condensation pressure (0.055 bar) to a value lower than the exhaust gas pressure, that is equal to 1 bar;
- 2–3: the compressed water is heated up to saturated conditions in an economizer, where in the hot side the compressed steam, downstream the first compression stage, is cooled down to the saturation;
- 3–4: the saturated water is first partially vaporized in two heaters, corresponding to two intercoolings of the compressed steam, and then completely vaporized in a heat recovery steam generator where the exhaust gas is cooled down to 105°C ;
- 4–5: the saturated steam is compressed up to the exhaust gas pressure;
- 5–6/18–6: the exhaust gas is partially recirculated and mixed with the compressed steam;
- 6–7, 7–8, 8–9, 9–10, 11–12, and 12–13: the mixed steam is compressed in four intercooled compression stages, where the intercoolings are executed down to the saturation;
- 13: after heating without mixing in the high pressure turbine blade cooling, not reported in Fig. 1, the compressed steam is split in two streams, one feeds the combustion chamber to mitigate the combustion temperature, and the other is mixed with natural gas;
- 13–14: in a countercurrent plug-flow tubular reactor, [26,27], the steam–natural gas mixture reacts endothermically to produce a syngas stream, whose components are CO , H_2 , CO_2 , and unreacted steam and CH_4 , using the heat provided internally by the exhaust gas (chemical heat recovery);
- 14–15: the syngas burns with pure compressed oxygen provided in stoichiometric amount in atmosphere of steam which mitigates the combustion temperature; this implies that NO_x are not produced in the combustion;
- 15–16: the exhaust gas, whose components are steam (about 90% in volume) and CO_2 , expands down to 1 bar in a steam– CO_2 turbine; the turbine blades are cooled by the compressed steam upstream the splitting described above;
- 16–17: the exhaust gas is cooled to provide the heat necessary to the endothermic reforming reaction;
- 17–18: the exhaust gas is cooled down to 105°C to vaporize the low pressure steam;

- 18–19: the exhaust gas, that has not been recirculated, expands down to the condensation pressure (0.055 bar);
- 19–1: the water in the low pressure gas condenses so that the CO_2 is separated in gas phase to be stored in liquid phase in a successive step without emissions into the atmosphere.

The cycles B and C differentiate from the cycle A only in the high-pressure steam production process. In particular, the cycle B has essentially the following differences in comparison with the cycle A: the pressure of the saturated steam is higher than the exhaust gas pressure; the recirculated exhaust gas is compressed in two intercooled stages (9–10, 10–11, and 11–4), and it is mixed (3–11) with the saturated steam downstream the intercooling (10–11); the vaporisation of the water is executed in the heat recovery steam generator and in the recirculated exhaust gas intercooling. It is important to note that in the intercooling of the compressed recirculated exhaust gas, the pinch point between the hot side and the cold side has been established equal to about 10°C .

In the cycle C, the water is pumped directly up to the highest pressure of the cycle (1–2); the exhaust gas, which is partially recirculated, is compressed in two intercooled stages (11–12, 12–13, and 13–6); with the heat recovered in the intercooling (12–13), saturated intermediate pressure steam is produced (3–5) and then mixed with the intercooled compressed gas; downstream the second compression stage, the recirculated gas is mixed with the high pressure steam (4–6) produced by the exhaust gas cooling (2–4 and 10–11).

The cycles here proposed may be considered as the integration of a top steam intercooled regenerated Brayton cycle and a bottom steam Rankine cycle (cycles A and B have one pressure level, whereas the cycle C has two pressure levels) where the energy input is provided by the top cycle. For cycle A, B, and C the Rankine cycle thermodynamic transformations are 1–2–3–4–5–6–18–19, 1–2–3–10–9–12, and 1–2–4–6–5–1–3–5–12–11–14, respectively, as in Fig. 1.

In the cycles proposed, once fixed the working fluid mass flow to mitigate the combustion temperature to a defined value, three features have been introduced to reduce the heat to be provided by the exhaust gas in the saturated steam production: (1) the compression is subdivided in liquid and vapor phase so to decrease the saturation pressure; (2) the compression in vapor phase is intercooled and the heat released is recovered in the steam production process; (3) the exhaust gas is partially recirculated so to reduce the steam mass flow necessary in the combustion temperature mitigation.

The chemical heat recovery in the reformer makes it possible to increase the heat exchange efficiency because the average temperature difference is lower than in standard heat exchangers (see, for example, [28]). The overall steam reforming process is endothermic and so the heat exchange, that in standard heat exchangers is governed only by temperature difference between the hot and cold side, is due also to the reaction heat absorption. For each mole of methane 206 kJ are required in the reforming reaction. The water–shift reaction, which is always present in the reforming process, provides exothermically 41 kJ for each mole of reactant and reduces the overall heat requirements. The methane conversion increases with low pressure, high equilibrium temperature, and high steam-to-methane molar ratio.

Thermodynamic Performance Analysis

The cycle operative behavior has been simulated with the well known process simulator ASPEN PLUS, [29], evaluating the most important performance parameters, as η and sw.

First of all, for each cycle the most meaningful operative independent process variables have been selected. For cycle B and C the combustion pressure (HP) and the firing temperature (TIT), which is the temperature of the exhaust gas downstream the first nozzle of the turbine, are the essential variables. For cycle A, the low saturation pressure of the steam (SP) has to be taken into

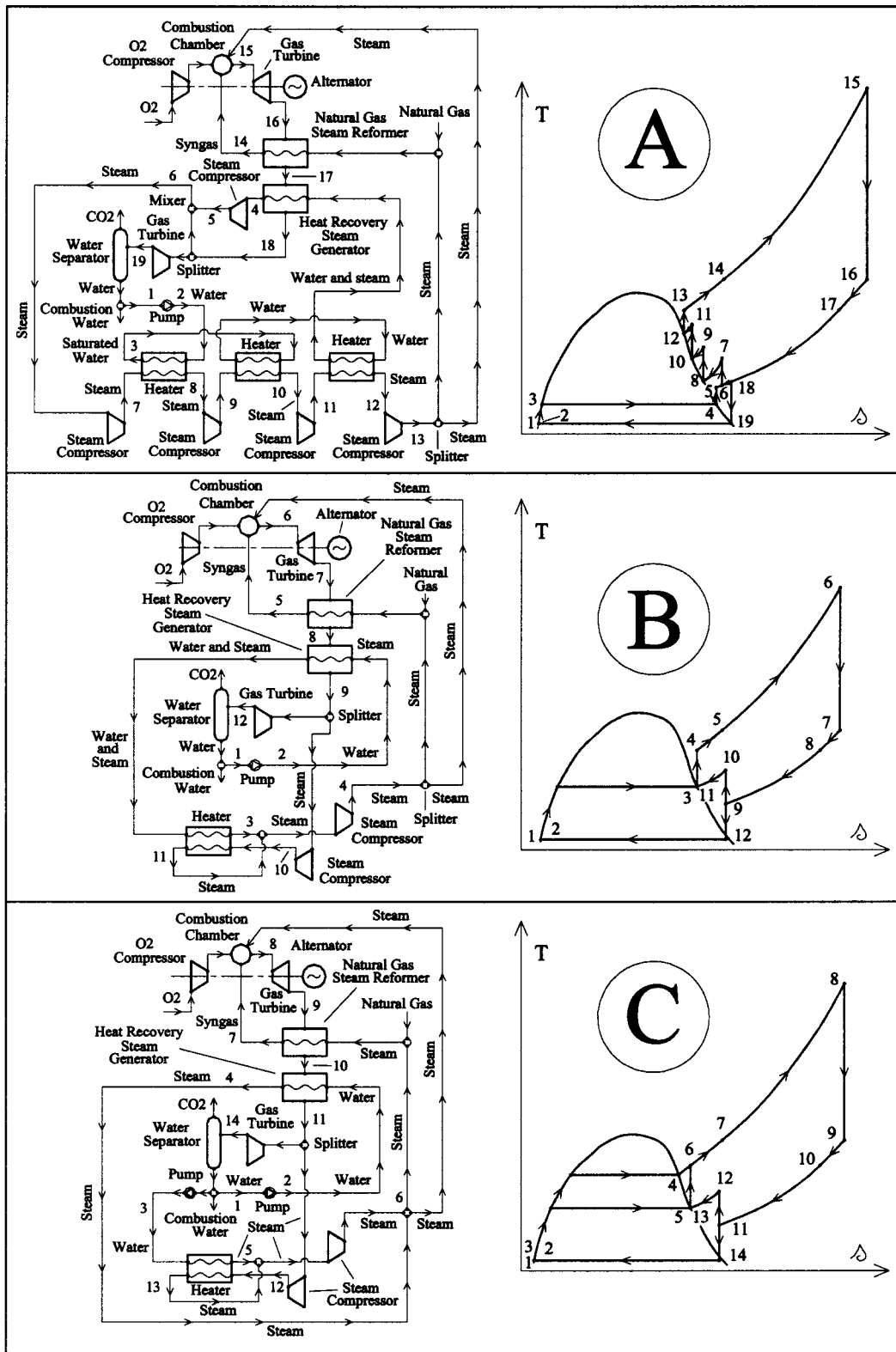


Fig. 1 Process flow diagram and relative qualitative temperature-specific entropy plane of the cycles proposed

account as further independent variable. The simulations have been executed varying the operative variables selected. HP assumes values from 10 bar to 40 bar in step of 5 bar. When the reforming pressure is higher than about 40 bar, the methane conversion is practically negligible and the chemical heat recovery

becomes a simple heat exchange due to temperature difference. TIT assumes values from 1225°C to 1375°C in step of 50°C, which are standard firing temperatures in modern power generation equipment. SP assumes four values, from 0.55 bar to 0.85 bar in step of 0.10 bar. Hence, $7 \times 4 \times 4 = 112$ and $7 \times 4 = 28$ simula-

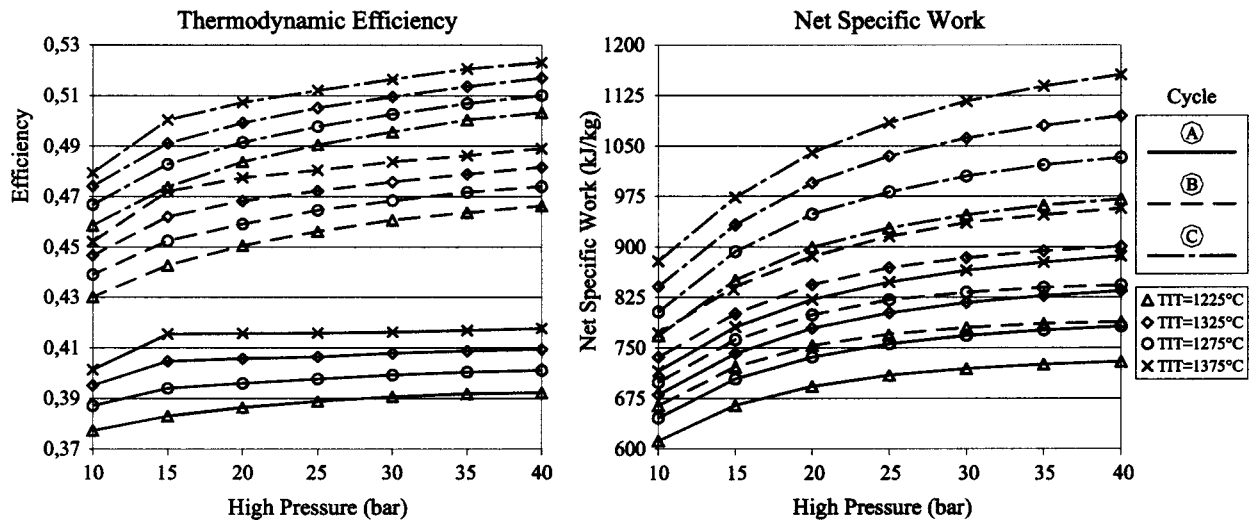


Fig. 2 Thermodynamic efficiency and net specific work of the cycles proposed

tions have been executed for the cycle A and for cycles B and C, respectively.

The operative assumptions to perform the simulations have been: (1) the natural gas, whose volume composition is $\text{CH}_4 = 95.04\%$, $\text{CO}_2 = 0.20\%$, $\text{N}_2 = 2.65\%$, $\text{C}_2\text{H}_6 = 2.11\%$, is supplied at 1 bar and 15°C ; (2) the oxygen production plant has not been taken into account; (3) the oxygen stream is supplied at 1 bar and 15°C with a volume purity equal to 96% (4% of argon); (4) the isentropic efficiency of compressors, turbines and pumps is, respectively, 0.90, 0.93, 0.80; (5) the mechanical efficiency of the turbomachinery is 0.99; (6) the difference between the combustion temperature at the outlet of the combustion chamber and the firing temperature has been established equal to 70°C via blade cooling with the working fluid downstream the compression; this has been simulated with a heat exchanger between the combustion chamber and the turbine [30]; (7) further cooling of the turbine has been simulated mixing some intermediate pressure working fluid with the exhaust gas at the middle of the expansion path, [30]; (8) in the heat exchangers, including the reformer, the pinch point is equal to 10°C ; (9) the working fluid mass flow (recirculated flow plus saturated steam) is fixed; (10) the pressure ratios of the intercooled steam compressor stages are equal; (11) to calculate the thermodynamic properties, the Redlich-Kwong-Soave equation of state and the steam NBS/NRC tables have been selected for steam- CO_2 mixtures and pure steam, respectively; (12) the pressure drop in the heat exchangers and reactors is 1% of the inlet pressure; (13) the heat loss in the heaters is equal to 1%; (14) the steam-to-methane molar ratio has been fixed equal to 3, which may be considered a standard value, [31]; (15) the liquefaction of CO_2 , that is executed at 70 bar and 28.6°C , has been simulated with an intercooled three-stage compressor and a water-cooled condenser.

In the evaluation of η and sw , the LHV of the fuel has been supposed equal to 47.8 MJ/kg, adopting the combustion heat values available in the software, and the overall net power has been decreased by the energy expense due to the oxygen production (0.24 kWh/kg, [2], which is a standard value with consolidated cryogenic technologies, [32]). In Fig. 2, η and sw (ratio between the overall net power and the exhaust gas mass flow) are reported for each version in function of the operative independent variables. For simplicity, the results of the cycle A are reported only when SP is 0.85 bar, because both η and sw increase monotonically with SP. Once established HP and TIT, when SP increases, the pressure ratio of the pump increases whereas that of the intercooled compressor decreases. This fact reduces the power consumption due to the steam compression.

Once fixed the operative variables, η and sw improve from cycle A to cycle C. The bottom Rankine subcycle η and sw grow markedly with the saturation pressure, as is well known. The best cycle is the cycle C whose η reaches about 52.3%. In the operative ranges of the independent variables, η grows monotonically: when TIT increases, the average temperature of heat introduction increases; when HP grows, η of both subcycles increases. The Brayton subcycle η starts to decrease with HP only for values higher than 40 bar.

sw has always an increasing trend with both HP and TIT. In the cycles B and C, the Rankine subcycle sw grows monotonically with HP. The Brayton subcycle sw assumes a decreasing trend with HP only when HP is higher than 40 bar. When TIT increases, the power produced in the high pressure turbine grows. The highest value of sw (for cycle C) is about 1150 kJ/kg.

Among the cycles proposed, the best one is the cycle C: Once fixed, the operative variables, the compression, is executed at most in the liquid phase with the lowest energy consumption (the area inside the qualitative temperature-specific entropy diagram assumes clearly the largest value).

Regression and 2^K Factorial Design Sensitivity Analysis

Using the numerical values of η and sw (the available operative conditions of cycles A, B, and C are 112, 28, and 28, respectively), reported above, a deep sensitivity analysis based on the regression technique has allowed us to define an explicit tool to predict the thermodynamic performance of a power plant based on one of the cycles proposed. In particular, adopting a suitable consolidated software, with the least-squares estimation method, all numerical results have been fitted to obtain approximated explicit functions that model the dependence of η and sw on the operative independent variables. With these functions, it is possible to predict approximately the process performances with a generic set of operative variables within the ranges analyzed without running further simulations.

The functions, used to approximate the dependence of η and sw on the operative variables and listed in the following, have proved to be the best set after detailed statistical comparisons among many functions:

Table 1 Regression parameters

| Regression Parameters | Average Quadratic Error | Coefficient of Determination |
|-----------------------|-------------------------|------------------------------|
| η_A | $1.038 \cdot 10^{-3}$ | $9.969 \cdot 10^{-1}$ |
| sw_A | $1.235 \cdot 10^0$ | $9.999 \cdot 10^{-1}$ |
| η_B | $9.209 \cdot 10^{-4}$ | $9.981 \cdot 10^{-1}$ |
| sw_B | $1.347 \cdot 10^0$ | $9.999 \cdot 10^{-1}$ |
| η_C | $6.994 \cdot 10^{-4}$ | $9.991 \cdot 10^{-1}$ |
| sw_C | $1.569 \cdot 10^0$ | $9.999 \cdot 10^{-1}$ |

$$\eta_A(\text{HP, SP, TIT}) = 4.541 \cdot 10^{-2} + 1.229 \cdot 10^{-3} \cdot \text{HP} + 4.388 \cdot 10^{-2} \cdot \text{SP} + 3.521 \cdot 10^{-4} \cdot \text{TIT} + 1.667 \cdot 10^{-5} \cdot \text{HP} \cdot \text{SP} - 7.404 \cdot 10^{-7} \cdot \text{HP} \cdot \text{TIT} - 2.374 \cdot 10^{-5} \cdot \text{SP} \cdot \text{TIT} - 1.433 \cdot 10^{-6} \cdot \text{HP}^2 + 4.242 \cdot 10^{-3} \cdot \text{SP}^2 - 5.377 \cdot 10^{-8} \cdot \text{TIT}^2 - 8.779 \cdot 10^3 / \text{HP}^6 - 1.095 \cdot 10^1 / \text{TIT} - 1.824 \cdot 10^{-2} / \text{SP};$$

$$sw_A(\text{HP, SP, TIT}) = 1.013 \cdot 10^1 - 1.618 \cdot 10^1 \cdot \text{HP} - 2.131 \cdot 10^2 \cdot \text{SP} + 7.518 \cdot 10^{-1} \cdot \text{TIT} + 7.242 \cdot 10^{-1} \cdot \text{HP} \cdot \text{SP} + 1.151 \cdot 10^{-2} \cdot \text{HP} \cdot \text{TIT} + 2.872 \cdot 10^{-2} \cdot \text{SP} \cdot \text{TIT} - 6.870 \cdot 10^{-3} \cdot \text{HP}^2 - 1.045 \cdot 10^2 \cdot \text{SP}^2 - 6.408 \cdot 10^{-5} \cdot \text{TIT}^2 - 1.094 \cdot 10^3 \text{HP}^{-0.5}, \text{ (kJ/kg)};$$

$$\eta_B(\text{HP, TIT}) = 1.206 \cdot 10^{-1} + 2.130 \cdot 10^{-3} \cdot \text{HP} + 3.180 \cdot 10^{-4} \cdot \text{TIT} - 6.320 \cdot 10^{-7} \cdot \text{HP} \cdot \text{TIT} - 1.084 \cdot 10^{-5} \cdot \text{HP}^2 - 5.392 \cdot 10^{-8} \cdot \text{TIT}^2 - 1.268 \cdot 10^2 / \text{HP}^4;$$

$$sw_B(\text{HP, TIT}) = 1.210 \cdot 10^2 - 1.737 \cdot 10^1 \cdot \text{HP} + 8.585 \cdot 10^{-1} \cdot \text{TIT} + 1.406 \cdot 10^{-2} \cdot \text{HP} \cdot \text{TIT} - 3.202 \cdot 10^{-2} \cdot \text{HP}^2 - 1.032 \cdot 10^{-4} \cdot \text{TIT}^2 - 1.109 \cdot 10^3 / \text{HP}^{0.5}, \text{ (kJ/kg)};$$

$$\eta_C(\text{HP, TIT}) = 1.624 \cdot 10^{-1} + 2.722 \cdot 10^{-3} \cdot \text{HP} + 3.070 \cdot 10^{-4} \cdot \text{TIT} - 8.795 \cdot 10^{-7} \cdot \text{HP} \cdot \text{TIT} - 1.270 \cdot 10^{-5} \cdot \text{HP}^2 - 5.350 \cdot 10^{-8} \cdot \text{TIT}^2 - 1.565 \cdot 10^1 / \text{HP}^3;$$

$$sw_C(\text{HP, TIT}) = 1.018 \cdot 10^2 - 1.969 \cdot 10^1 \cdot \text{HP} + 1.187 \cdot 10^0 \cdot \text{TIT} + 1.746 \cdot 10^{-2} \cdot \text{HP} \cdot \text{TIT} - 4.915 \cdot 10^{-2} \cdot \text{HP}^2 - 2.353 \cdot 10^{-4} \cdot \text{TIT}^2 - 1.419 \cdot 10^3 / \text{HP}^{0.5}, \text{ (kJ/kg)};$$

where the unit measures of each coefficient are omitted for simplicity and η_A (HP, SP, TIT), sw_A (HP, SP, TIT), η_B (HP, TIT), sw_B (HP, TIT), η_C (HP, TIT), sw_C (HP, TIT) are the estimated functions of η and sw for the cycles A, B, and C, respectively. The values of the regression parameters reported in Table 1 demonstrate the goodness of the fitting executed. The fitted functions, reported above, make it possible to predict, with very good approximation, the performance behavior of the power generation processes proposed. This may be useful in the automatic procedure of cost optimization of the new power generation plant.

To highlight clearly the main effects and the interactions between the independent operative variables on η and sw , a 2^k factorial design sensitivity analysis has been performed. In this kind of analysis, the energy expense to produce 1 kg of pure oxygen (E_{O_2}) has been added to the independent variable set. Its extreme values are 0.10 kWh/kg and 0.32 kWh/kg. This makes it possible to analyze the effect of the available oxygen production

Table 2 Performance data in the sensitivity analysis for cycle A

| HP, bar | SP, bar | TIT, °C | E_{O_2} , kWh/kg | η_A , % | sw_A , kJ/kg |
|---------|---------|---------|--------------------|--------------|----------------|
| 10 | 0.55 | 1225 | 0.10 | 40.13 | 647.7 |
| 40 | 0.55 | 1225 | 0.10 | 41.67 | 769.7 |
| 10 | 0.55 | 1375 | 0.10 | 42.63 | 757.5 |
| 40 | 0.55 | 1375 | 0.10 | 44.25 | 935.1 |
| 10 | 0.85 | 1225 | 0.10 | 41.95 | 680.1 |
| 40 | 0.85 | 1225 | 0.10 | 43.45 | 808.2 |
| 10 | 0.85 | 1375 | 0.10 | 44.37 | 790.8 |
| 40 | 0.85 | 1375 | 0.10 | 45.99 | 976.0 |
| 10 | 0.55 | 1225 | 0.32 | 33.49 | 540.5 |
| 40 | 0.55 | 1225 | 0.32 | 35.03 | 647.1 |
| 10 | 0.55 | 1375 | 0.32 | 35.99 | 639.6 |
| 40 | 0.55 | 1375 | 0.32 | 37.62 | 794.8 |
| 10 | 0.85 | 1225 | 0.32 | 35.31 | 572.5 |
| 40 | 0.85 | 1225 | 0.32 | 36.82 | 684.7 |
| 10 | 0.85 | 1375 | 0.32 | 37.73 | 672.5 |
| 40 | 0.85 | 1375 | 0.32 | 39.35 | 835.1 |

technology on the process performances. The extreme values of the other operative variables are those used in the simulations. The numerical values of η and sw in the sensitivity analysis are reported in Tables 2 and 3. Figure 3 reports the main effects of the operative variables on η and sw . In the operative ranges analyzed, about η and sw the most important variables are always E_{O_2} and HP, respectively. The decrease of E_{O_2} from 0.32 kWh/kg to 0.10 kWh/kg implies a large improvement of the performances of the power generation process (η grows 6.6% on average). About η , TIT is more important than HP only for cycle A. For each cycle, the only interaction effect not negligible is that between HP and TIT about sw . For cycle A, B, and C, the results equal $+2.644 \cdot 10^1$ kJ/kg, $+3.087 \cdot 10^1$ kJ/kg, and $+3.794 \cdot 10^1$ kJ/kg, respectively.

Conclusions

Three new gas turbine combined cycles with internal combustion of natural gas with pure oxygen in steam atmosphere without CO_2 and NO_x emissions have been proposed. They integrate many features of several literature proposals: steam intercooled compression, partial exhaust gas recirculation, internal chemical heat recovery with syngas production in steam-natural gas tubular reformer, exhaust gas expansion down to subatmospheric pressure, and CO_2 separation from the exhaust gas without any capture technology.

Cycle C, which is the integration of a top intercooled regenerative Brayton cycle and a bottom two-pressure reheat Rankine cycle, is the best one, because the power consumption due to steam compression is lower than in the other cycles.

A wide thermodynamic analysis has permitted the discovery that in the operative ranges of the selected process variables, the thermodynamic performances improve monotonically. Thermodynamic efficiency and net specific work explicit functions, obtained with the regression analysis of the numerical results of the simu-

Table 3 Performance data in the sensitivity analysis for cycle B and C

| HP, bar | TIT, °C | E_{O_2} , kWh/kg | η_B , % | η_C , % | sw_B , kJ/kg | sw_C , kJ/kg |
|---------|---------|--------------------|--------------|--------------|----------------|----------------|
| 10 | 1225 | 0.10 | 47.25 | 50.08 | 729.5 | 838.9 |
| 40 | 1225 | 0.10 | 50.85 | 54.55 | 860.1 | 1052.3 |
| 10 | 1375 | 0.10 | 49.43 | 52.16 | 844.3 | 956.1 |
| 40 | 1375 | 0.10 | 53.12 | 56.54 | 1040.0 | 1249.5 |
| 10 | 1225 | 0.32 | 40.61 | 43.44 | 627.0 | 727.7 |
| 40 | 1225 | 0.32 | 44.21 | 47.92 | 747.8 | 924.3 |
| 10 | 1375 | 0.32 | 42.79 | 45.52 | 730.8 | 834.3 |
| 40 | 1375 | 0.32 | 46.49 | 49.90 | 910.0 | 1102.8 |

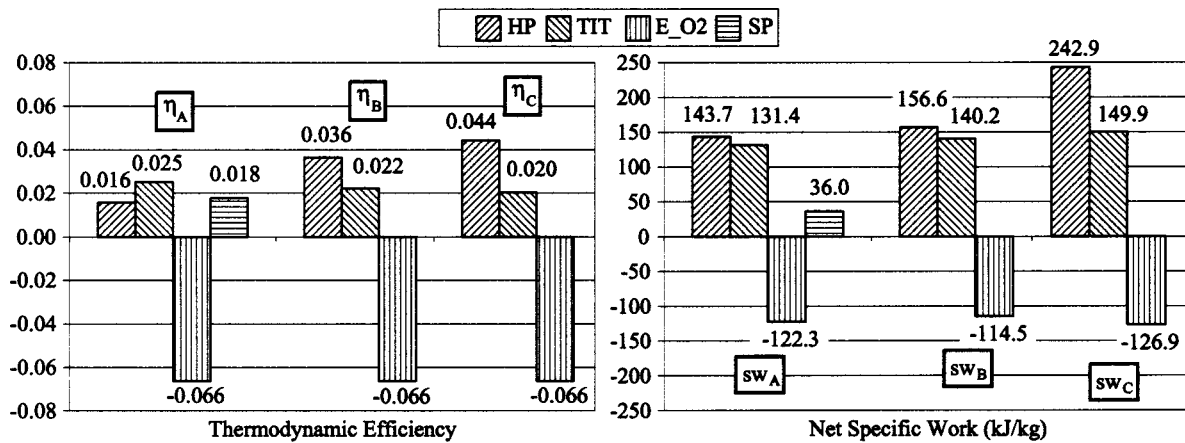


Fig. 3 Main effects of the operative variables on thermodynamic efficiency and net specific work with the 2^k factorial design sensitivity analysis

lations, may be used as useful tools to predict the process performance behavior with a generic set of operative variables. A 2^k factorial design analysis has highlighted the high importance of the energy consumption due to the oxygen production. To define the actual profitability of an eventual power plant based on the power generation processes proposed, it will be necessary to evaluate the process technological feasibility and to perform detailed economic and scenario analyses. These will be the topics of following papers.

Acknowledgments

The authors want to thank Franco Donatini (ENEL-Produzione Ricerca, Pisa) for his support provided during the research, a part of which has been described in this paper.

Nomenclature

- E_{O_2} = energy consumption to produce 1 kg of pure oxygen (kWh/kg)
 HP = combustion pressure (bar)
 LHV = lower heating value (kJ/kg)
 SP = low saturation pressure in cycle A (bar)
 sw = net specific work (kJ/kg)
 TIT = firing temperature ($^{\circ}$ C)

Greek

- η = LHV-based thermodynamic efficiency

Subscripts

- A = relative to cycle A
 B = relative to cycle B
 C = relative to cycle C

References

- Mathieu, P., and De Ruyck, J., 1993, "CO₂ Capture in CC and IGCC Power Plants Using a CO₂ Gas Turbine," *Proceedings of IGTI Cogen-Turbo Congress*, Bournemouth, UK, ASME, New York, pp. 77–83.
- Dechamps, P. J., Distelmans, M., Mathieu, P., and Pirard, N., 1994, "Performances of Combined Cycle Power Plants Using CO₂ Gas Turbine," *Proceedings of FLOWERS'94 Conference*, Florence, Italy, SG Editoriale, Padova, pp. 671–682.
- Yantovski, E. I., 1996, "Zero Emission Fuel-Fired Power Plants Concept," *Energy Convers. Manage.*, **37**, pp. 867–877.
- Ulizar, I., and Pilidis, P., 1997, "A Semiclosed-Cycle Gas Turbine With Carbon Dioxide-Argon as Working Fluid," *J. Eng. Gas Turbines Power*, **119**, pp. 612–616.
- Mathieu, P., and Nihart, R., 1999, "Zero-Emission MATIANT Cycle," *J. Eng. Gas Turbines Power*, **116**, pp. 116–120.
- Jackson, A., Neto, A. C., Whellens, M. W., and Audus, H., 2000, "Gas Turbine Performance Using Carbon Dioxide as Working Fluid in Closed Cycle Opera-

- tion," *Proceedings of ASME TURBOEXPO 2000*, Munich, Germany, ASME Paper No. 2000-GT-153.
- Pak, P. S., and Suzuki, Y., 1994, "A CO₂-Recovering Nonpolluting High-Efficiency Gas-Turbine Power-Generation System Utilizing Saturated Steam as Its Working Gas," *Electr. Eng. Jpn.*, **114**, pp. 86–97 (translated from Denki Gakkai Ronbunshi, 1993, 113-B, pp. 266–272).
- Jericha, H., Sanz, W., Woisetschlager, J., and Fesharaki, M., 1995, "CO₂-Retention Capability of CH₄/O₂-Fired Graz Cycle," *Proceedings of 21th CIMAC World Congress on Combustion Engines*, Interlaken, Switzerland, CIMAC, London.
- Anderson, R., Brandt, H., Mueggenburg, H., Taylor, J., and Viteri, F., 1998, "A Power Plant Concept Which Minimizes the Cost of Carbon Dioxide Sequestration and Eliminates the Emission of Atmospheric Pollutants," *Proceedings of 4th International Conference on Greenhouse Gas Control Technologies*, Interlaken, Switzerland, Elsevier Science Ltd., Oxford.
- Bolland, O., Undrum, H., and Nilsen, M., 2000, "Natural Gas Fired Power Cycles With Integrated CO₂ Capture," *Proceedings of 5th International Conference on Greenhouse Gas Control Technologies*, Cairns, Australia, CSIRO Publishing, Collingwood.
- Freund, P., 1998, "Abatement and Mitigation of Carbon Dioxide Emissions From Power Generation," *Proceedings of Power-Gen '98*, Milan, Italy, Pennwell, London.
- Bolland, O., and Undrum, H., 1999, "Removal of CO₂ From Natural Gas Fired Combined Cycle Plants," *Proceedings of Power-Gen '99*, Frankfurt, Germany, Pennwell, London.
- Fiaschi, D., and Manfrida, G., 1999, "A New Semi-Closed Gas Turbine Cycle With CO₂ Separation," *Energy Convers. Manage.*, **40**, pp. 1669–1678.
- Ishida, M., and Jin, H., 1994, "A New Advanced Power-Generation System Using Chemical-Looping Combustion," *Energy*, **19**, pp. 415–422.
- Jin, H., and Ishida, M., 2001, "Reactivity Study on a Novel Hydrogen Fueled Chemical-Looping Combustion," *Int. J. Hydrogen Energy*, **26**, pp. 889–894.
- Hendriks, C. A., and Blok, K., 1992, "Carbon Dioxide Recovery Using a Dual Gas Turbine IGCC Plant," *Proceedings of First International Conference on Carbon Dioxide Removal*, Amsterdam, Netherlands, Pergamon, Oxford.
- Audus, H., Kaarstad, O., and Skinner, G., 1998, "CO₂ Capture by Pre-Combustion Decarbonization of Natural Gas," *Proceedings of 4th International Conference on Greenhouse Gas Control Technologies*, Interlaken, Switzerland, Elsevier Science Ltd., Oxford.
- Andersen, T., Kvamsdal, M., and Bolland, O., 2000, "Gas Turbine Combined Cycle With CO₂-Capture Using Auto-Thermal Reforming of Natural Gas," *Proceedings of ASME TURBOEXPO 2000*, Munich, Germany, ASME Paper No. 2000-GT-162.
- Lozza, G., and Chiesa, P., 2000, "Natural Gas Decarbonization to Reduce CO₂ Emission From Combined Cycles. Part A: Partial Oxidation," *Proceedings of ASME TURBOEXPO 2000*, Munich, Germany, ASME Paper No. 2000-GT-0163.
- Lozza, G., and Chiesa, P., 2000, "Natural Gas Decarbonization to Reduce CO₂ Emission From Combined Cycles. Part B: Steam-Methane Reforming," *Proceedings of ASME TURBOEXPO 2000*, Munich, Germany, ASME Paper No. 2000-GT-0164.
- Cai, R., and Fang, G., 1991, "Analysis of a Novel Hydrogen and Oxygen Combined Cycle," *Int. J. Hydrogen Energy*, **16**, pp. 249–254.
- Bannister, R. L., Newby, R. A., and Yang, W. C., 1999, "Final Report on the Development of a Hydrogen-Fuelled Combustion Turbine Cycle for Power Generation," *J. Eng. Gas Turbines Power*, **121**, pp. 38–45.
- Sugisita, H., Mori, H., and Uematsu, K., 1998, "A Study of Thermodynamic Cycle and System Configurations of Hydrogen Combustion Turbines," *Int. J. Hydrogen Energy*, **23**, pp. 705–712.
- Inoue, H., Kobayashi, N., and Koganezawa, T., 2001, "Research and Development of Methane-Oxygen Combustor for Carbon Dioxide Recovery Closed-

- Cycle Gas Turbine," *Proceedings of 23th CIMAC World Congress on Combustion Engine Technology for Ship Propulsion, Power Generation, Rail Traction*, Hamburg, Germany, CIMAC, London.
- [25] Kesser, K. F., Hoffman, M. A., and Baughn, J. W., 1994, "Analysis of a Basic Chemically Recuperated Gas Turbine Power Plant," *J. Eng. Gas Turbines Power*, **116**, pp. 277–284.
- [26] Adelman, S. T., Hoffman, M. A., and Baughn, J. W., 1995, "A Methane-Steam Reformer for a Basic Chemically Recuperated Gas Turbine," *J. Eng. Gas Turbines Power* **117**, pp. 17–23.
- [27] Dybkjær, I., 1995, "Tubular Reforming and Autothermal Reforming of Natural Gas—An Overview of Available Processes," *Fuel Process. Technol.*, **42**, pp. 85–107.
- [28] Abdallah, H., Facchini, B., Danes, F., and De Ruyck, J., 1999, "Exergetic Optimization of Intercooled Reheat Chemically Recuperated Gas Turbine," *Energy Convers. Manage.*, **40**, pp. 1679–1686.
- [29] ASPEN PLUS User Guide, release 10.2.1, 2000.
- [30] Carcasci, C., and Facchini, B., 2000, "Comparison Between Two Gas Turbine Solutions to Increase Combined Power Plant Efficiency," *Energy Convers. Manage.*, **41**, pp. 757–773.
- [31] Strait, M., Allum, G., and Gidwani, N., 1997, "Synthesis Gas Reformers," <http://www.owl.net.rice.edu/~ceng403/nh3ref97.html>.
- [32] Smith, A. R., and Klosek, J., 2001, "A Review of Air Separation Technologies and Their Integration With Energy Conversion Processes," *Fuel Process. Technol.*, **70**, pp. 115–134.

Thermoeconomic Analysis of Gas Turbine Plants With Fuel Decarbonization and Carbon Dioxide Sequestration

M. Bozzolo

M. Brandani

A. Traverso

A. F. Massardo

Mem. ASME

Thermochemical Power Group,
Dipartimento di Macchine,
Sistemi Energetici e Trasporti,
Università di Genova,
Genova, Italy

In this paper the thermoeconomic analysis of gas turbine plants with fuel decarbonization and carbon dioxide sequestration is presented. The study focuses on the amine (MEA) decarbonization plant layout and design, also providing economic data about the total capital investment costs of the plant. The system is fuelled with methane that is chemically treated through a partial oxidation and a water-gas shift reactor. CO₂ is captured from the resulting gas mixture, using an absorbing solution of water and MEA that is continuously recirculated through an absorption tower and a regeneration tower: the decarbonized fuel gas is afterwards burned in the gas turbine. The heat required by CO₂ sequestration is mainly recovered from the gas turbine exhausts and partially from the fuel treatment section. The reduction in efficiency and the increase in energy production costs due to fuel amine decarbonization is evaluated and discussed for different gas turbine sizes and technologies (microturbine, small size regenerated, aeroderivative, heavy duty). The necessary level of carbon tax for a conventional plant without a fuel decarbonization section is calculated and a comparison with the carbon exergy tax procedure is carried out, showing the good agreement of the results. [DOI: 10.1115/1.1587744]

Introduction

The Third Conference of the Parties to the Framework Convention on climate change at Kyoto, Japan, required industry to seek new solutions to restrict the production and the emission of greenhouse gases from human activities. For the power industry such restrictions mainly apply to carbon dioxide which is emitted into the atmosphere when fossil fuels (methane, coal, oil) are burnt to produce energy.

Fossil fuels are at present, and will be for the following decades, the most important source for satisfying the world's energy demands. Unfortunately this precludes the possibility of drastically reducing carbon dioxide emissions, despite the increases in power plant conversion efficiency and the exploitation of low C/H content fuels, such as methane.

Nuclear and renewable energy could be alternative solutions but the use of nuclear energy raises political and security issues and renewables present economic and infrastructural problems.

Therefore, research efforts are being directed towards innovative power plants capable of first concentrating and then removing carbon dioxide from fossil fuels. Three main strategies have been proposed:

A Exhaust Gas Treatment. With very few changes to existing gas turbines, it would be possible to install a chemical treatment plant able to operate on the whole exhaust flow downstream from the gas turbine, [1,2].

B Fuel Decarbonization. Hydrogen is not directly available in nature, but it can be produced by properly treating hydrocarbons: A partial oxidation or a steam-methane reforming reaction followed by a water-gas shift reaction could be used to achieve this goal, [3].

C Use of Carbon Dioxide as the Working Fluid. It is possible to build a power plant where the expander flow is composed only of carbon dioxide and water [4].

The proposed available technologies to separate carbon dioxide from a syngas are based on the principles of:

1 *Chemical Absorption.* The use of an aqueous solution of blended amines represents the most mature technology that can be transferred to power plants, [1,3,5,6].

2 *Physical Absorption.* The technique is based on the variation of CO₂ solubility within a solvent at different pressures, [5,6].

3 *Adsorption.* Some materials can adsorb a particular gas: The flow is led to licking up the adsorbent bed, [5,6].

4 *Cryogenic.* Carbon dioxide can be removed from a syngas using low temperature condensation, [5,6].

5 *Separation Using Membranes.* Separation is achieved by compression of the feed stream, which forces the gaseous components with the higher permeability values to permeate through the membrane, [5,6].

The TPG (Thermomechanical Power Group) of the University of Genoa has investigated models of simple-cycle gas turbine plants with fuel decarbonisation and CO₂ sequestration. The aim of this work is to explain what the use of a fuel treatment and CO₂ chemical absorption section involves in terms of performance, efficiency, capital costs, and cost of energy. The study focuses on four different gas turbines: a microturbine Turbec T-100, a Nuovo Pignone PGT-2, a heavy-duty Siemens V64.3a, and an aeroderivative GE-LM6000.

To carry out thermodynamic and thermoeconomic analysis the in-house TEMP code (ThermoEconomic Modular Program), [7,8], was used. Three new modules were added to the code to simulate a partial oxidation reactor, a water-gas shift reactor and a chemical absorption plant for CO₂ sequestration. Thermodynamic results and chemical compositions of streams were verified with the help of the commercial code PRO/II, [5,9].

Each TEMP module is provided with a specific "cost/costing function" which evaluates the capital cost of the component on

Contributed by the International Gas Turbine Institute (IGTI) of THE AMERICAN SOCIETY OF MECHANICAL ENGINEERS for publication in the ASME JOURNAL OF ENGINEERING FOR GAS TURBINES AND POWER. Paper presented at the International Gas Turbine and Aeroengine Congress and Exhibition, Amsterdam, The Netherlands, June 3–6, 2002; Paper No. 2002-GT-30120. Manuscript received by IGTI, December 2001, final revision, March 2002. Associate Editor: E. Benvenuti.

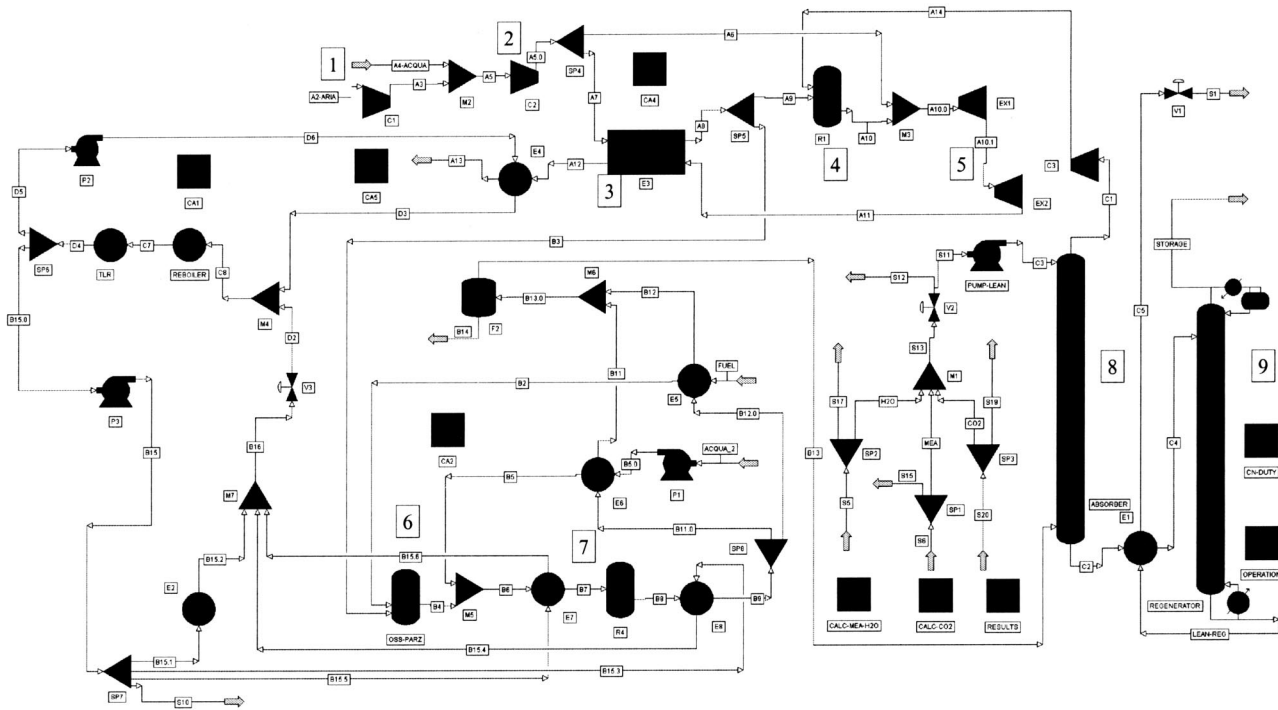


Fig. 1 Layout of the complete plant model in PROII. 1. LP compressor, 2. HP compressor, 3. regenerator, 4. combustion chamber, 5. expanders, 6. partial oxidation reactor, 7. water gas shift reactor, 8. absorber column, 9. regenerator column.

the basis of thermodynamic and physical parameters. This approach allows capital costs and cost of energy to be estimated straightforwardly.

Plant Layout

This work is based on a national test case, [3], proposed for the study of very low CO₂ emission power plants. The complete plant consists of three sections (see Fig. 1): The first section is the power section, represented by a gas turbine with a heat recovery system; the second is the fuel decarbonization section, represented by partial oxidation and water-gas shift reactors; the third is the carbon dioxide separation unit represented by a chemical absorption plant using an aqueous solution of blended amines, [5].

In the test case the regenerated 2.3 MW_e Nuovo Pignone PGT-2 gas turbine was employed to represent the power section. The machine includes two centripetal compressors working at on-design conditions with a polytropic efficiency of 0.845. A water injection chamber (Component M2 in Fig. 1) is placed between them: the air flow coming from the low pressure compressor is cooled by water injection and the mixture is afterwards sent to the high pressure compressor. Pressurised air enters the regenerator at 12.5 bar and is heated by hot gases coming from the expander. The turbine inlet temperature is set at 1080°C. A cooling flow equal to 6.5% of the compressor inlet air mass flow is also considered (Stream A6). Hot gases are reduced to 1.055 bar and are then sent to the regenerator and then to the heat recovery system in which excess heat is used for cogeneration. Downstream from the gas regenerator a fraction of the air flow is split into two streams in Component SP5 from which 10% of the total flow is sent to the fuel decarbonization section. Operating conditions for the whole plant are set so that the turbine inlet temperature is the same as the simple gas turbine cycle: The inlet methane mass flow is chosen to produce the necessary flow rate of hydrogen to obtain a 1080°C turbine inlet temperature. Methane is preheated by gases coming from the water-gas shift reactor, then sent to the partial oxidation reactor where it reacts with the pressurised air coming from the power section. The mixture leaves the reactor at such a

temperature that the incoming water flow can completely vaporize inside the mixer (Component M5). Actually, to obtain a high carbon monoxide efficiency conversion during the water-gas shift reaction the water must be in a gaseous state. The syngas from the water-gas shift reactor is split into two streams that preheat the fuel and the water and then it is carried to the carbon dioxide separation section where it enters the first column (absorber) from the bottom. Clean gas, composed mainly of hydrogen and nitrogen, leaves the tower from the top and is sent to the power section, while the products of the reaction, basically monoethanolamine, water and carbon dioxide, leave the tower from the bottom and are carried to the second column (regenerator) in which the chemical bond between the carbon dioxide and amines is broken by heat provided by the reboiler. Since the heat required is at relatively low temperature, about 180°C, it should be recovered from the plant for economical operation. In this case 70% of the heat comes from turbine exhaust gases, while 30% comes from the coolers of the syngas. Carbon dioxide is available at the top of the regenerator column and should be stored after being compressed and liquefied. However, this aspect of the process is beyond the scope of this work.

The flue gas leaving the top of the absorber column mainly consists of hydrogen and nitrogen; afterwards it is compressed and injected into the gas turbine combustion chamber, where it reacts with the air coming from the regenerator. The nontraditional fuel molar composition is likely to need apt redesign of the combustion chamber, [10].

Partial Oxidation for Fuel Decarbonization

A partial oxidator is a chemical reactor where hydrocarbons react with the incoming air flow without reaching complete combustion, thanks to the use of specific catalysts, [11].

In a partial oxidation reactor fed by methane the main chemical reaction is



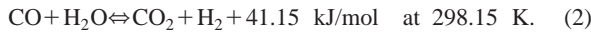
Table 1 Molar composition (%) of the gas mixture at the outlet of the partial oxidation reactor

| | T.E.M.P. | PRO II |
|------------------|----------|--------|
| CH ₄ | 0.25 | 0.28 |
| H ₂ | 32.70 | 32.38 |
| CO | 16.35 | 16.31 |
| CO ₂ | 1.70 | 1.75 |
| H ₂ O | 5.30 | 5.33 |
| N ₂ | 43.70 | 43.95 |

The reaction shows a favourable chemical equilibrium, [12], for a wide range of temperatures: It is thus possible to choose the operating temperature of the reactor on the basis of the requirements of the whole plant. The partial oxidation reactor is simulated by the TEMP code with a new module called "Oxipar." The program calculates the thermodynamic conditions and the molar composition of the mixture in a user-defined number of sections inside the reactor. In each single section fuel reacts with the incoming air flow according to the reactions of partial oxidation and complete combustion ($\text{CH}_4 + 2\text{O}_2 \rightleftharpoons \text{CO}_2 + 2\text{H}_2\text{O}$). In this case methane mass flow is chosen to obtain a 1080°C turbine inlet temperature. The program assumes a first attempt temperature and solves the mass-action law in an iterative way in order to obtain the molar composition at equilibrium. In that respect, it is necessary to evaluate the chemical equilibrium of the reactions through equilibrium constants, provided by the in-house code LNK, [5]. All data given by the new TEMP module were verified using the commercial code PRO/II (see Table 1).

As oxygen is poisonous for the absorber column catalysts, the partial oxidation reactor is expected to completely consume the incoming oxygen.

The reactor outlet temperature is set so that incoming water for the water-gas shift reaction can completely vaporize: In this way the reactor operating temperature depends on the incoming water mass flow. A unitary steam to carbon ratio is assumed, [13]. Carbon monoxide coming from the partial oxidation reactor can be converted into hydrogen by a water-gas shift reaction:



In order to obtain a high carbon monoxide efficiency conversion, water must be in a gaseous state. Liquid water can be injected directly into the partial oxidation reactor or downstream from it to obtain complete vaporization. The water-gas shift reaction is exothermic and it shows favorable chemical equilibrium at low temperatures. This is the reason why the flow from the partial oxidator must be cooled before it enters the shift reactor.

The water-gas shift reactor is simulated in the TEMP code by a new module named "Shift Reactor." Again, the program calculates the thermodynamic conditions and the molar composition of the mixture in a user-defined number of sections inside the reactor. In each section the gas mixture reacts with vapor according to the water-gas shift reaction. The results have been verified with the help of PRO/II. The comparison between the two codes is reported in Table 2.

Gas outlet temperature is 230°C. Downstream from the reactor the mixture is split into two streams that preheat the incoming

Table 2 Molar composition (%) of the gas mixture at the water-gas shift reactor outlet

| | T.E.M.P. | PRO II |
|------------------|----------|--------|
| CH ₄ | 0.20 | 0.24 |
| H ₂ | 39.20 | 38.91 |
| CO | 0.30 | 0.28 |
| CO ₂ | 14.33 | 14.48 |
| H ₂ O | 10.40 | 10.89 |
| N ₂ | 35.57 | 35.20 |

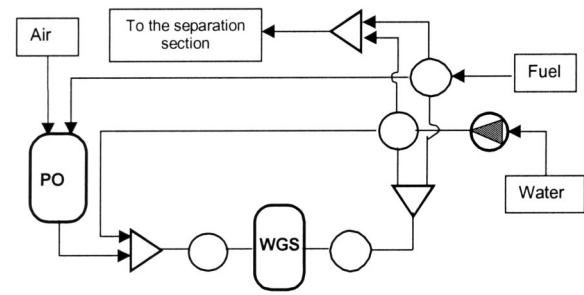


Fig. 2 Fuel decarbonization section

methane and water flows (see Fig. 2). It passes through a water knockout drum and then it enters the CO₂ separation section.

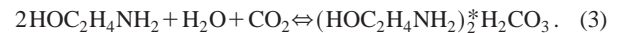
The present paper mainly focuses on the CO₂ separation plant; in that respect, partial oxidation and water-gas shift reactor design problems have not been analyzed in depth and their capital costs have been preliminarily estimated on the basis of the required catalyst surface: Operating temperature and pressure, mass flow and catalyst type are the most influential parameters, [5].

Carbon Dioxide Absorption With Amines

Of all the techniques reported in open literature, chemical absorption using an aqueous solution of blended amines represents the most mature technology for separating carbon dioxide from a syngas, [5]. The separation plant (see Fig. 3) consists of an absorber column (AC) and a regenerator column (RC).

Flue gas (Stream no. 1) enters the first column from the bottom and comes into contact with the counter flow the water and monoethanolamine absorbing solution (Stream no. 5). Hydrogen leaves the tower from the top (fuel stream) while the CO₂ rich solution (Stream no. 3) enters the regenerator column after being preheated. The chemical bond between the carbon dioxide and amines is broken by heat provided by the reboiler (component RE). CO₂ leaves the column from the top while the aqueous amine solution is carried back to the absorber column. The condenser at the top of the tower (CN) is necessary to ensure a small and gradual temperature gradient through the column.

The most commonly used columns for chemical absorption systems are plate towers or packed towers, [5,12,13]. Plate towers should be preferred when a chemical reaction occurs between the flue gas and the absorbing solution. In this model the two columns are plate towers as a chemical reaction takes place, [6]:



The right-hand side reaction is favored by low temperatures (37–50°C), while the left-hand side one is favored by high temperatures (120–180°C). The flue gas entering the absorber column

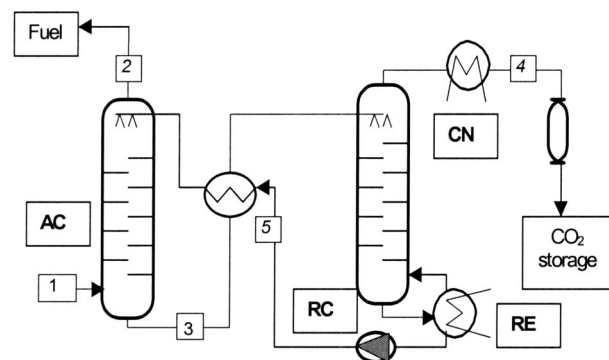


Fig. 3 Chemical absorption separation plant

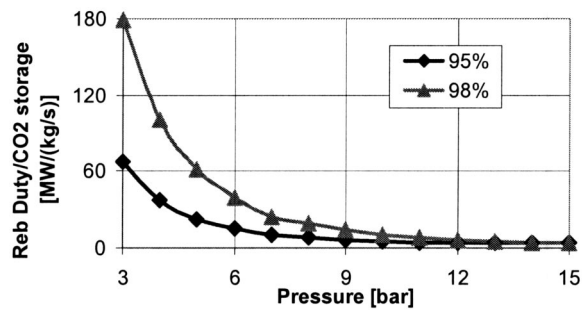


Fig. 4 Reboiler duty versus pressure

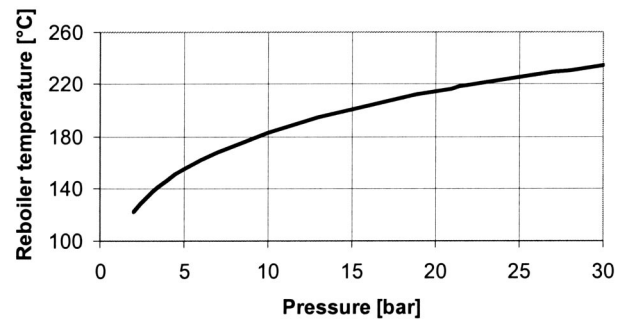


Fig. 5 Reboiler temperature versus pressure

must be kept at a low temperature; in the present model the flue gas temperature is 43°C. A challenging problem is avoiding poisoning components: The most important impurity in the flue gas, apart from SO₂ and NO₂, is oxygen. Oxygen can react with the aqueous solution of amines and cause the formation of stable salts which become very difficult to regenerate. This is why the oxygen must be completely burnt in the partial oxidation reactor.

The chemical absorption system is simulated in the TEMP code by the new module called “CO₂ Sequestration.” The first part of the program calculates the thermodynamic and chemical composition of outlet streams (“fuel” and “CO₂ storage”, see Fig. 3), the second part evaluates the tower design and the costs of the entire separation plant.

The program calculates the mass flow of the aqueous solution of amines required by the absorption process on the basis of the mass fraction of carbon dioxide inside the incoming flue gas. For every kg/s of CO₂ entering the absorber column, 19.84 kg/s of water and 4.86 kg/s of amines are needed for the process; for the present plant (Fig. 3), 0.52 kg/s of carbon dioxide from the bottom and 2.52 kg/s of monoethanolamine plus 10.31 kg/s of water from the top. The solution strength, that is to say the ratio between MEA and water, cannot be greatly increased because of corrosion problems inside the tower, [6].

Flue gas inlet pressure is the most important parameter for the operating conditions of the plant: It influences not only the thermodynamic and chemical operating conditions, but also the size of the towers. The model works properly in a large range of pressures, from 2 to 30 bar, and it is able to simulate the match between the separation plant and a large number of gas turbines (heavy-duty, aeroderivative, and microturbines). The program calculates the number of trays of the absorber column on the basis of the inlet pressure; the regenerator column has a fixed number of trays for every operating pressure. Tray number is a very important parameter to evaluate pressure losses, and the size and cost of the columns.

The regenerator column is meant to be very pressure sensitive: Figure 4 shows the duty delivered by the reboiler to the column with respect to the operating pressure and different solvent regeneration percentages.

The required duty has been adimensionalised by relating it to the amount of CO₂ entering the system in kilograms per second. According to the results, higher regeneration percentages mean greater energy requirements. A 95% regeneration efficiency means that 95% of the total CO₂ flow rate entering the regenerator column is stored, while 5% is pumped back to the absorber column. In the present model, efficiency is fixed at 95% so that the heat recovery system of the whole plant can satisfy reboiler duty. Another challenging problem is reboiler operating temperature; reboiler temperature increases with operating pressure (Fig. 5).

It is important to note that reboiler temperature is not influenced by regeneration efficiency. A remarkable fact is that an operating pressure increase causes reboiler duty to decrease and its temperature to rise: An agreement between these two parameters must be found in order to avoid a nonacceptable efficiency reduction for

the integrated plant. To reduce reboiler duty the aqueous solution of amines and carbon dioxide entering the regenerator column is preheated by the lean solution leaving the column from the bottom (Fig. 3).

The second part of the “CO₂ sequestration” module evaluates column sizes and system costs. In the model the two towers are plate columns, so that size calculations are the same as for the distillation columns, [12]. One of the most important parameters is rising gas velocity: If it is too low, very strong irregularities in the liquid-phase flow may occur, if too high, entrainment flooding may cause column malfunction. Attention must also be paid to the gas-liquid ratio in order to avoid downflow flooding. Once the gas velocity and mass flow are chosen, column diameter and thickness can be evaluated. Column costs are calculated on the basis of plate number, plate spacing, vessel diameter, and thickness, [12].

Test Case Thermodynamic Results

The regenerated Nuovo Pignone PGT-2 is capable of producing 2.35 MW_e and 3.27 MW_{th} for cogeneration with a net electrical efficiency of 0.3. Inlet air mass flow is 10.4 kg/s, compression ratio is 12.5. Exhaust gases leave the heat recovery system at 117°C with a carbon dioxide specific emission of 634 g/kWh.

For the complete plant equipped with fuel decarbonization and CO₂ sequestration sections, TEMP calculates an electric power of 2.30 MW_e, almost the same as the simple gas turbine cycle, but net efficiency decreases dramatically to 0.227. Methane mass flow entering the plant (Stream 16 in Fig. 6) is estimated at 0.202 kg/s, 27.3% more than the simple gas turbine cycle (turbine inlet temperature is the same for the gas turbine simple cycle and the complete cycle). An output partial oxidation reactor temperature of 933°C is reached using 9.4% of the inlet fuel flow for complete combustion, so that incoming water for the water-gas shift reactor can completely vaporise. As the water-gas shift reaction has a favorable chemical equilibrium at low temperatures, the gas mixture to the reactor is cooled to 151°C in component 41 (Fig. 6); an additional water flow (Stream 21) is injected into the shift reactor in order to obtain a 97.8% carbon monoxide conversion efficiency. The syngas leaves the reactor at 231°C, preheats the incoming methane and water flows, enters the water knockout drum (component 47 in Fig. 6) and is sent to the carbon dioxide separation section (component 16) at 43°C.

The sequestration plant operating pressure is related to the gas turbine compression ratio: in the present plant, the reboiler works at 10.1 bar and requires a 1.33 MW duty at 182.4°C. The required heat is recovered from the recovery system downstream from the gas turbine (component 11) and from the heat exchanger before the water-gas shift reactor (component 41). This restricts the complete plant to only 3 MW_{th} for cogeneration. Fuel leaving the absorber column is compressed up to 14 bar and then is injected into the gas turbine combustion chamber. Fuel mass flow rate is 0.92 kg/s (low heating value is equal to 8.96 MJ/kg); the molar composition is reported in Table 3.

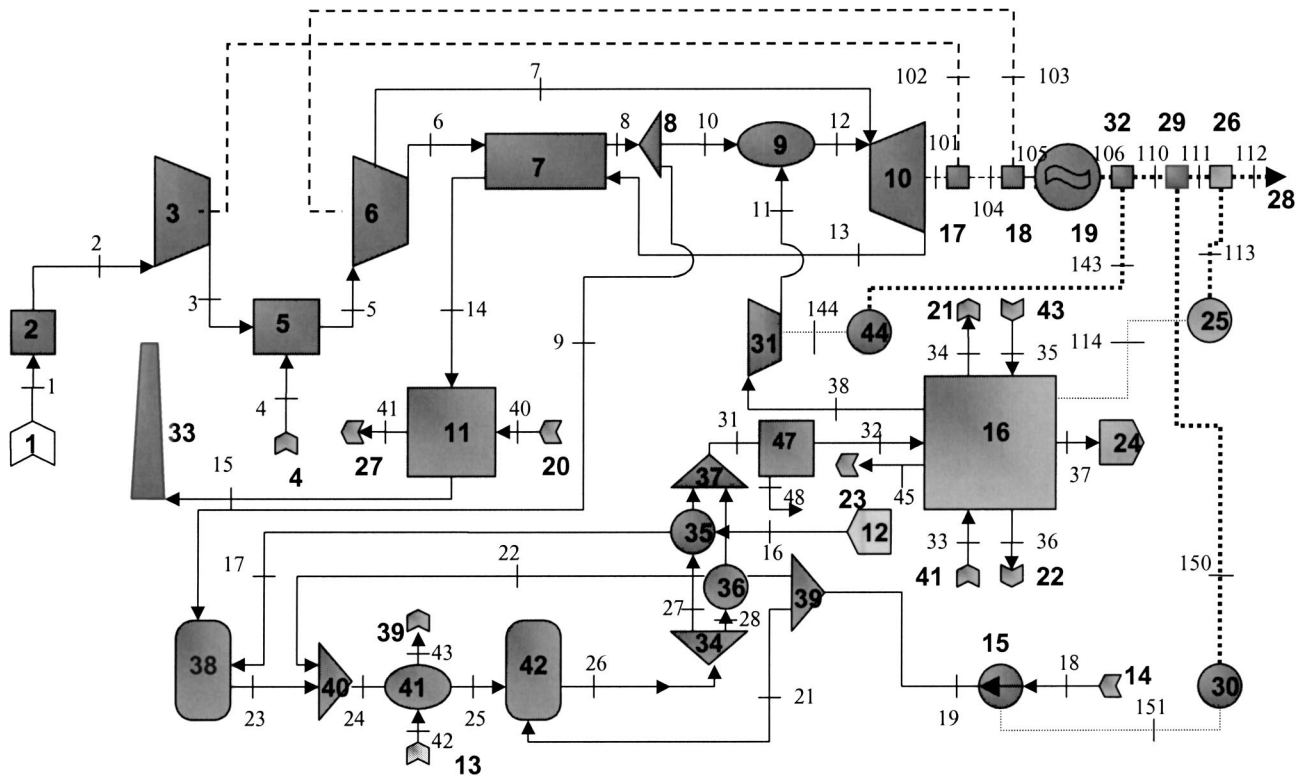


Fig. 6 Plant layout with T.E.M.P. code

The presence of traces of carbon monoxide in the fuel composition is responsible for the carbon dioxide specific emission of the plant which is lowered to 34.6 g/kWh.

Different Gas Turbine Plants

The present study focuses on three other gas turbine plants.

Case(2) The simple cycle Siemens heavy-duty V64.3a gas turbine has a net power output of 68 MW_e with an efficiency of 0.347. Inlet air mass flow is 191 kg/s, compression ratio is 16.1. Small plant layout differences have been adopted for the fuel decarbonization and CO₂ sequestration sections. The heat recovery system downstream from the gas turbine is meant to be a steam generator and no cooling is adopted before the water-gas shift reactor. In the present study 8.8% of the outlet compressor air flow is sent to the partial oxidation reactor: Outlet temperature is enough to vaporize the inlet water flow for the following water-gas shift reaction. A water flow is injected into the shift reactor in order to reduce the reaction temperature so that a 95.5% carbon monoxide conversion efficiency can be achieved. Methane inlet mass flow is 5.8% more than the simple gas turbine cycle for the same turbine inlet temperature. The reboiler requires a 49.5 MW duty at 196°C and works at 13 bar. The heat is recovered from the gas turbine exhaust gases in the heat recovery steam generator. The complete plant produces 70.1 MW_e, with a net efficiency of 0.321. Electric power is 2.1 MW_e more than the simple gas turbine cycle: This is due to the hydrogen combustion reaction (H₂ + O₂ ⇒ H₂O) whose product is steam only. This fact causes the

expanding fluid to have higher heat capacity, higher enthalpy and finally allows the expander to produce higher work. Plant carbon dioxide specific emission is 33.4 g/kWh (it was 573 g/kWh).

Case (3) The simple cycle General Electric aeroderivative LM-6000 gas turbine produces 43.7 MW_e with a 0.41 net efficiency. Inlet air mass flow is 127 kg/s, compression ratio is 29.6. In this case 9% of the outlet compressor air flow is sent to the decarbonization section. Methane inlet mass flow is 11.2% more than the simple gas turbine cycle; carbon monoxide conversion efficiency is 97.2%. As a consequence of a 25.4 bar operating pressure, the reboiler works at a high temperature, 225°C, and requires a 25.4 MW duty, which is completely recovered from the HRSG downstream from the gas turbine. The plant is capable of 44 MW_e net power output with a net efficiency of 0.356 and a carbon dioxide specific emission of 20.7 g/kWh (it was 479 g/kWh).

Case (4) The regenerated micro-gas turbine Turbec T-100 is capable of producing 100 kW_e with a net efficiency of 0.3. Inlet air mass flow, 0.78 kg/s, passes through the centrifugal compressor and is preheated in the regenerator by hot gases coming from the centrifugal expander. The compression ratio is 4.5, the turbine inlet temperature is 950°C as no blade cooling is adopted. As far as complete plant layout is concerned, an important change has been made: A compressor operating on the air flow fraction destined for the fuel decarbonization section has been inserted before the partial oxidation reactor. Such a device enables sequestration plant operating pressure to be chosen apart from the gas turbine compression ratio. The complete plant produces 98 kW_e with an overall efficiency of 0.22 and a carbon dioxide specific emission of 44.3 g/kWh (it was 640 g/kWh).

The installation of a fuel treatment-carbon dioxide absorption plant reduces whole plant efficiency for many reasons. First of all the reboiler at the bottom of the regeneration column needs to be fed at a high temperature (Fig. 5), and a plant with low compression ratio requires much more heat to be recovered from the sys-

Table 3 Molar composition (%) of the fuel entering the combustion chamber

| H ₂ | N ₂ | CO | CH ₄ | H ₂ O | CO ₂ |
|----------------|----------------|-----|-----------------|------------------|-----------------|
| 52.2 | 47 | 0.4 | 0.2 | 0.2 | 0 |

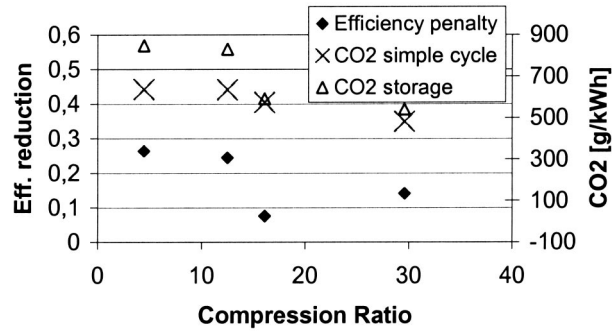


Fig. 7 Net efficiency reduction and CO₂ specific production versus pressure ratio

tem. That is the main reason why efficiencies of smaller gas turbines (Cases (1) and (4)) are more significantly reduced than larger ones. Turbine exhausts and heat recovery exchangers in the fuel treatment section do not provide enough heat to feed the chemical absorption section; so, an increase in the amount of fuel being introduced is needed, lowering the net system efficiency. Referring to the PGT-2, the necessary heat is recovered after the partial oxidation reactor, where part of the introduced fuel is burnt in order to raise outlet temperature. A different solution is adopted in the microturbine-based system, where regenerator size is reduced in order to recover more heat from the gas turbine exhausts; a larger methane flow is then converted in the fuel treatment section. A fired exhaust recovery system could be a third solution, [5].

Figure 7 shows the percentage reduction of efficiency compared to the simple cycle case for the considered plants together with carbon dioxide specific storage of the complete plant configuration and carbon dioxide specific emission of the simple cycle case.

Thermoeconomic Results

The installation of fuel decarbonisation and carbon dioxide sequestration systems is responsible for a considerable increase in plant complexity which affects overall efficiency, capital costs, and cost of energy (COE). The TEMP code is provided with “cost/costing equations,” [8], that evaluate single component capital costs on the basis of thermodynamic and physical parameters. In the framework of this work, the compressor, combustor, expander, and generator costing equations have been updated to obtain values conforming to current literature for the simple gas turbine cycle, [14]. New costing equations have been set up for partial oxidation and water-gas shift reactor modules and for the CO₂ separation section. As previously described, the latter capital cost is mainly affected by operating pressure, mass flow, column size, plate type, plate number, and plate spacing.

The thermoeconomic analysis was firstly carried out on the simple cycle: The results were verified with the data published in [14]. Then, such an analysis was extended to the complete plant, in order to estimate both capital cost and variable cost increases that lead to a significantly higher cost of electricity.

As far as investment cost is concerned, Fig. 8 shows, as an example, the percent capital cost allocation of the Siemens V64.3a simple cycle and complete plant configuration. The compressor is the most expensive component requiring about 35.5% of the total investment, followed by the expander (21%) and the generator (13%). The carbon dioxide absorption plant has almost the same influence on total costs as the heat recovery steam generator (HRSG) with 11%, while partial oxidation and water-gas shift reactors (REACT) make up less than 3%. The complete plant capital cost is estimated to be 39.5% higher than the simple cycle case.

Cost allocation for the other gas turbines examined is similar to the Siemens machine. However, the total capital investment in-

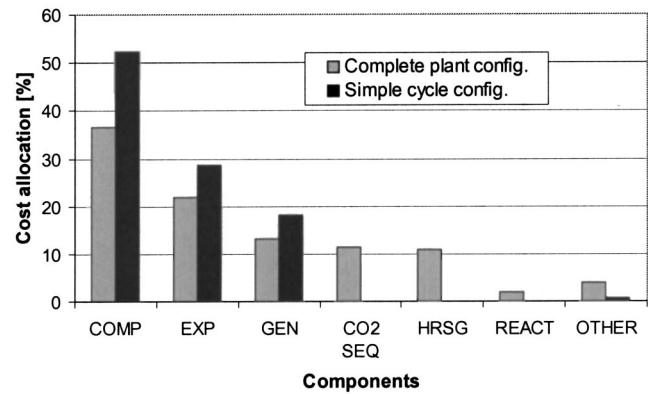


Fig. 8 Capital cost allocation for Siemens V64.3a

crease varies considerably: the Nuovo Pignone PGT-2 capital cost increase is the highest, about 60% more than the simple cycle, the Turbec T-100 one is about 49%, while the LM6000 one is the lowest, about 32%. Such an enhanced initial expenditure directly affects the cost of electricity, which is further penalized by the net efficiency decrease.

Figure 9 shows COE versus the overall efficiency for the simple cycle and complete plant configurations.

COE becomes considerably higher (and net efficiency considerably lower) when fuel decarbonization and CO₂ sequestration sections are included in the plant: compared to simple cycle cases, the COE increase goes from 47% for the Siemens V64.3a to 164% for the Turbec T100. Such a result clearly demonstrates that carbon dioxide sequestration becomes economically feasible and sustainable in a deregulated energy market only if a heavy carbon-tax (CT) is imposed on power plant carbon dioxide emissions. The break-even point between the imposition a carbon tax and the use of a sequestration plant has been evaluated for the gas turbines considered: Figure 10 shows the break-even (or economically equivalent) carbon tax versus net electrical efficiency. The resulting CT strongly depends on complete plant efficiency and size: The Siemens V64.3a shows the lowest equivalent carbon tax value with \$45 per ton of carbon dioxide emitted if in the simple cycle configuration; the LM6000 and PGT-2 require, respectively, \$63/tonCO₂ and \$90/tonCO₂ carbon taxes.

An alternative approach to deal with the problem of global warming is the carbon exergy tax (CET) proposed by the authors, [15–17]. Such a complex procedure, based on the internal thermoeconomic analysis of energy systems, allows a carbon tax to be evaluated for each power plant through properly pricing the internal irreversibilities of energy systems. The aim is to penalize the most inefficient cycles and to strongly push the energy market towards the most innovative and environmentally sustainable so-

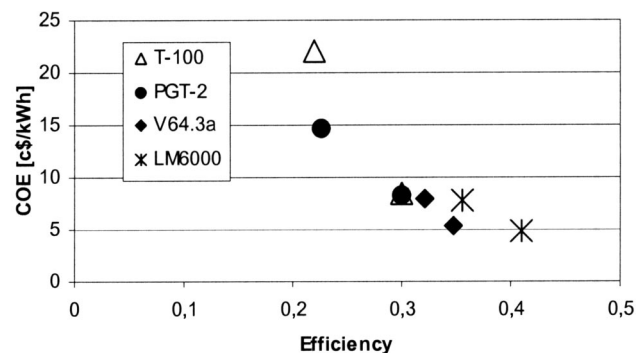


Fig. 9 Cost of electricity (8000 equivalent hours)

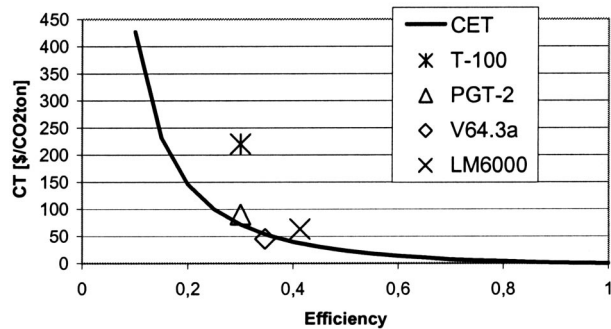


Fig. 10 CET curve and equivalent CT

lutions. In [16], a new simplified approach for plants only producing electrical power that well approximates the results of the complete CET procedure is shown to be possible, and it is called the generalized CET. The generalized CET curve for the considered gas turbine cycles is reported in Figure 10. Except for the T-100 microturbine, which is likely to be the less apt configuration for CO₂ sequestration because of its very small size, the resulting Carbon Tax is in surprisingly good agreement with the evaluated break-even CTs. This unexpected link demonstrates that the Generalized CET can be an effective tool in a deregulated energy market to encourage the spread of low-CO₂-emitting plants by making them competitive with conventional configurations.

Conclusions

The thermo-economic models of four differently sized gas turbine plants with fuel decarbonization and carbon dioxide sequestration have been successfully built and verified. The CO₂ separation section, based on the use of an aqueous solution of blended amines, has been investigated in depth and a preliminary design study has been carried out in order to evaluate its capital cost.

The results of the thermo-economic analysis show that the considerable total investment cost increase is accompanied by a significant net efficiency decrease, causing the COE to reach very high values. The break-even carbon tax that can make CO₂ sequestration economically feasible when applied to simple gas turbine cycles is shown to be in the range of \$45–90/tonCO₂ for conventional machines and very much higher for very small size gas turbines, which appear to be definitively excluded from CO₂ sequestration.

The generalized carbon exergy tax approach, proposed by the authors, seems to be an effective tool for encouraging the spread of low-CO₂-emitting plants by making them competitive with conventional configurations.

Acknowledgments

This work has been sponsored by MURST of Italy through a Cofin.99 grant.

The authors wish to thank D. Watson (Rolls-Royce) for his invaluable help in developing the CO₂ sequestration analysis.

References

- [1] Corti, A., Lombardi, L., and Manfreda, G., "Absorption of CO₂ With Amines in a Semiclosed GT Cycle: Plant Performance and Operating Costs," ASME Paper No. 98-GT-450.
- [2] Cau, G., and Cocco, D., 2000, "Performance Assessment of a Semi-Closed Chemically Recuperated Gas Turbine Systems," ASME Paper No. 2000-GT-161.
- [3] Lozza, G., and Chiesa, P., 2000, "Natural Gas Decarbonization to Reduce CO₂ Emission From Combined Cycles. Part A: Partial Oxidation," ASME Paper No. 2000-GT-163.
- [4] Jackson, A. J. B., Neto, A. C., Whellens, M. W., and Audus, H., 2001, "Gas Turbine Performance Using Carbon Dioxide as Working Fluid in Closed Cycle Operation," ASME Paper No. 2000-GT-153.
- [5] Bozzolo, M., and Brandani, M., 2001, "Study of Power Plants With CO₂ Sequestration Fed by Hydrogen From Fuel Decarbonization," Degree thesis, University of Genoa.
- [6] Squeri, S., and Schiappacasse, R., 1999, "CO₂ Capture and Sequestration Study," Degree thesis, University of Genoa.
- [7] Agazzani, A., and Massardo, A. F., 1997, "A Tool for Thermo-economic Analysis and Optimization of Gas, Steam, and Combined Plants," ASME J. Eng. Gas Turbines Power, **119**, pp. 885–892.
- [8] Massardo, A. F., and Scialò, M., 2000, "Thermo-economic Analysis of Gas Turbine Based Cycle," ASME J. Eng. Gas Turbines Power, **122**, pp. 664–671.
- [9] Simulation Sciences Inc., PRO/II 5.5 User's guide.
- [10] Bozza, F., Cameretti, M. C., and Tuccillo, R., 2001, "Una metodologia di analisi integrata di turbine a gas a bassa emissione di CO₂," X Convegno TESEC Sergio Stecco, Genova, pp. 441–456.
- [11] Alpino, A., and Oliva, M., 2000, "Modellizzazione di un ossidatore parziale ed integrazione con impianti di potenza tradizionali," Degree thesis, University of Genoa.
- [12] Perry, H., and Green, D., 1997, *Perry's Chemical Engineers' Handbook*, 7th ed., McGraw-Hill, New York.
- [13] Bosio, A., Bozzolo, M., Brandani, M., and Massardo, A. F., 2001, "Modellizzazione di un impianto a gas da 2.3 MW_e con emissioni nulle di biossido di carbonio," X Convegno TESEC Sergio Stecco, Genova, pp. 481–496.
- [14] *Gas Turbine World Handbook 2000–2001*, Pequot, CT.
- [15] Borchellini, R., Massardo, A. F., and Santarelli, M., 2000, "An Analytical Procedure for the Carbon Tax Evaluation," Energy Conversion and Management Journal, **41**, pp. 1509–1531.
- [16] Traverso, A., Santarelli, M., Massardo, A. F., and Cali, M., 2002, "A New Generalized Carbon Energy Tax for CO₂ Emission Internalisation: An Effective Rule to Control Global Warming," ASME Turbo Expo 2002, Amsterdam, submitted.
- [17] Traverso, A., 2000, "Thermo-economic Analysis of STIG, RWI and HAT Cycles With Carbon Dioxide (CO₂) Emissions Penalty," Degree thesis, University of Genoa.

Comparative Analysis of Off-Design Performance Characteristics of Single and Two-Shaft Industrial Gas Turbines

J. H. Kim

Senior Researcher,
Aeropropulsion Department,
Korea Aerospace Research Institute,
Daejeon 305-600, Korea

T. S. Kim

Assistant Professor,
Department of Mechanical Engineering,
Inha University,
Incheon 402-751, Korea

J. L. Sohn

BK 21 Assistant Professor

S. T. Ro

Professor,
Fellow ASME

School of Mechanical and Aerospace
Engineering,
Seoul National University,
Seoul 151-742, Korea

Off-design steady performance and operating characteristics of single and two shaft gas turbines for electric power generation have been investigated comparatively. A set of balance equations has been derived based on validated component models. A simultaneous calculation scheme has been employed, which is flexible to various engine configurations. Part-load performance analyses of two commercial gas turbines have been carried out to compare operating characteristics between single and two shaft engines. The predicted performance characteristics of both engines coincide soundly with the manufacturer's data and also correspond with the inherent characteristics of each configuration. The adoption of the variable inlet guide vane (VIGV) modulation has been addressed in order to examine the possibility of leveling up the heat recovery capacity by maintaining a high turbine exhaust temperature (TET) when those gas turbines are used for combined cycle plants. Maintaining TET at its design value as far as the VIGV modulation allows has been simulated and it has been determined that the TET control is possible at up to 40% and 50% load in the single and two shaft engine, respectively. Combined cycle performances have also been investigated for two engine configurations in different operating modes. While the VIGV modulation produces a favorable influence over the combined cycle performance of the single-shaft configuration, the two-shaft engine does not appear to be effectively improved by the VIGV modulation since the degradation of gas turbine performance counteracts the advantage of the higher performance of the bottoming (steam turbine) cycle. [DOI: 10.1115/1.1615252]

Introduction

Gas turbines for electric power generation usually operate at part-load conditions for a considerable amount of the time. Regardless of gas turbine configurations, performance generally degrades with a reduction in power. Accordingly, attention should be paid to the task of enhancing the part-load performance of the gas turbine itself and furthermore, the performance of applied systems such as the combined cycle and cogeneration power plants. Most gas turbines developed for electric power generation (heavy-duty) have a single-shaft configuration as shown in Fig. 1. The speed of the generator driven by the gas turbine should remain constant during the load variation. Therefore, the single shaft engine is advantageous in the event of the load being shed because the compressor acts as a very efficient brake. For this reason, regulation of output speed is easier to achieve than other configurations, [1]. Aeroderivative gas turbines have long been representatives of multishaft power generation engines. Recently, a couple of heavy-duty engines with the two-shaft configuration shown in Fig. 2 have also been introduced. Meanwhile, during the part-load operation of modern single shaft heavy-duty gas turbines, the airflow rate is actively controlled by modulating the setting angles of the variable inlet guide vane (VIGV) and the variable stator vanes (VSVs) in order to maintain the highest possible exhaust gas temperature (design temperature or higher). Thus, heat recovery capacity is greater compared with the maximum airflow control (fuel only control). Practical mass reduction limit is 10% to 30%

corresponding to 20% to 50% in load reduction, [2,3]. In multi-shaft engines, compressor shaft speed and thus airflow rate decrease as power reduces. Their part-load exhaust temperatures are higher than those of single shaft engines without VIGV control.

Out of these descriptions, a question arises as to which of the two alternatives (single and two-shaft engines) are preferred, considering the part-load performance of both the gas turbine and the heat recovery system. Another factor for consideration is how much the heat recovery performance would be affected when the VIGV modulation is employed in the two shaft engine. This study aims at answering these questions through a comparative off-design performance analysis at part-load conditions. A program has been developed to analyze the part-load performance of gas turbines. In particular, the compressor model adopts an improved stage-by-stage calculation enabling a practical estimation of VIGV and VSV control. The program has been validated by the accurate prediction on the part-load performance of actual single and two shaft engines. Subsequently, for single and two-shaft gas turbines with similar design parameters (pressure ratio, turbine inlet temperature, etc.) and performance (efficiency and power), analysis has been carried out to compare the part-load performance. The adoption of VIGV modulation has been investigated to examine the possibility of leveling up the heat recovery capacity when the gas turbines are used for combined cycle plants. Variation of performance parameters and the range of VIGV controlled operations has been analyzed in detail. Combined cycle performances have likewise been investigated for two engine configurations in different operating modes.

Off-Design Performance Analysis

The performance and operating characteristics of a gas turbine in off-design conditions depend on individual components such as

Contributed by the International Gas Turbine Institute (IGTI) of THE AMERICAN SOCIETY OF MECHANICAL ENGINEERS for publication in the ASME JOURNAL OF ENGINEERING FOR GAS TURBINES AND POWER. Paper presented at the International Gas Turbine and Aeroengine Congress and Exhibition, Amsterdam, The Netherlands, June 3–6, 2002; Paper No. 2002-GT-30132. Manuscript received by IGTI, December 2001, final revision, March 2002. Associate Editor: E. Benvenuti.

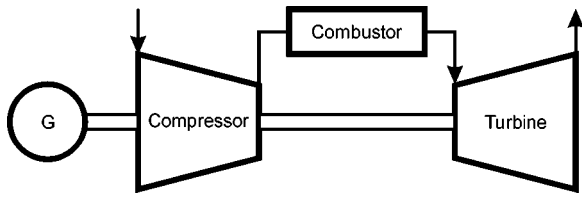


Fig. 1 The schematic diagram of a single-shaft gas turbine

the compressor and the turbine. When they are linked together in an engine, the potential operating range of these components becomes considerably reduced. It is, therefore, very important to accurately estimate the performance characteristics of each component when attempting to predict the overall performance of the gas turbine. The performance characteristics of each component can be obtained using its mathematical model or actual test data. Once the operating characteristics of each component has been specified, the performance and operating characteristics of the gas turbine during off-design conditions can be derived using thermofluid dynamic and mechanical matching.

In the present study, component models have been adopted from previous studies, [4,5]. Special efforts have been made to estimate characteristics of multistage axial flow compressors and turbines including the effect of intensive turbine blade cooling. Mass, momentum, and energy balances for each component (each stage in the cases of compressor and turbine in particular) have been considered for thermofluid dynamic matching. Work compatibility has also been taken into account in order to describe mechanical matching, for example, between compressor and gas generator turbine, or power turbine and load. These whole balances are consequently represented by a set of balance equations. The performance and operating characteristics of a gas turbine engine is then obtained by solving these equations simultaneously. This simultaneous calculation scheme is more flexible to various engine configurations than other previous iterative sequential schemes, [1,6], where the detailed calculation procedure must be modified as engine configurations change. In this study, without altering the calculation structure, a new component can be added without difficulty and the balance equations will correspond to the new components. This method can also be applied to a transient analysis by merely adding unsteady terms to the balance equations. In practice, the balance equations for off-design performance prediction in the present study are derived from the basic governing equations in the previous studies, [4,5], with unsteady terms neglected as follows:

$$\text{mass: } \dot{m}_{i+1} - \dot{m}_i = 0 \quad (1)$$

$$\text{momentum: } \dot{m}_{i+1}u_{i+1} - \dot{m}_i u_i + p_{i+1}A_{i+1} - p_i A_i - F = 0 \quad (2)$$

$$\text{energy: } \dot{m}_{i+1}H_{i+1} - \dot{m}_i H_i - \dot{Q} + \dot{W}_s = 0 \quad (3)$$

where

$$F = \dot{m}_{i+1}^* u_{i+1}^* - \dot{m}_i u_i + p_{i+1}^* A_{i+1} - p_i A_i \quad (4)$$

$$\dot{W}_s = \dot{m}_i (H_i - H_{i+1}^*) \quad (5)$$

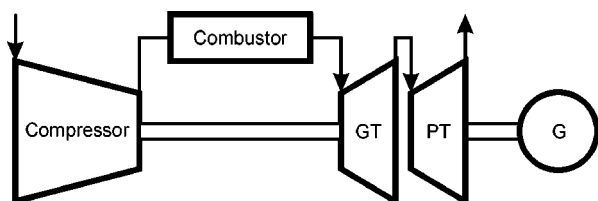


Fig. 2 The schematic diagram of a two-shaft gas turbine

These equations have been applied to each control volume corresponding to a component or a subcomponent (for example, a stage) with suitable F , \dot{Q} , and \dot{W}_s , which must be specified at every off-design condition. The force and shaft power in the balance equations have been determined by component characteristics, which can be derived from either characteristic maps or off-design models. In the above two equations, "*" represents the value evaluated from component characteristics at a given inlet condition.

Component Models

Compressor. Multistage axial flow compressors of modern heavy-duty gas turbines usually incorporate VIGV and VSVs for stable startup and enhancement of exhaust heat recovery at part-load in combined cycle plants. In addition, some portion of the compressed air is extracted from intermediate stages of the compressor for surge protection and turbine blade cooling. As such, the operating characteristics of modern compressors are too complicated to be handled by conventional methods, which generate a performance map first and then utilizes it in an engine simulation. An efficient method, proposed by the authors of this paper, [4,7], is used in the present analysis to calculate the performance of modern multistage axial flow compressors. The method requires stage performance maps but it differs from the conventional sequential stage-stacking method in that all interstage state variables are calculated simultaneously. Such a feature is very suitable for whole engine simulation, which is also based on simultaneous calculation. Generalized stage characteristics, [8], have been used, which are represented by relations among flow coefficient, pressure coefficient, temperature coefficient, and efficiency. At changed vane setting angles, stage characteristics are modified by adopting an analytical approach, [9]. The feasibility of the method can be found in previous papers, [4,7], where comparisons between predicted characteristics and field data for both fixed and variable geometry compressors have been presented.

Once the characteristics of the compressor have been specified, "*" values can be obtained at given inlet conditions. After that, the power required to drive the compressor can be determined by the following equation:

$$\dot{W}_c = \sum_i^{n_c} \dot{m}_i (H_i - H_{i+1}^*) \quad (6)$$

Turbines. Modern multistage axial flow turbines also have complicated operating characteristics mainly due to blade cooling. The bleed air from the compressor is entrained into the turbine blade rows for blade cooling and thus influences stage characteristics. Therefore, the effect of coolant flow must be considered in evaluating stage characteristics. For this reason, a row-by-row prediction method for the cooled turbine, [10], has been employed to obtain performance characteristics. An expansion pressure ratio has been obtained in off-design conditions by the following Stodola equation:

$$\frac{\dot{m}_{in} \sqrt{T_{T,in}}}{P_{in}} = K \sqrt{1 - \left(\frac{P_{out}}{P_{in}}\right)^2} \quad (7)$$

K has been deduced from design point values and kept constant at off-design conditions. Total pressure loss due to the blade cooling has been evaluated by using the model proposed by Kim et al. [11]. The amount of the coolant flow entrained to the turbine blade rows at off-design conditions has been determined using the following equation:

$$\dot{m}_c = K_c p_c \sqrt{\frac{2(1 - p_T/p_c)}{RT_c}} \quad (8)$$

The coolant flow is driven by static pressure differences between points where the coolant is extracted and injected. K_c is also obtained from design conditions and p_T is static pressure at

row inlet and exit for nozzle and rotor, respectively. As in the compressor model, the turbine power can be obtained by an equation similar to Eq. (6).

Combustor and Guide Ducts. Total pressure losses in the combustor, inlet and exhaust ducts in off-design conditions have been corrected using the following equation [1]:

$$\frac{(\Delta P/P)_{in}}{(\Delta P/P)_{in,d}} = \frac{(\dot{m}\sqrt{T/P})_{in}^2 R}{(\dot{m}\sqrt{T/P})_{in,d}^2 R_d} \quad (9)$$

The addition of thermal energy caused by combustion can be treated as heat transfer to the combustor and introduced in the energy balance equation of the combustor using the following form:

$$\dot{Q} = \eta_{comb} \dot{m}_f (LHV + \Delta H_{T_0 - T_f}) \quad (10)$$

The subscript 0 indicates a reference point where the low heating value (LHV) is defined. η_{comb} designates combustion efficiency. Changes in gas composition and thermodynamic properties subsequent to combustion have also been taken into account.

Work Compatibility. Since steady-state off-design conditions are being dealt with in this study, the net power produced by the engine should be equal to the power or load required at any speed. Otherwise, the engine will not be in equilibrium and will either accelerate or decelerate depending on whether there is a surplus or deficiency of power. In the case of a single-shaft gas turbine, a turbine drives both the compressor and the output load (electric generator) at a constant speed. The following equation therefore represents the work compatibility:

$$\dot{W}_T - \dot{W}_C - \dot{W}_L = 0 \quad (\text{at a constant speed}). \quad (11)$$

In the two-shaft configuration, the gas generator turbine drives the compressor and the power turbine drives the output load. Unlike the single-shaft engine, the gas generator shaft is not linked to the load; hence its speed is reduced as power diminishes. For a given power or gas generator speed, the power turbine speed may vary over a wide range, depending on the load characteristics (mechanical drive, for example). In the present study, however, the power turbine speed has been fixed at the rated speed because it must drive an electric generator. Two equations for work compatibility are required in the case of two shaft engine and are presented as follows:

$$\dot{W}_C - \dot{W}_{GT} = 0 \quad (\text{at variable speeds}) \quad (12)$$

$$\dot{W}_{PT} - \dot{W}_L = 0 \quad (\text{at a constant speed}). \quad (13)$$

Numerical Treatment

As mentioned in the previous section, the balance equations and component characteristics in each component comprise a set of algebraic equations. With a given fuel flow rate and VIGV angle, performance characteristics such as net power and TET can be obtained by solving this equation set. Static pressure, temperature, and axial velocity at each station (control surface) are state variables to be solved. Therefore, there are $3(n+1)$ variables for n control volumes and three of them are given as known values, which are the inlet total temperature, pressure, and exhaust static pressure of the engine. Consequently, the remaining $3n$ variables can be obtained as solutions of the equation set since there are $3n$ equations (mass, momentum and energy balance equations for n control volumes). The speed of the shaft linked to the load that should be kept constant in electric power generation is a known variable both in a single and two shaft engine at steady-state part-load conditions. Hence, work compatibility Eqs. (11) and (13) are not those to be solved but are rather to be used as criteria for determining the fuel flow rate and VIGV angle corresponding to the required power (\dot{W}_L) and TET. In the case of the two shaft engine, however, the work compatibility equation for the gas gen-

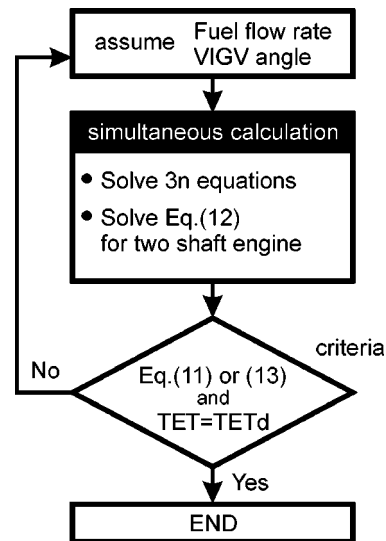


Fig. 3 Calculation procedure for off-design performance analysis at part-load conditions

erator represented by Eq. (12) should be included in the simultaneous calculation in order to solve the gas generator speed. With the purpose of solving these state variables including the gas generator speed, the multivariable Newton-Raphson method has been employed.

In actual situations, the net power and TET of an engine are controlled by modulating fuel flow rate and VIGV angle. Numerical simulation is carried out in the same manner, that is, the fuel flow rate and VIGV angle are modulated numerically so as to obtain the required power (\dot{W}_L) and TET as shown in Fig. 3. As mentioned in the previous section, balance equations corresponding to new components are simply added to the “simultaneous calculation” module shown in Fig. 3 when a new engine configuration is simulated.

Results and Discussion

Gas Turbines. The performance and operating characteristics of both a single and a two-shaft version of *Titan*TM 130 (Solar Turbines Inc.) at steady-state part-load conditions have been investigated in the present study. Because they incorporate almost the same components (except for turbines) and have the same power capacity level, an investigation of off-design performance of the two engines might indicate inherent differences between the two configurations and could present reasonable comparative results. The design point performance parameters and specifications of both engines are shown in Table 1, which have mostly been provided from technical brochures, [12,13], and supplemented with reference to Rocha and Etheridge [14], Rocha and Kurz [15], and Farmer [16].

As seen in the component models, the majority of off-design characteristics have been evaluated by corrections based on design point performances. Therefore, also required are detailed design point performances and specifications such as stage efficiencies, stage pressure ratios, and the amount of bleed air, etc., which are hardly obtainable in most commercial engines. Accordingly, the design point analysis has been carried out based on the previous work, [17], so as to obtain such performance data. The predicted compressor and turbine stage efficiencies were 88%, 87%, and 88% and 89% for the single and two-shaft engines, respectively. As far as the total amount of coolant flow is concerned, it was estimated at 16.5% and 15.7% of the inlet airflow rate for the single and two-shaft engines, respectively. These predicted data

Table 1 Design point performance parameters and specifications of Titan™ 130 engines

| Gas Turbine Configuration | Single Shaft | Two Shaft |
|---------------------------|--------------|------------|
| Electrical power, MW | 13.5(13.5) | 14.5(14.5) |
| Cycle efficiency, % | 33.3(34.2) | 35.7(36.1) |
| Compressor† | 14 stages | 14 stages |
| Speed, rpm | 11,220 | 11,220 |
| Inlet airflow rate, kg/s | 48 | 47.7 |
| Pressure ratio | 17 | 16.4 |
| Gas Generator Turbine | 3 stages | 2 stages |
| Firing temperature, °C | 1,149 | 1,149 |
| Exit temperature, °C | 489(501) | |
| Power Turbine | | 2 stages |
| Speed (rated), rpm | | 7,970 |
| Exit temperature, °C | | 492(497) |

†The compressor incorporates one VIGV and five VSVs. The values inside the parentheses are results of simulation.

are thought to be reasonable compared with typical values of modern engines. The simulated outputs are also shown in Table 1, and are very similar to the actual data.

To show the validity of the off-design analysis program, a comparison between field data and simulation results for a single-shaft gas turbine, [4], is exemplified in Fig. 4. Simulated results coincide in accordance with manufacturer's data. TET has been kept constant for considerable power range through VIGV modulation. Maximum airflow reduction is 30%, which corresponds to a 50% power reduction. This has been realized by the modulation of four VSVs in addition to VIGV. The related VIGV and VSV modulation has been adopted for the simulation of the present gas turbines equipped with five VSVs as well as VIGV. Adopted from the example calculation is the criterion regarding the limitation of the airflow reduction during VIGV modulation, which will be explained further on.

At part-load conditions, the performance and operating characteristics of the two engines were initially investigated without the incorporation of VIGV modulation. Figure 5 displays operating lines, known as "equilibrium running lines," over the part-load on the compressor characteristic map. The compressor characteristic map (constant speed lines in particular) is produced by an independent compressor map generation routine that adopts the same models as this work, [7]. While the single-shaft engine operates at a constant speed, the gas generator speed of the two shaft engine varies up to about 70% of the rated speed at no load, which results in a drastic reduction in inlet airflow rate. Upon reference to performance charts of the typical two shaft engine used in Walsh and Fletcher [6], about 75% of the rated speed at no load is observed. This coincides soundly with the results of this study.

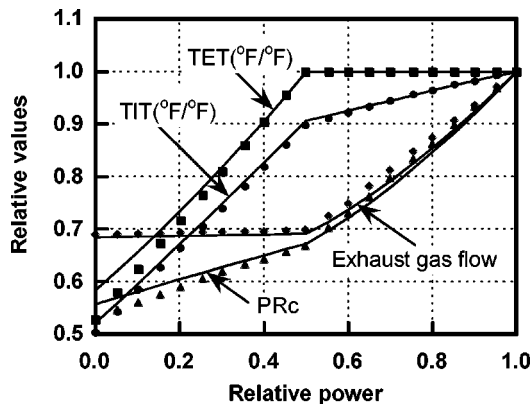


Fig. 4 Predicted part-load characteristics compared with engine data of Siemens V64.3 (lines: prediction, marks: data from [3])

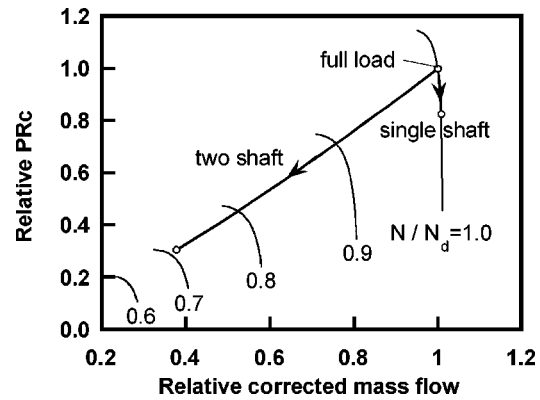


Fig. 5 Equilibrium running lines of the Titan™ 130 single and two-shaft gas turbines

Variations in parameters of the single and two shaft engine are shown in Fig. 6 and Fig. 7, respectively, compared with the data provided by Solar Turbine Inc, [12,13]. The overall operating characteristics predicted in this study are in good agreement with the corresponding data from the manufacturer and these results further confirm the validity of the component models. Clear distinction between single and two shaft engines is the inlet airflow rates at identical load capacities, as shown in Fig. 5, Fig. 6, and Fig. 7. Compared with the single-shaft engine, the two-shaft engine requires greater specific power (power per unit airflow rate)

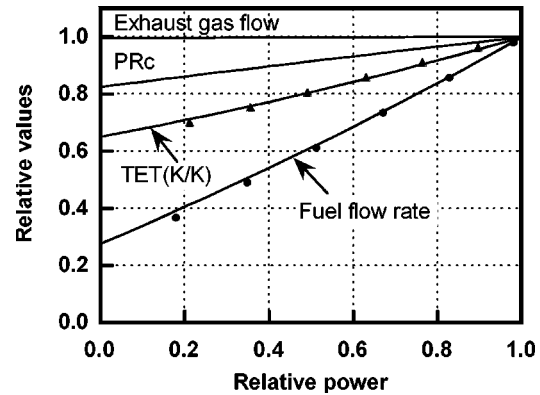


Fig. 6 Predicted part-load characteristics compared with engine data of the single-shaft version of Titan™ 130 (lines: prediction, marks: data from [12])

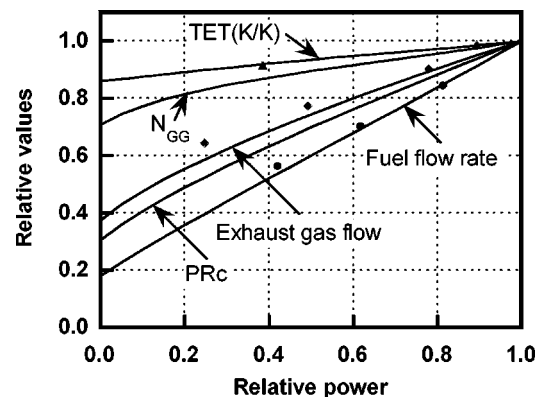


Fig. 7 Predicted part-load characteristics compared with engine data of the two shaft version of Titan™ 130 (lines: prediction, marks: data from [13])

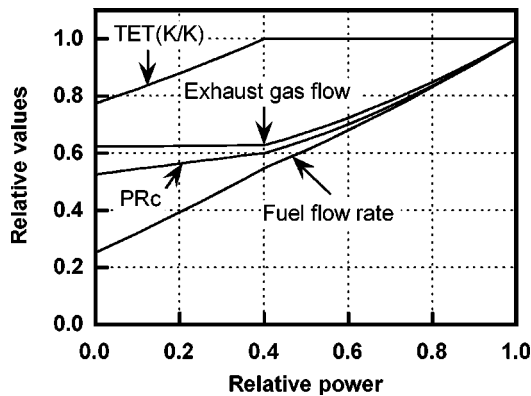


Fig. 8 Predicted part-load characteristics of the single shaft version of *Titan*[™] 130 with VIGV modulation

in order to produce equivalent power due to the larger reduction in the inlet airflow rate. Accordingly, the two-shaft engine operates at higher temperatures (TRIT, TET) over the part-load conditions so as to acquire greater specific powers, as shown in Fig. 7.

At present, it does not seem that the VIGV and five VSVs are actively modulated during load changes except for the surge margin control purpose taking place during startup and shutdown, [14]. In this study, however, their active modulation to control TET has been examined with the intention of enhancing the heat recovery capacity. It is assumed that the design point VIGV and VSV angles are 15° and that they are connected by a common link device driven by an actuator, [7]. The criterion for maximum possible airflow reduction by VIGV closing has been deduced from the results of the previous study, [4], where the part-load operating characteristics of Siemens V64.3 and GE 7F were evaluated. According to the result analysis, it has been found that the first stage has the largest normalized flow coefficient at maximum VIGV closing and that its value is within 1.25–1.3, corresponding to a nearly zero pressure rise in the generalized curve by Muir et al. [8]. This can be an appropriate criterion for determining the load up to which the VIGV closing can be continued.

The performance and operating characteristics of the two engines with VIGV modulation are investigated and results are shown in Fig. 8 and Fig. 9. In the case of the single-shaft engine, it is predicted that the inlet air-flow rate can be reduced up to about 60% of the design point value and TET can remain constant up to 40% load reduction. This TET control range is even greater than that of the Siemens V64.3 shown in Fig. 4 because the present engine adopts a greater number of VSVs. An enhancement of heat recovery, therefore, can be expected by the adoption of the VIGV and VSVs in a single-shaft engine. The two-shaft engine

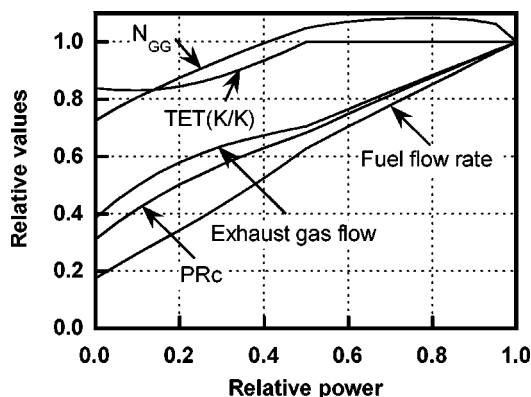


Fig. 9 Predicted part-load characteristics of the two shaft version of *Titan*[™] 130 with VIGV modulation

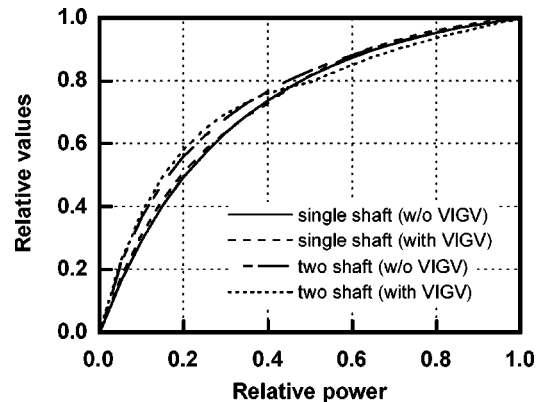


Fig. 10 Thermal efficiencies of the *Titan*[™] 130 single and two shaft gas turbines in different operating modes

can operate at the design point TET up to 50% load by the VIGV modulation. However, a great difference in mass flow rate and pressure ratio cannot be found compared with the two shaft engine without VIGV modulation. From these results, it can be found that the VIGV modulation in two shaft engines does not change the equilibrium working line shown in Fig. 5. However, the closing of VIGV changes operating characteristics of the compressor themselves such that constant speed lines as shown in Fig. 5, shift to lower mass flow rate regions. For a given mass flow rate and pressure ratio, therefore, the gas generator operates at an increased speed as shown in Fig. 9. Thermal efficiencies of the single and two-shaft engines in two different operating modes are shown in Fig. 10. Without VIGV modulation, the efficiency of the two shaft engine is higher than that of the single-shaft engine. Compressor efficiency varies a great deal due to the change in VIGV and VSV angles and may affect the engine efficiency. VIGV modulation reduces compressor efficiency as shown in Fig. 11. In particular, the degradation in engine efficiency during VIGV modulation for the two shaft case may be explained by a drastic decrease in compressor efficiency. Once the VIGV is fully closed, compressor efficiency improves as power decreases further, which results in engine efficiency comparable to or rather higher than the case without VIGV modulation.

Combined Cycle Consideration. In this section, the performance characteristics of combined cycles adopting the single and two-shaft gas turbines have been analyzed. Special attention has been given to the effect of VIGV modulation. A single pressure bottoming system (heat recovery steam generator and steam turbine) has been analyzed with an off-design calculation routine. A detailed analysis method can be found in Ref. [18]. The design

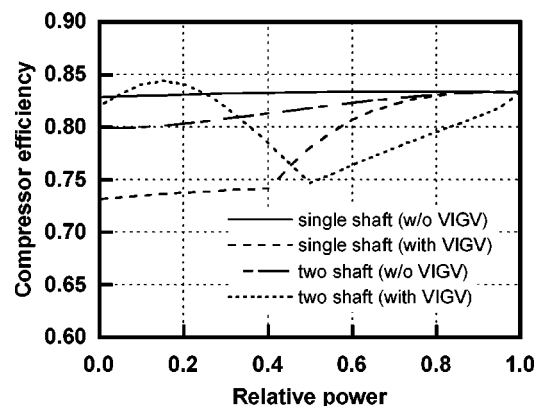


Fig. 11 Compressor efficiencies of the *Titan*[™] 130 single and two shaft gas turbines in different operating modes

Table 2 Design point performance parameters of the combined cycle

| Gas Turbine Configuration | Single Shaft | Two Shaft |
|------------------------------|--------------|-----------|
| Steam pressure, kPa | 3000 | 3000 |
| Condensing pressure, kPa | 4.2 | 4.2 |
| Steam turbine power, MW | 6.17 | 6.00 |
| Combined cycle power, MW | 19.72 | 20.50 |
| Combined cycle efficiency, % | 49.8 | 51.1 |

calculation is performed for given gas turbine exhaust data (TET and mass flow) with both the specified heat transfer information on the heat recovery sections and the steam turbine efficiency. The main features of the off-design calculation include sliding pressure operation, heat transfer data correction, and constant turbine swallowing capacity. Major design parameters are summarized in Table 2. Figure 12 shows the variation of steam turbine power with gas turbine power and Fig. 13 depicts the variation of combined cycle efficiency. Without VIGV modulation for both single and two-shaft engines, the two-shaft case exhibits higher heat recovery capacity and results in far better combined cycle efficiency, which is due to the much-increased TET. It is noticeable that the VIGV modulation for the single-shaft gas turbine brings about a very large increase in steam turbine power and thus achieves a considerable improvement in combined cycle efficiency, which also comes from the increased TET. This is the reason why VIGV modulation has been adopted in modern single-shaft gas turbine power plants.

It should also be noted that the VIGV modulated single-shaft engine results in even higher combined cycle efficiency than the

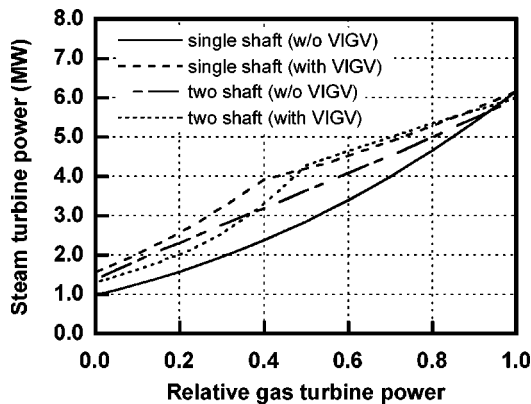


Fig. 12 Variations in steam turbine power with gas turbine power in different operating modes

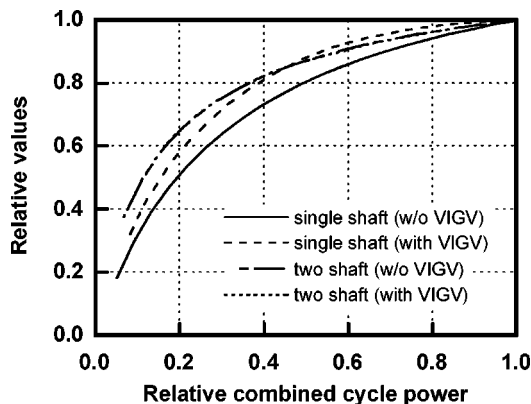


Fig. 13 Variations in combined cycle efficiency with combined cycle power in different operating modes

simple (without VIGV modulation) two shaft engine in the higher power range (over 50%). In the lower power range, the two shaft engine is superior to the VIGV modulated single shaft engine, which is mainly due to the higher gas turbine performance as indicated in Fig. 10. In the two shaft engine, VIGV modulation results in higher steam turbine power for a given gas turbine as in the single shaft case. However, the relatively lower gas turbine efficiency (see Fig. 10) counteracts the bottoming cycle advantage. Hence, the overall combined cycle efficiency is not effectively influenced by the VIGV modulation as shown in Fig. 13 where both efficiencies fall on the same line. As explained previously, the lower gas turbine efficiency is mainly due to the decreased compressor efficiency. Therefore, if the compressor performance were prevented from degrading, improved combined cycle efficiency could be achieved.

Conclusion

Part-load behavior of two gas turbines of single and two-shaft configurations with similar design parameters (pressure ratio, turbine inlet temperature, etc.) and performance (efficiency and power) has been comparatively investigated. A practical estimation of VIGV and VSV control is possible due to a novel compressor model adopting an improved stage-by-stage calculation. For the simple mode, efficiency of the two-shaft engine is higher than that of the single-shaft engine, especially in the lower power region. In the VIGV modulated single shaft case, the maximum airflow reduction is estimated to be as much as 40%, corresponding to a 60% reduction in power. In the two shaft engine, the VIGV modulation reduces the thermal efficiency in the higher power range due to a considerable reduction in the compressor efficiency. In the combined cycle application, the VIGV modulation increases the combined cycle efficiency considerably in the case of the single shaft engine. The VIGV modulated single-shaft engine exhibits even higher efficiency than the simple two shaft engine in the higher power range but shows lower efficiency in the lower power range. The combined cycle efficiency of the two-shaft engine does not appear to be effectively improved by the VIGV modulation since the degradation of gas turbine performance counteracts the advantage of higher bottoming system performance.

Acknowledgment

This work was supported by the Brain Korea 21 project.

Nomenclature

- A = area
- F = force
- H = total enthalpy
- \dot{m} = mass flow rate
- N = rotational speed
- n = number of stages or control volumes
- P = total pressure
- p = static pressure
- PR = total to total pressure ratio
- \dot{Q} = heat transfer rate
- R = gas constant
- T = total temperature
- TIT = turbine inlet temperature
- TRIT = turbine rotor inlet temperature (firing temperature)
- u = axial velocity
- VIGV = variable inlet guide vane
- VSV = variable stator vane
- \dot{W} = power

Subscripts

- C = compressor
- c = coolant
- d = design point

f = fuel
 GG = gas generator shaft
 GT = gas generator turbine
 i = control volume index
 in = inlet
 L = load
 out = outlet
 PT = power turbine
 s = shaft
 T = turbine

References

- [1] Cohen, H., Rogers, G. F. C., and Saravanamuttoo, H. I. H., 1996, *Gas Turbine Theory*, 4th Ed., Longman Group Limited, London.
- [2] Rowen, W. I., and Van Housen, R. L., 1983, "Gas Turbine Airflow Control for Optimum Heat Recovery," *ASME J. Eng. Power*, **105**, pp. 72–79.
- [3] Jansen, M., Schulenberg, T., and Waldinger, D., 1992, "Shop Test Result of the V64.3 Gas Turbine," *ASME J. Eng. Gas Turbines Power*, **114**, pp. 676–681.
- [4] Kim, J. H., Song, T. W., Kim, T. S., and Ro, S. T., 2001, "Model Development and Simulation of Transient Behavior of Heavy Duty Gas Turbines," *ASME J. Eng. Gas Turbines Power*, **123**, pp. 589–594.
- [5] Kim, J. H., Song, T. W., Kim, T. S., and Ro, S. T., 2002, "Dynamic Simulation of Full Start-up Procedure of Heavy Duty Gas Turbines," *ASME J. Eng. Gas Turbines Power*, **124**, pp. 510–516.
- [6] Walsh, P. P., and Fletcher, P., 1998, *Gas Turbine Performance*, 1st Ed., Blackwell Science Ltd., London.
- [7] Song, T. W., Kim, T. S., Kim, J. H., and Ro, S. T., 2001, "Performance Prediction of Axial Flow Compressors Using Stage Characteristics and Simultaneous Calculation of Interstage Parameters," *Proc. Inst. Mech. Eng., Part A, J. Power Energy*, **215**, pp. 89–98.
- [8] Muir, D. E., Saravanamuttoo, H. I. H., and Marshall, D. J., 1989, "Health Monitoring of Variable Geometry Gas Turbines for the Canadian Navy," *ASME J. Eng. Gas Turbines Power*, **111**, pp. 244–250.
- [9] Klapproth, J. F., 1958, "Effects of Stage Characteristics and Matching on Axial-Flow-Compressor Performance," *Trans. ASME*, **80**, pp. 1290–1291.
- [10] Kim, T. S., and Ro, S. T., 1997, "The Effect of Gas Turbine Coolant Modulation on the Part Load Performance of Combined Cycle Plants—Part 1: Gas Turbines," *Proc. Inst. Mech. Eng., Part A, J. Power Energy*, **211**, pp. 443–451.
- [11] Kim, J. H., Kim, T. S., Lee, J. S., and Ro, S. T., 1996, "Performance Analysis of a Turbine Stage Having Cooled Nozzle Blades With Trailing Edge Ejection," *ASME Paper 96-TA-12*.
- [12] Solar Turbines Inc., 1999, TITAN 130-Gas Turbine Generator Set, technical brochure, www.solarturbines.com.
- [13] Solar Turbines Inc., 1999, TITAN 130-Gas Turbine Mechanical-Drive Package, technical brochure, www.solarturbines.com.
- [14] Rocha, G., and Etheridge, C. J., 1998, "Evolution of The Solar Turbines TITAN 130 Industrial Gas Turbine," *ASME Paper 98-GT-590*.
- [15] Rocha, G., and Kurz, R., 2001, "Field and Application Experience of the TITAN 130 Industrial Gas Turbine," *ASME Paper 2001-GT-0224*.
- [16] Farmer, R., 2001, *Gas Turbine World 2000–2001 Handbook*, Pequot Publishing Inc., CT.
- [17] Kim, T. S., and Ro, S. T., 1995, "Comparative Evaluation of the Effect of Turbine Configuration on the Performance of Heavy-Duty Gas Turbines," *ASME Paper 95-GT-334*.
- [18] Kim, T. S., and Ro, S. T., 1997, "The Effect of Gas Turbine Coolant Modulation on the Part Load Performance of Combined Cycle Plants—Part 2: Combined Cycle Plant," *Proc. Inst. Mech. Eng., Part A, J. Power Energy*, **211**, pp. 453–459.

Steady and Dynamic Performance and Emissions of a Variable Geometry Combustor in a Gas Turbine Engine

Y. G. Li

R. L. Hales

School of Engineering,
Cranfield University,
Bedford MK43 0AL, England

One of the remedies to reduce the major emissions production of nitric oxide (NO_x), carbon monoxide (CO), and unburned hydrocarbon (UHC) from conventional gas turbine engine combustors at both high and low operating conditions without losing performance and stability is to use variable geometry combustors. This type of combustor configuration provides the possibility of dynamically controlling the airflow distribution of the combustor based on its operating conditions and therefore controlling the combustion in certain lean burn conditions. Two control schemes are described and analyzed in this paper: Both are based on airflow control with variable geometry, the second including fuel staging. A model two-spool turbofan engine is chosen in this study to test the effectiveness of the variable geometry combustor and control schemes. The steady and dynamic performance of the turbofan engine is simulated and analyzed using an engine transient performance analysis code implemented with the variable geometry combustor. Empirical correlations for NO_x , CO, and UHC are used for the estimation of emissions. Some conclusions are obtained from this study: (1) with variable geometry combustors significant reduction of NO_x emissions at high operating conditions and CO and UHC at low operating condition is possible; (2) combustion efficiency and stability can be improved at low operating conditions, which is symbolized by the higher flame temperature in the variable geometry combustor; (3) the introduced correlation between nondimensional fuel flow rate and air flow ratio to the primary zone is effective and simple in the control of flame temperature; (4) circumferential fuel staging can reduce the range of air splitter movement in most of the operating conditions from idle to maximum power and have the great potential to reduce the inlet distortion to the combustor and improve the combustion efficiency; and (5) during transient processes, the maximum moving rate of the hydraulic driven system may delay the air splitter movement but this effect on engine combustor performance is not significant. [DOI: 10.1115/1.1615253]

Introduction

In recent years, more attention to aircraft emissions has been paid with the emergence of environmental concerns of a global nature, such as climate change and depletion of the ozone layer. Different combustion technologies have been developed in order to reduce gas turbine emissions. These can be classified into the following combustor concepts, following the review by Wulff and Hourmouziadis [1]: variable geometry combustors, staged combustors, lean premixed combustors, rich-burn, quick-quench, lean-burn (RQL) combustors, and catalytic combustors.

The variable geometry concept provides the flexibility to control the airflow distribution inside a combustor and therefore has the very attractive ability to reduce the emissions on both high and low operating conditions without losing combustor performance. It also has great potential to improve combustion efficiency at low power operating conditions, Schultz [2], and facilitate engine re-light at altitude, Schultz [3]. At the same time it certainly introduces more complicated mechanical and control issues. Typical low emissions variable geometry combustor configurations are those proposed by Schultz [2,3], Gupta et al. [4], Fletcher [5], Saintsbury and Sampath [6], Fletcher and Adkins [7], Hayashi et al. [8], and Li et al. [9].

Contributed by the International Gas Turbine Institute (IGTI) of THE AMERICAN SOCIETY OF MECHANICAL ENGINEERS for publication in the ASME JOURNAL OF ENGINEERING FOR GAS TURBINES AND POWER. Paper presented at the International Gas Turbine and Aeroengine Congress and Exhibition, Amsterdam, The Netherlands, June 3–6, 2002; Paper No. 2002-GT-30135. Manuscript received by IGTI, December 2001, final revision, March 2002. Associate Editor: E. Benvenuti.

Gas turbines, especially aero gas turbines, work in a wide range of environmental and operational conditions and their combustors experience dramatic variation of inlet pressure, temperature, air flow rate and fuel flow rate. The control of the variable geometry and therefore the air flow distribution in all working conditions is one of the effective methods to keep the combustors working stably, reliably, efficiently and with low emissions.

The objective of this paper is to assess the effectiveness on the control of emissions production in gas turbine combustors with two variable geometry combustor control schemes. The analysis is based on a typical two-spool large turbofan engine by using an in-house gas turbine analysis computer code, MacCallum [10], implemented with a variable geometry combustor model and empirical emissions models (Lefebvre [11] and Reeves and Lefebvre [12]). The dynamic combustor performance and emissions characteristics in engine environment with different control schemes are analyzed and compared.

Emissions Simulation

There are three basic types of methods of predicting gas turbine combustion emissions: empirical correlations such as that of Lefebvre [11] based on combustor emissions measurement, analytical methods using a stirred reactor assumption and simplified chemical reactions, and the computational combustion dynamics (CCD). CCD is able to provide a detailed description of the flow field and emissions production mechanism but is numerically too expensive for performance analysis. The analytical methods have more universal suitability but are more complicated than the empirical

models. In order to get fast emissions prediction within the engine performance calculation environment with acceptable accuracy, Lefebvre's NO_x and CO empirical correlation, [11], and Reeves and Lefebvre's UHC empirical model, [12], are used in this study. These empirical correlations were developed based on large number of emissions measurements of gas turbine combustors and reflect the influence of basic combustor fluid dynamic parameters. It is assumed that the exhaust concentrations of NO_x and CO are proportional to the product of the mean residence time in the combustion zone, the chemical reaction rates and mixing rates. UHC is normally associated with poor atomization, inadequate burning rates, chilling effects of film-cooling air, or any combination of these. Therefore, the parameters that determine the production of NO_x, CO, and UHC are the combustor inlet pressure, temperature, mass flow rate, flame temperature, and combustor geometry. The empirical correlations of emissions used in this study are as follows:

$$(\text{NO}_x) = \frac{9 \times 10^{-8} P_2^{1.25} V_c \exp(0.01 T_{st})}{\dot{m}_A T_f} \text{ (g/kg} \cdot \text{fuel)} \quad (1)$$

$$(\text{CO}) = \frac{86 \dot{m}_A T_f \exp(-0.00345 T_f)}{(V_c - V_{ev}) \left(\frac{\Delta P}{P_2}\right)^{0.5} P_2^{1.5}} \text{ (g/kg} \cdot \text{fuel)} \quad (2)$$

$$(\text{UHC}) = \frac{11764 \dot{m}_A T_f \exp(-0.00345 T_f)}{(V_c - V_{ev}) \left(\frac{\Delta P}{P_2}\right) P_2^{2.5}} \text{ (g/kg} \cdot \text{fuel)} \quad (3)$$

The NO_x model suggests that in the combustion of a heterogeneous fuel-air mixture it is the stoichiometric flame temperature T_{st} that determines the formation of NO_x. However, for lean burn combustors where the maximum attainable temperature is the adiabatic flame temperature T_f , the equation may still be used provided that T_f is substituted for T_{st} . The flame temperature of the combustor primary zone is estimated with the formula of Gülder [13], where combustor inlet pressure, temperature, mass flow rate, air flow ratio to the primary zone, and fuel flow rate are required.

Model Engine and its Performance Calculation

A representative civil aero turbofan engine is chosen for the analysis and has the following basic performance parameters:

| | |
|----------------------------|------------|
| Total mass flow rate: | 191.5 kg/s |
| Total pressure ratio: | 16.7 |
| Bypass ratio: | 3.03 |
| Turbine entry temperature: | 1300 K |

In the combustor, the proportion of air flow to the primary combustion zone is 0.34 for the conventional configuration, which is typical for conventional gas turbine combustors.

The calculation of combustor performance is based on enthalpy balance so whatever is the air flow ratio to the primary combustion zone the total fluid dynamic performance of the combustor is almost the same if small changes in pressure loss and combustion efficiency are ignored. The performance analysis of a variable geometry combustor is carried out by replacing the combustor of the engine with the variable geometry combustor. The engine is supposed to run in the same operating conditions and therefore the combustor works in the same engine environment.

Emissions Control Strategy

The emissions characteristics are shown in Fig. 1, where the emissions indices are plotted against equivalence ratio in the combustor primary zone. Equivalence ratio close to the stoichiometric condition enhances thermal NO_x production, while lean and rich equivalence ratios enhance CO and UHC production. There are two narrow low-emissions windows, one in lean burn and the other in rich burn, where all the emissions are at a relatively low

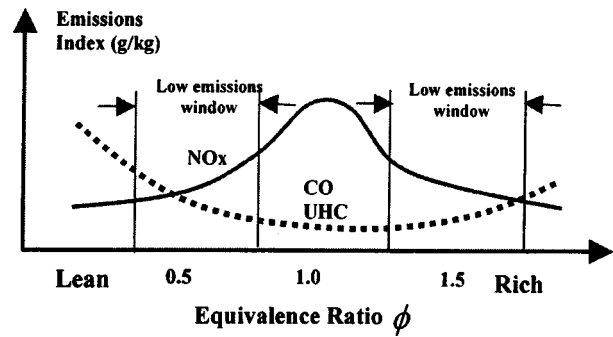


Fig. 1 Emissions characteristics

level. Because of the additional difficulties with rich burn control, the current analysis focuses on lean burn control.

Among all the emissions produced by gas turbines, CO and UHC emissions can be reduced significantly by improving combustion efficiency. The NO_x production is mainly determined by the combustor inlet pressure, inlet temperature, flame temperature, and residence time in the primary combustion zone and fuel type. According to Steele et al. [14], the flame temperature has the most significant effect on the NO_x production.

According to Eqs. (1) to (3), there are several parameters, such as combustor inlet pressure, temperature, mass flow rate, combustor geometry, and fuel flow rate, which influence the emissions production. In order to maintain a certain level of engine performance for given gas turbine thermal cycles, the combustor inlet pressure, temperature, mass flow rate, and fuel flow rate cannot be changed. The only parameters that can be changed are the air flow distribution and fuel flow distribution within the combustor, which can be achieved with variable geometry and fuel staging respectively. Many fuel staging methods have been developed, but only the circumferential staging is analyzed in this study.

In conventional gas turbine combustors, the combustion system is designed for a certain high-power operation condition, producing an unwanted effect on the requirements for combustion stability and low limit of weak extinction at idle. Such a design requires an equivalence ratio in the primary zone which is very close to unity at the maximum working point; the flame temperature and therefore the NO_x emissions are very high in this situation. In order to reduce the NO_x emissions at high power level based on the lean burn concept, the equivalence ratio in the primary zone must be within the lean burn low emissions window (Fig. 1) so the air flow rate to the primary zone must be increased. Such a change will definitely result in poor combustion stability at low operating conditions. One of the remedies to the problem is to vary the air flow rate to the primary zone by changing the combustor geometry according to the operating conditions. Due to difficulties in measuring and controlling the absolute air flow rate to the primary zone but being relatively easy to control the air flow ratio to the primary zone because air flow ratio is approximately proportional to cross-sectional area ratio, the air flow ratio is chosen to be the control parameter.

The variable geometry combustor suggested in this paper is schematically shown in Fig. 2 where an air flow splitter driven by a hydraulic system can move forward and backward to vary the cross-sectional area ratio and therefore the air flow ratio to the primary zone. The suggested position of the air splitter has the advantages that it is located at the upstream of the combustor chamber and is relatively distant from the hottest gas. The control target is chosen to be the flame temperature, an indirect measure of combustion stability and the emissions production of the combustor.

The engine operates over a wide range of environmental and operational conditions and therefore the air flow splitter may have to move to an extreme position to satisfy the control target; this

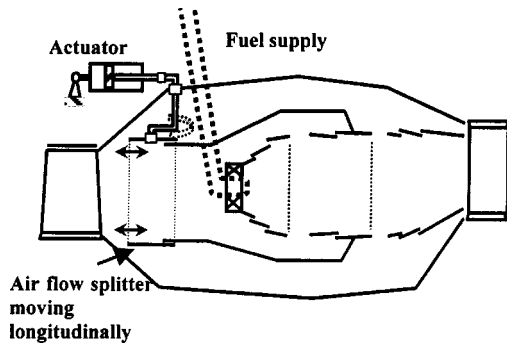


Fig. 2 Variable geometry combustor

may cause severe distortion to the air flow field and result in large pressure loss. Such a distortion may be crucial to the life of the combustor chamber because the amount of cooling air may also be far away from its design value. Therefore a circumferential fuel staging is introduced in this study to reduce the range of movement of the air flow splitter.

Control Scheme A. The starting point for the control system is to introduce a flame temperature predictor and to control the flame temperature in the combustor primary zone to a set point value. The flame temperature in the primary zone can be adequately predicted with combustor inlet pressure, temperature, mass flow rate, fuel flow rate, and combustor geometry parameters. Generally, the best flame temperature range for lean-burn low-emissions combustion is between 1900 K and 2300 K. Outside of the range, a higher flame temperature will enhance NO_x production and a lower flame temperature will carry the risk of weak extinction and unstable combustion. For illustration, a constant flame temperature in the primary combustion zone of 1900 K is chosen in this study. The introduced inferential control system is schematically shown in Fig. 3 and is called Control Scheme A. The accuracy of the control relies on the measurement accuracy of those relevant combustor parameters and the prediction of flame temperature. The drawback of such a control scheme is that the control system may introduce more complexity to the combustor design and manufacture and require more attention to its reliability due to the existence of many sensors and the flame temperature predictor. Accurate measurement of air flow rate to the combustor is even more difficult.

Control Scheme B. An alternative simplified inferential control scheme may be used to prevent the above problem if there is a relationship between the flame temperature and another control parameter. It is observed that the air flow rate required in the primary zone to keep the flame temperature constant as the gas turbine changes its power is approximately proportional to the fuel flow rate into the combustor. Taking into account the wide range of environmental and operating conditions, a nondimensional fuel flow rate

$$WF_{nd} = \frac{\dot{m}_f \sqrt{T_2}}{P_2} \quad (4)$$

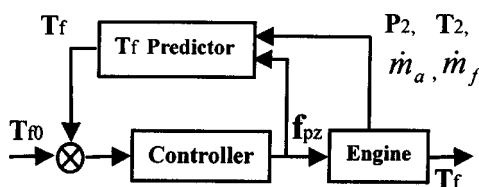


Fig. 3 Control Scheme A

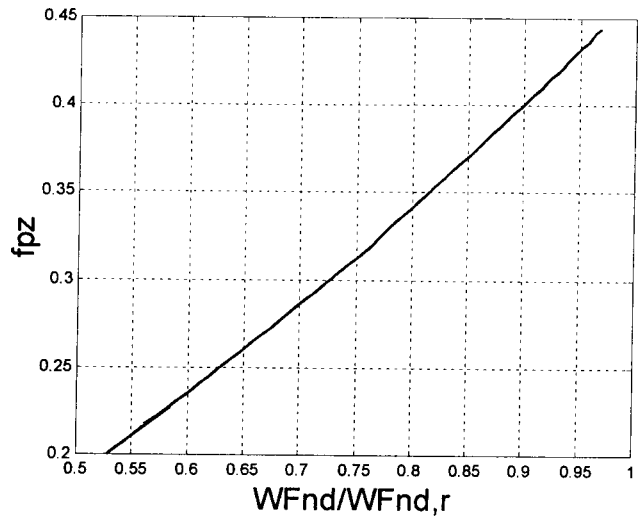


Fig. 4 Air flow ratio versus nondimensional fuel flow rate

is chosen to be the indirect control parameter.

A throttle-back performance of the model turbofan engine at standard day at sea level is calculated while adjusting the air flow ratio to the combustor primary zone with Control Scheme A to keep the flame temperature at 1900 K. As a result of the calculation, the variation of the air flow ratio to the primary zone f_{pz} with the nondimensional fuel flow rate ($WF_{nd}/WF_{nd,r}$) is demonstrated in Fig. 4 and shows almost linear relationship, which provides the possibility of a flame temperature control scheme based on the information of nondimensional fuel flow rate. A linear relationship between the air flow ratio to the combustor primary zone and the nondimensional fuel flow rate is introduced as follows:

$$f_{pz} = a \cdot \left(\frac{WF_{nd}}{WF_{nd,r}} \right) + b \quad (5)$$

where a and b are case-dependent constants.

Fuel staging may be necessary when the total fuel/air ratio of the combustor is below a certain level and the air flow ratio to the primary zone is significantly below its design value. The advantage of the fuel staging is that the air flow splitter does not have to move far from its design position in most of the engine operation conditions to meet the control requirement; accordingly the air flow field upstream of the combustor should not distort dramatically. It would be better to control the fuel staging based on the total air/fuel ratio of the combustor, but unfortunately accurate

Table 1 Fuel staging scheme

| No. | CN/CN_r | Injectors fueled f_{inj} |
|-----|-------------|----------------------------|
| 1 | ≥ 0.94 | 100% |
| 2 | < 0.94 | 60% |

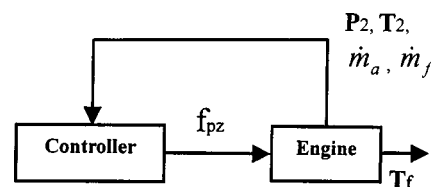


Fig. 5 Control Scheme B

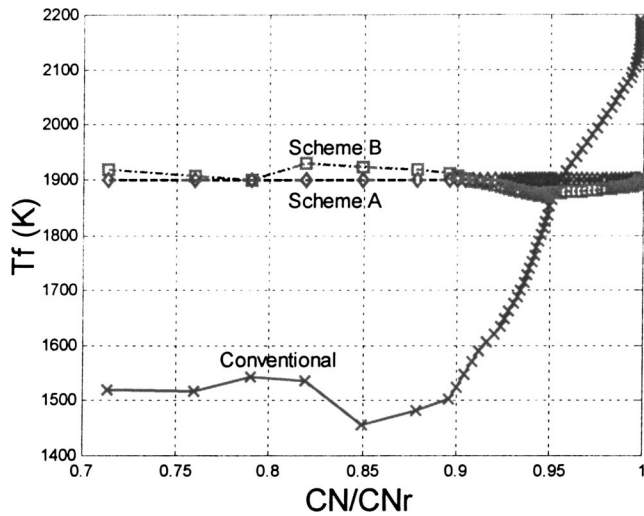


Fig. 6 Flame temperature

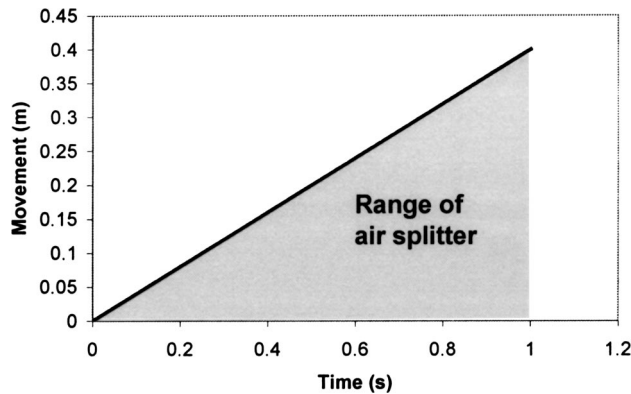


Fig. 7 Hydraulic system capability

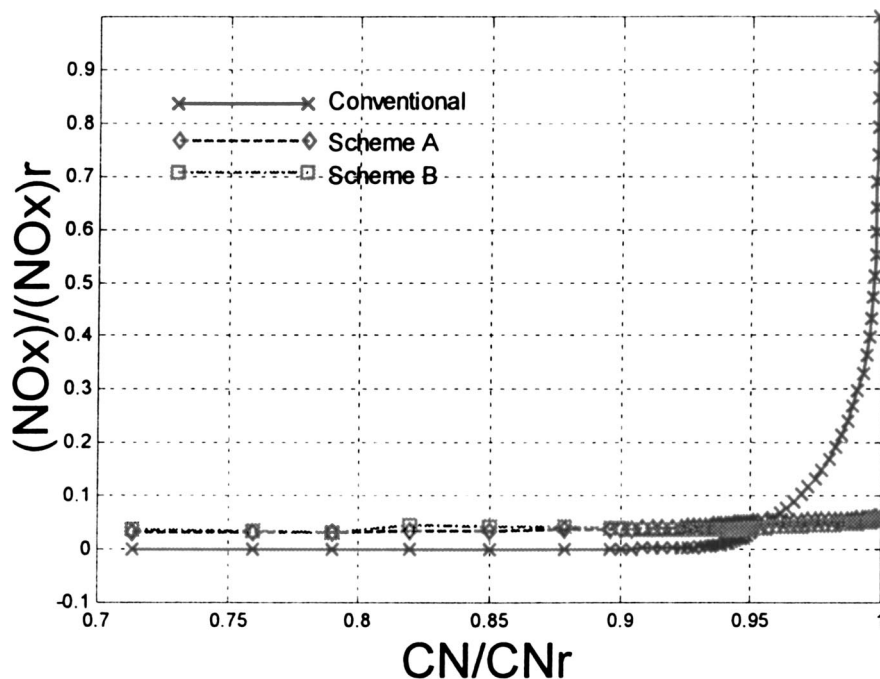


Fig. 8 Index of NO_x emissions

air/fuel ratio is difficult to measure. One of the methods to control the fuel staging is to use the HP spool rotational speed as an indirect measure of the engine power level or the total air/fuel ratio in the combustor. A two-step fuel staging scheme is chosen in this study which is illustrated in Table 1 where all fuel injectors are fueled when the HP spool nondimensional rotational speed is greater than 0.94 and 60% injectors are fueled when the nondimensional rotational speed is below 0.94.

With fuel staging, Eq. (5) is now modified to the following form:

$$f_{pz} = \left[a \cdot \left(\frac{WF_{nd}}{WF_{nd,r}} \right) + b \right] \cdot \left(\frac{1}{f_{inj}} \right). \quad (6)$$

At the point of staging, the total fuel flow remains constant but the number of injectors fueled changes, so the fuel flow per injector changes. The control scheme based on the above relations is called Control Scheme B and is schematically shown in Fig. 5.

The advantage of using the parameter WF_{nd} for control is that all the parameters in Eq. (4) are measurable and the control system can be simplified significantly. When the Eq. (5) is used in the control system to control the air flow ratio to the primary zone, the effectiveness of the flame temperature control can be observed in Fig. 6 where the flame temperature is plotted against HP spool speed. It can be seen that assuming such a linear air flow ratio control is very effective compared to the original inferential Control Scheme A and the maximum control error is about 40 K at about 82% nondimensional speed. Such a level of flame temperature variation would not adversely affect combustion performance.

Transient Performance Calculation

Details of gas turbine transient performance modeling issues can be found in Refs. [15,16]. The computer code for gas turbine transient performance calculation used in this study was developed by Maccallum [10] and the prediction accuracy has been assessed during the calculation of Rolls-Royce RB183 engines.

The air splitter located at the upstream end of the combustor, which is the salient part of the variable geometry combustor, is controlled by the engine control system and driven by a hydraulic

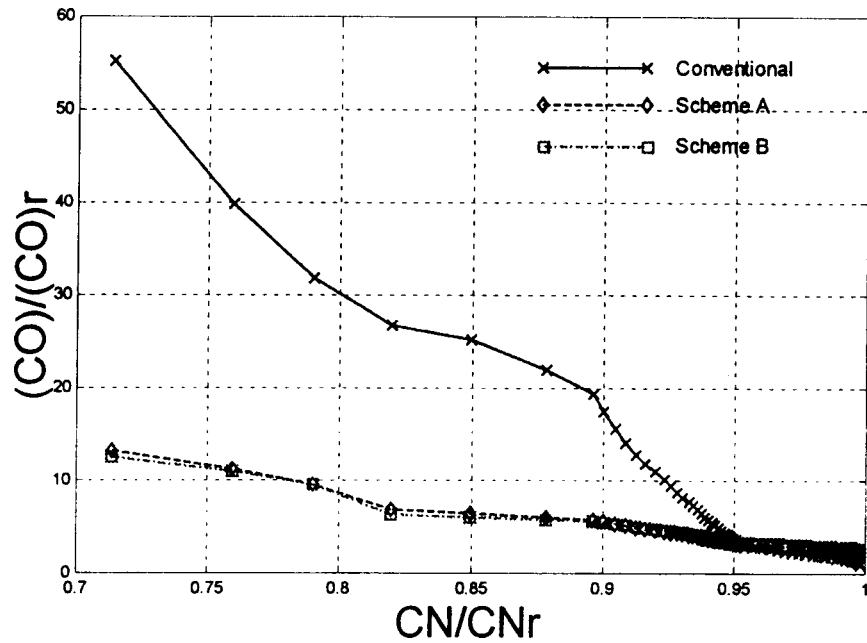


Fig. 9 Index of CO emission

system. The moving speed of the air splitter, if not high enough, may have influence on the combustor transient performance. The critical scenarios would be rapid acceleration and deceleration processes and fuel staging.

A simple model is used to describe the moving speed of the air splitter, Fig. 7, where a maximum moving speed of 0.4 m/s is assumed. If the required moving speed of the air splitter is less than 0.4 m/s, the hydraulic system would be able to drive the air splitter to the required position, which is the case in most situations. If the required moving speed of the air splitter is higher than what the hydraulic system can drive, the movement of the air splitter will be delayed. Details of the influence of the delay will be described in the next section.

Comparisons and Analysis

Steady State Behavior. When the turbofan engine is throttled back from its maximum operating condition at standard day at sea level, the performance and emissions of the engine combustor produced by the conventional configuration and variable geometry combustors with different control schemes are compared as follows. In the analysis, the indices of emissions produced by the combustor with conventional configuration at maximum power level at sea level are chosen to be the reference values ($(NO_x)_r$, $(CO)_r$ and $(UHC)_r$) for the convenience of comparison.

In the combustors with conventional configuration where the air flow ratio to the primary combustion zone is chosen to have a

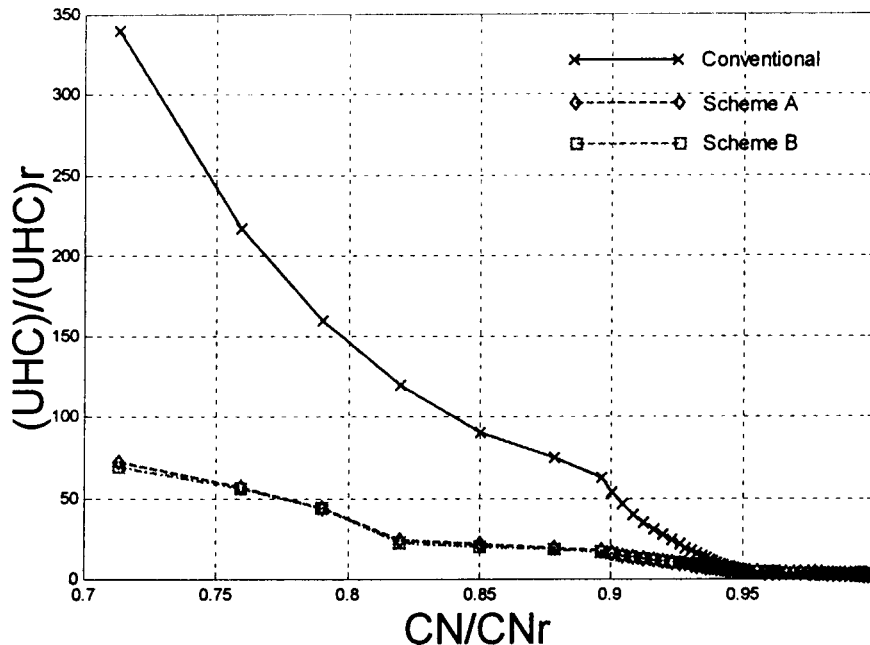


Fig. 10 Index of UHC emission

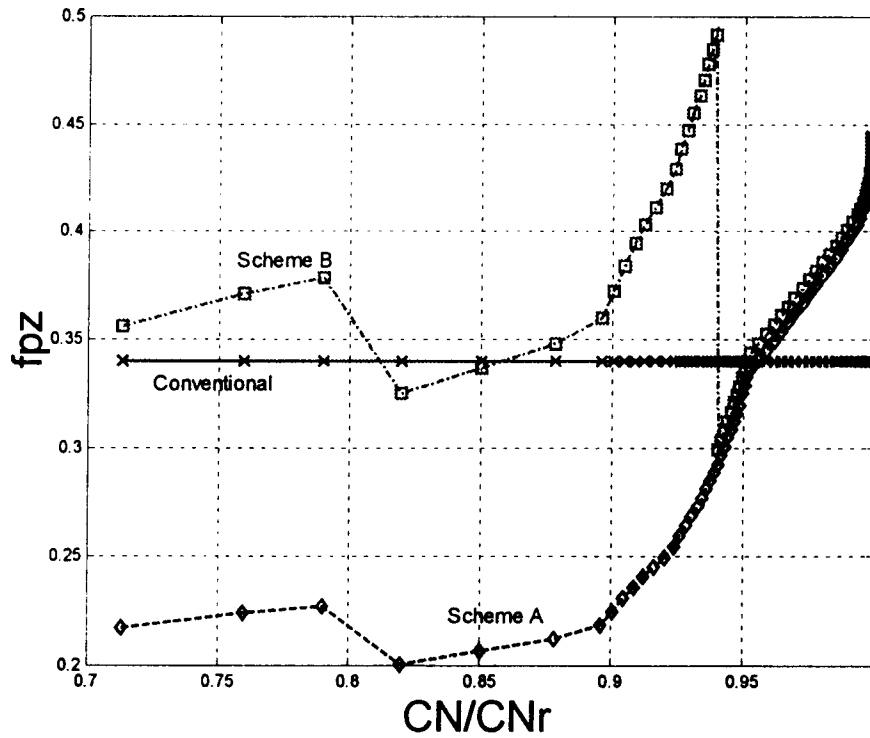


Fig. 11 Air flow ratio to primary zone

constant value of 34%, the flame temperature will reach around 2200 K at maximum operating condition at sea level, Fig. 6; as a consequence, a large amount of NO_x will be produced, Fig. 8. When the engine throttles back the flame temperature decreases significantly and a large amount of CO and UHC may be produced, Figs. 9 and 10. With the control schemes it can be seen that the flame temperature can be kept almost exactly at the set point value in Control Scheme A and very close to the set point value in Control Scheme B (within 40 K). Correspondingly, with both control schemes the air flow ratio to the primary zone will be increased to around 45% at the maximum operating condition at sea

level, Fig. 11. As a consequence of the application of the control schemes, the NO_x index can be reduced by a factor of 14 at maximum engine power level and kept almost constant with slight reduction at low engine power level. At about 72% of nondimensional HP spool rotational speed the geometry control brings a reduction of CO and UHC emissions indices by around a factor of 4.4 and reduces CO and UHC gradually as the high engine power level is approached.

The benefit of the fuel staging can be seen in Fig. 11. The air flow ratio to the primary zone in Control Schemes A and B is at a level substantially different to the value at design point in most of

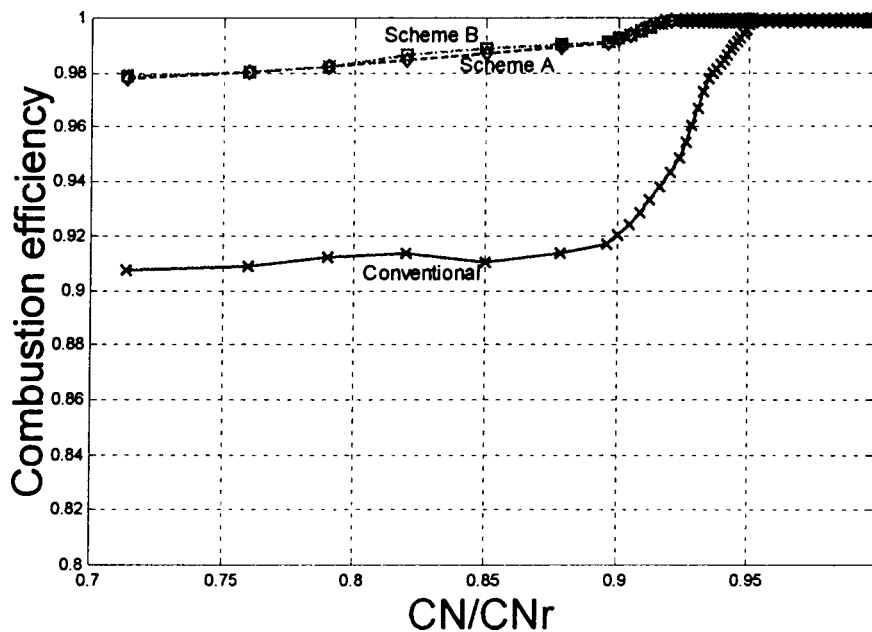


Fig. 12 Combustion efficiency

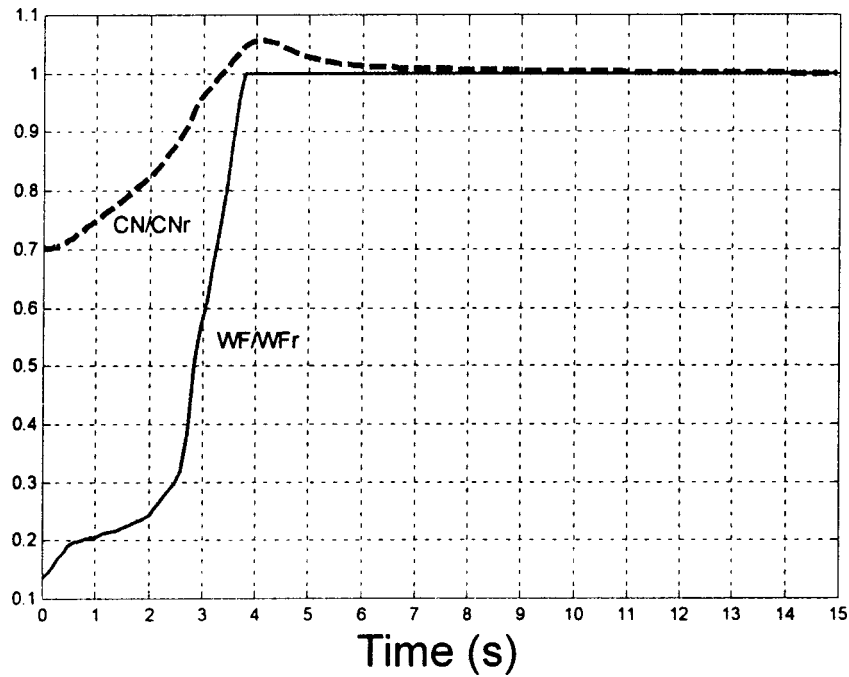


Fig. 13 Fuel flow rate and rotational speed

the engine operation conditions. With the introduction of fuel staging in Control Scheme B, the air flow ratio f_{pz} to the primary zone can take values much closer to its design point in most of the engine operation conditions, which is beneficial to the air flow field at the combustor inlet.

Compared with the conventional combustor configuration, the fuel/air mixture in the primary zone of the variable geometry combustor (whatever fuel staged or not) becomes richer at low operating conditions. Correspondingly, the flame temperature increases (Fig. 6), which is a great benefit to the combustion stability and efficiency. A correction factor $(T_f/T_{f,r})^s$ which is the ratio of flame temperature at off-design point to that at design

point for the same combustor is introduced in the calculation of combustion efficiency. In this way, the combustion efficiency better reflects the combustion conditions for both the conventional and variable geometry combustors, and its effect can be seen in Fig. 12. The improvement of the combustion efficiency in the variable geometry combustor has certain benefit to specific fuel consumption (sfc) but little influence on other engine performance parameters.

It can be seen from Fig. 6 and Figs. 8 to 12 that the variable geometry combustor has a great potential to reduce the emissions and improve the combustor performance. Control Scheme B pro-

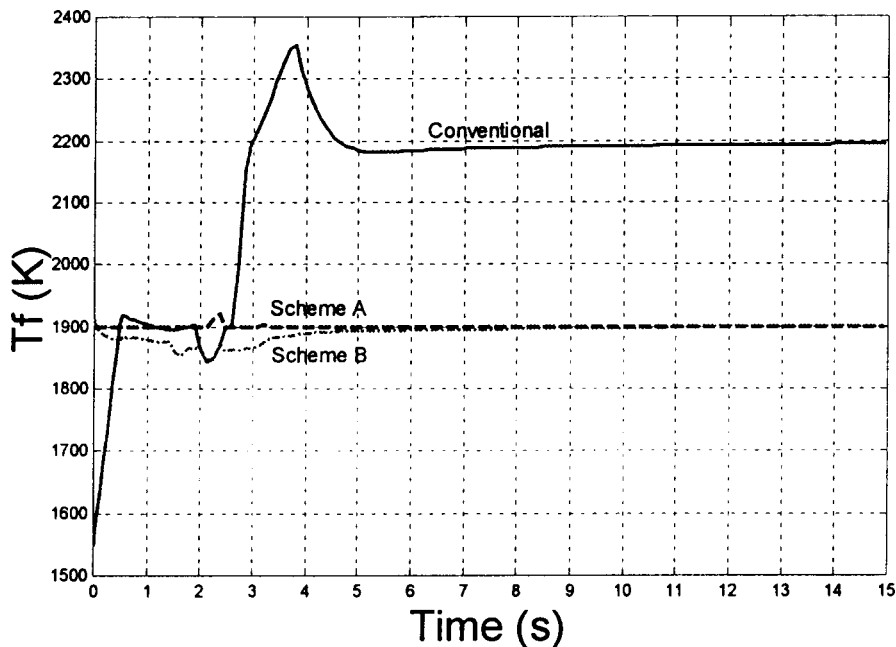


Fig. 14 Flame temperature

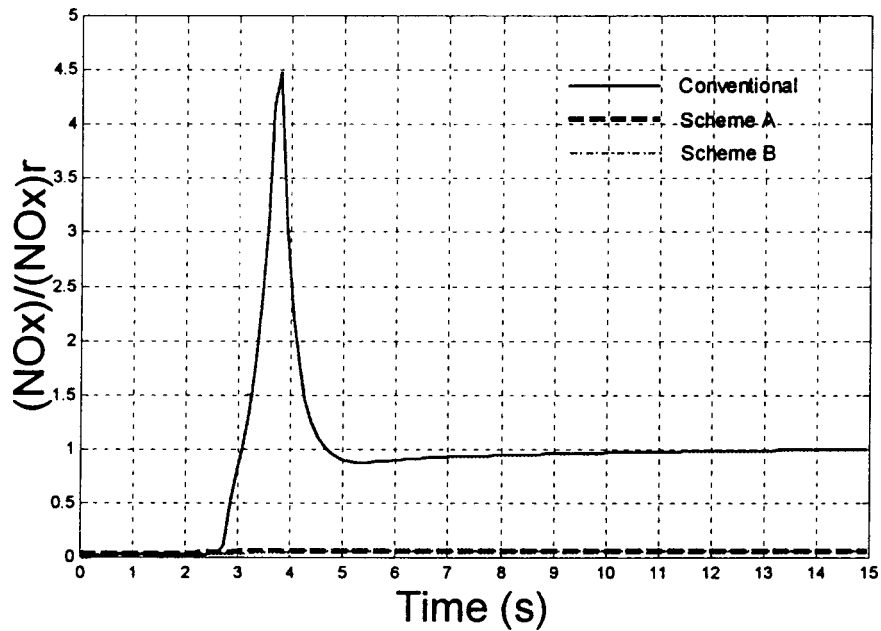


Fig. 15 Index of NO_x emissions

vides equivalent control effect to that of Control Scheme A; the difference in the performance and emissions production is very small.

Dynamic Behavior. An acceleration process of the engine from steady idle to its maximum power at sea level was simulated with the computer code, where the variations of the fuel flow rate and corresponding HPC rotational speed are illustrated in Fig. 13. It shows a rapid increase in fuel flow rate in the first 0.5 second, slow acceleration in the following 2.0 seconds and a further steep acceleration in the next 1.3 seconds. A steady state is attained after around 7 seconds.

The flame temperature in the conventional combustor increases rapidly during the acceleration and reaches its top value of about

2350 K at the end of the acceleration at about 3.8 second, Fig. 14, which causes a jump in NO_x emissions accordingly, Fig. 15. With the variable geometry combustor controlled by Schemes A and B, the flame temperature varies around the set point value with control error of less than 40 K, which results in much lower NO_x emissions over operating conditions.

Much lower flame temperature (Fig. 14) in the conventional combustor in the first 0.5 second, especially at idle, causes much higher CO and UHC emissions, Figs. 16 and 17. These emissions can be reduced significantly with the variable geometry combustor. With the increase in engine power level, little difference in CO and UHC emissions exist between the two control schemes, Figs. 16 and 17.

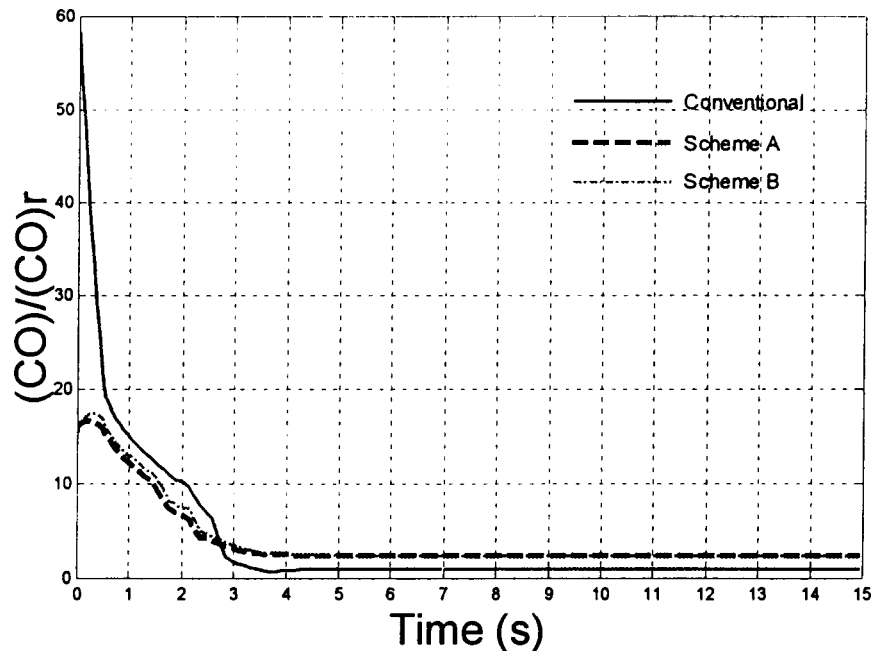


Fig. 16 Index of CO emission

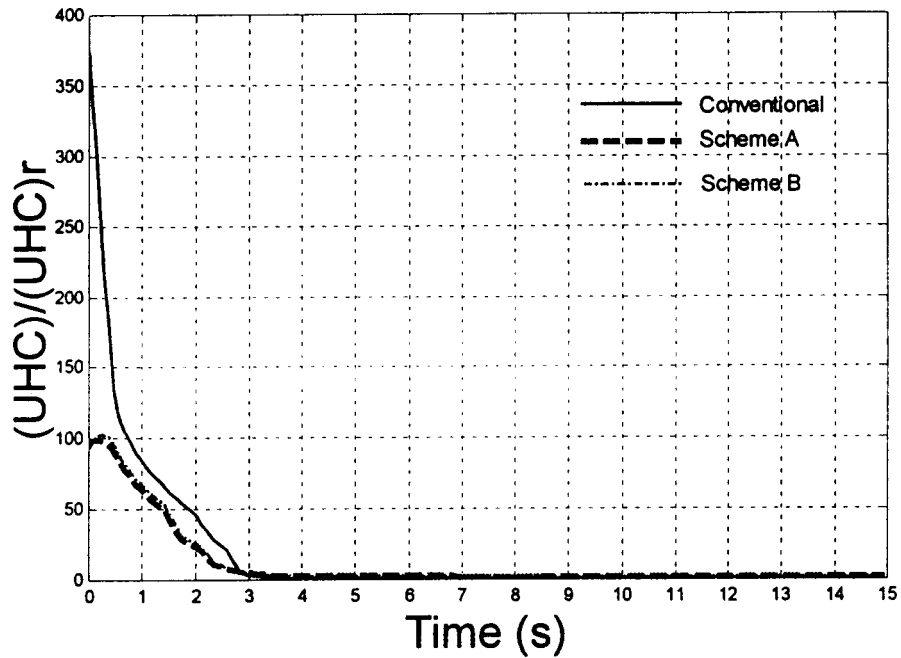


Fig. 17 Index of UHC emission

The primary zone air flow ratios with Control Schemes A and B in the variable geometry combustor, Fig. 18, have larger values than those in the steady state situations, Fig. 11, during the acceleration (in the first 3.2 seconds). This is because the air flow ratio to the primary zone is controlled by the corrected fuel flow rate, Eq. (6), and the fuel flow rate at a specific rotational speed during a transient is larger than that required to keep the same rotational speed at steady state. The two schemes exhibit a difference in air flow ratios until 2.2 seconds after the acceleration starts, at which time fueling is staged under Scheme B.

The air splitter is constrained by the hydraulic system. Therefore the combustion conditions during transient may be influenced

by the speed limit of the air splitter. This can be seen in Fig. 14 where the flame temperature in the variable geometry combustor with Control Schemes A and B has sudden jumps at about 2.2 seconds when fuel staging is switching and at about 3.2 seconds when a steep acceleration occurs. The maximum flame temperature jump is less than 20 K so the influence is not significant.

The difference in combustion efficiencies between the conventional combustor and the variable geometry combustor during the acceleration is shown in Fig. 19. Maximum efficiency difference occurs at idle due to maximum flame temperature difference but the difference reduces when the engine power increases.

In general, the combustor performance difference between the

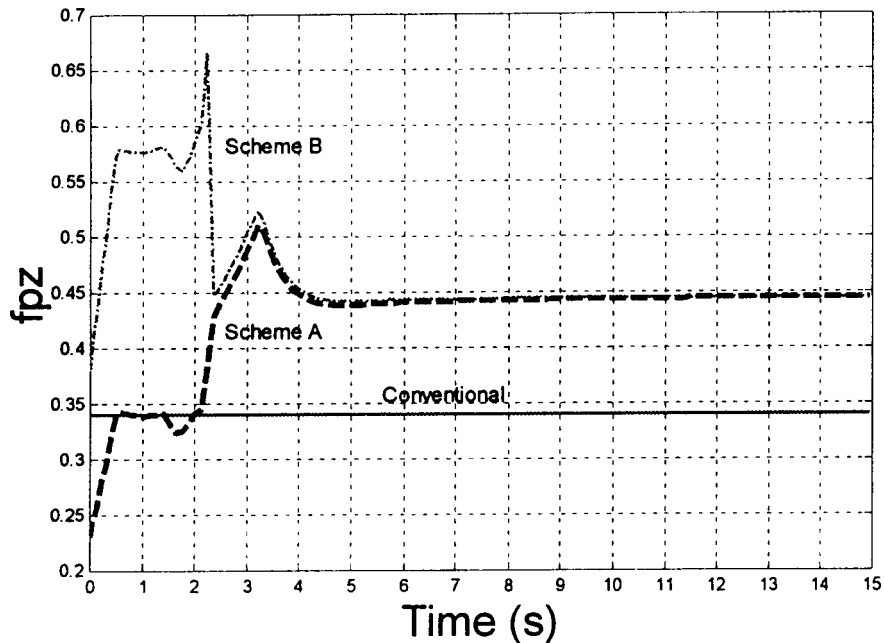


Fig. 18 Air flow ratio to primary zone

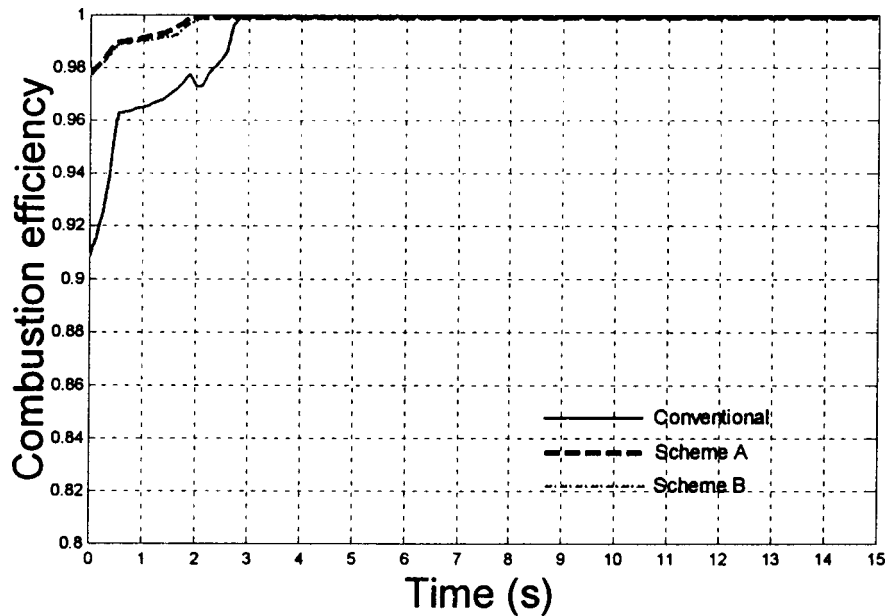


Fig. 19 Combustion efficiency

conventional combustor and the variable geometry combustor during the acceleration is obvious but the difference between the two control schemes is very small.

Conclusions

The proposed variable geometry combustor combined with appropriate control schemes can significantly reduce emissions production for engine operation at or near ground level, compared to a combustor with conventional configuration. Fuel staging can reduce the range of movement of the air flow splitter at most of the operational conditions and therefore is beneficial to the air flow field at combustor inlet.

The introduced linear relationship between the non-dimensional fuel flow rate and air flow ratio to the combustor primary zone for the control of flame temperature

$$f_{pz} = \left[a \cdot \left(\frac{WF_{nd}}{WF_{nd,r}} \right) + b \right] \cdot \left(\frac{1}{f_{inj}} \right)$$

is effective and can simplify the control system.

The speed limit of the air flow splitter has little influence on combustor performance. The variable geometry combustor has a potential to improve combustion stability, efficiency and specific fuel consumption compared to the conventional configuration.

The inferential Control Scheme A is able to provide good control accuracy of flame temperature but embodies significant complexity. The simplified Control Scheme B provides equivalent control accuracy.

Nomenclature

- CN = engine high pressure (HP) spool nondimensional rotational speed (N/\sqrt{T})
- N = rotational speed (rpm)
- (CO) = carbon monoxide index (g/kg)
- (NO_x) = nitric oxide index (g/kg)
- P_2 = combustor inlet pressure (kPa)
- ΔP = combustor liner pressure drop (kPa)
- T_2 = combustor inlet temperature (K)
- T_f = flame temperature in primary combustion zone (K)
- T_{st} = stoichiometric flame temperature (K)

- (UHC) = unburned hydrocarbon index (g/kg)
- V_c = volume of combustor chamber (m^3)
- V_{ev} = fuel evaporation volume (m^3)
- WF_{nd} = nondimensional fuel flow rate
- a, b = constants
- f_{inj} = proportion of injectors fueled
- f_{pz} = air flow ratio to primary zone
- \dot{m}_A = air flow rate to combustor (kg/s)
- \dot{m}_f = fuel flow rate (kg/s)

Subscripts

- nd = nondimensional
- pz = primary zone
- r = reference value at engine maximum operation condition at sea level
- 0 = control set point
- 2 = combustor inlet

References

- [1] Wulff, A., and Hourmouziadis, J., 1997, "Technology Review of Aeroengine Emissions," *Aerospace Science and Technology*, (8), pp. 557–572.
- [2] Schultz, D. F., 1975, "Ground Idle Performance Improvement of a Double-Annular Combustor by Using Simulated Variable Combustor Geometry," NASA TM X-3176.
- [3] Schultz, D. F., 1975, "Variable Combustor Geometry for Improving the Altitude Relight Capability of a Double Annular Combustor," NASA TM X-3163.
- [4] Gupta, A. K., Ramavajjala, M. S., and Chomiak, J., 1988, "Burner Geometry Effects on Combustion and NO_x Emission Characteristics of Variable Geometry Swirl Combustor," Paper No. AIAA-89-0488.
- [5] Fletcher, R. S., 1973, "The Automotive Gas Turbine," conference on Developments in Automotive Power Plants to Reduce Fuel Consumption, Air Pollution and Noise, Queen Mary College, London, Apr.
- [6] Saintsbury, J. A., and Sampath, P., 1974, "Atmospheric Tests of a Variable Combustor Geometry for Reducing Gas Turbine Emissions," ASME/CSME Conference, Montreal, May.
- [7] Fletcher, R. S., and Adkins, R. C., 1976, "The Variable Geometry Combustor," AGARD Conference (48 PEP Meeting), Paris, Sept.
- [8] Hayashi, S., Yamada, H., and Shimodaira, K., 1996, "Engine Testing of a Natural Gas-Fired, Low- NO_x , Variable Geometry Gas Turbine Combustor for a Small Gas Turbine," ASME Paper No. 96-GT-455.
- [9] Li, Y. G., and Hales, R. L., 2002, "Gas Turbine Emissions Control Using Variable Geometry Combustor and Fuel Staging," Paper No. AIAA-2002-0079.
- [10] Maccallum, N. R. L., 1984, "Computational Models for the Transient Performance of RB183-02 (Spey) and RB183-03 (Tay) Engines," Technical Report RR/1, University of Glasgow, Aug. 13.

- [11] Lefebvre, A. H., 1984, "Fuel Effects on Gas Turbine Combustion—Liner Temperature, Pattern Factor and Pollutant Emissions," Paper No. AIAA-84-1491.
- [12] Reeves, C. M., and Lefebvre, A. H., 1986, "Fuel Effects on Aircraft Combustor Emissions," ASME Paper No. 86-GT-212.
- [13] Gülder, Ö. L., 1986, "Flame Temperature Estimation of Conventional and Future Jet Fuels," ASME J. Eng. Gas Turbines Power, **108**, pp. 376–380.
- [14] Steele, R. C., Jarrett, A. C., Malte, P. C., Tonouchi, J. H., and Nicol, D. G., 1997, "Variables Affecting NO_x Formation in Lean-Premixed Combustion," ASME J. Eng. Gas Turbines Power, **119**, pp. 102–107.
- [15] Maccallum, N. R. L., and Qi, O. F., 1989, "The Transient Behavior of Aircraft Gas Turbines," IMechE Seminar (Seminar S777) on Gas Turbines: Technology and Development, Institute of Mechanical Engineering, London, Nov.
- [16] Pilidis, P., 1983, "Digital Simulation of Gas Turbine Performance," Ph.D. dissertation, Department of Mechanical Engineering, University of Glasgow, Glasgow, Scotland.

A New Generalized Carbon Exergy Tax: An Effective Rule to Control Global Warming

A. Traverso

e-mail: alberto.traverso@unige.it

A. F. Massardo

e-mail: massardo@unige.it

Thermochemical Power Group,
Dipartimento di Macchine,
Sistemi Energetici e Trasporti,
Universita di Genova, Italy,
Genova 16145, Italy

M. Santarelli

e-mail: santa@athena.polito.it

M. Cali

e-mail: cali@polito.it

Dipartimento di Energetica,
Politecnico di Torino,
Torino, Italy

An instrument for promoting CO₂ emission reductions, taking the Kyoto Protocol goal into account, could be the assignment to energy conversion plants of a monetary charge linked to their specific emission intensity, usually called carbon tax. There are two main problems closely connected with this approach: the estimation of the charge (that must be related to the "external" cost associated with CO₂ emission) and the choice of the strategy to determine the amount of the imposed charge. In this paper an analytical procedure proposed by the authors and called carbon exergy tax (CET) for the evaluation of CO₂ emission externalities is presented. It is based on the thermo-economic analysis of energy systems, which allows second law losses to be quantified in monetary terms: the resulting cost represents the taxation that is to be applied to the energy system under examination, calculated without any arbitrary assumption. Since the complete procedure of the CET evaluation is too complex to become a feasible instrument of energy policy, hereby, after applying the procedure to some conventional and advanced power plants, gas, oil, and coal-fueled, a new generalized approach, based on the results of the complete CET procedure, is proposed. The generalized CET evaluation requires much less information about the energy system and thus a simple and effective energy policy rule to manage global warming is obtained and available. [DOI: 10.1115/1.1610013]

Introduction

The criteria that will influence the evolution of the energy market this century will be based on the need to preserve the environment (both locally and globally) through new technologies and sustainable use of existing resources. This need is also ratified by the guidelines of the various framework programs of the European community and by international agreements such as the Kyoto Protocol. In particular, the global warming problem, linked to CO₂ emissions, requires an energy policy approach at an international level devoted to CO₂ regulation: The energy policy should aim at punishing the inefficient use of fossil energy sources that determines a larger emission of CO₂ than a more efficient use. Two main approaches are possible to deal with the global warming issue: the political approach and the economic approach, [1–3], already discussed by the authors, [4,5]. The former "forces," the latter "suggests" and makes low CO₂ emission energy systems more competitive than conventional solutions. The carbon exergy tax (CET), proposed by the authors in the framework of the economic approach, [6–9], allows the CO₂ emission external cost to be evaluated on the basis of efficient utilization of exergy resources. The idea is not to punish the energy production activity (CO₂ emissions are not toxic and moreover they are inevitably emitted in large quantities during hydrocarbon combustion processes) but the inefficient use of fossil fuels.

The carbon exergy tax should push the deregulated energy market towards the most efficient and advanced conversion technologies and towards renewable resources (they should not be taxed since they do not emit carbon dioxide); in addition, the CET is an effective regulation for making CO₂ sequestration economically feasible, [10–14].

In the present work the carbon exergy tax evaluation procedure is briefly presented and is applied to power plants of different

types and sizes, in order to discuss its effect on the economic promotion of low CO₂ emission configurations such as the HAT or fuel-cell hybrid cycles. After that, a generalized approach that maintains the same features of the rigorous CET method, but requires much less information about the energy system, is shown to be possible. In this way a feasible proposal for CO₂ emission taxation is issued and its ability to effectively contribute to the economic management of global warming is assessed.

Carbon Exergy Tax (CET): Analytical Approach

The CO₂ "external cost" should conceptually be equal to the cost of the CO₂ emission damage caused to the environment: Once this cost is evaluated, it should be charged to the emitting plant since it must repay the society for polluting the atmosphere. When a procedure is being considered for the calculation of such an "externality" of CO₂ emissions, it should be taken into account that carbon dioxide is not toxic and is even necessary for life. The CET method shifts attention away from the effects (global warming) to the causes (exploitation of fossil resources) of CO₂ production: to punish the inefficient use of scarce energy resources that determines a larger emission of CO₂ than an efficient use. The proposed procedure is based on the concept of the *inefficiency penalty* (Π_e), and the *index of CO₂ emission* ($I_{CO_2}^*$) and it highlights system inefficiencies that cause larger amounts of CO₂ to be released into the environment. Both terms (Π_e and $I_{CO_2}^*$) depend on the technical characteristics of the system, contained in the vector \mathbf{x} . The meaning and the expressions of Π_e and $I_{CO_2}^*$ are presented in the following.

Inefficiency Penalty. The inefficiency penalty term has this expression:

$$\Pi_e(\mathbf{x}) = 3600 \cdot N \cdot \{C_{irr}(\mathbf{x}) + C_w(\mathbf{x})\} \quad (1)$$

where the *cost of destroyed exergy* is

$$C_{irr}(\mathbf{x}) = \sum_{i=1}^{NC} c_{e_i} [\Psi_e(\mathbf{x}) - \Psi_o(\mathbf{x})]_i \quad (2)$$

Contributed by the International Gas Turbine Institute (IGTI) of THE AMERICAN SOCIETY OF MECHANICAL ENGINEERS for publication in the ASME JOURNAL OF ENGINEERING FOR GAS TURBINES AND POWER. Paper presented at the International Gas Turbine and Aeroengine Congress and Exhibition, Amsterdam, The Netherlands, June 3–6, 2002; Paper No. 2002-GT-30139. Manuscript received by IGTI, December 2001, final revision, March 2002. Associate Editor: E. Benvenuti.

and the cost of residual exergy is

$$C_w(\mathbf{x}) = \sum_{w=1}^{NC} c_w \Psi_w(\mathbf{x}). \quad (3)$$

In order to assign a weight to the irreversibilities and the residual exergy, corresponding to their relevance in terms of resource waste, the unit inefficiency penalty is evaluated in this manner:

c_e : the cost of a unit of irreversibility produced by a component i is calculated on the product of the economic fuel cost of the system (e.g., cost of natural gas) and the unit exergetic cost (k^*) of the exergy input flow of the same component, which is

$$c_{e_i} = c_f \cdot k_i^*(\mathbf{x}). \quad (4)$$

c_w : the cost of a unit of the residual exergy. Residual exergy is related to the exergy ejected into the biosphere through exhausts and/or heat from the condenser, as it is considered to be a potential product which is wasted; its unit cost is given by

$$c_w = c_f \cdot k_p^*(\mathbf{x}). \quad (5)$$

The irreversibility cost is linked to the fuel cost because irreversibility means waste of fuel.

Index of CO₂ Emission. The index of CO₂ emission $I_{CO_2}^*$ is defined as

$$I_{CO_2}^* = \frac{I_{CO_2}}{I_{CO_2,ref}} = \frac{1}{I_{CO_2,ref}} \frac{G_{CO_2}}{\Psi_p} \quad (6)$$

where $I_{CO_2,ref}$ is assumed to be equal to 1 kg/kWh. The assumption is only made to define the $I_{CO_2}^*$ as a nondimensional parameter.

When plants for electrical generation only are considered, the following formula can be derived:

$$I_{CO_2}^* = \frac{1}{I_{CO_2,ref}} \cdot \frac{\alpha \cdot [C]}{LHV} \frac{1}{\eta} \quad (7)$$

where the relationship between $I_{CO_2}^*$ and the system thermal efficiency η is expressed. Parameter α , that is CO₂ production per mass of C , is equal to 3.664 for all fuels.

Charge for the CO₂ Emitted by the Plant.

$$C_{CO_2} = I_{CO_2}^* \cdot \Pi_\varepsilon. \quad (8)$$

To better outline the influence of plant operating conditions the following relationship can be developed:

$$C_{CO_2} = \frac{1}{I_{CO_2,ref}} \cdot \alpha \cdot [C] \cdot G_F \cdot 3600 \cdot N \cdot \left[\frac{\sum_{i=1}^{NC} c_{e_i} [\Psi_e(\mathbf{x}) - \Psi_o(\mathbf{x})]_i}{\Psi_p(\mathbf{x})} + \frac{\sum_{i=1}^{NC} c_{w,i} \Psi_{w,i}(\mathbf{x})}{\Psi_p(\mathbf{x})} \right]. \quad (9)$$

CET. Finally the expression of CET is

$$CET = \frac{C_{CO_2}}{G_{CO_2}} = I_{CO_2}^* \cdot \frac{\Pi_\varepsilon}{G_{CO_2}} = \frac{1}{I_{CO_2,ref}} \frac{\Pi_\varepsilon}{\Psi_p}. \quad (10)$$

It is important to note that the CET expression, as already discussed in [4,8], is only obtained through an objective thermo-economic procedure, without subjective assumptions.

When the CET, calculated according to (10), is charged to the emitted CO₂, it causes a non-negligible increase in the energy cost that mainly depends on plant conversion efficiency and the type of fuel (composition and cost): The least polluting plants will suffer the smallest increase. In that respect, the CET represents an economic penalty linked to the inefficient utilisation of energy resources.

It is also possible to determine an equivalent tax imposed on fuel cost, called the fuel carbon exergy tax (FCET), whose expression is

$$FCET = \frac{C_{CO_2}}{G_F \cdot LHV} \frac{\$/yr}{kJ/yr} \Rightarrow [\$/kJ]. \quad (11)$$

Finally, considering plants for electrical generation only, it is possible to evaluate the absolute increase of the electricity cost due to the imposition of the CET, defined as Δc_{el} :

$$\Delta c_{el} = \frac{CET \cdot G_{CO_2}}{W_{el}} \quad (12)$$

Software Tool and Case Studies

All the results presented here are calculated using the in-house TEMP (thermo-economic modular program) code, [15–17], recently upgraded to predict complex mixed air-steam cycle performance, [18,19]. At present 64 modules are available, and they allow the thermoeconomic and exergoeconomic, [20], analysis of a large number of energy cycles such as the following to be obtained: steam, gas turbine, combined, and advanced cycles (mixed gas-steam cycles, fuel cells—SOFC and MCFC—and hybrid cycles, partial oxidation cycles, chemical recovery cycles, [21]). The system to be calculated is defined as an ensemble of interconnected components. It is possible to calculate the internal irreversibility of each component (that determines an exergy expenditure) and its capital cost (that determines a monetary expenditure). Thermo-economic results are given at two different levels: at the inner level as an estimate of the average unit cost (c), the unit exergetic cost (k^*) and the marginal cost (λ) at each connection; at the outer level as an evaluation of the thermal efficiency, the generated power, the generated heat, the electrical and thermal energy costs. In addition, it is possible to carry out plant through-life cost analysis, calculating financial parameters such as internal rate of return, payback period, net present value, and others. In the end plant thermodynamic and economic features are completely and fully described.

The TEMP code is also provided with an optimization tool that allows energy system thermoeconomic optimization to be obtained with different objective functions: the most important are thermal efficiency and the cost of electricity. The nonlinear optimization algorithm is described in [15], and it has been recently upgraded with the introduction of a genetic algorithm.

In the present paper, the complete CET calculation procedure has been applied to some conventional and advanced power plants differently fuelled (coal, oil, and natural gas; see Table 1) and sized (0.5–350 MW; see Table 2). Of the conventional power systems, a natural gas and oil-fueled 30 MW simple gas turbine cycle (GT), a natural gas-fueled 50 MW one-pressure-level steam injected gas turbine (STIG), a natural gas-fueled 200 MW three-level-pressure combined cycle (CC3LP), and the coal-fueled standard ENEL (320 MW) have been considered in order to represent the state of the art of power plants.

Among advanced power systems, the following configurations have been studied in order to comprehend a wide range of possible future plants.

An oil-fueled 354 MW externally fired combined cycle (EFCC), [22] and a coal-fueled 356 MW pressurised fluid bed combustor plant (PFBC), [23], have been considered as examples of solid and liquid fuel exploitation. The EFCC cycle scheme is similar to the CC3LP cycle one considered, but with the addition of a high-temperature ceramic heat exchanger between the gas turbine compressor and turbine: It is the most challenging component and at the present such a pressurised heat exchanger has never been built on such a large scale, because of problems regarding material high temperature corrosion, thermal stress, leakage, and ceramic tube fouling, [24].

Table 1 Fuel composition, LHV, and exergy

| Coal | | Oil | | Natural Gas | |
|------------------|---------------|------------------|---------------|-----------------|----------------|
| Comp | Mass Fraction | Comp | Mass Fraction | Comp | Molar Fraction |
| C | 85 | C | 87.13 | CH ₄ | 93.0 |
| H | 1.0 | H | 12.6 | N ₂ | 7.0 |
| O+N | 3.0 | O | 0.044 | | |
| S | 1.0 | N | 0.006 | | |
| H ₂ O | 2.5 | S | 0.22 | | |
| Ash | 7.5 | H ₂ O | 0.0 | | |
| LHV | 29500 kJ/kg | LHV | 44720 kJ/kg | LHV | 44270 kJ/kg |
| Ex _f | 31060 kJ/kg | Ex _f | 47650 kJ/kg | Ex _f | 45800 kJ/kg |

The pressurized fluid bed combustor plant scheme is a typical two-pressure-level combined cycle that has been modified in order to burn the coal in a PFBC. The PFBC replaces the original turbine natural gas combustor. The resulting scheme is an air-cooled PFBC. This is the only alteration to the original combined cycle, which remains the same for the bottoming steam cycle section. Coal is burned in the presence of a sorbent at temperatures around 1125 K: Above 1200 K there is the risk of a synerization of the fluidised bed; below 1025 K the combustion efficiency is too low; however, the most influential factor for bed temperature is the need for an *in situ* desulphuration, which operates well at a temperature around 1125 K, [23].

A 50 MW regenerated water injected gas turbine cycle (RWI) and a 50 MW humid air gas turbine cycle (HAT), [19], have been studied as examples of future applications of natural gas for power generation. The introduction of water into the compressed air after flue gas heat recovery is a very promising technique for increasing gas turbine efficiency and specific work and, moreover, an effective technical device for drastically reducing NO_x emissions. The RWI cycle carries out compressed air intercooling and aftercooling through water injection, which is a more irreversible process than the evaporation of water inside the humidification tower in the HAT cycle. This fact justifies the lower efficiency of the RWI to that of the HAT cycle. However, the HAT cycle does not require high-quality water: Conceptually it could work even with sea-quality water.

On the other hand, the STIG and RWI cycles require very high-quality water. At present water injection is implemented in a few commercial gas turbines for air intercooling, while no working HAT cycle is operating in the world, except for the pilot plant installed at the University of Lund, [25].

Two innovative power plants have been considered as examples of sub-MW applications for distributed power generation: the natural gas-fueled 500 kW micro HAT cycle (mHAT) and the natural gas and oil-fueled 500 kW externally fired micro gas turbine (EFmGT), [26]. Their layouts are simplified versions of the large-size HAT and EFCC cycles: The former (mHAT) does not carry out compressed air intercooling and aftercooling, the

latter (EFmGT) is similar to the EFGT without the bottoming cycle (steam section). Present microturbine technology has been considered.

Thermoeconomic Results

To calculate electrical power cost, the assumptions reported in Table 3 are necessary. The cost of electricity without any penalization has been evaluated for all the power plants considered and referred to the first construction year (2002), except for microsystems, whose economic data in open literature are not yet detailed enough and, however, are expected to lower by much in next years. The presence of innovative components such as the humidification tower in the HAT cycle and the ceramic heat exchanger in the EFCC cycle require some rough preliminary assumptions to calculate capital costs: for the humidification tower, a cost equal to the economizer cost has been considered; for the high-temperature heat exchanger, a cost equal to ten times the cost of a metallic recuperator with the same exchanging surface has been supposed, in order to also comprehend external combustor cost and the major operating and maintenance costs.

It should be noted that capital costs do not affect CET values, because they only depend on the process irreversibilities, which are economically evaluated using the fuel cost c_f (see Eq. (4) and Eq. (5)).

Figure 1 shows the COE of each plant before and after CET imposition. Considering the unpenalized COE, the HAT cycle has the lowest electricity cost (3.74 c\$/kWh), despite the fact that it does not achieve the high efficiency of the three-level-pressure combined cycle: This is due to the high specific work (800 kJ/kg) and the absence of the bottoming cycle which make the HAT cycle a compact and cheap power plant. The oil-fueled EFGTCC has an electricity cost similar to the CC3LP (3.84 c\$/kWh): In

Table 3 Main economic assumptions. When double values, the first is for a simple gas turbine cycle.

| | |
|---|-----------------------|
| O&M cost (% of purchased equipment cost) | 4% |
| Inflation | 2.5% |
| Nominal escalation rate of purchased equipment cost | 2.5% |
| Nominal escalation rate of fuel cost | 3.0% |
| Construction initial year (1 Jan) | 2002 |
| Construction time | 1–2 years |
| Plant economic life (book life) | 15–20 years |
| Plant Life for tax purposes | 10 years |
| Debts—financing fraction | 50% |
| Preferred stocks—financing fraction | 15% |
| Common equities—financing fraction | 35% |
| Debts—required annual return | 5.5% |
| Preferred stocks—required annual return | 6% |
| Common equities—required annual return | 6.5% |
| Average income tax rate | 30% |
| Coal price | 2.4e-6 \$/kJ |
| Oil price | 3.2e-6 \$/kJ |
| Natural gas price | 4.0e-6 \$/kJ |
| Demineralized water price | 0.5 \$/m ³ |
| Equivalent operating hours | 4000–8000 |

Table 2 Main plant characteristics

| Plant | Fuel type | Net Power [MW] | Efficiency |
|---------------|-----------------|----------------|------------|
| PFBC | Coal | 356 | 0.420 |
| EFCC3LP | Oil | 354 | 0.502 |
| Standard ENEL | Coal | 320 | 0.423 |
| CC3LP | Natural Gas | 200 | 0.537 |
| HAT | Natural Gas | 50 | 0.528 |
| RWI | Natural Gas | 50 | 0.486 |
| STIG | Natural Gas | 50 | 0.459 |
| GT | Natural Gas | 30 | 0.398 |
| GToil | Oil | 30 | 0.393 |
| mHAT | Natural Gas | 0.5 | 0.317 |
| EFmGT | Natural Gas+Oil | 0.5 | 0.292 |

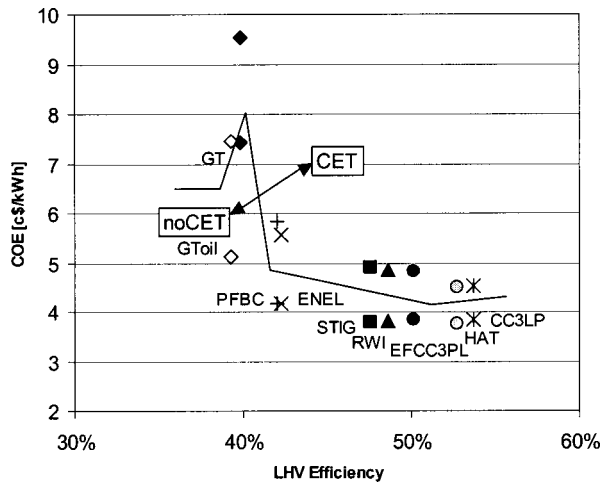


Fig. 1 Cost of electricity with or without CET

fact, even if it burns cheaper fuel (oil instead of natural gas), it is heavily affected by the capital costs of the high-temperature heat exchanger and NO_x and SO_x abatement equipment. The coal-fueled plants (standard ENEL and PFBC combined cycle) show low conversion efficiencies (less than 44%) that do not allow their COE to compete with the other systems, despite the low cost of coal (Table 3). Simple gas turbine COEs demonstrate that such a technology can stand alone only for peak power purposes: For that reason 4000 equivalent operating hours have been set for a simple GT, while 8000 have been set for the other plants.

If the CET is applied to all power plants (CET and FCET values are discussed in depth in the following paragraph), a considerable increase in the COE can be observed (Fig. 2): up to 30 percent for natural gas-fueled plants and over 35 percent for oil-fueled and coal-fueled plants.

Among the non-gas-fueled plants, only the EFGTCC shows a COE increase lower than 30 percent, because of the great impact of capital costs on the total revenue requirement. Oil-fueled and coal-fueled plants suffer a greater penalization due to the higher mass content of carbon fuel, which is taken into account by the index of CO_2 emission ($I_{\text{CO}_2}^*$).

In Fig. 3 the hyperbolic relationship between $I_{\text{CO}_2}^*$ and plant LHV efficiency is shown. Each different fuel (or mixture of fuels) has its own hyperbole as a function of plant efficiency (Eq. (7)).

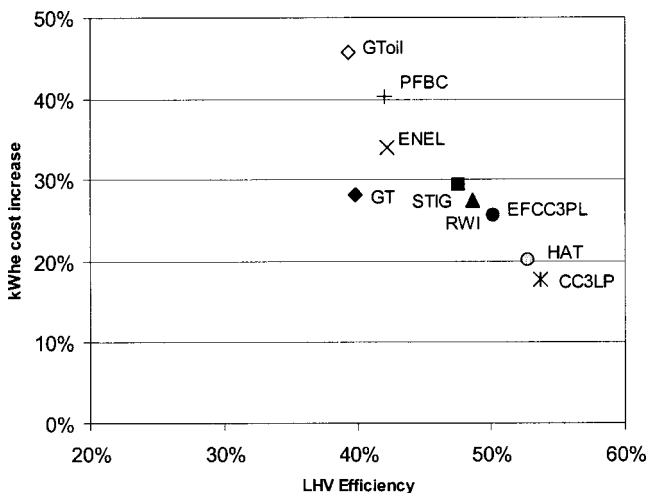


Fig. 2 Electricity cost increase with CET

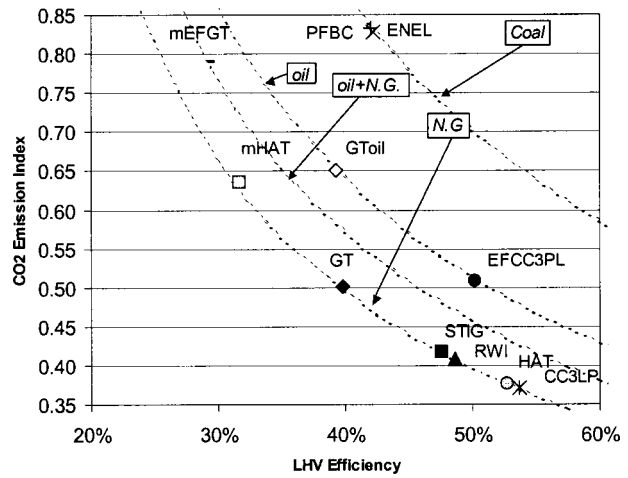


Fig. 3 CO_2 emission index versus LHV efficiency

Values of $[C]$ and LHV for fuels are reported in Table 1: Regarding fuel mixtures, LHV and $[C]$ are averaged on mass flow rates.

The following relationship between the values of $I_{\text{CO}_2}^*$ for fuel "x" and fuel "y" for the same plant efficiency η can be derived from Eq. (7):

$$\frac{I_{\text{CO}_2x}^*}{I_{\text{CO}_2y}^*} = \frac{[C]_x \text{LHV}_y}{[C]_y \text{LHV}_x} \quad (13)$$

The most efficient plants with low CO_2 emissions, such as HAT and CC3LP, are the least penalized and so they become the most economic choice for investment; on the other hand, the oil-fueled and coal-fueled plants, due to the high carbon content of their fuel, cease to be competitive. In this way economic savings match environmental issues because the most efficient and less-emitting plants become the most attractive solutions for the energy market.

Generalized Carbon Exergy Tax (CET)

The complete procedure for CET evaluation, fully described in the previous paragraphs, is too complex to become a feasible instrument of energy policy. In addition, many thermodynamic data are required to carry out the complete thermo-economic analysis: often the necessary information is not available or not even directly accessible. Here it is shown that the results of the complete method allow a simplified approach to be developed: The simplified CET and FCET are named "generalized" because they can be easily applied to all power plants. The generalized CET and FCET evaluations require much less information about the energy system and thus offer a simpler and more effective energy policy regulation to manage global warming.

Figures 4 and 5 show the CET and FCET for the studied plants: A hyperbolic-like curve can be traced to interpolate the calculated values, but the analytical correlation is more complex. In the present paper the following function is proposed:

$$y = a \left(\frac{1}{x} - 1 \right)^b \quad (14)$$

where y represents the generalized CET (GenCET) or the generalized FCET (GenFCET) and x stands for LHV efficiency. Such an equation has two important characteristics that belong to the complete CET procedure:

1. taxation equal to infinite for a zero-efficiency and
2. taxation equal to zero for a unit-efficiency.

It is important to state that in (14) only two parameters are used: "a" and "b." The former defines the level of taxation

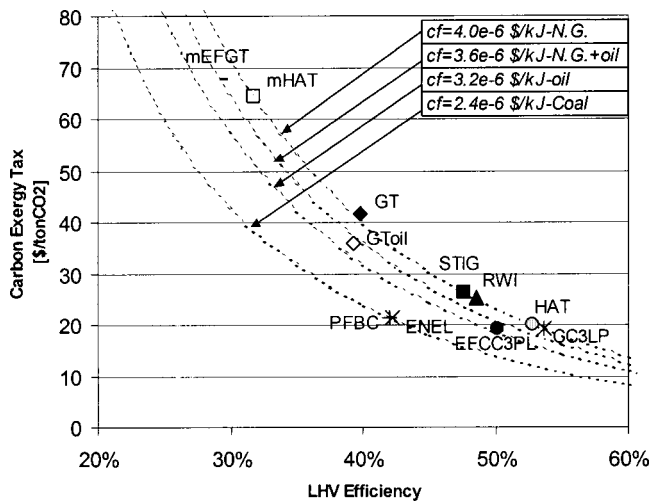


Fig. 4 CET and generalized CET versus LHV efficiency

(it is the GenCET or GenFCET applied to a plant achieving 50 percent efficiency), while the latter influences the curve trend. Values of “a” and “b” for generalized CET and FCET are shown in Table 4.

Considering the carbon exergy tax, GenCET curves (dotted curves in Fig. 4) depend only on the fuel cost c_f used in (4,5) to calculate the charge, and do not depend on fuel carbon content and fuel LHV (for fuel mixtures, c_f is averaged on mass flow rates): c_f is the driving factor for GenCET and ensures market-linked taxation. This is a very interesting result because a single generalized CET law can be defined and then applied to all power systems according to their fuel cost, whatever their size and whatever type of fossil fuel is used.

For midsize and large-size plants, with calculated efficiencies in the range 43–53 percent, the resulting CET is always in the interval 30–15 \$/tonCO₂: These values are in good agreement with the

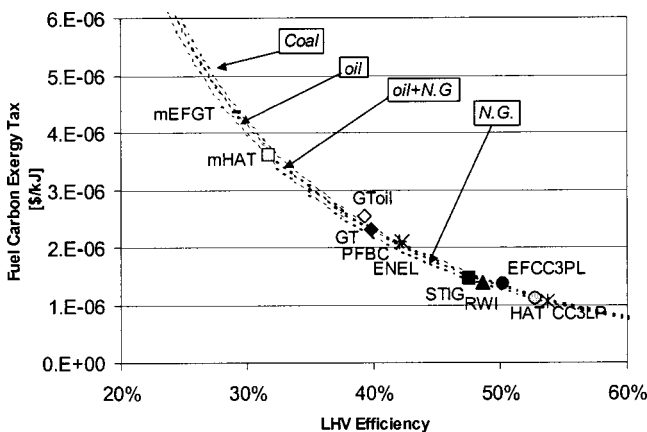


Fig. 5 FCET and generalized FCET versus LHV efficiency

Table 4 Values of “a” and “b” for generalized CET and FCET (Figs. 4 and 5)

| | Coal | Oil | N.G. + Oil | N.G. |
|----------------------------|----------|----------|------------|----------|
| GenCET | | | | |
| a [\$/tonCO ₂] | 13.943 | 18.590 | 20.914 | 23.238 |
| b | 1.325 | 1.325 | 1.325 | 1.325 |
| GenFCET | | | | |
| a [\$/kJ] | 1.406e-6 | 1.330e-6 | 1.334e-6 | 1.284e-6 |
| b | 1.325 | 1.325 | 1.325 | 1.325 |

break-even carbon tax indicated in [13] to economically sustain CO₂ sequestration. In addition, the detailed thermoeconomic analysis of the CO₂ sequestration facility integrated with a simple gas turbine cycle with original efficiencies in the range 36–41 percent, carried out in [27], shows that only a carbon tax at the 45–65 \$/tonCO₂ level can make CO₂ sequestration economically feasible: such a value is very close to the generalized CET correspondent for such an efficiency range. In that respect, it is very interesting to note that an objective and nonarbitrary method like the CET, for penalising the CO₂ emissions through an internalisation of costs connected to plant inefficiencies, is capable of giving similar results: It means that the calculated external “thermoeconomic” cost for CO₂ emissions is equal to the “technical” cost for preventing such emissions from happening. This unforegone link demonstrates the reliability of thermoeconomics as an analytical and powerful tool for energy system analysis and the capabilities of the CET as an effective regulation for managing global warming.

The FCET (Fig. 5), that is the equivalent charge imposed on the fuel price, depends not only on fuel cost but also on fuel carbon content and LHV, as issued by (11). So, coal is more heavily charged than oil and oil more heavily charged than natural gas, even if there is little difference between them.

However, fuel costs increase by up to 100 percent for small-size applications while by no more than 50 percent for midsize and large-size plants: However, such a considerable cost rise is justified only by an international energy policy aimed at globally reducing CO₂ emissions.

The calculated FCET for the EFmGT cycle is an average charge, because it has to be divided between the two fuels (natural gas and oil): For instance, an equal percent cost increase criterion can be used.

When comparing CET (and FCET) values with GenCET (and GenFCET) curves for oil-fueled plants, the former seem to be too high: In fact, they lie above the corresponding generalized curve, which has been calculated on the basis of the results of gas-fueled plants. Such a problem would not be present if exergy efficiency replaced LHV efficiency in the abscissa. The relationship between the two efficiencies is

$$\frac{\eta_{ex}}{\eta} = \frac{LHV}{Ex_f} \quad (15)$$

Generalized curves have been based on gas-fueled plant CETs (and FCETs). Generalized curves for the other fuels have been obtained moving the curves based on gas-fueled plants proportionally to fuel cost (and, for FCETs, also to $I_{CO_2}^*$). Since the ratio expressed by (15) is equal to 0.975 for natural gas and 0.938 for oil, if exergy efficiency replaced LHV efficiency in Figs. 4 and 5, the oil-fueled plant CET and FCET would be “pushed back” more than those of gas-fueled plants in such graphics and would “ride” the generalized curve.

To obtain an easy-to-apply method for CO₂ emission penalization, LHV efficiency has been preferred to exergy efficiency because it is much more diffused in the energy system field: However, referring to the complete CET evaluation, the exergy efficiency would be conceptually more correct.

Parameters “a” and “b” in (14) have been calculated in the efficiency range 30–55 percent, but such a correlation can be extended to the whole range.

In fact, Fig. 6 demonstrates that the proposed correlation well represents the carbon exergy tax results: The extrapolated value of CET compared with the one calculated in [21] for the hybrid gas turbine-fuel cell plant called FCGT4 and achieving 73.2 percent LHV efficiency, shows a quite satisfactory agreement: the published CET is 8.21\$/tonCO₂; actually, considering the different assumptions regarding fuel equivalent cost and fuel composition, the reference value becomes 6.7\$/tonCO₂; the generalized CET correlation gives the value of 6.14\$/tonCO₂.

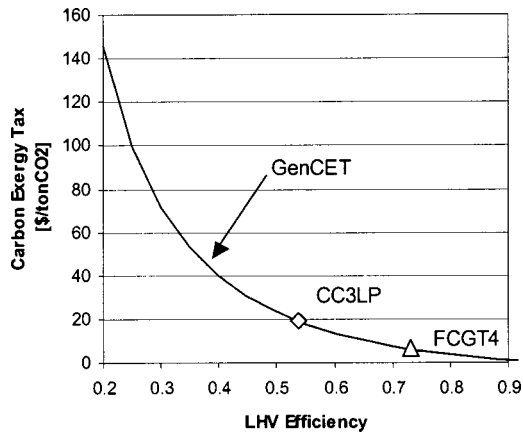


Fig. 6 Wide-range efficiency generalized CET with c_f equal to $4.0e-6$ \$/kJ

Since the CET rises dramatically at low efficiencies and becomes quite flat at high efficiencies, an upper limit for the CET (e.g., 70\$/ton_{CO₂}) and a target LHV efficiency (e.g., 70 percent), after which no carbon tax would be charged, could be imposed in order to strongly push the energy market beyond such a limit, favoring the implementation of the most innovative solutions, such as hybrid fuel cell systems.

Conclusions

An effective and generalized method for CET and FCET evaluation has been developed and it can easily be applied to all power plants. It is based on the rigorous results of CET calculation and it takes into account plant net efficiency and the type of fossil fuel. Such a method only requires the following information about the energy system:

- net LHV efficiency,
- average fuel cost,
- average carbon mass fraction $[C]$ for the employed fuels, and
- average LHV for the employed fuels.

In a deregulated energy market, CO₂ emission penalization through a generalized CET can

- push the energy industry towards the most innovative, efficient, and environmentally sustainable technical solutions,
- make CO₂ sequestration economically feasible and competitive,
- increase the utilization of renewables, and
- help countries to achieve the Kyoto targets and, in that respect, to improve the life of all the people in the world.

In this paper only plants for electrical generation have been studied, without considering cogeneration systems. In that respect, while the complete thermoeconomic procedure for CET evaluation can be immediately applied to cogenerative systems, the generalized method should be further developed.

Acknowledgments

The authors gratefully acknowledge the support of a mURST “Cofinanziamento 1999” grant.

Nomenclature

- c_f = economic fuel cost (\$/kJ)
 c_e = unit inefficiency penalty of input exergy flow (\$/kJ)
 c_w = unit inefficiency penalty of residual exergy flow (\$/kJ)

- C_{CO_2} = charge to emitted CO₂ (\$/yr)
 C_{irr} = destroyed exergy cost(\$/s)
 C_w = residual exergy cost(\$/s)
 $[C]$ = fuel carbon mass fraction (kg_C/kg_{fuel})
CET = carbon exergy tax (\$/ton_{CO₂})
COE = cost of electricity (\$/kWh)
 Ex_f = fuel exergy content (kJ/kg)
FCET = fuel carbon exergy tax (\$/kJ)
GenCET = generalized CET (\$/kJ)
GenFCET = generalized FCET (\$/kJ)
 $I_{CO_2}^*$ = index of CO₂ emission (kg/kWh)
 $I_{CO_2,ref}^*$ = reference index of CO₂ emission (kg/KWh)
 G_{CO_2} = emitted CO₂ mass flow rate (ton/yr)
 G_F = fuel mass flow rate (kg/s)
 k^* = unit exergetic cost (kJ/kJ)
 k_i^* = unit exergetic cost of input exergy flow of the i th component (kJ/kJ)
 k_p^* = unit exergetic cost of the exergy product of the plant (kJ/kJ)
LHV = low heating value (kJ/kg)
 N = equivalent operating hours
NC = number of components of the plant
 p = pressure (bar)
 N = number of components of the plant
 T = temperature (K)
 \mathbf{x} = vector of plant technical characteristics
 W_{el} = plant electrical power output (kW)

Greek Letters

- α = CO₂ production per mass of C (kg_{CO₂}/kg_c)
 η = plant LHV efficiency
 η_{ex} = plant exergy efficiency
 Δc_{el} = electricity cost increase due to CET(\$/kj)
 Π_e = inefficiency penalty (\$/yr)
 Ψ_e = input exergy flow (kW)
 Ψ_{irr} = exergy destroyed (kW)
 Ψ_o = output exergy flow (kW)
 Ψ_p = plant product exergy content (kWh/yr)
 Ψ_w = residual exergy rejected by the plant (kW)

References

- [1] OECD, 1994, “Managing the Environment: The Role of Economic Instruments,” Organization for Economic Cooperation and Development, Paris.
- [2] Goodstein, E. S., 1999, *Economics and the Environment*, Prentice-Hall, Englewood Cliffs, NJ.
- [3] Parkin, M., Powell, M., and Matthews, K., 1997, *Economics*, Addison-Wesley, Reading, MA.
- [4] Borchellini, R., Massardo, A. F., and Santarelli, M., 2000, “An Analytical Procedure for the Carbon Tax Evaluation,” *Energy Convers. Manage.*, **41**, Sept.
- [5] Borchellini, R., Massardo, A. F., and Santarelli, M., 2000, “A Carbon Tax Evaluation Based on the Efficient Use of Energy Resources,” *Int. J. Appl. Thermodyn.*, **3**(3), pp. 129–145.
- [6] Santarelli, M., 1998, “Considerazioni Termodinamiche, Economiche ed Ambientali nella Analisi ed Ottimizzazione di Sistemi Energetici,” Ph.D. thesis, Dipartimento di Energetica, Politecnico di Torino, Torino, Italy.
- [7] Santarelli, M., Borchellini, R., and Massardo, A. F., 1999, “Environmental Optimization for Combined Plants Including CO₂ Influence,” IGTI Turbo Ekpo ’99, Indianapolis, IN, June, ASME, New York.
- [8] Santarelli, M., Traverso, A., Cali, M., and Massardo, A. F., 2001, “La Metodologia dell’Efficiency Penalty Quale Criterio Termoeconomico di Penalizzazione delle Emissioni di CO₂,” X Convegno Tecnologie E Sistemi Energetici Complessi “Sergio Stecco,” Genova.
- [9] Massardo, A. F., Santarelli, M., and Borchellini, R., 2000, “Carbon Exergy Tax (CET): Impact on Conventional Energy Systems Design and Its Contribution to Advanced Systems Utilisation,” *ECOS 2000*, University of Twente, The Netherlands, July, ASME, New York.
- [10] Langeland, K., and Wilhelmsen, K., 1993, “A Study of the Costs and Energy Requirement for Carbon Dioxide Disposal,” *Energy Convers. Manage.*, **34**(9–11).
- [11] Summerfield, I. R., Goldthorpe, S. H., Williams, N., and Sheikh, A., 1993, “Costs of CO₂ Disposal Options,” *Energy Convers. Manage.*, **34**(9–11).
- [12] Schiappacasse, R., and Squeri, S., 1999, “CO₂ Capture and Sequestration Study,” degree thesis, DIMSET, Università di Genova, Genova, Italy.

- [13] Santarelli, M., Borchiellini, R., and Massardo, A. F., 1999, "Carbon Tax vs CO₂ Sequestration Effects on Environmental Analysis of Existing Power Plants," *ECOS '99*, Tokyo, Japan, June, ASME, New York.
- [14] Brandani, M., and Bozzolo, M., 2001, "Study of Power Plants With CO₂ Sequestration Fed by Hydrogen From Fuel Decarbonisation," degree thesis, DIMSET, Università di Genova, Genova, Italy.
- [15] Agazzani, A., and Massardo, A. F., 1997, "A Tool for Thermo-economic Analysis and Optimization of Gas, Steam, and Combined Plants," *ASME J. Eng. Gas Turbines Power*, **119**, pp. 885–892.
- [16] Agazzani, A., Massardo, A. F., and Frangopoulos, C. A., 1998, "Environmental Influence on the Thermo-economic Optimization of a Combined Plant With NO_x Abatement," *ASME J. Eng. Gas Turbines Power*, **120**, p. 557.
- [17] Massardo, A. F., and Scialò, M., 2000, "Thermo-economic Analysis of Gas Turbine Based Cycle," *ASME J. Eng. Gas Turbines Power*, **122**.
- [18] Traverso, A., 2000, "Thermo-economic Analysis of STIG, RWI and HAT cycles With Carbon Dioxide (CO₂) Emissions Penalty," degree thesis, DIMSET, Università di Genova, Genova, Italy.
- [19] Traverso, A., and Massardo, A. F., 2001, "Thermo-economic Analysis of Mixed Gas-Steam Cycles," *Applied Thermal Engineering*, **22**, Elsevier, New York, 1–21.
- [20] Lozano, M., and Valero, A., 1993, "Theory of the Exergetic Cost," *Energy-Int. J.*, **18**, p. 939.
- [21] Massardo, A. F., and Lubelli, F., 2000, "Internal Reforming Solid Oxide Fuel Cell-Gas Turbine Combined Cycles (IRSOFC-GT): Part A—Cell Model and Cycle Thermodynamic Analysis," *ASME J. Eng. Gas Turbines Power*, **122**.
- [22] Consonni, S., Macchi, E., and Farina, F., 1996, "Externally Fired Combined Cycles (EFCC). Part A/B," *ASME Paper Nos. 96-GT-92/93*.
- [23] Cohen, H., Rogers, G. F. C., and Saravanamuttoo H. I. H., 1996, *Gas Turbine Theory*, 4th Ed., Longman House, London.
- [24] Ansaldo Ricerche (ARI), 2001, private communication, Genova, Italy.
- [25] Rosén, Per M., 2000, "Evaporative Cycles—In Theory and in Practice," doctoral thesis, Lund Institute of Technology, Sweden.
- [26] Magistri, L., Traverso, A., Scarpellini, R., and Zito, D., 2001, "Sviluppo di un Sistema a Combustione Esterna con Microturbina a Gas per la Generazione Distribuita," *Tecnologie e Sistemi Energetici Complessi "Sergio Stecco"*, Genova.
- [27] Bozzolo, M., Brandani, M., Massardo, A. F., and Traverso, A., "Thermo-economic Analysis of a Gas Turbine Plant With Fuel Decarbonisation and CO₂ Sequestration," *ASME Paper No. GT-2002-30120*.

A New Scaling Method for Component Maps of Gas Turbine Using System Identification

C. Kong

e-mail: cdgong@mail.chosun.ac.kr

J. Ki

e-mail: kijayoung@hanmir.com

M. Kang

e-mail: k0914@stmail.chosun.ac.kr

Department of Aerospace Engineering,
Chosun University,
#375 Seosuk-dong,
Dong-gu,
Kwangju 501-759, Korea

A scaling method for characteristics of gas turbine components using experimental data or partially given data from engine manufacturers was newly proposed. In case of currently used traditional scaling methods, the predicted performance around the on-design point may be well agreed with the real engine performance, but the simulated performance at off-design points far away from the on-design point may not be well agreed with the real engine performance generally. It would be caused that component scaling factors, which were obtained at on-design point, is also used at all other operating points and components' maps are derived from different known engine components. Therefore to minimize the analyzed performance error in the this study, first components' maps are constructed by identifying performances given by engine manufacturers at some operating conditions, then the simulated performance using the identified maps is compared with performances using currently used scaling methods. In comparison, the analyzed performance by the currently used traditional scaling method was well agreed with the real engine performance at on-design point but had maximum 22% error at off design points within the flight envelope of a study turboprop engine. However, the performance result by the newly proposed scaling method in this study had maximum 6% reasonable error even at all flight envelope. [DOI: 10.1115/1.1610014]

Introduction

Performance simulation is one of the most important activities not only to minimize risk and cost in development phase but also to monitor engine health in operation phase.

In order to simulate gas turbine performance it is absolutely needed that a condition, which each engine performance must follow its own components' performance, should be satisfied, [1]. Generally components' characteristics are obtained from component performance tests at various operating and environmental conditions. However, it can be usually done in case of engine development stage. Moreover, it is not generally disclosed to engine users because of very expensive and important technical data. Therefore engine users or engineers, who are observing engine performance, have been mostly utilizing the known engine components' characteristics by scaling.

Even though there are various scaling methods, current traditional methods are mostly using a technique, where first the scaling factors for the derived maps are derived from comparison between a design point data of original known performance maps and a new design point then scaled maps can be obtained by multiplying the derived scaling factors to off-design point data of the original performance maps, [2,3]. However, this technique may be reasonable if the derived scaling factors are close to 1.0 because it means having similar performance between the original engine and the scaled engine. Therefore, the performance analysis result using this technique nearby the on-design point may be usually agreed well with the measured performance result of the scaled engine. However, if calculation at off-design points is performed far away from the on-design point, it has generally a drawback that the error of calculation by this technique may increase. Therefore, in order to reduce the analyzed performance error, a new scaling method for characteristics of gas turbine components

using experimental data or partially given data from engine manufacturers was proposed. This method can be realized using the following procedure: it is that first after obtaining the scaling maps with the scaling factors of components from the known performance data or the known experimental data by engine manufacturers at some operation points, and then constructing the new component maps using the system identification technique, which build a mathematical model between input (scaling factors at some given conditions) and output parameters (pressure ratio, mass flow rate, and efficiency) with polynomial equations, and finally analyzing the engine performance with the identified maps.

For this study, P&WC PT6A-62 turboprop engine was used for a calculation example, which has been a power plant of Korean indigenous basic trainer KT-1. Basic data for identification of component maps are uninstalled performance at sea level, 3000 m (10,000 ft), 6000 m (20,000 ft) and 9000 m (30,000 ft) altitudes, and standard atmosphere conditions.

After analyzing performance at deferent altitude and flight M.N. conditions with uninstalled and installed conditions using the newly obtained component maps, their results were compared with the results using component maps obtained from the currently used scaling method.

Engine Specification

The engine selected for analysis is the PT6A-62 free-turbine turboprop engine. The engine's shaft horsepower is 857.9 kW (1150 hp) at sea level, but flat rated at around 708.7 kW (950 hp). The engine has a compressor with three axial stages and a single centrifugal stage, a reversed flow combustor, single-stage compressor turbine with cooled NGV and blades, and a two-stage uncooled power turbine.

The selected propeller for PT6A-62 of the Korean basic trainer was Hartzell HC-E4V-3Exl/E9512CX model, which is four blades, constant speed of 2000 rpm, featherable, and 95 inches diameter, [4]. The station number and layout for performance analysis of the study engine is shown in Fig. 1.

Table 1 shows the performance data at maximum takeoff condition, which were provided by the engine manufacturer, [5].

Contributed by the International Gas Turbine Institute (IGTI) of THE AMERICAN SOCIETY OF MECHANICAL ENGINEERS for publication in the ASME JOURNAL OF ENGINEERING FOR GAS TURBINES AND POWER. Paper presented at the International Gas Turbine and Aeroengine Congress and Exhibition, Amsterdam, The Netherlands, June 3–6, 2002; Paper No. 2002-GT-30150. Manuscript received by IGTI, Dec. 2001, final revision, Mar. 2002. Associate Editor: E. Benvenuti.

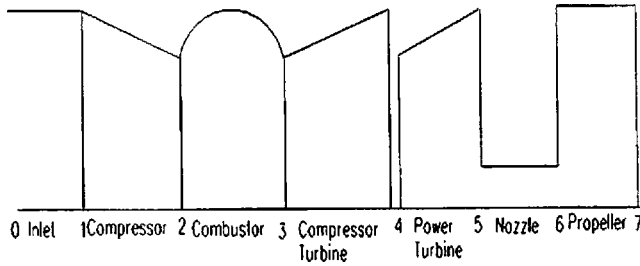


Fig. 1 Station number and layout of the study engine

Traditional Scaling Method

The currently used traditional scaling method is a way to obtain scaled component maps by multiplying scaling factors derived at the on-design point to the original component maps at off-design points: The scaling equations used in this method are expressed as follows, [2]:

$$PR = \frac{PR_D - 1}{PR_{M.D.} - 1} (PR_M - 1) + 1 \quad (1)$$

$$\dot{m} = \frac{\dot{m}_D}{\dot{m}_{M.D.}} \dot{m}_M \quad (2)$$

$$\eta = \frac{\eta_D}{\eta_{M.D.}} \eta_M \quad (3)$$

As shown in the first column of Table 2, there are the design point performance data taken from compressor, compressor turbine and power turbine maps, which are obtained from GAS-TURB program, [6]. And the second column has the design point data taken by PT6A-62 turboprop engine, and the third column has the calculated scaling factors using above equations.

This method may usually be effective if the scaling factors of scaled component maps are close to 1.0 range of 1.0. However, if they are far away from 1.0, this method may generally be inaccurate.

Table 1 Performance data by engine manufacturer

| Variable | Values |
|---|-------------------------------------|
| Atmospheric condition | Sea level static standard condition |
| Mass flow rate (kg/s) | 4.18 |
| Fuel flow rate (kg/s) | 0.0818 |
| Shaft horse power (hp) | 1150 |
| S.F.C. (kg/kw·hr) | 0.3433 |
| Nozzle throat area (m ²) | 0.058 |
| Gas generator rotational speed (100% rpm) | 37468 |
| Propeller rotational speed (100% rpm) | 2000 |

Table 2 The scaling factor using traditional scaling method

| Component | | M.D. (GASTURB) | Design data (PT6A-62) | S.F. |
|--------------------|--------|----------------|-----------------------|--------|
| Compressor | PR | 15.275 | 9.4 | 0.5885 |
| | MFP | 7.2245 | 4.18 | 0.5786 |
| | η | 0.8076 | 0.77 | 0.9535 |
| Compressor turbine | PR | 2.4252 | 3.34367 | 1.6445 |
| | MFP | 46.499 | 16.5848 | 0.3498 |
| | η | 0.8011 | 0.88 | 1.0985 |
| Power turbine | PR | 2.5844 | 2.5538 | 0.9807 |
| | MFP | 64.9699 | 48.9868 | 0.7540 |
| | η | 0.8635 | 0.88 | 1.0191 |

Table 3 The scaling factor using novel scaling method

| Alt. | | 0 m | 3048 m | 6096 m | 9144 m |
|--------------------|--------|--------|--------|--------|--------|
| Compressor | PR | 0.5885 | 0.5716 | 0.5500 | 0.4664 |
| | MFP | 0.5786 | 0.5538 | 0.5455 | 0.5461 |
| | η | 0.9535 | 0.9535 | 0.9535 | 0.9535 |
| Compressor turbine | PR | 1.6636 | 1.4822 | 1.3675 | 1.3053 |
| | MFP | 0.3466 | 0.3498 | 0.3498 | 0.3498 |
| | η | 1.0985 | 1.0985 | 1.0985 | 1.0985 |
| Power turbine | PR | 0.9808 | 1.1904 | 1.3153 | 1.4264 |
| | MFP | 0.7379 | 0.7054 | 0.7031 | 0.7023 |
| | η | 1.0191 | 1.0191 | 1.0191 | 1.0191 |

Newly Proposed Scaling Method

Generally the design point performance, for instance performance at maximum takeoff power condition, would be revealed to engine users. Therefore each component performance can be approximately calculated using well-known thermodynamic equations and the revealed performance. From these calculated pressure ratio, mass flow rate and efficiency of each component, the scaling factors can be obtained using Eqs. (1), (2), and (3).

If performance data, such as power, specific fuel consumption ratio, etc., at some off-design points can be known from engine manufacturers or experimental tests, scaling factors at some conditions can be calculated. In this case, if component maps, which are obtained with scaling factors at some conditions, can be performed by the system identification, the closer component maps to real engine may be obtained, where the system identification defines that it builds a mathematical model between input values and output values of a system.

In this study, the mathematical model was built using polynomial equations, where the input value was the scaling factor of each component map which was obtained from engine manufacturers' performance data at the flight M.N. 0, and the altitude 0, 3048 m (10,000 ft), 6096 m (20,000 ft), and 9144 m (30,000 ft), and the output values were performance parameters such as pressure ratio, mass flow parameter, and efficiency of each component using the obtained scaling factors. Component maps used in the present study were maps for compressor, compressor turbine, and power turbine and each component has 20 beta-lines per a corrected rotational speed, where the corrected rotational speed defines as follows:

$$CN = \frac{N}{\sqrt{\theta}} \quad (4)$$

where θ is $T_1/288.15$. Therefore the corrected rotational speed is 100% at sea level, 103.63% at 3048 m (10,000 ft), 107.68% at 6096 m (20,000 ft), and 112.4% at 9144 m (30,000 ft), respectively.

Calculation Example. First, pressure ratio, mass flow parameter, and efficiency were calculated to obtain the scaling factors for compressor, compressor turbine, and power turbine using air mass flow rate, fuel flow rate, shaft horsepower at the flight M.N. 0, and the altitude 0, 3048 m (10,000 ft), 6096 m (20,000 ft), and 9144 m (30,000 ft), which were obtained from the PT6a-62 engine manufacturer's performance data, [3]. Table 3 shows scaling factors at four conditions obtained using Eqs. (1), (2), and (3). Secondly, four sets of component maps were derived using each set of scaling factors obtained at four conditions.

It can be assumed that pressure ratio, mass flow parameter, and efficiency have the following linear function for the corrected rotational speeds at each beta-line:

$$y = ax + b \quad (5)$$

where y is the pressure ratio, mass flow parameter, and efficiency, respectively, and x is the corrected rotational speed. Polynomial coefficients a and b were calculated using polyfit that is an m-file

of the MATLAB program. And then polynomial equations from each beta-line were derived using polyval.m of the MATLAB program. However, the scaling factors for component efficiencies are fixed at the design point value because they are almost constant at four conditions and exhibit simplification of calculation.

Finally, each component map was identified from 70% rpm to 110 rpm using the derived polynomial equations.

Figure 2 shows comparison between component maps obtained by the newly proposed scaling method (solid curves) and component maps obtained by the traditional scaling method (dotted curves).

Steady-State Performance Analysis

In the steady-state performance analysis at off-design points, the following assumptions and equations were considered.

The airflow passed through the intake, the compressor, the compressor turbine, and the power turbine must be constant. Therefore, the following flow compatibility equations can be applied to this type of the engine, [1].

$$\frac{\dot{m}_a \sqrt{T_{03}}}{P_{03}} = \frac{\dot{m}_a \sqrt{T_{01}}}{P_{01}} \times \frac{P_{01}}{P_{02}} \times \frac{P_{02}}{P_{03}} \times \sqrt{\frac{T_{03}}{T_{01}}} \quad (6)$$

$$\frac{\dot{m}_a \sqrt{T_{04}}}{P_{04}} = \frac{\dot{m}_a \sqrt{T_{03}}}{P_{03}} \times \frac{P_{03}}{P_{04}} \times \sqrt{\frac{T_{04}}{T_{03}}} \quad (7)$$

The work done by the compressor and the turbine connected with the same shaft must be the same. Therefore, work compatibility of the gas generator presents as the following equation:

$$\eta_m C_{Pg} \Delta T_{034} = C_{Pa} \Delta T_{012} \quad (8)$$

The steady-state performance analysis was carried out at the uninstalled and installed conditions. Figure 3 shows the flow chart of the steady state program, which satisfies the above conditions.

Performance Analysis at Uninstalled Condition. At the uninstalled condition, the bleed air for cooling and heating in a cockpit and the accessory power extraction were not considered. In addition, the pressure losses at inlet duct and at nozzle caused by engine installation to the aircraft were ignored, [3].

When both gas generator and power turbines were running at 100% rpm, the uninstalled performance was analyzed in the changes of the altitude using the developed program. Where the altitude interval from sea level to 9144 m (30,000 ft) was 1534 m (5000 ft) and the flight Mach number was fixed at zero.

Table 4 and Fig. 4 show the result that the manufacturer's performance data (M.D.) are compared with the results using the newly proposed scaling method (N.M.) and the traditional method (T.M.), respectively.

In investigation of the analysis results, the performance using the traditional scaling method, was well agreed upon with real engine performance data at the on-design point, but the performance at off-design points did not agreed well with real engine performance data. However, in the case of the new scaling method, it was noted that the analysis results at overall operation range have a relatively reasonable error within 5%. Therefore, in this study, it was confirmed that the newly proposed scaling method would be more effective than the traditional scaling method.

Performance Analysis at Installed Condition. When an engine is installed on an aircraft, it happens that the temperature rises and the pressure drops in the inlet duct, the bleed air loss is due to cooling and heating for the cockpit and the power loss is due to accessory power extraction. Moreover, the effective exhaust area was influenced by the exhaust pressure loss, [3,5].

In this study, the performance was analyzed at both ECS (Environmental Control System) off condition and maximum operation of ECS. Table 5 shows loss values, which were provided by the PT6A-62 engine manufacturer.

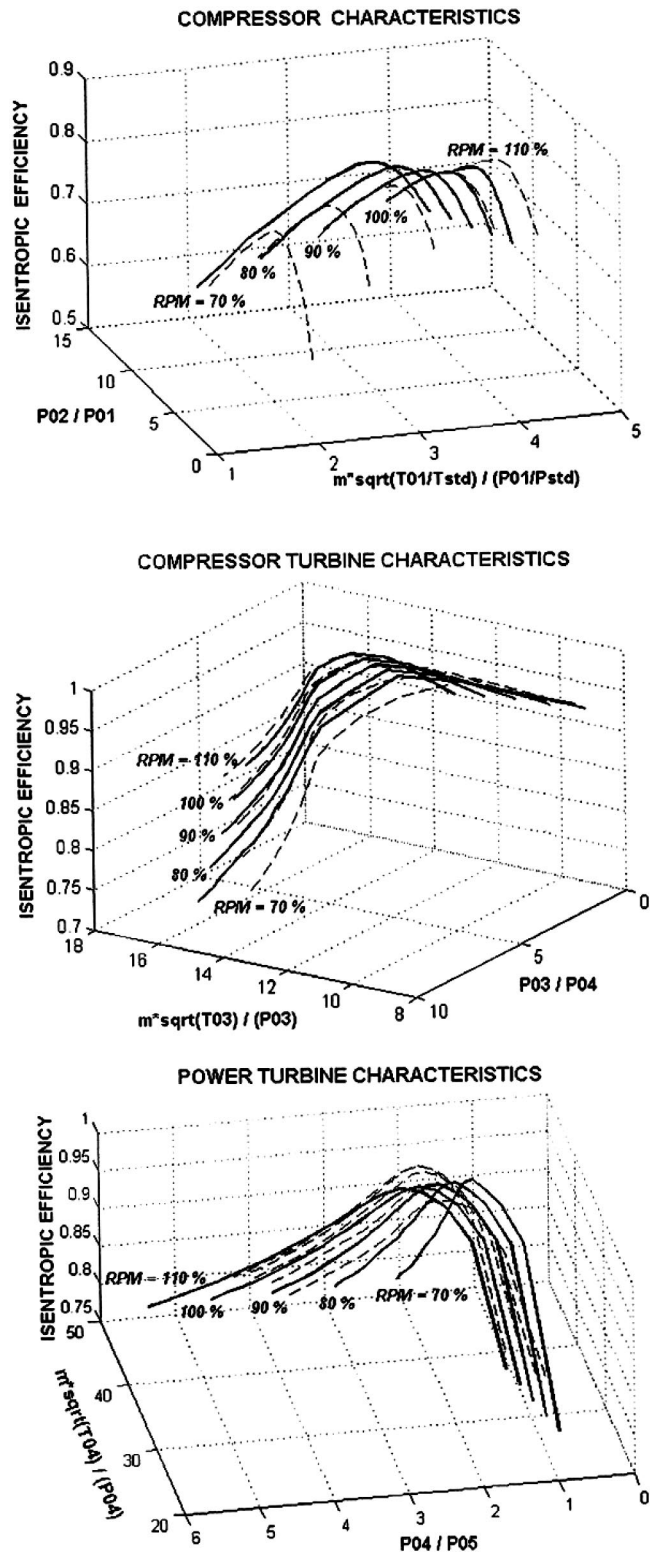


Fig. 2 Comparison between component maps obtained by the newly proposed scaling method (solid curves) and component maps obtained by the traditional scaling method (dotted curves)

Table 6 and Fig. 5 show the result that the manufacturer's performance data (M.D.) are compared with the results using the newly proposed scaling method (N.M.) and the traditional method (T.M.) in installed performance analysis at the ECS off condition, flight M.N.=0.27, 0.38, 0.48, and sea level.

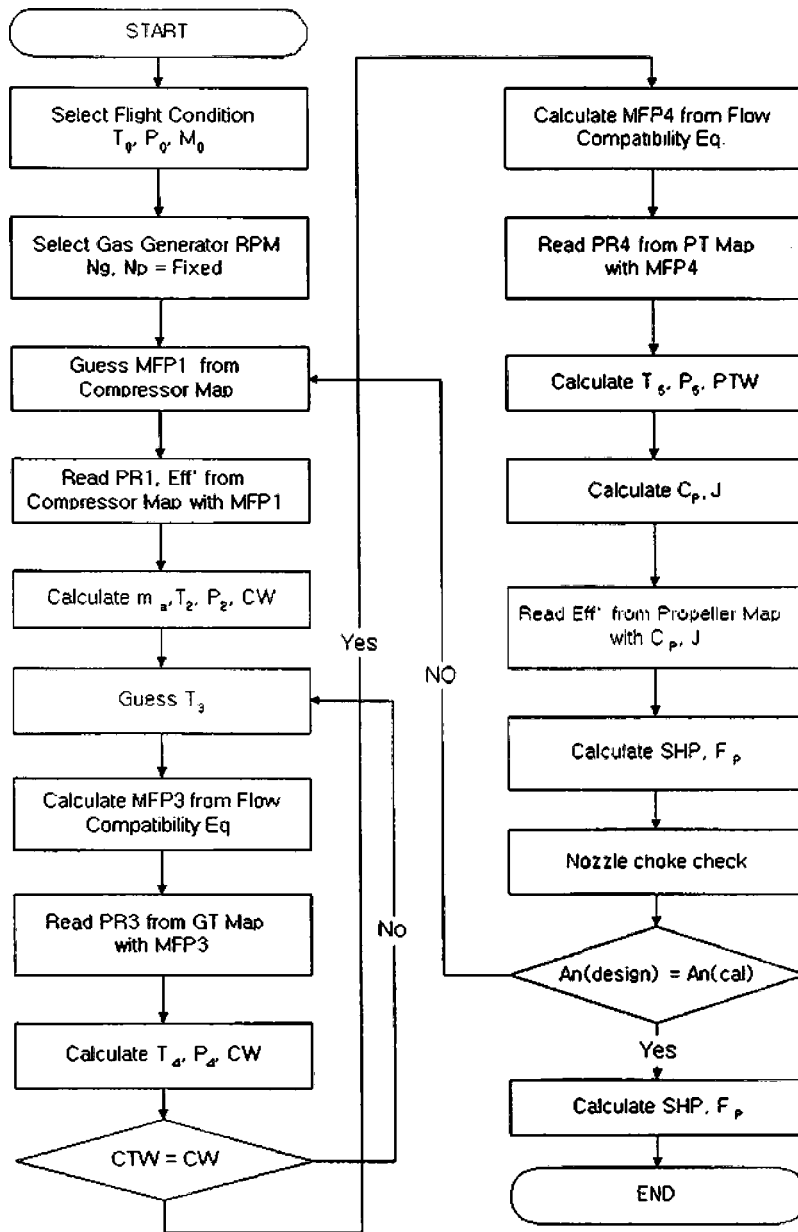


Fig. 3 Flow chart of steady state performance calculation program

Table 7 and Fig. 6 show the result that the manufacturer's performance data (M.D.) are compared with the results using the newly proposed scaling method (N.M.) and the traditional method (T.M.) in installed performance analysis at ECS maximum condition, flight M.N.=0.27, 0.38, 0.48, and sea level.

In this investigation, it was found that the analysis results using the newly proposed scaling method at overall operation range have a relatively reasonable error within 6%. Therefore, it could be stated that the newly proposed scaling method would be more effective than the traditional scaling method.

Conclusion

In this study, in order to reduce the analysis performance error of the traditional scaling method, a new scaling method for characteristics of gas turbine components using experimental data or partially given data from engine manufacturers was proposed.

Flow of the newly proposed scaling method is as follows: obtaining the scaling maps with the scaling factors of components from the known performance data or the known experimental data

Table 4 Uninstall performance with altitude variation

| Alt. | Variable | M.D. | T.M. | % Err | N.M. | % Err |
|------|--------------|--------|--------|-------|--------|-------|
| 0 | m_a (kg/s) | 4.18 | 4.1821 | 0.05 | 4.18 | 0. |
| | m_f (kg/s) | 0.0818 | 0.0818 | 0.00 | 0.0819 | 0.12 |
| | SHP | 1150. | 1150.2 | 0.02 | 1149.8 | 0.01 |
| 1524 | m_a (kg/s) | 3.357 | 3.6729 | 9.41 | 3.5029 | 4.35 |
| | m_f (kg/s) | 0.0724 | 0.0693 | 4.28 | 0.0703 | 2.90 |
| | SHP | 1070. | 977.7 | 8.63 | 1037.9 | 3.01 |
| 3048 | m_a (kg/s) | 3.0385 | 3.2560 | 7.16 | 3.0902 | 1.70 |
| | m_f (kg/s) | 0.0642 | 0.0622 | 3.12 | 0.0608 | 5.30 |
| | SHP | 980. | 866.2 | 11.6 | 934.3 | 4.67 |
| 4572 | m_a (kg/s) | 2.63 | 2.7744 | 5.49 | 2.6263 | 0.14 |
| | m_f (kg/s) | 0.0562 | 0.0507 | 9.79 | 0.0540 | 3.92 |
| | SHP | 868. | 710.0 | 18.2 | 833.7 | 3.95 |
| 6096 | m_a (kg/s) | 2.23 | 2.3658 | 6.09 | 2.2325 | 0.11 |
| | m_f (kg/s) | 0.0466 | 0.0442 | 5.15 | 0.0447 | 4.08 |
| | SHP | 740. | 608.7 | 17.7 | 705.0 | 4.73 |
| 7620 | m_a (kg/s) | 1.88 | 1.9795 | 5.29 | 1.8802 | 0.01 |
| | m_f (kg/s) | 0.0393 | 0.0353 | 10.2 | 0.0376 | 4.33 |
| | SHP | 625. | 488.5 | 21.8 | 591.3 | 5.40 |
| 9144 | m_a (kg/s) | 1.57 | 1.6619 | 5.85 | 1.5680 | 0.13 |
| | m_f (kg/s) | 0.0334 | 0.0303 | 9.28 | 0.0319 | 4.49 |
| | SHP | 520. | 412.2 | 20.7 | 514.9 | 0.99 |

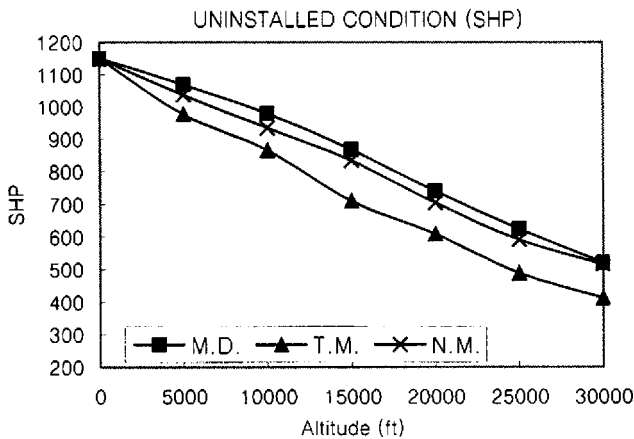
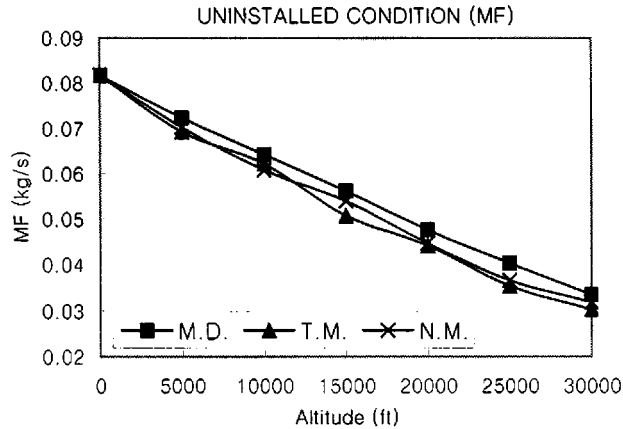
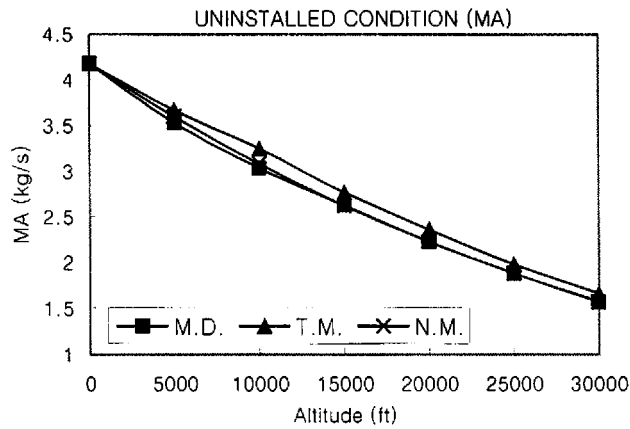


Fig. 4 Results of uninstal performance analysis with altitude variation (flight Mach No.=0)

Table 5 Loss by install to an aircraft

| Coefficient | ECS off | ECS max |
|------------------------|----------------------|----------------------|
| Inlet efficiency | 1.0 | 0.9922 |
| Inlet temp. rise | 3K | 3K |
| Bleed air loss | 0% | 5.25% |
| Power extraction | 3.73 kW | 5.22 kW |
| Effective exhaust area | 0.0477m ² | 0.0477m ² |

Table 6 Installed performance at the ECS off condition

| M.N. | Variable | M.D. | T.M. | % Err. | N.M. | % Err. |
|------|--------------|-------|-------|--------|-------|--------|
| 0.27 | m_a (kg/s) | 2.245 | 2.405 | 7.14 | 2.278 | 1.49 |
| | m_f (kg/s) | 0.047 | 0.040 | 14.68 | 0.047 | 0.43 |
| | SHP | 712. | 574.8 | 19.27 | 720.3 | 1.17 |
| 0.38 | m_a (kg/s) | 2.381 | 2.493 | 4.72 | 2.373 | 0.34 |
| | m_f (kg/s) | 0.049 | 0.042 | 15.31 | 0.049 | 1.02 |
| | SHP | 764. | 596.8 | 21.89 | 749.6 | 1.88 |
| 0.48 | m_a (kg/s) | 2.522 | 2.602 | 3.16 | 2.488 | 1.34 |
| | m_f (kg/s) | 0.049 | 0.043 | 11.84 | 0.047 | 4.08 |
| | SHP | 792. | 624.6 | 21.13 | 747.0 | 5.69 |

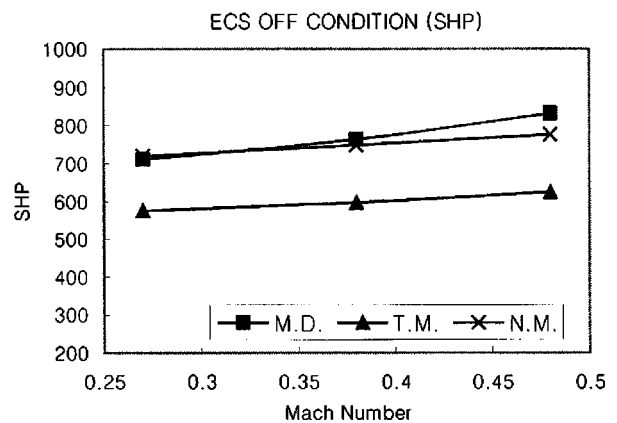
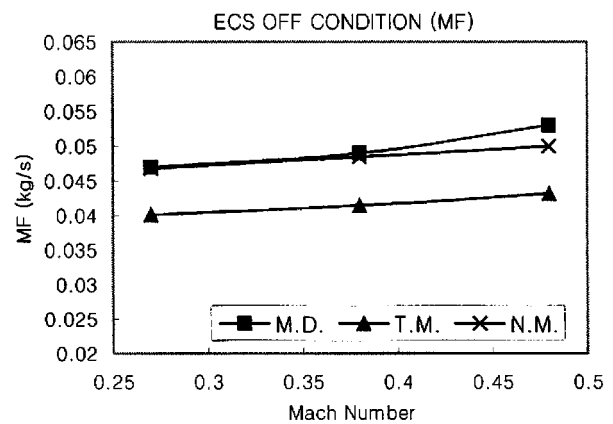
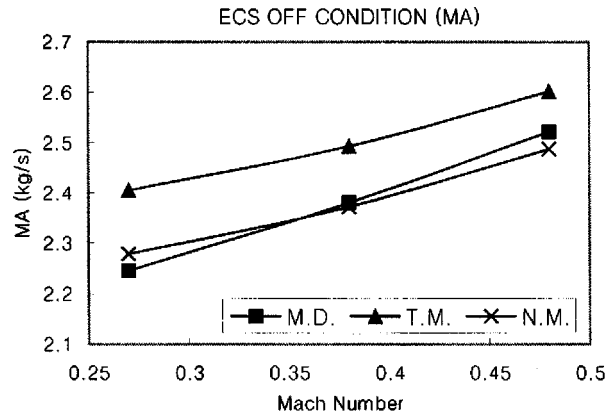


Fig. 5 Results of installed performance analysis at ECS off condition (flight Mach No.=0.27, 0.38, and 0.48, altitude=0 m)

Table 7 Installed performance at the ECS max condition

| M.N. | Variable | M.D. | T.M. | % Err. | N.M. | % Err. |
|------|--------------|-------|-------|--------|-------|--------|
| 0.27 | m_a (kg/s) | 2.223 | 2.404 | 8.2 | 2.300 | 3.45 |
| | m_f (kg/s) | 0.046 | 0.040 | 12.4 | 0.046 | 0.22 |
| | SHP | 600. | 546.0 | 9.0 | 612.1 | 2.01 |
| 0.38 | m_a (kg/s) | 2.249 | 2.491 | 10.8 | 2.383 | 6.0 |
| | m_f (kg/s) | 0.048 | 0.042 | 13.3 | 0.048 | 0.42 |
| | SHP | 653. | 566.6 | 13.2 | 686.0 | 5.05 |
| 0.48 | m_a (kg/s) | 2.386 | 2.599 | 8.91 | 2.493 | 4.47 |
| | m_f (kg/s) | 0.049 | 0.043 | 11.6 | 0.047 | 3.27 |
| | SHP | 716. | 592.5 | 17.2 | 712.5 | 0.49 |

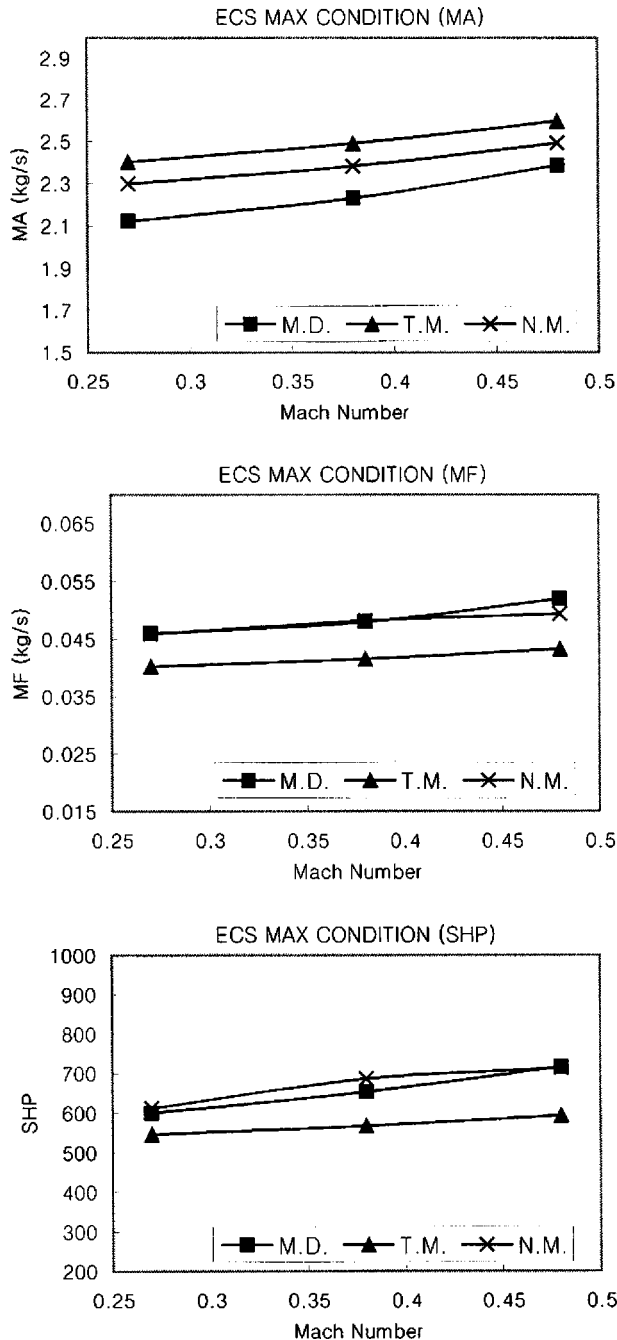


Fig. 6 Results of installed performance analysis at ECS maximum condition (flight Mach No.=0.27, 0.38, and 0.48, altitude=0 m)

by engine manufacturers at some operation points, and then constructing the new component maps using the system identification technique, which build a mathematical model between input (scaling factors at some given conditions) and output parameters (pressure ratio, mass flow rate, and efficiency) with polynomial equations, and finally analyzing the engine performance with the identified maps.

For this study, a P&WC PT6A-62 turboprop engine was used for a calculation example. After analyzing performance in uninstalled and installed conditions at different altitude and variation of flight M.N. using component maps obtained from the newly proposed scaling method, their results were compared with the results using component maps obtained from the traditional scaling method. In this investigation, it was found that the analysis results using the newly proposed scaling method at overall operation range have a relatively reasonable error within 6%. Therefore it could be stated that the newly proposed scaling method would be more effective than the traditional scaling method.

Acknowledgment

This study was supported by research funds from Chosun University, 2003.

Nomenclature

- CN = corrected rotational speed
- C_p = specific heat at constant pressure
- M.D. = provided data by manufacturer
- MFP = mass flow parameter
- M.N. = flight Mach number
- \dot{m} = mass flow rate
- \dot{m}_a = air mass flow rate
- \dot{m}_f = fuel flow rate
- N = true rotational speed
- N.M. = new scaling method for component maps
- PR = pressure ratio
- rpm = revolution per minute
- S.F. = scaling factor
- SHP = shaft horse power
- T.M. = traditional scaling method for component maps
- η = isentropic efficiency

Subscripts

- C = compressor
- CT = compressor turbine
- D = design point map values of scaled components
- M = arbitrary map values
- $M.D.$ = design point map values of original components
- a = air
- g = combustion gas
- m = mechanical
- 1, 2 = inlet and outlet station of compressor
- 3, 4 = inlet and outlet station of compressor turbine
- 5 = outlet station of power turbine
- 6 = nozzle throat

References

- [1] Cohen, H., Rogers, G. F. C., and Saravanamuttoo, H. I. H., 1996, *Gas Turbine Theory*, 4th Ed., Longman, London.
- [2] Sellers, J. F., and Daniele, C. J., 1975, "DYNGEN-A Program for Calculating Steady-State and Transient Performance of Turbojet and Turbofan Engines," NASA-TN D-7901.
- [3] Kong, C. D., and Ki, J. Y., 2001, "Performance Simulation of Turboprop Engine for Basic Trainer," ASME Paper No. 01-GT-391.
- [4] Kong, C. D., 2000, "Propulsion System Integration of Turboprop Aircraft for Basic Trainer," ASME Paper No. 00-GT-10.
- [5] Na, J. J., 1996, "A Study on PT6A-62 Engine Install Performance Analysis," Agency of Defense Development, Technical Report.
- [6] Kurzke, K., 1999, *GASTURB 8.0 Manual*.
- [7] Douglas, I. E., 1986, "Development of a Generalized Computer Program for Gas Turbine Performance Simulation," Ph.D. thesis, Cranfield University, Cranfield, UK.

- [8] Kong, C. D., and Chung, S. C., 1999, "Real Time Linear Simulation and Control for Small Aircraft Turbojet Engine," *KSME Int. J.*, **13**, pp. 656–666.
- [9] Palmer, J. R., and Yan, C.-Z., 1985, "TURBOTRANS—A Programming Language for the Performance Simulation of Arbitrary Gas Turbine Engines With Arbitrary Control Systems," *Int. J. Turbo Jet Engines*, **2**, pp. 19–28.
- [10] Schobeiri, M. T., Attia, M., and Lippke, C., 1994, "GETRAN: A Generic, Modularly, Structured Computer Code for Simulation of Dynamic Behavior of Aero-and Power Generation Gas Turbine Engines," *ASME J. Eng. Gas Turbines Power*, **116**, pp. 483–494.
- [11] Seldner, K. et al., 1972, "Generalized Simulation Technique for Turbojet Engine System Analysis," NASA-TN-D-6610.

Off-Design Performance Analysis of a Hybrid System Based on an Existing Molten Fuel Cell Stack

P. Bedont

e-mail bedont@ari.ansaldo.it
Ansaldo Fuel Cells,
Genova, Italy

O. Grillo

A. F. Massardo

e-mail: massardo@unige.it

Thermochemical Power Group (TPG),
Dipartimento di Macchine Sistemi Energetici e
Trasporti,
Università di Genova,
Genova, Italy

This paper addresses the off-design analysis of a hybrid system (HS) based on the coupling of an existing Ansaldo Fuel Cells (formerly Ansaldo Ricerche) molten carbonate fuel cell (MCFC) stack (100 kW) and a micro gas turbine. The MCFC stack model at fixed design conditions has previously been presented by the authors. The present work refers to an off-design stack model, taking into account the influence of the reactor layout, current density, air and fuel utilization factor, CO₂ recycle loop, cell operating temperature, etc. Finally, the design and off-design model of the whole hybrid system is presented. Efficiency at part load condition is presented and discussed, taking into account all the constraints for the stack and the micro gas turbine, with particular emphasis on CO₂ recycle control. [DOI: 10.1115/1.1587742]

Introduction

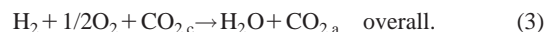
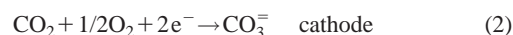
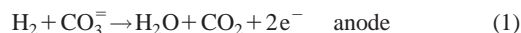
Fuel cells are electrochemical reactors that allow an efficient and ecological conversion of energy. High efficiency, close to 50%, also at part-load condition, and low pollution, make fuel cells a very interesting system for distributed power generation. Molten carbonate fuel cells (MCFCs) have been analyzed in this paper. Their name comes from the electrolyte employed, a mixture of alkaline carbonate (K,Na), inserted into a ceramic matrix (LiAlO₂); the anode and cathode are made of Ni powder, via a proper tape-casting process. MCFCs belong to the "high temperature" fuel cell class: the operating range is about 600–700°C, in which the electrolyte has a good ionic conductivity.

In this work the MCFC stack has been considered with reference to an existing Ansaldo fuel cells plant, named a fuel cell system (FC), [1], based on a molten carbonate fuel cell stack (100 kW size), a sensible heat reformer (SHR), and two catalytic burners. In a previous paper, the MCFC group performance was presented and analyzed by the authors, [2]. As already discussed in the cited paper, the MCFC operating temperature (600–700°C) well matches the gas turbine inlet one; therefore, in a pressurized hybrid system configuration, an MCFC stack substitutes the turbine combustor. Such a plant configuration is attracting wide interest as a solution to some of the key problems of small-size turbines (low efficiency and NO_x emission, due to the presence of the combustor) and MCFC stacks (high cost). The on-design efficiency of such an MCFC hybrid system has been evaluated as close to 60%, as discussed by the authors for a small-size hybrid system (electrical power around 130 kW), [3].

The small size of the plant and its application in the distributed power field justify the study of its performance at part load condition. For this reason, the design and off-design performance of the hybrid system (HS), based on the Ansaldo fuel cells (FC), is presented and discussed in this paper, on the basis of a model realized by coupling the design/off-design models of the micro gas turbine and the MCFC unit.

1 Molten Carbonate Fuel Cell (MCFC) Stack and Model

The fuel cell system is made of a molten carbonate fuel cell, shown in Fig. 1, a sensible heat reformer (SHR), and two catalytic burners; the presence of blowers is due to pressure loss compensation. The whole plant is pressurized at 0.35 MPa. Figure 2 shows the proof of concept power plant Ansaldo Fuel Cells MCFC, while Fig. 3 shows a simplified process scheme of the whole hybrid system, obtained by the coupling of an MCFC group (FC-represented inside the dashes) and a gas turbine. As shown in the scheme, the electrochemical reactions taking place in the MCFC stack are reported below:



Besides the electrochemical one, the water-gas shift reaction, whose equation is as follows, takes place in the anode:



The stack is fed with a mixture of H₂, CO, CO₂, H₂O (anodic side) and with air and CO₂ (cathodic side). The products of the overall reaction are electrical power, heat, steam, and the transfer of CO₂ (in the form of CO₃⁻) from the cathode to the anode through the electrolyte. A plant simulation model was previously realized in Fortran language, [1]. Such a model, positively tested by experimental data, allows a thermal-economic analysis of the plant. Nevertheless, being a variable geometry model, it only allows the analysis of the design point conditions, [4]. Thus, in order to study the off-design working conditions of the plant, a new model, written in Simulink, a graphic toolbox of Matlab language, was developed, [5]. The model structure is based upon the energy balance equation. From Nernst's equation, it is possible to evaluate the thermodynamic voltage, corresponding to the open circuit condition. When electrical current is drawn from the stack, voltage losses arise due to irreversibility; these losses can be classified as ohmic losses, owing to the ohmic resistance of the stack elements, and polarization losses, mainly due to an impoverishment of the anodic and cathodic gases, [6].

In the model realized, input data are stack area, chemical and thermodynamic characteristics of inlet flow rates, temperature, pressure and composition, current density. The starting assumptions are reported below:

Contributed by the International Gas Turbine Institute (IGTI) of THE AMERICAN SOCIETY OF MECHANICAL ENGINEERS for publication in the ASME JOURNAL OF ENGINEERING FOR GAS TURBINES AND POWER. Paper presented at the International Gas Turbine and Aeroengine Congress and Exhibition, Amsterdam, The Netherlands, June 3–6, 2002; Paper No. 2002-GT-30115. Manuscript received by IGTI, Dec. 2001, final revision, Mar. 2002. Associate Editor: E. Benvenuti.

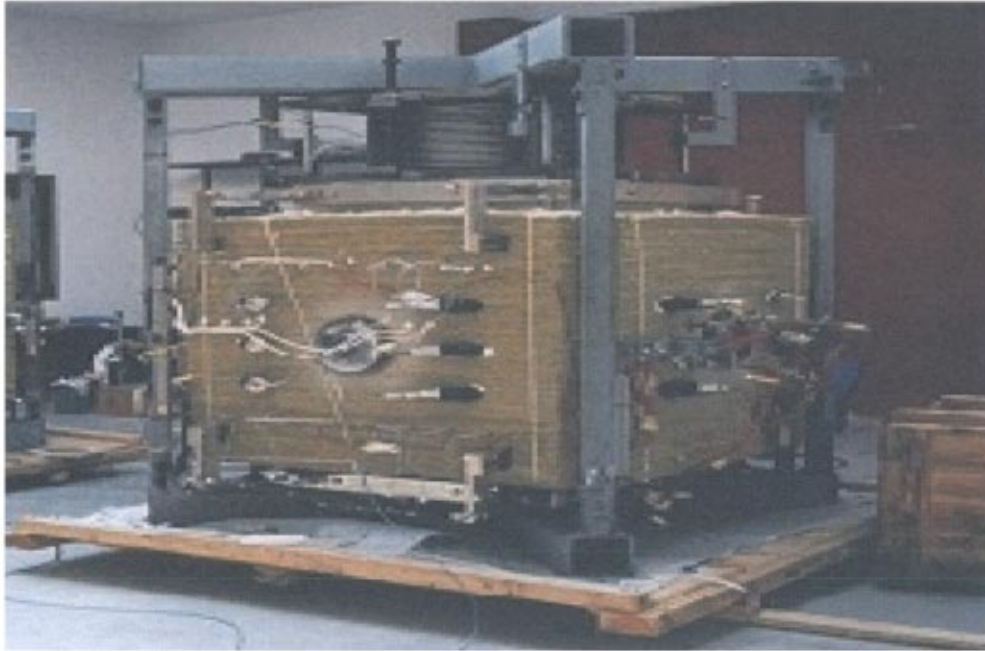


Fig. 1 Molten carbonate fuel cell (MCFC) stack (Ansaldo Fuel Cells)

- cathodic flow rate composition: O_2 , N_2 , H_2O , CH_4 , and CO_2 ;
- anodic flow rate composition: H_2 , CH_4 , CO , CO_2 , and H_2O ;
- shift reaction at equilibrium;
- operating temperature considered as the average value between outlet gas temperatures.

Current value is known, as it depends on input data; the unknown term is the equilibrium temperature. The calculation is based on the stack energy balance equation, whose terms are calculable thanks to a first attempt value of T_{eq} . In particular, the program evaluates:

1. composition of outlet flow rates, since the shift equilibrium constant depends on the operating temperature, and the electrochemical reaction rate depends on current value (input data);
2. outlet flow rate specific heat;
3. heat flow rate associated with both electrochemical and shift reactions;
4. thermodynamic voltage and voltage losses, from which it is possible to calculate the electrical power value, since the current is known.

The calculation of heat transmission is based on the hypothesis



Fig. 2 Proof of concept power plant Ansaldo Fuel Cells MCFC

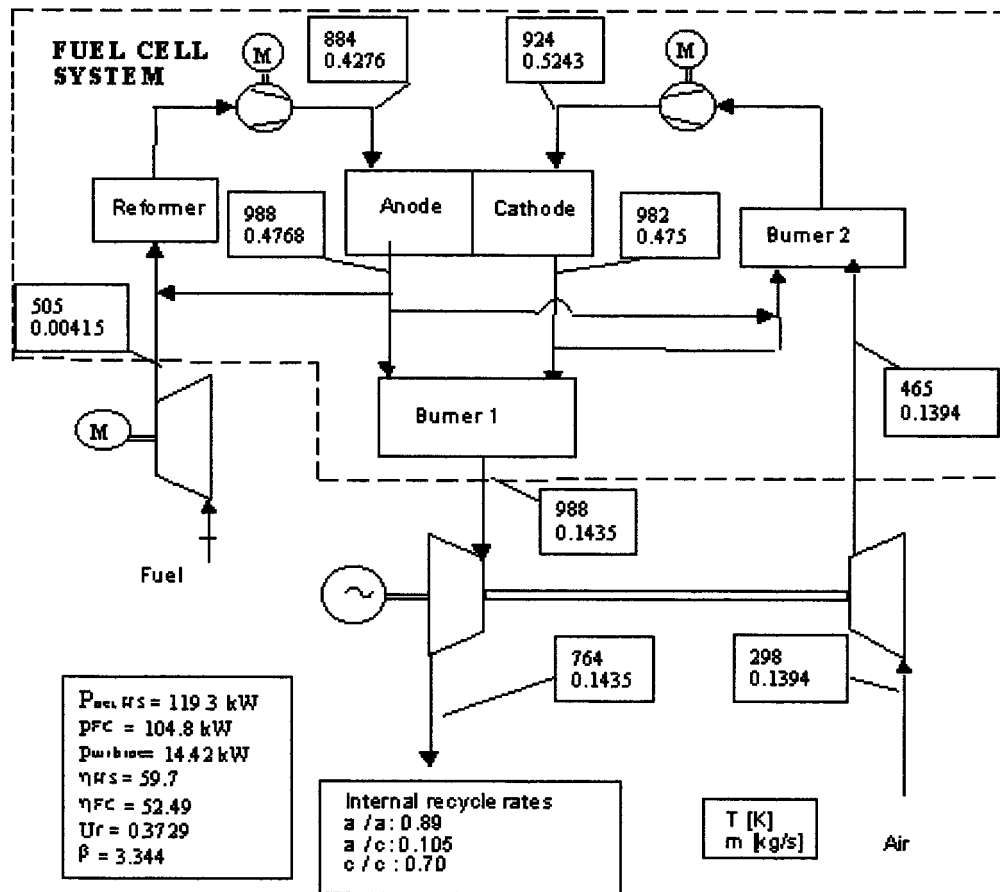


Fig. 3 Hybrid system simplified layout (fuel cell system is represented inside dashed boundary)

of sharing the electrochemical heat flow rate between the anode and cathode, on a fixed percentage; this assumption has been adopted in a previous modelization, [7]. The model makes an assumption of 3% of the electric power value for thermal dissipation. From the energy balance equation, it is possible to calculate outlet mass temperature and a new value of operating temperature for each electrode until data convergence. Moreover, the MCFC model takes into account internal gas recycles; at design point, their value is 89% anode to anode and 70% cathode to cathode, in order to recover effluent gas sensible heat, and 10.5% anode to cathode, in order to recycle CO_2 . A sensible heat reformer is a catalytic reactor whose function is to convert methane into a hydrogen richer mixture. Reactant sensible heat, thanks to the anodic exhausts recycle, provides the necessary energy so that the reforming reaction can occur (endothermic reaction). The model structure is based upon the energy balance equation. Input data are the chemical and thermodynamic characteristics (temperature, pressure, and composition) of the inlet flow rates. The unknown term is again equilibrium temperature. Thanks to a starting assumption of its value, it is possible to evaluate the composition of the outlet flow rates (since both reforming and shifting equilibrium constants depend on operating temperature), the specific heat of the outlet flow rates, and the heat flow rate associated with both the reforming and shifting reactions. From the balance equation it is possible to calculate the outlet temperature and a new value for the operating temperature until data convergence. The model for the burners, working at a fixed percentage of the reacted fuel, is also based upon the energy balance equation.

2 Fuel Cell System Performance

In order to understand the results of the overall plant simulation, the performance of the fuel cell system alone (not inserted in the hybrid system), is presented and discussed.

2.1 Design Point Performance. The operating conditions are reported in Table 1. The chemical and thermodynamic characteristics of the inlet flow rate at design point are shown in Table 2 since Table 3 shows the anode/cathode inlet and outlet compositions.

The FC supplies a net power of 104.3 kW (evaluated as the difference between the electrical power and the one absorbed by blowers) with an efficiency of 52.2%. Pressurization of the stack has not been considered in the evaluation of the performance. The

Table 1 Operating condition at design point

| Operating Condition | | |
|---------------------|-----------------------|-------|
| m fuel in | 0.00415 kg/s | |
| m air in | 0.139 kg/s | |
| Current density | 1580 A/m ² | |
| Recycle Rates | Anode to anode | 89% |
| | Anode to cathode | 10.5% |
| | Cathode to cathode | 70% |

Table 2 Chemical and thermodynamic characteristics of the FC inlet flow rate

| | T (°C) | p (MPa) | Composition % (Molar Fraction Rate) | |
|---------|----------|-----------|-------------------------------------|-------|
| Air in | 192 | 0.35 | O_2 | 20 |
| | | | N_2 | 80 |
| | | | H_2 | 6.15 |
| | | | H_2O | 4.17 |
| Fuel in | 232 | 0.35 | CH_4 | 89.68 |

Table 3 Chemical composition in the stack

| Molar Fraction Rate % | Cathode | | Anode | |
|-----------------------|---------|--------|-------|--------|
| | Inlet | Outlet | Inlet | Outlet |
| O ₂ | 11.12 | 9.48 | 0 | 0 |
| N ₂ | 71.64 | 76.92 | 0 | 0 |
| CO ₂ | 8.14 | 3.83 | 59.77 | 63.02 |
| H ₂ O | 9.07 | 9.74 | 24.25 | 27.7 |
| CH ₄ | 0.03 | 0.03 | 0.59 | 0.56 |
| CO | 0 | 0 | 5.80 | 4.52 |
| H ₂ | 0 | 0 | 9.59 | 4.20 |

single-pass fuel utilization factor, defined as the ratio between reacted fuel (H₂+CO) and fuel at the stack inlet (H₂+CO), is 0.4.

The model results have been verified, from a design point only, by comparison with

- the results of the above mentioned model, written in Fortran language, [4];
- the results of another simulation, [8].

The calculation error for temperature and composition values, in each module of the plant, is always less than 2%, [5].

2.2 Off-Design Performance. To evaluate off-design FC performance, it is necessary to make some considerations on operating limits and working conditions:

- stack inlet temperature greater than 580°C, in order to guarantee the molten condition of the carbonate;
- inlet cathode minimum percentage of CO₂: 9% (mass fraction rate).

At the first attempt, the FC off-design analysis was performed by prescribing a proportional reduction of both inlet flow rates (air and fuel) and current density, at fixed recycle rates. Following this operating procedure, the stack was fed with an excessive air flow rate, making the anode inlet temperature decrease under the operating values, already at 90% of rated power, as shown in Fig. 4. Therefore, to permanently keep the inlet temperatures over the limit, different operating conditions were adopted; they are illustrated in Figs. 5 and 6. Part-load condition is obtained by reducing fuel inlet flow rate and current density in proportion to the power generated (Fig. 5); the air inlet flow rate undergoes a greater reduction percentage, since a decrease in the air-to-fuel ratio is necessary to avoid the results shown in Fig. 4. In order to recover the outlet flow rate enthalpy, the plant works at increasing recycle rates (as for anode to anode and cathode to cathode ones). Despite its reduction, the anode to cathode recycle rate has to guarantee a sufficient percentage of CO₂ to the cathode. Following these operating conditions, FC thermodynamic efficiency increases by reducing the power supplied by the plant, as shown in Fig. 7. This fact can be explained on the basis of the cell characteristic curve:

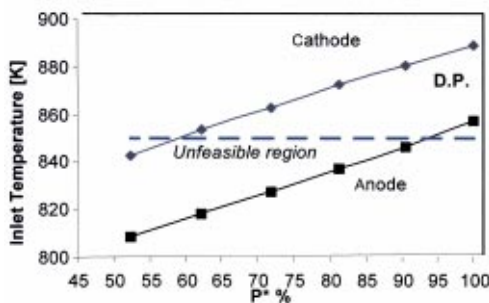


Fig. 4 Stack inlet temperatures by reducing power at fixed recycle rates

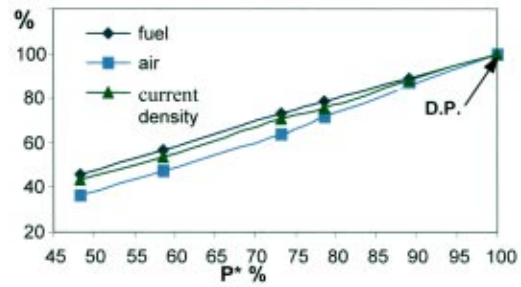


Fig. 5 Operating parameters at part-load condition

since the reactant content in the cell inlet streams is substantially constant. Under this condition, the reduction in current density produces a consequent increase in cell voltage. The lowering of the operating temperature has no particular influence on the ohmic losses and on the cell voltage, (Fig. 8), [5].

The parameters connected with the exploitation of the inlet flow rates are reported in Fig. 9. At rated power, the percentage of methane converted into hydrogen decreases, because of the lower temperature. The fuel (U_f) and oxygen (U_o) utilization rates are defined as the ratio between the reacted flow rate and the one fed to the stack ("single pass"). They both decrease, since the reacted flow rates depend on the imposed current density value (decreasing proportionally with rated power), while the percentage of reactant supplied to the stack is subjected to lower reductions thanks to the increase in the internal recycles. This definition of the fuel utilization rate does not take into account the recycle of the flow rate at the anode outlet. Actually, also considering the recycled fraction as reacted flow rate, the fuel utilization rate ($U_{f, total}$) increases by reducing the power, according to the plant efficiency trend, (Fig. 7), [9].

It is necessary to underline that the described operating conditions cannot be adopted after the coupling of the fuel cell system

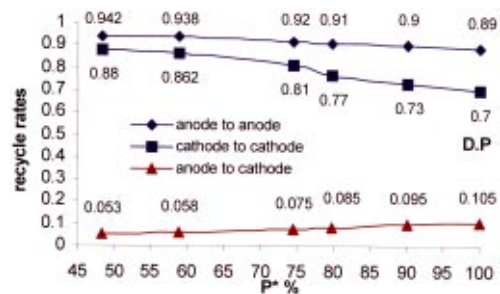


Fig. 6 Internal recycle rates at part-load condition

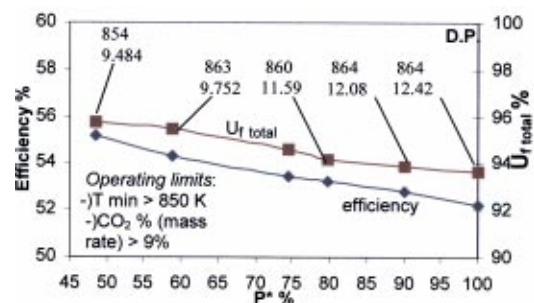


Fig. 7 CU efficiency and plant fuel utilization rate at part-load condition

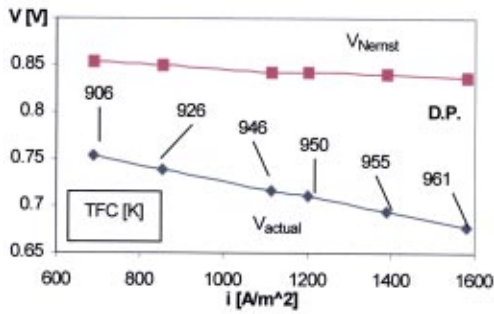


Fig. 8 Cell voltage and Nernst potential versus current density

with an MGT, without employing any dedicated solution, since the inlet air flow rate depends on the compressor and expander matching condition.

3 Molten Carbonate Fuel Cell (MCFC)—Hybrid System

Hybrid cycles are derived from the integration of high-temperature fuel cell technology (MCFC and SOFC) and small size gas turbines, whose temperature and pressure working conditions well match a pressurized stack, [3,10]. Figure 3 shows a schematic representation of a hybrid system FC-GT plant layout. The FC effluent gas enthalpy is exploited in a gas turbine, supplying additional power and that necessary to move the inlet air compressor. An auxiliary compressor performs the anode pressurization. The hybrid system model has also been written in Simulink [5]; simulation has been realized by coupling the FC model with the gas turbine and compressor models. In order to determine the matching of the air compressor and gas turbine, the unknown terms are compressor flow rate; pressure ratio; and compressor and turbine isentropic efficiencies, depending on operating conditions. Simulation requires an external loop for pressure ratio calculation and an internal one for flow rate and efficiency evaluation (for both turbine and compressor models). The input data for the compressor module are air inlet pressure and temperature, rotational speed and first-guess pressure ratio. The model is based on the compressor, [11], and expander maps, [12] (efficiency and pressure ratio versus nondimensional flow rate).

3.1 Hybrid System Design Performance. There are different ways to choose the design point of a hybrid system; for example, starting with the data of an existing stack and looking for a suitable turbine (if it exists). Another way of defining the HS design point, when the gas turbine has been defined, is an MCFC group designed to be fed with the same air flow rate, to operate at the turbine pressure, and to have an exhaust temperature equal to the turbine inlet one (TIT).

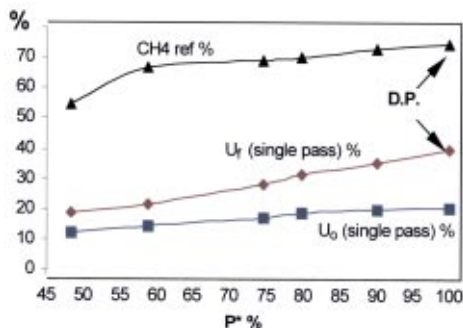


Fig. 9 Fuel cell system utilization rates at part-load condition

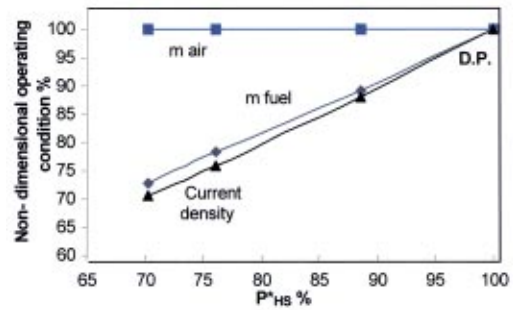


Fig. 10 Hybrid system (HS) operating parameters at part-load condition

In this study, the HS design point is the operating condition where turbine and compressor flow rates, rotational speed, and the pressure ratio are compatible with the existing fuel cell system design point parameters. In particular, they are: $m_{\text{fuel}} = 0.00415 \text{ kg/s}$; $m_{\text{air}} = 0.1394 \text{ kg/s}$; inlet temperature: 25°C ; inlet pressure: 0.1013 MPa ; pressure ratio: 3.4; current density: 1580 A/m^2 .

As shown in Fig. 3, the HS efficiency is close to 60%, which is noteworthy, taking into account the small size of the plant. Net power supplied by the hybrid system is 119 kW, 89% coming from the stack and 11% from the turbine. Power absorbed by the air compressor is about 23 kW (60% of the power supplied by the turbine expander). All the data regarding internal recycle rates at design point are equal to the fuel cell system ones (Fig. 3).

3.2 Hybrid System Off-Design Performance at Constant Turbine Rotational Speed. When a variable speed control system is not available, the only possible way of varying the power supplied by a system, including a gas turbine, is to vary the overall fuel flow rate. Air flow rate, in fact, depends on the compressor working condition; this is a limit for hybrid system efficiency at part load operation, since the stack does not work at its optimal condition. In order to manage the heat produced into the stack, and to avoid an excessive and undesirable cooling of the stack, as already discussed for the FC off-design behavior, two possibilities can be considered: increasing the cathodic recycle or supplying more fuel to the anodic side. The first one is limited by pressure losses, the second one causes a reduction in the whole efficiency, [7].

Figure 10 shows the fuel flow rate and current density operating conditions. The fuel reduction percentage is less than the power one, in order to keep the stack temperature over the operating limit ($T_{\text{min}} > 580^\circ\text{C}$), to the detriment of stack efficiency. The diagram also shows the inlet air flow rate, even if it is not an operating parameter (it depends on the MGT matching point), in order to better visualize the different working conditions between the FC alone and the FC inserted into the hybrid system (See also Fig. 5). The air inlet flow rate value remains almost constant, according to the compressor and expander maps, [5]. Figure 11 shows the internal recycle rates at part load condition; the cathode-to-cathode rate increases, as well as the anode-to-anode one, in order to avoid an excessive cooling of the electrodes, to the detriment of the CO_2 recycle.

Owing to the recycle rates values, the exhaust catalytic burner is almost inactive at design point; it is more used at part load condition, since the increase of cathode to cathode recycle rate causes a decrement of the air to fuel ratio. Figure 12 shows the performance of both the hybrid system and the FC at part load condition. The efficiency of the whole plant is calculated as the ratio between the net power produced and the LHV of the feeding fuel, while the FC efficiency is the ratio between the power supplied by the stack alone and the LHV of the fuel supplied to the plant. At a fixed turbine rotational speed, the FC efficiency is

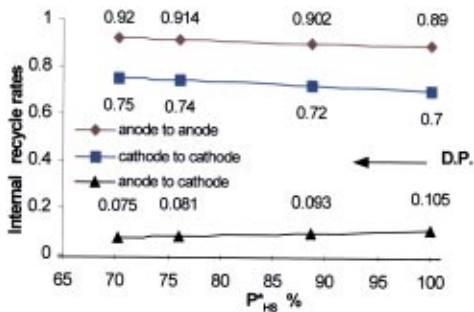


Fig. 11 Internal recycle rates at part-load condition

penalised by its insertion in the hybrid system, even if the plant fuel utilization rate ($U_{f, total}$) increases at rated power (since it takes into account the recycled flow rates, too). The impossibility of reducing the fresh air flow rate results in an excessive cooling of the stack; this leads to increase the fuel supply to the anode (in comparison to that supplied before the insertion into the hybrid system, at the same part load condition). Moreover, the operating temperature reduction causes an increase in electrical losses, besides limiting the operating range at rated power. Due to these facts and the results of the modelling, it is impossible to reduce the power below 75% of the design point value.

Figure 13 shows the sharing of net power between the stack and gas turbine, at part load condition: the FC net power is calculated as the difference between the electrical power and the power absorbed by the blowers (including the anodic compressor). The turbine net power is the difference between the power supplied by the turbine expander and that absorbed by the air compressor.

At part-load condition, the contribution of the stack increases since the turbine power is penalised by the reduction of the turbine inlet temperature (Fig. 13). Figure 14 shows the cell voltage and Nernst potential at part load condition. The first increases, but

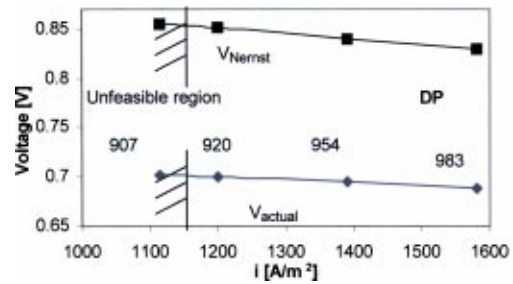


Fig. 14 Actual and Nernst potential of the cell against current density

undergoes the contrasting effects of Nernst potential increase, due to the greater average concentration of reactant, and electrical loss increase, due to the reduction in the operating temperature.

The utilization rate trends are shown in Fig. 15. The fuel utilization rate (single pass), defined as the ratio between reacted ($H_2 + CO$) and supplied ($H_2 + CO$) fuel, decreases by reducing the inlet flow rate. Reacted H_2 , in fact, decreases by reducing the current density value, while the anodic inlet flow rate is substantially constant, thanks to the increase in the internal recycle. The oxygen utilization rate decreases because the reduction in current density is not followed by a fresh air reduction. The assessment of operating limit feasibility (inlet flow rate temperatures and percentage of CO_2 supplied to the cathodic side) is reported in Figs. 16 and 17. The impossibility of reducing the air flow rate in the proper way causes a cooling of the stack; to 75% of the power supplied by the plant; an increase of the cathode-to-cathode internal recycle keeps the stack temperature over the operating limit. At 70% of nominal power, the cathodic inlet temperature prevents a further reduction of the fuel inlet flow rate. With regard to the cathodic flow rate composition, the inlet percentage of CO_2 is sufficient to allow the electrochemical reaction to occur until 75%

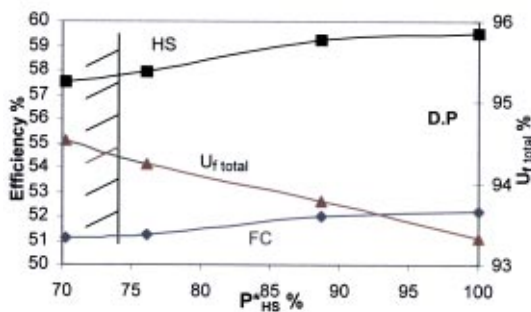


Fig. 12 Hybrid system (HS) and fuel cell system (FC) efficiency versus net nondimensional power supplied by the plant

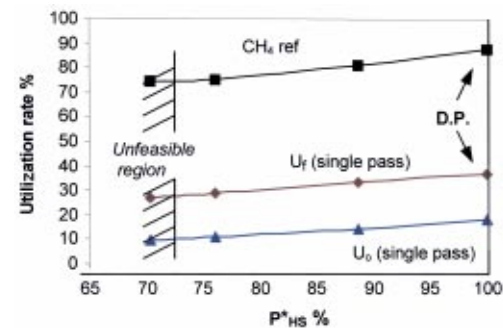


Fig. 15 Fuel and oxygen utilization rates, and CH_4 converted by sensible heat reformer, versus nondimensional power supplied by the hybrid system

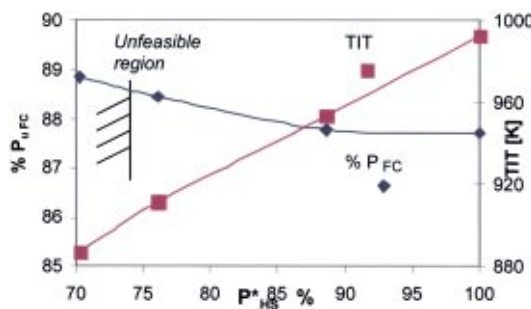


Fig. 13 Percentage of net power supplied by the stack and inlet turbine temperature versus net nondimensional power supplied by the whole hybrid system

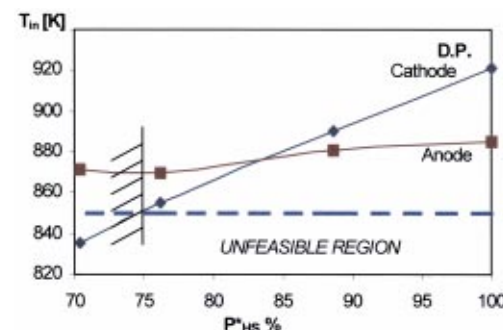


Fig. 16 Inlet temperature at part-load condition

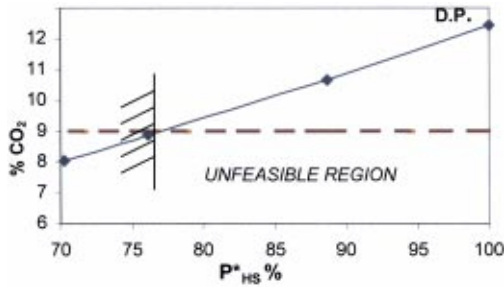


Fig. 17 Inlet cathodic percentage of CO_2 (mass fraction rate) at the part-load condition

of rated power is reached; its decrease is due to the reduction of the anode to cathode recycle rate and the excessive flow of fresh air in the cathodic flow.

3.3 Hybrid System Off-Design Performance at Variable Turbine Rotational Speed: Preliminary Results. At a fixed rotational speed, the impossibility of reducing the air flow rate, places the stack at nonoptimal operating conditions, and only a 25% reduction of power is possible. The typical operational mode of large-size gas turbine plants does not usually involve the possibility of changing the rotational speed of the turbine. This is because typical plants do not include an inverter, and thus, the rotational speed of the gas turbine is chosen on the basis of the alternate current frequency required by the end user electrical network. On the contrary, a hybrid system requires the presence of an inverter, which converts the electrical current produced by the fuel cell and the alternator; thus, this configuration allows the operation of the turbine at a variable rotational speed (variable frequency). This opportunity is of fundamental importance for operating the plant at very high efficiency and, above all, for enlarging the operating range at part-load condition. At variable speed, reducing the power, as shown in Fig. 18, according to the different compressor working maps, [11], can decrease the air inlet flow rate. When a variable speed control is available, a reduction in power supplied by the plant to 50% of design point value is possible. Fuel cell system performance is shown in Fig. 19: It is increased by reducing the turbine rotational speed, since this operating condition allows working at rated power with stack temperature and inlet flow rate ratio almost constant. Hybrid system performance is illustrated in Fig. 20; the overall efficiency of the plant is very high, even at part-load condition. At a fixed power supplied by the plant, decreasing the rotational speed increases efficiency; for example, at 75% of rated power, the efficiency value is 58% at 85,000 rpm and 59.5% at 80,000 rpm. By reducing the power supplied to 50% of nominal value, the operating pressure decrease is about 0.106 MPa.

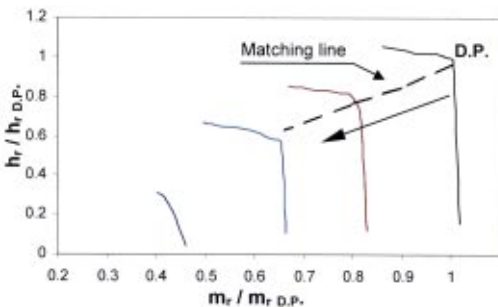


Fig. 18 Air compressor working points at part load conditions, when a variable turbine rotational speed is available

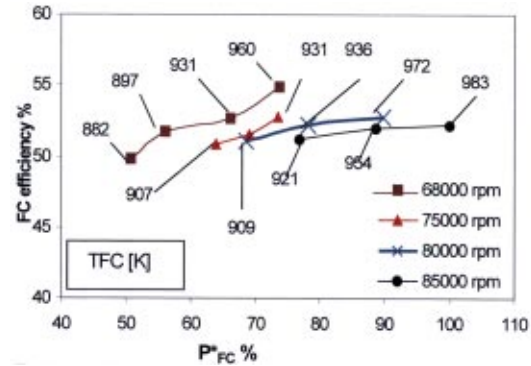


Fig. 19 Fuel cell efficiency at different turbine rotational speed versus net nondimensional power supplied by the hybrid system

Conclusions

In this paper, the design and off-design performance of a hybrid system (HS), based on the coupling of a small-size gas turbine with an existing molten carbonate fuel cell system (MCFC) has been presented and discussed. The turbine and stack models have been presented and discussed. The coupling of a small size non-regenerated turbine with an MCFC has shown a potential for efficiency close to 60% at design point and always over 55% at part-load condition. With regard to the stack group, an existing plant, known as a fuel cell system (100 kW) and realised by Ansaldo Fuel Cells, has been considered. The different behavior of the stack at part load condition, when both fuel and air flow rates and current density are reduced, has been presented for two cases: at fixed or variable recycle rates:

- at fixed recycle rates, the stack temperature (anodic side) decreases under the operating limit already at 90% of rated power (Fig. 4);
- at variable recycle rates, the stack works at optimal condition and its efficiency increases by reducing power to 50% of nominal value (Fig. 7); feasibility of operating limits is shown in Fig. 7, too.

Hybrid system off-design performance has been analyzed for two different gas turbine rotational speed control systems: fixed and variable. In both cases, the analysis has required the modification of the stack internal recycle rates, in order to verify the operating limits (minimum temperature and inlet cathodic percentage of CO_2).

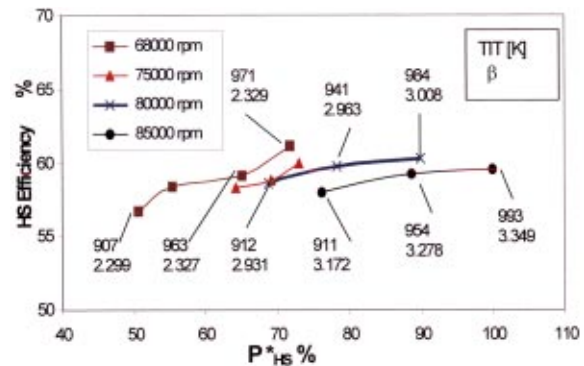


Fig. 20 Hybrid system efficiency at different rotational speed versus net nondimensional power supplied by the plant

At a fixed rotational speed, owing to the impossibility of reducing the air flow rate, as it depends on compressor and expander matching condition:

- part-load working is possible to 75% of rated power; a further fuel flow rate decrease does not allow the verification of the operating limit on temperature and percentage of CO₂ (Figs. 16 and 17);
- stack efficiency is penalized by a temperature decrease (51% at 70% of rated power against 52% at design point) (Fig. 12);
- owing to the stack performance, the overall plant efficiency decreases (57.5% at 70% of rated power to 59.5% at design point) (Fig. 12).

At variable turbine rotational speeds, the opportunity of varying the air flow rate, according to the different compressor working maps, allows stack feeding with the apt ratio between air and fuel; thus:

- part load working is possible to 50% of rated power, with very high efficiency, at part load condition, too (Fig. 20);
- a rotational speed control system allows working at around constant stack operating temperature and FC efficiency increases by reducing the power generated (Fig. 19).

Acknowledgments

This work has been partially sponsored by MIUR of Italy through the Contract FISR 2000, No. 10203–836.

Nomenclature

- T = temperature (K)
 TIT = inlet turbine temperature (K)
 TFC = fuel cell temperature (K)
 β = pressure ratio
 V = stack electrical potential (V)
 i = current density (A/m²)
 p = pressure (Pa)
 h = specific enthalpy (J/kg)
 c_p = specific heat (J kg⁻¹ K⁻¹)
 m = flow rate (kg/s)
 U = utilization rate (%)
 P = net power (W)

Superscript

- * = nondimensional value referred to design point one

Subscripts

- a = anode
 c = cathode
 f = fuel
 ref = reforming
 D.P. = design point
 HS = hybrid system
 FC = fuel cell system
 in = inlet
 out = outlet
 eq = equilibrium
 min = minimum
 0 = reference condition

References

- [1] Parodi, F., and Sanderson, R. A., 1994, "100 kW MCFC Power Plant: Ansaldo System Analysis," *Proceedings of the 1994 Fuel Cell Seminar*, FCS Organizing Committee, San Diego, CA.
- [2] Bosio, B., and Massardo, A. F., 2000, "Assessment of Molten Carbonate Fuel Cell Models and Integration With Gas and Steam Cycles," *ASME J. Eng. Gas Turbines Power*, to be published.
- [3] Bedont, P., and Massardo, A. F., 2001, "Heat Recovering and Pressurisation for an Existing 100 kW_e Molten Carbonate Fuel Cell," TESEC Congress, Genoa, June (in Italian).
- [4] Bedont, P., 1999, "Molten Carbonate Fuel Cells Modelisation and Integration With Power Generation Plants," Master thesis, University of Genoa (in Italian).
- [5] Grillo, O., 2001, "Design and Part Load Performance of a Hybrid System Based on a Molten Carbonate Fuel Cell and a Microgasturbine," Master thesis, University of Genoa (in Italian).
- [6] Hirschenhofer, J. H., Stauffer, D. B., and Engleman, R. R., 1994, *Fuel Cells Handbook* (revision 3), US-DOE, Morgantown, WV.
- [7] Bosio, B., 1999, "Development of Fuel Cell Technology," Ph.D. thesis, Politecnico di Torino (in Italian).
- [8] Bosio, B., Arato, E., and Parodi, F., 2001, "Fuel Cell Power Plant Process Analysis Using Aspen Plus," *Proceedings of the 4th Conference on Process Integration, Modelling and Optimization for Energy Saving and Pollution Reduction*, Florence, Italy.
- [9] Bosio, B., Parodi, F., Arato, E., and Costamagna, P., 1999, "Process Analysis of a Molten Carbonate Fuel Cell Pilot Plant," *Proceedings of the Ichea P4 Conference*, May, Florence, Italy, AIDIC-Servizi, Milano, p. 651.
- [10] Costamagna, P., Magistri, L., and Massardo, A. F., 2001, "Design and Part Load Performance of a Hybrid System Based on a Solid Oxide Fuel Cell Reactor and a Micro Gas Turbine," *Journal of Power Resources*, **96**, pp. 352–368.
- [11] Huchida, H., Shiraki, M., Bessho, A., and Yagi, Y., 1994, "Development of a Centrifugal Compressor for 100 kW Automotive Ceramic Gas Turbine," ASME Paper No. 94-GT-73.
- [12] Pullen, K. R., Baines, N. C., and Hill, S. H., 1992, "The Design and Evaluation of a High Pressure Ratio Radial Turbine," ASME Paper No. 92-GT-93.

J. C. Bailey
GE Corporate Research and Development,
Niskayuna, NY 12309

J. Intile

T. F. Fric

GE Power Systems,
Greenville, SC 29602

A. K. Tolpadi
GE Power Systems,
Schenectady, NY 12345

N. V. Nirmalan

R. S. Bunker

GE Corporate Research and Development,
Niskayuna, NY 12309

Experimental and Numerical Study of Heat Transfer in a Gas Turbine Combustor Liner

Experiments and numerical simulations were conducted to understand the heat transfer characteristics of a stationary gas turbine combustor liner cooled by impingement jets and cross flow between the liner and sleeve. Heat transfer was also aided by trip-strip turbulators on the outside of the liner and in the flowsleeve downstream of the jets. The study was aimed at enhancing heat transfer and prolonging the life of the combustor liner components. The combustor liner and flow sleeve were simulated using a flat-plate rig. The geometry has been scaled from actual combustion geometry except for the curvature. The jet Reynolds number and the mass-velocity ratios between the jet and cross flow in the rig were matched with the corresponding combustor conditions. A steady-state liquid crystal technique was used to measure spatially resolved heat transfer coefficients for the geometric and flow conditions mentioned above. The heat transfer was measured both in the impingement region as well as over the turbulators. A numerical model of the combustor test rig was created that included the impingement holes and the turbulators. Using CFD, the flow distribution within the flow sleeve and the heat transfer coefficients on the liner were both predicted. Calculations were made by varying the turbulence models, numerical schemes, and the geometrical mesh. The results obtained were compared to the experimental data and recommendations have been made with regard to the best modeling approach for such liner-flow sleeve configurations.

[DOI: 10.1115/1.1615256]

Introduction

The combustor systems of modern high-efficiency, low-emission turbine engines have been under continual development and improvement over the last decade. While firing temperatures have been increasing to gain efficiency, simultaneous requirements have been enforced to reduce emissions levels, especially for power producing gas turbines. Today's combustions systems seek to limit NO_x emissions to 9 ppm or less on dry fuel, and 25 ppm or less prior to reduction measures on the turbine exhaust gases. To achieve such stringent emissions levels it is necessary to maintain combustion zone temperatures as low as possible, which in turn requires more air to be utilized in the premixing process and reaction zones. Such systems put a large burden on the combustor liner, requiring that this structure be cooled without the use of cooling air bleed as hot-side film cooling. While the geometry of many combustor liners is relatively simple, cooling must be achieved through back-side convective methods alone. Due to the extremely long operating intervals of power turbines, combustor liner cooling must be predictable and reliable to assure system durability and long life.

Methods for the cooling of combustor liners are of many forms. Older power turbine engine product designs utilize combustion dilution air and film cooling of various types, similar to their aircraft engine counterparts. One common cooling geometry used shingled combustor liners with continuous slots as investigated by Chin et al. [1]. Another typical film cooled combustor liner geometry is that of full-coverage, multihole, or effusion cooling as described in the various research of Crawford et al. [2], Metzger et al. [3], Andrews et al. [4,5], Al Dabagh et al. [6], Martiny et al. [7,8], and Fric et al. [9]. An excellent summary of combustor liner

cooling by film cooling methods, and combined film and convective cooling methods, is presented by Schulz [10].

In lieu of film cooling, combustor liners generally utilize impingement, convection, and convective surface enhancement cooling techniques. The use of impingement jets for the cooling of various regions of modern gas turbine engines is widespread, most especially within the high pressure turbine. Since the cooling effectiveness of impingement jets is very high, this method of cooling provides an efficient means of component heat load management given sufficient available pressure head and geometrical space for implementation. Regular arrays of impingement jets are used within turbine airfoils and endwalls to provide relatively uniform and controlled cooling of fairly open internal surface regions. Such regular impingement arrays are generally directed against the target surfaces by the use of sheet metal baffle plates, inserts, or covers which are fixed in position relative to the target surface. These arrangements allow for the design of a wide range of impingement geometries, including in-line, staggered, or arbitrary patterns of jets. A summary of applicable impingement heat transfer research may be found in Martin [11].

Cases involving the use of a single line of impinging jets, or arrays of circular jets, are of particular applicability to the cooling of combustor liners. Metzger and Korstad [12] investigated the effects of a crossflow on a single line of circular jets within a channel. The relative strengths of the jet flow and crossflow as determined by other system parameters such as target spacing and Reynolds number are extremely important to the resulting heat transfer on the target wall. Several studies have also been performed to correlate the heat transfer under an array of impinging circular jets, primarily for normal impingement on flat surfaces. Kercher and Tabakoff [13] tested a matrix of square arrays of in-line jets over ranges of target spacing and jet Reynolds number, correlating streamwise heat transfer with geometry and flow parameters. The range of parameters in [13] included jet average Re up to 30,000, jet-to-jet spacing x/D of 3 to 12.5 jet diameters, and target spacing z/D from 1 to 5. In a series of studies of Florschuetz et al. [14–16] the heat transfer to a flat plate beneath

Contributed by the International Gas Turbine Institute (IGTI) of THE AMERICAN SOCIETY OF MECHANICAL ENGINEERS for publication in the ASME JOURNAL OF ENGINEERING FOR GAS TURBINES AND POWER. Paper presented at the International Gas Turbine and Aeroengine Congress and Exhibition, Amsterdam, The Netherlands, June 3–6, 2002; Paper No. 2002-GT-30183. Manuscript received by IGTI, Dec. 2001, final revision, Mar. 2002. Associate Editor: E. Benvenuti.

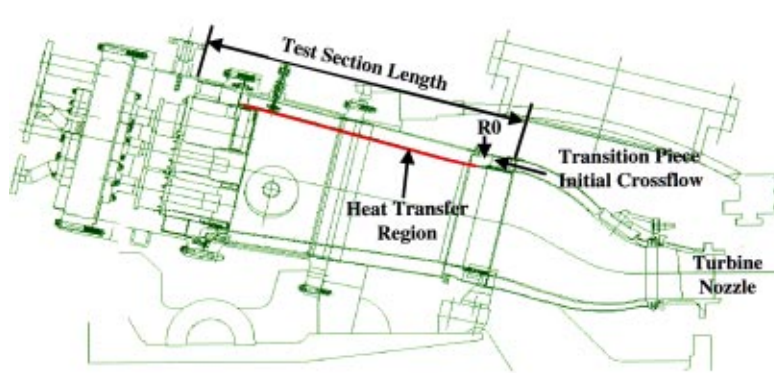


Fig. 1 Cross-section of typical "F" class combustor system per [23]

nonsquare arrays of impingement jets was determined, including in-line and staggered arrays and various effects of initial and developing crossflow. Various jet array geometries were investigated in these studies, providing a major portion of the current database for heat transfer correlations of impingement arrays. In particular, [14] presents correlations covering jet average Re up to 70,000, jet-to-jet spacing x/D and y/D of 5 and 4 to 15 and 8 jet diameters, target spacing z/D from 1 to 3, and crossflow ratios up to 0.8.

Many studies, both experimental and computational, exist in the literature concerning fundamental means for enhancing internal heat transfer within dominantly turbulent flow configurations. These include turbulation of passages by various repeated surface features, impingement jets and arrays of jets, swirling flows, pin-banks, roughness, and much more. One of the most common means for enhancing heat transfer coefficients within internal passages, and especially the serpentine passages of many turbine blade designs, is the use of turbulators, also known as rib rougheners. Basic turbulator research leading to widely used data and correlations was performed by Webb et al. [17], Burggraf [18], and Han et al. [19,20]. These and other researchers have concentrated on turbulators of relative height e/D less than 0.2, but greater than that typically associated with uniform surface roughness. The general findings of all such research has been that surface-averaged heat transfer coefficients within stationary, turbulated passages may be enhanced by factors from 1.8 to 2.8, while the friction factors or required pumping power are increased by factors of 3 to 10. Many parameters are variable in turbulated passages, and many more in serpentine circuits, but the range of effects has remained much the same over the years.

In integral structures of airfoils, endwalls, or liners, the total heat transfer distribution is important to the proper assessment of thermal-mechanical loading in the component. It is important also to include the variations in geometry and flow conditions. Ferrara et al. [21] present a study of various regions of cooling for a convective and film-cooled combustor liner. They developed an analysis tool including impingement, turbulated, and film cooling methods. Smith and Fahme [22] specifically focus on a nonfilm cooled combustor liner design for low emissions, which utilizes only convective flow over turbulators.

The present study explores heat transfer distributions for a combustor liner model utilizing both impingement jet cooling, high Reynolds number turbulated flow between the liner and flow-sleeve, and variable passage geometry. An experimental model is used to obtain full-surface heat transfer distributions under engine representative conditions. A CFD numerical model precisely representing the experiment provides predictions of full-surface heat transfer, as well as direct comparisons to data with both two-layer and wall-function turbulence modeling methods.

Experimental Apparatus and Method

For the present study a test rig has been built to evaluate heat transfer coefficients and pressure drop in a large gas turbine reverse flow combustion system similar to Fig. 1. This system is very similar to the low NO_x design described in detail by Vandervort [23]. The combustion system model is composed of an inner liner to contain hot combustion gases and an outer flow sleeve to contain and control cooling flow. The experimental facility used in this study is a cold flow parallel plate test section. The test section geometry is modeled and scaled to match the annulus geometry of the combustion liner and flow sleeve assembly. The test section is equivalent to a quarter sector of the combustor system. The annulus spacing is matched at each streamwise location. The test section is approximately 35.1 cm wide and 113.4 cm long. The average passage height is 3.9 cm, varying from 2.9 to 4.4 cm. The side walls and flow sleeve are aluminum. The test surface is 0.76-mm thick aluminum with 2.54 cm of acrylic backing for insulation and mechanical support. The test section is contained in a three-piece ASME pressure vessel that is 61 cm in diameter and 220 cm long when assembled. Each section of the vessel contains a pipe nozzle for air feed or air exhaust. The test section bolts to flanges inside the pressure vessel (Fig. 2), which provide sealing between the three sections creating separate plenums.

The test is operated using room temperature cooling air supplied from dedicated compressors. There are two controlled cooling flows, each measured with a standard ASME square edge orifice station. The first cooling flow is brought in as initial cross flow from one plenum supply. Secondary cooling flow is brought in through a second plenum feeding five rows of impingement jets. Both flows are metered and controlled independently. The combined cooling flows exhaust into the vessel top section, where a valve controls the back pressure. Figure 2 shows the flow circuit of the test section. Passage pressures are monitored with static

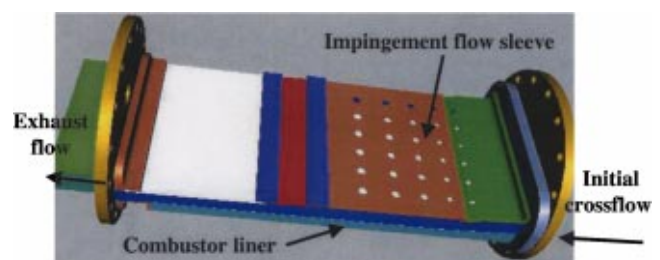


Fig. 2 Parallel plate test section module

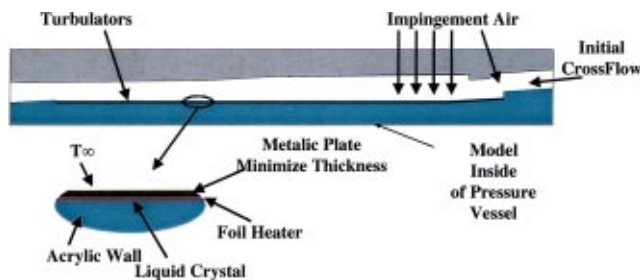


Fig. 3 Flow cross-section and detailed surface construction

pressure taps in the flow sleeve at 13 axial positions. The inlet pressure profile is measured with five static pressure taps distributed spanwise (circumferentially) before the first row of cooling jets. Air temperatures are measured at the orifice stations, each section of the vessel, and axially at five locations in the test section (equally spaced from inlet to exit). There were also five thermocouples spread spanwise at the channel exit to check uniformity. Under all present test conditions, the inlet crossflow is quite uniform in distribution, and all heat transfer tests show excellent spanwise distribution uniformity for each impingement row and the total downstream flow. Nominal rig flow conditions are listed below:

- Passage Re (ave.) 8.4×10^5
- Jet Re_j range 1.7×10^5 to 2.8×10^5
- G_j/G_c range 0.26 to 0.6
- Cross flow 0.98 kg/sec
- Impingement flow 1.69 kg/sec
- Impingement pressure 558 kPa
- Air inlet temperature 22°C
- Passage Mach number 0.02–0.09

The impingement jet diameters are not uniform. Each row has different jet size, hence the range of jet Reynolds numbers and crossflow ratios. There are six spanwise rows of impingement jets. The average target distance-to-diameter ratio of these jets is 2.3. The average jet array spacing streamwise and spanwise is 4. Sharp, square turbulators with full fillet radius are machined in the liner surface over the latter 50% of the flow path. The turbulators are transverse to the flow, with height of 0.76 mm, a pitch-to-height ratio of 10, and an average height-to-channel height ratio of 0.022.

Liner wall temperatures are measured utilizing the liquid crystal video thermography method of Farina et al. [24]. A wide band liquid crystal pre-applied to a mylar sheet was calibrated over its entire color band. The liquid crystal type was Hallcrest 40–45°C. A curve fit of liquid crystal hue versus calibration temperature was then used to calculate liner wall temperatures. The liner heater system shown in Fig. 3 was a stack up consisting of 2.54 cm of acrylic insulation, liquid crystal sheet, adhesive, foil heater, adhesive, and a 0.76-mm nominal aluminum plate. A thin aluminum plate was used to allow for machining of turbulator trip strips on the liner cold side while minimizing thermal resistance. A uniform heat flux boundary condition is created by applying high-current, low-voltage DC power to the foil heater. Liquid crystal images were taken with an RGB CCD camera. Site glasses in the rig provided viewing of the test section with the camera as well as lighting access. Figure 4 shows the lighting and camera setup. Each data set is comprised of four to eight images taken at different heat flux settings. Heat losses were measured to be less than 2% of the total power input. The definition of local heat transfer coefficient used in this study is

$$h = Q_{\text{wall}} / (T_{\text{surface}} - T_{\text{air inlet}})$$

where Q_{wall} is the power input to the heater divided by the heater area. The wall surface temperature is calculated using a one-dimensional temperature drop from the liquid crystal surface to



Fig. 4 Test rig pressure vessel (left) and internal test section (right, jets inactive)

the flow path surface. The impingement air supply temperature is used for $T_{\text{air inlet}}$, and is the same as the initial crossflow supply temperature. The heat up of the air over the heated test section length was less than 1.1°C, while the minimum temperature potential between the surface and the air inlet was 11°C. Because the impingement region “ h ” is more appropriately based on the supply air temperature, this same basis was used for the entire test region in order to allow full-surface comparisons. Experimental uncertainty in “ h ,” as calculated using the methods of Kline and McClintock [25], is between 8 and 15%. Higher uncertainty is associated with higher heat transfer coefficients. The flow rate uncertainty is $\pm 1\%$.

Computational Technique and Model

A fully three-dimensional, steady CFD analysis was performed to validate the heat transfer coefficients within the impingement zone of the liner/flow sleeve geometry. The purpose of this model was to validate current methods and practices used to predict the local heat transfer coefficients on the liner. As CFD is becoming the primary tool for providing three-dimensional heat transfer boundary conditions for FEA lifting predictions, it is extremely important to understand and validate the CFD methods and models, detail the deficiencies, and provide a set of guidelines for “best practices.”

Symmetry conditions were used to reduce the size of the computational model to that of 1/6th of the test rig geometry. Both the fluid and solid domain of the test rig were explicitly modeled as a conjugate heat transfer problem with temperature dependent properties. The model and results were created using StarCD-HPC Version 3.1 Patch B.

The computational domain and boundary conditions are shown in Fig. 5. The experimental test rig consisted of a series of heat fluxes to allow the liquid crystals to respond within their temperature limits over the liner surface. The CFD model surface heat flux corresponds to the average experimental condition. The flow was assumed compressible using the ideal gas law relating pressure, density, and temperature. The heat fluxes were applied uniformly across the liner. The cross flow rate into the flow sleeve was assumed to be uniform. The impingement flow rates into the large

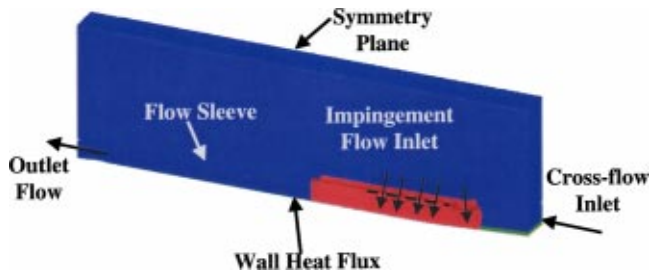


Fig. 5 Computational domain

plenum region of the CFD model closely resembled that of the test rig. An assumed turbulence intensity magnitude of 10% was used for both inlet flows. The turbulent viscosity was assumed to be 100 times the laminar value to evaluate the inlet turbulence length scale. The definition of the heat transfer coefficient in the CFD predictions was kept the same as that for the experiments.

The CFD models consisted of two volumes corresponding to the impingement zone and the turbulator zone of the liner. For each zone the cell discretization was chosen such that either the wall-function approach of Launder and Spalding [26] or the two-layer turbulence model/mesh approach of Norris and Reynolds [27] could be used. Thus two models were created for comparison. One model consisted of a wall-function mesh in the turbulator zone and the impingement zone. A second model used a two-layer mesh for both the zones. The two models contained 1.1 and 3.7 million cells, respectively, and required either one or three days to converge using available parallel resources. Generally, 2500 iterations were required for convergence of the solutions. The turbulator meshes used are shown in Figs. 6 and 7. The size of the first cell layer for the turbulators using the wall-function mesh varied between y^+ values of 30 and 50. For the two-layer mesh the first cell layer varied between y^+ values of 0.75 and 1.5. The grid density of these models was based upon the experi-

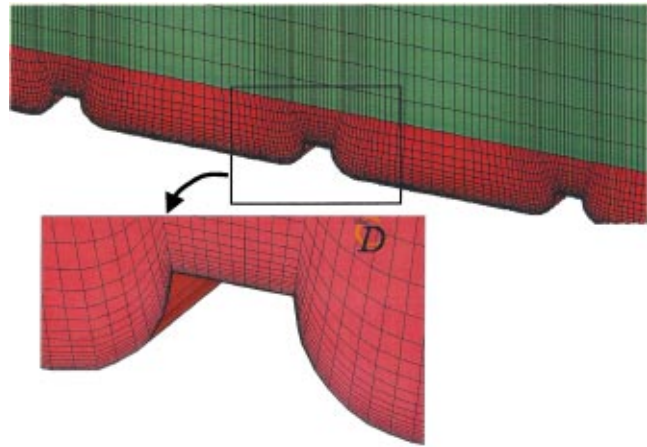


Fig. 7 Two-layer discretization scheme

ence of previous similar in-house CFD analyses shown to provide good results, as well as maximum available computational resources for reasonable turn-around time.

The convective terms in the governing equations were discretized using the monotone advection and reconstruction scheme (MARS) [28]. Results shown in this paper include the standard $k-\epsilon$ model, [26], and the two-layer model, [27].

Results and Discussion

The distribution of the heat transfer coefficient for this sector model is of value to design engineering in that the flow rate variation, both in the flow sleeve holes and crossflow, can be adjusted to account for variations found in field operation.

Before making a comparison of test data and CFD predictions, some fundamental test data effects are of value. As noted in the experimental description above, the test surface was composed of a thin, heated aluminum plate, smooth under the impingement

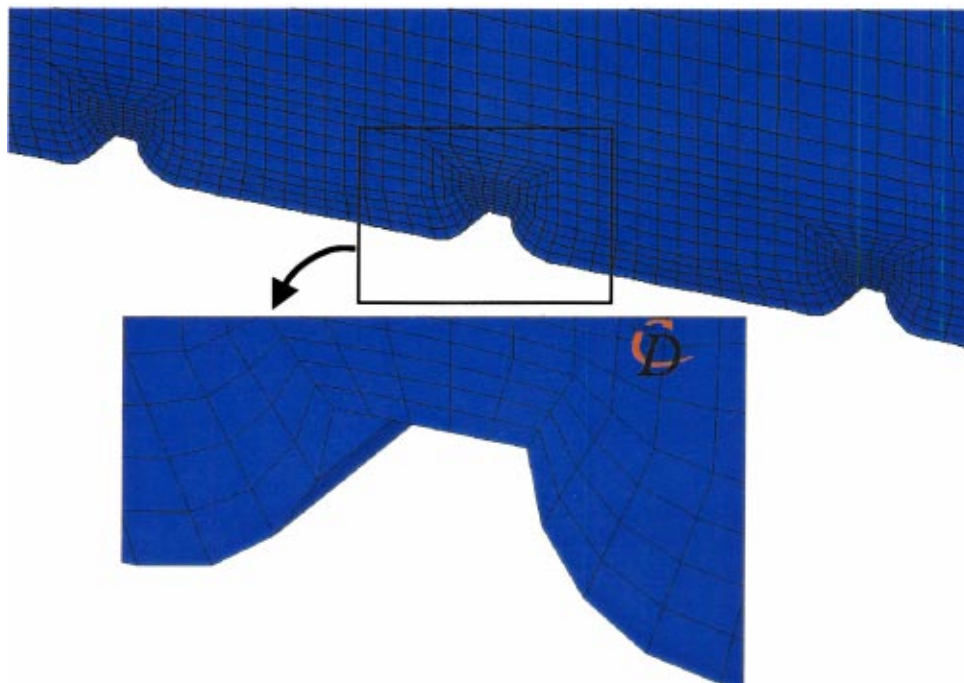


Fig. 6 Wall-function discretization scheme

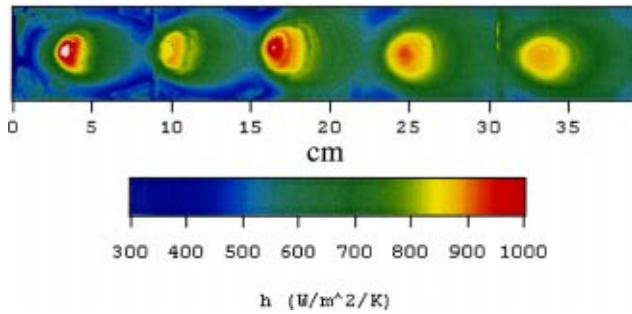


Fig. 8 Impingement heat transfer data with bare surface heater

region and turbulated downstream of impingement. Since the heater is a thin foil of Inconel, it can also represent a smooth test surface without the presence of the aluminum plate. Figure 8 shows the impingement region heat transfer coefficients obtained by impingement directly onto the heater surface. This method eliminates any surface conduction effects or corrections, and so provides the most detailed local heat transfer results. The interaction of the first jets with the initial crossflow is seen, both in the shaping of the jet thermal footprint and in the upstream bow wave. Subsequent jet impingement locations show less intensity due to increased crossflow (remember that the jets do not have the same diameter or Re_{jet}). Regarding these jets as individuals for the moment, the peak impingement heat transfer is from 900 to 1000 $W/m^2/K$. Using a very simple expression for peak impingement Nusselt number, the present conditions result in $Nu = C * Re_{jet}^{0.7} Pr^{0.33}$, with C between 0.12 and 0.18. While no literature data exist for impingement jets at the present Re with crossflow, this approximate valuation is in the same range as data of Perry [29] and also the evaluations provided by [11] for jets without crossflow. As an additional point, a visual comparison of the spanwise-averaged data of Fig. 8 can be made with the impingement-smooth case in Fig. 9 for which the aluminum plate was employed. This comparison shows the effect of the thin plate on spanwise-averaged results to be negligible.

The heat transfer data for three different liner cooling configurations are shown in Fig. 9. Each case has the same total flow rate. In this data, since some of the data include machined surface turbulators, all of these tests were conducted using the thin alumi-

num surfaces above the heaters. The data are presented as spanwise or circumferentially averaged heat transfer coefficients across the middle 50% of the test plate, thereby eliminating any endwall effects. Any sharp changes in the data are usually due to the interface between adjacent foil heaters. The baseline configuration for this study is that with both impingement and downstream turbulators; this is compared to CFD and literature data later. The second configuration presents a convection only case, without impingement, in which 100% of the flow is present at the inlet to the channel (2.67 kg/s). In this condition, the thermal entry region effect is observed to decay, approaching a heat transfer coefficient of about 320 $W/m^2/K$, which is the value for turbulent, fully developed smooth duct flow based on accepted literature. In the present case, this shows a combined thermal and hydrodynamic entry length of about ten passage heights, which is somewhat less than typically observed under more ideal conditions. The downstream turbulated wall is seen to enhance the heat transfer by a factor of about 2. The third configuration uses impingement in the upstream region, but eliminates the turbulators in the downstream region. Taking the turbulators away causes a redistribution of the pressure in the entire test section, due to the significant fraction of total pressure loss contributed by the turbulators. As a result, the impingement jet Re numbers are altered, and the impingement heat transfer shows a more uniform jet-to-jet magnitude. The average impingement region heat transfer is the same for both impingement configurations. The downstream smooth surface heat transfer again decays to the turbulent, fully developed level from accepted literature, but with a small increase due to channel convergence. The most striking feature of these results is the 40 to 50% enhancement in the turbulated region caused by the use of impingement upstream. This enhancement is essentially constant along the channel length, and felt to be due to the elevated bulk fluid turbulence levels created by the impingement jets. Recall that this configuration uses relatively large jets at very high Reynolds numbers (up to $2.8e5$), as well as relatively small turbulators of only 2.2% blockage. Under such conditions, an elevated turbulence level generated in the bulk flow might be expected to provide significant enhancement when aided by the turbulators. This has been shown to be a very repeatable effect in this and other geometries tested.

Figure 10(a) shows the predicted velocity vectors in a cross section through the centerline of the model in the impingement region. The vectors show good penetration of the impingement flow through all the holes. The crossflow under the holes is quite strong but the impinging jets are able to penetrate and reach the

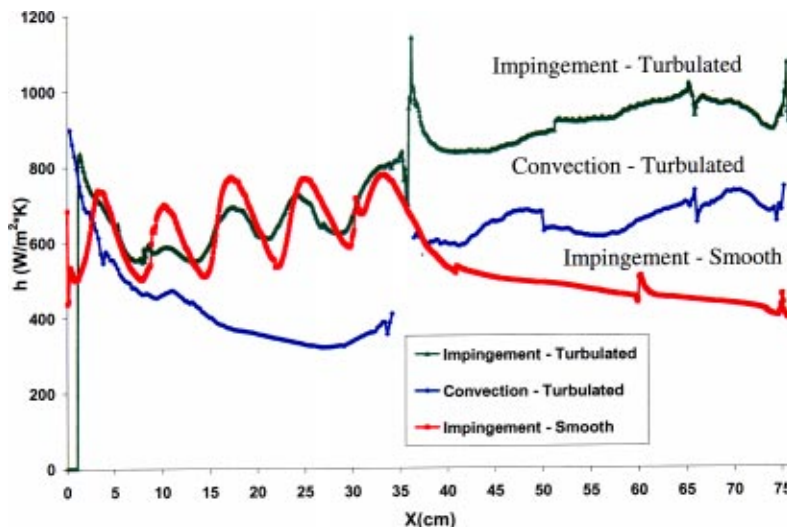


Fig. 9 Comparison of circumferentially averaged test data for varying geometries

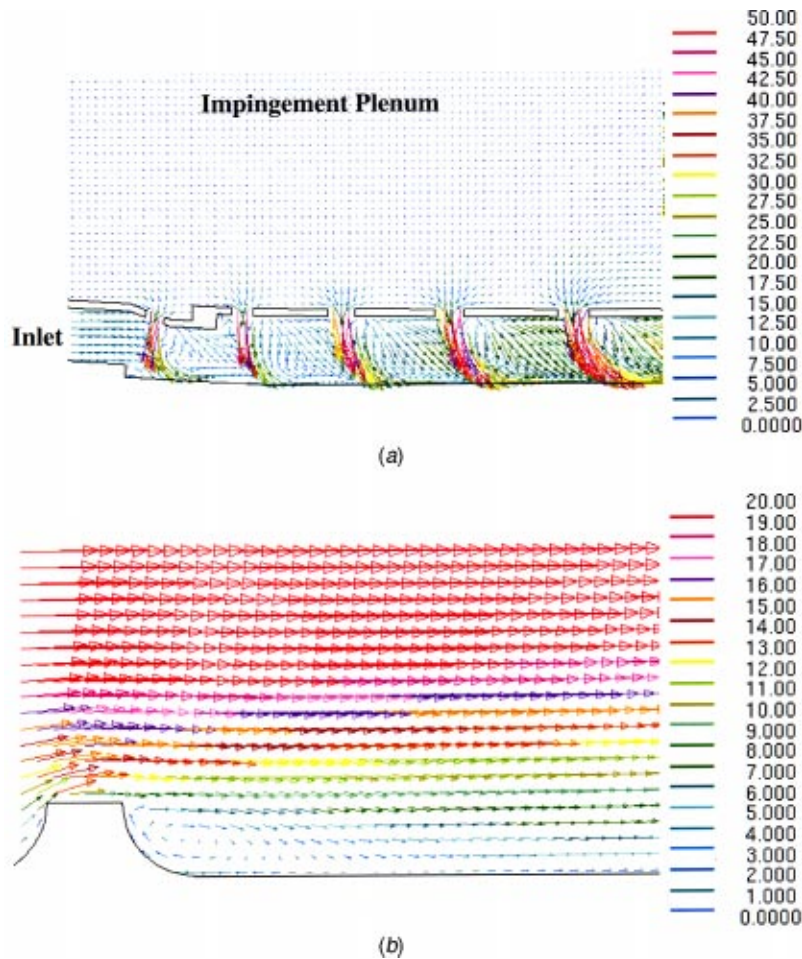


Fig. 10 (a) Computed velocities for impingement region (m/s); (b) Computed velocities for flow past a turbulator (m/s)

lower plate. A very small area of recirculation may be seen behind the jets. Figure 10(b) shows the velocity vectors around a turbulator approximately halfway down the turbulator section of the plate. The boundary layer above the turbulator and also between the turbulators can be discerned. The two-layer model is able to capture the recirculation zone behind the turbulator. The zone length is about 1.5 turbulator heights. Reattachment of the flow is evident at about four step heights downstream.

The experimental and predicted distributions of liner flow pressure drop are compared in Fig. 11. The inlet static pressure is that of the supply air entering as initial crossflow, upstream of the heated test surface (hence the negative location). The flow path static pressure measurements are in the flow sleeve surface. The liner cooling pressure drop is normalized to the inlet pressure, providing a common measure of combustor system performance in the form of pressure loss fraction. Measurement uncertainty

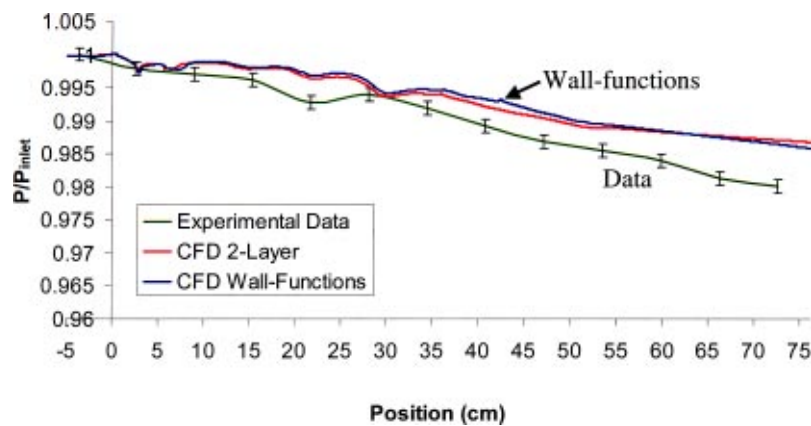


Fig. 11 Comparison of liner pressure drop for experimental data and CFD predictions

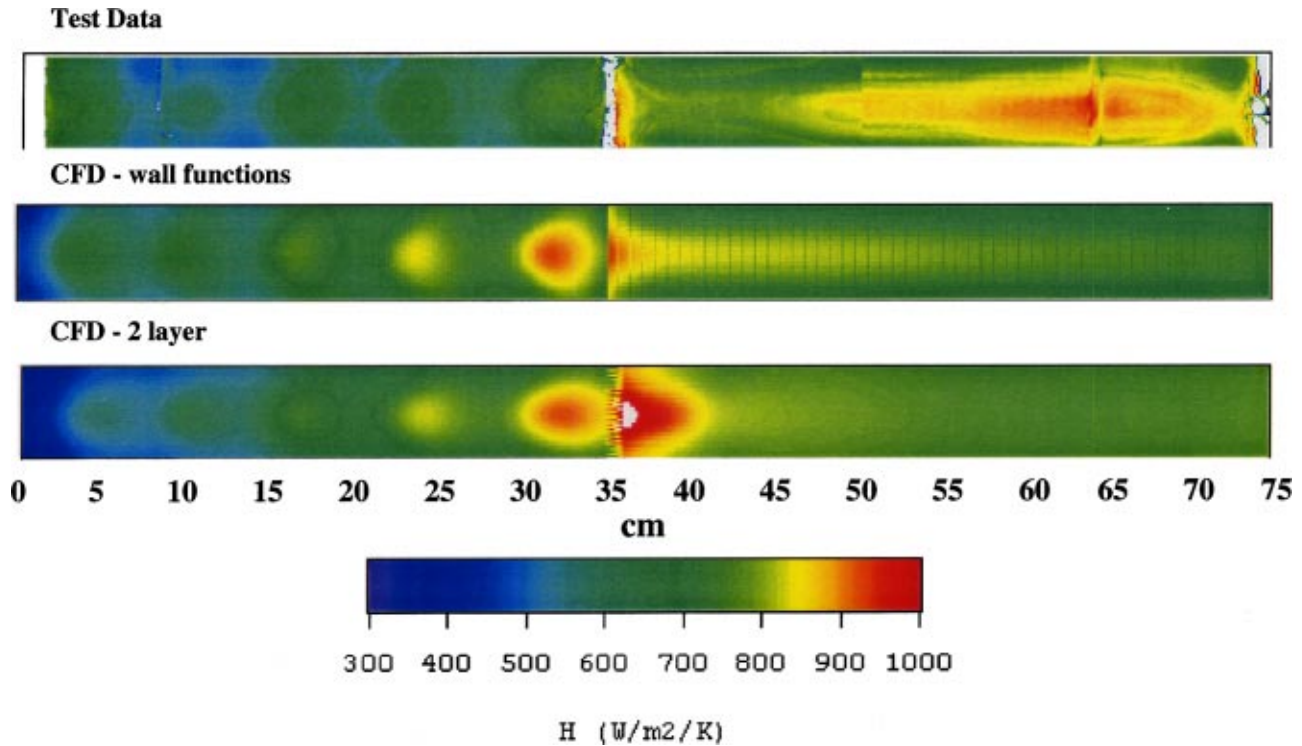


Fig. 12 Comparison of liner heat transfer for experimental data and CFD predictions

bars are shown on the experimental data indicating the $\pm 0.05\%$ accuracy of the pressure transducer used. The CFD static pressures are those predicted in the cells adjacent to the flow sleeve surface. The CFD predictions are seen to consistently underpredict the pressure loss throughout most of the liner channel; the two-layer model prediction is only slightly closer to the data overall. This underprediction is not surprising in the region of the impingement jets, considering the significant shear layers involved with crossflow mixing. The continued small divergence of experimental and predicted loss in the turbulated region is less expected. It is speculated that this is due in part to the continued jet mixing which occurs for a considerable distance, as well as the additional turbulence from the liner surface; i.e., these effects are not completely captured by the turbulent shear stress terms in the transport models. The result is that pressure loss over the computational region is about 30% less than actual.

Figure 12 shows the predictions of the heat transfer coefficient

as obtained using the wall function approach and the two-layer approach, compared with the test data. The test data in this figure represent the center region of the test section. The first half of the surface represents the impingement zone and the second half represents the turbulators. In the impingement region, the heat transfer is somewhat underpredicted over the first hole and universally overpredicted over the last four holes with the wall function turbulence model. With the two layer approach, the heat transfer is underpredicted over the first half of the impingement region and overpredicted over the latter half but clearly shows better agreement with the data. In the turbulator zone that follows, the predictions with both approaches appear to be significantly underpredicting data, although the two-layer approach predictions are higher and much closer to the data. For instance, the peak in the heat transfer in the vicinity of the first turbulator is predicted only by the two-layer approach.

Figure 13 presents an error plot of the CFD predictions relative

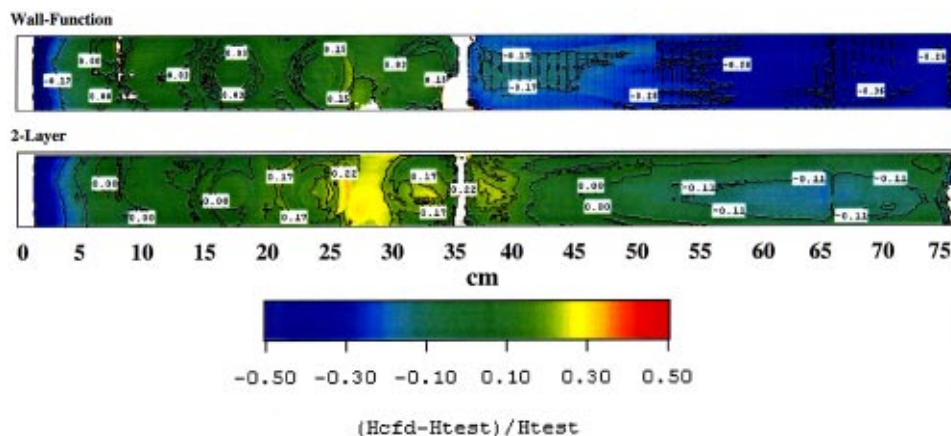


Fig. 13 Relative error in heat transfer coefficients between test data and CFD predictions

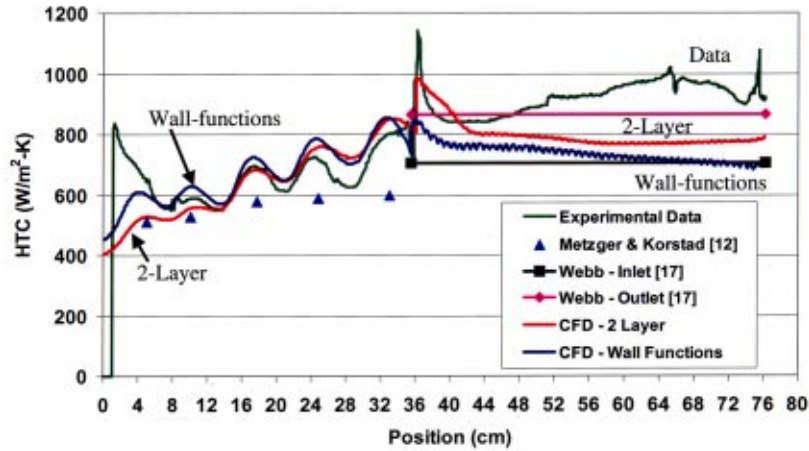


Fig. 14 Comparison of circumferentially averaged heat transfer coefficient across liner

to the data. The fractional difference

$$\{(h_{cfd} - h_{test}) / h_{test}\}$$

is calculated at all locations on the surface and plotted. Consistent with the observations in Fig. 12, the heat transfer is always underpredicted over the turbulators. The wall function approach results in much more deviation relative to the data, as much as -25%. In the impingement region, the deviation from the data is less with the two-layer approach.

The local heat transfer coefficients were spanwise-averaged and a one-dimensional heat transfer coefficient distribution along the flow direction generated. Figure 14 presents both the test data and predicted heat transfer coefficients. The bulk temperature used for definition of the heat transfer coefficient was the inlet temperature of the crossflow. The calculated CFD heat transfer coefficients have the peaks and valleys within the impingement zone (0–36 cm) for both models, however, the levels predicted are not the same. Barring the first hole, the wall function approach overpredicts the data over the remainder of the impingement region. The two-layer approach underpredicts the data initially, perfectly agrees with the data over the middle hole and then overpredicts the data. Past the last impingement jet, the wall function model does not capture the large elevation of the average heat transfer coefficient at the start of the turbulators. The two-layer approach is able to capture the large increase in heat transfer coefficients. Overall, in the impingement region, the two-layer approach is the better one to use. Using the jet Reynolds numbers and the cross flow to jet momentum ratios, the heat transfer coefficient under each of the five holes was calculated based on the correlation due to Metzger and Korstad [12]. The correlation of [12] falls below the data, as well as both the CFD predictions, universally at all the five jet locations. This is to be expected since the Re range of [12] is far below that of the present test, and the available correlations are all based on uniform jet sizing. Still, the comparison is reasonably good.

For the turbulator zone (>36 cm), the wall-function mesh significantly underpredicts the average heat transfer coefficient relative to the data. The two-layer calculation is able to predict the initial spike of the heat transfer over the turbulators although further downstream, it ends up underpredicting the data. However, without any doubt, the two-layer method gives results that are far closer to the data as compared to wall functions. The correlation due to Webb et al. [17] was used to estimate and compare the heat transfer coefficients here. There are two reference locations involved in the passage, one corresponding to the inlet of the turbulated section and the second corresponding to the exit of the turbulated section. Based on the conditions at these two locations,

two heat transfer coefficients are plotted as bounding values, both assuming fully developed roughened flow as in [17]. It can be seen that the correlation of [17] underpredicts the data almost universally. The correlation of [17] is based upon turbulators in a circular tube flow, not parallel plates, and furthermore is only valid to Re of 10^5 . Moreover, it is to be expected that the upstream conditions of the present test section will have an influence on the turbulated section heat transfer. It is interesting that the two-layer prediction falls almost entirely midway between the predictions using [17].

Based on these averaged as well as the local heat transfer predictions, it is clear that the two-layer approach is recommended for more accurate impingement and turbulator heat transfer predictions. However, the use of a two-layer turbulence model/mesh for a real gas turbine combustor liner containing turbulators may be practically infeasible because the number of cells required could exceed available computer pre/post processing limits. In this study, a two layer approach was used over 1/6th of the test rig geometry (resulting in a 3.7 million cell mesh) to understand its impact on the heat transfer predictions and demonstrate its superiority over the wall function approach. In a fully three-dimensional CFD simulation of a combustor liner, a judgment call therefore has to be made between the accuracy of predictions and the available computer resources.

Conclusions

Experiments and numerical simulations were conducted to understand the heat transfer characteristics of a stationary gas turbine combustor cooled by impingement jets and also comprised of turbulators for heat transfer enhancement. A flat-plate test rig was constructed corresponding to a one-quarter circumferential section of the combustor unwrapped. The Reynolds number through the impingement holes and the momentum ratios were matched to realistic combustor conditions. The turbulators in the test rig also modeled the relative shape and size as those in a real combustor liner. A steady-state liquid crystal method was used to obtain the local heat transfer coefficient distributions. A numerical model of the exact test rig was created and CFD was used to calculate the heat transfer coefficients. Two turbulence models were used: (1) wall function, and (2) two layer. Overall, the latter approach gave predictions that were more accurate and much closer to the data. However, the computational requirements with this approach could prove to be very prohibitive leaving the CFD practitioner with a difficult choice to make.

Nomenclature

| | |
|---------------|---|
| A_{cf} | = passage crossflow area |
| A_j | = jet area |
| A_h | = heater area |
| D | = jet diameter (mm) |
| h | = heat transfer coefficient (W/m ² /K) |
| G_c | = crossflow mass velocity= m_{cf}/A_{cf} |
| G_j | = jet mass velocity= m/A_j |
| m | = jet mass flow rate (kg/s) |
| m_{cf} | = passage cross flow rate (kg/s) |
| Q_{total} | = total heater power (W) |
| Pr | = Prandtl number |
| Re | = channel Reynolds number based on $2\times$ height |
| Re_j | = jet Reynolds number= $(4m)/(D/\mu)$ |
| T_{air} | = plenum supply temperature (°C) |
| $T_{surface}$ | = liner wall temperature |
| μ | = viscosity |

References

- [1] Chin, J., Skirvin, S., Hayes, L., and Burggraf, F., 1961, "Film Cooling With Multiple Slots and Louvers—Part 1: Multiple Continuous Slots," *ASME J. Heat Transfer*, **83**, pp. 281–286.
- [2] Crawford, M., Kays, W., and Moffat, R., 1980, "Full-Coverage Film Cooling Part I: Comparison of Heat Transfer Data for Three Injection Angles," *ASME J. Eng. Power*, **102**, pp. 1000–1005.
- [3] Metzger, D. E., Takeuchi, D., and Kuentler, P., 1973, "Effectiveness and Heat Transfer With Full-Coverage Film Cooling," *ASME J. Eng. Power*, **95**, pp. 180–184.
- [4] Andrews, G. E., Al Dabagh, A. M., Asere, A. A., Bazdidi-Tehrani, F., Mkpadi, M. C., and Nazari, A., 1992, "Impingement/Effusion Cooling," AGARD CP-527, *Heat Transfer and Cooling in Gas Turbines*, Paper Number 30.
- [5] Andrews, G. E., Khalifa, I. M., Asere, A. A., and Bazdidi-Tehrani, F., 1995, "Full Coverage Effusion Film Cooling With Inclined Holes," *ASME Paper 95-GT-274*.
- [6] Al Dabagh, A. M., Andrews, G. E., Abdul Husain, R. A. A., Husain, C. I., Nazari, A., and Wu, J., 1990, "Impingement/Effusion Cooling: The Influence of the Number of Impingement Holes and Pressure Loss on the Heat Transfer Coefficient," *ASME J. Turbomach.*, **112**, pp. 467–476.
- [7] Martiny, M., Schulz, A., and Wittig, S., 1995, "Full-Coverage Film Cooling Investigations: Adiabatic Wall Temperatures and Flow Visualization," *ASME Paper 95-WA/HT-4*.
- [8] Martiny, M., Schulz, A., and Wittig, S., 1997, "Mathematical Model Describing the Coupled Heat Transfer in Effusion Cooled Combustor Walls," *ASME Paper 97-GT-329*.
- [9] Fric, T. F., Campbell, R. P., and Rettig, M. G., 1997, "Quantitative Visualization of Full-Coverage Discrete-Hole Film Cooling," *ASME Paper 97-GT-328*.
- [10] Schulz, A., 2001, "Combustor Liner Cooling Technology in Scope of Reduced Pollutant Formation and Rising Thermal Efficiencies," *Heat Transfer in Gas Turbine Systems*, Ann. NY. Acad. Sci., **934**, pp. 135–146.
- [11] Martin, H., 1977, "Heat and Mass Transfer Between Impinging Gas Jets and Solid Surfaces," *Advances in Heat Transfer*, **13**, Academic Press, San Diego, CA, pp. 1–60.
- [12] Metzger, D., and Korstad, R., 1972, "Effects of Crossflow on Impingement Heat Transfer," *ASME J. Eng. Power*, **94**, pp. 35–41.
- [13] Kercher, D., and Tabakoff, W., 1970, "Heat Transfer by a Square Array of Round Air Jets Impinging Perpendicular to a Flat Surface Including the Effect of Spent Air," *ASME J. Eng. Power*, **92**, pp. 73–82.
- [14] Florschuetz, L., Truman, C., and Metzger, D., 1981, "Streamwise Flow and Heat Transfer Distributions for Jet Array Impingement With Crossflow," *ASME J. Heat Transfer*, **103**, pp. 337–342.
- [15] Florschuetz, L., Berry, R., and Metzger, D., 1980, "Periodic Streamwise Variations of Heat Transfer Coefficients for Inline and Staggered Arrays of Circular Jets With Crossflow of Spent Air," *ASME J. Heat Transfer*, **102**, pp. 132–137.
- [16] Florschuetz, L., Metzger, D., and Su, C., 1984, "Heat Transfer Characteristics for Jet Array Impingement With Initial Crossflow," *ASME J. Heat Transfer*, **106**, pp. 34–41.
- [17] Webb, R. L., Eckert, E. R. G., and Goldstein, R. J., 1971, "Heat Transfer and Friction in Tubes With Repeated-Rib Roughness," *Int. J. Heat Mass Transfer*, **14**, pp. 601–617.
- [18] Burggraf, F., 1970, "Experimental Heat Transfer and Pressure Drop With Two-Dimensional Turbulence Promoter Applied to Two Opposite Walls of a Square Tube," *Augmentation of Convective Heat and Mass Transfer*, Bergles and Webb, eds., ASME, New York, pp. 70–79.
- [19] Han, J. C., Glicksman, L. R., and Rohsenow, W. M., 1978, "An Investigation of Heat Transfer and Friction for Rib-Roughened Surfaces," *Int. J. Heat Mass Transfer*, **21**, pp. 1143–1156.
- [20] Han, J. C., Park, J. S., and Lei, C. K., 1984, "Heat Transfer Enhancement in Channels With Turbulence Promoters," *ASME Paper 84-WA/HT-72*.
- [21] Ferrara, G., Innocenti, L., Migliorini, G., Facchini, B., and Dean, A. J., 2000, "Heat Transfer Analysis in a Modern DLN Combustor," *ASME Paper 2000-GT-254*.
- [22] Smith, K., and Fahme, A., 1999, "Backside Cooled Combustor Liner for Lean-Premixed Combustion," *ASME Paper 99-GT-239*.
- [23] Vandervort, C. L., 2001, "9 ppm NO_x/CO Combustion System for "F" Class Industrial Gas Turbines," *ASME J. Eng. Gas Turbines Power*, **123**, pp. 317–323.
- [24] Farina, D. J., Hacker, J. M., Moffat, R. J., and Eaton, J. K., 1994, "Illuminant Invariant Calibration of Thermochromic Liquid Crystals," *Exp. Therm. Fluid Sci.*, **9**, pp. 1–9.
- [25] Kline, S. J., and McClintock, F. A., "Describing Uncertainties in Single-Sample Experiments," *Mech. Eng. (Am. Soc. Mech. Eng.)*, Jan.
- [26] Launder, B. E., and Spalding, D. B., 1974, "The Numerical Computation of Turbulent Flows," *Comput. Methods Appl. Mech. Eng.*, **3**, pp. 269–289.
- [27] Norris, L. H., and Reynolds, W. C., 1975, "Turbulent Channel Flow With a Moving Wavy Boundary," Report No. FM-10, Department of Mechanical Engineering, Stanford University, Stanford, CA.
- [28] STARCD, 2001, Version 3.1B manual.
- [29] Perry, K. P., 1954, "Heat Transfer by Convection From a Hot Gas Jet to a Plane Surface," *Proc. Inst. Mech. Eng.*, **168**, pp. 775–780.

Disintegration of Oil Jets Emerging From Axial Passages at the Face of a Rotating Cylinder

A. Glahn
M. F. Blair

United Technologies Research Center,
411 Silver Lane, M/S 129-19,
East Hartford, CT 06108

K. L. Allard
Pratt & Whitney,
400 Main Street,
East Hartford, CT 06108

S. Busam
O. Schäfer
S. Wittig

Institut für Thermische Strömungsmaschinen,
Universität Karlsruhe,
Kaiserstrasse 12,
Karlsruhe 76128, Germany

A fundamental study has been performed to examine the disintegration of oil films emerging from axial passages at the face of a rotating cylinder. The investigation has been conducted in parallel to a similar study on atomization processes at rotating radial holes (Glahn, A. et al., 2001, "Disintegration of Oil Films Emerging From Radial Holes Inside a Cylinder," ASME Paper No. 2001-GT-0202) and has used the same approaches in simulating one of the droplet generation sources in aeroengine lubrication systems. Both papers aim to contribute to the establishment of a database that can be used for the development of droplet generation models directly applicable to engine conditions. As with the parallel investigation, the near-term objectives of fundamental oil film disintegration studies are (i) to determine droplet sizes under relevant aeroengine bearing compartment operating conditions, and (ii) to measure individual droplet diameter/velocity relationships. The long-term objective is to incorporate this information into advanced design systems such as CFD-based tools. In the present study, flow visualization has been used to identify the dominant disintegration processes. Droplet diameters and velocities have been obtained for relevant engine operating conditions. Data are presented in terms of both characteristic diameters and size-class resolved droplet velocities and flow angles. A comparison of droplet sprays measured in the present study with those generated by disintegration of oil films at the rim of a rotating disk (Glahn, A. et al., 2000, "Droplet Generation by Disintegration of Oil Films at the Rim of a Rotating Disk," ASME Paper No. 2000-GT-0279) has been enabled by introducing nondimensional parameters for atomization products and operating conditions. [DOI: 10.1115/1.1586310]

Introduction

Some of the consequences of current aeroengine development trends for lubrication system designs have been discussed in several prior publications on bearing compartment two-phase flow and internal heat transfer. Most recently, Glahn et al. [1] pointed out that high pressure, high temperature, and high rotational speeds of the turbine rotor significantly reduce the design margin for lubrication system components and especially bearing compartments. Improved design tools are required to meet the challenges of current and future engine developments.

In recent years, progress has been made on several subtasks involved in the overall design process, [2–8]. All these studies were helpful in getting an overall picture of the flow phenomena involved in bearing compartments. They establish a database for validation purposes and some of them appear to be directly applicable for certain aspects of the engine design. However, the development of a design system and its adaptation to different geometrical and operational boundary conditions requires a platform that is able to integrate these submodels.

A viable approach would be to use CFD methods to predict the two-phase air/oil flow in lubrication system components. A study presented by Glahn et al. [9] suggested the feasibility of such an approach. However, a prerequisite for a successful implementation of these tools into a standard design environment is the availability of boundary conditions and the development of submodels which describe the complex phase interaction mechanism and atomization effects prevailing in these parts. Therefore, further studies of film behavior and atomization processes are essential.

Glahn et al. [1] report on the first phase of a multiyear, fundamental investigation into generic oil system atomization processes by examining the disintegration of oil films at the rim of a rotating disk. The present paper is a continuation of this effort and deals with the disintegration of oil films emerging from axial passages at the face of a rotating cylinder. This study has been conducted in parallel with an investigation of oil film breakup processes at rotating radial holes, [10]. Both studies aim at simulating droplet generation sources in aeroengine bearing compartments and gearboxes. The present paper focuses on the oil film disintegration downstream of rotating axial holes and passages that exist in intershaft oil flow configurations and gear support systems.

The objectives of the study were as follows: (i) to identify disintegration modes relevant to aeroengine bearing compartment operating conditions, (ii) to determine droplet sizes under those operating conditions, and (iii) to measure individual droplet diameter/velocity relationships.

Following a brief description of the experimental setup, results are presented in terms of samples from the visualization work, typical spatial droplet diameter distributions, characteristic diameters, and droplet velocities as a function of flow rate and rotational speed. Nondimensional parameters for atomization products and operating conditions are introduced that are useful in comparing droplet sprays measured in the present study with those generated by disintegration of oil films at the rim of a rotating disk, [1]. Conclusions drawn from this comparison will summarize the paper.

Experimental Setup and Techniques

Test Rig. The test facility used for the fundamental oil film disintegration studies reported in this paper is basically the same used by Glahn et al. [1]. Minor modifications similar to those undertaken in a parallel study by Glahn et al. [10] are highlighted in the following section. The rotating disk used in the prior inves-

Contributed by the International Gas Turbine Institute (IGTI) of THE AMERICAN SOCIETY OF MECHANICAL ENGINEERS for publication in the ASME JOURNAL OF ENGINEERING FOR GAS TURBINES AND POWER. Paper presented at the International Gas Turbine and Aeroengine Congress and Exhibition, New Orleans, LA, June 4–7, 2001; Paper 2001-GT-0201. Manuscript received by IGTI, December 2000, final revision, March 2001. Associate Editor: R. Natole.

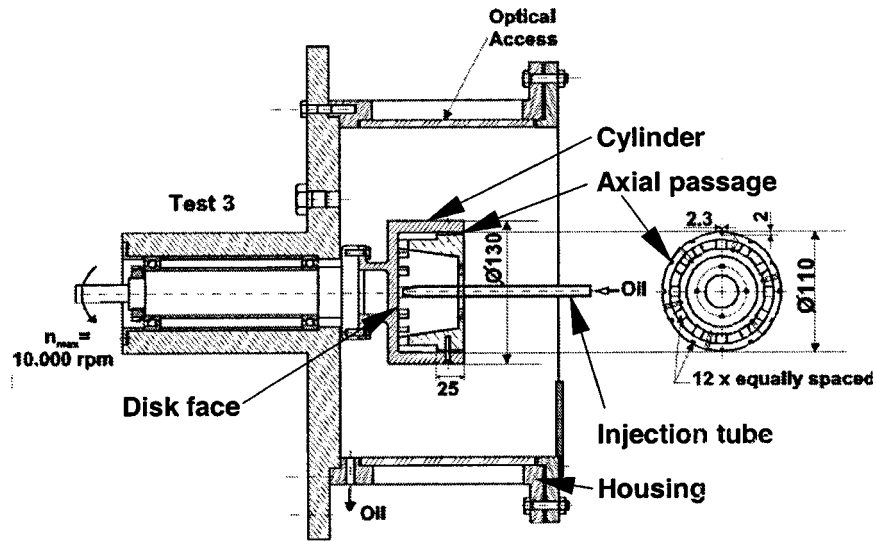


Fig. 1 Rotating Cylinder test rig

tigation has been replaced by a rotating outer cylinder that supports an insert which forms the axial passages (Fig. 1). Rotational speeds and physical dimensions of this arrangement had to be chosen such that two goals were met: (i) to provide relevant bearing compartment operating conditions and (ii) to guarantee full optical access to the rotating holes.

The first goal was met based on a simulation of the relevant Weber number which is the parameter dominating the atomization process. By using a test fluid (Dow Corning 200 Fluid 5cS) with the same fluid properties at room temperature that turbine oil would have at 373 K, engine Weber numbers are obtained for

$$1 \approx \left(\frac{\omega_T}{\omega_E} \right)^2 \left(\frac{D_C}{D_S} \right)^3 \quad (1)$$

The conclusion to be drawn from Eq. (1) is that it would be favorable to simulate the Weber number by aiming for a larger cylinder diameter and keeping the rotational speeds at a moderate level. For this investigation, a maximum rotational speed of $N_T = 10,000$ rpm and a cylinder diameter of $D_C = 0.13$ m (5.12 in.) have been chosen. The exit diameter of the rotating axial passages is $D_P = 0.11$ m (4.33 in.). These values translate into an engine condition of $N_E = 16,000$ rpm and a shaft diameter of $D_S = 0.10$ m (3.94 in.) which are expected to be typical values for current aeroengine designs.

The cylinder diameter of $D_C = 0.13$ m in combination with a relatively short cylinder length of about $L_C = 0.07$ m (2.76 in.) also supports the second design requirement by enabling a cantilever arrangement and, therefore, full optical access from the non-drive side. The cylinder is located in a stationary housing with an inner diameter of 0.301 m (11.85 in.). The housing consists of an aluminum frame supporting a transparent thermoplastic that allows optical access for flow visualization studies throughout the whole circumference. The shaft is positioned by spindle bearings and driven by an electromotor in combination with a flexible coupling and a flat belt.

Oil is pumped out of a reservoir through an electrical oil heater ($T_{\max} = 473$ K for $\dot{m} = 0.1$ kg/s) into the rig. It is fed along the centerline onto the spinning disk face using a tube with an inner diameter of $6 \cdot 10^{-3}$ m (0.236 in.). The oil is driven by centrifugal forces along the inner cylinder wall until it reaches an annulus from where it is evenly distributed to 12 axial passages that are equally spaced along the circumference. As shown in the next section on flow visualization results, oil is discharged through the axial passages as a thin film that eventually separates and disintegrates into droplets. The atomized oil is collected at the stationary,

transparent housing walls. Gravitation forces the oil to flow downward into the oil sump from where it is scavenged back into the reservoir.

Measurement Techniques. As in the previous investigation focussing on the disintegration of oil films at the rim of a rotating disk, [1], the experimental objectives of this study required applying techniques for flow visualization as well as laser Doppler techniques for the droplet sizing and velocimetry.

The first task, aimed at identifying the oil film breakup mechanisms, used two types of flow visualization arrangements. In one setup, stroboscopic illumination along with a simple video camera was employed to obtain a detailed full-access documentation of oil flow patterns. At high rotational speeds, however, the open housing of the test rig had to be covered in order to avoid oil droplet penetration into the laboratory room. Utilization of a simple transparent cover in combination with standard video equipment had limitations due to droplet coalescence and film flow formation at the inner wall. Therefore, another recording system was adapted with an endoscope optic ($6.5 \cdot 10^{-3}$ m diameter, 110° apex angle) in front of the video camera. For both arrangements all flow phenomena were monitored on a screen, recorded on videotape, and examined in detail using digital image processing.

For quantitative measurements of spray characteristics, a single particle counter, Aerometrics' PDPA, was used. In recent years, the PDPA has become a standard technique for atomization studies. Thus, a lengthy description of the measuring principle is avoided here and the interested reader is referred to the specific literature (e.g., Bachalo and Houser [11]). However, the adaptation of this measuring technique to the current test is special because it used a backscatter arrangement at an off-axis angle of 130 deg, which became available for measurements due to a relatively high index of refraction for oil that is greater than 1.4. A comprehensive analysis of this type of measurement configuration is given by Willmann et al. [12].

Test Matrix for Droplet Sizing and Velocimetry. Measurements for the characterization of sprays generated by the disintegration of oil films emerging from rotating axial passages were carried out for some 152 different combinations of operating condition and measurement location. As indicated in Fig. 2(a,b) variations of operating conditions included three different rotational speeds and two different flow rates. Measurements of spatial spray characteristics were configured to obtain axial and radial droplet size and velocity distributions and assumed a (time-averaged) axi-

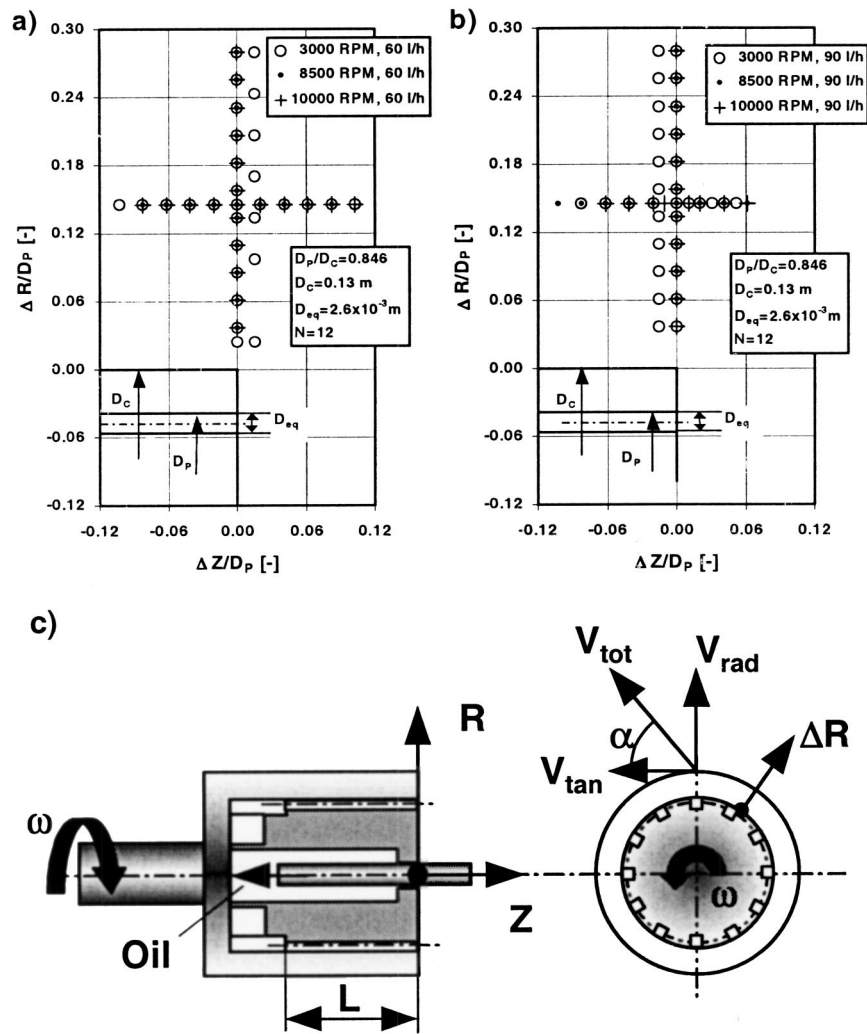


Fig. 2 Test matrix for droplet size and velocity measurements. (a) Configuration 3: $D_{eq} = 2.6 \cdot 10^{-3}$ m, $L/D_{eq} = 10$, $q = 1.67 \cdot 10^{-5}$ m³/s. (b) Configuration 3: $D_{eq} = 2.6 \cdot 10^{-3}$ m, $L/D_{eq} = 10$, $q = 2.50 \cdot 10^{-5}$ m³/s. (c) Nomenclature.

symmetric flow pattern. The circumferential measurement location and the nomenclature used in the subsequent discussion of test results are introduced in Fig. 2(c). Note the use of a right-hand side cylindrical coordinate system that is aligned with the centerline of the rotor (Z -axis) and the face of the rotating cylinder at the exit side of the axial passages (R -axis), respectively.

Experimental Results

Flow Visualization. Flow visualization studies were performed in order to identify the fundamental oil film break-up mechanisms that have to be considered in the modeling and analysis of quantitative test results. Figure 3 shows typical results gained from the full-access flow visualization.

A close examination of the picture visualizing oil atomization at very low rotational speeds (Fig. 3(a)) shows that a thin continuous oil film separates from the surface at the outer pitch diameter (D_p) of the rotating axial passage. The thin film extends radially outward from the OD side of the passage and is bent in the circumferential direction. At low speeds, equilibrium between the surface tension force at the free edge and the kinetic energy of the liquid sheet is maintained over almost the entire radial gap between cylinder and housing. From further video and photo analysis it was concluded that the oil film thickens at the edges of the sheet. The following two effects are expected to cause this behavior: (i) oil

accumulates in the corners of the noncircular rotating passages and (ii) surface tension tries to minimize the overall surface area. The thick edges of the oil film eventually disintegrate into ligaments and subsequently droplets. At higher rotational speeds (Fig. 3(b)) the same mechanisms occur, but the oil film breaks up more rapidly. The oil film disintegration appears to be completed at about $\Delta R/D_p = 0.10$, about twice the radial distance between oil film exit location and the rim of the cylinder ($5 \cdot 10^{-3}$ m, 0.2 in.).



Fig. 3 Full-access visualization of axial jet disintegration. (a) $\omega = 105$ rad/s, $q = 1.67 \cdot 10^{-5}$ m³/s, $\nu_L = 5 \cdot 10^{-6}$ m²/s. (b) $\omega = 524$ rad/s, $q = 1.67 \cdot 10^{-5}$ m³/s, $\nu_L = 5 \cdot 10^{-6}$ m²/s.

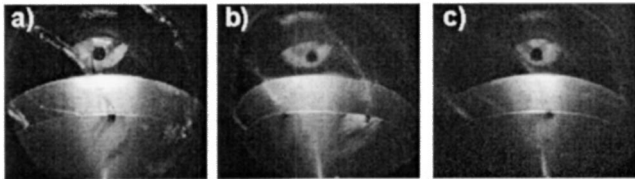


Fig. 4 Endoscope visualization of axial jet disintegration. (a) $\omega=314$ rad/s, $q=2.50 \cdot 10^{-5}$ m³/s, $\nu_L=5 \cdot 10^{-6}$ m²/s. (b) $\omega=890$ rad/s, $q=2.50 \cdot 10^{-5}$ m³/s, $\nu_L=5 \cdot 10^{-6}$ m²/s. (c) $\omega=1047$ rad/s, $q=2.50 \cdot 10^{-5}$ m³/s, $\nu_L=5 \cdot 10^{-6}$ m²/s.

In Fig. 4, samples from the endoscope visualization are shown for rotational speeds and flow rates that reflect test conditions as defined in (Fig. 2(b)). Though the viewport is much smaller than before and the endoscope optic distorts the image, the previous observations are confirmed. In addition, the impact of rotational speed on the droplet spray is visualized. A jet, which is characterized best at relatively low speed (Fig. 4(a)) as oil mist, transitions into a cloud or fog flow (Fig. 4(b,c)).

The qualitative flow investigation strongly suggests that the processes driving the atomization of oil films at rotating axial passages and rotating disks are somewhat similar. However, it is recognized that (i) the disintegration of oil films emerging from axial passages starts at discrete locations as opposed to a continuous rim and (ii) the turning from an axial to a radial flow direction with possible reattachment at the face of the cylinder will have an impact on the spray characteristics.

Typical results from the quantitative flow measurements are discussed in the following sections in terms of actual dimensional quantities. In order to assess differences in the atomization quality relative to rotating disk oil film disintegration, nondimensional quantities are introduced and compared in the subsequent sections.

Typical Droplet Sizes and Velocities. Figure 5 summarizes results obtained at a radial distance of $\Delta R=16 \cdot 10^{-3}$ m from the rim of the rotating cylinder ($\Delta R/D_p=0.145$). Measurements were acquired along an axial traverse ranging from about $0.10 < \Delta Z/D_p < 0.10$. In Fig. 5(a), results are presented in terms of arithmetic mean droplet diameter (D_{10}), area-averaged droplet diameter (D_{20}), volume-averaged droplet diameter (D_{30}), and a combination of the latter two, the so-called Sauter mean diameter (D_{32}). The shape of the curves shows a distinct asymmetry relative to the face of the disk ($\Delta Z/D_p=0$) with maximums in the diameter distribution located above the cylinder surface ($\Delta Z/D_p = -0.02$ to -0.04). As will be seen in the discussion of droplet flow velocities (Fig. 6), differences in the relative velocities between oil fragments and surrounding airflow are expected to be responsible for the shape of the size distribution curve. In the annular gap between rotating cylinder and stationary housing, the air velocity is higher than in the rather quiescent environment in front of the cylinder. Thus the relative velocity between the droplets that are spun off the cylinder at high speed and the air is smaller at negative $\Delta Z/D_p$ -values and the droplet size distribution is skewed towards larger diameters in this region. The decline in droplet sizes at both ends of the measured traverse is due to the fact that only small particles are able to diffuse into these regions. Arithmetic mean diameters in the center of the distribution ($\Delta Z/D_p=0$) are in the range of $D_{10}=55 \mu\text{m}$, whereas Sauter mean diameters are about twice as large.

Similar conclusions relative to the droplet propagation can be drawn from another set of characteristic diameters that is shown in (Fig. 5(b)). Diameters $D_{v,x}$ that define the diameter at which the fraction x of the total droplet volume has been accumulated are plotted against the axial coordinate. In the center of the droplet spray ($\Delta Z/D_p=0$), a value of $D_{v,0.1}=67 \mu\text{m}$ was obtained. Thus, a conclusion that can be drawn in comparison with (Fig.

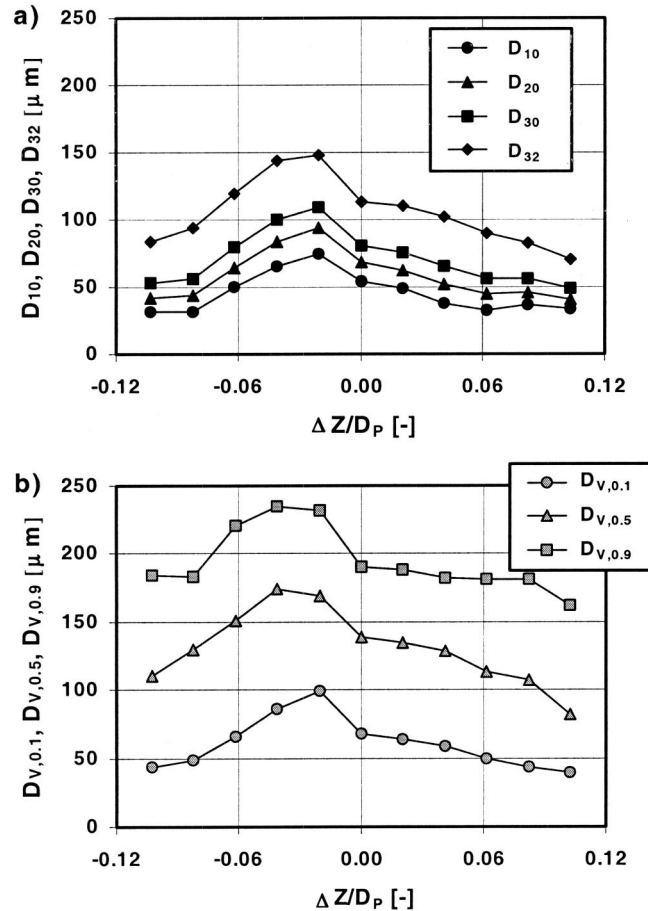


Fig. 5 $N=3000$ rpm, $q=1.67 \cdot 10^{-5}$ m³/s, $L/D_{eq}=10$, $\Delta R/D_p=0.145$. Axial profiles of (a) Mean diameters, (b) Cumulative diameters.

5(a)) is that the average diameter (D_{10}) of the spray contributes less than 10% to the overall volume. A much better overview on the volume distribution can be obtained from a combination of all three cumulative diameters given in (Fig. 5(b)), e.g. by tracking the mass mean diameter ($D_{v,0.5}$) and recognizing significant contributions to the volume distributions up to $D_{v,0.9}=200 \mu\text{m}$ ($\Delta Z/D_p=0$). However, it should be pointed out that cumulative diameters are sensitive to the correct and statistically relevant acquisition of a few large droplets at the upper limit of the measurement range. In the present study, a minimum of 10,000 valid samples was acquired for each of the 152 measurements. In addition to that, a huge number of exploratory measurements were conducted in order to find the best suitable combination of instrument settings and to avoid conditioned sampling.

The overall trend of the velocity distributions was briefly discussed above. Figure 6(a) summarizes size-class resolved droplet velocities for three droplet classes and compares this data with ensemble-averaged velocities. The positive leg of the velocity distribution ($\Delta Z/D_p > 0$) does not show any size dependency of the droplet velocity indicating a uniform flow behavior and a narrow size distribution. The negative leg, however, shows the effects of larger droplets by moving the ensemble-averaged values ("spray") above those of rather small size classes.

In Fig. 6(b), droplet flow angles corresponding to the velocity distributions discussed above are shown. The distribution displays a fairly homogeneous behavior for the whole spray and is almost symmetrical relative to $\Delta Z/D_p=0$.

Analogous to the presentation of axial profiles of diameters and velocities, Fig. 7 presents data for a radial traverse measured at

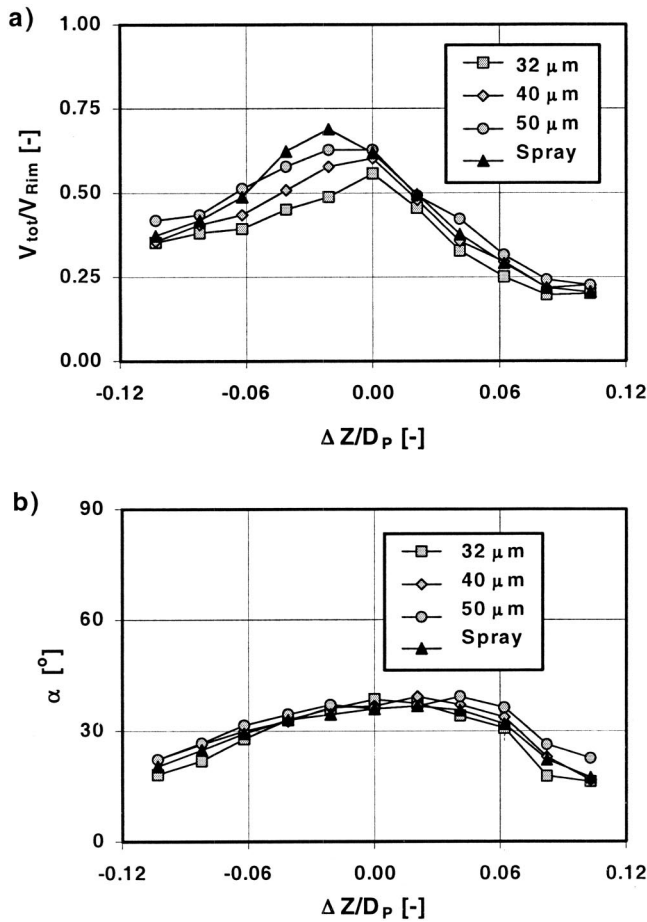


Fig. 6 $N=3000$ rpm, $q=1.67 \cdot 10^{-5}$ m³/s, $L/D_{eq}=10$, $\Delta R/D_p=0.145$. Axial profiles of (a) Droplet and spray velocities, (b) Droplet and spray flow angles.

the location $\Delta Z/D_p=0$, i.e., aligned with the exit plane of the axial passages at the face of the cylinder. It is interesting to note that values for D_{10} , D_{20} , and $D_{V,0.1}$ remain approximately constant for radial distances greater than $\Delta R/D_p=0.10$. Characteristic diameters that are more dependent on the upper limit of the measured size distribution display the ongoing atomization process of larger oil fragments by showing variations up to a distance of about $\Delta R/D_c=0.20$ where the atomization process is completed. For the subsequent analysis and correlation of test results, only those data at locations beyond where the mass mean diameter ($D_{V,0.5}$) has converged into a constant level were considered. In most cases this requirement was met at about $\Delta R/D_p=0.145$.

Droplet velocities decrease as the particles move radially outward (Fig. 8(a)). Again, ensemble-averaged velocity information has been combined with size-class resolved data. For the relatively high speed of $N=8500$ rpm considered here, the ensemble-average velocity is close to that of the 32 μm class which reflects the finer atomization at high rotational speeds. As expected, larger droplets maintain a higher velocity at a given radius which reflects the dependency of the droplet/gas interaction on the droplet Reynolds number.

In comparison with the lower speed case (Fig. 6(a)) the droplet velocity relative to the rim speed of the rotating cylinder seems to decrease with increasing rotational speed. Opposite to that, the droplet flow angle does not depend on either rotational speed or droplet size.

Impact of Rotational Speed and Flow Rate on the Spray Characteristic. In the present study, data sets have been ac-

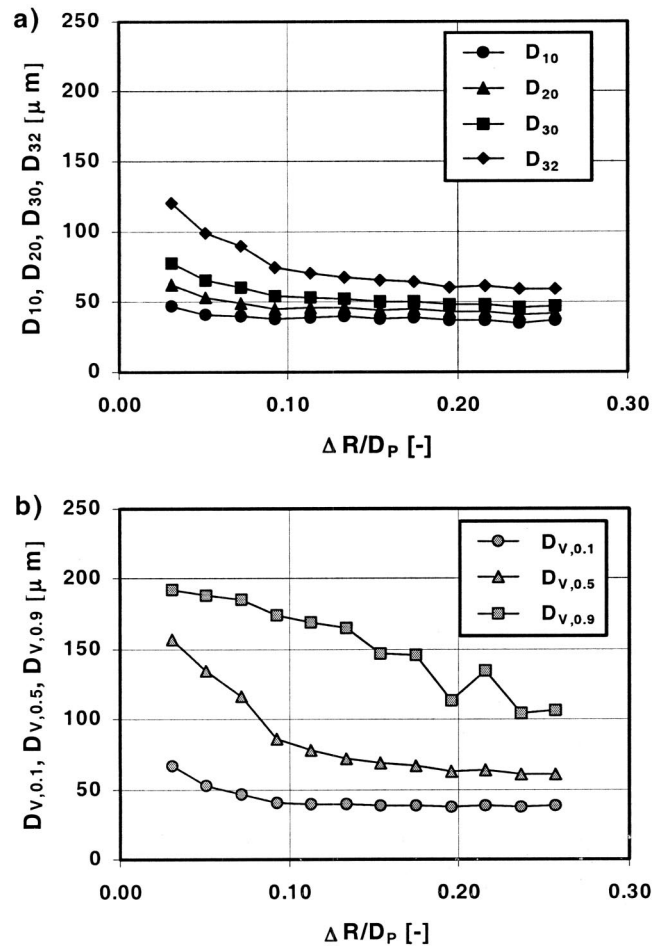


Fig. 7 $N=8500$ rpm, $q=1.67 \cdot 10^{-5}$ m³/s, $L/D_{eq}=10$, $\Delta Z/D_p=0.0$. Radial profiles of (a) Mean diameters, (b) Cumulative diameters.

quired for 6 different operating conditions. An overview and comparison of the atomization quality gained for these conditions is presented in Fig. 9. Arithmetic mean diameters (D_{10}) are plotted against rotational speeds with the flow rate as a curve parameter. Apparently, the latter does not have an identifiable impact on the droplet generation though it has to be mentioned that the variation examined here was relatively small. However, small and even negligible effects of flow rates are also known from other oil film disintegration studies, [1,10]. Opposite to that, the rotor speed has a significant impact on the droplet size. Figure 9 suggests a relationship $D_{10} \sim N^{-0.33}$.

Comparison With Oil Film Disintegration at the Rim of a Rotating Disk. Similar observations to those reported here were made by Glahn et al. [1] for oil film atomization studies at the rim of a rotating disk. Therefore, it is believed to be instructive to compare the spray characteristics generated under these different circumstances.

In order to compare the disintegration process in different configurations, nondimensional parameters are required. The previous study by Glahn et al. [1] adopted Hinze and Milbourn's [13] suggestion of using a modified Weber number

$$We^* = \frac{1}{8} \frac{\rho_L \omega^2 D^3}{\sigma} \quad (2)$$

and a nondimensional flow rate

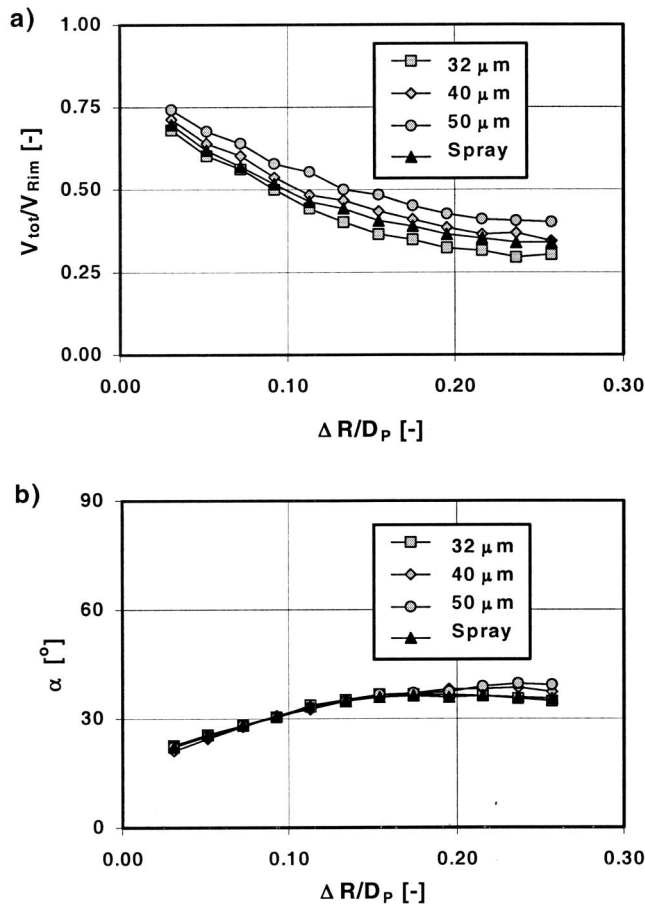


Fig. 8 $N=8500$ rpm, $q=1.67 \cdot 10^{-5} \text{ m}^3/\text{s}$, $L/D_{eq}=10$, $\Delta Z/D_p=0.0$. Radial profiles of (a) Droplet and spray velocities, (b) Droplet and spray flow angles.

$$V^+ = \frac{\rho_L q^2}{\sigma \cdot D_D^3} \quad (3)$$

for the characterization of disintegration processes and atomization products. However, an invariance relative to the flow rate has been observed in the present study and, therefore, only the Weber number as defined in Eq. (2) will be used subsequently to scale operating conditions. Note that the diameter to be used is the disk

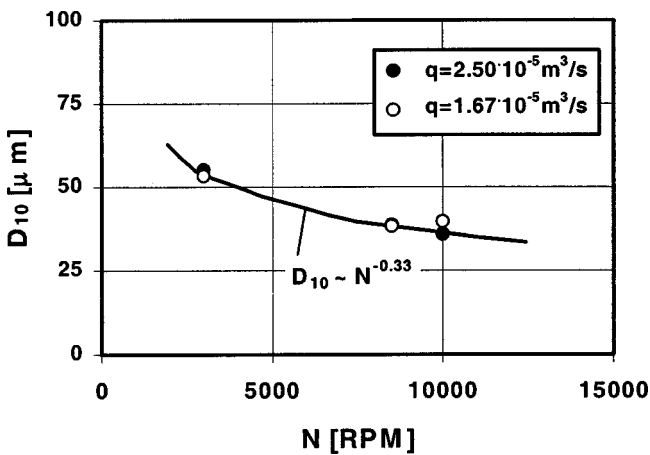


Fig. 9 Arithmetic mean droplet diameter versus operating conditions

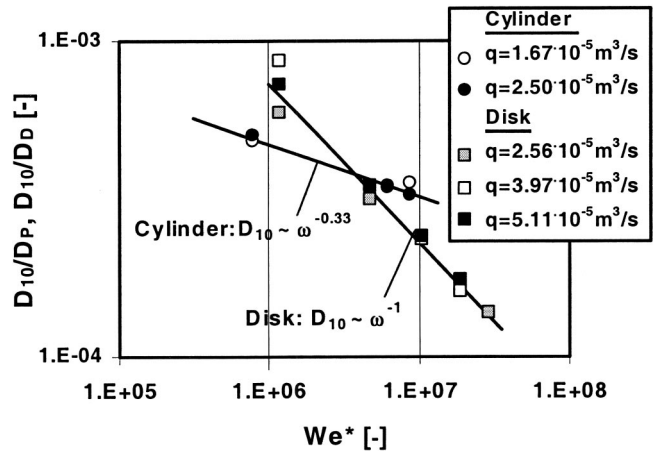


Fig. 10 Average spray diameters compared with those generated at the rim of a rotating disk

diameter, D_D , in the case of Glahn et al.'s [1] data while the pitch diameter of the rotating axial passages, D_p , is the proper dimension in the current study. The same diameters have been used to normalize measured mean diameters, D_{10}/D_D and D_{10}/D_p , respectively.

In Fig. 10, normalized arithmetic mean diameters of sprays generated by rotating axial passages and rotating disks are compared for various Weber numbers. The slopes of the trendlines that combine data point from different geometries have been included in the figure and indicate a similar though more pronounced impact of aerodynamic to surface tension impact on the rotating disk oil film atomization process. Furthermore, it is interesting to note that in the most relevant range of $10^6 < We^* < 10^7$, nondimensional mean diameters differ merely by some 30%. This is remarkable because oil film atomization processes at rotating disks offer the opportunity of predicting the diameter distribution based on an assessment of the oil film thickness at the face of the disk (Glahn et al. [10]). A comparison with the latter case, therefore, enables at least a rough estimate of droplet sizes generated by rotating axial passages at the face of a rotating cylinder.

As seen before in Figs. 5 and 7, the sprays considered here are non-homogeneous, i.e., the spray has to be regarded as a spectrum of drop sizes distributed about a mean value (D_{10}). Thus, in addition to this mean diameter, another parameter is needed in order to be able to calculate this distribution. The data obtained in the present study has been approximated best by use of a log-normal distribution of droplet sizes, [14]:

$$\frac{dn_d}{dD_d} = \frac{1}{\sqrt{2\pi}D_d s_g} \exp\left[-\frac{1}{2s_g^2}(\ln D_d - \ln D_{10})^2\right], \quad (3)$$

where s_g is the geometric standard deviation and n_d is the number of droplets per size class D_d . Measured standard deviations are shown in Fig. 11 for both geometries at a comparable flow rate. Though the data show some scatter, no distinct dependence on the Weber number has been identified. Oil film disintegration at the rim of a rotating disk apparently produces a narrower droplet size distribution than rotating axial passages. The latter case is reasonably well characterized by a constant value of

$$s_g = 0.335. \quad (4)$$

From Fig. 10 and 11, the mean droplet diameter and the spectrum of the size distribution can be estimated from known dimensions and operating conditions. Besides that, additional information relative to the droplet motion, namely flow velocity and flow angle, are required. Again, an attempt has been made to relate the current oil film atomization process to that prevailing at the rim of a rotating disk. Such a comparison is shown in Fig. 12 for the

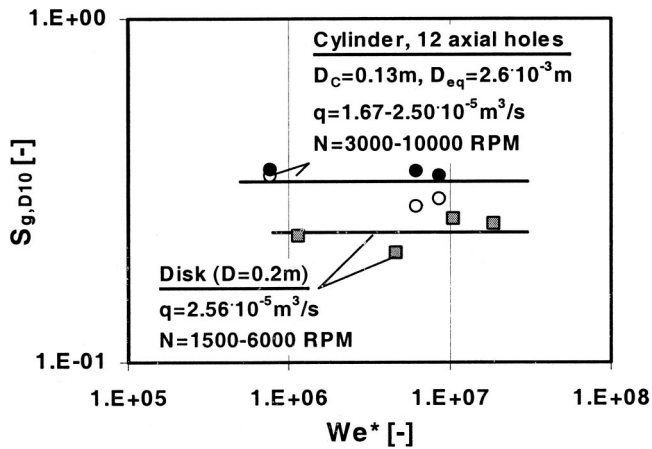


Fig. 11 Standard deviation of droplet diameter distribution

normalized mean velocity, V_{tot}/V_{rim} , and the flow angle, α , respectively. Note that the dimensions used in the definition of a “rim velocity” have to be consistent with those used before, i.e., for rotating axial passages, the pitch radius has to replace the rim radius to calculate the reference velocity. Using this scaling parameter yields identical relationships between droplet velocity and operating conditions in terms of Weber numbers for both configurations:

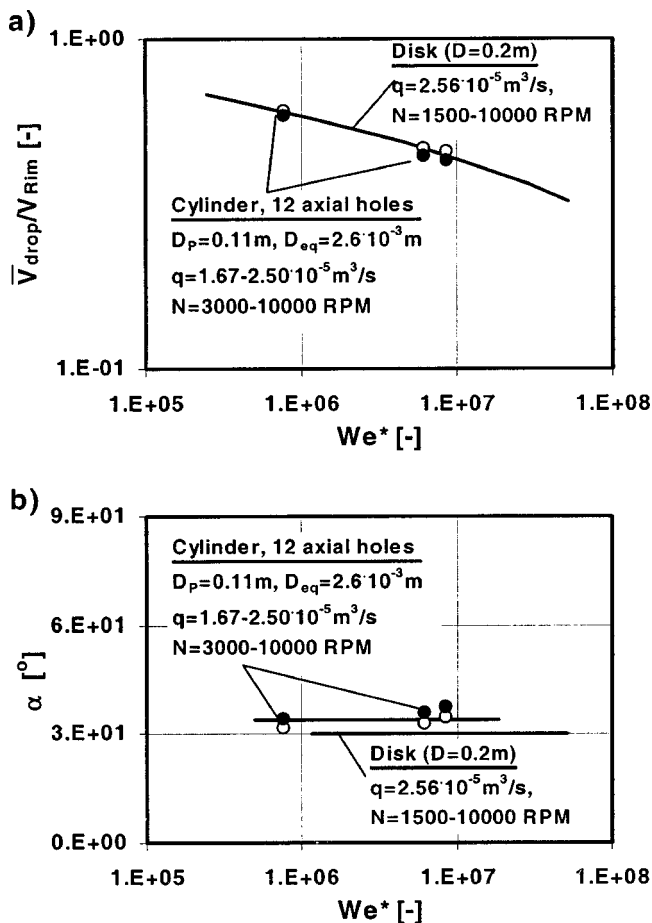


Fig. 12 Spray characteristics compared with those of droplet flows emerging from the rim of a rotating disk. (a) Initial droplet velocity. (b) Initial droplet flow angle.

$$\frac{\bar{V}_d}{V_{rim}} = 1.5 - 0.1327 \cdot \ln(We^{*0.5}). \quad (5)$$

As mentioned before, the flow angle is invariant to both operating conditions and remains constant at

$$\alpha = 34^\circ. \quad (6)$$

Conclusions

The disintegration of oil films emerging from axial passages at the face of a rotating cylinder is one of the droplet generation sources inside aeroengine lubrication system components. In order to establish a database for the development of atomization models, which are required in advanced design tools, this situation was studied experimentally and the following conclusions were drawn:

All measurements were carried out for a 5cS liquid, thus in terms of the fluid properties at relevant engine conditions.

The breakup process shows similarities to those observed at the rim of a rotating disk. It consists of the separation of a thin oil film from the outer most part of the inner surface of the rotating passage and the subsequent disintegration of this film into ligaments and droplets.

The droplet size distribution is driven by the rotational speed. No impact of oil flow rates has been detected which suggests an indifference relative to a variation of oil Reynolds numbers (based on the hydraulic diameter of the axial passage). The effect of the passage length was not investigated though it can be expected that the disintegration results are different for very short passages. More data are needed to establish these characteristics.

By introducing nondimensional parameters for the description of atomization products, a quantitative comparison of the disintegration processes at rotating axial passages with those at the rim of rotating disks has been enabled. This comparison confirms phenomenological interpretations of the oil film breakup and offers the opportunity to scale droplet size distributions and flow characteristics to other operating conditions.

Acknowledgments

The authors are grateful to Lou Dobek, Pratt & Whitney, East Hartford, for his encouragement and support of the work presented here.

Nomenclature

- D = diameter (m)
- $D_{10,20,30}$ = averaged droplet diameters based on number, surface area, and volume (m)
- $D_{V,x}$ = characteristic droplet diameter, representing the fraction x of the total droplet volume accumulated at the specified diameter (m)
- N = rotational speed (rpm)
- n = number
- q = volumetric flow rate (m^3/s)
- R, φ, Z = cylindrical coordinates (m, deg, m)
- s = standard deviation
- T = temperature (K)
- V = velocity (m/s)
- V^+ = nondim. volumetric flow rate
- We^* = modified Weber number
- α = flow angle, $\tan \alpha = V_{rad}/V_{tan}$ (deg)
- ρ = density (kg/m^3)
- μ = dynamic viscosity ($kg/(m \cdot s)$)
- σ = surface tension (N/m)
- ω = angular velocity (rad/s)

Subscripts

- C = cylinder
- D = disk
- $d(drop)$ = droplet

E = engine conditions
 L = liquid
 P = pitch
rad = radial
 T = test conditions
tan = tangential
tot = total

References

- [1] Glahn, A., Busam, S., Blair, M. F., Allard, K. L., and Wittig, S., 2000, "Drop-let Generation by Disintegration of Oil Films at the Rim of a Rotating Disk," ASME Paper No. 2000-GT-279.
- [2] Wittig, S., Glahn, A., and Himmelsbach, J., 1994, "Influence of High Rotational Speeds on Heat Transfer and Oil Film Thickness in Aero Engine Bearing Chambers," ASME J. Eng. Gas Turbines Power, **116**(2), pp. 395–401.
- [3] Chew, J., 1996, "Analysis of the Oil Film on the Inside Surface of an Aero-Engine Bearing Chamber Housing," ASME Paper No. 96-GT-300.
- [4] Glahn, A., and Wittig, S., 1996, "Two-Phase Air Oil Flow in Aero Engine Bearing Chambers—Characterization of Oil Film Flows," ASME J. Eng. Gas Turbines Power, **118**(3), pp. 578–583.
- [5] Glahn, A., and Wittig, S., 1999, "Two-Phase Air Oil Flow in Aero Engine Bearing Chambers—Assessment of an Analytical Prediction Method for the Internal Wall Heat Transfer," Int. J. Rotating Mach., **5**(3), pp. 155–165.
- [6] Glahn, A., Busam, S., and Wittig, S., 1997, "Local and Mean Heat Transfer Coefficients Along the Internal Housing Walls of Aero Engine Bearing Chambers," ASME Paper No. 97-GT-261.
- [7] Zaidi, S. H., Ishaq G., Aroussi A., Azzopardi, B. J., 1998, "Two-Phase Flow Study Around a Rotating Liquid Film Using Laser Techniques," *Proceedings of the VSJ-SPIE98*, Dec. 6–9, Yokohama, Japan.
- [8] Busam, S., Glahn, A., and Wittig, S., 1999, "Internal Bearing Chamber Wall Heat Transfer as a Function of Operating Conditions and Chamber Geometry," ASME J. Eng. Gas Turbines Power, accepted for publication.
- [9] Glahn, A., Kurreck, M., Willmann, M., and Wittig, S., 1996, "Feasibility Study on Oil Droplet Flow Investigations Inside Aero Engine Bearing Chambers—PDDPA Techniques in Combination with Numerical Approaches," ASME J. Eng. Gas Turbines Power, **118**, pp. 749–755.
- [10] Glahn, A., Blair, M. F., Allard, K. L., Busam, S., Schäfer, O., and Wittig, S., 2001, "Disintegration of Oil Films Emerging From Radial Holes Inside a Rotating Cylinder," ASME Paper No. 2001-GT-0202.
- [11] Bachalo, W. D., and Houser, M. J., 1984, "Phase Doppler Spray Analyzer for Simultaneous Measurements of Drop Size and Velocity Distributions," Opt. Eng., **23**, pp. 583–590.
- [12] Willmann, M., Glahn, A., and Wittig, S., 1997, "Phase-Doppler Particle Sizing with Off-Axis Angles in Alexander's Darkband," Part. Part. Syst. Charact., **14**(3), pp. 122–128.
- [13] Hinze, J. O., and Milborn, H., 1950, "Atomization of Liquids by Means of a Rotating Cup," ASME J. Appl. Mech., **17**, pp. 145–153.
- [14] Lefebvre, A. H., 1989, *Atomization and Sprays*, Hemisphere, Washington, DC.

A. Glahn
M. F. Blair

United Technologies Research Center,
411 Silver Lane, M/S 129-19,
East Hartford, CT 06108

K. L. Allard
Pratt & Whitney,
400 Main Street,
East Hartford, CT 06108

S. Busam
O. Schäfer
S. Wittig

Institut für Thermische Strömungsmaschinen,
Universität Karlsruhe,
Kaiserstr. 12,
Karlsruhe 76128, Germany

Disintegration of Oil Films Emerging From Radial Holes in a Rotating Cylinder

A fundamental study has been performed to examine the disintegration of oil films emerging from radial holes in a rotating hollow cylinder. The configuration investigated is an abstraction of one of the droplet generation sources in an aeroengine bearing compartment; similar configurations may also occur inside gearboxes. The paper aims to contribute to both the determination of directly applicable droplet characteristics and the establishment of a database that can be used for the development of droplet generation models. Similar to a prior paper on droplet generation processes at the rim of a rotating disk (Glahn, A. et al., 2000, "Droplet Generation by Disintegration of Oil Films at the Rim of a Rotating Disk," ASME Paper No. 2000-GT-0279,) the near-term objectives of the study are (i) to determine droplet sizes under relevant aeroengine bearing compartment operating conditions, and (ii) to measure individual droplet diameter/velocity relationships. The long-term objective is to incorporate this information into advanced CFD-based design tools. Therefore, special emphasis has been directed towards a correlation of test results that enables determination of boundary conditions for a two-phase (oil droplets/air) simulation of lubrication system components. Based on the results of the present paper, droplet flow boundary conditions in terms of mean diameter, standard deviation of the diameter distribution, starting velocity, and flow angle are available for oil droplets generated by disintegration of oil films emerging from rotating radial holes and rotating disks. [DOI: 10.1115/1.1586311]

Introduction

The major development driver for new engines is still the desire to increase the gas turbine's efficiency. This goal is accomplished by increases of both the overall pressure ratio and the turbine inlet temperature. Although beneficial for the cycle performance of the engine, the combination of high pressure, high temperature, and high rotational speeds of the turbine rotor leads to specific problems within the heat management of the engine's lubrication system, [1]. As a consequence, the design margin for the lubrication system and especially the bearing compartments becomes smaller and design tool improvements are required to meet the challenges of current and future engine developments.

In recent years, progress has been made on several subtasks involved in the overall design process. Wittig et al. [2] report on the identification of bearing compartment flow patterns. The characterization of oil film flows was subject of studies by Chew [3] and Glahn and Wittig [4]. Glahn et al. [5], Busam et al. [6], and Glahn and Wittig [7] investigated the heat transfer along the internal bearing chamber housing walls. Droplet flows in a rotating, annular two-phase flow environment were studied for air/water mixtures at low speeds by Zaidi et al. [8]. All these studies were helpful in getting an overall picture of the flow phenomena involved in bearing compartments. They help to establish a database for validation purposes and some of them appear to be directly applicable for certain aspects of the engine design. However, the development of a design system and its adaptation to different geometrical and operational boundary conditions requires a platform that is able to integrate these submodels. A viable approach would be to use CFD methods to predict the two-phase air/oil flow in lubrication system components. A study presented by

Glahn et al. [9] suggested the feasibility of such an approach. However, a prerequisite for a successful implementation of these tools into a standard design environment is the availability of boundary conditions and the development of submodels which describe the complex phase interaction mechanism and atomization effects prevailing in these parts. Therefore, further studies of film behavior and atomization processes are required.

Glahn et al. [10] report on the first phase of a multiyear, fundamental investigation into generic oil system atomization processes: specifically the disintegration of oil films at the rim of a rotating disk. The present paper is a continuation of this effort and deals with the disintegration of oil films emerging from radial holes in a rotating cylinder. This is a generic representation of one of the droplet generation sources in an aeroengine bearing compartment, e.g., under-race lubrication oil supply arrangements or intershaft oil flow configurations; similar configurations may also occur inside gearboxes.

As in the previous study, the objectives were as follows: (i) to identify disintegration modes relevant with respect to aeroengine bearing compartment operating conditions, (ii) to determine droplet sizes under those operating conditions, and (iii) to measure individual droplet diameter/velocity relationships.

The current experimental paper aims to contribute to both the definition of directly usable droplet characteristics and the establishment of a database that can be used for model development. Following a brief description of the experimental setup, results are presented in terms of samples from the visualization work, typical spatial droplet diameter distributions, characteristic diameters, and droplet velocities as a function of flow rate and rotational speed. A theory is developed that enables comparison of oil film atomization by rotating radial holes with that of a rotating disk. From this theory, correlations are developed for all atomization products, namely the mean droplet diameter, the standard deviation of the diameter distribution, the mean droplet velocity, and the droplet flow angle.

Contributed by the International Gas Turbine Institute (IGTI) of THE AMERICAN SOCIETY OF MECHANICAL ENGINEERS for publication in the ASME JOURNAL OF ENGINEERING FOR GAS TURBINES AND POWER. Paper presented at the International Gas Turbine and Aeroengine Congress and Exhibition, New Orleans, LA, June 4-7, 2001; Paper 2001-GT-0202. Manuscript received by IGTI, December 2000, final revision, March 2001. Associate Editor: R. Natole.

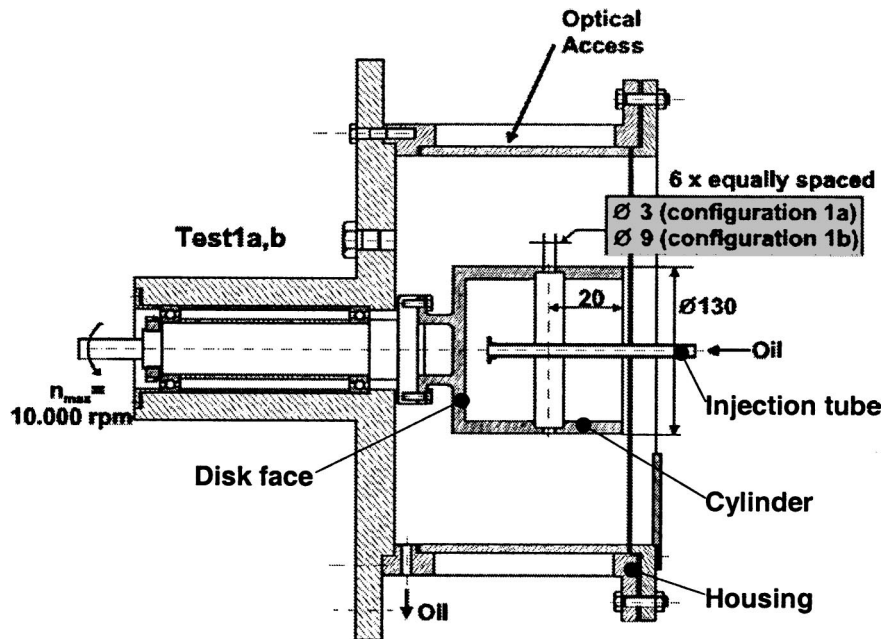


Fig. 1 Rotating cylinder test rig

Experimental Setup and Techniques

Test Rig. The test facility used for the fundamental oil film disintegration studies reported in this paper is the same as was used by Glahn et al. [10]. However, the rotating disk used in the prior investigation has been replaced by a rotating cylinder. The rotational speeds and the physical dimensions of the cylinder had to be chosen such that two goals were met: (i) to achieve an investigation relevant to bearing compartment operating conditions and (ii) to aim for a design that guarantees full optical access to the rotating holes.

The first goal was met based on a simulation of the relevant Weber number which is the parameter dominating the atomization process. By using a test fluid (Dow Corning 200 Fluid 5cS) with the same fluid properties at room temperature as turbine oil at 373 K, engine Weber numbers are obtained for

$$1 \approx \left(\frac{\omega_T}{\omega_E} \right)^2 \left(\frac{D_C}{D_S} \right)^3. \quad (1)$$

Equation (1) suggests that it would be favorable to simulate the Weber number by aiming for a higher cylinder diameter and keeping the rotational speeds at a moderate level. For this investigation, a maximum rotational speed of $N_T = 10,000$ rpm and a cylinder diameter of $D_C = 0.13$ m (5.12 in.) have been chosen. These values translate into an engine condition of $N_E = 16,000$ rpm and a shaft diameter of $D_S = 0.10$ m (3.94 in.) which are expected to be typical values for current aeroengine designs.

The cylinder diameter of $D_C = 0.13$ m in combination with a relatively short cylinder length of about $L_C = 0.096$ m (2.76 in.) also supports the second design requirement by enabling a cantilever arrangement and, therefore, full optical access from the non-drive side. As shown in Fig. 1, the cylinder is located in a stationary housing with an inner diameter of 0.301 m (11.85 in.). The housing consists of an aluminum frame supporting a transparent thermoplastic that allows optical access for flow visualization studies throughout the whole circumference. The shaft is positioned by spindle bearings and driven by an electro-motor in combination with a flexible coupling and a flat belt.

Oil is pumped out of a reservoir through an electrical oil heater ($T_{\max} = 473$ K for $\dot{m} = 0.1$ kg/s) into the rig. It is fed along the centerline onto the spinning disk face using a tube with an inner

diameter of $6 \cdot 10^{-3}$ m (0.236 in.). The oil is driven by centrifugal forces along the inner cylinder wall until it reaches a groove from where it is evenly distributed to six radial holes that are equally spaced around the circumference. As shown in the next section on flow visualization results, oil is discharged through the radial holes as a thin film that separates from the hole wall and disintegrates into droplets. The atomized oil is collected at the stationary, transparent housing walls. Gravitation forces the oil to flow downward into the oil sump from where it is scavenged back into the reservoir.

Measurement Techniques. As in the previous investigation focussing on the disintegration of oil films at the rim of a rotating disk (Glahn et al., [10]), the experimental objectives of this study required applying techniques for flow visualization as well as laser Doppler techniques for the droplet sizing and velocimetry.

For the first task, aimed at identifying the oil film breakup mechanisms, stroboscopic illumination along with a simple video camera was used to obtain a detailed documentation of oil flow patterns. All flow phenomena were monitored on a screen, recorded on videotape, and examined in detail using digital image processing.

For quantitative measurements of spray characteristics, a single particle counter, Aerometrics' PDPA, was used. In recent years, the PDPA has become a standard technique for atomization studies. Thus, a lengthy description of the measuring principle is avoided here and the interested reader is referred to the specific literature (e.g., Bachalo and Houser [11]). However, the adaptation of this measuring technique to the current test is special because it used a backscatter arrangement at an off-axis angle of 130 deg, which became available for measurements due to a relatively high index of refraction for oil that is greater than 1.4. A comprehensive analysis of this type of measurement configuration is given by Willmann et al. [12].

Test Matrix for Droplet Sizing and Velocimetry. Measurements for the characterization of sprays generated by the disintegration of oil films emerging from rotating radial holes were carried out for two configurations and 224 different combinations of operating condition and measurement location. As indicated in Fig. 2(a,b), variations of operating conditions included three different rotational speeds and four different flow rates. Measure-

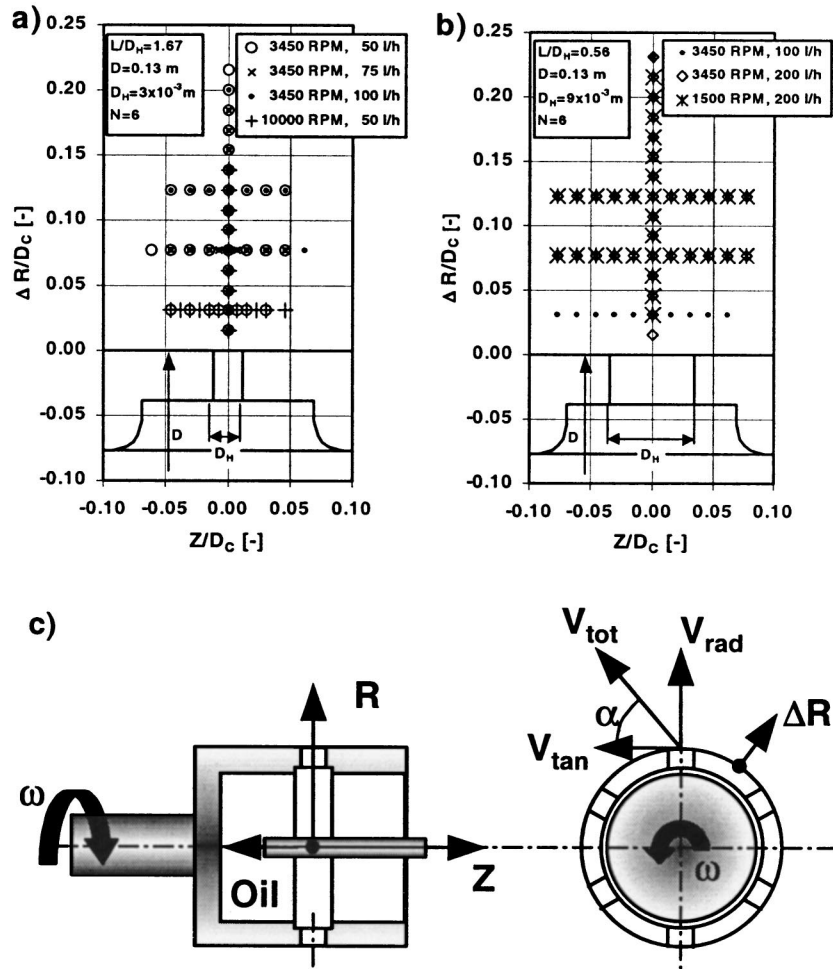


Fig. 2 Test matrix for droplet size and velocity measurement. (a) Configuration 1A: $D_H=3 \cdot 10^{-3}$ m, $(L/D)_H=1.67$. (b) Configuration 1B: $D_H=9 \cdot 10^{-3}$ m, $(L/D)_H=0.56$. (c) Nomenclature.

ments of spatial spray characteristics were designed to obtain axial and radial droplet size and velocity distributions and assumed a (time-averaged) axisymmetric flow pattern. The circumferential measurement location and the nomenclature used in the subsequent discussion of test results are introduced in Fig. 2(c). Note the use of a right-hand side cylindrical coordinate system that is aligned with the centerline of the rotor (Z -axis) and the centerline of the radial hole (R -axis), respectively.

Experimental Results

Flow Visualization. Flow visualization studies were performed in order to identify the fundamental oil film break-up mechanisms to be considered in the modeling and analysis of quantitative test results. Figure 3 shows typical results gained from the flow visualization. The picture in the left-hand side (Fig. 3(a)) shows in some detail that a thin continuous oil film separates from the inner surface of the rotating radial hole ($D_H=9 \cdot 10^{-3}$ m). This separation process occurs along the whole circumference of the hole. The thin film extends radially outward from the rim of the hole (initially forming a hollow fluid cylinder) until equilibrium is reached between the surface tension force at the free edge and the kinetic energy of the liquid sheet. The oil film thickens at the edges of the sheet and then disintegrates into ligaments and droplets (Fig. 3(b)). This process is very similar to the disintegration of oil films at the rim of a rotating disk, [10,13,14].

The qualitative flow investigation strongly suggests that the processes driving the atomization of oil films at rotating radial holes and rotating disks are basically the same. This information was used to derive a nondimensional description of disintegration products and their subsequent correlation with operating conditions. However, some typical results will be discussed first in

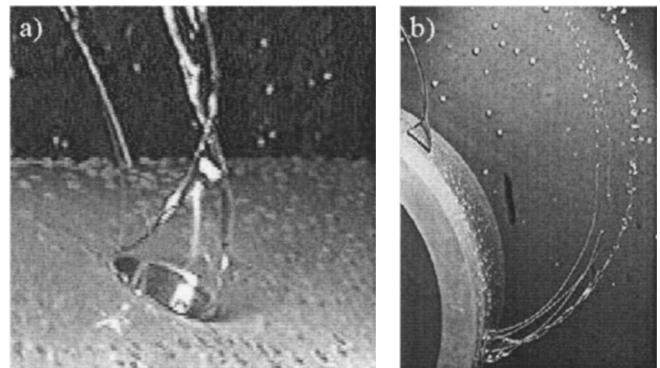


Fig. 3 Oil atomization at a rotating radial hole ($D_H=9 \cdot 10^{-3}$ m); (a) sheet separation, (b) droplet trajectory

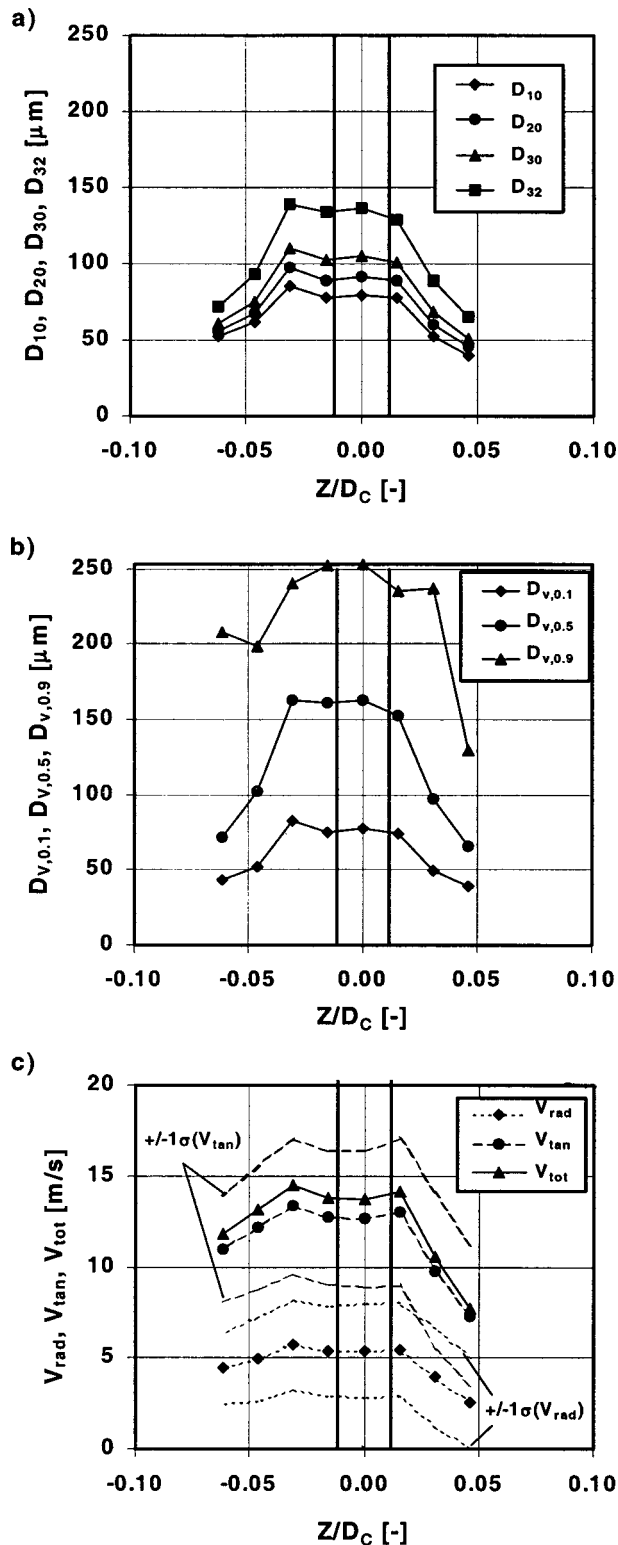


Fig. 4 $N=3450$ rpm, $q=1.39 \cdot 10^{-5}$ m³/s, $L/D_H=1.67$, $\Delta R/D_C=0.077$. Axial profiles of (a) mean diameters, (b) cumulative diameters, (c) mean velocities and velocity range.

terms of actual dimensional quantities, which are often more suitable than nondimensional quantities to develop an initial understanding of the droplet flow phenomena.

Typical Droplet Sizes and Velocities. Figure 4 summarizes results obtained for configuration 1A at a radial distance of ΔR

$=10 \cdot 10^{-3}$ m from the rim of the rotating cylinder. Measurements were acquired along an axial traverse ranging from about $-0.07 < Z/D_C < 0.05$. The axial location of the radial holes is indicated by vertical lines at $R_H/D = \pm 0.0115$. Results are presented in terms of characteristic diameters, mean velocities, and velocity distributions.

Figure 4(a) shows the arithmetic mean droplet diameter (D_{10}), the area-averaged droplet diameter (D_{20}), the volume-averaged droplet diameter (D_{30}), and a combination of the latter two, the so-called Sauter mean diameter (D_{32}), which represents a droplet with the same volume-to-surface ratio as the whole spray. The shape of the curves reflects the jet-like flow of oil into the annulus between rotating cylinder and stationary housing. Larger droplets are concentrated in a region more or less aligned with the center-line of the radial holes. Only smaller droplets separate from this flow path and penetrate into regions beyond $\pm Z/D_C=0.02$. Arithmetic mean diameters in the center of the distribution are approximately $D_{10}=75 \mu\text{m}$, whereas Sauter mean diameters are about twice as large.

Similar conclusions relative to the droplet propagation can be drawn from another set of characteristic diameters that is shown in Fig. 4(b). Diameters $D_{v,x}$ that define the diameter at which the fraction x of the total droplet volume has been accumulated are plotted against the axial coordinate. In the center of the droplet spray ($Z/D_C=0$), a value of $D_{v,0.1}=75 \mu\text{m}$ was obtained. Thus, a conclusion that can be drawn from the combined results of Fig. 4(a) and 4(b) is that the average diameter (D_{10}) of the spray contributes only 10% to the overall volume. A much better overview on the volume distribution can be obtained from a combination of three cumulative diameters. However, cumulative diameters are sensitive to the correct and statistically relevant acquisition of a few large droplets at the upper limit of the measurement range. In the present study, a minimum of 10,000 valid samples was acquired for each of the 224 measurements. In addition to that, a huge number of exploratory measurements were conducted in order to find the best suitable combination of instrument settings and to avoid conditioned sampling.

Mean radial and tangential velocities are shown in Fig. 4(c). The velocity distributions along the axial traverse support the phenomenological explanation of droplet distributions given above. Only low inertia droplets outside of the core of the droplet spray can be decelerated significantly by the surrounding air. Note that the $\pm 1\sigma$ velocities for both components are about $\pm 40\% - 50\%$ of the mean velocities. This rather broad distribution of velocities reflects the fact that they represent the whole spray, i.e., large variations in droplet size and, therefore, droplet Reynolds number.

Analogous to the presentation of axial profiles of diameters and velocities, Fig. 5 shows data for a radial traverse measured at the location $Z/D_C=0$, i.e., aligned with the radial holes. It is interesting to note that values for D_{10} and $D_{v,0.1}$ remain approximately constant for radial distances greater than $\Delta R/D_C=0.05$. All other characteristic diameters display the ongoing atomization process of larger oil fragments by showing continuously decreasing droplet sizes up to a distance of about $\Delta R/D_C=0.18$ at which the atomization process is completed. For the subsequent analysis and correlation of test results, only those data were considered for which this "completed atomization" condition was reached. The velocity distributions (Fig. 5(c)) show the expected transition from a tangentially orientated flow (in the stationary frame of reference) to a more and more radially orientated flow vector. The spread of measured velocities ($\pm 1\sigma$) was approximately the same as for the axial distribution and does not change significantly with increasing radii.

Size Class Resolved Droplet Velocity Distributions. The previous discussion of typical traverse data included mean and velocity range information useful for an overall understanding of the flow situation. However, these velocities represent the whole spray and are affected not only by operating conditions such as rotational speed and flow rate but also by the atomization quality,

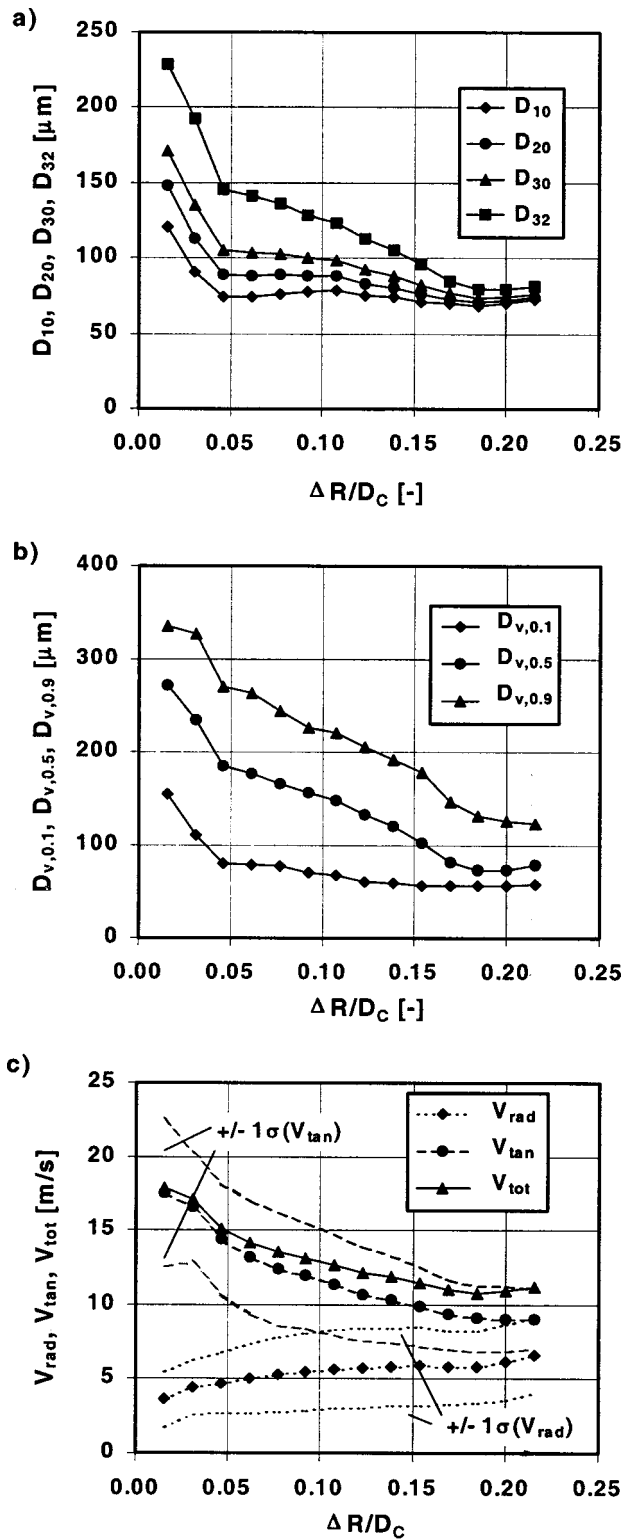


Fig. 5 $N=3450$ rpm, $q=1.39 \cdot 10^{-5}$ m³/s, $L/D_H=1.67$, $Z/D_C=0.0$. Radial profiles of (a) mean diameters, (b) cumulative diameters, (c) Mean velocities and velocity range.

i.e., the diameter distribution. An analysis of cause/effect relationships on the droplet flow has to be based on individual size-class resolved velocities that enable a better separation of droplet generation mechanisms from droplet propagation phenomena. Samples from such an analysis are given in Figs. 6 and 7. Both

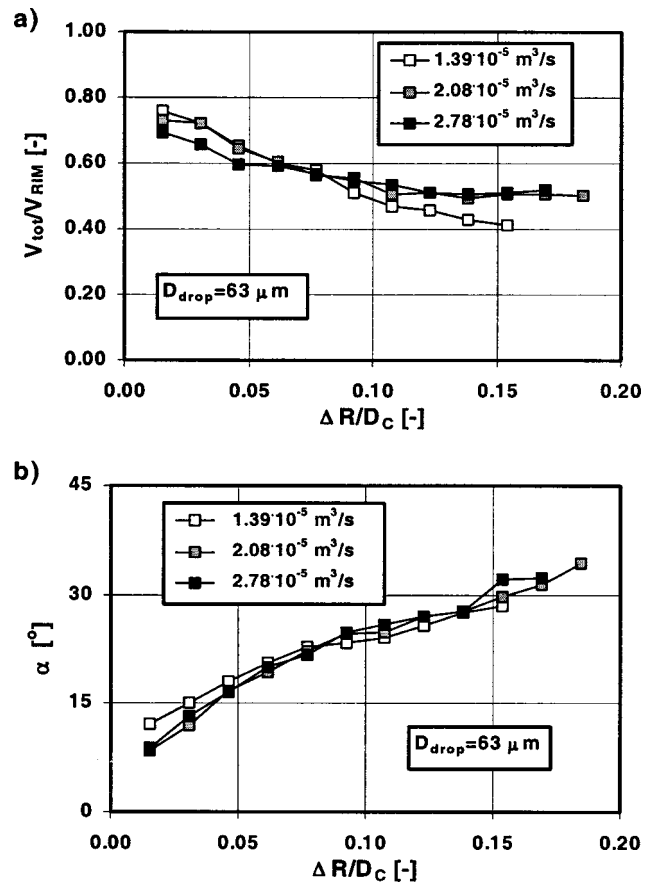


Fig. 6 $N=3450$ rpm, $L/D_H=1.67$, $Z/D_C=0.0$. Effect of flow rate on (a) droplet velocities based on rim speed, (b) flow angles.

figures contain droplet velocities based on the rim speed of the rotating cylinder and flow angles relative to the tangential direction (Fig. 2(c)).

In Fig. 6, the effect of the oil flow rate on the droplet velocity and the flow angle is shown for a droplet diameter class of $D_{drop}=63 \mu\text{m}$ along a radial traverse. The overall impact of the flow rate on both parameters is small. The droplet velocity decreases with increasing distance from the cylinder until it reaches a constant level of about $V_{tot}/V_{rim}=0.5$. For the lowest flow rate, however, the velocity distribution seems to have a slightly steeper slope than those measured for higher flow rates. Similar observations were made for other size classes.

A possible reason for this difference in the flow behavior is the slower disintegration process that has been observed for these lower flow rates. The droplet flow angle increases from an almost tangential orientation to values slightly above 30 deg (at $\Delta R/D_C=0.18$). No dependence on the oil flow rate has been observed.

In contrast to the relatively weak dependence on the oil flow rate displayed in Fig. 6, rotational speed has a substantial impact on both droplet velocity and flow angle. Figures 7(a–c) show the results for droplets with $D_{drop}=40 \mu\text{m}$ for three speed conditions and a constant flow rate of $q=5.44 \cdot 10^{-5}$ m³/s. Note that the distances ($\Delta R/D_C$) from the cylinder to the first data point for Fig. 7 are inversely dependent on the rotational speed. These “innermost” data points indicate the location where the first statistically meaningful 40 μm droplet data could be obtained. This result indicates that the film breakup/atomization process depends on the rotor speed. While Fig. 7(a) demonstrates that the absolute velocity of the droplets increases directly with the rotational speed, Figs. 7(a) and 7(b) show that the radial decrease of the

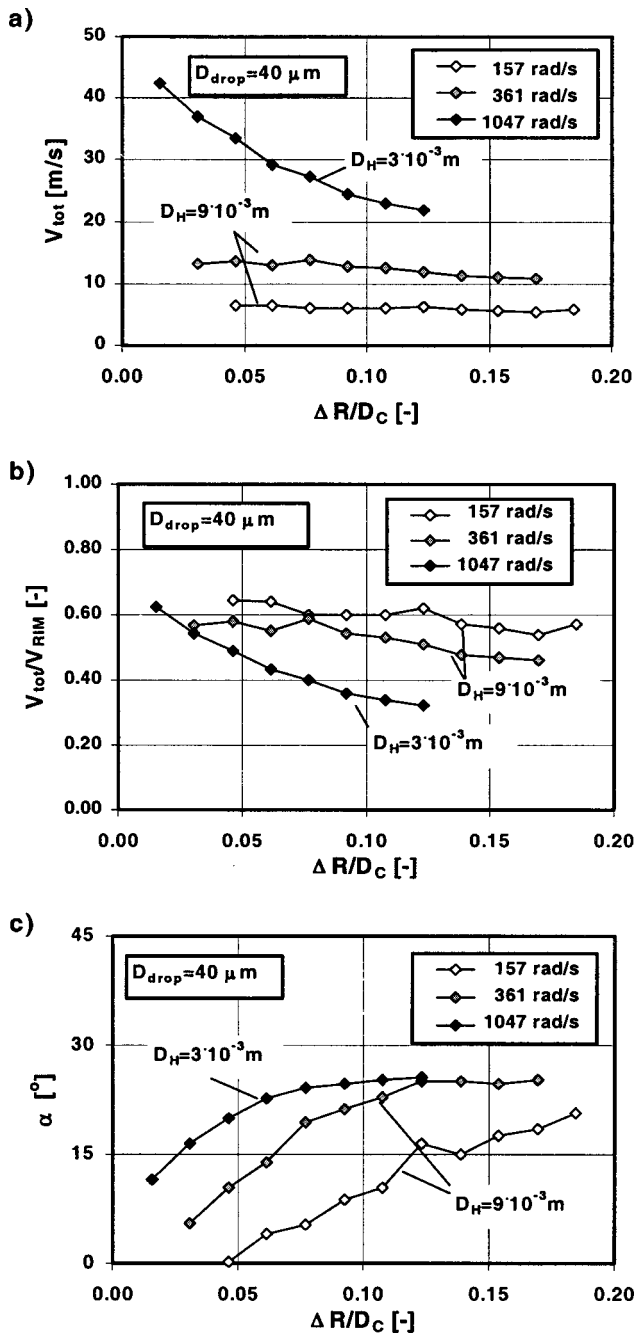


Fig. 7 $q=5.44 \cdot 10^{-5} \text{ m}^3/\text{s}$, $L/D_H=0.56$, $Z/D_C=0.0$. Effect of rotational speed on (a) absolute droplet velocities, (b) droplet velocities based on rim speed, (c) flow angles

droplet velocity is also highly speed dependent. For the analysis of these flow conditions it is helpful to examine the equation of motion for a single liquid particle in air:

$$\frac{d\mathbf{V}_d}{dt} = \frac{18 \cdot \mu_G}{\rho_d \cdot D_d^2} (\mathbf{V}_G - \mathbf{V}_d). \quad (2)$$

Note that Eq. (2) is valid for small droplet Reynolds numbers, where the coefficient of drag can be approximated by $C_W = 24/\text{Re}_D$. This condition is met for the droplet size and velocity range considered in Fig. 7. It can readily be concluded from the equation of motion that the deceleration of a liquid droplet of given size does not scale with the characteristic velocity of its generation mechanism (Fig. 7(a) shows that the rotor speed deter-

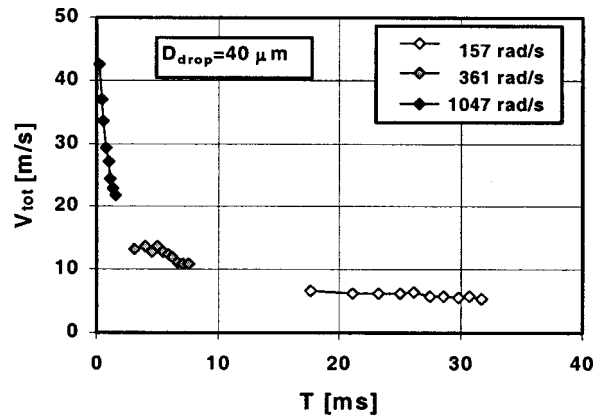


Fig. 8 Deceleration of droplets at various rotational speeds

mines the initial droplet velocity) but depends on the absolute velocity magnitude. The stronger deceleration at higher cylinder speeds has been visualized in Fig. 8 by transferring the measured spatial velocity distributions into the time domain. The time increment has been calculated from the radial location and the measured radial velocity component.

As noted above, the data indicate that the droplet generation due to oil film disintegration occurs much more rapidly at higher rotor speeds. The film breakup process is driven by the ratio of destabilizing aerodynamic forces to surface tension forces, thus depending on some function of the Weber number which is proportional to the square of the relative velocity. Therefore, the velocity distributions shown in Figs. 7(a,b) are a result of superimposed effects of stronger deceleration and earlier onset of deceleration. The latter is a result of an earlier completion of the atomization process for higher speeds which enables the acquisition of relatively small droplets ($40 \mu\text{m}$ diameter) at smaller radii. The relative magnitude of these effects could be determined based on further studies with independent simulations of droplet Weber number and Reynolds numbers, respectively.

Another consequence of different time scales involved in the disintegration process is that of significantly different flow angles (Fig. 7(c)). Close to the rotating surface, droplet flow angles show a steeper angle for higher rotational speeds but also a more rapid transition into a constant flow angle characteristic. That is consistent with a faster breakup process as discussed above.

Impact of Hole Diameter, Rotational Speed, and Flow Rate on the Spray Characteristic. Data sets have been acquired from two rotating hole geometries in the present study. Furthermore, similarities to the disintegration processes at the rim of a rotating disk have been identified that suggest an incorporation of this kind of data into the subsequent data analysis. In order to compare the three different configurations, nondimensional parameters are required. The previous study by Glahn et al. [10] adopted Hinze and Milborn's [13] suggestion of using a modified Weber number

$$\text{We}^* = \frac{1}{8} \frac{\rho_L \omega^2 D_D^3}{\sigma} \quad (3)$$

and a nondimensional flow rate

$$V^+ = \frac{\rho_L q^2}{\sigma \cdot D_D^3} \quad (4)$$

for the characterization of disintegration processes and atomization products. Though it was not introduced as such, it is interesting to note that the nondimensional flow rate as defined in Eq. (4) is basically the ratio of radial inertia to surface tension forces, thus a radial Weber number. Recognizing this physical interpretation of

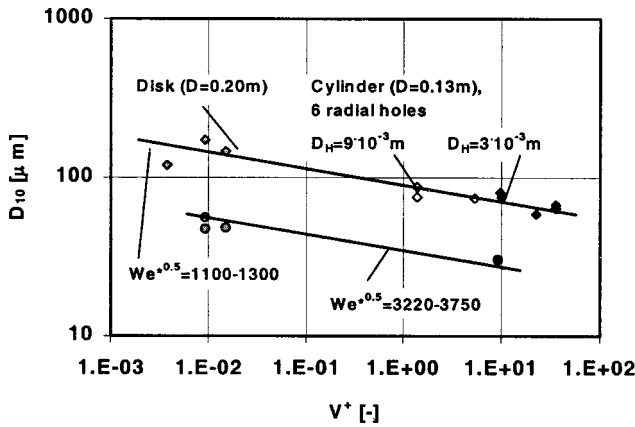


Fig. 9 Arithmetic mean droplet diameter versus nondimensional volumetric flow rate

the nondimensional flow rate, it is useful to rewrite Eq. (4) to account for the specifics of the rotating hole configurations:

$$V^+ = \frac{\rho_L q^2}{n^2 \cdot \sigma \cdot D_H^3}, \quad (5)$$

with n as the number of holes with diameter D_H . Note that Eqs. (4) and (5) are identical if the rim of the rotating disk is treated in terms of the flow rate impact as a single hole ($n=1$) with a diameter $D_H=D_D$.

In Fig. 9, arithmetic mean diameters of sprays generated by the three different configurations are compared for various flow rates and two rotational speeds. V^+ as defined in Eq. (5) appears to be a proper scaling parameter for this comparison though the impact of the flow rate on the diameter seems to be relatively small. In contrast to the weak dependence on flow rate, rotational speeds significantly influence the atomization quality. This is highlighted by lines of constant speed (note that $We^{*0.5} \sim \omega$) which demonstrate an almost linear relationship between speed increase and diameter reduction. Both observations relative to the impact of operating parameters are consistent with conclusions drawn from the rotating disk studies by Glahn et al. [10].

Correlation of Test Results. Employing the type of data reduction shown in Fig. 9, the test results could have been expressed as a function of some power law representation of V^+ and We^* . Such an approach would lead to correlations that could predict the mean diameter, D_{10} , and the Sauter mean diameter, D_{32} , within a confidence range of about 30% and 50%, respectively. Considering the complexity of the flow problem, this would already be a satisfactory result. However, in the current study, an attempt has been made to relate the atomization product more closely to its generation mechanisms, i.e., to the oil film flow conditions at the atomizer edge. It is hoped that this approach will further enhance the understanding of the disintegration process, will lead to a broader applicability of subsequent model formulations, and will result in a higher confidence level towards these models.

It has been shown by flow visualization that the droplet spray in rotating disk and rotating cylinder configurations is generated by disintegration of thin oil films and, therefore, it is instructive to compare the size of the droplets with the thickness of the oil sheet prior to its break up.

For the calculation of film conditions at the rim of a rotating disk or at the exit plane of a rotating radial hole, a simple model has been derived that is explained in some detail in the Appendix. According to this model, the oil film thickness can be calculated from

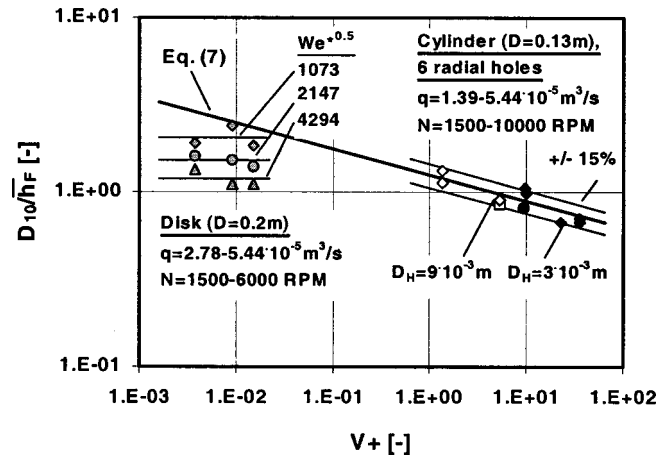


Fig. 10 Mean diameter based on oil film thickness at the rim of the hole/disk

$$\bar{h}_F = \left(\frac{6 \cdot q \cdot \nu_L}{\omega^2 \cdot D_{D,C} \cdot n \cdot \pi \cdot D_{D,H}} \right)^{1/3}. \quad (6)$$

Note that different diameters have to be used in Eq. (6) if it is desired to compute the oil film thickness at the rim of a rotating disk (D_D) or the oil film thickness at the exit of a rotating hole (D_C and D_H).

In Fig. 10, measured mean droplet diameters D_{10} have been related to film thicknesses calculated from Eq. (6) and plotted for various rotational speeds as a function of non-dimensional flow rates V^+ . It is most interesting to note that all data acquired for the test case of a rotating cylinder with radial holes seem to group around a value of unity, i.e., droplet and film dimensions are approximately the same. More accurate information may be obtained by use of the following equation:

$$\frac{D_{10}}{\bar{h}_F} = 1.25 \cdot (V^+)^{-0.15}. \quad (7)$$

Equation (7) represents data for engine relevant variations of flow rate and speed and predicts mean diameters within a relatively narrow scatterband of $\pm 15\%$. The same equation also gives a reasonable estimate for the size of droplets generated for low speed conditions at the rim of a rotating disk ($We^*=1073$). For higher disk speeds, which are more applicable to engine situations, ratios of droplet diameter to film thickness also approach a value of 1.

As seen before in Figs. 4 and 5 and in the previous study by Glahn et al. [10], the sprays considered here are nonhomogeneous, i.e., the spray has to be regarded as a spectrum of drop sizes distributed about a mean value (D_{10}). Thus, in addition to the mean diameter, another parameter is needed in order to be able to calculate the droplet size distribution.

The data obtained in the present study can be approximated best by use of a log-normal distribution of droplet sizes, [14]:

$$\frac{dn_d}{dD_d} = \frac{1}{\sqrt{2\pi} D_d s_g} \exp \left[-\frac{1}{2s_g^2} (\ln D_d - \ln D_{10})^2 \right], \quad (8)$$

where s_g is the geometric standard deviation and n_d is the number of droplets per size class D_d . It has also been recognized that the standard deviation is not only affected by the flow rate but also by the hole diameter. The latter has an impact because a broader oil column at the exit of the rotating hole (Fig. 3) has the tendency to shield oil film fragments at its leeward side from high aerodynamic forces. Although the majority of droplets eventually reach comparable size (Fig. 10), the larger hole and especially the rotating disk with its continuous oil film maintain a small but recog-

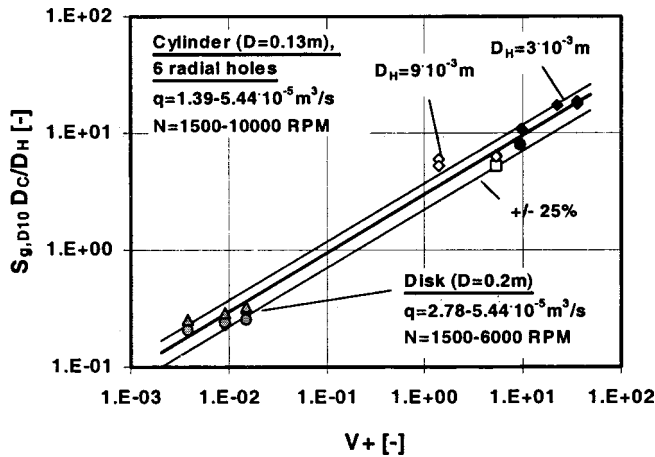


Fig. 11 Standard deviation of droplet diameter distribution

nizable number of larger droplets which influence the standard deviation. This circumstance was considered in Fig. 11 by referring the measured standard deviation to the nondimensional hole diameter, D_H/D_C . Note that for the case of the rotating disk D_H and D_C become equal to the disk diameter D_D .

For the relationship between standard deviation, hole diameter, and flow rate, the following simple equation has been found to represent measured data within about $\pm 25\%$:

$$s_g = 2.91 \cdot (V^+)^{0.5} \cdot \frac{D_H}{D_C} \quad (9)$$

By use of Eqs. (6) to (9), the mean droplet diameter and the spectrum of the size distribution can be calculated from known dimensions and operating conditions. Besides that, additional information relative to the droplet dynamics, namely flow velocity and flow angle, are required. Again, an attempt has been made to relate droplet to oil film flow characteristics. However, a comparison of both oil film velocity components shows that the tangential velocity, i.e., the rim speed of the disk or the cylinder, is about one to two orders of magnitude larger than the radial oil film velocity. Therefore, the droplet's average total velocity has been related simply to the rim speed and the result of this comparison is shown in Fig. 12 as a function of Weber numbers, We^* . Almost identical characteristics for the three different configurations have been observed though the high-speed datapoint for the smaller of the two radial holes deviates from the overall trend by roughly 20%. The relationship between droplet velocity and operating conditions in terms of Weber numbers is represented by

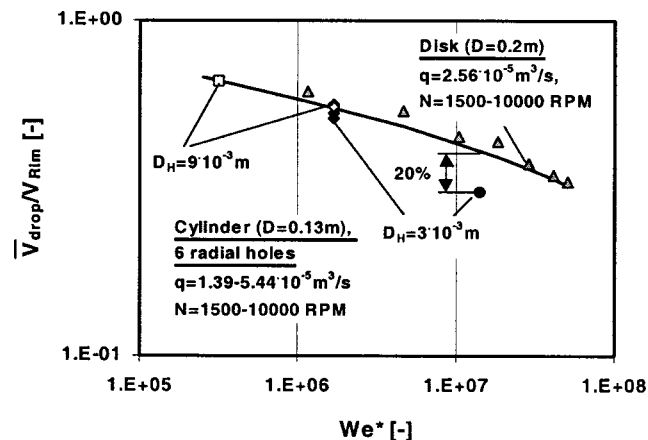


Fig. 12 Droplet velocity after completed disintegration

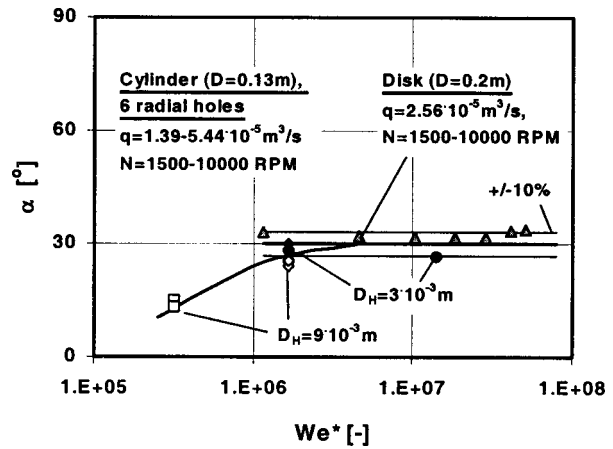


Fig. 13 Droplet flow angle after completed disintegration

$$\frac{\bar{V}_d}{V_{rim}} = 1.5 - 0.1327 \cdot \ln(We^{*0.5}) \quad (10)$$

No significant impact of the flow rate on the average droplet velocity has been observed and Eq. (10) appears to be applicable for all flow rates relevant to engine designs.

As the final quantity required for a characterization of oil film disintegration processes in rotating disk and rotating cylinder configurations, the droplet flow angle has to be defined in terms of operating conditions. This has been done in Fig. 13 for same test conditions that have been considered in Fig. 12 for the droplet velocity. The flow angle, however, appears to be only weakly dependent on variations in either flow rate or rotational speed. In fact, for intermediate and high rotational speeds the flow angle is represented best by a constant value of

$$\alpha = 30 \text{ deg}, \quad We^* > 2 \cdot 10^6 \quad (11)$$

For the rotating cylinder with radial holes at low angular velocities,

$$\alpha = 34 \cdot \log(We^{*0.5}) - 78, \quad We^* < 2 \cdot 10^6 \quad (12)$$

describes the relationship between flow angle and shaft speeds.

Conclusions

The disintegration of oil films emerging from radial holes inside a rotating cylinder is one of the droplet generation sources inside an aeroengine lubrication system component. In order to establish a database for the development of atomization models, which are required in advanced design tools, this situation was studied experimentally and the following conclusions were drawn:

All measurements were carried out for a 5cS liquid, thus in terms of the fluid properties at relevant engine conditions.

The breakup process is basically the same as observed at the rim of a rotating disk and consists of the separation of a thin oil film from the inner surface of the rotating hole and the subsequent disintegration of this film into ligaments and droplets.

The atomization quality, i.e., the droplet size distribution, is mainly driven by the rotational speed. The impact of oil flow rates is much weaker.

A dimensional analysis confirmed similarities between film disintegration processes at rotating cylinders and rotating disks. A nondimensional flow rate and a modified Weber number were identified as suitable scaling parameters for a comparison of different geometries.

A comparison of mean droplet sizes and oil film flow conditions prior to separation and disintegration shows that averaged droplet diameters and film thicknesses are approximately the same, thus $D_{10}/\bar{h}_F \approx 1$ appears to be a reasonable estimate for the average

diameter. A simple model for the calculation of oil film properties was developed and included as an Appendix to this paper.

Within the limited range of geometrical variations investigated, results obtained from dimensional analysis and comparisons with the simple film model suggest that the ratio of hole diameter to hole length does not have a significant effect on the disintegration products.

Based on the results of the present paper, droplet flow boundary conditions in terms of mean diameter, standard deviation of the diameter distribution, starting velocity, and flow angle are available for oil droplets generated by disintegration of oil films emerging from rotating radial holes and rotating disks.

Acknowledgments

The authors are grateful to Lou Dobek, Pratt & Whitney, East Hartford, for his encouragement and support of the work presented here.

Nomenclature

| | |
|-----------------|--|
| D | = diameter (m) |
| $D_{10,20,30}$ | = averaged droplet diameters based on number, surface area, and volume (m) |
| $D_{V,x}$ | = characteristic droplet diameter, representing the fraction x of the total droplet volume accumulated at the specified diameter (m) |
| h_F | = oil film thickness (m) |
| N | = rotational speed (rpm) |
| n | = number |
| q | = volumetric flow rate (m ³ /s) |
| R, φ, Z | = cylindrical coordinates (m, deg, m) |
| ΔR | = radial distance from rim (m) |
| T | = temperature (K) |
| V | = velocity (m/s) |
| V^+ | = nondim. volumetric flow rate |
| v | = radial oil film velocity (m/s) |
| We^* | = modified Weber number |
| α | = flow angle, $\tan \alpha = V_{rad}/V_{tan}$ (deg) |
| ρ | = density (kg/m ³) |
| μ | = dynamic viscosity (kg/(m·s)) |
| ν | = kinematic viscosity (m ² /s) |
| σ | = surface tension (N/m) |
| ω | = angular velocity (rad/s) |

Subscripts

| | |
|-----------------|---------------------|
| C | = Cylinder |
| D | = Disk |
| $d(\text{rop})$ | = Droplet |
| E | = Engine conditions |
| F | = Film |
| G | = Gas |
| H | = Hole |
| L | = liquid |
| max | = maximum value |
| rad | = radial |
| S | = shaft |
| T | = test conditions |
| tan | = tangential |
| tot | = total |

Appendix

The following assumptions and models have been used to calculate oil film flow properties, i.e., film thickness and film velocity, at the rim of a rotating disk and a radial hole in a rotating cylinder, respectively.

Considering a rotating frame of reference, axisymmetric flow conditions ($\omega^2 r \gg g$), assuming no interfacial shear stress between the co-current gas stream and the film surface, and neglecting tangential relative motion between the hole/disk surface and

the oil film, the radial velocity profile for the oil film along the rotating surface can be written in wall coordinates as

$$\frac{dv_F^+}{dy_F^+} = \frac{1 - \sigma_{CF} \cdot \gamma_F^+}{1 + \nu_i/\nu_F}, \quad (A1)$$

with σ_{CF} as a parameter that describes the impact of centrifugal forces versus frictional forces on the film profile

$$\sigma_{CF} = \frac{\omega^2 r \cdot \nu_F}{v_\tau^3}. \quad (A2)$$

This approach is an analogy to film flow calculations that have been verified by Glahn and Wittig [4,7] for oil film flows in the stationary frame of reference. In those situations the gravitational acceleration, g , has been used in Eq. (A2) instead of the centrifugal acceleration, $\omega^2 r$.

Assuming that the oil film is thin in comparison with either the hole diameter or the disk diameter, a film Reynolds number can be calculated from

$$Re_F = \frac{q}{n \cdot \pi \cdot D_H \cdot \nu_F} = \bar{v}_F^+ \cdot \bar{h}_F^+. \quad (A3)$$

Integration of Eq. (A1) and substitution into Eq. (A3) requires an assumption for the eddy viscosity term, ν_i/ν_F . In the present study, Glahn and Wittig's [4,7] proposal of a turbulent velocity profile as well as a laminar approach ($\nu_i/\nu_F=0$) have been used. However, differences in calculated film thicknesses and velocities were negligible because the \bar{h}_F^+ values of the film flows considered here were usually less than 12–14. Thus, for the sake of simplicity, a laminar oil film profile has been assumed in the following.

The assumption of no interfacial shear translates into

$$\bar{h}_F^+ = \frac{1}{\sigma_{CF}}. \quad (A4)$$

With Eq. (A4), the integration of (A1) and substitution of \bar{v}_F^+ into Eq. (A3) readily leads to

$$\frac{q}{n \cdot \pi \cdot D_H \cdot \nu_F} = \frac{1}{3 \cdot \sigma_{CF}^2} \quad (A5)$$

which can be rearranged to

$$\bar{h}_F = \left(\frac{6 \cdot q \cdot \nu_L}{\omega^2 \cdot D_{D,C} \cdot n \cdot \pi \cdot D_{D,H}} \right)^{1/3} \quad (A6)$$

and

$$\bar{v}_F = \left(\frac{q^2 \cdot \omega^2 \cdot D_{D,C}}{6 \cdot n^2 \cdot \pi^2 \cdot D_{D,H}^2 \cdot \nu_F} \right)^{1/3}. \quad (A7)$$

Note that for the rotating disk, Eq. (A7) can further be simplified to

$$\bar{v}_F = \left(\frac{\rho_F \cdot q^2 \cdot \omega^2}{6 \cdot \pi^2 \cdot D_D \cdot \mu_F} \right)^{1/3} \quad (A8)$$

which is identical to Hinze and Milborn's [13] result in the event of $\varphi=90$ deg, i.e., when the equation derived for a rotating cup with opening half-angle φ is applied to the test case of a rotating disk.

References

- [1] Zimmermann, H., Kammerer, A., Fischer, R., and Rebhahn, D., 1991, "Two-Phase Flow Correlations in Air/Oil Systems of Aero Engines," ASME Paper No. 91-GT-54.
- [2] Wittig, S., Glahn, A., and Himmelsbach, J., 1994, "Influence of High Rotational Speeds on Heat Transfer and Oil Film Thickness in Aero Engine Bearing Chambers," ASME J. Eng. Gas Turbines Power, **116**(2), pp. 395–401.
- [3] Chew, J., 1996, "Analysis of the Oil Film on the Inside Surface of an Aero-Engine Bearing Chamber Housing," ASME Paper No. 96-GT-300.
- [4] Glahn, A., and Wittig, S., 1996, "Two-Phase Air Oil Flow in Aero Engine

- Bearing Chambers—Characterization of Oil Film Flows,” ASME J. Eng. Gas Turbines Power, **118**(3), pp. 578–583.
- [5] Glahn, A., Busam, S., and Wittig, S., 1997, “Local and Mean Heat Transfer Coefficients along the Internal Housing Walls of Aero Engine Bearing Chambers,” ASME Paper No. 97-GT-261.
- [6] Busam, S., Glahn, A., and Wittig, S., 1999, “Internal Bearing Chamber Wall Heat Transfer as a Function of Operating Conditions and Chamber Geometry,” ASME Journal of Engineering for Gas Turbines and Power, accepted for publication.
- [7] Glahn, A., and Wittig, S., 1999, “Two-Phase Air Oil Flow in Aero Engine Bearing Chambers—Assessment of an Analytical Prediction Method for the Internal Wall Heat Transfer,” Int. J. Rotating Mach., **5**(3), pp. 155–165.
- [8] Zaidi, S. H., Ishaq G., Aroussi A., and Azzopardi, B. J. 1998. “Two-Phase Flow Study Around a Rotating Liquid Film Using Laser Techniques,” *Proceedings of the VSJ-SPIE98*, Dec. 6–9, Yokohama, Japan.
- [9] Glahn, A., Kurreck, M., Willmann, M., and Wittig, S., 1996, “Feasibility Study on Oil Droplet Flow Investigations Inside Aero Engine Bearing Chambers—PDPA Techniques in Combination with Numerical Approaches,” ASME J. Eng. Gas Turbines Power, **118**(4), pp. 749–755.
- [10] Glahn, A., Busam, S., Blair, M. F., Allard, K. L., and Wittig, S., 2000, “Drop-let Generation by Disintegration of Oil Films at the Rim of a Rotating Disk,” ASME Paper No. 2000-GT-279.
- [11] Bachalo, W. D., and Houser, M. J., 1984, “Phase Doppler Spray Analyzer for Simultaneous Measurements of Drop Size and Velocity Distributions,” Opt. Eng., **23**, pp. 583–590.
- [12] Willmann, M., Glahn, A., and Wittig, S., 1997, “Phase-Doppler Particle Sizing with Off-Axis Angles in Alexander’s Darkband,” Part. Part. Syst. Charact., **14**(3), pp. 122–128.
- [13] Hinze, J. O., and Milborn, H., 1950, “Atomization of Liquids by Means of a Rotating Cup,” Journal of Applied Mechanics, pp. 145–153.
- [14] Lefebvre, A. H., 1989, *Atomization and Sprays*, Hemisphere, Washington, DC.

Mechanical Surface Treatment Technologies for Gas Turbine Engine Components

W. Zhuang

e-mail: wyman.zhuang@dsto.defence.gov.au

B. Wicks

Air Vehicle Division,
Aeronautical and Maritime Research Laboratory,
Defence Science and Technology Organization,
Melbourne, VIC 3207, Australia

Various mechanical surface treatment technologies have been invented and developed to induce a protective layer of compressive residual stress at the surface of gas turbine engine components where the operating loads are tensile dominated. The benefits of these surface treatments are to prevent crack initiation, to retard propagation of small cracks, and even to resist corrosion and wear damage. In this paper the literature on these technologies and their effects on component reliability and durability is reviewed, with an emphasis on shot peening (SP), laser shock peening (LSP), and low plasticity burnishing (LPB). The relative advantages of these three surface treatment technologies, as well as their limitations, are identified and evaluated. The most important issues for these three technologies, and the relative merits of the resultant residual stress fields, are presented and discussed with a view to enhancing gas turbine engine component operating lives. [DOI: 10.1115/1.1610011]

Introduction

For gas turbine engines, fatigue and corrosion damage, often initiated from the surfaces of components, represents a threat to the safety and availability of aircraft [1,2]. The inspection requirements for fatigue and corrosion damage, the maintenance to replace critical components, and the rework required to remove fatigue and corrosion damage considerably increase operating costs. The down-time required to perform these inspections and repairs significantly impacts on aircraft airworthiness and readiness.

Various surface treatment and modification technologies have been developed to induce a protective layer at the surface of gas turbine engine components to enhance wear, corrosion and fatigue properties. Some of these technologies, such as plating, coating, ion implantation, heat treatment for surface hardening, and shot peening are well established and routinely applied to engine components in manufacturing and maintenance, [3–7]. However, these technologies have a number of limitations. For instance, shot peening (SP) induces only a shallow compressive residual stress layer (about 0.2 mm deep) at the surface, with a large degree of cold work (strain hardening) that can cause damage to the microstructure of materials and promote accelerated relaxation of the beneficial compressive residual stresses, [8]. In this regard, although shot peening is routinely applied to engine components, engine manufacturers are unable to quantify the benefits and hence cannot allow the operators to derive any benefit in the form of extended component replacement intervals. In particular there is a lack of confidence in the development and sustainment of the residual stresses over long periods of service, [7].

These shortcomings have led to the development of advanced mechanical surface treatment technologies, such as laser shock peening (LSP) and low plasticity burnishing (LPB). LSP was first developed in early 1970s as a fatigue enhancement surface treatment for metallic materials, [9,10]. Recently, based on the principle of roller and ball burnishing used originally for refinement of surface finishes, a new concept—low plasticity burnishing—was patented by Lambda Research in Cincinnati, Ohio, [11]. The published data have demonstrated that both LSP and LPB are able to introduce large and deep compressive residual stresses with low

cold work at the surface that not only can increase fatigue initiation life but also can decrease fatigue crack growth rates, although they have very different features and capabilities that will be presented and discussed in this paper.

It is worth noting that there are other kinds of surface treatment technologies under research and development. It is impossible for this paper to exhaustively review and cover all of these technologies, and this paper highlights only the mechanical type of surface treatment technologies and their applications to gas turbine engines. The technical features and induced residual stress fields will be presented and discussed and the paper will conclude with a statement of the future research requirements for this area, including the generation and relaxation of residual stresses, and the likely implications for gas turbine engine life assessment, life extension, and repair.

Shot Peening (SP)

The Basic Shot Peening Process. The shot peening process is a traditional and inexpensive mechanical surface treatment method, and it is currently applied to many aircraft structures and engine components. The process is shown schematically in Fig. 1. Hard shots (metallic shots or glass or ceramic beads) in an air-blast repeatedly bombard the surface of the workpiece resulting in local plastic surface deformation. Since the plastically deformed surface layer tends to stretch/expand and the adjacent layer of elastic material beneath restrains the expansion there is a compressive residual stress field generated in the surface layer balanced by subsurface tensile residual stresses.

A simple Heyn spring model can be used to describe the balanced residual stress field in the depth direction of a component produced by the shot peening process, [12], as shown in Fig. 2, based on the principle of local plastic deformation. Two compressive surface springs are balanced by five tensile springs in the core. The model shows that there are basically two features for the residual stresses induced by shot peening. The first feature is a high level of compressive residual stresses at the surface. The second is a low level of tensile residual stresses over a large section in the subsurface region to maintain the component in equilibrium.

The Development of Shot Peening. The development of the shot peening process has taken place in three stages, [13]. The first stage involved manual control with the quality of the SP process being heavily dependent on the skill of the operator. The second

Contributed by the Manufacturing Materials and Metallurgy Division of THE AMERICAN SOCIETY OF MECHANICAL ENGINEERS for publication in the ASME JOURNAL OF ENGINEERING FOR GAS TURBINES AND POWER. Manuscript received by the Manufacturing Materials and Metallurgy Division Nov. 2001; final revision received Feb. 2003. IGTT Chair: S. Gollahalli.

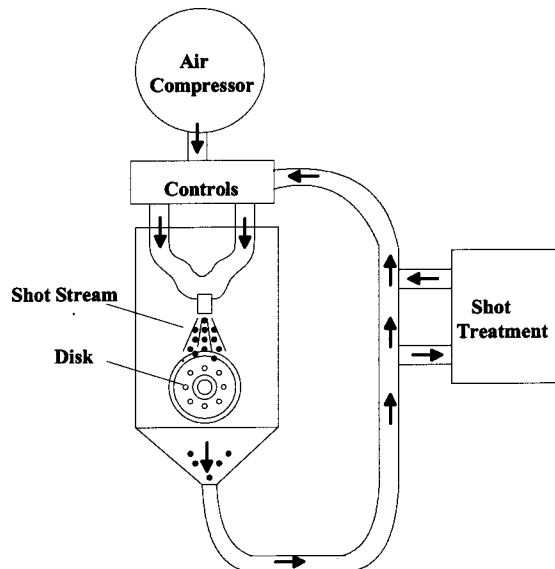


Fig. 1 Schematic of air-blast shot peening

stage involved hydraulic control, which was developed to ensure the accuracy and repeatability of the SP process. The third stage of development involved the use of Computerized Numerical Control (CNC), which not only maintained control of the SP process but also allowed monitoring of the process to achieve the required residual stress field and surface finish.

A further stage of development of the SP process is expected which will quantify the benefits with concomitant nondestructive monitoring of compressive residual stresses and the elimination of surface damage.

The Effect of Shot Peening Control Parameters. Although shot peening is simple to apply, it is much more difficult to develop a model of the mechanism and the subsequent induced deformation and residual stress relaxation. It is equally difficult to quantify the SP benefits and the effect on the fatigue behavior of shot peened components. In general, of the various important shot peening parameters (shot size, shape, mass, density, hardness, velocity, coverage, etc.), the Almen intensity and the coverage are the important parameters that can be controlled once the media has been selected for shot peening for controlling the quality of the shot peening process.

An Almen strip intensity indirectly represents the compressive residual stress profile of a shot peened component. The Almen strip is a piece of steel (the 1070 steel) which is measured for flatness with an indicator, and then peened. The change in flatness is called the Almen arc height, or Almen intensity, [14]. The Al-

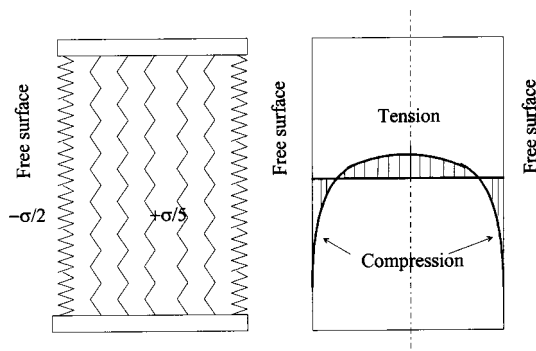


Fig. 2 The Heyn spring model for the generation of residual stresses

men intensity can be easily measured using an Almen gauge which is commercially available. From the Almen intensity the approximate depth of compressive residual stress at the surface may be calculated. However, there is a possibility that shot peening with different shot sizes may generate the same Almen intensity, but induce different residual stress distributions at the surface, [8]. Further the steel selected for Almen strip is heat treated so that it neither work hardens nor softens. Differences in yield strength and work hardening behavior of actual components will result in quite different stress distributions that are determined by destructive residual stress measurements by either mechanical or X-ray diffraction techniques.

The coverage is related to the amount of surface area treated by shot peening. Complete coverage means that the surface area is impacted at least once and totally by shot particles. The commonly used specification of 200% coverage implies that the area is impacted for twice the time required for 100% coverage. The definition of the coverage is obviously arbitrary since there is no such way to control the shots impacting on the area exactly once or twice without overlapping, [15]. The coverage may be estimated using the Peenscan method which uses the color change of a fluorescent tracer liquid under a UV light to estimate different coverage. Similarly, fluorescent indicator or fluorescent marker is also applicable.

Applications of Shot Peening to Gas Turbine Engines. One of the main merits of the SP process is that it can be applied to large and irregular surfaces of components at relative low cost. Because of the enhancement in fatigue life produced by the process, shot peening was applied initially to a variety of gas turbine engine components, such as crankshafts, connecting rods, ring gears and so on in the 1940s, [16]. A wide range of materials has since been SP treated, including steel, titanium, and aluminum alloys relevant to the aircraft industry.

To ensure the quality of shot peening, a military specification, MIL-S-13165 has been established to guide the SP process for gas turbine blades and metallic components, [17]. Subsequently, a modified SP process with a shot deflector was developed by General Electric Company to enhance the fatigue strength of bolt holes in engine turbine disks, [6]. The diameter of bolt hole is 6.5 mm. The depth of compressive residual stresses which can be achieved is about 0.15 mm.

Laser Shock Peening (LSP)

The Basic Laser Shock Peening Process. Laser shock peening was first developed for enhancing the fatigue life of metal parts in the early 1970s, but the LSP process has only recently been applied to gas turbine engine components such as fan blades and compressor blades. The main reason for the delay in applying the process has been the low repetition rate of the original pulsed Nd-glass laser system—about one cycle every eight minutes, [18]. A new laser system developed by LSP Technologies, Inc. in Dublin, OH is a high-energy, pulsed neodymium-glass laser which reduces pulse duration to 15 to 30 nanoseconds and produces output energy per pulse of 200 joules or more, [19].

Figure 3 shows the basic process of laser shock peening. A coat of black paint is first applied to the area of the component to be peened. A high energy pulsed laser is then used to vaporize the opaque coating into a plasma. As the plasma explosively expands, a powerful shock wave is generated that impacts and propagates into the components due to the presence of a transparent layer confining the energy outwards. The intensity of the shock wave travelling within the component can exceed two times the dynamic yield strength of the material at the surface and the shock wave then gradually disperses through the thickness, [20]. The shock wave penetrates a relatively deep surface layer to plastically deform the material to produce a relatively deep compressive residual stress layer.

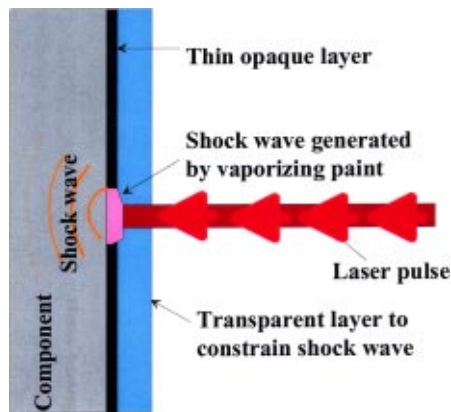


Fig. 3 Schematic of the laser shock peening process on a flat surface

The Control Parameters for Laser Shock Peening. The residual stress distribution induced by the LSP process is strongly dependent on the type and intensity of the process and the material properties. In principle, by increasing the intensity and exposure, the depth of the compressive residual stresses can be increased from 0.9 mm to 1.8 mm depending on the material, [20].

Since the compressive residual stresses have to be balanced by equivalent tensile residual stresses, the increasing intensity of LSP will not necessarily increase the depth of the compressive stresses for thin-wall structures. Further, based on the test results from Smith in 2000, it is expected that the percentage of cold work increases with the increase of pulse number from one to three.

Applications of Laser Shock Peening in Gas Turbine Engines. The LSP process has been successfully applied to enhance the fatigue resistance of engine materials such as A17075-T7351, [21], IN718, [8], Ti-6-4, [22], and Ti-6-2-4-6, [20]. However, one of the significant barriers to the application of LSP is the slow processing rate, which is mainly due to the inability to remove the black coating rapidly for multiple shots.

The first production application of LSP was in 1997 on a United States military aircraft gas turbine engine blade after a Rapid-Coater™ Processing System was developed. Following this successful application, the LSP has been used to enhance fatigue-prone engine components, such as blades, disks, and gears on the F-14 Tomcat, the F-16 Falcon, and the B-1B Lancer. Most recently, a F119 integrally bladed rotor has been attached to a robot for the LSP processing, [23].

Low Plasticity Burnishing

The Basic Low Plasticity Burnishing Process. Low plasticity burnishing (LPB) has been developed as an improved surface enhancement technology that can induce deep compressive residual stress layers reaching to 1.0 mm with a low degree of cold work (about 5%), and a proportionate increase in the stability of the residual stress layers. The basic LPB process is shown in Fig. 4. Rather than using shots to bombard the component surface, a hydraulically floated ball is used to press and roll freely along the surface so that near-surface layers are deformed plastically. A series of overlapping passes are applied until the intended surface area has been treated. By using X-ray diffraction stress measurement system, it was found that great depths of compressive residual stress can be induced by the LPB process. Because the rolling ball minimizes plasticity (no shearing due to sliding), less cold work is generated at the surface, [8].

The Effect of Low Plasticity Burnishing Processing Parameters. There are several LPB processing parameters that affect

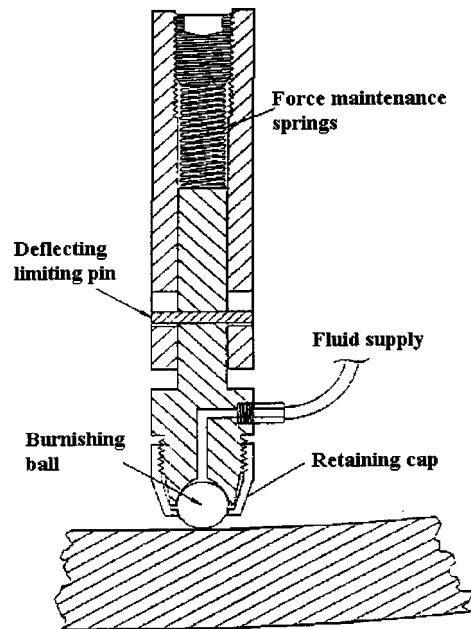


Fig. 4 Scheme of the LPB process on a flat surface

the resultant residual stresses at the surfaces. The most important parameters are the LPB burnishing force, the burnishing ball diameter, the feed and speed.

The effect of the LPB burnishing loads on residual stresses has been investigated, [24]. Two levels of burnishing loading were chosen to represent the low and high LPB conditions. It was demonstrated that the compressive residual stresses in IN718 increase with the LPB burnishing load. Like increasing laser intensity in the LSP process, increasing the burnishing load will increase the percentage of cold work, not necessarily increasing the depth of the compressive stresses for thin-wall structures.

Based on studies performed on a lathe, high-speed coverage can be achieved without significant difference in the residual stress distributions. The use of a 0.030 in. (0.76 mm) feed appears to be excessive. Any feed below that is probably a reasonable maximum for both residual compression at the surface and finish.

High chromium steel, beta-silicon nitride, and tungsten carbide burnishing balls have been tested. The results, [8], show that the effect of burnishing ball modulus on residual stresses is almost negligible. So far no results have been published on the effect of the size of the LPB burnishing ball.

Applications of Low Plasticity Burnishing in Gas Turbine Engines. LPB has been demonstrated as a cost-effective surface enhancement technology with process speeds comparable to those of conventional machining operations such as surface milling. It has been demonstrated that LPB can (i) improve fatigue strength of the engine materials, IN718, [8], Ti-6-4, [24], and Al 7075-T6, [25]; (ii) increase resistance to foreign object damage, [8]; and (iii) eliminate corrosion damage, [25].

The advantages of LPB have attracted attention from USAF and US Navy. It is currently being investigated for application to both F404 (F/A-18 aircraft) and T56 (C-130 and P-3C aircraft). Figure 5 is an example of the LPB application to an engine compressor blade using four-axis mode in CNC milling machine, [26].

Evaluation and Comparison

Residual Stress Profiles. In general, shot peening with small shots generates a low Almen intensity and a shallow depth of plastic deformation, resulting in shallower compressive residual stresses. A comparison of residual stress profiles induced by SP, LSP, and LPB for engine material IN718 is shown in Fig. 6, [27].

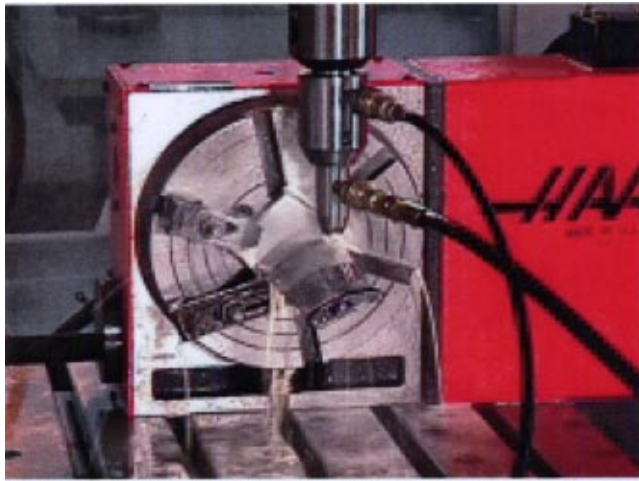


Fig. 5 An engine compressor blade under PPB processing using a four-axis mode in CNC mill

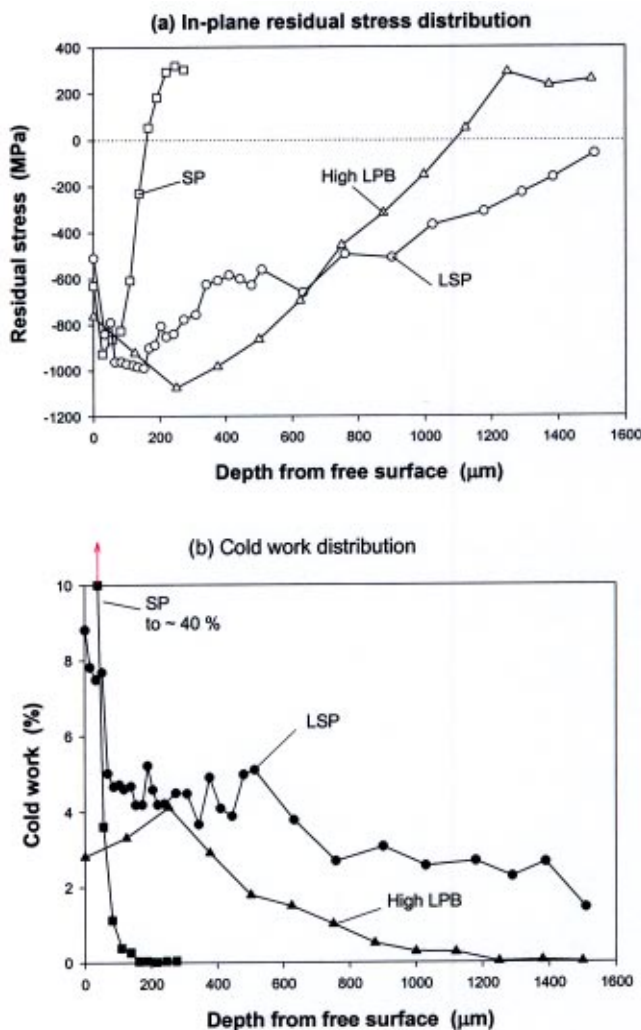


Fig. 6 Residual stress and cold work distributions in IN 718 after SP, LSP, and LPB

Table 1 Comparison of surface treatment technologies

| Surface Treatment Technology | Speed | Coldwork | Depth (mm) | Relative Cost |
|------------------------------|----------|----------|------------|---------------|
| SP | Fast | High | ~0.2–0.5 | Low |
| LPB | Moderate | Low | ~1.0 | Moderate |
| LSP | Slow | Low | ~1.5 | High |

Figure 6(a) shows that, after the SP process, high compressive residual stresses are confined to a shallow surface layer (0.2 mm) while low tensile residual stresses spread deeper through the cross section. Unfortunately, the degree of cold work can be exceptionally high (up to 30–40%) at the surface, Fig. 6(b).

Residual Stress Relaxation. Although the mechanism of residual stress relaxation needs to be investigated, it has been found that the degree of cold work induced during residual stress generation will influence the rate of thermal relaxation of the residual stresses. A comparison study of thermal relaxation for a variety of surface treatment technologies has been conducted, [8], and the results indicated that compressive residual stresses at heavily cold worked SP'd surfaces relaxed very rapidly, compared with that of a low cold worked surface produced by LSP and LPB.

Figure 6 indicates that, using laser shock peening, the depth of compressive residual stress is significantly greater than that produced by shot peening for the same peak compressive residual stress. The degree of cold working is beneficially less ($\approx 9\%$ or less).

Figure 6 also indicates that LPB can generate great depths of compressive residual stress. Because the rolling ball minimizes plasticity (no shearing due to sliding), less cold work ($\approx 4\%$) is generated at the surface. Deep compressive residual stresses decrease fatigue crack growth rates, in addition to prolonging initiation life, and hence further increase the life of treated components, [28].

Comparison of The Features of Each Process

It is known that a deep and high-magnitude compressive layer at the surface ($\sim 1\text{ mm}+$ by LPB and LSP) can significantly resist both crack initiation and short crack propagation. Very low cold work (2–5%) can improve both thermal stability and resistance to thermal and cyclic load relaxation of these residual stresses. Moreover, application of the process to industrial components requires a process which is adaptable to existing CNC machine tools, at speeds comparable to conventional machining operations such as surface milling. A comparison of the applicability of the three surface treatment technologies is summarized in Table 1.

In summary Table 1 shows that

- LPB can generate deep and large compressive residual stresses, comparable to LSP;
- High cold work by SP is achieved by repeated applications of shot peening; and
- LSP is the most expensive and slow process and the most difficult to incorporate into an overhaul shop environment.

Conclusions

A review has been made of three mechanical surface treatment technologies and their application to aircraft engine component life extension and repair. The two most advanced technologies, laser shock peening and low plasticity burnishing are described and compared with shot peening, a well-established process. The advantages of the technologies are highlighted as well as the limitations.

The review has indicated that neither LSP nor LPB has been fully understood and effectively applied to engine components. Further research work is needed for the better understanding in the following areas:

- the mechanism of residual stress generation and relaxation by all the mechanical surface treatment technologies and
- the effectiveness of these surface treatment technologies for engine component fatigue life extension and damage repair in an overhaul shop environment.

References

- [1] James, D., 1991, "Ageing aircraft—The AATF Present Programme," *Proceedings of an International Conference on Ageing Aircraft and Structural Airworthiness*, Washington, DC, Nov. 19–21, pp. 15–26.
- [2] Ratwani, M. M., Koul, A. K., Immarigeon, J-P., and Wallace, W., 1997, "Ageing Airframes and Engines," AGARD-CP-600 Vol. 1.
- [3] Lessells, J. M., and Brodrick, R. F., 1956, "Shot-Peening as Protection of Surface-Damaged Propeller-Blade Materials," *Proceedings of The International Conference on Fatigue of Metals*, London, Sept. 10–14, pp. 617–627.
- [4] Levine, S. R., 1978, "High Temperature Surface Protection," *Surface Treatments for Protection*, The Chameleon Press Ltd., London.
- [5] Meetham, C. W., 1978, "The Protection of Compressor and Turbine Components of the Aero Gas Turbine Engine," *Surface Treatments for Protection*, The Chameleon Press, Ltd., London.
- [6] Happ, M. B., 1984, "Shot Peening Bolt Holes in Aircraft Engine Hardware," *Proceedings of The Second International Conference on Shot Peening*, Chicago, IL, pp. 43–49.
- [7] Bailey, P. G., and Whalen, J. M., 1990, "Shot Peen Controls and Aircraft Engine Requirements," *Surface Engineering*, S. A. Meguid, ed., Elsevier, New York, pp. 379–385.
- [8] Prevey, P. S., 2000, "The Effect of Cold Work on the Thermal Stability of Residual Compression in Surface Enhanced IN718," *Proceedings of the 20th ASM Materials Solutions Conference & Exposition*, St. Louis, MO, Oct. 10–12.
- [9] Metz, S. A., and Smidt, F. A., 1971, "Production of Vacancies by Laser Bombardment," *Appl. Phys. Lett.*, **19**, pp. 207–208.
- [10] Fairand, B. P., Wilcox, B. A., Gallagher, W. J., and Williams, D. N., 1972, "Laser Shock-Induced Microstructural and Mechanical Property Changes in 7075 Aluminum," *J. Appl. Phys.*, **43**, pp. 3893–3895.
- [11] U.S. Patent 5,826,453, Oct. 1998, other patents pending.
- [12] Sigwart, H., 1956, "Influence of Residual Stresses on the Fatigue Limit," *Proceedings, International Conference on Fatigue of Metals, Institution of Mechanical Engineers*, London.
- [13] Bailey, P. G., Lombardo, D. R., Popp, H. G., and Thompson, R. A., 1996, "Full Assurance Shot Peening of Aircraft Gas Turbine Engine Components," *Proceedings of The Six International Conference on Shot Peening*, San Francisco, CA, pp. 320–327.
- [14] Kirk, D., 1999, "Shot Peening," *International Journal of Aircraft Engineering and Aerospace Technology*, **71**, pp. 349–361.
- [15] Lombardo D., and Bailey, P., 1996, "The Reality of Shot Peening Coverage," *Proceedings of The Six International Conference on Shot Peening*, San Francisco, CA, pp. 493–504.
- [16] Brookman, J. G., and Kiddle, L., 1946, "The Prevention of Fatigue Failures in Metal Parts by Shot Peening," *The Failure of Metals by Fatigue*, Melbourne University Press, Melbourne, Australia.
- [17] Eckersley, J. S., 1990, "Effect of Shot Peening Process Controls on Consistent Treatment," *Surface Engineering*, S. A. Meguid, ed., Elsevier, New York, pp. 417–427.
- [18] Vaccari, J. A., 1992, "Laser Shocking Extends Fatigue Life," *American Machinist*, July, pp. 62–64.
- [19] Clauer, A. H., Walters, C. T., and Ford, S. C., 1983, "The Effects of Laser Shock Processing on the Fatigue Properties of 2024-T3 Aluminum," *Lasers in Materials Processing*, American Society for Metals, Metals Park, OH, pp. 7–22.
- [20] Clauer, A. H., 1996, "Laser Shock Peening for Fatigue Resistance," *Surface Performance of Titanium*, J. K. Gregory, H. J. Rack, and D. Eylon, eds., TMS, Warrendale, PA, pp. 217–230.
- [21] Peyre, P., Fabbro, R., Berthe, L., and Dubouchet, C., 1996, "Laser Shock Processing of Materials, Physical Processes Involved and Examples of Applications," *J. Laser Appl.*, **8**, pp. 135–141.
- [22] Ruschau, J., John, R., Thompson, S., and Nicholas, T., 1999, "Fatigue Crack Growth Rate Characteristics of Laser Shock Peened Ti-6Al-4V," *ASME J. Eng. Mater. Technol.*, **121**, pp. 321–329.
- [23] LSPT 2001, 2001, website publications of LSP Technologies, Inc.
- [24] Prevey, P. S., and Shepard, M. J., 2000, "Surface Enhancement of Ti-6Al-4V Using Low Plasticity Burnishing," *Proceedings of 11th AeroMat Conference*, Bellevue, WA, June.
- [25] Prevey, P. S., and Cammett, J. T., 2000, "Low Cost Corrosion Damage Mitigation and Improved Fatigue Performance of Low Plasticity Burnished 7075-T6," *Proceedings of 4th International Conference Aircraft Corrosion Workshop*, Solomons, MD, Aug.
- [26] Cammett, J. T., and Prevey, P. S., 2001, *Fatigue Strength Restoration in Corrosion Pitted 4340 Alloy Steel via Low Plasticity Burnishing*, Lambda-Research, Cincinnati, OH.
- [27] Zhuang, W., and Halford, G., 2001, "Investigation of Residual Stress Relaxation Under Cyclic Load," *Int. J. Fatigue*, **23**, pp. S31–S37.
- [28] Telesman, J., Kantzos, P., Gabb, T., and Prevey, P., 1999, "Effect of Residual Stress Surface Enhancement Treatments on Fatigue Crack Growth in Turbine Engine Alloys," *The Third Joint FAA/DoD/NASA Conference on Aging Aircraft*, Albuquerque, NM, Sept.

Imbalance Response of a Rotor Supported on Flexure Pivot Tilting Pad Journal Bearings in Series With Integral Squeeze Film Dampers

L. San Andrés
Professor

O. De Santiago
Research Assistant

Mechanical Engineering Department,
Texas A&M University,
College Station, TX 77843-3123

Measurements of the imbalance responses of a massive 45 kg rotor supported on series (flexure pivot) tilting pad bearings and integral squeeze film dampers (SFDs) are presented. The rotor-bearing configuration is of interest in compressor applications where often oil lubricated dampers are introduced in series with fluid film bearings to relocate critical speeds, enhance the overall system damping, and reduce the risks of rotordynamic instabilities due to seals and impellers, for example. Coast-down experiments from 9000 rpm are conducted for increasing levels of rotor imbalance, and equivalent system damping coefficients identified from the peak amplitude of rotor response while traversing cylindrical mode critical speeds. The tests performed with locked (inactive) and active SFDs demonstrate the effectiveness of the flexible damped support in reducing the system critical speed and improving the overall rotor response with reduced transmitted forces to ground. The SFDs allow safe rotor operation with values of imbalance twice as large as the maximum sustained by the rotor supported on tilting pad bearings alone. The experiments reveal a linear relationship between the peak amplitude of vibration at the critical speeds and the imbalance displacement, even for rotor motions larger than 50% of the tilting pad bearing and damper clearances. The tests also show little cross-coupling effects with the shaft centerline moving along a nearly vertical path. The rotor-bearing system remained stable in the entire range of operation and without the appearance of subsynchronous vibration or nonlinear damper jump response.

[DOI: 10.1115/1.1492831]

Introduction

Current turbomachinery design demands higher power-to-weight ratios. These systems require flexible supports in order to locate and traverse critical speeds and to reduce midspan rotor excursions. Furthermore, there exists a demand for increased tolerance to imbalance and sudden loads for satisfactory engine performance, which accrues additional requirements to the rotor supports for vibrational energy dissipation. Tilting pad journal bearings (TPJBs) are extensively used in land turbines and compressors due to their inherent stability, long life, and low power consumption. Recently, flexure pivot tilting pad journal bearings (FPJBs) have been implemented due to their easiness of installation and reduced number of parts (De Choudhury et al. [1]). However, tilting pad bearings may possess large stiffness coefficients that inhibit damping to properly dissipate vibrational energy at the support locations. Introducing a flexible support in series with the tilting pad bearing allows to relocate critical speeds in nearly rigid rotors and provides a means to increase viscous damping by using squeeze film dampers (SFD).

Squeeze film dampers derive their behavior from a lubricant being squeezed in the annular space between a nonrotating cylindrical journal and its housing. A rolling bearing usually connects the rotating shaft with the damper journal, and an elastic element (spring) centers the journal within the damper housing. Squirrel

cage spring centered dampers are the most commonly employed design. Their most distinctive feature is the relatively large axial length required by the elastic support in comparison to the damper hydrodynamic length, often requiring three to four times as much length as the damper itself. The integral squeeze film damper (ISFD) recently advanced by Zeidan [2] provides advantages such as short axial length, light weight, and easiness of installation. In this case, the cylindrical journal is replaced by a set of arcuate segments (pads), their number depending on the particular application. Thin structural EDM webs (springs) provide the support flexibility and connect the inner and outer rings. The thin gap between the sector pads and the outer ring forms the squeeze film lands. Each pad can be manufactured with different clearances to counter the static deflection due to the rotor weight. Additionally, the ISFD can be split for ease of installation and retrofit.

Integral squeeze film dampers provide satisfactory damping forces to rotor-bearing systems to safely traverse critical speeds. De Santiago et al. [3] and De Santiago and San Andrés [4] present experimental results on integral squeeze film dampers (ISFDs) supporting a three-disk rigid rotor subjected to rotating loads induced by calibrated imbalance masses. In the tests, a pair of stiff ball bearings connected the shaft to the damper journal. Measurements of the rotor synchronous response demonstrate the ability of the ISFDs to attenuate rotor vibrations in the range of operation from zero to 9000 rpm, both for the first (cylindrical) and second (conical) modes of vibration. De Santiago and San Andrés [5] incorporated end plate seals on the faces of the ISFDs and observed enhanced damping capability. The particular construction of the centering springs enables larger damping coefficients for tighter end seals without a severe reduction in the through lubricant flow, which could cause excessive lubricant temperature rise.

Contributed by the International Gas Turbine Institute (IGTI) of THE AMERICAN SOCIETY OF MECHANICAL ENGINEERS for publication in the ASME JOURNAL OF ENGINEERING FOR GAS TURBINES AND POWER. Paper presented at the International Gas Turbine and Aeroengine Congress and Exhibition, New Orleans, LA, June 4–7, 2001; Paper 2001-GT-0257. Manuscript received by IGTI, December 2000, final revision, March 2001. Associate Editor: R. Nafise.

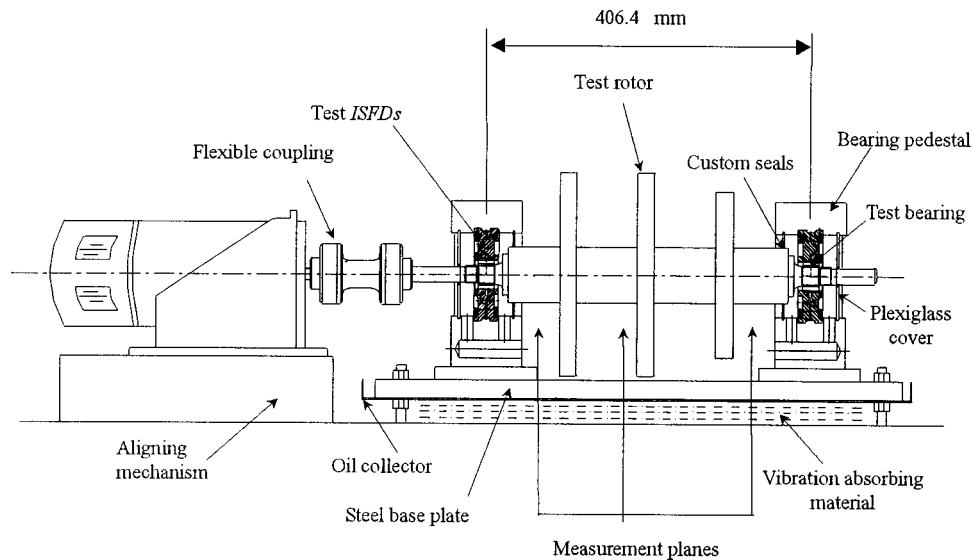


Fig. 1 Test rig for measurements of imbalance response of rotor supported on tilting pad bearings and squeeze film dampers

Several applications of the FPJB-SFD bearing combination have already been implemented in industrial turbomachinery (Edney and Nicholas [6] and Zeidan [2]).

Experiments on the dynamic response of a rigid rotor mounted on a pair of flexure pivot TPJBs in series with Integral SFDs follow. The aim of the tests is to determine the combined effect of these elements on the location of critical speeds and estimation of the rotor-bearing system damping ratio, and to demonstrate their effectiveness on reducing amplitudes of rotor vibration. The experiments extend prior work in a comprehensive research program dedicated to study and to demonstrate the effectiveness of novel squeeze film dampers and bearings for applications in turbomachinery.

Test Rig Description

Figure 1 depicts the test rig with a 7.5 kW (10 HP) DC motor driving the rotor up to a top speed of 9000 rpm through a flexible coupling and a drawn cup-type roller clutch. The rotor mass is 43.5 kg (95.9 lb) and consists of a 76.2 mm (3 in.) diameter shaft, 686 mm (27 in.) long. The total vibrating mass is 45.3 kg including one half of the coupling weight. The rotor has three equally spaced, press-fit disks 25.4 mm (1 in.) thick. The drive end and middle disks are 279 mm (11 in.) in diameter whereas the free end disk has a diameter of 229 mm (9 in.). Each disk has 12 threaded holes, equally spaced on its circumference, for installation of calibrated imbalance masses. The span distance between the support bearing centerlines is 406.4 mm (16 in.).

Hardened steel rings mounted on the shaft provide the sliding surfaces at the fluid film bearing locations. Two identical pedestals bolted to a metal base plate hold the test bearings and provide grooves for lubricant feeding into the damper lands, as well as drainage ducts for oil return. The pedestals also have transparent side covers allowing visualization of the bearing assembly. Custom-made plastic hose seals prevent leakage of lubricant to the pedestal's exterior while allowing free rotor lateral motions. A plastic pin facing the rotor free-end constrains axial motions since no thrust bearings are installed in the test apparatus. The rotor, bearing pedestals, and support steel plate rest on a steel-reinforced concrete table.

The facility includes a 151 L (40-gallon) lubricant reservoir with one main pump and a circulation system with a heater and a cooler to maintain the lubricant temperature at a desired preset value. The lubrication system provides oil to the tilting pad bear-

ings and squeeze film dampers through separate lines and allows for independent control of the supply pressure to the bearing and damper elements.

Eddy current proximity probes located at three axial planes and in two orthogonal directions measure the rotor vibration during coast down. Piezoelectric accelerometers with magnetic bases record the pedestals' vibrations. A data acquisition system records the rotor response and acceleration at both supports as functions of the rotor speed and stores the data in a personal computer. Type K thermocouples and meters display reservoir, inlet, and exit lubricant temperatures from the test bearings as well as ambient temperature for reference, and the motor temperature for safe operation. A light beam optical tachometer displays the rotor speed and provides a reference signal to the data acquisition system for phase angle measurements. Turbine-type flow meters digitally display the overall and individual lubricant consumption of the test bearings and dampers, and gauges display the lubricant supply pressure into each bearing and damper. The lubricant employed in all tests is an ISO VG 10 turbine oil with a viscosity (μ) of 21.6 cP at 17°C (63°F) and 8.40 cP at 40°C (104°F).

Design of the Flexure Pivot-Tilting Pad Bearing

The rotor support assembly consists of three elements in series: the flexure pivot tilting pad journal bearings (FPJBs), the integral squeeze film dampers (ISFDs), and the bearing pedestals. Figure 2 depicts the FPJB-ISFD bearing combination. The tilting pad bearing is incorporated into the existing ISFD previously tested by De Santiago et al. [3], whose main dimensions are given in Table 1.

The objective of the bearing design is to furnish a rotor support with engineered location of critical speeds through the appropriate choice of the combined stiffness as well as optimum damping coefficients. The two fluid films in series possess combined stiffness and damping force coefficients that can be optimized as described by Barrett et al. [7]. Given a rotor-bearing system, there exists a specific value of the bearing to damper damping ratio (β) that minimizes the rotor response for given values of bearing to damper stiffness ratio (α) and damper damping ratio (ζ) at any rotor speed (ω) (frequency ratio $f = \omega/\omega_n$). In the design of the flexure pivot journal bearing, the optimum bearing to support damping ratio (β_{opt}) is selected at the undamped natural frequency of the original system (i.e., $f = 1$).

Prior measurements show the bearing supports (pedestals) to be flexible with asymmetric stiffness coefficients in the vertical and

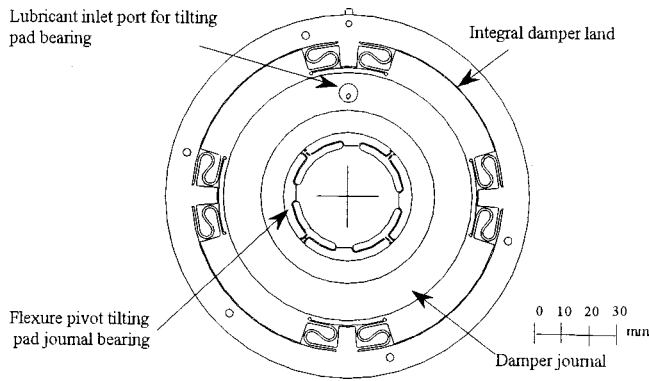


Fig. 2 Assembled ISFD and tilting pad bearing

horizontal directions as shown in Table 2. On the other hand, the integral dampers have (both from design and static tests) a radial stiffness very close to 3.5 MN/m. The effective stiffness of the combined bearing pedestals and integral dampers found from impact tests on the rotor supported on ball bearings and ISFDs equals $K_{sV}=5.6$ MN/m and $K_{sH}=4.83$ MN/m in the vertical and horizontal directions, respectively.

Desired bearing stiffness coefficients (K_{bV}, K_{bH}) that render an isotropic support (i.e., $K_{EV}=K_{EH}$) are estimated from the simple

Table 1 Integral squeeze film damper main characteristics

| | | |
|-------------------------------|----------|-----------------|
| Outer diameter: | 126 mm | (4.961 in) |
| Land Radius: | 48.26 mm | (1.900 in) |
| Axial Length: | 23.0 mm | (0.910 in) |
| Land radial clearance: | 0.229 mm | (0.009 in) |
| Pad arc extent: | 52 deg | 4 pads |
| Nominal web radial stiffness: | 3.5 MN/m | (20,000 lbf/in) |

Table 2 Measured stiffness of pedestal supports and integral dampers

| Effective rotor mass: 45.3 kg | | Drive end | | Free end | |
|--|------------|----------------|-----------------------|---------------|--|
| | | MN/m, (lbf/in) | | MN/m (lbf/in) | |
| <i>ISFD</i> structural stiffness (from static measurements) | Vertical | 3.66 | 3.50 | | |
| | Horizontal | 3.80 | 3.53 | | |
| Pedestal support stiffness (from impact tests) | Vertical | 30.50 | 28.20 | | |
| | Horizontal | 13.95 | 10.10 | | |
| Equivalent support stiffness (series <i>ISFD</i> and pedestal) | Vertical | 3.26 | 3.11 | | |
| | Horizontal | 2.99 | 2.62 | | |
| <i>Effective</i> support stiffness (from rotor bump tests on two supports)* | Vertical | 5.60 | $\omega_{nV} = 56$ Hz | | |
| | Horizontal | 4.83 | $\omega_{nH} = 52$ Hz | | |

Average system damping from imbalance response measurements, *rotor on *ISFDs* only (ball bearings):

Vertical: 4.36 ± 0.13 kN.s/m (24.9 lbf.s/in), $\zeta_{sV} = 0.137$; Horizontal: 3.14 ± 0.10 kN.s/m (17.9 lbf.s/in), $\zeta_{sH} = 0.106$

Table 3 Flexure pivot tilting pad bearing main dimensions and operating conditions

| | 4 pads (70° arc) | |
|-----------------------------------|-----------------------------|---------------------------------------|
| | ISO units | English units |
| Bearing nominal diameter: | 30.15 mm | 1.187 in |
| Bearing axial length: | 22.9 mm | 0.902 in |
| Pad radial clearance: | 0.127 mm \pm 0.005 mm | 0.0050 in \pm 0.0001 in |
| Pad preload: 0.405 (r_p) | 0.0508 mm | 0.002 in |
| Pivot offset: | 0.50 | |
| Bearing radial clearance: | 0.076 mm | 0.003 in |
| Pad rotational stiffness: | 40 N-m/rad | 354 lbf-in/rad |
| Clearance on back of pads: | 0.178 mm (typ) | 0.007 in (typ) |
| Average inlet lubricant viscosity | 15.76 cP at 24.4° C (76° F) | |
| Operating speed range: | 0-10,000 rpm | |
| Static load between pads | | |
| drive end bearing | 247.3 N | 55.53 lbf (51.90 psi – specific load) |
| free end bearing | 198.2 N | 44.50 lbf (41.56 psi – specific load) |

series relationship $K_E = K_s K_b / (K_s + K_b)$. The condition of support isotropy is needed to keep the vertical and horizontal first critical speeds as close as possible. The *desired* values of bearing stiffness obtained are $K_{bV} = 27.6$ MN/m, and $K_{bH} = 4.7 K_{bV}$. Note that these predicted stiffness values define a strongly anisotropic fluid film bearing. A computational analysis (San Andrés [8]) generates the synchronous stiffness and damping coefficients for a four pad, load between pads, flexure pivot TPJB. The fluid film model is laminar with adiabatic thermal boundaries.

Table 3 gives the geometry of the FPJB, lubricant properties and operating conditions. With the current hardware, the predictions show that the maximum attainable bearing stiffness asymmetry ($K_{xx} \neq K_{yy}$) is on the order of $K_{bV}/K_{bH} = 1/1.008$ at 3000 rpm. However, these bearing stiffness coefficients yield an equivalent support stiffness asymmetry (K_{EV}/K_{EH}) of only 1.12 at this speed, which is considered satisfactory.

The predicted FPJB force coefficients at 3000 rpm, ($f \approx 1$) combined with the pedestal-ISFD effective stiffness and damping ratios (ζ) for the open-ended ISFDs (see Table 2), yield optimum bearing to support damping ratios of $\beta_{optV} = 21.2$, and $\beta_{optH} = 26.7$. Table 2 includes the measured values of support damping, i.e., overall system damping for the open ends ISFD and bearing pedestals. The selected tilting pad bearing is expected to provide damping coefficients that are smaller than those needed for optimum damping conditions (slightly over 50% of the optimum damping). Figure 3 depicts predictions of the rotordynamic force coefficients representing the combined pedestals, ISFDs and FPJBs for the drive end bearing as a function of the rotor speed. The force coefficients for the free end bearing support are very similar to the coefficients in the drive end, the only difference being the carrying load and the structural stiffness of the pedestals.

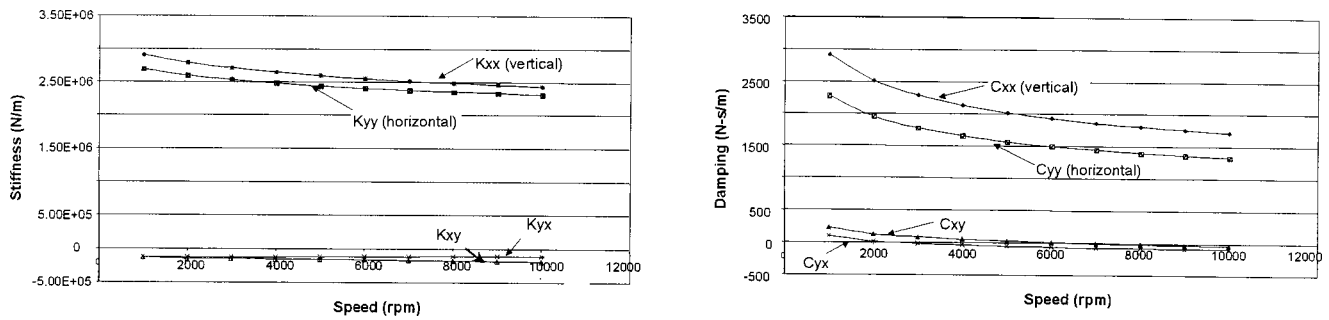


Fig. 3 Predicted equivalent stiffness and damping synchronous force coefficients for tilting pad bearings and integral dampers, including supports flexibility. Drive and support.

Experimental Results

Coast-down imbalance response tests serve to evaluate the effectiveness of the series bearing combination in limiting orbit amplitudes when the rotor traverses the first critical speed. In these experiments, the rotor speed is brought up to 9000 rpm and then the motor power is shut off. The rotor disengages from the motor through the clutch action, continues spinning after the motor stops and decelerates until it reaches rest. The experimental results evidence the very low friction in the FPJBs since it takes more than ten minutes for the decelerating rotor to come to a full stop. In all the synchronous response measurements, the baseline response to remnant imbalance is subtracted (vector form) from the responses

due to known imbalance masses inserted at a radius of 114.3 mm (4.5 in.) on the rotor middle disk and exciting the first (cylindrical) mode of vibration.

The current bearing support configuration allows conducting measurements with locked squeeze film dampers. These experiments are of importance to isolate the effect of the tilting pad bearings on the dynamic response of the rotor. Bronze shims inserted within the integral damper film lands and lateral plates tightly pressed against the damper journal and housing ring effectively eliminated (locked) any damper journal motions relative to its housing. Table 4 sums the imbalance conditions and recorded feed lubricant temperatures. The largest imbalance displacement

Table 4 Measured responses at the first critical speed of rotor supported on FPJBs with locked dampers

Bearing diametrical clearance (between pivots) = 0.152 mm (0.006 in)

| Peak-peak amplitude (mm) and critical speed (rpm) VERTICAL DIRECTION | | | | | |
|--|--------------|--------------------------------|----------------------------|---------------|----------------|
| Imbalance mass <i>m</i> | Av. Oil Temp | Imbalance distance <i>u</i> | Average pk-pk Amplitude | Standard dev. | Critical speed |
| gr | °C (°F) | μm | mm | mm | rpm |
| 3.5 | 22.7 (72.9) | 8.81 | 0.063 | 0.006 | 5742 |
| 5.0 | 24.6 (76.4) | 12.6 | 0.069 | 0.006 | 5800 |
| 6.9 | 24.2 (75.7) | 17.4 | 0.099 | 0.009 | 5750 |
| 8.9 | 22.4 (72.3) | 22.4 | 0.117 | 0.011 | 5775 |

The imbalance distance is calculated from $u = (m r / M)$ where u is the imbalance distance, m is the imbalance mass, $r = 114.3$ mm (4.5 in) is the radius of the disk where the imbalance mass is attached, and $M = 45.3$ kg is the rotor mass (for the fundamental mode of vibration).

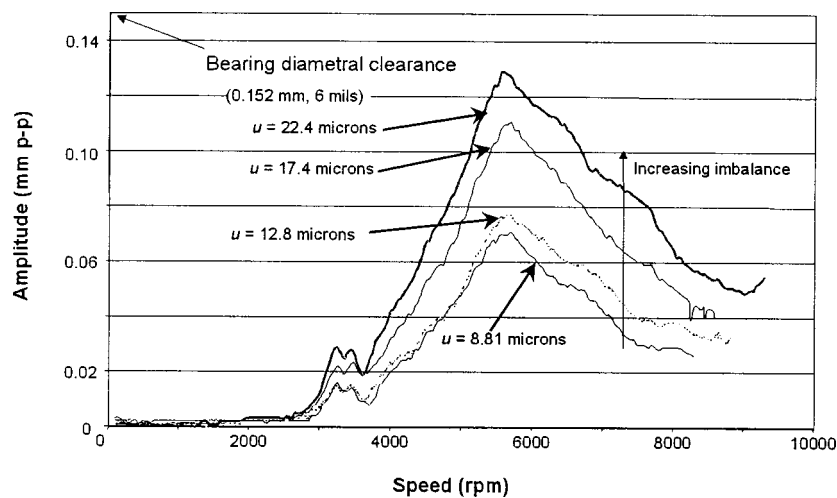


Fig. 4 Summary of imbalance response of rotor supported on FPJBs. Measurement at rotor midspan (vertical direction). Locked ISFDs.

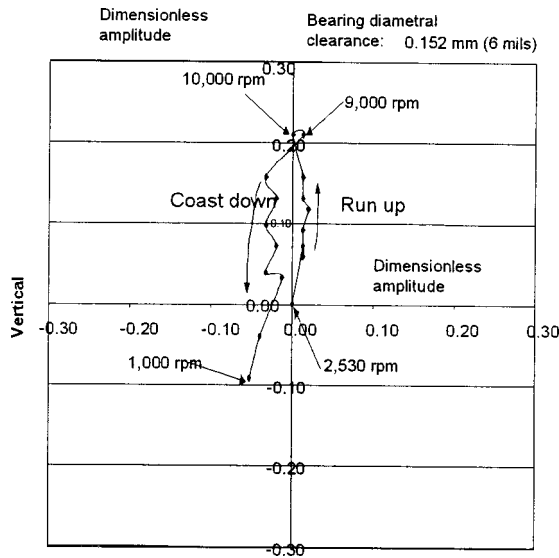


Fig. 5 Shaft centerline motion for test with no imbalance. Rotor supported on FPJBs in series with ISFDs. Drive end, static load: 247.3 N.

(u) corresponds to 22.4 microns, i.e., approximately 30% of the FPJB assembled radial clearance. Figure 4 shows the rotor synchronous response at midspan in the vertical direction. The amplitudes of rotor vibration are consistently larger in this direction than in the horizontal direction, the critical speeds occurring at

about 5750 rpm. Table 4 also gives the peak-peak amplitudes of response at the first critical speed in the vertical direction as well as the location of the critical speeds. The largest imbalance ($u = 22.4$ microns) excites rotor motions up to $\sim 80\%$ of the assembled bearing clearance at the drive end location. The measurements show the linearity of the response, i.e., amplitudes of motion proportional to the imbalance displacement, even though these motions are rather large relative to the bearing clearance. Predictions of rotor response from a transfer matrix model of the rotor supported on the tilting pad bearings (XLTRC [9]) show good correlation with the location of the experimental critical speeds and response amplitudes in the vertical direction.

A test with no imbalance in the rotor evidences the rotor lift within the bearing clearance with the dampers active (unlocked). Figure 5 shows in dimensionless form the centerline travel of the rotor at the drive end for increasing rotor speeds. The FPJB minimum diametral clearance (0.152 mm) is used to set dimensionless rotor displacements. The main direction of the shaft centerline motion is along a vertical line thus denoting small cross-coupled forces. The coordinate (0,0) denotes the beginning of the test with the rotor at its lowest position and in contact with the pads. At the highest speed of ~ 9000 rpm, the rotor has lifted to about 20% of the bearing diametral clearance. Note that the rotor center does not return to the same start position, thus revealing some static sag at the end of the experiment. This may be attributed to the bearing construction and some thermal-induced bow on the rotor.

Imbalance response experiments were conducted next to assess the dynamic behavior of the rotor supported on tilting pad bearings in series with the ISFDs. The squeeze film lands are open to ambient in the current tests, i.e., without end seals installed. Table 5 sums the imbalance conditions and inlet lubricant temperatures.

Table 5 Measured responses at the first critical speed of rotor supported on series FPJB-ISFDs with locked dampers

ISFD diametral clearance = 0.458 mm (0.018 in)

| Imbalance mass m | Av. Oil Temp | Imbalance distance u | VERTICAL DIRECTION | | | HORIZONTAL DIRECTION | | |
|--------------------|--------------|------------------------|-------------------------|---------------|----------------|-------------------------|---------------|----------------|
| | | | Average pk-pk Amplitude | Standard dev. | Critical speed | Average pk-pk Amplitude | Standard dev. | Critical speed |
| gr | °C (°F) | μm | mm | mm | rpm | mm | mm | rpm |
| 2.67 | 24.8 (76.7) | 6.99 | 0.047 | 0.004 | 3041 | 0.041 | 0.002 | 2900 |
| 5.33 | 23.5 (74.4) | 14.02 | 0.117 | 0.006 | 2975 | 0.079 | 0.008 | 2850 |
| 6.88 | 23.2 (73.8) | 18.08 | 0.147 | 0.007 | 2908 | 0.109 | 0.010 | 2800 |
| 9.07 | 24.0 (75.2) | 23.84 | 0.179 | 0.011 | 2883 | 0.117 | 0.015 | 2700 |
| 10.8 | 23.5 (74.3) | 28.32 | 0.212 | 0.012 | 2833 | | | |
| 13.3 | 24.9 (76.9) | 35.03 | 0.249 | 0.016 | 2750 | 0.188 | 0.008 | 2850 |
| 15.9 | 25.8 (78.4) | 42.07 | 0.284 | 0.015 | 2700 | 0.227 | 0.014 | 2750 |
| 18.7 | 25.9 (78.6) | 49.06 | 0.322 | 0.014 | 2716 | 0.309 | 0.013 | 2700 |

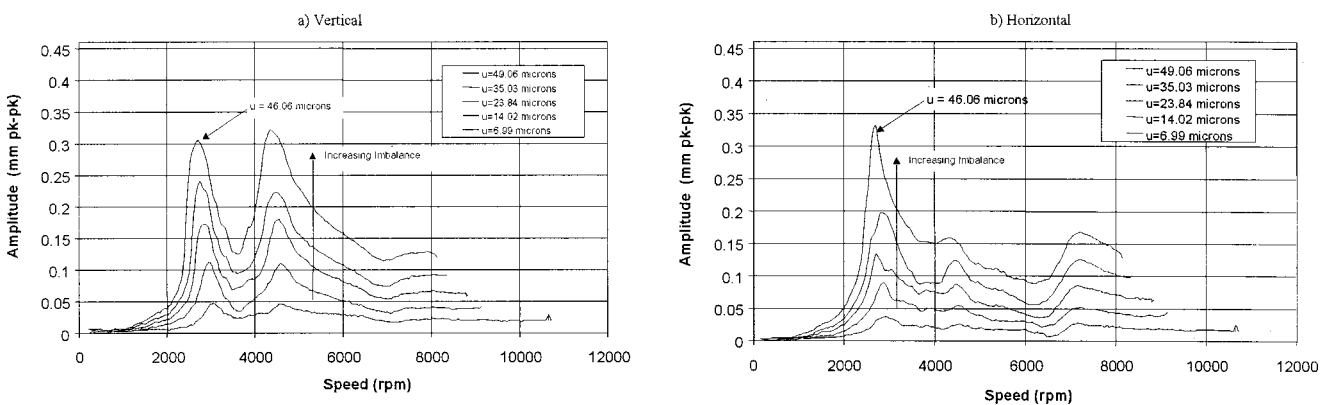


Fig. 6 Summary of imbalance response of rotor supported on series FPJB-ISFDs. Measurements at rotor midspan in the vertical and horizontal directions. ISFDs active.

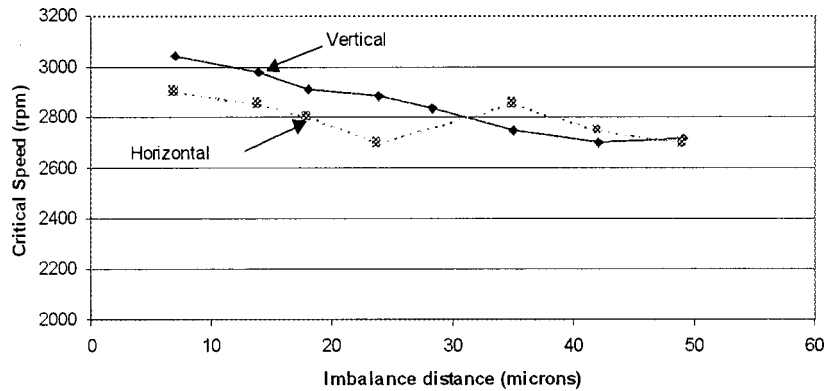


Fig. 7 Measured first critical speed versus imbalance distance for tests on rotor supported on series FPJB-ISFDs

The largest imbalance displacement (u) corresponds to 49 microns (18.7 grams), i.e., larger than twice the largest value tested with the FPJBs alone. Figure 6 depicts the rotor synchronous response, vertical and horizontal, at midspan for increasing imbalances. Similar measurements were recorded at the free and drive ends and are not shown for brevity. Note that the amplitudes of rotor vibration in the two directions are nearly identical while crossing the (new) lower critical speed at approximately 2700 rpm. The peak response in the vertical direction at about 4500 rpm is due to a resonance of the bearing pedestals. No subsynchronous vibrations were ever observed in any of the experiments. For identical imbalance conditions, the peak amplitudes of vibration for the rotor with the dampers active are larger than those recorded

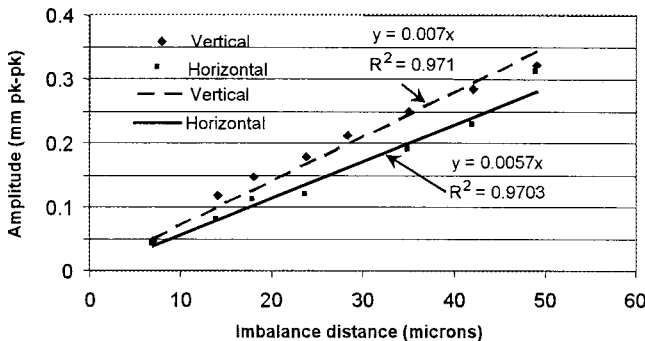


Fig. 8 Average peak-peak rotor response at first critical speed versus imbalance distance for rotor supported on FPJB-ISFDs. Vertical direction and horizontal planes.

with the locked dampers. However, operation with the dampers results in an increased tolerance to imbalance due to the larger clearances in the ISFDs. Note that the maximum available clearance with the two elements is 0.610 mm [0.152 (TPJB) + 0.458 (ISFD)].

Table 5 includes the peak-peak amplitudes of rotor response at the first critical speed as well as estimates of the average amplitude and standard deviation in the three planes of measurement. Figure 7 shows the average value of critical speeds (vertical and horizontal) versus the imbalance displacement. Note the remarkable reduction in critical speed of almost 10% for the largest imbalance condition tested.

Figure 8 depicts the average peak amplitudes of motion at the critical speed versus the imbalance distance. Note that the rotor amplitudes of motion are proportional to the imbalance displacement (u), in spite of the fact that the largest rotor motions are about 70% of the damper radial clearance. The equivalent system damping ratios (ζ) are estimated from the peak responses using the amplification factor (Q) at the first critical speed as, i.e., from $2\zeta^2 = -1 \pm \sqrt{1 + 1/Q^2}$. The simple analysis implies rigidity of the rotor, as the experiments demonstrate from the measurements of displacements at three planes. The amplification factors Q from the linear regressions given in Fig. 8 are equal to 3.5 and 2.85 in the vertical and horizontal directions, respectively. Thus, the corresponding system damping ratios are $\zeta_V = 0.141$ and $\zeta_H = 0.173$ for the configuration of rotor mounted on tilting pad bearings and active integral dampers. These values of system damping ratio are compared with results obtained in prior experiments for the rotor supported on integral dampers and ball bearings, $\zeta_{sV} = 0.137$ and $\zeta_{sH} = 0.106$ (De Santiago et al. [3]). Thus, the present test configuration shows a marked increase in system damping of about

Table 6 Calculated rotordynamic properties of test rotor supported on FPJBs only (locked dampers) and FPJBs in series with active ISFDs

| | | | |
|--|---|-----------------------|-------------------------|
| Rotor on FPJBs only: | Critical speed: | Vertical 5,900 rpm | Horizontal 5,600 rpm |
| Average experimental critical speed in the vertical direction is 5,750 rpm | | | |
| Rotor on FPJB-ISFDs: | Rotor speed: 3,000 rpm | Vertical | Horizontal |
| | Nat. Frequencies: | 2,991 cpm | 3,100 cpm |
| | Damping ratio: | 0.127 | 0.134 |
| | Mode: Cylindrical Forward | | |
| | Rotor speed: 6,000 rpm | | |
| | Nat. Frequency: | 5933 cpm | |
| | Damping ratio: 0.144. | Mode: Conical Forward | |
| | Experimental system damping ratios: $\zeta_{v,b} = 0.141$ $\zeta_{h,b} = 0.173$ | | |
| | Average critical speeds: Vertical 3,000-2,700 rpm, Horizontal: 2,900-2,700 rpm | | |

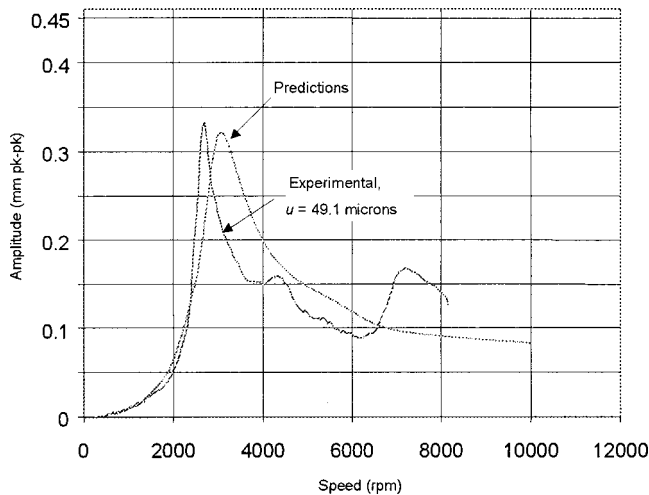


Fig. 9 Comparison of predicted and measured horizontal synchronous response for 18.6 gram imbalance ($u=49$ microns). Measurements at rotor midspan (integral dampers active).

60% for motions in the horizontal direction. The increase in damping ratios for motions in the vertical direction is more modest (only 2.9%) since the rotor displacements in this direction now are similar to the displacements in the horizontal direction.

A transfer matrix model of the test rotor on the bearing supports, i.e., series FPJBs and ISFDs, predicts the system damped eigenvalues (natural frequencies and damping ratios) as well as the rotor imbalance response. Table 6 presents the calculated system critical speeds and damping ratios for rotor speeds below 9000 rpm. All predicted modes of vibration are well damped within the range of test speeds. The predicted damping ratios for the cylindrical mode of vibration ($\zeta_V=0.127$, $\zeta_H=0.134$) compare relatively well with the values derived from the measurements ($\zeta_V=0.141$, $\zeta_H=0.173$), the differences being 5% and 26% in the vertical and horizontal directions, respectively. Figure 9 shows a comparison of the experimental and predicted synchronous rotor response for the largest imbalance (18.6 gram), $u=0.049$ mm. Note that the test response in the vertical direction shows the resonance of the support not well accounted for in the predictive model. In general, there is good agreement between the predicted and experimental responses, the horizontal response being slightly closer to the experimental measurements than the vertical amplitudes.

Conclusions

Measurements of the imbalance response of a three disk massive rotor supported on flexure pivot tilting pad bearings in series with integral squeeze film dampers are detailed. This support configuration shows many advantages over the common ball bearing-SFD arrangement. These are namely, ease of installation and retrofit (split elements), reduced number of parts and weight, and as demonstrated by the measurements, much larger viscous damping action with increased tolerance to disk imbalances.

Coast-down experiments from 9 krpm were conducted for increasing levels of disk imbalance. The measurements show the rotor center line moves in a nearly vertical direction, thus evidencing little cross coupled effects in the flexure pivot bearings. System damping coefficients are identified from the peak amplitude of rotor response (Q -factor) while traversing cylindrical mode critical speeds (~ 5700 rpm for locked SFDs and 3200 rpm for active SFDs). The tests performed with locked (inactive) and active ISFDs demonstrate the effectiveness of the flexible damped support in relocating the system critical speed and improving the

overall rotor response with reduced transmitted forces to ground. The ISFDs allow the rotor to operate safely with values of imbalance twice as large as the maximum sustained by the rotor supported on tilting pad bearings only.

Predicted system damping ratios compare well with those estimated from the peak amplitude responses. Critical speeds are also favorably predicted. Further experimental effort is needed to develop parameter identification techniques that will allow the accurate estimation of the bearing and damper force coefficients over frequency ranges of interest.

Acknowledgments

The support of the TAMU Turbomachinery Research Consortium and National Science Foundation are gratefully acknowledged.

Nomenclature

- C = system damping coefficient (N.s/m, lbf.s/in.)
- f = frequency ratio, ω/ω_n
- K = bearing and support stiffness (N/m, lbf/in.)
- m = imbalance mass attached to rotor middle disk (kg)
- M = rotor mass for the first mode of vibration (45.3 kg, 99.8 lbf)
- Q = rotor-bearing system amplification factor at first critical speed
- r = rotor middle disk radius for location of imbalance masses (114.3 mm, 4.5 in.)
- R^2 = linear regression correlation factor
- u = $m \cdot r / M$, imbalance distance (m, in.)
- X, Y = coordinates of motion, vertical and horizontal
- α = K_b / K_s , bearing-to-support stiffness ratio
- β = C_b / C_s , bearing-to-support damping ratio
- μ = lubricant viscosity (Pa-s)
- ω = frequency of imbalance excitation, synchronous with rotor speed (rad/s)
- ω_n = system natural frequency of rotor supported on ISFDs and rigid bearings (rad/s)
- ζ = $C/2M\omega_n$, system damping ratio

Subscripts

- V, H = vertical, horizontal (X, Y)
- s = refers to support (pedestal-ISFD) properties
- b = refers to tilting pad bearing properties
- E = equivalent "static" property
- opt = optimum value

References

- [1] De Choudhury, P., Hill, M. R., and Paquette, D. J., 1992, "A Flexible Pad Bearing System for a High Speed Centrifugal Compressor," *Proceedings of the 21st Turbomachinery Symposium*, Dallas, TX, pp. 57–64.
- [2] Zeidan, F., 1995, "Application of Squeeze Film Dampers," *Turbomach. Int.*, **11**, (Sept./Oct.), pp. 50–53.
- [3] De Santiago, O., Oliveras, J., and San Andrés, L., 1999, "Imbalance Response of a Rotor Supported on Open-Ends Integral Squeeze Film Dampers," *ASME J. Eng. Gas Turbines Power*, **121**, pp. 718–724.
- [4] De Santiago, O., and San Andrés, L., 2000, "Dynamic Response of a Rotor-Integral Squeeze Film Damper to Couple Imbalances," *ASME Paper No. 2000-GT-388*.
- [5] De Santiago, O., and San Andrés, L., 1999, "Imbalance Response and Damping Force Coefficients of a Rotor Supported on End Sealed Integral Squeeze Film Dampers," *ASME Paper No. 99-GT-203*.
- [6] Edney, S. L., and Nicholas, J. C., 1999, "Retrofitting a Large Steam Turbine With a Mechanically Centered Squeeze Film Damper," *Proceedings of the 28th Turbomachinery Symposium*, Houston, TX, pp. 29–40.
- [7] Barrett, L. E., Gunter, E. J., and Allaire, P. E., 1978, "Optimum Bearing and Support Damping for Unbalance Response and Stability of Rotating Machinery," *ASME J. Eng. Gas Turbines Power*, **100**, pp. 89–94.
- [8] San Andrés, L., 1996, "Turbulent Flow, Flexure-Pivot Hybrid Bearing for Cryogenic Applications," *ASME J. Tribol.*, **118**, pp. 190–200.
- [9] XLTRC, 1998, *Rotordynamics Analysis Software*, TAMU Turbomachinery Laboratory.

Contact Stresses in Dovetail Attachments: Alleviation via Precision Crowning

G. B. Sinclair

Department of Mechanical Engineering,
Louisiana State University,
Baton Rouge, LA 70803-0100

N. G. Cormier

General Electric Aircraft Engines,
Evendale,
Cincinnati, OH 45215

Previous studies of contact stresses in dovetail attachments provide verified finite element stresses as well as some simple physical models of such stresses. Generally there is good agreement between the finite element analysis and the simple physical models. Together the two identify a pinching mechanism as leading to large fluctuations in hoop stresses at the edges of contact. These fluctuating hoop stresses can be expected to be a major contributor to the fatigue of dovetail attachments. The present study investigates a method of alleviating the fluctuating hoop stresses. This method entails crowning of the contacting flat on a blade. Such crowning is in two orthogonal directions on the blade flat. Two-dimensional finite element analyses are made in both directions. These analyses indicate that significant reductions in fluctuating hoop stresses can be achieved by the method, provided the crowning is controlled sufficiently precisely. [DOI: 10.1115/1.1584477]

1 Introduction

1.1 Motivation and Background. Single tooth attachments or “dovetails” are used to secure fan and compressor blades to disks in gas turbines. A section through a typical dovetail is shown in Fig. 1(a). Therein the base of the blade is pulled as a result of the centripetal acceleration of its remainder, while it is restrained by contact with the disk on two flats (e.g., $C-C'$ in Fig. 1(a)). At the edges of these contact regions, fretting can occur when loads vary. This fretting can lead to fatigue crack initiation and ultimately to failures (e.g., in the disk at C , the blade at C'). The primary intent of this work is to try to devise means of reducing the incidence of such failures.

This research builds on an earlier stress analysis of a dovetail attachment with a section as in Fig. 1(a) (Sinclair et al., [1]). This stress analysis uses finite elements. It also builds on an earlier development of simple companion physical models (Sinclair and Cormier [2]). These models are largely analytical. Preliminary to devising an approach for reducing fatigue failures in dovetail attachments, we summarize the findings of these two papers. We begin with some results for nominal contact stresses during loading up, then we discuss results for peak contact stresses during loading up, then stresses during unloading.

1.2 Nominal Contact Stresses During Loading Up. A free-body diagram for half of the blade section of Fig. 1(a) is given in Fig. 2. The loading of this half-blade comes from the centripetal acceleration of its self mass, F_ω , and that of the portion of the blade not shown, F_b . These “forces” are balanced by normal and shear forces, N and T , acting on a contact region of extent $2a$ inclined at an angle α . By virtue of symmetry, there are no counterbalancing forces on the centerline and only a horizontal force there, H . All these forces are per unit thickness in the out-of-plane direction in Fig. 2.

In general there can be a moment reaction on the contact region, M (per unit thickness). This is balanced by an equal and opposite moment on the centerline, which also has a further moment M_F to offset the moment produced by F_ω and F_b about the head of N .

A highly simplified model in [2] indicates that the blade slips relative to the disk during loading up if

$$\tan \alpha > \mu, \quad (1)$$

where μ is the coefficient of friction. Typically in gas turbine engines $\alpha \approx \pi/4$ whereas $\mu \leq 0.4$ (Hamdy and Waterhouse, [3]), so that (1) predicts slip during loading up. The finite element analysis of [1] confirms this is the case.

Given slipping during loading up,

$$T = \mu N. \quad (2)$$

Then resolving vertically leads to the following expressions for the nominal contact and shear stress:

$$\bar{\sigma}_c = \frac{F_\omega + F_b}{2a(\cos \alpha + \mu \sin \alpha)}, \quad \bar{\tau}_c = \mu \bar{\sigma}_c. \quad (3)$$

In (3), $\bar{\sigma}_c$ is taken to be positive when compressive (as in Fig. 1(b)), and bars atop stresses denote nominal values. The finite element analysis in [1] tracks the results in (3) during loading up to within 3%. This analysis also furnishes nominal bending stresses due to M : There is no corresponding formula in terms of F_ω , F_b for these stresses because they are statically indeterminate.

1.3 Peak Contact Stresses During Loading Up. While it is fairly easy to obtain accurate nominal stresses with finite elements, it is not so easy to obtain accurate edge-of-contact stresses (i.e., stresses at C , C' in Fig. 1(a),(b)). There are challenges to obtaining such stresses even within two-dimensional elasticity. While contact is conforming at C , C' and stresses therefore non-singular provided contact inequalities are policed,¹ the policing of these inequalities requires elements that are small relative to local radii of curvature and here these local radii are small themselves. In addition there are locally high stresses, and even infinite stress gradients, at the edges of contact. An illustration of this for the normal contact stress σ_c is given in Fig. 3. This is for maximum load (rpm) and when there is no friction, the situation producing the highest σ_c (cf., (3)). Normalization is by σ_0 , a stress representative of the loading and defined by

¹See, e.g., [1], Section 2, for a discussion of contact inequalities and their roles in conforming contact problems.

Contributed by the International Gas Turbine Institute (IGTI) of THE AMERICAN SOCIETY OF MECHANICAL ENGINEERS for publication in the ASME JOURNAL OF ENGINEERING FOR GAS TURBINES AND POWER. Paper presented at the International Gas Turbine and Aeroengine Congress and Exhibition, New Orleans, LA, June 4–7, 2001; Paper 2001-GT-0550. Manuscript received by IGTI, Dec. 2000, final revision, Mar. 2001. Associate Editor: R. Natole.

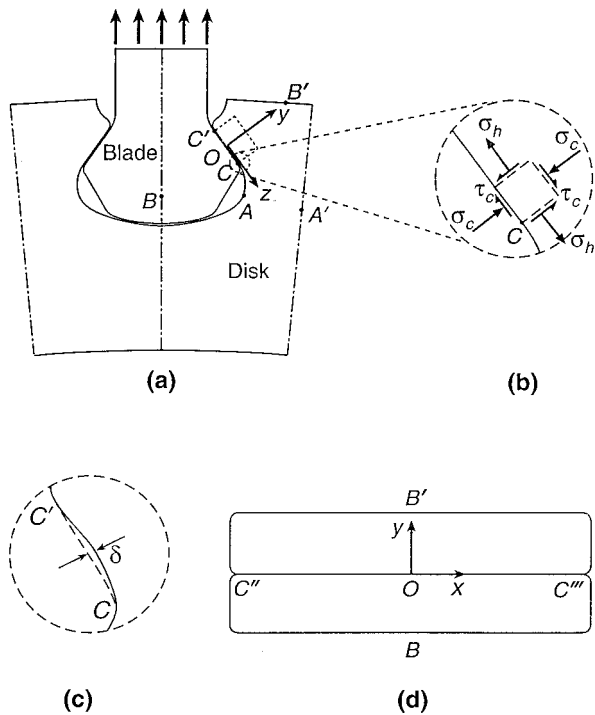


Fig. 1 Dovetail attachment configuration: (a) section of overall attachment, (b) closeup of disk near lower contact point with stresses acting, (c) in-plane crown on blade flat, (d) out-of-plane section BB'

$$\sigma_0 = \frac{F_w + F_b}{b}, \quad (4)$$

where b is the half-blade width (Fig. 2). The sharp peaks in Fig. 3 are not equal because of the presence of bending contributions (i.e., the presence of M). For the higher of the two peaks, the value of σ_c^{\max} can be expressed by

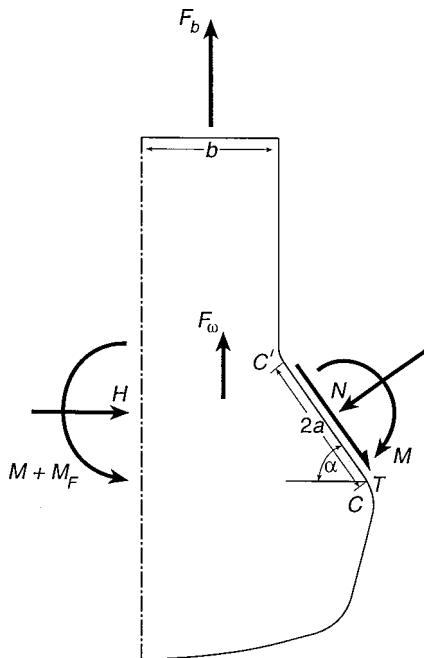


Fig. 2 Free-body diagram of half of the blade section

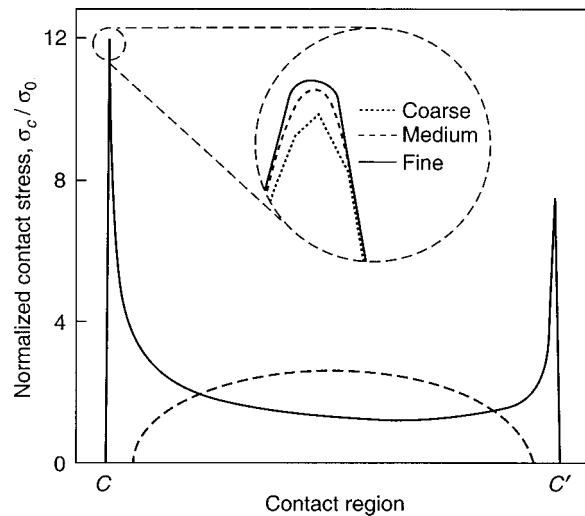


Fig. 3 Contact stress distributions ($\mu=0$)

$$\sigma_c^{\max} = 6.3\bar{\sigma}_c. \quad (5)$$

Hence, at maximum load, a *stress concentration factor* of 6.3 in effect ($\bar{\sigma}_c = 1.9\sigma_0$, thus the lower factor in (5) than in Fig. 3).

Crucial to determining the peak contact stress of Fig. 3 with finite elements is to try and ensure *convergence*: Only then can one be reasonably sure that peak stresses are being accurately calculated. Furthermore, convergence can be nonuniform in conforming contact problems because of changing contact extents. Under these circumstances, it is relatively easy to be misled as to convergence with just a two-grid check. Consequently in [1] and here we adopt the following convergence checks. We employ a sequence of at least three grids: a coarse, a medium, and a fine. The last two of these grids are formed from their respective predecessors by successively halving element sides. Then if the coarse grid has n elements, the medium and fine have $4n$ and $16n$, respectively. On this sequence, we judge a contact stress to be *converging* if

$$|\sigma_c^C - \sigma_c^M| > |\sigma_c^M - \sigma_c^F|, \quad (6)$$

wherein superscripts indicate the grid used in the evaluation. Provided (6) holds, we judge this contact stress to have *converged* if

$$|\sigma_c^M - \sigma_c^F| < \varepsilon |\sigma_c^F|, \quad (7)$$

wherein ε is the level of accuracy sought. We view $\varepsilon=0.10$ (i.e., 10%) as a satisfactory level of accuracy for present purposes, $\varepsilon=0.05$ (5%) as good, and $\varepsilon=0.01$ (1%) as excellent.²

In order to meet the convergence criteria of (6), (7) for the dovetail attachment of Fig. 1(a), [1] uses a submodeling procedure (Cormier et al. [5]). This choice results in three, successively refined, global grids, followed by three, successively refined, submodel grids. Convergence is only achieved on the latter three-grid sequence. Thereon (6) is complied with as illustrated in the close-up in Fig. 3. Further, (7) is complied with to within a good level of accuracy (the actual $\varepsilon=0.017$ or 1 2/3%; [1], Section 4). These are the only edge-of-contact stresses we are aware of in the literature that comply with (6), (7) (see [1], Section 1, for a review). The sides of the elements in the fine submodel grid are 0.5% of the local radii of curvature: This is 30 times smaller than elements used in any analysis reported in the literature and referenced in [1]. The submodeling procedure enables this level of resolution to be achieved without undue computational effort.

²For stress analysis in general, some justification for convergence checks of this genre is given in Sinclair [4].

With friction present, slipping during loading up leads to local shear stresses, τ_c of Fig. 1(b), with

$$\tau_c = \mu \sigma_c \quad (8)$$

The shear contact stresses in [1] comply with (8) to within 3.5%. These shears pull the material within the disk just before C , and push the material just ahead of C' . Accordingly the hoop stress σ_h (Fig. 1(b)) is tensile at C and compressive at C' in the disk. The converse holds true for the blade. Thus the peak tensile hoop stresses occur at C in the disk, C' in the blade.

For Hertzian contact in the presence of slip, Poritsky [6] has that the hoop stress at the edge of contact, σ_h^{\max} , is given by

$$\sigma_h^{\max} = 2\tau_c^{\max} = 2\mu\sigma_c^{\max} \quad (9)$$

For the maximum coefficient of friction considered here, 0.4, this means hoop stresses that are quite comparable in magnitude to the normal contact stresses. This is indeed found to be the case in [1]. There the peak value of the converged hoop stress at C at maximum load is 88% of the peak normal contact stress when $\mu=0.4$.³

1.4 Contact Stresses During Unloading. Unloading can occur with reductions in engine rpm. It can also occur with variations in stiff-wise bending (i.e., bending out-of-plane in Fig. 1(a)). Irrespective of the source, two different responses can be identified.

Without friction, N and σ_c^{\max} during unloading take on the same values as during loading up for corresponding loads (to within 0.5%, [1], Section 4.2). With friction, N and σ_c^{\max} during unloading increase, at least initially. This result is contrary to any one-dimensional physical reasoning. However, it can be explained with two-dimensional reasoning.

Consider what happens at the section through the disk at AA' in Fig. 1(a). With unloading, $F_\omega + F_b$ in Fig. 2 is reduced. Therefore so is the radially outward pull on the disk at AA' . Consequently the material above AA' in the disk retracts radially inward. Because the periodic symmetry line through A' is not parallel to the central symmetry line through B (Fig. 1(a)), this retraction is accompanied by a tendency for the disk contact region to move laterally towards the centerline. Without friction, the blade can slip radially inwards and thereby accommodate lateral motion of the disk contact region. With friction, the blade can stick and get pinched by lateral motion of the disk contact region. It is this *pinching mechanism* that increases N and σ_c^{\max} during unloading. A simple analysis in [2], Section 2.5, shows that indeed sticking and pinching during unloading is consistent with increases in N , hence σ_c^{\max} . Results from the analysis for [1] and reported in [2] confirm sticking with pinching and quantify the increases in N and σ_c^{\max} (e.g., a 20% unload leads to a 13% increase in σ_c^{\max} when $\mu=0.4$).

One consequence of this pinching is that T and τ_c^{\max} drop significantly on unloading. This is because there are two sources of reduction in the shear force T . The first is the expected reduction occurring because there is less load to be balanced (i.e., because $F_\omega + F_b$ in Fig. 2 is less). The second is the less-expected reduction occurring because the normal reaction is increased and consequently is balancing a greater share of the load (i.e., because the vertical component of N in Fig. 2 is increased). Results from the analysis for [1] reported in [2], Section 2.5, confirm and quantify the significant drops that can occur in T and τ_c^{\max} (e.g., a 20% unload leads to a 68% decrease in τ_c^{\max} when $\mu=0.4$).

³There are other contributions to the σ_h in the dovetail attachment that are not present in the configuration in Poritsky [6], so that precise compliance with (9) is not to be expected.

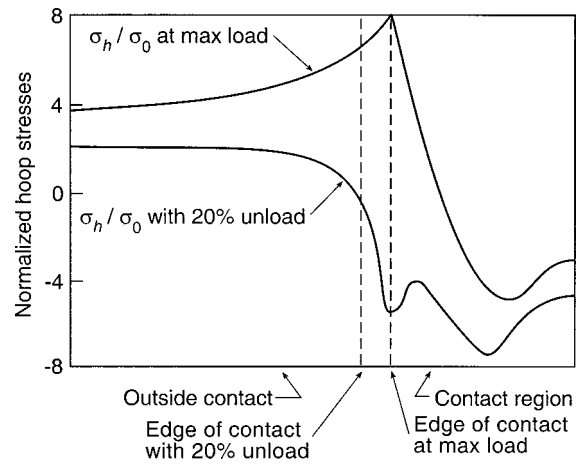


Fig. 4 Hoop stress variation near the edge of contact for 20% unloading ($\mu=0.4$)

A further consequence of this pinching is that it produces large fluctuations in the peak hoop stress, σ_h^{\max} . In the first instance, this is because σ_h^{\max} is largely due to τ_c^{\max} (recall (9)), and τ_c^{\max} drops significantly with unloading and pinching. In the second instance, this is because σ_h^{\max} can go from being tensile just outside of the contact region to compressive and within the contact region as N and the contact region grow with unloading and pinching. These effects in combination are illustrated in Fig. 4. Therein a 20% reduction in load changes σ_h^{\max}/σ_0 from 8.0 to -5.2 when $\mu=0.4$.

The foregoing large fluctuations in hoop stresses are from an elastic analysis. With yielding and plastic flow, these fluctuations can be expected to be lessened. Even so, large fluctuations in elastic stresses are the harbingers of fatigue failure (cf., S-N curves). It would seem reasonable that finding a means for lowering these fluctuations would offer a potential way for reducing the incidence of fatigue failures in dovetail attachments.

1.5 Objective and Scope. The primary objective of the present work, then, is to reduce the large fluctuations in hoop stresses that attend unloading of dovetail attachments. One clear means of doing this is to lower friction. Our understanding is that the industry has introduced surface treatments to this end. Any further improvements in this regard would be all to the good. Here, instead, we adopt a different tactic.

The tensile σ_h^{\max} prior to unloading largely stems from τ_c^{\max} (as in the first of (9)): τ_c^{\max} in turn is directly proportional to σ_c^{\max} (as in the second of (9)). It follows that reducing σ_c^{\max} reduces the σ_h^{\max} that can fluctuate at the outset. Here therefore we seek to reduce σ_c^{\max} at maximum load.

The method chosen for implementing this tactic is *precision crowning*. This method places a crown in the shape of an arc of a circle with a small height δ on the blade contact flat (Fig. 1(c)). The intent is to promote Hertzian-like normal contact stresses (indicated with a broken line in Fig. 3). Frictionless Hertzian contact of a cylinder on a flat has a stress concentration factor of $4/\pi$ (Hertz [7]). The dovetail attachment of Fig. 1(a) with its blend radii has a stress concentration factor of 6.3 when $\mu=0$ (see (5)). Hence provided we can approach the same contact extent with crowning as without, a marked reduction in σ_c^{\max} may be possible.

In order for contact to spread throughout most of the available contact extent (CC' of Fig. 1(a)), the height of δ of the crown must be comparable to the elastic approach (i.e., the elastic deflection of the crown center). Typically elastic approaches under Hertzian contact are too small to be manufactured. In the jet en-

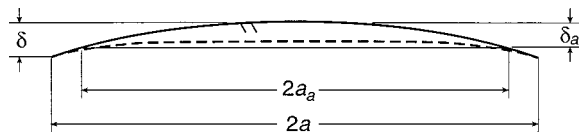


Fig. 5 Crown profiles

gine industry, however, loads are high enough relative to elastic moduli that this need not be the case, albeit some precision may be required in the manufacture.⁴

If precision crowning in the plane of Fig. 1(a) is successful in reducing σ_c^{\max} and thereby fluctuations in hoop stresses, then to be consistent a similar crowning needs to be employed in the out-of-plane direction. That is, for section BB' of Fig. 1(a) shown in Fig. 1(d). Absent crowning, this cross section can be expected to produce a double-peak, normal, contact stress similar to that of Fig. 3. Accompanying shear stresses out of the plane of Fig. 1(d) would have a similar scaled distribution and lead to large hoop stresses. With crowning, this cross section can be expected to produce a more Hertzian-like normal contact stress with correspondingly reduced shear and hoop stresses.

In what follows, therefore, we first assess the effects of in-plane precision crowning in Section 2. Thereafter, in Section 3, we assess the effects of out-of-plane precision crowning. This latter activity requires a special development in order to keep the analysis two-dimensional and thus be able to check convergence fairly readily.⁵ The paper closes in Section 4 with some remarks in light of the results found for precision crowning in both planes.⁶

2 In-Plane Precision Crowning

2.1 Crown Heights. The major concern of this analysis is when the fluctuations in hoop stresses are worst. That is, when friction is at its likely maximum ($\mu=0.4$, Hamdy and Waterhouse [3]). However, we need precision crowning to work for any level of friction if it is to be really effective. Consequently we also evaluate precision crowning for $\mu=0$ as a lower bound check.

Although the hoop stresses unload without any dramatic fluctuations for the frictionless case, it is this case which sets the *minimum crown height*. To see this, consider Fig. 5. This depicts an exaggerated crown in the form of a circular arc of central height δ spanning the maximum available contact extent $2a$ between CC' of Fig. 1(a). At the ends of this arc, the crown surface is smoothly blended into the blade (this blending is not shown in Fig. 5). Even with such blending, we want to avoid contact with this part of the blade. Otherwise we can expect a normal contact stress with large peaks at the edges of contact (cf., Fig. 3). Under load, therefore, we want the actual contact extent, $2a_a$, to be distinctly less than $2a$, say about 90% of $2a$. And we want this for the maximum normal load, and this occurs for the frictionless case. Hence this case sets δ .

More specifically, the elastic approach δ_a under load (Fig. 5) can be estimated from Hertzian formulas (see, e.g., Johnson, [10], Appendix 3). Thus

$$\delta_a = \frac{4(1-\nu^2)N}{\pi E}, \quad (10)$$

⁴For an in-plane geometry like that of Fig. 1(a), Evans [8] suggests barreling a contact flat to position the line of action of N . While such barreling profiles consist of curved arcs as do precision crowns, the heights involved are considerably larger. Pape and Neu [9] also employ a similar curved geometry, with a far larger height than that for precision crowning, in fretting test pieces.

⁵In 3D, the exacting convergence checks of (6), (7) can be expected to involve two-three orders of magnitude more degrees-of-freedom than in 2D.

⁶As an aside here, we report that we did consider a third tactic for reducing fluctuations in σ_h , namely varying α of Fig. 2. We could not find an α which resulted in any real reduction.

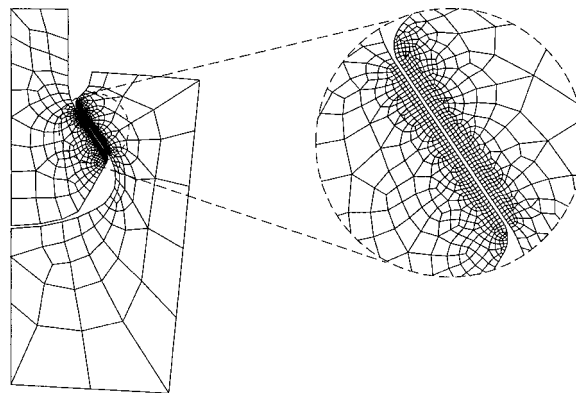


Fig. 6 Coarse finite element grid for in-plane analysis

where E is the Young's modulus and ν Poisson's ratio. These moduli are taken to be the same for both the blade and the disk. Further,

$$\frac{\delta}{\delta_a} = \left(\frac{a}{a_a}\right)^2. \quad (11)$$

From (10), (11), for the specifications given in [1], we obtain a minimum δ of $25.4 \mu\text{m}$ ($1/1000$ in) for 87% contact when $\mu=0$ and N is a maximum. That is, $a_a=0.87a$ when $\delta=25.4 \mu\text{m}$. This crown height we denote by δ_0 .

To see if precision crowning is effective within some range above the minimum δ_0 , we consider higher crown heights of $2\delta_0$ and $4\delta_0$ for $\mu=0.4$. If it is effective, this would enable precision crowning to be performed at a higher δ than δ_0 with some tolerance. To check our expectation with respect to edge-of-contact peaks in σ_c , we also consider a lower crown height of $\delta_0/2$ for $\mu=0$. After all, the estimate of the minimum δ_0 came from Hertzian formulas, and even with crowning the dovetail attachment of Fig. 1(a) is not strictly a Hertzian configuration.

Absent the crown, a precise formulation for the in-plane contact problem attending Fig. 1(a), including contact inequalities, is given in [1], Section 3.1. The only change needed for this formulation to be applicable here is the minor realignment of the s coordinate on the blade in [1] so that it now follows the crowning.

2.2 Finite Element Analysis. To police the contact inequalities in the foregoing formulation within a finite element analysis, we use the point-to-surface contact elements of ANSYS [11], CONTAC 48. There are some input parameters required to run CONTAC 48. Here we take these to be the same as in [1], Section 3.2.

Following ANSYS [11] recommendations for the analysis of contact problems, we use the CONTAC 48 elements in conjunction with ANSYS four-node quadrilateral elements, PLANE 42. The latter are arranged in a sequence of three grids to enable convergence to be checked in accordance with (6), (7). The coarse grid has relatively small elements arranged uniformly in the critical areas bordering the contact elements (Fig. 6; no crown is included in this figure, but for δ_0 it would be barely discernible anyway, even in the closeup). The remainder of this grid is meshed with elements of increasing size as they get further from the contact elements. This is done with the convenient mesh-generation command AMESH (ANSYS, [11]). Grid refinement within the uniform element region is completely systematic with element sides being successively halved to form successive grids. Grid refinement with the AMESH command follows a similar sizing pattern but is not completely systematic. Thus the number of elements only roughly quadruples with grid refinement. Table 1 gives the actual numbers of four-node quadrilateral elements used. The corresponding numbers of contact elements used are comparable.

Table 1 Summary of finite element grids

| Grid | Number of Elements | |
|--------|--------------------|-----------------------|
| | In-Plane Analysis | Out-of-Plane Analysis |
| Coarse | 915 | 800 |
| Medium | 2,604 | 3,200 |
| Fine | 8,314 | 12,800 |

2.3 Results. For maximum load and $\mu=0$, $\delta=\delta_0$, the peak, normal, contact stress is converging in the sense of (6), and converged in the sense of (7) to within $\varepsilon=0.002$ (0.2%). The resulting σ_c is actually the stress shown in Fig. 3 with a broken line. It acts over 88% of $2a$, in close agreement with the prediction from Hertz theory (87). Moreover, it is *practically indistinguishable from a Hertzian contact stress* distribution over $2a$. That is, in terms of the coordinates in Fig. 1(a), this stress is essentially given by

$$\sigma_c = \frac{2N}{\pi a_a} \sqrt{1 - \left(\frac{z}{a_a}\right)^2} \quad (12)$$

With (12), the central maximum value in terms of the original, nominal, normal, contact stress of (3) can be expressed by

$$\sigma_c^{\max} = 1.4\bar{\sigma}_c \quad (13)$$

This is more than a *factor of four lower* than σ_c^{\max} without crowning (cf., (5)). Also with (12), *bending* contributions have been completely removed.

Given the preceding close accord with Hertz theory, it is not surprising that for $\delta=\delta_0/2$ we get edge-of-contact peaks in σ_c . Hertz theory has that this happens whenever $\delta \leq 0.75 \delta_0$ (see (11)), and indeed it does. The values of the peak stresses so produced are uneven, revealing the presence of a bending contribution. While stresses for the larger of the peaks have yet to converge on the sequence of grids used here, the fine grid value is already a factor of two greater than σ_c^{\max} of (13). Further grid refinement can only be expected to increase this factor. As anticipated, then, crowning which leads to contact regions extending off the circular crown arc should be avoided.

For maximum load and $\mu=0.4$, $\delta=\delta_0$, $2\delta_0$, $4\delta_0$, the peak normal and shear contact stresses are converging in the sense of (6) and converged in the sense of (7) to within $\varepsilon=0.002$ (0.2%). The peak hoop stress is converging in the sense of (6) and converged in the sense of (7), but only to within $\varepsilon=0.04$ (4%). There is a step discontinuity in the derivative of the hoop stress at its peak which slows convergence.⁷

Even with friction present, σ_c for all crown heights at maximum load continue to closely follow *Hertzian distributions*. Thus *no bending* is present. Further, τ_c also follow Hertzian distributions (cf., (8)).

Peak values of the contact stresses at maximum load when $\mu=0.4$ are given in Table 2 for the varying crown heights. Also

Table 2 Stresses at maximum load with in-plane precision crowning ($\mu=0.4$)

| δ/δ_0 | σ_c^{\max}/σ_0 | τ_c^{\max}/σ_0 | σ_h^{\max}/σ_0 |
|-------------------|----------------------------|--------------------------|----------------------------|
| 0 | 9.0 | 3.5 | 8.0 |
| 1 | 2.3 | 0.9 | 3.0 |
| 2 | 3.2 | 1.3 | 3.7 |
| 4 | 4.5 | 1.8 | 4.0 |

⁷A similar discontinuity in σ_h is present in the solution in Poritsky [6].

Table 3 Reduction in hoop stress fluctuations with in-plane precision crowning ($\mu=0.4$)

| δ/δ_0 | $\Delta\sigma_h/\sigma_0$, 20% Unload | $\Delta\sigma_h/\sigma_0$, 40% Unload |
|-------------------|---|---|
| 0 | 13.2 | 20.7 |
| 1 | 3.0 | 4.4 |
| 2 | 3.7 | 5.9 |
| 4 | 4.4 | 7.4 |

included for comparison are corresponding values without crowning (from [1]).

Confirmation of the Hertzian nature of the normal contact stress can be obtained by comparing peak values. From Hertz theory (see, e.g., Johnson, [10], Appendix 3),

$$\sigma_c^{\max} | / \sigma_c^{\max} | = \sqrt{\delta_1 / \delta_2}, \quad (14)$$

where δ_1 is one crown height, δ_2 another. With δ doubling, therefore, the ratio of the second σ_c^{\max} to the third, as well as the ratio of the third to the fourth, should be $1/\sqrt{2}$ in Table 2. In fact, both ratios are 0.7, in good agreement with this Hertzian prediction.

With crowning, the peak shear stresses of Table 2 satisfy (8) to two figures. This is better agreement with this shear check than obtained in [1] without crowning. Presumably this is because stresses are less concentrated with crowning.

Both σ_c^{\max} and σ_h^{\max} values are significantly lowered in Table 2 by crowning. Even for a crown height of $4\delta_0$, both are *lowered by a factor of two*.

While promising, the results of Table 2 are not the critical ones. Rather it is the fluctuations in hoop stresses that attend unloading, $\Delta\sigma_h$, that are key. Table 3 presents values for $\Delta\sigma_h$ for 20 and 40% unloading for the varying crown heights. Also included for comparison are corresponding values without crowning (from the analysis for [1]). Clearly these fluctuations are markedly reduced. Even for a crown height of $4\delta_0$, reductions approach a *factor of three*. These results suggest that, here, in-plane precision crowning would be effective with crown heights in the range

$$\delta = 2\delta_0 \pm \delta_0 \quad (15)$$

Hence for the present dovetail attachment, precision crowning could be implemented with a 50% tolerance in the crown height.

3 Out-of-Plane Precision Crowning

3.1 Loading Mechanism. While the means of loading for the in-plane section of Fig. 1(a) is clear, the means of loading for the out-of-plane section of Fig. 1(d) is not so clear. Though a pressure is to be expected between the upper disk section and the lower blade section in Fig. 1(d), it is not obvious what agency produces this pressure, at least from Fig. 1(d). In Fig. 1(a), however, this agency can be discerned. Therein the dotted segment of the disk can be thought of as acting like a cantilever beam with a uniform distributed load on its under side. From beam theory, then, we have the standard result

$$p = - \frac{dV}{dz}, \quad (16)$$

wherein p is the pressure due to varying shear force, V , and z is as in Fig. 1(a). Thus the basic loading mechanism for the section of Fig. 1(d) is *shear transfer* out of the plane of this section.

To explain further, Fig. 7 shows a uniform nominal pressure p with the stress resultants it induces acting on a geometry corresponding to the dotted segment of Fig. 1(a). With these resultants as Saint-Venant end conditions, it is straightforward to construct a

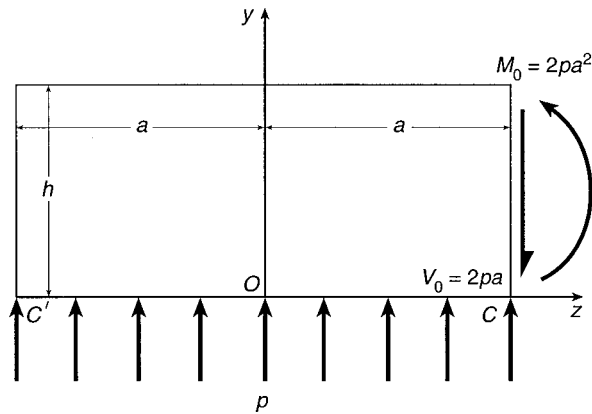


Fig. 7 Nominal pressure and stress resultants acting on a segment of the disk above contact flat

two-dimensional, elastic, stress field which reflects shear load transfer. The approach for this construction is described in Timoshenko and Goodier [12], Chap. 3. Thus

$$\sigma_z = p \frac{h-2y}{10h^3} [30(z+a)^2 + 3h^2 - 5(h-2y)^2], \quad (17)$$

$$\sigma_y = -p \frac{h+2y}{h^3} (h-y)^2, \quad \tau_{yz} = -6p \frac{h-y}{h^3} y(z+a),$$

with all other stress components being zero, where h is the height of the segment (Fig. 7), and y and z are as in Fig. 1(a). This stress field complies with the stress equations of equilibrium and compatibility and the boundary conditions indicated in Fig. 7 on $y=0, h$, as well as reproducing the stress resultants indicated in Fig. 7 on $z=\pm a$. That this is so may be verified directly by substitution. Away from the ends $z=\pm a$, as at the central section BB' , we can expect the stresses in (17) to be physically representative of the stresses attending shear transfer.

Associated displacements for the stress field of (17) are those in the y and z directions, v and w , respectively. These are both functions of y and z alone (i.e., independent of x of Fig. 1(d)).

Complementary fields are active within the blade section of Fig. 1(a). Together these fields produce a nominal contact pressure p for the section in Fig. 1(d).

3.2 Plane Strain With Simulated Shear Transfer. The expectation for the central section BB' of Fig. 1(a) shown in Fig. 1(d) is that fields do not vary appreciably in the out-of-plane direction of Fig. 1(d). That is, in terms of the coordinates in Fig. 1, $\partial/\partial z$ is a null operator in Fig. 1(d). This is the essential condition for a state of plane strain in the xy -plane. Accordingly we look to use a plane strain analysis for the section in Fig. 1(d).

In the xy -plane, a *plane-strain state* has that the only displacements are those in the x and y directions, u and v , respectively. Furthermore, these displacements are functions of x and y alone. Then the existing companion stress components are $\sigma_x, \sigma_y, \tau_{xy}$, and σ_z . These stresses satisfy the following field equations: the stress equations of equilibrium,

$$\begin{aligned} \sigma_{x,x} + \tau_{xy,y} + F_x &= 0, \\ \sigma_{y,y} + \tau_{xy,x} + F_y &= 0, \end{aligned} \quad (18)$$

where coordinates preceded by a comma denote partial differentiation with respect to that coordinate and F_x, F_y are body-force components; and the stress equations of compatibility,

$$\nabla^2(\sigma_x + \sigma_y) = 0, \quad \sigma_z = \nu(\sigma_x + \sigma_y), \quad (19)$$

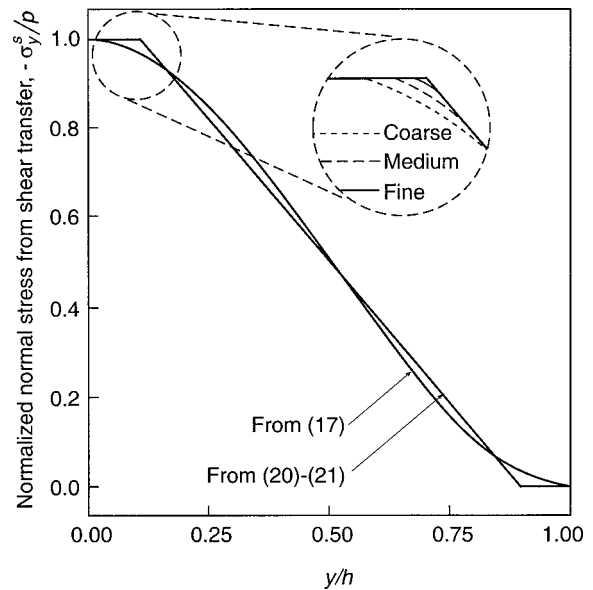


Fig. 8 Comparison of normal stress with shear load transfer and simulating body force

where ∇^2 is the Laplacian operator in x, y -coordinates.

To proceed with a plane-strain analysis of the section in Fig. 1(d), we need to provide loading. This loading comes from shear transfer and fields like that of (17). Clearly these are *not plane-strain* fields in the xy -plane. Actually they are plane stress fields in the yz -plane.

To introduce the effects of (17) in a way which is compatible with plane strain in the xy -plane, we *simulate the shear transfer* with a *body force*, F_y . We take F_y to be as simple as possible which yet produces a distribution similar to σ_y of (17). We also set Poisson's ratio $\nu=0$ so that the only displacement attending this F_y and σ_y is v , and this v is a function of y alone. Then these three elements in the simulation are admissible contributors to a plane-strain state in the xy -plane.

Specifically the fields we take for simulating shear transfer are thus as follows, distinguished by a superscript s . For $0 \leq y/h \leq 1/10$,

$$\sigma_y^s = -p, \quad F_y = 0, \quad v^s = -\frac{py}{E}; \quad (20)$$

for $1/10 \leq y/h \leq 9/10$,

$$\sigma_y^s = \frac{p}{8h} (10y-9h), \quad F_y = -\frac{5p}{4h}, \quad (21)$$

$$v^s = \frac{p}{160Eh} (100y^2 - 180yh + h^2);$$

for $9/10 \leq y/h \leq 1$,

$$\sigma_y^s = 0, \quad F_y = 0, \quad v^s = -\frac{ph}{2E}; \quad (22)$$

with all other stresses and displacements being zero. Corresponding fields act in the blade section ($-1 \leq y/h \leq 0$) with F_y replaced by $-F_y$. In (20)–(22) and these corresponding fields, h is now taken so that the cross section these fields apply to spans BB' of Fig. 1.

Figure 8 presents a comparison of σ_y^s with σ_y of (17). Typically the two agree to within 2% of p . The maximum discrepancy between the two is 3.5%. This sort of agreement is judged to be sufficient for the proof-of-concept analyses being undertaken here.

In combination then we have the plane-strain stresses for the cross section in Fig. 1(d) determined via finite element analysis together with the simulated shear transfer stress. That is, on distinguishing the former by the superscript f ,

$$\sigma_x = \sigma_x^f, \quad \sigma_y = \sigma_y^f + \sigma_y^s, \quad \tau_{xy} = \tau_{xy}^f, \quad (23)$$

with $F_x = 0$, F_y as in (20)–(22) times signum (y), and $\nu = 0$. These stresses satisfy (18), (19) with $\sigma_z = 0$ because $\nu = 0$ rather than its actual value. We do not expect, though, that setting $\nu = 0$ effects the in-plane stresses significantly: This is something we check with finite element analysis. In fact, with F_y prescribed to be as in (20)–(22) times signum (y), the finite element analysis also calculates σ_y^s . This is also something we check and see how well finite elements do this.

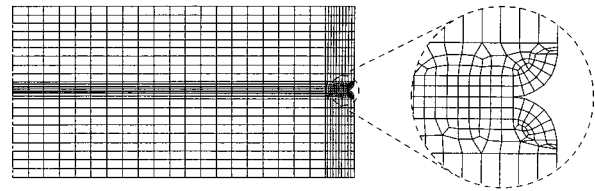
3.3 Crown Heights. For the analysis of the cross section in Fig. 1(d) with and without crowning, we restrict attention to the frictionless case $\mu = 0$. This is because when $\mu \neq 0$ a shear stress is induced which acts out of the plane of Fig. 1(d), and therefore cannot be captured with a plane-strain analysis. However, as in Section 2.1, $\mu = 0$ is the critical case when sizing crown heights if one is to prevent contact expanding out to the blending at the ends of crowns.

The basic crown profile continues to be as show schematically in Fig. 5. That is, a circular arc blended into the blade at its ends (this blending not being shown in Fig. 5). Now, though, crown heights need to be considerably larger if contact is not to expand off the circular arc. This is because of *bending* contributions to the *deformation*. These contributions are not accounted for in (10), (11), and consequently these equations cannot be used to size crown heights. Instead an actual effective value of crown height can be found using finite element analysis. Such analysis leads to a baseline, out-of-plane, crown height, δ'_0 , of 5 mm (1/5 in). This results in contact over 81% of $C''C'''$ at maximum load.

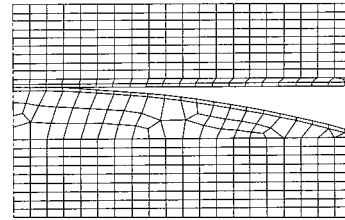
This baseline crown height is sizable within the confines of dovetail attachments in jet engines. To provide a smaller, out-of-plane, crown height, we introduce a flat on the central portion of the crown profile which then smoothly blends into two outer circular arcs with a common radius (indicated by the broken line in Fig. 5). In a first analysis, we take the extent of the flat to be a , or half of the available contact region. This greatly reduces bending contributions so that the crown height is reduced to $\delta'_0/4$ (again, though, this is something that needs to be checked with finite element analysis).

With or without either crown profile, the symmetry of the section in Fig. 1(d) enables analysis to be confined to $x \geq 0$. Without crowning, the stress analysis problem for the section in Fig. 1(d) can then be stated as follows. Throughout this half section we seek the plane-strain stresses σ_x , σ_y , τ_{xy} satisfying: the stress equations of equilibrium (18) with $F_x = 0$, F_y as in (20)–(22) when $y \geq 0$, and an equal and opposing F_y when $y \leq 0$; the stress equation of compatibility, (19) with $\nu = 0$; frictionless contact conditions, which match normal stresses and displacements while setting shears to zero, on $y = 0$ between $x = 0$ and C''' ; symmetry conditions on $x = 0$ for $-h \leq y \leq h$; stress-free conditions on the remainder of the boundary of this half-section; and contact inequalities, which prohibit tensile contact stresses within the contact region and overlapping of displacements without.

The stress-free conditions in the preceding are not really appropriate on the bottom of the blade (i.e., at $y = -h$). This is because this “edge” is actually still inside the blade, being at B in Fig. 1(a). We do not expect the choice of boundary conditions at this location to be that significant, however. This is because the body force in the blade is yet to start acting when $y = -h$. As a check on this expectation, we also enforce symmetry conditions on this edge. Symmetry conditions are also not really appropriate here.



(a)



(b)

Fig. 9 Coarse finite element grids for out-of-plane analysis: (a) without crown, (b) with circular crown

They are, though, perhaps more appropriate than stress-free conditions because they would be correct if the section BB' intersected the centerline at $\pi/2$ instead of $\sim \pi/4$.

The foregoing formulation can be perturbed to accommodate either of the crown profiles considered simply by altering the blade surface at $y = 0$ to conform to these profiles. With these perturbations, the blade occupies a region wherein $-h \leq y \leq \delta$ while the disk now occupies a region wherein $\delta \leq y \leq \delta + h$, where δ is either δ'_0 or $\delta'_0/4$ depending on the profile.

3.4 Finite Element Analysis. As previously, we use the point-to-surface contact elements of ANSYS, [11], CONTACT 48, in conjunction with ANSYS four-node quadrilateral elements, PLANE 42. The latter are arranged in sequences of grids to enable convergence to be checked via (6), (7).

For the original cross section, high stresses are expected near the outer blend radii (cf., the original in-plane section). To try and capture these stresses, the coarse grid for this cross section has relatively small elements near its blend radius (Fig. 9(a)). The coarse grids with crowning are not expected to need this type of refinement and thus are more uniform in their element sizes (e.g., Fig. 9(b) for δ'_0). Both types of grid have a completely uniform arrangement of elements throughout most of their vertical extents away from the contact surfaces to facilitate the introduction of the body force simulating shear transfer. As a result, grid refinement is systematic (to the nearest 100 of elements). The actual numbers of four-node quadrilateral elements used are included in Table 1 for the original cross section (i.e., for a grid sequence with coarse grid as in Fig. 9(a)). Fewer quadrilateral elements are used for the crowned profiles (about 40% less), but grid refinement remains systematic. The numbers of contact elements used are comparable to the numbers of quadrilateral elements for respective grids.

In addition to the foregoing grids, we run the three grids for the original cross section with the blend radius removed. Then, with perfect alignment of the disk and blade edges, the stress field produced reduces to simply σ_y^s of (20)–(22). This checks the ability of our finite element analysis to calculate σ_y^s .

For the coarse grids of Fig. 9, we run our finite element analysis with Poisson's ratio equal to 0.0 and 0.3. This checks the effects on stresses of making the simplification $\nu = 0$. We also run these

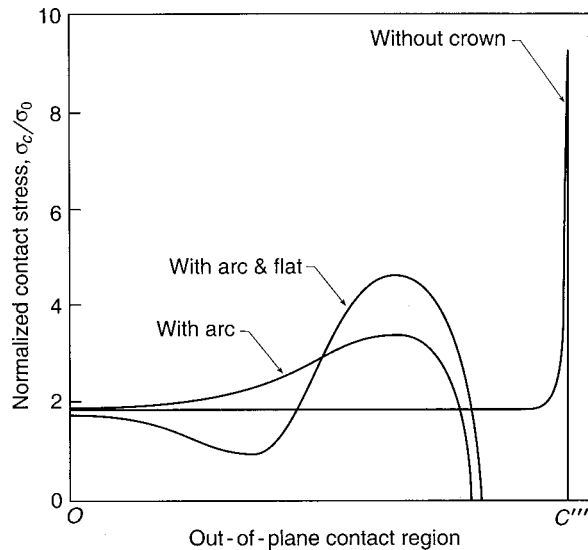


Fig. 10 Out-of-plane contact stress distributions ($\mu=0$)

grids with stress-free and symmetry conditions on their lower edges. This checks the effects of boundary condition choice.

3.5 Results. For our first check on the finite element calculation of σ_y^s of (20)–(22), we find results from all three grids lie on top of the analytical result except near the two discontinuities at $y/h=1/10, 9/10$. These results are converging in the sense of (6) as indicated in the closeup in Fig. 8. They have converged in the sense of (7) to within $\varepsilon=0.008$ provided $|\sigma_c^F|$ on the right-hand side of (7) is replaced by p (to avoid dividing by zero when estimating ε for $y/h=9/10$). That is, finite element results for σ_y^s have converged to within 0.8% of p , an excellent level of accuracy for present purposes.

For our check on the effects of Poisson's ratio, we find results for σ_c with $\nu=0, 0.3$ to be close (within 5%). This is not unexpected. Peak contact stresses in Hertzian contact differ by only 5% when ν varies from 0 to 0.3 (see, e.g., Johnson, [10], Appendix 3).

For our check on boundary condition choice, we find no differences in the contact stress with stress-free or symmetry conditions on the lower edge of the original cross section of Fig. 1(d). With crowning, though, stresses are about 8% higher with the symmetry condition. This is because it restrains bending deformation. Henceforth, therefore, we only report crowning results with *symmetry conditions*, thereby minimizing any reductions in σ_c afforded by crowning.

At maximum load, results for the contact stress for the original cross section are shown in Fig. 10. These stresses are for the fine grid. The peak stresses for this cross section are not converging in the sense of (6) on the grid sequence used. Further grid refinement can only be expected to increase the peak contact stress for this cross section.

At maximum load, results for the contact stress for the circular crown of height δ'_0 are included in Fig. 10. These are for the fine grid. The peak stresses for this crown are converging in the sense of (6), and have converged in the sense of (7) to within $\varepsilon=0.005$. Peak values of σ_c with this crown are a *factor of 2.7 less* than the low estimate of peak σ_c for the original cross section.

At maximum load, results for the contact stress for the crown with a flat and a height of $\delta'_0/2$ are also included in Fig. 10. These are from only a medium grid because of its close agreement with coarse grid results (e.g., peak stresses differ by less than 1.5%). Peak values of σ_c with this crown are still a *factor of two less* than the low estimate of peak σ_c for the original cross section.

The reductions in σ_c attending either crown profile can be expected to reduce the τ_c out of the plane of Fig. 1(d) induced during loading up. Hence these profiles can be expected to reduce σ_h of Fig. 1(b), and thus fluctuations in the hoop stress at the edges of contact.

4 Concluding Remarks

In dovetail attachments, *fluctuations in hoop stresses* at the edges of contact can occur. A pinching mechanism can amplify these changes in hoop stresses over those in loading. As a result, fluctuations in hoop stresses can be more than an order of magnitude greater than variations in loading. Moreover, these fluctuations include hoop stresses which are tensile at maximum load and compressive at reduced load. Such fluctuating hoop stresses can be expected to be a major contributor to fatigue failure in dovetail attachments. The principal objective of the work described here is to offer a method of alleviating these fluctuations.

The peak hoop stresses at maximum load largely result from the shear contact stresses. These stresses in turn are directly proportional to the normal contact stresses. Thus reducing the normal contact stresses at maximum load should reduce the hoop stresses that can fluctuate. This is the tactic adopted here, with *crowning* being chosen as the method for reducing contact stresses.

Crowns in both *in-plane* (Fig. 1(a)) and *out-of-plane* (Fig. 1(d)) directions are analyzed via finite elements. The finite element analysis employs point-to-surface contact elements to ensure convergent edge-of-contact stresses. For the in-plane configuration, a state of plane strain applies keeping analysis two-dimensional. For the out-of-plane configuration, plane strain is not strictly applicable. However, by simulating shear load transfer with body forces, it can be approximately treated as such. While it seems likely that this approach yields physically reasonable stresses, ultimately this is something that needs to be checked with a full three-dimensional analysis. Given confirmation, plane strain with simulated shear transfer then furnishes stress analysts with a means of keeping analysis two-dimensional in dovetail attachments, with consequent reductions in computational effort.

Results from crowning in both directions indicate that *significant reductions* in hoop stress fluctuations can be achieved via this means. For the in-plane direction, crown heights are small. Hence some precision is expected to be required in their manufacture. Nonetheless, even with crown heights varying by $\pm 50\%$, hoop stress fluctuations can be reduced by a factor of three. For the out-of-plane direction, quite a range of crown profiles is available which can reduce hoop stresses by a further factor of two. All told, then, crowning shows some promise of alleviating hoop stress fluctuations in dovetail attachments.

Acknowledgments

We are pleased to acknowledge the benefit of technical discussions with engineers at General Electric Aircraft Engines (GEAE). We are also grateful for the financial support of this work by GEAE.

References

- [1] Sinclair, G. B., Cormier, N. G., Griffin, J. H., and Meda, G., 2002, "Contact Stresses in Dovetail Attachments: Finite Element Modeling," *ASME J. Eng. Gas Turbines Power*, **124**, pp. 182–189.
- [2] Sinclair, G. B., and Cormier, N. G., 2002, "Contact Stresses in Dovetail Attachments: Physical Modeling," *ASME J. Eng. Gas Turbines Power*, **124**, pp. 325–331.
- [3] Hamdy, M. M., and Waterhouse, R. B., 1981, "The Fretting Wear of Ti-6Al-4V and Aged Inconel 718 at Elevated Temperatures," *Wear*, **71**, pp. 237–248.
- [4] Sinclair, G. B., 1998, "FEA of Singular Elasticity Problems," *Proceedings of the Eighth International ANSYS Conference*, ANSYS Inc., Canonsburg, PA, **1**, pp. 225–236.
- [5] Cormier, N. G., Smallwood, B. S., Sinclair, G. B., and Meda, G., 1999, "Aggressive Submodelling of Stress Concentrations," *Int. J. Numer. Methods Eng.*, **46**, pp. 889–909.
- [6] Poritsky, H., 1950, "Stresses and Deflections of Cylindrical Bodies in Contact

- With Application to Contact of Gears and Locomotive Wheels," ASME J. Appl. Mech., **17**, pp. 191–201.
- [7] Hertz, H., 1882, "On the Contact of Elastic Solids," *Journal für die reine und angewandte Mathematik*, **92**, pp. 156–171 (in German; for an account in English, see Johnson, [10], Chap. 4).
- [8] Evans, N. M., 1992, "Attachment of a Gas Turbine Engine Blade to a Turbine Rotor Disc," Patent No. 5, 110, 262, U.S. Patent Office.
- [9] Pape, J. A., and Neu, R. W., 1999, "Influence of Contact Configuration in Fretting Fatigue Testing," *Wear*, **225–229**, pp. 1205–1214.
- [10] Johnson, K. L., 1985, *Contact Mechanics*, Cambridge University Press, Cambridge, UK.
- [11] ANSYS personnel, 1995, *ANSYS User's Manual*, Revision 5.2, I, ANSYS Inc., Canonsburg, PA.
- [12] Timoshenko, S. P., and Goodier, J. N., 1970, *Theory of Elasticity*, 3rd Ed., McGraw-Hill, New York.

Computation of the Optimal Normal Load of a Friction Damper Under Different Types of Excitation

D. Cha
A. Sinha

Department of Mechanical Engineering,
The Pennsylvania State University,
University Park, PA 16802

In this paper, forced responses of a frictionally damped turbine blade are investigated for three different types of excitation: white noise excitation, narrowband random excitation, and deterministic sinusoidal excitation. To determine the steady-state nonlinear response, the harmonic balance method is used for sinusoidal excitation, and the equivalent linearization method is used for white noise and narrowband random excitations. Using a new set of nondimensionalized variables, the optimal value of normal load of a friction damper is found to be almost independent of the nature of excitation. The effectiveness of the damper in reducing the vibration level is also examined for the aforementioned three different types of excitation. [DOI: 10.1115/1.1584474]

1 Introduction

The fatigue failure of turbine blades can be caused by excessive resonant stresses. In order to reduce the resonant amplitude of a turbine blade, friction dampers are used in practice. In many situations, a friction damper can be designed as a blade-to-ground (B-G) damper which is composed of a linear spring and a Coulomb friction element, as shown in Fig. 1, [1]. The B-G damper provides slip between points experiencing relative motion and dissipate the system energy. The single-degree-of-freedom model used for the investigation, shown in Fig. 2, represents the fundamental mode of a blade with B-G friction damper.

Many researchers have worked on the calculation of the optimal normal load of a friction damper. While the harmonic balance method (HBM) is widely used for sinusoidal excitation, [1–5], the equivalent linearization method (ELM) is commonly used for the white noise excitation to investigate the steady-state nonlinear response, [6–8]. It has been reported that turbine blades can experience random loads, [9–11]. However, the system responses to random and deterministic excitations are different in nature. Hence the optimal normal load obtained for one type of external force may not work effectively for other types of excitation.

In this paper, three different types of excitation are considered: white noise excitation, narrowband random excitation, and sinusoidal excitation. Using a new set of nondimensionalized variables, the performance of the friction damper is plotted under different loading conditions. The resulting curves of responses with these variables are independent of the intensity of external force and are not sensitive to the change in the frequency band of excitation. Therefore, the optimal value of normal load can be easily obtained irrespective of the excitation characteristics. It is noted that this approach can be easily applicable in the actual situation, because instead of the measurements of external forces, only the experimental data of response when the friction damper is fully stuck are required.

First, the ELM and HBM are briefly described. Then, the analytical results from ELM only are compared with those from time

integration because the accuracy of HBM has been established in the literature. Lastly, the nondimensionalized variables are used to obtain the optimal value of normal load.

2 Formulation

Let m , k , and c be the mass, stiffness, and damping coefficient, respectively. The governing differential equation of motion for the system shown in Fig. 2 can be written as follows:

$$m\ddot{x} + c\dot{x} + kx + f_G = F(t) \quad (1)$$

where f_G is the hysteretic force of the friction damper and can be defined as follows:

- (i) when friction damper is stuck: $K_G|x - d_G| \leq \mu_f F_N$

$$f_G = K_G(x - d_G) \quad (2a)$$

- (ii) when friction damper is slipping: $K_G|x - d_G| = \mu_f F_N$

$$f_G = \mu_f F_N \text{sign}(\dot{d}_G) \quad (2b)$$

where d_G , K_G , μ_f , and F_N represent the displacement, the stiffness, the friction coefficient and normal load of friction damper, respectively. For such systems, analytical calculation of the response depends on the characteristic of external force, $F(t)$.

Case I: White Noise Excitation. If the external force, $F(t)$, is assumed as an ergodic and Gaussian white noise, $w(t)$, with zero mean, the equivalent linearization method (ELM) can be used to obtain the statistics of response. The autocorrelation of the external force is given as follows:

$$R_w(\tau) = E[w(t)w(t + \tau)] = Q_0 \delta(\tau) \quad (3)$$

where Q_0 is the intensity, $\delta(\tau)$ is the dirac-delta function, and $E[\cdot]$ is the expected value.

The nonlinear force of the friction damper can also be described, [6], as

$$\begin{aligned} f_G(\dot{x}, y_G; x_c, K_G) = & K_G y_G [U(y_G + x_c) - U(y_G - x_c)] \\ & + K_G x_c [U(y_G - x_c)U(\dot{x}) \\ & - U(-y_G - x_c)U(-\dot{x})] \end{aligned} \quad (4)$$

where

Contributed by the International Gas Turbine Institute (IGTI) of THE AMERICAN SOCIETY OF MECHANICAL ENGINEERS for publication in the ASME JOURNAL OF ENGINEERING FOR GAS TURBINES AND POWER. Paper presented at the International Gas Turbine and Aeroengine Congress and Exhibition, Indianapolis, IN, June 7–10, 1999; ASME Paper 99-GT-413. Manuscript received by IGTI, Oct. 1998; final revision received by the ASME Headquarters, Mar. 1999. Associate Editor: D. Wisler.

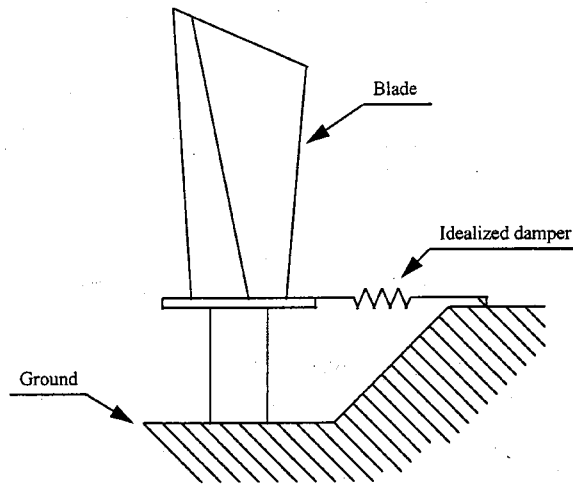


Fig. 1 A blade-to-ground damper

$$\dot{y}_G = h_G(\dot{x}, y_G; x_c) = \dot{x}[U(y_G + x_c) - U(y_G - x_c) + U(y_G - x_c)U(-\dot{x}) + U(-y_G - x_c)U(\dot{x})] \quad (5a)$$

$$y_G = x - d_G \quad (5b)$$

$$x_c = \frac{\mu_f F_N}{K_G} \quad (5c)$$

Note that $U(\cdot)$ is the unit step function. Using ELM, the equations of motion, Eq. (1) and Eq. (5a), can be expressed as

$$m_t \ddot{x} + c\dot{x} + kx + c_G^x \dot{x} + k_G^x y_G = w(t) \quad (6a)$$

$$\dot{y}_G = c_G^y \dot{x} + k_G^y y_G \quad (6b)$$

where

$$c_G^x = E \left[\frac{\partial f_G}{\partial \dot{x}} \right], \quad (7a)$$

$$k_G^y = E \left[\frac{\partial f_G}{\partial y_G} \right] \quad (7b)$$

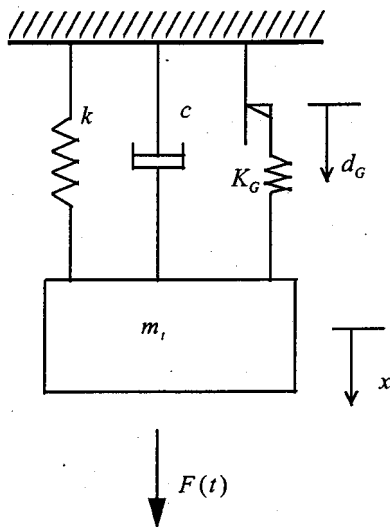


Fig. 2 Equivalent single-degree-of-freedom system

$$c_G^y = E \left[\frac{\partial h_G}{\partial \dot{x}} \right], \quad (7c)$$

$$k_G^y = E \left[\frac{\partial h_G}{\partial y_G} \right]. \quad (7d)$$

These coefficients are evaluated by assuming a joint Gaussian probability distribution of the multidimensional response process and presented in the Appendix A.

Introducing the state variables, $z(t)$, the Eq. (6a) and (6b) can be written as

$$\dot{z} = Az + Bw(t) \quad (8)$$

where

$$z^T = [x \quad \dot{x} \quad y_G]^T \quad (9a)$$

$$A = \begin{bmatrix} 0 & 1 & 0 \\ \frac{-k}{m_t} & \frac{-(c+c_G^x)}{m_t} & \frac{-k_G^x}{m_t} \\ 0 & c_G^y & k_G^y \end{bmatrix}, \quad (9b)$$

$$B = \begin{bmatrix} 0 \\ \frac{1}{m_t} \\ 0 \end{bmatrix}. \quad (9c)$$

Since $E[w(t)] = 0$, it has been shown that $E[z(t)] = 0$. Let P be the correlation matrix of state variables: i.e.,

$$P = E[z(t)z(t)^T]. \quad (10)$$

Then the correlation matrix, P , satisfies the following algebraic equation under steady-state conditions.

$$AP + PA^T = B_R \quad (11)$$

where

$$B_R = -BQ_0B^T. \quad (12)$$

Note that the variance of the blade's displacement, R_x , is obtained from the correlation matrix of the system response P : i.e.,

$$R_x = \sigma_x^2 = (P)_{1,1}. \quad (13)$$

Because the linearized coefficients, c_G^x , k_G^x , c_G^y , and k_G^y , are functions of $E[\dot{x}^2]$, $E[y_G^2]$, and $E[\dot{x}y_G]$, which are the elements of correlation matrix P , Eq. (11) is solved numerically to evaluate the correlation matrix P , [7].

Case II: Narrowband Excitation. If the external excitation, $F(t)$, is assumed as a narrow band excitation, $g(t)$, which can be generated by passing the white noise excitation, $w(t)$, through the bandpass filter: i.e.,

$$\ddot{g} + 2\xi_F\omega_F\dot{g} + \omega_F^2g = \omega_F^2w(t) \quad (14)$$

where ξ_F and ω_F are damping ratio and natural frequency of the bandpass filter, respectively. Using ELM, the governing differential equation, Eq. (1) and Eq. (5a), are given by

$$m_t \ddot{x} + c\dot{x} + kx + c_G^x \dot{x} + k_G^x y_G = g(t) \quad (15a)$$

$$\dot{y}_G = c_G^y \dot{x} + k_G^y y_G. \quad (15b)$$

If the state vector is selected as

$$z^T = [g \quad \dot{g} \quad x \quad \dot{x} \quad y_G]^T, \quad (16)$$

then Eqs. (14), (15a), and (15b) can be represented in the state-space form as

$$\dot{z} = Az + Bw(t) \quad (17)$$

where

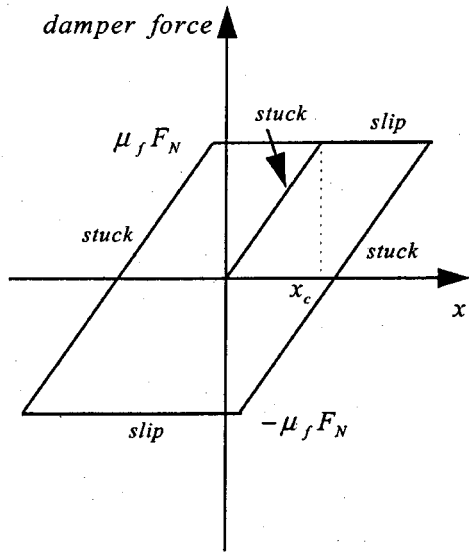


Fig. 3 Hysteretic characteristic of a friction damper (sinusoidal response)

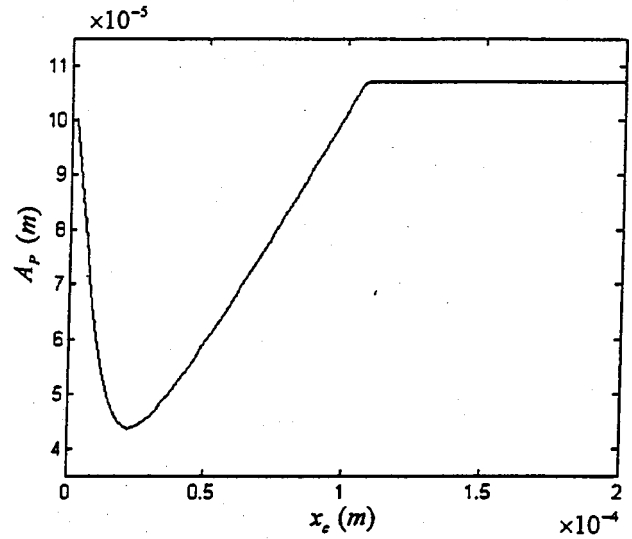


Fig. 4 A_p as a function of x_c (sinusoidal excitation)

$$A = \begin{bmatrix} 0 & 1 & 0 & 0 & 0 \\ -\omega_F^2 & -2\xi_F\omega_F & 0 & 0 & 0 \\ 0 & 0 & 0 & 1 & 0 \\ \frac{1}{m_t} & 0 & \frac{-k}{m_t} & \frac{-(c+c_G^x)}{m_t} & \frac{-k_G^x}{m_t} \\ 0 & 0 & 0 & c_G^y & k_G^y \end{bmatrix} \quad (18a)$$

$$B = [0 \ \omega_F^2 \ 0 \ 0 \ 0]^T \quad (18b)$$

Therefore, Eq. (11) can be used again to calculate the correlation matrix P .

Case III: Deterministic Sinusoidal Excitation. When the external force is assumed to correspond to a particular engine order excitation,

$$F(t) = f_0 \cos(\omega t), \quad (19)$$

and the harmonic balance method (HBM) is used for the analysis of system response. It is assumed that the steady-state response is almost sinusoidal: i.e.,

$$x(t) = A_x \cos(\omega t + \phi). \quad (20)$$

Then, in steady state, the damper force will be periodic with the fundamental frequency same as ω . The resulting nonlinear force-displacement relationship of a friction damper is shown in Fig. 3. The displacement of the friction damper, d_G , is expanded in a Fourier series and only the terms with the fundamental frequency are considered, [1,12]. Therefore the nonlinear force of the friction damper can be represented as

$$f_G = K_G(x - d_G) = K_G(a_d \cos(\omega t + \phi) + b_d \sin(\omega t + \phi)) \quad (21)$$

where

$$a_d = A_x(\theta_c - 0.5 \sin(2\theta_c))/\pi \quad (22a)$$

$$b_d = -A_x \sin^2(\theta_c)/\pi \quad (22b)$$

$$\theta_c = \cos^{-1}(1 - 2x_c/A_x). \quad (22c)$$

It should be noted that $a_d = A_x$ and $b_d = 0$ when there is no slip at the friction damper: i.e., $A_x \leq x_c$ where the slip distance x_c is defined by Eq. (5c). Analytically, the peak response of the blade,

A_p , and the resonant frequency, ω_p , can be obtained, [1]. The numerical procedure is presented in Appendix B. The HBM is frequently used for the analysis of response to sinusoidal excitation and its accuracy has been proved in previous papers, [1,4,12]. The peak response of the blade, A_p , is plotted in Fig. 4 as a function of x_c when the amplitude of the sinusoidal excitation, f_0 , is chosen to be 1 N.

3 Accuracy of Equivalent Linearization Method (ELM)

The computational efficiency of ELM makes it an attractive approach to find the response of a nonlinear system. However, its accuracy depends on the system characteristics because the ELM is an approximation to replace nonlinear terms by linear ones which minimize the error between them, [13]. Therefore, the analytical results by ELM are compared with those from the numerical integration of the differential Eq. (1). The nominal values of modal parameters are given in Table 1 and are representative of a high pressure turbine stage, [14]. The analytical results are obtained by solving Eq. (11) iteratively with the MATLAB routine "lyap," [15]. For the time integration, the MATLAB routine "randn" is used to generate the Gaussian white noise excitation. It yields random numbers which have Gaussian distribution with zero mean and specified standard deviation. The time response is generated at 30,000 instants with the time interval equal to 5×10^{-5} sec. The external excitation, $w(t)$, is assumed to be constant during the time interval to facilitate the numerical integration of differential equation.

For the white noise excitation, the intensity of external force, Q_0 , is taken to be $1 N^2$ and the variance of displacement of blade, R_x , is shown in Fig. 5 as a function of the slip distance, x_c . The optimal value of x_c is close to 0.46×10^{-3} m. These results obtained analytically from Eq. (11) are compared with results from the numerical integration of differential equation. Three different values of slip distance, $x_c = 0.1 \times 10^{-3}$, 0.46×10^{-3} , and 2.98×10^{-3} m, are chosen and the results are presented in Table 2. The responses at 30,000 discrete times are divided into six batches of 5000 successive data where each batch is considered as a result of

Table 1 System parameters

| | | | |
|--------------------|------------------|--------------------|--------------------|
| $m_t = 0.0114$ kg, | $c = 1.45$ Ns/m, | $k = 430,000$ N/m, | $K_G = 43,000$ N/m |
|--------------------|------------------|--------------------|--------------------|

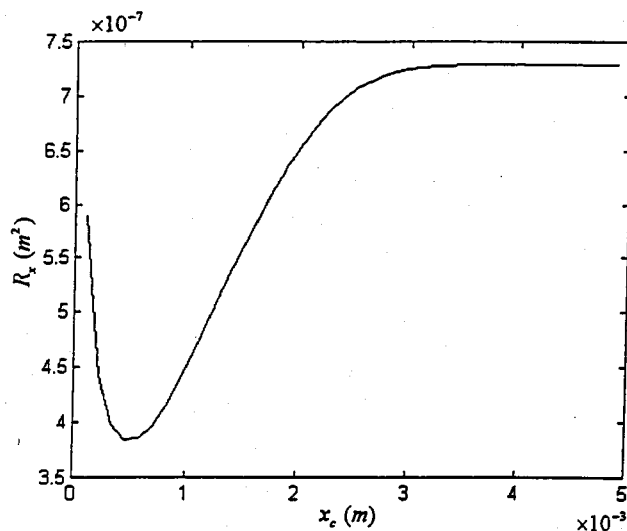


Fig. 5 R_x as a function of x_c (white noise excitation)

an independent simulation, [16]. Therefore, the value of R_x has been computed for each of six batches separately. It is found that R_x of each batch fluctuates around the analytical result. However, the average value of six batches compares well with the analytical result.

The bandpass filter is used to generate narrow band excitation with ξ_F equal to 0.01, Eq. (14). The bandpass filter amplifies the white noise excitation at frequencies which are close to the resonant frequency of the filter ω_F . Therefore, the exciting force to the bladed disk system has the dominant frequency band near the resonant frequency of the filter ω_F . In the Fig. 6(a), R_x for the narrow band excitation is plotted as a function of x_c and ω_F . Because the bandpass filter amplifies the white noise excitation, $w(t)$, near the resonant frequency of the filter, ω_F , the actual force on blade, $g(t)$, can be increased by as much as the quality factor of the bandpass filter, Q_f , which can be defined as

$$Q_f = \frac{1}{2\xi_F}. \quad (23)$$

Therefore, the intensity of external white noise excitation, Q_0 , is chosen to be 10^{-4} N^2 . From analytical results, shown in Fig. 6(a),

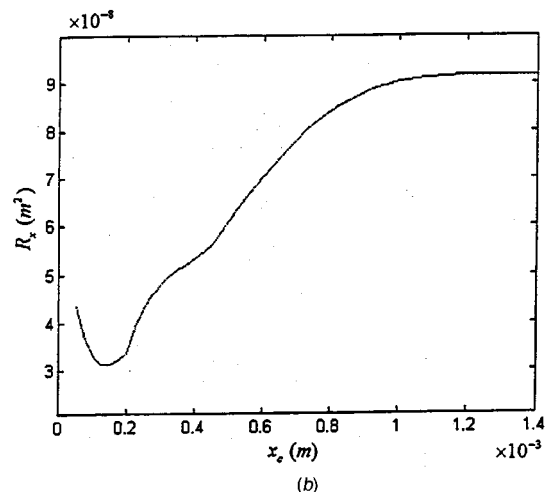
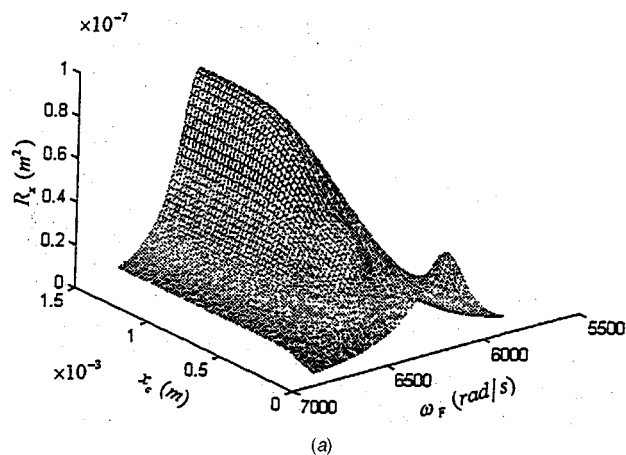


Fig. 6 (a) R_x as a function of x_c and ω_F (narrowband excitation); (b) peak value of R_x as a function of x_c (narrowband excitation)

five different points are selected to compare with the results from time integration. The results are presented in Table 3. The average values obtained using all 30,000 data are reasonably close to analytical results, however, the values of six batches show large fluctuation and the errors are increased compared to the results for

Table 2 The response correlation, R_x , for white noise excitation (units: $\times 10^{-7} \text{ m}^2$) (optimal $x_c = 0.00046 \text{ m}$)

| Batch number | 1 | 2 | 3 | 4 | 5 | 6 | Average | ELM |
|---------------------------|-------|-------|-------|-------|-------|-------|---------|-------|
| $x_c = 0.0001 \text{ m}$ | 7.154 | 5.951 | 5.273 | 6.474 | 4.001 | 4.802 | 5.609 | 5.894 |
| $x_c = 0.00046 \text{ m}$ | 4.195 | 3.526 | 3.286 | 4.203 | 2.857 | 2.855 | 3.487 | 3.837 |
| $x_c = 0.00298 \text{ m}$ | 6.628 | 7.177 | 8.373 | 8.484 | 8.246 | 7.387 | 7.716 | 7.247 |

Table 3 The response correlation, R_x , for narrow band excitation (units: $\times 10^{-8} \text{ m}^2$) (optimal $x_c = 0.00015 \text{ m}$)

| Batch number | 1 | 2 | 3 | 4 | 5 | 6 | Average | ELM |
|---------------------------------|-------|-------|-------|-------|-------|-------|---------|-------|
| $x_c = 0.00005 \text{ m}$ | 5.815 | 4.279 | 3.793 | 6.080 | 3.011 | 3.036 | 4.336 | 4.332 |
| $\omega_F = 6170 \text{ rad/s}$ | | | | | | | | |
| $x_c = 0.00015 \text{ m}$ | 2.919 | 2.740 | 2.783 | 3.210 | 1.792 | 1.548 | 2.499 | 3.131 |
| $\omega_F = 6270 \text{ rad/s}$ | | | | | | | | |
| $x_c = 0.0003 \text{ m}$ | 3.501 | 4.119 | 4.330 | 4.645 | 5.041 | 4.225 | 4.310 | 4.802 |
| $\omega_F = 6450 \text{ rad/s}$ | | | | | | | | |
| $x_c = 0.0006 \text{ m}$ | 6.327 | 7.622 | 9.550 | 8.700 | 10.02 | 8.565 | 8.465 | 7.030 |
| $\omega_F = 6420 \text{ rad/s}$ | | | | | | | | |
| $x_c = 0.000975 \text{ m}$ | 6.945 | 8.158 | 13.78 | 9.658 | 13.31 | 9.286 | 10.99 | 8.988 |
| $\omega_F = 6440 \text{ rad/s}$ | | | | | | | | |

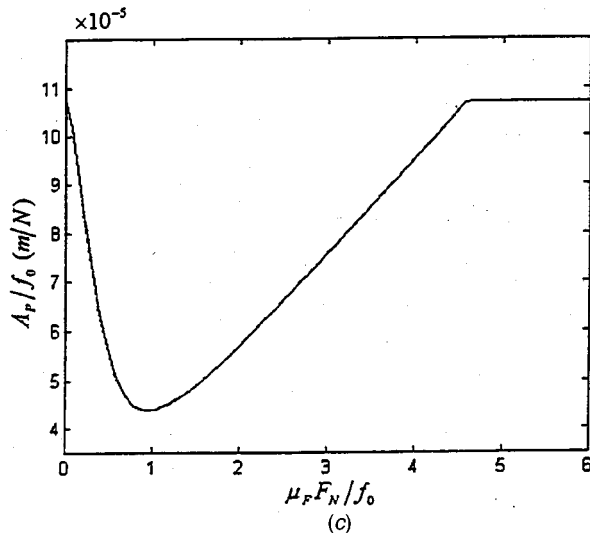
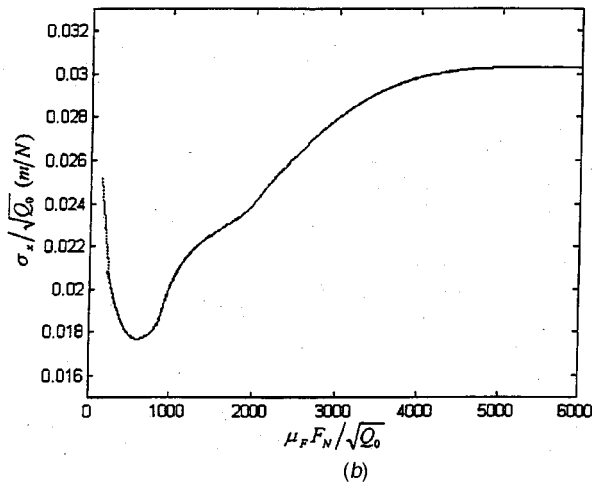
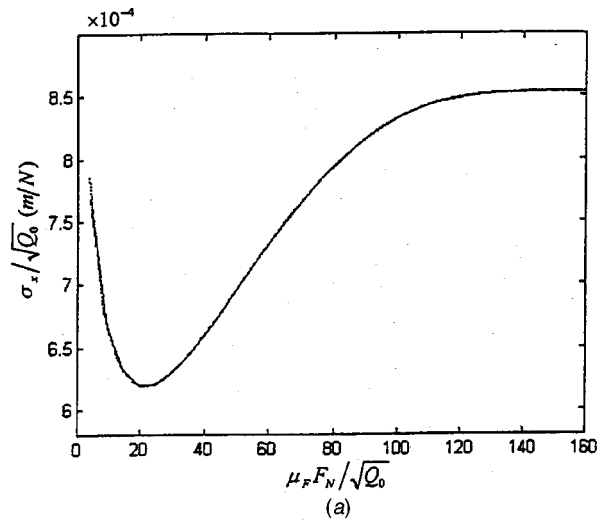


Fig. 7 (a) $\sigma_x/\sqrt{Q_0}$ as a function of $\mu_f F_N/\sqrt{Q_0}$ (W.N.); (b) peak value of $\sigma_x/\sqrt{Q_0}$ as a function of $\mu_f F_N/\sqrt{Q_0}$ (N.B.); (c) A_p/f_0 as a function of $\mu_f F_N/f_0$ (S.)

white noise excitation. To study the effect of the normal load only, the peak values of R_x in Fig. 6(a) are estimated for many different values of x_c , and are plotted in Fig. 6(b) as a function of x_c . It shows a trend similar to the results for white noise excitation, Fig. 5. The optimal value of x_c is close to 0.15×10^{-3} m, and corre-

sponding ω_F is 6270 rad/s. It should be noted again that the normal load, F_N , is proportional to the slip distance x_c , Eq. (5c).

In comparison with the results from time integration, Tables 2 and 3, the results from ELM are greater than those from numerical simulation when x_c is around that for the minimum value of R_x . It implies that the ELM seems to be underestimating the effect of damper when normal load is close to its optimal value. When x_c is increased, the R_x from ELM is smaller than that from the time integration; i.e., the ELM overestimates the effect of friction damper when the normal load is much greater than the optimal value. However, the ELM is shown to be well suited in the study of normal load optimization because the trend of analytical results are fairly close to that of simulation results. The error of ELM near the minimum value of R_x for the narrowband excitation is greater than that for white noise. Furthermore, the maximum errors are approximately 10% and 25% for white noise and narrowband excitation, respectively.

4 Optimization of the Normal Load

The optimal value of the normal load, which minimizes the response of the system, depends on the intensity and the type of external force. Therefore, the optimum normal load can be determined easily if the external force is known. However, in the actual situation, the intensity and frequency band of external force are not known.

First, the normalized variables, $\sigma_x/\sqrt{Q_0}$ and $\mu_f F_N/\sqrt{Q_0}$ for random excitation and A_p/f_0 and $\mu_f F_N/f_0$ for sinusoidal excitation, are used to eliminate the effect of intensity of external force. Note that Q_0 is the intensity of white noise and f_0 is the amplitude of sinusoidal forcing function. Three different levels of external forces are selected for each type of excitation. The intensity, Q_0 , are selected as 1, 5 and 10 N^2 for white noise excitation and 10^{-5} , 5×10^{-5} , and 10^{-4} N^2 for narrow band excitation. The amplitudes of sinusoidal excitation are chosen as 1, 5 and 10 N. In Fig. 7, the resulting curves are independent of the level of external force. They can be referred to as system performance curves to determine the optimum normal load when the type of external force is only known. However, the optimum value of normalized slip load is considerably different with each type of external force.

Next, the nondimensionalized variables, σ_x/σ_{st} and x_c/σ_{st} for random excitation and $\text{rms}(x_p)/\text{rms}(x_{st})$ and $x_c/\text{rms}(x_{st})$ for sinusoidal excitation, are used to determine the optimum normal load. The definition of each new variable is given as follows:

(i) random excitation:

$$\sigma_{st}^2 = E[x_{st}^2] \quad (24a)$$

x_{st} = response when the friction damper is fully stuck

In the case of narrow band excitation, ω_F is chosen such that σ_{st} is maximum.

$$(24b)$$

(ii) sinusoidal excitation:

$$\text{rms}(\cdot) = \text{root mean square value} \quad (25a)$$

$$x_p(t) = A_p \cos(\omega_p t + \phi_p) \quad (25b)$$

$$x_{st}(t) = A_{st} \cos(\omega_{st} t + \phi_{st}) \quad (25c)$$

$$A_p = \text{peak amplitude at a given normal load} \quad (25d)$$

$$A_{st} = \text{resonant amplitude when the friction damper is fully stuck} \quad (25e)$$

It should be noted that the standard deviation and the rms value are mathematically equivalent when the mean value is equal to zero. Therefore, the nondimensionalized variables are similar in nature for both the random and sinusoidal excitations.

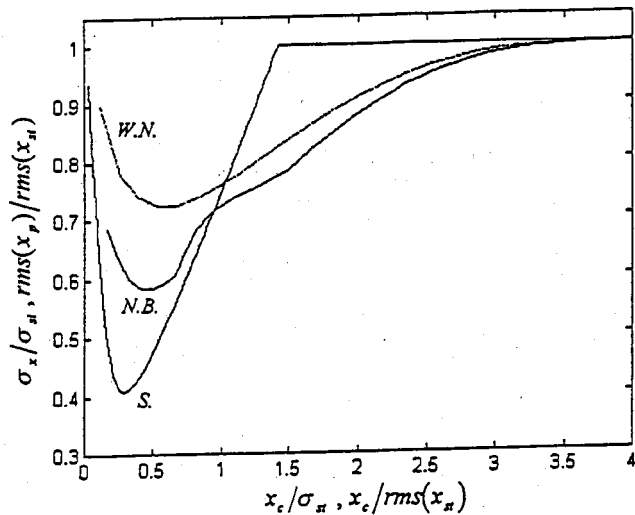


Fig. 8 σ_x/σ_{st} versus x_c/σ_{st} for white noise excitation, peak value of σ_x/σ_{st} versus x_c/σ_{st} for narrow band excitation, $rms(x_p)/rms(x_{st})$ versus $x_c/rms(x_{st})$ for sinusoidal excitation ($K_G=43,000$ N/m)

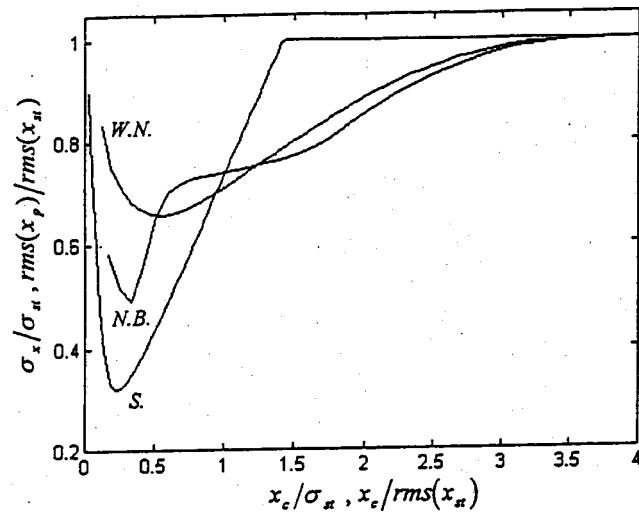


Fig. 9 σ_x/σ_{st} versus x_c/σ_{st} for white noise excitation, peak value of σ_x/σ_{st} versus x_c/σ_{st} for narrow band excitation, $rms(x_p)/rms(x_{st})$ versus $x_c/rms(x_{st})$ for sinusoidal excitation, ($K_G=64,500$ N/m)

In Fig. 8, the resulting curves show similar scales. It is also seen that the system performance with x_c/σ_{st} or $x_c/rms(x_{st})$ equal to 0.5 is fairly good for any types of excitation. Hence, the near-optimal normal load can be calculated as

$$F_N^* = \alpha_{xc} \frac{K_G \sigma_{st}}{\mu_f} \quad \text{or} \quad \alpha_{xc} \frac{K_G rms(x_{st})}{\mu_f} \quad (26)$$

where $\alpha_{xc} = 0.5$.

When the stiffness of friction damper, K_G , is increased to 64,500 N/m, the near-optimal value of α_{xc} can be chosen as 0.42 which provides good performance for any types of excitation, as shown in Fig. 9. The minimum value of σ_x/σ_{st} and those with the near-optimal values of x_c/σ_{st} are represented in Table 4. These results indicate that the near-optimum normal load can be determined by the factor α_{xc} which is independent of the intensity and frequency band of excitation. Since σ_{st} can be measured experi-

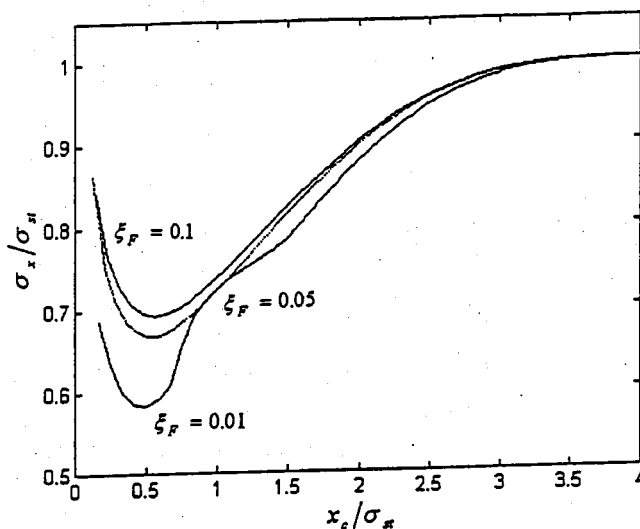


Fig. 10 Peak value of σ_x/σ_{st} versus x_c/σ_{st} ($\xi_F=0.01, 0.05$, and 0.1)

Table 4 The performance of friction damper

| K_G | Excitation | Minimum Value | | Near-Optimal Value | |
|--------------|-------------|-------------------|------------------------|--------------------|------------------------|
| | | x_c/σ_{st} | σ_x/σ_{st} | x_c/σ_{st} | σ_x/σ_{st} |
| 43,000 (N/m) | white noise | 0.5388 | 0.7256 | 0.5 | 0.7295 |
| | narrowband | 0.4953 | 0.5843 | | 0.5848 |
| | periodic | 0.2906 | 0.4094 | | 0.4749 |
| 64,500 (N/m) | white noise | 0.5509 | 0.6584 | 0.42 | 0.6663 |
| | narrowband | 0.3362 | 0.4930 | | 0.5596 |
| | periodic | 0.2431 | 0.3216 | | 0.3910 |

mentally, the normal load obtained by Eq. (26) will yield near-optimal performance regardless of the external force characteristics.

It is found that the friction damper becomes less effective with increase of frequency band of external force and more effective with increase of friction damper stiffness, K_G , Table 4, Fig. 8 and 9. The effect of frequency band of narrow band excitation is shown in Fig. 10 when $\xi_F=0.01, 0.05$, and 0.1. With the increase of ξ_F , the bandwidth of excitation increases and resulting curves approach the curve of white noise excitation.

5 Conclusions

A new set of nondimensionalized variables, σ_x/σ_{st} and x_c/σ_{st} or $rms(x_p)/rms(x_{st})$ and $x_c/rms(x_{st})$, is used to compare the performance of a friction damper under three different types of excitation: white noise excitation, narrowband random excitation, and deterministic sinusoidal excitation. The resulting curves of responses with these nondimensionalized variables are independent of the level of external force and the optimal value of x_c/σ_{st} or $x_c/rms(x_{st})$, α_{xc} , is not sensitive to the bandwidth of excitation. If σ_{st} or $rms(x_{st})$ is measured experimentally, the optimal normal load can be obtained based on the optimal value of α_{xc} , without any information about the external force. The performance of blade-to-blade (B-B) and B-G dampers in a multi-degree-of-freedom model of a rotor stage is currently being examined.

Nomenclature

- A = system matrix in the state-space analysis
- A_p = peak amplitude of sinusoidal response
- A_x = amplitude of sinusoidal response

B = input matrix in the state-space analysis
 B_R = input matrix of Lyapunov equation
 c = damping coefficient
 c_G^x, k_G^x ,
 c_G^y, k_G^y = equivalent linear coefficients of damper
 d_G = displacement of damper
 $E[\]$ = expected value
 $F(t)$ = external force vector
 F_N = normal load of friction damper
 f_G = hysteretic force of damper
 f_0 = amplitude of sinusoidal excitation
 $g(t)$ = narrowband excitation
 K_G = stiffness of damper
 k = modal stiffness of blade
 m_t = modal mass of blade
 P = correlation matrix of state variables
 Q_0 = intensity of white noise excitation
 Q_f = quality factor of the bandpass filter
 $R_w(\tau)$ = correlation matrix of white noise excitation
 $R_x(\tau)$ = correlation matrix of blade displacement
 $U(\cdot)$ = unit step function
 $w(t)$ = white noise excitation
 x_c = slip distance of damper
 x_i = displacement of i th blade
 x_p = sinusoidal response with peak amplitude at a given normal load
 x_{st} = response of a blade when the friction damper is fully stuck, defined in Eq. (24b)
 y_G = relative displacement of damper
 z = state variables
 α_{xc} = defined in Eq. (26)
 σ_{st} = standard deviation of x_{st} , defined in Eq. (24a)
 σ_x = standard deviation of blade displacement
 μ_f = friction coefficient
 ξ_F = damping ratio of bandpass filter
 ω_F = resonant frequency of bandpass filter

Appendix A

Expressions for Equivalent Linear Coefficients c_G^x , k_G^x , c_G^y , and k_G^y . Assuming a joint Gaussian probability distribution of the multidimensional response process, the equivalent linear coefficients are obtained as follows, [6]:

$$c_G^x = \frac{K_G x_c}{\sigma_x \sqrt{2\pi}} \operatorname{erfc}\left(\frac{x_c}{\sigma_{y_G} \sqrt{2(1-\rho_G^2)}}\right) \quad (A1)$$

$$k_G^x = K_G \operatorname{erf}\left(\frac{x_c}{\sigma_{y_G} \sqrt{2}}\right) - \frac{K_G x_c}{\sigma_{y_G} \sqrt{2\pi}} \exp\left(\frac{-x_c^2}{2\sigma_{y_G}^2}\right) \operatorname{erfc}\left(\frac{\rho_G x_c}{\sigma_{y_G} \sqrt{2(1-\rho_G^2)}}\right) \quad (A2)$$

$$c_G^y = \frac{1}{2} \left[1 + \operatorname{erf}\left(\frac{x_c}{\sigma_{y_G} \sqrt{2}}\right) \right] - \frac{1}{\sqrt{\pi}} \int_{x_c/\sigma_{y_G} \sqrt{2}}^{\infty} e^{-v^2} \operatorname{erf}\left(\frac{\rho_G v}{\sqrt{1-\rho_G^2}}\right) dv \quad (A3)$$

$$k_G^y = \frac{-\rho_G x_c \sigma_x}{\sigma_{y_G}^2 \sqrt{2\pi}} \exp\left(\frac{-x_c^2}{2\sigma_{y_G}^2}\right) \left[1 + \operatorname{erf}\left(\frac{\rho_G x_c}{\sigma_{y_G} \sqrt{2(1-\rho_G^2)}}\right) \right] - \frac{\sigma_x \sqrt{1-\rho_G^2}}{\sigma_{y_G} \pi} \exp\left(\frac{-x_c^2}{2(1-\rho_G^2)\sigma_{y_G}^2}\right) \quad (A4)$$

where

$$\sigma_x^2 = E[\dot{x}^2], \quad (A5a)$$

$$\sigma_{y_G}^2 = E[y_G^2] \quad (A5b)$$

$$\rho_G = \frac{E[\dot{x}y_G]}{\sigma_x \sigma_{y_G}}. \quad (A5c)$$

The coefficient c_G^y requires a numerical integration. However, it can be approximated for small values of ρ_G as

$$c_G^y = \frac{1}{2} \left[1 + \operatorname{erf}\left(\frac{x_c}{\sigma_{y_G} \sqrt{2}}\right) \right] - \frac{1}{\sqrt{\pi}} \frac{\rho_G}{\sqrt{1-\rho_G^2}} \exp\left(\frac{-x_c^2}{2\sigma_{y_G}^2}\right). \quad (A6)$$

Appendix B

Calculation of A_p and ω_p for Sinusoidal Excitation. The peak response of the blade, A_p , and the corresponding frequency, ω_p , can be obtained by the algorithm available in the literature, [1,4].

1 Define nondimensional parameters as

$$\varepsilon_d = \frac{K_G}{k + K_G}, \quad (B1)$$

$$f_d = \frac{f_0}{K_G x_c} \quad (B2)$$

$$\xi_d = \frac{c}{2\sqrt{m(k + K_G)}}. \quad (B3)$$

2 The nondimensional peak response, A_m , and the corresponding frequency, ω_m , are obtained by solving the following nonlinear algebraic equations:

$$A_m = \Gamma + \sqrt{\Gamma + \frac{2\varepsilon_d}{\pi \xi_d \omega_m}} \quad (B4)$$

$$\omega_m = \sqrt{1 - \frac{\varepsilon_d}{\pi} (\pi - \theta_d + 0.5 \sin(2\theta_d))} \quad (B5)$$

$$\Gamma = \frac{\varepsilon_d (f_d - 4/\pi)}{4 \xi_d \omega_m} \quad (B6)$$

$$\theta_d = \cos^{-1}\left(1 - \frac{2}{A_m}\right). \quad (B7)$$

It should be noted that the allowable ranges for the parameters are $A_m \geq 1$ and $(1 - \varepsilon_d) \leq \omega_m \leq 1$.

3 The peak response of the blade, A_p , and the corresponding frequency, ω_p , are calculated as

$$A_p = A_m x_c, \quad (B8)$$

$$\omega_p = \omega_m \sqrt{\frac{k + K_G}{m}}. \quad (B9)$$

References

- [1] Griffin, J. H., 1980, "Friction Damping of Resonant Stresses in Gas Turbine Engine Airfoils," ASME J. Eng. Gas Turbines Power, **102**, pp. 329–333.
- [2] Srinivasan, A. V., and Cutts, D. G., 1983, "Dry Friction Damping Mechanisms in Engine Blades," ASME J. Eng. Gas Turbines Power, **105**, pp. 332–341.
- [3] Menq, C.-H., Griffin, J. H., and Bielak, J., 1986, "The Influence of a Variable Normal Load on the Forced Vibration of a Frictionally Damped Structure," ASME J. Eng. Gas Turbines Power, **108**, pp. 300–305.
- [4] Cameron, T. M., Griffin, J. H., Kielb, R. E., and Hoosac, T. M., 1990, "An Integrated Approach for Friction Damper Design," ASME J. Vib. Acoust., **112**, pp. 175–182.
- [5] Sanliturk, K. Y., Imregun, M., and Ewins, D. J., 1997, "Harmonic Balance Vibration Analysis of Turbine Blades With Friction Dampers," ASME J. Vib. Acoust., **119**, pp. 96–103.
- [6] Asano, K., and Iwan, W. D., 1984, "An Alternative Approach to the Random Response of Bilinear Hysteretic Systems," J. Earthquake Eng. Struct. Dyn., **12**, pp. 229–236.
- [7] Sinha, A., 1990, "Friction Damping of Random Vibration in Gas Turbine

- Engine Airfoils," *International Journal of Turbo and Jet Engines*, **7**, pp. 95–102.
- [8] Roberts, J. B., and Spanos, P. D., 1990, *Random Vibration and Statistical Linearization*, Chichester: John Wiley and Sons, Chichester.
- [9] Whitehead, D. S., 1960, "The Analysis of Blade Vibration due to Random Excitation," *Reports and Memoranda R & M 3253*, Cambridge University, Cambridge, UK.
- [10] Sogliero, G., and Srinivasan, A. V., 1980, "Fatigue Life Estimates of Mistuned Blades via a Stochastic Approach," *AIAA J.*, **18**(83), pp. 318–323.
- [11] Minkiewicz, G., and Russler, P., 1997, "Dynamic Response of Low Aspect Ratio Blades in a Two Stage Transonic Compressor," *AIAA Paper No. 97-3284*.
- [12] Chen, S., and Sinha, A., 1990, "Probabilistic Method to Compute the Optimal Slip Load for a Mistuned Bladed Disk Assembly With Friction Dampers," *ASME J. Vibr. Acoust.*, **112**, pp. 214–221.
- [13] Socha, L., and Soong, T. T., 1991, "Linearization in Analysis of Nonlinear Stochastic Systems," *Appl. Mech. Rev.*, **44**, pp. 399–422.
- [14] Griffin, J. H., and Sinha, A., 1985, "The Interaction Between Mistuning and Friction in the Forced Response of Bladed Disk Assemblies," *ASME J. Eng. Gas Turbines Power*, **107**, pp. 205–211.
- [15] *MATLAB Manual*, 1995, The MathWorks, Inc.
- [16] Deo, N., 1980, *System Simulation With Digital Computer*, Prentice-Hall, Englewood Cliffs, NJ, pp. 153–154.

Engine Torque Nonuniformity Evaluation Using Instantaneous Crankshaft Speed Signal

N. Cavina
F. Ponti

DIEM—University of Bologna,
Viale Risorgimento 2,
40136 Bologna, Italy

The paper presents the development of a methodology for evaluating the torque nonuniformity between the various cylinders of an internal combustion engine (ICE). This nonuniformity can be due, for example, to pathological operating conditions such as misfires or misfuels, as well as to other abnormal operating conditions. Between the nominal torque production and the one corresponding to the absence of combustion there exist, in fact, a series of possible intermediate conditions. Each of them corresponds to a value of produced torque that lies between the nominal value and the one corresponding to the lack of combustion (due for example to statistical dispersion in manufacturing or aging in the injection system). The diagnosis of this type of nonuniformity is a very important issue in today's engine control strategies design. The use of the developed methodology should in fact allow the control strategy to adopt the appropriate interventions if the diagnosed nonuniformity is related to different behavior of the injectors. In order to evaluate this torque production variability between the various cylinders, information hidden in the instantaneous crankshaft speed fluctuations has been processed using a suitable methodology. The procedure has been validated running a supercharged 2.0 liters V6 engine, and a 1.2 liters L4 engine, in a test cell. During the tests, the in-cylinder pressure signal has been acquired together with the instantaneous engine speed, in order to determine a correlation between speed fluctuations and the indicated torque produced by each cylinder. The actual cylinder-by-cylinder torque nonuniformity can then be evaluated on-board by processing engine speed. The procedure is able to diagnose the absence of combustion (due for example to a misfire or a misfuel) as well as abnormal combustions that do not necessarily involve lack of combustion, with the accuracy needed for on-board use. Control interventions to injection and ignition time commands of one or more cylinders should, in most cases, be able to re-establish torque production uniformity.

[DOI: 10.1115/1.1581892]

Introduction

The great interest of industry and research centers on the crankshaft instantaneous speed analysis for the misfire detection and torque estimation in internal combustion engines is due to the positive results obtained using different approaches based on this signal, [1–7].

A simple misfire diagnosis methodology developed by Bosch research, [2–4], is based on the evaluation of the time periods spent by the crankshaft to perform the rotation of a pre-defined angular sector, related to the combustion phase of each cylinder.

Knowledge of the combustion periods allows evaluating the crankshaft kinetic energy variation caused by each combustion by means of the following expression presented in [3]:

$$LU_i = \frac{\tau_{i+1} - \tau_i}{\tau_i^3} \quad (1)$$

where τ_i and τ_{i+1} are the time periods relative to two consecutive combustions. LU_i can be evaluated for each combustion; it contains information on the instantaneous crankshaft kinetic energy variations caused by abnormal combustions, such as misfires and other sources of torque production nonuniformity, or by gear shifts, cutoff.

The extension of these algorithms to engines with a high number of cylinders is a challenging application, due to the higher

uniformity that the engine torque production shows when the number of combustions within an engine cycle increases.

On the other hand, the information hidden in the engine speed fluctuation signal has been used in order to perform engine torque estimation, as demonstrated by previous studies, [8–11]. These algorithms usually require fast fourier transform (FFT) computation and are time-consuming. Their use on-board a vehicle is still limited by the capability of the engine control unit (ECU).

There exist, therefore, two main approaches for the evaluation of the torque, or the lack of it, using the instantaneous engine speed information: the first focusing on diagnostic purposes, the second one on control. This second approach is usually able to give also diagnostic information, but is more complex and involves algorithms that require high computing power.

This paper investigates if and how it is possible to obtain information useful for engine management and control even using a rough and simple approach based on engine speed analysis, a methodology normally used only for diagnostic purposes.

The algorithm has been tested on an L4 and a V6 engine in a test cell. It showed a good capability to diagnose the presence of accidental misfires even for the 6-cylinder engine. Furthermore, it has been demonstrated that it is possible to enlighten the presence of torque production nonuniformity (due for example to aging of the injectors) between the different cylinders for the L4 engine. This could allow, for example, the adoption of control interventions on injection and ignition time commands of one or more cylinders, in order to reestablish the torque production uniformity (due, for example, to aging of the injectors).

Other control applications could arise from the capability of detecting and quantifying the presence of torque nonuniformity. For example, the cycle reference information could be indirectly

Contributed by the Internal Combustion Engine Division of THE AMERICAN SOCIETY OF MECHANICAL ENGINEERS for publication in the ASME JOURNAL OF ENGINEERING FOR GAS TURBINES AND POWER. Manuscript received by the ICE Division, Oct. 2001; final revision received by the ASME Headquarters, Dec. 2002. Associate Editor: D. Assanis.

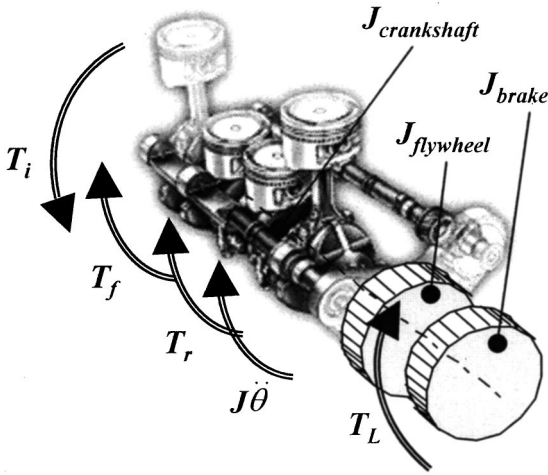


Fig. 1 Engine-brake dynamic model

obtained, for a sequential phased injection system, without using a magnetic pickup facing the camshaft. In fact, the instantaneous crankshaft position is usually measured by placing a magnetic pickup in front of a gear wheel connected to the crankshaft. One (or more) teeth of the wheel are usually missing to provide a reference position within the crankshaft revolution. Another pickup is normally placed in front of the camshaft, to differentiate one revolution to the other (within the same engine cycle), [12]. By using a torque nonuniformity detection algorithm it is possible to cause an abnormal injection and determine when the given cylinder is affected by the abnormal torque production. The crankshaft angular distance between the instant in which the abnormal injection is caused, and the instant in which the abnormal torque production is revealed gives the information regarding the actual cycle reference of the engine. In this way, the reference signal coming from a magnetic pickup facing the camshaft is no longer needed, and the cost of the sensor can be saved.

Effects of Engine Torque Production on Instantaneous Engine Speed

To evaluate the effects of the torques acting on the crankshaft over the instantaneous engine speed, a suitable model of the interactions between engine and vehicle dynamics is needed. The development of such a model has been carried out considering the engine connected to an eddy current brake, since this was the layout of the experimental tests. The results that have been obtained may be extended to on-board applications: In this case the vehicle equivalent inertia and the transmission line elasticity have to be taken into account.

Figure 1 depicts the engine-brake model considered in this study: T_i represents the overall indicated torque, T_r the overall reciprocating torque, T_f the friction torque, including in this term also the torque absorbed by the auxiliaries (oil pump, cooling system, . . .), and T_L the load torque. Newton's second law requires that

$$J\ddot{\theta} = T_i(\theta) - T_r(\theta) - T_L(\theta) - T_f(\theta) \quad (2)$$

where

$$J = J_{\text{crankshaft}} + J_{\text{flywheel}} + J_{\text{brake}}$$

and

$$T_i(\theta) = A_p r \sum_{m=1}^Z p_m(\theta) f(\theta).$$

In Eq. (2), the term J is assumed constant, since it models only the effect of the rotating inertias. The torque contribution due to

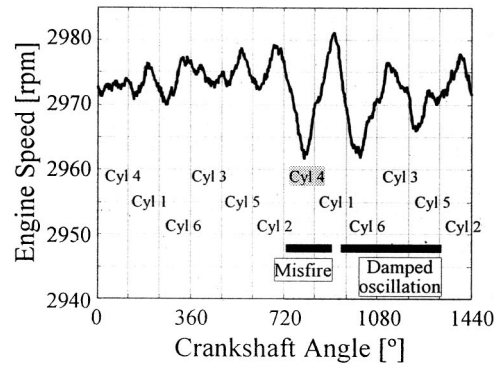


Fig. 2 Engine speed waveform for an accidental misfire in cylinder 4 of a V6 engine running in a test cell at 3000 rpm

the crank-slider mechanism angle-dependent inertia, [13,14], is taken into account by introducing the reciprocating torque $T_r(\theta)$, following a well-known approach, [11,14]:

$$T_r(\theta) = \sum_{m=1}^Z M_{eq} r^2 f(\theta) \left[f(\theta) \ddot{\theta} + \frac{df(\theta)}{d\theta} \dot{\theta}^2 \right]$$

where Z is the number of cylinders, and M_{eq} is the equivalent mass of the sliding part of the crank-slider mechanism, [11,14].

The approach presented considers the crankshaft as a unique inertia, thus neglecting its elasticity and damping. A more complex model, involving two inertias, could be designed in order to take into account also the elasticity and the damping of the crankshaft. The higher complexity of this model, anyway, is not compatible with the development of a simple algorithm for misfire and torque production nonuniformity detection. For this reason the simple single-inertia model will be used for the development of this work. The considerations that can be made using this simpler model will require some adjustments in order to take into account also the effects of the shaft elasticity on the instantaneous engine speed fluctuations, as it will be mentioned in the following.

Misfire Diagnosis and Torque Production Nonuniformity Evaluation

The presence of an accidental misfire in one cylinder will result in a lack of torque acting on the crankshaft, thus influencing the engine speed waveform. In particular, the instantaneous engine speed will show a characteristic behavior during the engine cycle portion in which the misfire occurs: The expansion stroke of the misfiring cylinder. A torsional damped vibration will follow due to the torque impulse on the crankshaft caused by the misfire.

Figure 2 shows the speed waveform for two engine cycles during which a misfire occurs in cylinder number 4 of a 2-liter V6 engine, where the effects of the misfire can be clearly seen.

In order to evaluate the effects of the misfire on the instantaneous engine speed, Eq. (2) has been considered. The attention has been focused on the speed trend during the expansion stroke of the various cylinders. When a lack of combustion takes place, the engine speed will decrease. Integrating Eq. (2) over the expansion stroke of each cylinder shows this effect.

Since the expansion strokes of engines with more than four cylinders overlap, for this kind of engines the integration is limited to a portion of the expansion stroke of each cylinder (for a 6-cylinder engine this portion will be 120 deg wide).

The integration yields:

$$\frac{1}{\Delta\theta} \int_0^{\Delta\theta} J \ddot{\theta} d\theta = \frac{1}{\Delta\theta} \int_0^{\Delta\theta} (T_i(\theta) - T_f(\theta) - T_r(\theta) - T_L(\theta)) d\theta$$

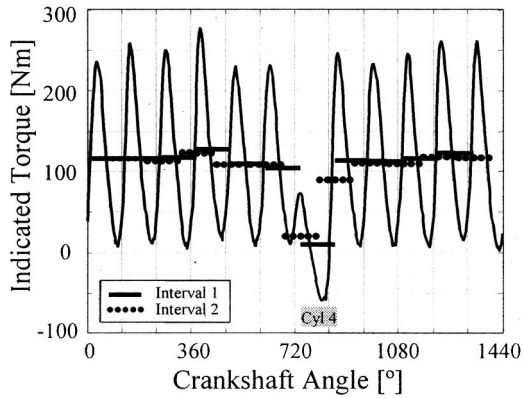


Fig. 3 Indicated torque mean value evaluation over different integration intervals for a V6 engine with cylinder 4 misfiring at the beginning of the second engine cycle

$$\frac{1}{\Delta\theta} \int_0^T J \ddot{\theta} dt = \overline{T_i(\theta)} - \overline{T_f(\theta)} - \overline{T_r(\theta)} - \overline{T_L(\theta)} \quad (3)$$

$$\frac{J[\dot{\theta}^2]_0^T}{2\Delta\theta} \cong \overline{T_i(\theta)} - \overline{T_f(\theta)} - \overline{T_L(\theta)}$$

where the mean values of the acting torques over the engine cycle portion taken into account are considered ($\overline{T_r} \cong 0$ over the portion of the expansion stroke considered), [11,13].

If the engine is running at steady-state operating conditions for a nonmisfiring cylinder, the corresponding value of the misfire detection parameter defined as

$$MD_i = -\frac{J[\dot{\theta}^2]_0^T}{2\Delta\theta} = \frac{J}{2\Delta\theta} [\dot{\theta}^2(0) - \dot{\theta}^2(T)] \quad (4)$$

will be approximately equal to zero, while for a misfiring cylinder it will assume positive values, since $\overline{T_i(\theta)}$ is negligible with respect to $-(\overline{T_f(\theta)} + \overline{T_L(\theta)})$ under such conditions.

The difference between the MD values for misfiring and nonmisfiring cylinders is therefore related to the lack of indicated torque in the misfiring cylinder. In order to maximize this difference (i.e., to optimize the signal-to-noise ratio for misfire detection) a proper placement of the integration interval for MD evaluation has to be done.

Figure 3 reports the indicated torque mean values over engine cycle portions of amplitude $4\pi/Z$ for a 6-cylinder engine. Two different intervals have been chosen: the first one centered on the expansion stroke of each cylinder (Interval 1), the second one starting 30 deg before and ending 90 deg after the top dead center (TDC) of each cylinder (see Fig. 4).

The difference between the indicated torque mean values of the misfiring cylinder and of the other cylinders is maximized choosing Interval 1.

On the other hand, it has to be noticed that in Fig. 3 the effects of the torsional vibrations following the misfire event are not considered. These torsional vibrations modify the situation described in Fig. 3, adding an oscillating torque component acting on the crankshaft after the misfire occurrence. The mean torque over each interval will be then different from those reported in Fig. 3. The effects of the oscillating torque are expected to be less relevant on the mean torque during Interval 2, since in this case the torque is evaluated at the beginning of the expansion stroke of the misfiring cylinder, and the torsional vibration is not yet completely excited.

This consideration is made clearer by looking at the values of the engine speed to be used to evaluate MD over Intervals 1 and 2.

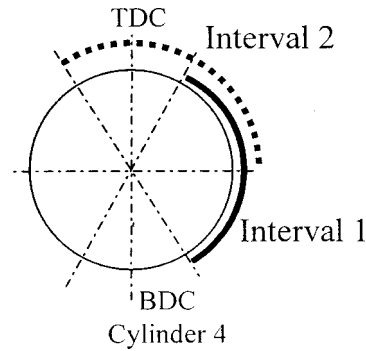


Fig. 4 Intervals investigated for optimal MD evaluation

In order to evaluate MD_i over Intervals 1 and 2 in fact the engine speed instantaneous values at the beginning and at the end of such intervals should be considered (see Eq. (4)). In order to minimize the effects of noise on the evaluation of the engine speed at the beginning and at the end of each of these intervals, the mean values of the speed over two engine cycle portions centered on these two points and having an amplitude of 120 deg have been used. Figure 5 shows how the parameter MD_i can be evaluated, for example, over Interval 2.

The (mean) engine speed values before and after each interval to be used for MD evaluation respectively over Interval 1 and 2 are reported in Fig. 6.

From Fig. 6 it is possible to observe that MD_i evaluated for the misfiring cylinder 4 over Interval 2 will show a high positive value, while MD_i evaluated over Interval 1 will show a small absolute value and will be negative. This is due to the presence of the speed increase related to the torsional vibration that follows the misfire event. Therefore, even if the previous considerations

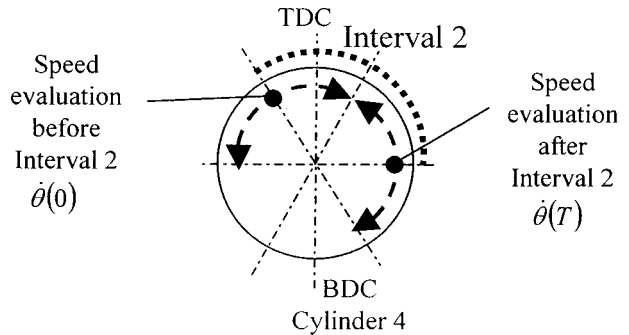


Fig. 5 Engine speed evaluation before and after Interval 2

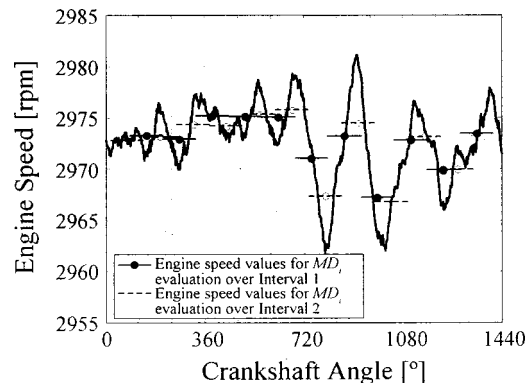


Fig. 6 Engine speed values to be used for MD_i evaluation over Intervals 1 and 2

made on the torque waveform suggest to choose Interval 1 for misfire diagnosis, better results are expected by choosing Interval 2. In fact, as already mentioned, the influence of the torsional vibration is less relevant over this last interval. For this reason, the detection algorithm has been designed using MD_i evaluated over Interval 2, with the engine speeds before and after such Interval obtained as described in Fig. 5. This will be the choice adopted from here on in this work.

The engine speed values before and after each Interval 2 have been obtained in this work from the knowledge of the time periods τ_i necessary for the crankshaft to cover the same angular sectors over which these engine speeds have to be evaluated (for example, by looking at Fig. 5, τ_i is the time interval needed to cover the angular interval $-90 \text{ deg} \rightarrow +30 \text{ deg}$, with respect to cylinder 4 TDC).

Once the time periods τ_i have been acquired and preprocessed to filter the effects of sensor-wheel interferences (such as mechanical tolerances of the teeth edges, eccentricity of the wheel and air gap variation during one revolution), the values of the engine speed at the beginning and at the end of Interval 2 can be obtained from

$$\dot{\theta}(0) = \frac{\Delta \theta}{\tau_i}; \quad \dot{\theta}(T) = \frac{\Delta \theta}{\tau_{i+1}} \quad (5)$$

When a misfire occurs, MD_i will suddenly increase assuming values related to the quantity $\overline{T_f(\theta)} + \overline{T_L(\theta)}$ (considering approximately $\overline{T_i} \cong 0$ in case of misfire—see Eq. (3)). In order to diagnose the presence of a misfire event it is then necessary to define threshold values to distinguish whether it occurred or not. These threshold values are strictly related for each engine operating condition to the quantity $\overline{T_f(\theta)} + \overline{T_L(\theta)}$ and can be mapped over the engine operating range as a function of manifold pressure and engine speed. Once this map has been stored in the ECU memory, misfire detection is possible comparing the actual value of MD_i to the threshold that can be obtained by entering the map with the actual values of manifold pressure and engine speed.


The same parameter MD used to detect misfiring cylinders could be suitable also to evaluate torque production nonuniformities between the various cylinders. In this case, the interest is focused on the actual value assumed by MD , rather than on its comparison with a threshold value. In fact it can supply information on the difference between the indicated torque developed by the various cylinders. Therefore, this parameter does not allow obtaining information on the absolute value of the torque produced by the cylinders but only on the relative difference that exists between them.

The evaluation of these nonuniformities should present more difficulties than the misfire detection, since the signal-to-noise ratio should be in this case lower (a misfire could be thought, in fact, as the torque nonuniformity of the maximum possible amplitude). On the other hand, it has to be noted that the torsional vibrations caused by the torque production nonuniformity (that is to be detected) are surely less evident than in the case of a misfire, and therefore the effect of these vibrations over the instantaneous engine speed waveform should be less relevant.

As already mentioned, the evaluation of the torque nonuniformity allows adopting control strategies (i.e., variations of injection and ignition commands of one or more cylinders), able in most cases to re-establish the desired torque production uniformity. The capability of detecting torque production nonuniformities can be used also to obtain a cycle reference information, without using a magnetic pickup facing the camshaft. In fact, cycle reference identification is usually performed using two pickups facing, respectively, the crankshaft and the camshaft. If the second pickup (the one facing the camshaft) is absent, the information obtained by the first one allows identifying the crankshaft position, but it is not sufficient to distinguish between the two-cycle positions at which that same crankshaft position is reached. In this case, the complete cycle reference information can be obtained by properly

Table 1 Main engine and sensor characteristics

| Engine characteristics | | |
|------------------------|-------------------------|-------------------|
| Type | Fiat - Alfa Romeo V6 TB | Fiat Fire L4 |
| Displacement | 2.0 liters | 1.2 liters |
| Cylinder bore | 80.0 mm | 70.8 mm |
| Stroke | 66.2 mm | 78.9 mm |
| Compression Ratio | 8.0:1 | 9.8:1 |
| Maximum Power | 151 kW @ 6000 rpm | 54 kW @ 6000 rpm |
| Maximum Torque | 280 Nm @ 2400 rpm | 106 Nm @ 4000 rpm |

| Pressure sensor characteristics | |
|---------------------------------|---|
| Kistler 6117B in the spark-plug |  |
| Range | 0-200 bar |
| Sensitivity | -15 pC/bar |
| Linearity | 0.6 % FSO |

introducing an abnormal injection in one cylinder immediately after the engine start, and by determining the engine cycle portion at which the torque nonuniformity appears on the engine speed.

Experimental Tests

Some experimental tests have been conducted to identify and validate the misfire detection and torque production nonuniformity evaluation methodology previously presented. The tests have been conducted running two different SI engines (a 2.0-liter V6 and a 1.2-liter L4 engine) in a test cell, both in steady-state and in transient conditions.

Both the engines have been equipped with pressure sensors inside the cylinders, in order to evaluate the real torque production of the single cylinders. The main characteristics of the engines used and of the sensors employed are reported in Table 1.

Two magnetic pickups were used, one facing the flywheel teeth and another one mounted in front of the camshaft pulley, to generate a cycle reference signal.

An important role in realizing these tests was performed by a Virtual ECU (VECU): This device, based on a particular configuration of the dSPACE Real Time System, allows controlling the engine actuators (ignition coils and/or injectors, for example) in any cylinder, independently of the original ECU. The VECU has been used to control ignition and injection of one single cylinder, inducing misfires (an example is shown in Fig. 7), misfuels or varying the injection time in order to cause also small torque nonuniformities.

The Virtual ECU used lookup tables (containing the original spark advance or injection time values) to generate the ignition or injection logical signals, which were sent to the drivers and then to the actuators.

Results

The misfire detection algorithm previously presented, with MD_i evaluated over Interval 2 as explained in Fig. 5, has been applied to the V6 engine whose characteristics are reported in Table 1. The steady-state operating conditions that have been investigated in order to determine the misfire detection threshold map are reported in Fig. 8.

For each operating condition of Fig. 8, one misfire has been induced every 30 cycles in cylinder #4. Using the instantaneous engine speed signal, the parameter MD has then been evaluated.

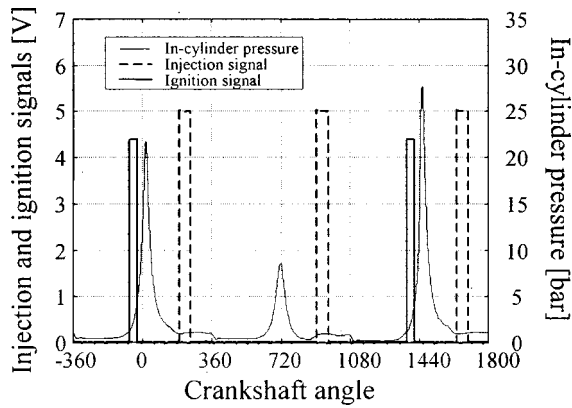


Fig. 7 Example of the Virtual ECU actuation signals to generate a misfire

As an example MD evaluated for the test at 4000 rpm engine speed and 160 Nm load torque has been reported in Fig. 9. Larger dots represent the combustions where a misfire has been induced.

A threshold value of 25 Nm has been chosen for MD in this operating condition in order to distinguish misfiring from non-misfiring combustions. When MD is higher than the chosen threshold a misfire is diagnosed in the cylinder whose combustion stroke is associated to the MD_i value that fell beyond the threshold. This threshold seems to enable the algorithm to detect all the misfires, while it causes a series of false alarms. These false alarms are related to the presence of the torsional vibration that follows the

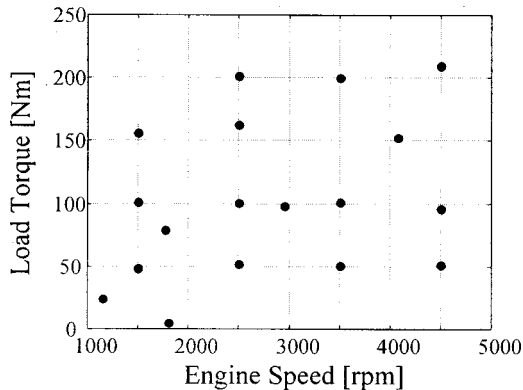


Fig. 8 Steady-state operating conditions investigated to determine the misfire detection threshold map

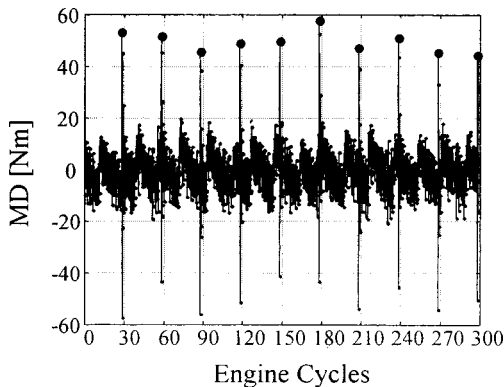


Fig. 9 MD evaluation for the test at 4000 rpm engine speed and 160 Nm load torque (larger dots represent the induced misfires)

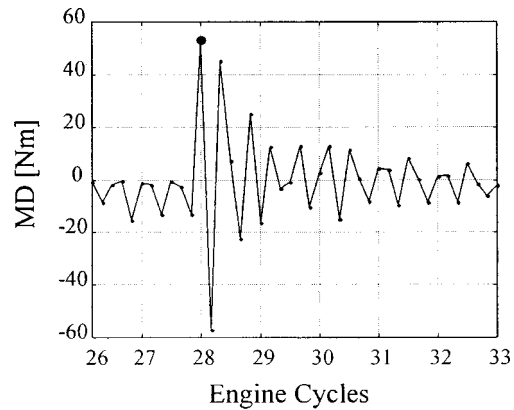


Fig. 10 MD evaluation for the test at 4000 rpm and 160 Nm in the vicinity of a misfire event

misfire event, especially at higher loads, as it can be seen in Fig. 10. The damped oscillation that follows the misfire causes, in fact, the overtaking of the chosen threshold one more time, two combustion periods after the one where the misfire has been induced. In order to avoid these false alarms the effects of the torsional vibration on the engine speed waveform have to be taken into account. This can be done, for example, by properly filtering the MD waveform after a misfire occurrence, as it will be explained in the following.

The MD waveforms after each misfire in Fig. 9 are always very similar to the one described in Fig. 10; these waveforms are determined by the crankshaft dynamic behavior that follows the misfire torque impulsive excitation. A unique pattern can then be isolated to represent the effects on MD related to a misfire event, computing the average of all the waveforms obtained after each misfire in Fig. 9. From Fig. 10 it is possible to notice that the misfire effect lasts, in this engine operating condition, for at least six combustions after the misfire event, and therefore the average waveform has been computed considering six MD values immediately after each missing combustion; the average waveform has been reported in Fig. 11.

The waveform identified can be used to avoid the false alarms previously described; in fact, once a misfire event has been diagnosed, the following MD values can be filtered by subtracting the corresponding values in Fig. 11. The result of such a signal processing algorithm is reported in Fig. 12.

In the case of a single misfire, such a procedure allows avoiding false alarms, while a multiple misfire detection would need the application of the same filtering technique once for each misfire

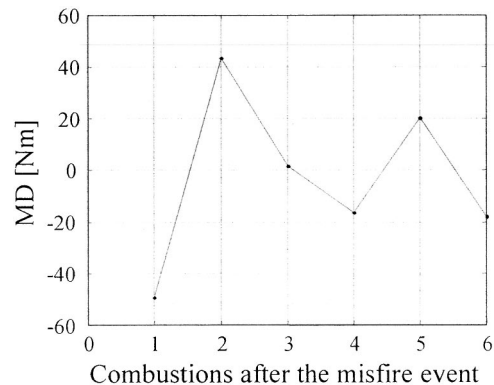


Fig. 11 MD waveform after a misfire for the test at 4000 rpm engine speed and 160 Nm load torque

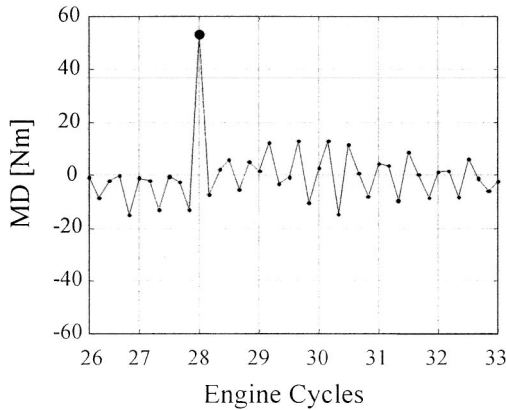


Fig. 12 MD evaluation for the test at 4000 rpm and 160 Nm in the vicinity of a misfire event, after the torsional vibration effects have been filtered away

detected. The case of multiple misfires has not been deeply investigated in this work, and will be the subject for future work on this topic.

Figure 13 shows the *MD* pattern for the engine running steady-state at 1150 rpm engine speed and 24 Nm load torque (1 misfire induced every 30 combustions in cylinder #4). Also in this case the choice of a threshold value able to detect all the misfires (3.5 Nm, for example) causes many false alarms. In this case they are not related to the presence of the torsional vibration, and therefore it is not possible to avoid them as previously described.

In order to better understand the nature of these false alarms the *MD* values related to the combustions inside cylinder #4 have been considered separately in Fig. 14, together with the indicated torque (obtained using in-cylinder pressure measurement) developed by that cylinder. When a misfire occurs a negative indicated torque value is measured. Such negative values are not located only in correspondence of induced misfire events (see Fig. 14). This means that in the operating condition considered (low load and low engine speed) the normal cyclic variability of the engine causes the presence of abnormal combustions that present effects similar to the induced misfires. It can be stated that under that operating conditions the engine presents partial burns cycles with very low torque produced. The false alarms are then the detection of the torque production nonuniformity related to the natural cyclic variability of the engine. The in-cylinder pressure signal acquired for cylinder #4 confirmed this statement.

Figure 15 reports *MD* versus the indicated torque values devel-

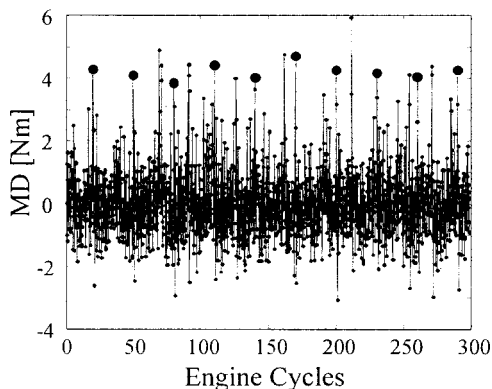


Fig. 13 MD evaluation for the test at 1150 rpm engine speed and 24 Nm load torque (larger dots represent the induced misfires)

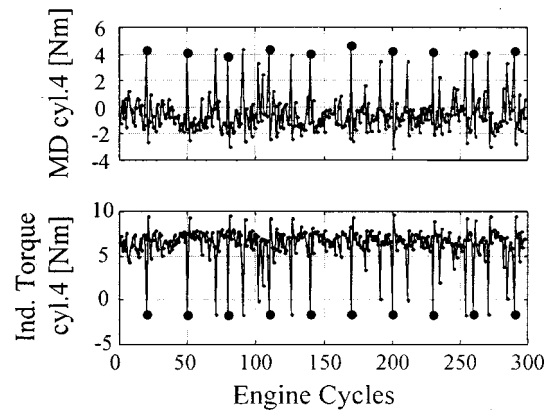


Fig. 14 MD and indicated torque values in cylinder #4 for the test at 1150 rpm and 24 Nm

oped by cylinder #4; the strict correlation between these two signals shows that it is possible to detect torque production nonuniformities using *MD*.

The same analysis has been conducted also for cylinder #6, where no misfires have been induced by the VECU. Figure 16 shows that *MD* overtakes twice the threshold chosen for the specific operating condition that is being considered, unveiling the presence of two misfires due to the cyclic variability of the engine.

Figure 17 shows that the same correlation, as for cylinder #4, exists between *MD* and the indicated torque developed by cylin-

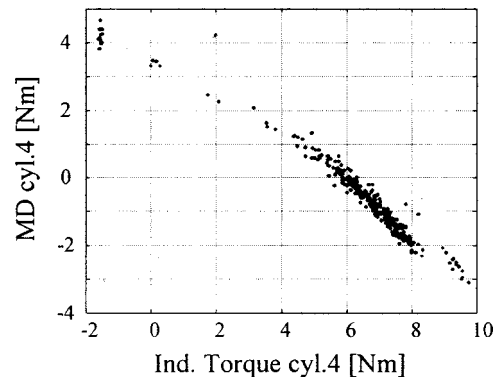


Fig. 15 MD versus indicated torque values in cylinder #4 for the test at 1150 rpm and 24 Nm

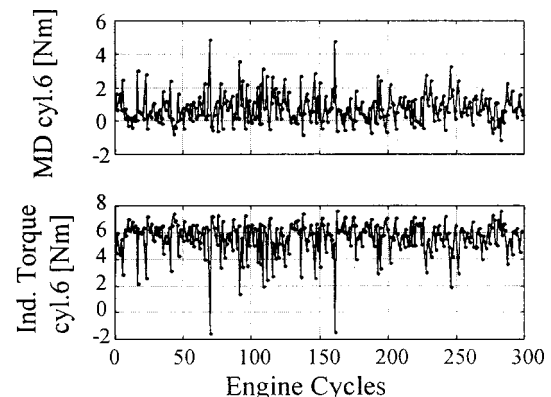


Fig. 16 MD and indicated torque values in cylinder #6 for the test at 1150 rpm and 24 Nm

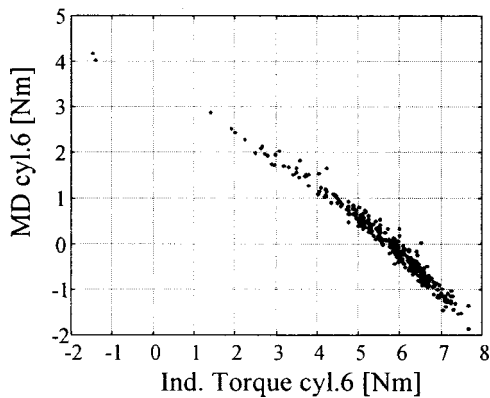


Fig. 17 *MD* versus indicated torque values in cylinder #6 for the test at 1150 rpm and 24 Nm

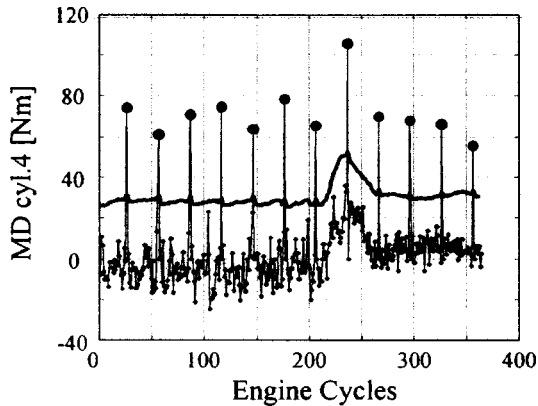


Fig. 18 *MD* evaluation for transient test #1 compared to the mapped threshold value (larger dots are the induced misfires)

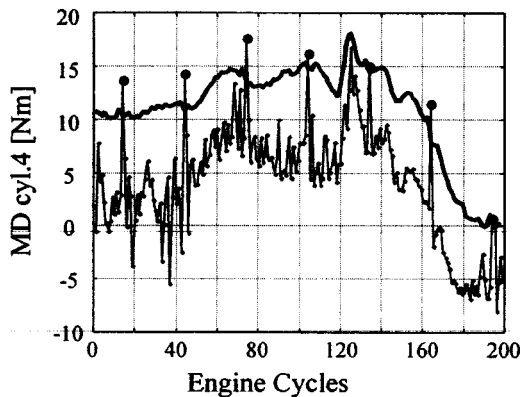


Fig. 19 *MD* evaluation for transient test #2 compared to the mapped threshold value (larger dots are the induced misfires)

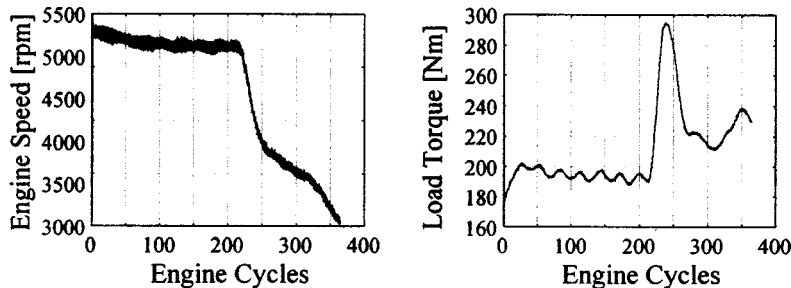


Fig. 20 Engine speed and load torque trends during transient test #1

der #6. As already mentioned this could allow detecting the entity of the torque production nonuniformities by monitoring the values of the parameter *MD*.

Once a threshold value has been chosen for each steady-state operating condition investigated, it is possible to obtain a map of the threshold values as a function of the engine operating conditions (in terms of engine speed and manifold pressure), to be used for misfire detection.

Figures 18 and 19 show the misfire detection capability during two speed and load transients where one misfire every 30 combustions has been induced in cylinder #4. Engine speed and load torque waveforms during these transient tests are reported, respectively, in Figs. 20 and 21. The methodology is able to detect all the misfires that have been induced, since *MD* falls beyond the mapped threshold value for every misfire. It has to be noted also the presence of false alarms, due to the presence of the torsional vibration. They can be avoided, as previously discussed, by filtering the effects of this torsional vibration on the engine speed waveform.

In order to verify the existence of a correlation between the torque production nonuniformities and the parameter *MD* also for another engine architecture, some steady-state tests have been performed on the L4 engine whose characteristics are reported in Table 1 (see Fig. 22).

For each steady-state operating condition the injection has been controlled using the Virtual ECU. The injectors have been controlled maintaining the same injection time as that imposed by the original ECU for all the cylinders except for cylinder #1, in order to simulate an injector malfunctioning condition in that cylinder. Smaller injection time adopted for cylinder #1 causes a different torque production between cylinder #1 and the other cylinders. In this case *MD* can be used to diagnose not only an accidental partial torque production (or a misfire in the worst case) in one cylinder, but also a systematic torque production difference between two cylinders. Figure 23 shows, as an example, the difference between the *MD* evaluated for cylinder #1 and #4, versus the difference between the indicated torque developed in those cylinders.

As it can be observed, the parameter *MD* gives in this case information related to the different torque production associated to each cylinder. This different behavior can be for example the result of a different air filling into the cylinders taken into account during the intake stroke, or can be due for example to a malfunction in one of the two injectors. The use of *MD* in such situations could help in developing a cylinder-by-cylinder torque production management and control strategy.

It has to be noted that the results presented here have been obtained with the engine mounted in a test cell. The approach that has been developed is still valid also on-board a vehicle. As previously mentioned, anyway, the different elasticity and inertia of the transmission line has to be considered for on-board applications, thus modifying the entity of the torsional vibration that follows a torque production nonuniformity.

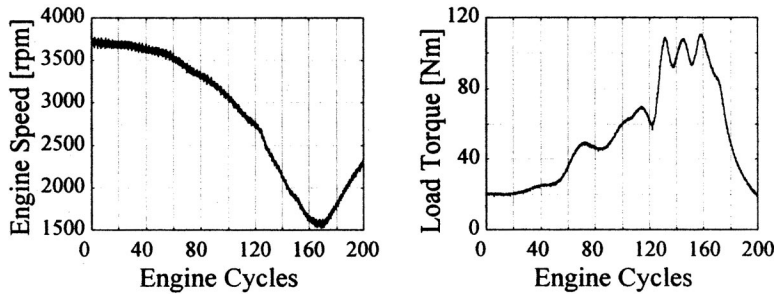


Fig. 21 Engine speed and load torque trends during transient test #2

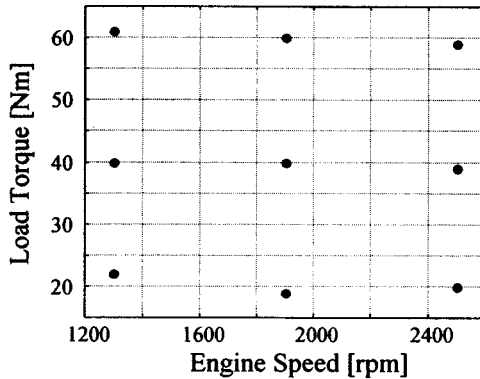


Fig. 22 Steady-state tests performed on the 1.2 liters L4 engine

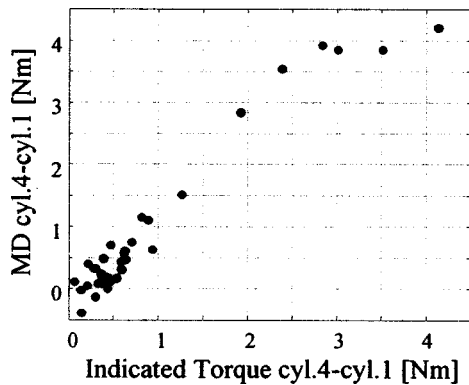


Fig. 23 Difference between the MD evaluated for cylinder #1 and #4, versus difference between the indicated torque developed in the same cylinders

Conclusions

The results obtained demonstrate the feasibility of detecting torque production nonuniformity and misfires from engine speed fluctuations. The MD parameter can in fact be used both as a misfire index (diagnosis is performed by comparing MD values, calculated for each combustion, with threshold values that depend on the engine operating condition), and to evaluate torque production differences between the cylinders (by comparing MD values related to the combustion of each cylinder, at the same engine operating condition). The developed methodology has been applied both to a V6 and an L4 engine, yielding good results in both cases. Therefore the extension of this approach to other engine architectures seems to be feasible. Anyway, the applicability of the methodology could be particularly challenging for engines that present combustions not evenly spaced. In this case, in fact, the angular portions over which the expansion strokes of different

cylinder overlap is higher than the case of an engine with the same number of cylinders and combustions evenly spaced.

Finally, the paper introduces the problem of the crankshaft torsional vibration effects on the engine speed fluctuations, that make the misfire detection critical in particular when multiple misfires are present in the same cycle. This topic will be further analyzed in future works.

The engine speed signal is already present in modern engine control systems, and the computing time required for the evaluation of the parameter MD seems to be compatible with the actual ECU computing power. This should allow an easy application on board a vehicle of the methodology presented, thus giving a benefit to actual engine control strategies. Rather than giving only a diagnostic information the procedure is, in fact, able to give information useful to design control strategies able to improve on-board engine torque management.

Acknowledgments

The authors would like to thank Dr. Gabriele Serra (Magna Marelli), Prof. Piero Azzoni and Borghi & Saveri Engine Brakes for the support and the contribution in the development of the present work.

Nomenclature

- τ_i = combustion period relative to the i th combustion [s]
 - LU_i = misfire detection parameter [$1/s^2$]
 - MD_i = misfire detection parameter [Nm]
 - θ = crank angle [rad]
 - $\dot{\theta}$ = crankshaft speed [rad/s]
 - $T_i(\theta)$ = indicated torque of the engine [Nm]
 - $T_L(\theta)$ = load torque [Nm]
 - $T_f(\theta)$ = friction and auxiliaries torque [Nm]
 - $T_r(\theta)$ = reciprocating torque [Nm]
 - J = crankshaft, flywheel, and brake equivalent inertia [$kg\ m^2$]
 - M_{eq} = equivalent mass of the sliding part of the crank-slider mechanism [kg]
 - r = crank-slider mechanism radius [m]
 - l = connecting rod length [m]
 - A_p = piston surface [m^2]
 - $p_m(\theta)$ = pressure inside m th cylinder [Pa]
 - $\lambda = r/l$
 - Z = number of cylinders
- $$f(\theta) = \frac{\sin(\theta) + \lambda \sin(2\theta)}{2\sqrt{1 - \lambda^2 \sin^2(\theta)}}$$
- $f(\theta)$ = crank slider mechanism function
 - $T_{im}(\theta)$ = indicated torque for m th cylinder [Nm]
 - T = expansion stroke portion duration [s]
 - $\Delta\theta$ = expansion stroke angular portion [rad]

References

- [1] California Air Resources Board, 1991, "Technical Status Update and Proposed Revisions to Malfunction and Diagnostic System Requirements Applicable to 1994 and Subsequent California Passenger Cars, Light-Duty Trucks, and Medium-Duty Vehicles—(OBD II)," CARB Staff Report.
- [2] Forster, J., Lohmann, A., Mezger, M., and Ries-Muller, K., 1997, "Advanced Engine Misfire Detection for SI-Engines," SAE Technical Paper 970855.
- [3] Klenk, M., Moser, W., Muller, W., and Wimmer, W., 1993, "Misfire Detection by Evaluating Crankshaft Speed—A Means to Comply With OBD II," SAE Paper 930399.
- [4] Plapp, G., Klenk, M., and Moser, W., 1990, "Methods of On-Board Misfire Detection," SAE Technical Paper 900232.
- [5] Azzoni, P. M., Moro, D., Porceddu-Cilione, C. M., and Rizzoni, G., 1996, "Misfire Detection in a High Performance Engine by the Principal Components Analysis Approach," SAE Technical Paper 960622.
- [6] Azzoni, P. M., Cantoni, G., Ceccarani, M., Mazzetti, S., Minelli, G., Moro, D., and Rizzoni, G., 1995, "Measurement of Engine Misfire in a Lamborghini V-12 Engine Using Crankshaft Speed Fluctuations," SAE Technical Paper 950837.
- [7] Azzoni, P. M., Minelli, G., and Moro, D., 1998, "Misfire Pattern Recognition in High Performance SI 12 Cylinder Engine," SAE Technical Paper 980521.
- [8] Cavina, N., Ponti, F., and Rizzoni, G., 1999, "Fast Algorithm for On-Board Torque Estimation," SAE Technical Paper 1999-01-0541.
- [9] Azzoni, P., Moro, D., Ponti, F., and Rizzoni, G., 1998, "Engine and Load Torque Estimation With Application to Electronic Throttle Control," SAE Technical Paper 980795.
- [10] Citron, S. J., O'Higgins, J. E., and Chen, L. Y., 1989, "Cylinder by Cylinder Engine Pressure and Pressure Torque Waveform Determination Utilizing Speed Fluctuations," SAE Technical Paper 890486.
- [11] Moro, D., Ponti, F., and Cavina, N., 1999, "In-Cylinder Pressure Reconstruction Based on Instantaneous Engine Speed Signal," *Proceedings of ICE Division*, Oct. 16–20, 1999, Ann Arbor, MI, ASME, New York.
- [12] Letenturier, P., and Benning, J., 1999, "Enhanced Engine Position Acquisition and Treatment," SAE Technical Paper 1999-01-0203.
- [13] Heywood, J. B., 1988, *Internal Combustion Engine Fundamentals*, McGraw-Hill, New York.
- [14] Moskwa, J., Wang, W., and Bucheger, D. J., 1998, "A New Methodology for Engine Diagnostics and Control Utilizing "Synthetic" Engine Variables: Theoretical and Experimental Results," *Proceedings of the ASME Dynamic Systems and Control Division*, DSC-Vol. 64, ASME, New York.

S. L. Yang

Associate Professor

Y. K. Siow

Graduate Research Assistant

C. Y. Teo

Graduate Student

Department of Mechanical Engineering—
Engineering Mechanics,
Michigan Technological University,
Houghton, MI 49931-1295

R. R. Tacina

A. C. Iannetti

P. F. Penko

Combustion Technology Branch
NASA Glenn Research Center,
Cleveland, OH 44135

Numerical Study of Lean-Direct Injection Combustor With Discrete-Jet Swirlers Using Reynolds Stress Model

The flowfield in a lean-direct injection (LDI) combustor with discrete-jet swirlers is described and analyzed using a computational fluid dynamics (CFD) code with a Reynolds stress turbulence model (RSTM). The results from the RSTM are compared to time-averaged laser-Doppler velocimetry (LDV) data, as well as results from the National Combustion Code (NCC) that has a cubic nonlinear κ - ϵ turbulence model, and from the KIVA code using the standard κ - ϵ model. The comparisons of results indicate that the RSTM accurately describes the flow details and resolves recirculation zones and high velocity gradients while the κ - ϵ models are unable to capture most flow structures. This confirms that, within the Reynolds averaging approach, the higher-order RSTM is preferred for simulating complex flowfields where separations, strong anisotropy, and high swirl are present. [DOI: 10.1115/1.1610012]

Introduction

Flame stability over a wide range of operating conditions is a basic requirement for through-flow combustion devices, such as gas turbine combustors. One common practice used to stabilize combustion is generation of swirling flow that entrains and recirculates a portion of the hot combustion products. For direct injection engine, recirculation zones also enhance the mixing of the incoming air with fuel. This effect is readily accomplished by the use of swirlers, such as discrete-jet swirlers, surrounding the fuel injector, [1].

Air swirlers are often used in many types of aircraft engines. In the lean direct injection (LDI) concept, a key feature is the injection of finely atomized fuel into the high-swirling airflow at the combustor dome that provides a homogeneous, lean fuel-air mixture. This allows for a better combustion efficiency and the reduction of NO_x and other pollutants. Another advantage of the LDI concept is that, with proper design of swirler configuration, a shorter combustor length is possible. Accordingly, to fully realize the potential of the LDI concept, a good understanding of the complex, turbulent swirling flow inside the combustor becomes essential.

To effectively calculate flowfield where swirl, wall effect, flow separation, and recirculation are present, a high-level turbulence model should be used. The most widely used turbulence model in current advanced CFD codes is the κ - ϵ model, such as the cubic nonlinear model, [2,3], used in the National Combustion Code (NCC), [4,5], and the standard κ - ϵ model, [6], in the KIVA code, [7]. Its popularity is due to the relative ease of implementation and its low CPU and memory overhead. It does, however, have considerable drawbacks for use in resolving flow with high gradients of velocity and swirl.

Regardless of the advantages of the κ - ϵ model, it has a tendency to yield inconsistent and diffusive results for complex flows because of its isotropic nature in modeling eddy viscosity. Without *ad hoc* modifications, the κ - ϵ model often cannot completely describe the large gradients in swirling and recirculating flows. For

more accurate calculations of the complex flowfield typical of an engine, or a combustor with high degree of swirl, use of a higher-order turbulence model is more appropriate.

Unlike the κ - ϵ models, the Reynolds stress turbulence model (RSTM) naturally resolves flow anisotropy, streamline curvature, sudden changes in strain rate, secondary motions, flow in rotation (swirl flow), etc. This is mainly due to the fact that each Reynolds stress component has its own transport equation. In addition, the production source terms in the RSTM are exact and need not be modeled. This greatly improves the accuracy and robustness of the solver. All in all, the RSTM represents the most comprehensive description of turbulent flows within the framework of the Reynolds averaging approach, [8]. Despite the added complexity due to the number of equations in the modeling, the applicability of the RSTM has been made feasible by present-day computer capacity.

In addition to obtaining a better understanding of the complex flow physics inside the combustor, the other purpose of this paper is to present cold-flow calculations of the flowfield in an LDI combustor with a discrete-jet swirler array using the KIVA-3V code, [7] with an RSTM [9]. It also aims to compare the RSTM results with the same calculations by KIVA's built-in standard κ - ϵ model, and the NCC's cubic nonlinear κ - ϵ model, which has been tuned for swirl flow calculations, [10,11]. All calculated results are compared to laser-Doppler velocimetry (LDV) data, [12], for the same configuration and operating conditions.

The National Combustion Code

The NCC is a research code under development at the NASA Glenn Research Center. It is a four-stage Runge-Kutta, preconditioned, massively parallel CFD code with super linear scalability, [4,5]. The NCC includes various advanced chemistry models, such as the intrinsically low-dimensional manifold and a generalized finite rate kinetic model. In addition, turbulence-chemistry interaction is modeled via the Magnussen model and a joint-scalar PDF model for turbulent reacting flow. Furthermore, the NCC uses a dynamic wall function for the effect of adverse pressure gradient, a low Reynolds number wall treatment, and unstructured grids for computations. The turbulence models in the code include the standard, quadratic, and cubic κ - ϵ models.

Contributed by the Internal Combustion Engine Division of THE AMERICAN SOCIETY OF MECHANICAL ENGINEERS for publication in the ASME JOURNAL OF ENGINEERING FOR GAS TURBINES AND POWER. Manuscript received by the ICE Division, Feb. 2002; final revision received Mar. 2003. Associate Editor: D. Assanis.

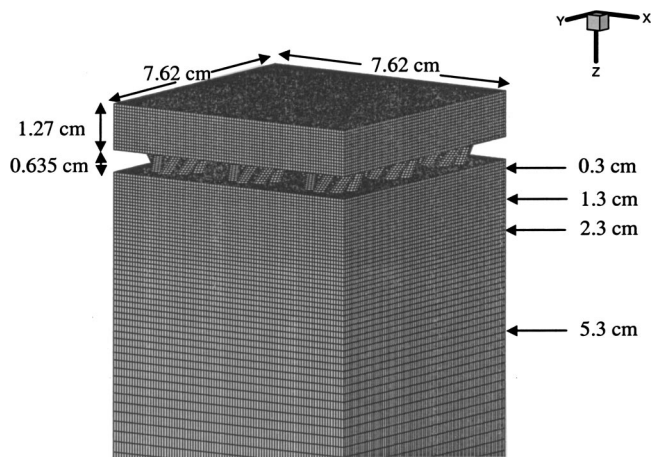


Fig. 1 Computational mesh

The cubic nonlinear κ - ϵ turbulence model is a second-order closure-scheme turbulence model, which uses both a nonlinear Reynolds stress-strain model, [13], and a cubic Reynolds stress-strain model, [14], for mean flow calculations. The model has been tuned and has fewer deficiencies than the standard κ - ϵ model, particularly in simulating the effects of flow rotation and curvature.

The KIVA-3V Code With Reynolds Stress Turbulence Model (RSTM)

The KIVA-3V computer code is the latest version of the KIVA-family CFD codes developed by the Los Alamos National Laboratory and is in use worldwide among the engine research communities, [7]. It solves transient, two and three-dimensional, chemically reactive fluid flow with fuel sprays. The turbulence models in the code include both the standard and RNG-variant κ - ϵ models. To better simulate complex, turbulent engine flow, the Speziale-Sarkar-Gatski (SSG) RSTM, [15], has been incorporated into the KIVA code, [9]. The SSG RSTM is considered a quasi-linear model, since it contains one quadratic term in the pressure-strain model. One advantage of using the SSG model is that, unlike most other RSTMs available in the literature, no wall-distance parameter is needed to account for wall reflection. This is a desirable feature for engine flow simulations, since the computational domain is often of a complex shape and may also be time-dependent. Details of the RSTM implementation, numerical issues, and code validation can be found in Yang et al. [9] and will not be repeated here.

Problem Description and Computational Mesh

The multipoint LDI combustor has a rectangular inlet section 1.27 cm long and is upstream of nine groups of swirlers arranged in a 3×3 pattern, as shown in Fig. 1. Each group of swirlers comprises eight flow passages, all of which orientated at 35 deg in the tangential direction, Fig. 2. Figure 3 illustrates the 3×3 swirler array arrangement and the relative location of the flow passages. A rectangular burner duct, either 7.62 cm or 17.78 cm long—depending on the grid density, is downstream of the swirler section. The duct has a cross section of 7.62 cm \times 7.62 cm. The inlet surface of the combustor lies in the XY -plane and the inlet velocity is in the positive Z (axial) direction.

The computational grids are constructed by using Pro-Engineer® to create a three-dimensional model, which is then exported in IGES format to the Gridgen®, [16], database. A Cartesian multiblocked structured mesh is then generated using Gridgen®. Next, the grids are exported from Gridgen® into the KIVA code where all blocks are appropriately interconnected. This pro-

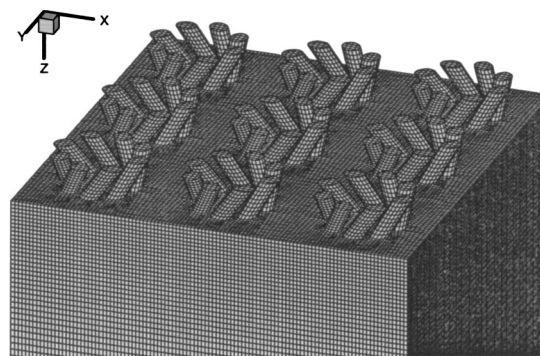


Fig. 2 Orientation of the discrete-jet swirler array

cedure not only allows for the construction of any complex geometry, but is also efficient in the use of time and resources.

To insure that the calculated results represent a converged solution, a grid dependency study was performed. Three grid densities were chosen for this purpose, namely coarse, medium, and dense grids. The grid densities are given in Table 1, along with the combustor length used in each computational model. Notice that, for the dense-grid case, the rectangular burner duct has a length of 7.62 cm. This length was chosen for CPU time consideration and was based on the LDV measurements. From the LDV data, there is no reversed flow at this location and the measured recirculation bubbles are no more than 5.3 cm in length. Comparisons of the LDV data with the numerical results among the three computational meshes show that the solution converges with grid density. Therefore, the dense-grid result is chosen for presentation.

Discrete-Jet Swirler Array Flow Physics

Swirl flow is created when air is forced through the small flow passages, inclined at an angle with respect to the cross-flow plane. As air enters and contracts through the small passages, air velocity increases, producing the so-called discrete jets. As each jet enters the combustor, it spreads, expands, and interacts with the neighboring jets and the bounding walls. Due to the orientation of the flow passages, azimuthal and radial velocity components, which are responsible for the creation of swirl, are developed. When the swirl reaches certain strength, reversed or recirculating flow regions will form near the top of the combustor.

Based on the arrangement of the swirler array shown in Fig. 3, the nine groups of swirlers can be classified, according to their geometric locations, into three types of swirler, namely “center,” “corner,” and “side,” [12]. Since the “center” swirler is not bounded by any solid walls but is instead surrounded by other swirlers, it is expected that it will receive the highest level of interactions with other swirlers. Two solid walls and two neighboring swirlers, on the other hand, bound the four “corner” swirlers. The remaining four “side” swirlers have three sides bounded by other swirlers and one side by a solid wall. On the basis of flow physics, the same swirler type is expected to behave similarly. Further discussion of the complex flow pattern inside the combustor will be given in the Results and Discussion section through the aid of both measured and CFD results.

Flow Conditions and Laser-Doppler Velocimetry (LDV) Measurements

For comparison, the operating conditions in this study are identical to the LDV measurements by Cai et al. [12] and an NCC study reported by Iannetti et al. [10,11]. The inlet axial velocity is 6.6 m/s. As in the KIVA code, wall functions are used for all solid walls. At the inlet, the turbulence intensity and length scale are

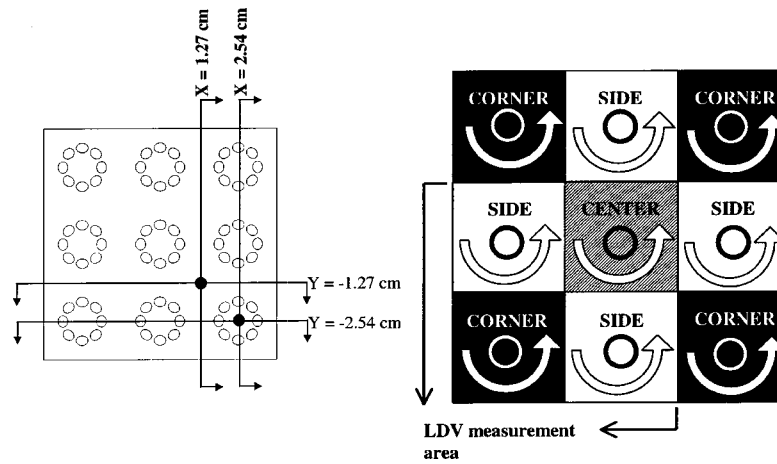


Fig. 3 Swirler array configuration and classification

assumed 10% of the inlet mean flow kinetic energy and 3% of the inlet opening, respectively. The outlet pressure is at the ambient condition.

The experimental method and assumptions reported in Ref. [12] are now briefly described. The measurements were made with a two-component LDV system, at 12 axial stations downstream of the discrete-jet swirlers. Due to geometric symmetry of the swirler array, only 4/9 of each cross section (Fig. 3) was covered during the experiment. In other words, the LDV system measured the axial (W) and a cross-flow velocity component (U) within the volume downstream of four neighboring swirlers. The third velocity component, V , was derived by assuming that the flowfield was antisymmetrical about the diagonal.

Results and Discussion

The primary objective of this study is to investigate the flow-field of an LDI combustor with multipoint swirler array in a square duct, and to compare results among the SSG RSTM, the standard $\kappa\text{-}\epsilon$ model in the KIVA code, the cubic nonlinear $\kappa\text{-}\epsilon$ model in the NCC, and the LDV measurements. As the measurements were made in a nonreacting flow, only cold-flow calculations are presented. In the NCC study, [10], tetrahedral grids were used with a total of 2.26 million cells and 2.28 million vertices. Comparisons of results are presented in XY -planes, i.e., at Z

$=0.3$ cm, 1.3 cm, 2.3 cm, and 5.3 cm. These cutting-plane locations are shown in Fig. 1. In addition to contour plots, line plots along two axial lines downstream of the swirlers are also presented for quantitative comparison. The first line is located at $X = 2.54$ cm, $Y = -2.54$ cm (at the center of the bottom, right corner-swirler), and the second at $X = 1.27$ cm, $Y = -1.27$ cm (between four swirlers at the bottom, right corner).

The results in the XY -planes show that the RSTM yields a better and more consistent agreement with the experiment than do both the $\kappa\text{-}\epsilon$ models. At $Z=0.3$ cm, Fig. 4, although the RSTM (Fig. 4(c)) calculated a slightly stronger forward velocity (red spots) at the jets, the size, shape, and strength of the reversed-velocity contours compare considerably well with the LDV data. The $\kappa\text{-}\epsilon$ models, Figs. 4(a–b), despite showing acceptable contours of forward velocity, had difficulty computing the reversed flow. In particular, the NCC $\kappa\text{-}\epsilon$ result displays a strong presence of recirculation zone (the blue regions) surrounding the center swirler. This suggests an overcompensation for the diffusiveness inherited in the standard $\kappa\text{-}\epsilon$ formulation.

Further downstream at $Z=1.3$ cm, Fig. 5 contains interesting yet serious differences among the turbulence models. The experimental measurements, Fig. 5(d), show kidney-shaped reversed-flow regions around the bounding walls, and a circular region at the center. This is caused by the high shear induced by the interactions among the co-rotating swirlers. The RSTM result, Fig. 5(c), agrees very well with the LDV data. The locations and magnitude of the recirculation zones are essentially resolved by the RSTM. The $\kappa\text{-}\epsilon$ models, on the other hand, each computed an inaccurate yet distinct profile. While the standard $\kappa\text{-}\epsilon$ model result, Fig. 5(b), may seem reasonable, the locations of the reversed-flow regions have shifted. More importantly, the size of these regions is much smaller compared to the LDV plot. This is an

Table 1 Grid density

| | Coarse | Medium | Dense |
|-----------------------|----------|----------|---------|
| Number of cells | 357,257 | 527,687 | 965,905 |
| Number of vertices | 360,450 | 528,618 | 967,312 |
| Burner length modeled | 17.78 cm | 17.78 cm | 7.62 cm |

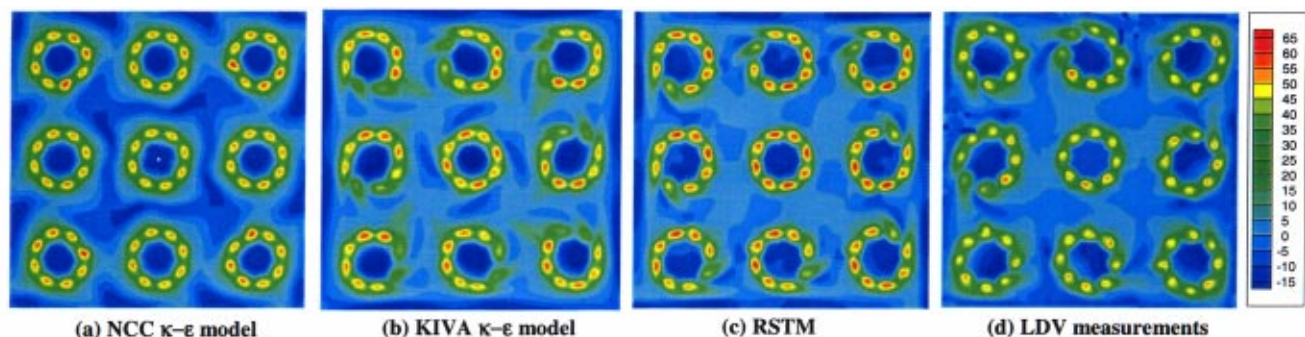


Fig. 4 Axial velocity (W) contours at $Z=0.3$ cm

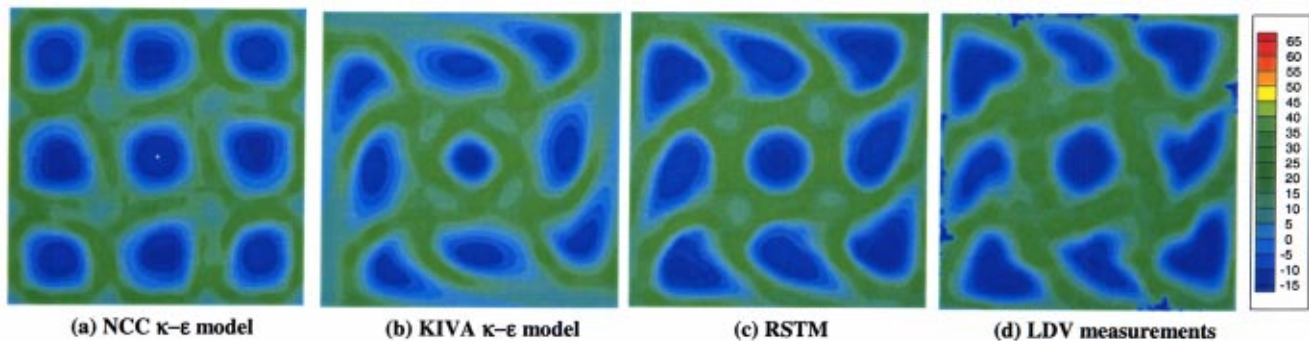


Fig. 5 Axial velocity (W) contours at $Z=1.3$ cm

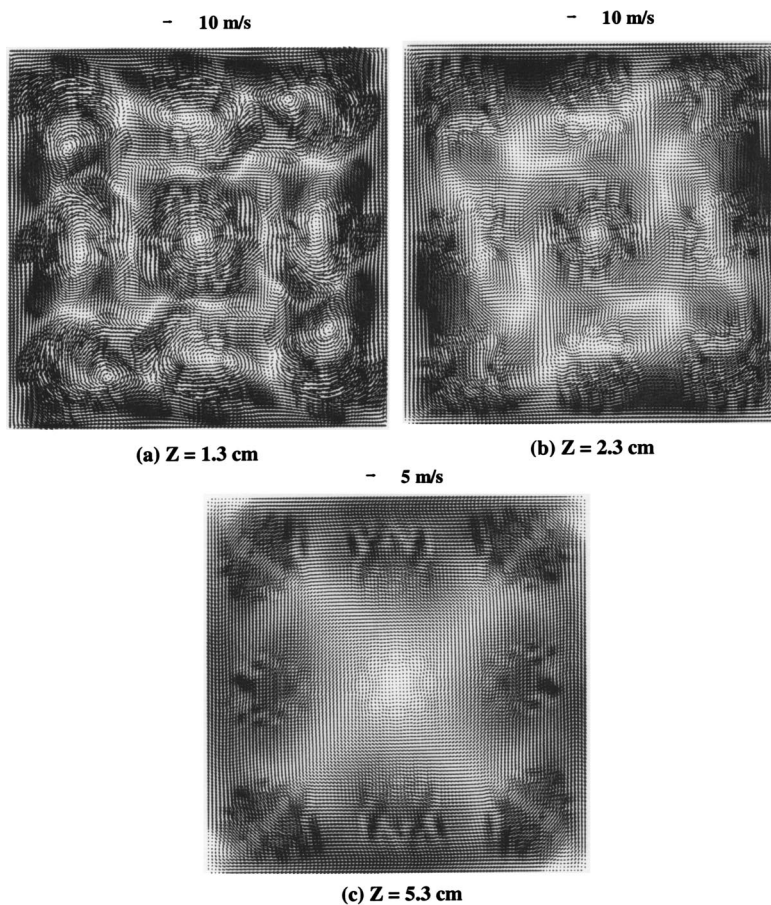


Fig. 6 $XY(UV)$ velocity vectors at different Z -planes, RSTM results

indication of the well-known diffusive nature of the standard $\kappa-\epsilon$ model. In contrast, the NCC's $\kappa-\epsilon$ model, Fig. 5(a), failed to resolve the recirculation structures. It instead calculated rather well-behaved and circular reversed flow regions, without much swirler-swirler interactions. In the NCC studies, [10,11], it was assumed that the combustor geometry was rotationally periodic every 90 deg. While this is true in geometric terms, the LDV data in both Figs. 4 and 5 show that the flowfield is not symmetrical about both the X and Y -axes. Therefore, a periodic boundary condition may not be appropriate for this particular geometry and swirler array configuration. Nevertheless, since the corner kidney-shaped recirculation is located away from the symmetry boundaries, the flow structure should be resolved regardless of the symmetry assumption. In addition, some of the NCC-computed recirculation

zones appear larger than the measured ones. This again suggests that the cubic nonlinear $\kappa-\epsilon$ model may have been overadjusted to counteract the diffusiveness found in the standard $\kappa-\epsilon$ model. Together, the results from both $\kappa-\epsilon$ models strongly indicate the downside of *ad hoc* modifications in turbulence modeling. Modifying the two-equation formulation on a case-by-case basis is problematic and therefore should be used with caution, particularly when large gradients, strong shear, and high swirl are expected.

While Fig. 5 characterizes the complex flow physics associated with the discrete-jet swirlers, Fig. 6 shows with velocity vectors how the swirling jets interact with each other and with the solid walls along the axial direction ($Z=1.3$ cm, 2.3 cm, and 5.3 cm). In Fig. 6(b), all the "corner" and "side" swirler vortex centers

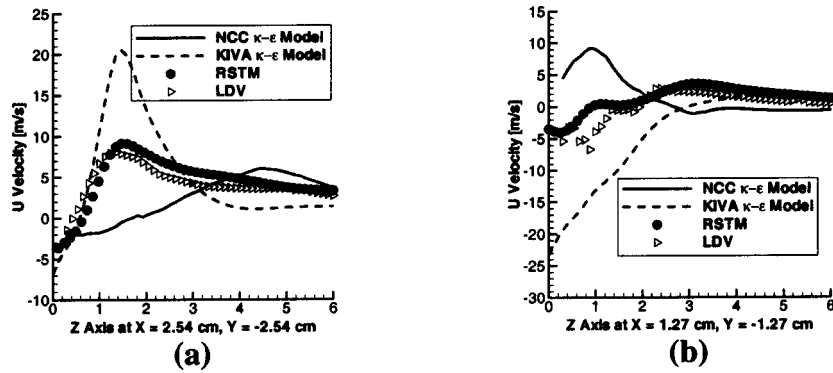


Fig. 7 *U* velocity

have shifted relative to each swirler group's center due to wall effect and swirling jet interactions. Smaller, secondary induced vortices due to these interactions are also visible. The center swirler, on the other hand, is able to preserve its characteristics while gaining strength from its neighbors, hence maintaining a nearly circular reversed-flow structure. Further downstream at $Z = 2.3$ cm, Fig. 6(b), due to jet spreading, expanding, and interacting processes and wall effect, those swirlers neighboring the wall gradually merge and eventually form a single, albeit weaker, swirl, Fig. 6(c).

The line plots in Figs. 7–10 quantitatively show, in further detail, how the RSTM computations give better agreement with the measurements than do the κ - ϵ calculations. Since in the LDV experiment two velocity components (U, W) were measured, it is appropriate to present comparisons in terms of these components. Figure 7 contains two line plots of U -velocity comparison among the measured and computed results. The first plot, Fig. 7(a), pre-

sents the U -velocity at different axial locations downstream of the bottom, right swirler. Immediately below the swirler, the LDV data shows small, negative U -velocity, which quickly becomes positive further downstream, reaches a peak, and gradually tapers off. This implies an axial shift of momentum from the presence of neighboring swirlers. Comparing the LDV measurements with the calculated results provides an obvious distinction among the different turbulence models. The RSTM agrees exceptionally well with the LDV data, while the two κ - ϵ models give contrasting profiles, particularly before $Z = 3.0$ cm where recirculation is strong. At $Z = 1.4$ cm, the KIVA's standard κ - ϵ model calculated a peak value approximately 175% higher than the measurements, while the NCC, unable to resolve the peak, computed much lower values.

Figure 7(b) contains a line-plot comparison along axial locations between the four bottom-right swirlers. The RSTM shows a close agreement with the LDV data, with a maximum offset near $Z = 1.0$ cm. The κ - ϵ results exhibit similar behavior as in Fig.

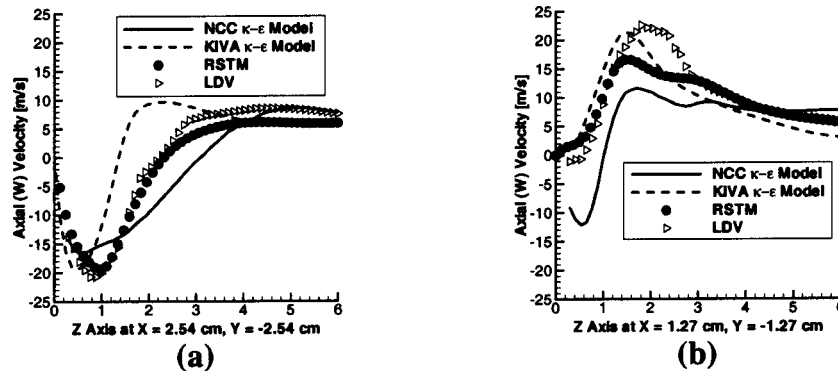


Fig. 8 Axial (W) velocity

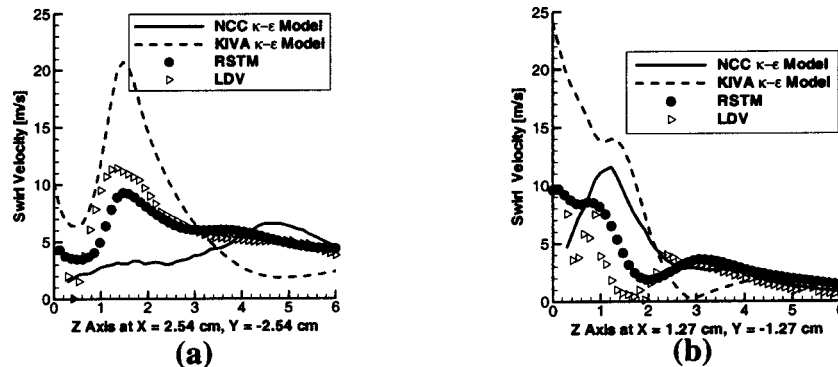


Fig. 9 Swirl velocity

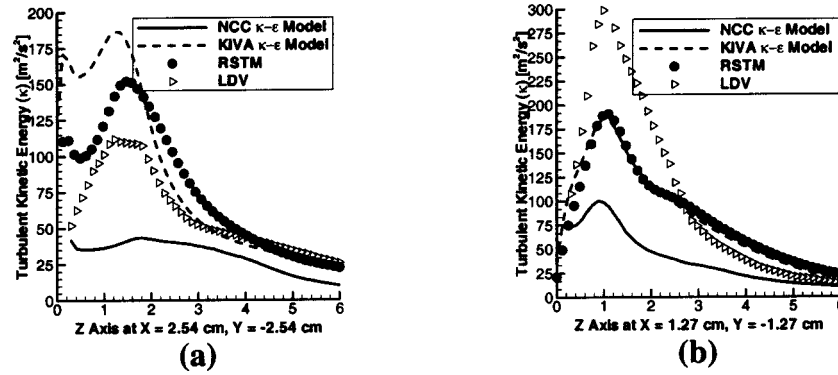


Fig. 10 Turbulence kinetic energy (κ)

7(a), except the standard κ - ϵ model calculated much lower values and the cubic nonlinear model, much higher. Both plots in Fig. 7 illustrate the inconsistency of κ - ϵ models when the flow is complex.

The line plots in Fig. 8 quantitatively present the axial velocity component (W). In Fig. 8(a), from the LDV data zero axial-velocity occurs at approximately $Z=2.2$ cm downstream of the swirler, which may be assumed to be the size of the recirculation bubble. The RSTM profile closely follows the LDV data, although a maximum offset of 25% occurs below the recirculation region. The NCC's κ - ϵ model computed a bubble size nearly twice the measured one, while the KIVA's model calculated only half, clearly displaying its diffusive nature. Figure 8(b) on the other hand, does not show as distinct a comparison as does Fig. 8(a). The RSTM result exhibits the general trend of the LDV profile for $Z < 1.0$ cm as well as $Z > 3.0$ cm. The NCC calculates a substantially stronger reversed flow in the $Z < 1.0$ cm region.

Although the V -velocity component was not directly measured in the LDV experiment, it would still be useful to show the line plots of swirl velocity and turbulence kinetic energy, κ . The plots that follow, therefore, serve as comparisons of trend rather than accuracy. The swirl velocity in Fig. 9(a) carries a characteristic similar to the U -velocity plot in Fig. 7(a). The swirl quickly peaks at about $Z=1.4$ cm, then gradually settles. The RSTM basically follows the trend and stays within 20% of the measured values. The highest swirl computed by the standard κ - ϵ model occurs at a Z value close to the measured one, and the cubic nonlinear κ - ϵ model was unable to resolve any swirl structure within the recirculation zone.

Figure 9(b) shows a more complex profile, particularly for $Z < 3.0$ cm. The measured swirl values are generally lower than those in Fig. 9(a), and fluctuate considerably inside the bubble. Both κ - ϵ models generally yield excessive swirl up to $Z = 2.5$ cm. Halfway downstream and onward, however, all computed results agree quite well with the LDV measurements.

The last set of figures contains the κ -levels at the same locations as in the preceding line plots. Figure 10(a) shows that the NCC's κ - ϵ model fails to capture the steep profile of the measurements, near $Z=1.5$ cm. Instead, the model gives a generally flat line that falls below the LDV data. Since eddy viscosity, μ_T , is directly proportional to the square of κ , a small κ value results in an even smaller μ_T . By the same token, the standard κ - ϵ model, having κ values much higher than the LDV data, has excessively large μ_T throughout the entire combustor length. In Fig. 10(b), all calculated results fall below the LDV data, although exhibiting similar trend.

Conclusion

An LDI combustor with a discrete-jet swirler array was modeled for cold-flow investigation. The complex flow physics associated with the swirler array was described with the aid of CFD

results and experimental data. The SSG RSTM was used to describe the turbulence inside the combustor. The RSTM-computed results were compared to LDV measurements, as well as results from the cubic nonlinear κ - ϵ turbulence model in the NCC, and the standard κ - ϵ model in the KIVA code: The result comparisons show that the RSTM accurately captured most of the flow characteristics. Both κ - ϵ models exhibited contrasting behaviors, either over or undercalculating eddy viscosity in regions of high swirl and strong recirculation. Similar conclusion was also achieved in a previous study of an LDI combustor with an axial swirler array, [17].

Accurate calculation of swirl and recirculation zones is important in deciding fuel spray locations as well as in the design of combustors. Within the Reynolds averaging approach, the RSTM has proven to be a proper choice in accurately calculating complex flow characteristics, given the general capacity and availability of current-generation computers. The RSTM computations required 178.4 μ sec per cycle per grid point on an SGI Origin 3400 platform, while the computation with KIVA's κ - ϵ model took 87.6 μ sec. The extra computational overhead from using the RSTM is justified by its accuracy and robustness. No *ad hoc* modifications are necessary for complex geometry and flow conditions. Future work may include study of similar combustor geometry with different swirl angles as well as with combustion and fuel spray.

Acknowledgment

The authors would like to thank NASA for their financial assistance under NASA Grant Contract #: NAG3-2088.

References

- [1] Lefebvre, Arthur H., 1983, *Gas Turbine Combustion*, Hemisphere, Washington, DC.
- [2] Shih, T.-H., Chen, K.-H., Liu, N.-S., and Lumley, J. L., 1998, "Modeling of Turbulent Swirling Flows," NASA-TM-113112.
- [3] Shih, T.-H., Chen, K.-H., and Liu, N.-S., 1998, "A Non-Linear k -epsilon Model for Turbulent Shear Flows," AIAA Paper 98-3983.
- [4] Stubbs, R. M., and Liu, N.-S., 1997, "Preview of the National Combustion Code," AIAA Paper 97-3314.
- [5] Quealy, A., Ryder, R., Norris, A., and Liu, N.-S., 2000, "National Combustion Code: Parallel Implementation and Performance," NASA TM-2000-209801.
- [6] Launder, B. E., and Spalding, D. B., 1974, "The Numerical Computation of Turbulent Flows," *Comput. Methods Appl. Mech. Eng.*, **3**, pp. 269-289.
- [7] Amsden, A. A., 1999, "KIVA-3V, Release 2, Improvements to KIVA-3V," Los Alamos National Laboratory, LA-13608-MS, Los Alamos, NM.
- [8] Hanjalic, K., 1999, "Second-Moment Turbulence Closures for CFD: Needs and Prospects," *Int. J. Comput. Fluid Dyn.*, **12**, pp. 67-97.
- [9] Yang, S. L., Peschke, B. D., and Hanjalic, K., 2000, "Second-Moment Closure Model for IC Engine Flow Simulation Using KIVA Code," *ASME J. Eng. Gas Turbines Power*, **122**, pp. 357-365.
- [10] Iannetti, A., Tacina, R., Jeng, S.-M., and Cai, J., 2001, "Toward Accurate Prediction of Turbulence, Three-Dimensional, Recirculation Flows With the NCC," Paper No. AIAA-2001-0809.
- [11] Iannetti, A., Tacina, R., Cai, J., and Jeng, S.-M., 2001, "Multi-Swirler Aerodynamics: CFD Predictions," AIAA Paper No. 2001-3575.

- [12] Jeng, S.-M, Cai, J., and Tacina, R., 2001, "Multi-Swirl Aerodynamics: Experimental Measurements," AIAA Paper No. 2001-3574.
- [13] Craft, T. J., Launder, B. E., and Suga, K., 1993, "Extending the Applicability of Eddy Viscosity Models Through the Use of Deformation Invariations and Non-Linear Elements," 5th IAHR Conference on Refined-Flow Modeling and Turbulence Measurement, Paris, Sept. 7–10.
- [14] Shih, T.-H., and Lumley, J. L., 1993, "Remarks on Turbulent Constitutive Relations," *Math. Comput. Modell.*, **18**(9-6).
- [15] Speziale, C. G., Sarkar, S., and Gatski, T. B., 1991, "Modeling the Pressure-Strain Correlation of Turbulence: An Invariant Dynamical Systems Approach," *J. Fluid Mech.*, **227**, pp. 245–272.
- [16] Gridgen CFD and FEA Pre-Processing, V.13.3, Pointwise, Inc.
- [17] Yang, S. L., Siow, Y. K., Peschke, B. D., and Tacina, R., 2003, "Numerical Study of Nonreacting Gas Turbine Combustor Swirl Flow Using Reynolds Stress Model," *ASME J. Eng. Gas Turbines Power*, **125**, pp. 804–811.

Development of an Exhaust Gas Recirculation Distribution Prediction Method Using Three-Dimensional Flow Analysis and Its Application

K. Yoshizawa

K. Mori

Y. Matayoshi

S. Kimura

Powertrain and Environment Research
Laboratory,
Nissan Research Center,
Nissan Motor Company, Ltd.,
1, Natsushima-cho,
Yokosuka 237-8523, Japan

A multidimensional computational fluid dynamics (CFD) method has been used to improve the exhaust gas recirculation (EGR) distribution in the intake manifold. Since gas flow in the intake system is affected by intake pulsation caused by the gas exchange process, a pulsation flow simulation is used. A one-dimensional gas exchange calculation is combined with three-dimensional intake gas flow calculation to simulate pulsation flow. This pulsation flow simulation makes it possible to predict the EGR distribution. The gas flow in the intake system was analyzed in detail. It was found that a reverse flow region formed downstream of the throttle valve. The size and shape of the reverse flow region greatly depend on the engine operating conditions. With a conventional EGR system, it is difficult to distribute EGR uniformly under various engine operating conditions. A new EGR system that uses a spiral flow to mix the fresh air and EGR gas has been developed to obtain a uniform EGR distribution. As a result of adopting this system, a uniform EGR distribution is obtained regardless of the engine operating conditions. This spiral flow EGR system was applied to a low-emission vehicle (LEV) put on the Japanese market. [DOI: 10.1115/1.1581896]

Introduction

Continuing concerns about air quality have necessitated further reductions of automotive emissions such as nitrogen oxides (NO_x) and carbon dioxide (CO_2). Recently, a heavy Exhaust Gas Recirculation (EGR) system has attracted much interest as a key technology for reducing exhaust emissions of internal combustion engines, because it has the potential to lower both NO_x and CO_2 levels simultaneously, [1]. Heavy exhaust gas recirculation (EGR) refers to an EGR rate of more than 30% in the cylinder. This kind of large EGR rate has become possible with development of direct-injection gasoline (DIG) engines, [2], since the fuel distribution in the cylinder is controlled more accurately than in port-injection gasoline engines. Under the application of heavy EGR, the EGR distribution in the intake system is an important factor. If the EGR distribution is not uniform, a cylinder with a large EGR gas concentration would cause unstable combustion. That would generate large emissions and also deteriorate drivability. Therefore, achieving a uniform EGR distribution is essential. However, time-consuming experimental research has so far been the only way to evaluate the EGR distribution in the intake manifold. Design and development lead time must be shortened in order to meet consumers' rapidly changing needs, [3]. Hence, there have been strong expectations for the development of a simulation method for predicting the EGR distribution.

In this connection, computational fluid dynamics (CFD) has been used. Since gas flow in the intake system is affected by intake pulsation caused by the gas exchange process, a pulsation flow simulation method is used, [4,5]. A one-dimensional gas exchange calculation and a three-dimensional intake gas flow calculation are used to simulate pulsation flow caused by the gas ex-

change process. This pulsation flow simulation makes it possible to predict the EGR distribution under the influence of intake pulsation. With this analysis method, the EGR distribution was accurately predicted to within 3–5%.

After validating the EGR distribution predicted with the pulsation simulation method, gas flow in the intake system was analyzed in detail. It was found that a reverse flow region formed downstream of the throttle valve. The size and shape of the reverse flow region greatly depend on the engine operating conditions. With a conventional EGR system, it is difficult to distribute EGR uniformly under various engine operating conditions, because the distribution is greatly influenced by the reverse flow region, [6].

A new EGR system has been developed to obtain a uniform EGR distribution. The EGR passage is connected to the intake manifold tangentially and recirculated exhaust gas flows into the manifold in a spiral manner. This spiral flow enhances the mixing of fresh air and recirculated exhaust gas and is less influenced by changes in the reverse flow region. The EGR distribution is improved by this newly developed mixing system. As a result of adopting this system, a uniform EGR distribution is obtained regardless of the engine operating conditions.

This spiral flow EGR system was then modified for production vehicle application, taking into account layout limitations and production cost. It has been applied to a low-emission vehicle (LEV) put on the Japanese market.

Exhaust Gas Recirculation (EGR) Distribution in Conventional EGR Systems and Engineering Tasks for Heavy EGR System

Figure 1 shows a schematic diagram of a conventional EGR system. The engine system comprises a collector, an intake manifold and an exhaust manifold. The throttle body, incorporating the throttle valve, is connected upstream of the collector. An EGR passage connects the exhaust manifold and the throttle body. In

Contributed by the Internal Combustion Engine Division of THE AMERICAN SOCIETY OF MECHANICAL ENGINEERS for publication in the ASME JOURNAL OF ENGINEERING FOR GAS TURBINES AND POWER. Manuscript received by the ICE Division, Feb. 7, 2002; final revision received Aug. 2002. Associate Editor: D. Assanis.

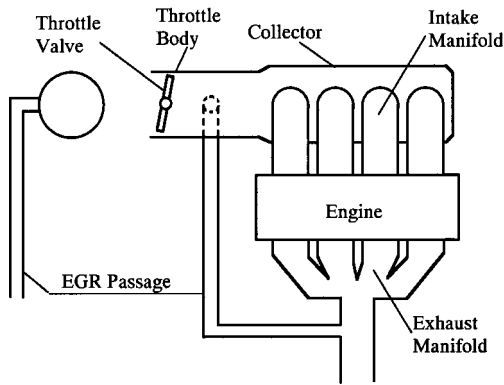


Fig. 1 Schematic diagram of conventional EGR system

this conventional system, EGR gas is introduced downstream of the throttle valve, i.e., far upstream of the collector, to allow enough time for mixing with the fresh air so as to attain a uniform EGR distribution.

Figure 2 shows the EGR distribution for different engine operating conditions. These results were obtained experimentally using the conventional EGR system shown in Fig. 1. The EGR rate of each cylinder is calculated by

$$EGRR(\text{cyl.}\#) = M_{\text{EGR}}(\text{cyl.}\#) / [M_{\text{EGR}}(\text{cyl.}\#) + M_{\text{air}}(\text{cyl.}\#)] \quad (1)$$

where EGRR is the EGR rate, M_{EGR} is the EGR gas mass flow, and M_{air} is the air mass flow. The CO_2 concentration in the air inducted into each cylinder was measured and the EGR gas mass flow was calculated. The EGR rate in each cylinder and its tendency vary depending on the engine operating conditions. These results suggest that it is difficult to achieve a uniform EGR distribution under different engine operating conditions.

Figure 3 shows the EGR rate in each cylinder for different average EGR rates. The EGR rate is increased assuming that heavy EGR is applied. The variance in the EGR rate becomes larger as the average EGR rate increases. These results suggest that if heavy EGR is applied with a conventional EGR system, the EGR rate variance would become unacceptably large. If the EGR gas concentration difference in each cylinder reached this level, the cylinder with a large EGR gas concentration would cause unstable combustion. That would generate large emissions and also deteriorate drivability. Accordingly, it would be difficult to apply heavy EGR with a conventional EGR system. Therefore, it is necessary to develop a robust EGR system that makes it possible to achieve a uniform EGR distribution under different engine operating conditions even when heavy EGR is applied.

However, time-consuming experimental research has so far been the only way to evaluate the EGR distribution in the intake system. Considerable time and cost are needed to study and de-

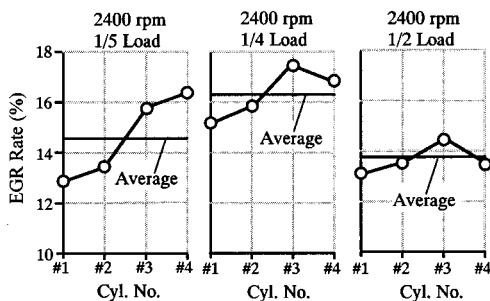


Fig. 2 Influence of engine operating conditions on EGR distribution

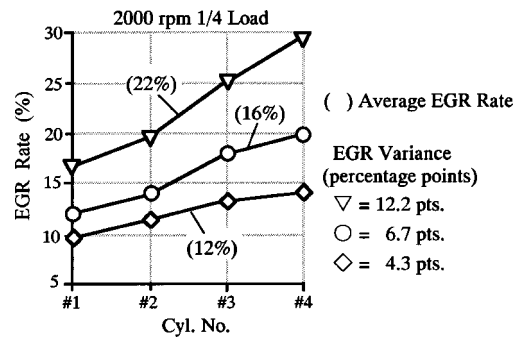


Fig. 3 Influence of average EGR rate on EGR variance

velop a heavy EGR system. Therefore, as a first step, CFD simulation was applied to predict the EGR distribution.

Exhaust Gas Recirculation (EGR) Distribution Prediction With Pulsation Flow Simulation

Pulsation Flow Simulation Method. When an engine is running, the gas exchange in the cylinders takes place intermittently. The gas flow in the collector and intake manifold is greatly affected by intake pulsations. Therefore, it is necessary to simulate the EGR gas flow and its diffusion under pulsation flow in order to predict the EGR distribution accurately, [7]. That requires a model of the entire engine system, including the intake and exhaust systems. However, it would be impractical to simulate the gas flow in the entire engine system with a three-dimensional model. Therefore, a pulsation flow simulation method was used, in which a one-dimensional gas exchange calculation and a three-dimensional exhaust gas flow calculation were combined.

Figure 4 shows an outline of the pulsation flow simulation method. In the pulsation simulation, the engine system model for calculating pulsation flow caused by the gas exchange process is one-dimensional. In the one-dimensional calculation, the entire engine system model is described as a combination of one-dimensional pipes and dimensionless containers. In the three-dimensional calculation, an intake system model that includes the throttle body, collector and intake manifold is used. First, a one-dimensional gas exchange simulation is run to obtain velocity, pressure, temperature, and density data for one cycle (720 crank angle degrees) that are necessary for a three-dimensional calculation. Next, the three-dimensional calculation is executed using the results of the one-dimensional calculation as the boundary conditions. It is possible to run both the one-dimensional gas exchange calculation and the three-dimensional flow calculation together at one time as shown in Fig. 4. The difference between the separate calculation method and the combined calculation method is neg-

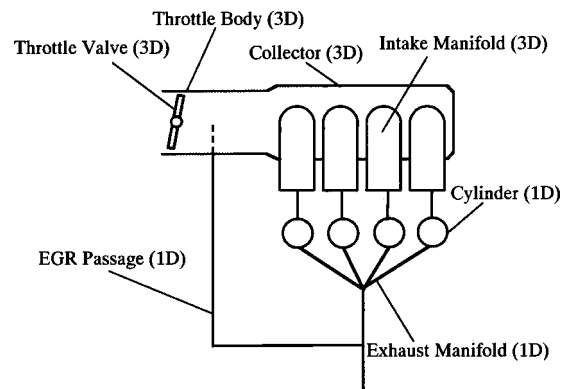


Fig. 4 Schematic diagram of pulsation flow simulation method

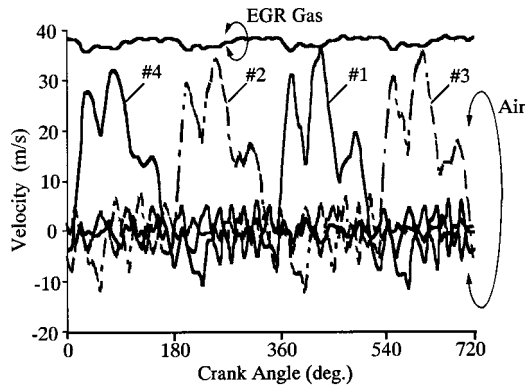


Fig. 5 One-dimensional gas exchange calculation results

ligible. Therefore, in this study, the separate calculation method was used, since it is easier to analyze both the one-dimensional and three-dimensional results in detail.

One-Dimensional Gas Exchange Calculation. An in-house gas exchange calculation code has been adopted for performing one-dimensional calculations, [8,9]. The data needed for the calculations are the engine specifications, intake and exhaust system dimensions and engine operating conditions. Figure 5 shows an example of the one-dimensional gas exchange calculation results. The velocities calculated at the EGR gas inlet and outlet of the intake manifold for one cycle are presented. Air was introduced into each cylinder in turn according to the ignition timing. Yet the EGR gas velocities are almost stable for the entire cycle, though some effect of the pulsation flow can be observed. These velocity data were used in the three-dimensional calculation as the boundary conditions.

Three-Dimensional Gas Flow Calculation. The general STAR-CD code was used for the three-dimensional calculation, [10]. Table 1 shows the flow analysis conditions. The flow was assumed to be compressible. The conservation equations of mass, momentum and energy, and the turbulence energy and its dissipation (κ - ϵ turbulence model) were used. The law of the wall was used at the wall boundary. The differencing scheme was upwind.

Figure 6 shows the computational grids and the boundary conditions. The computational grids consist of the collector and intake manifold, including the intake plenum, throttle body, throttle valve and the EGR gas introduction port. The number of grid points depends on the intake system configuration and it is generally between 150,000–200,000. The intake plenum is used for making the calculations stable. Boundary conditions are set at the inlet of the intake plenum, the inlet of the EGR gas introduction port and at the four outlets of the intake manifold runners.

Unsteady flow that varied with the crank angle degree was simulated using the one-dimensional gas exchange calculation results as the boundary conditions (Fig. 5). In this calculation, the EGR gas was marked to distinguish it from the fresh air by using a scalar definition as its physical properties. The EGR rate of each cylinder was calculated at the four outlets of the intake manifold runners by Eq. (1). The EGR gas mass of each cylinder was cal-

Table 1 Flow analysis conditions

| Program | STAR-CD |
|---------------------|--|
| Flow | Compressible Standard K- ϵ |
| Wall Boundary | Law of the Wall |
| Differencing Scheme | Upwind |

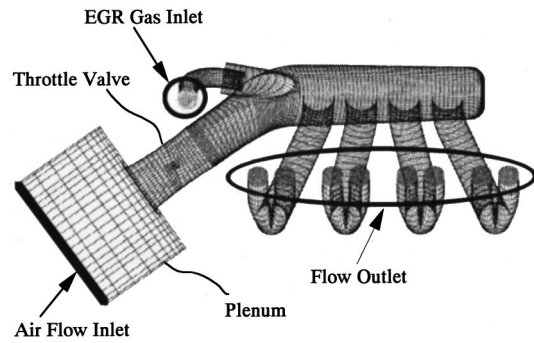


Fig. 6 Computational grid and boundary conditions

culated by multiplying the EGR gas concentration, the gas mass flow rate and a calculation time step at each crank angle, and totaling the results for one cycle. Specifically, the following expressions were used to calculate the EGR gas mass and the air mass.

$$M_{\text{EGR}}(\text{cyl.}\#) = \sum_{i=1,720} [C_{\text{EGR}}(\text{cyl.}\#) \cdot M_{\text{gas}}(\text{cyl.}\#) \cdot \Delta t] \quad (2)$$

$$M_{\text{air}}(\text{cyl.}\#) = \sum_{i=1,720} [(1 - C_{\text{EGR}}(\text{cyl.}\#)) \cdot M_{\text{gas}}(\text{cyl.}\#) \cdot \Delta t] \quad (3)$$

where C_{EGR} is the EGR gas concentration, M_{gas} is the total gas mass flow rate and Δt is the calculation time step (equivalent to one crank angle degree).

At the start of the calculation, namely, in the initial condition, there is no EGR gas in the intake manifold. Therefore, a certain amount of time is required for the EGR gas to diffuse through the intake manifold. In this case, eight to ten calculation cycles were needed before the results converged to show cycle-to-cycle stability, though it depended on the number of grid points and engine operating conditions. One of the factors influencing the calculation accuracy is the boundary conditions obtained by the one-dimensional gas exchange calculation. It is also important to model the throttle valve with a fine grid to prevent calculation divergence.

Figure 7 shows examples of the calculated results for the EGR gas concentration distribution. In this calculation, the EGR gas was introduced upstream of the collector. It is seen that the EGR

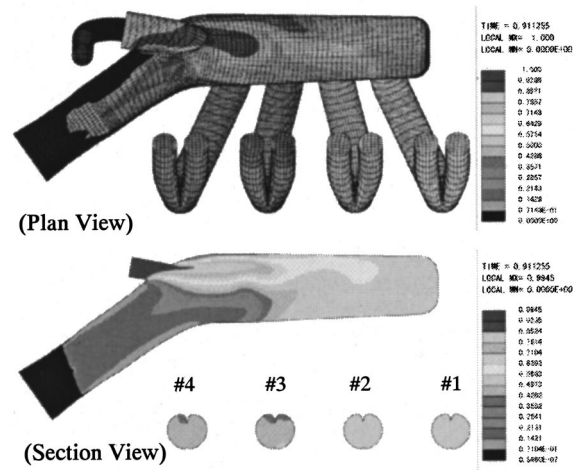


Fig. 7 Calculated results for EGR gas concentration distribution

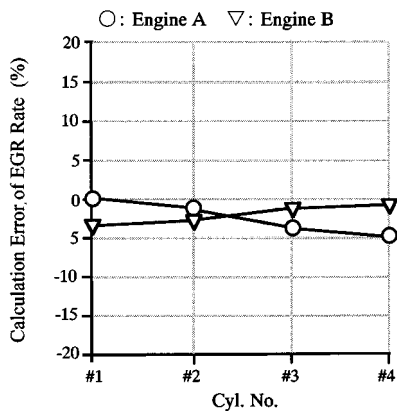


Fig. 8 Calculation error of EGR rate compared with experimental data

gas mixes with the fresh intake air coming from upstream of the throttle valve and diffuses in the collector. The EGR gas concentration decreases as the gas flows downstream.

An experiment was then conducted to validate the EGR rate predicted by the pulsation flow simulation method. To investigate the effect of the engine specifications, two types of four-cylinder engine were used. Figure 8 shows the calculation error of the EGR rate. The calculation error was calculated by

$$\text{ERROR}_{\text{EGR}} = (\text{EGRR}_{\text{pre}} - \text{EGRR}_{\text{mea}}) / \text{EGRR}_{\text{mea}} \cdot 100 \quad (4)$$

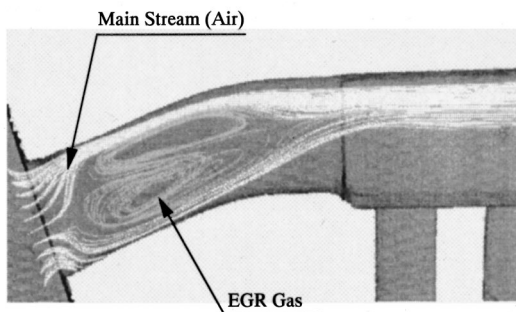


Fig. 9 Gas flow trace lines

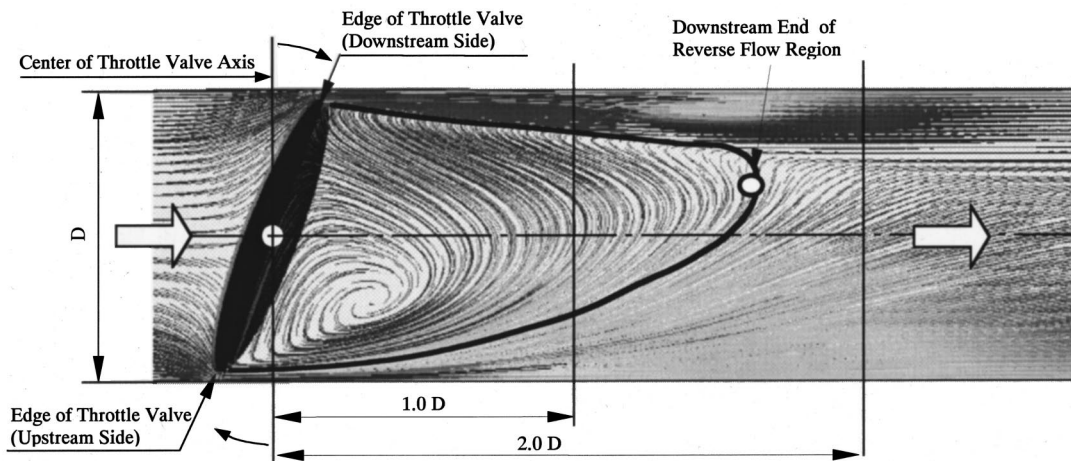


Fig. 10 Section view of reverse flow region

where $\text{ERROR}_{\text{EGR}}$ is the calculation error of the EGR rate, EGRR_{pre} is the predicted EGR rate, and EGRR_{mea} is the measured EGR rate. The calculation error was within 3–5% in both cases, though the predicted EGR rate was a little smaller than the measured one. These results confirmed the validity of the pulsation flow simulation. It is possible to predict the EGR rate quantitatively with this method.

Physical Phenomena in the Intake System and Their Effect on Exhaust Gas Recirculation (EGR) Distribution Characteristics

Gas Flow in the Intake System. After validating the EGR rate predicted with the pulsation flow simulation method, physical phenomena in the intake system that influence the EGR distribution were examined. As noted earlier, the EGR gas is introduced downstream of the throttle valve in conventional EGR systems (Fig. 1). In that case, the EGR rate variance in each cylinder and its tendency vary depending on the engine operating conditions (Fig. 2). To analyze this factor, physical phenomena in the intake system were investigated in detail.

Figure 9 shows gas flow trace lines in the throttle body obtained by the steady flow simulation. There is a reverse flow region downstream of the throttle valve. In this region, the fresh intake air is recirculating. In conventional EGR systems, the EGR gas would be induced into the reverse flow region and would show complex flow characteristics in this region under the strong influence of the recirculating flow. It is assumed that the intake flow in the throttle body has a large effect on the EGR distribution downstream.

A detailed analysis was then made of the reverse flow region. First, a steady-flow simulation using a simple throttle body model with a straight pipe was run to study the geometric features of the reverse flow region. A pulsation flow simulation was then conducted to analyze the effect of the engine operation conditions.

Reverse Flow Region Downstream of Throttle Valve. Figure 10 shows the steady-flow simulation results obtained with the simplified throttle body model. The gas velocities are shown in a side view section. The reverse flow region on the downstream side of the throttle valve edge is larger than that on the upstream side. The vortex center is located on the upstream side of the throttle valve edge (lower side in Fig. 10). Figure 11 shows the reverse flow region in a cubic form. The region of the computational grid having an upstream flow velocity was selected to show the reverse flow region.

The shape of the reverse flow region was analyzed for different throttle body sizes and engine operating conditions. In all cases,

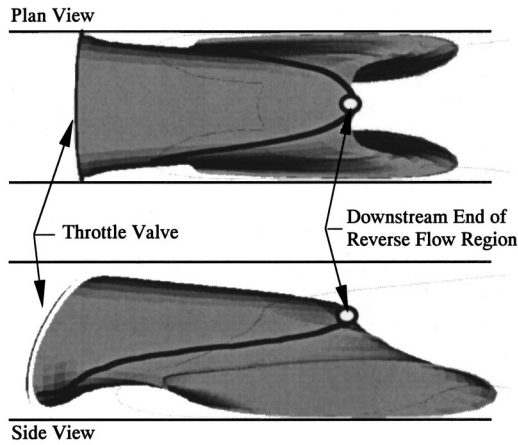


Fig. 11 Plan view and side view of reverse flow region

the reverse flow region was always just downstream of the throttle valve. Schematically, the location of the reverse flow region was similar for different throttle body sizes. The shape and size of the reverse flow region changed depending on the opening angle of the throttle valve and the gas mass flow rate. Figure 12 compares reverse flow regions for different engine loads. The reverse flow region became larger under a low load condition with a small throttle valve opening angle.

The size of the reverse flow region was then investigated quantitatively. It was found that the length between the throttle valve and the downstream end of the reverse flow region was similar for different throttle body sizes. The length was between 1.3–1.8 times the throttle body diameter (D), though the shape of the reverse flow region varied depending on the throttle valve opening angle.

In a conventional EGR system, the EGR gas is introduced downstream of the throttle valve. As explained above, the size of the reverse flow region varies depending on the engine operating conditions. In some cases, the EGR gas would be introduced into the reverse flow region and, in other cases, it would be introduced outside the region. It is assumed that the EGR gas flow in the intake system and the EGR distribution characteristics are significantly affected by changes in the reverse flow region.

Effect of EGR Gas Introduction Location on EGR Gas Flow. The effect of the EGR gas introduction location on the EGR gas flow was examined in detail. First, the EGR gas flow was analyzed when the EGR gas was introduced outside the reverse flow region. Figures 13 and 14 show the EGR gas trace lines

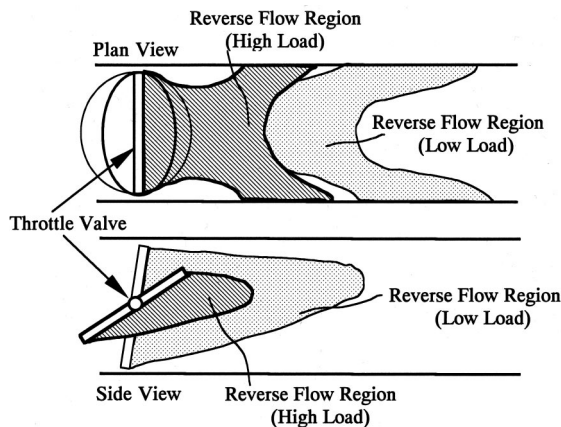


Fig. 12 Effect of throttle opening angle on reverse flow region

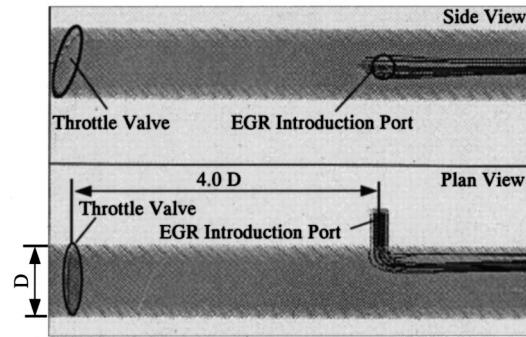


Fig. 13 Trace lines of EGR gas flow (position of EGR introduction port: $4.0 D$)

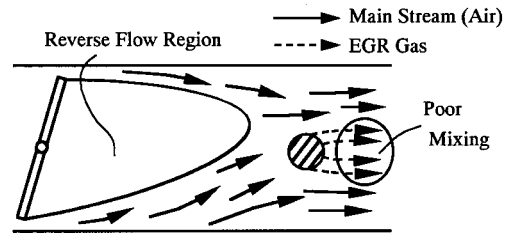


Fig. 14 Schematic gas flow pattern (EGR gas introduced outside reverse flow region)

and the schematic flow pattern, respectively. The EGR gas was introduced horizontally to the throttle valve axis at the center. The location of the EGR introduction pipe was $4.0 D$ downstream.

In this case, the EGR gas is caught between the upper and lower main streams of fresh air, and there is not enough turbulence for the EGR gas and fresh air to mix. As a result, the EGR gas is quickly carried away toward the collector before it diffuses sufficiently. This results in poor mixing and the EGR gas is concentrated in some parts of the collector. Therefore, it is assumed that the EGR rate to each cylinder would differ substantially.

The EGR gas flow was then analyzed when the EGR gas was introduced into the reverse flow region. Figures 15 and 16 show the EGR gas trace lines and the schematic flow pattern, respectively. Again, the EGR gas was introduced horizontally to the throttle valve axis at the center. The location of the EGR introduction pipe was $1.0 D$ downstream of the throttle valve. In this case, the EGR gas circulates in the reverse flow region, allowing more opportunity for it to mix with the fresh air. However, as explained earlier, the size and shape of the reverse flow region vary depending on the engine operating conditions. That means the mixing rate of the EGR gas and fresh air also varies accordingly. These

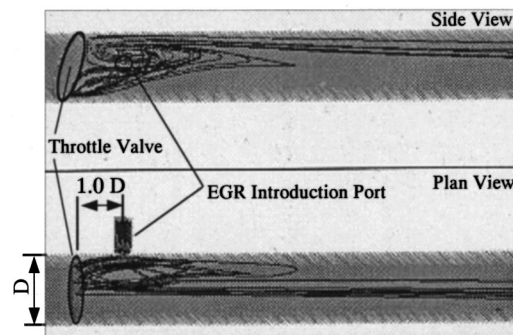


Fig. 15 Trace lines of EGR gas flow (position of EGR introduction port: $1.0 D$)

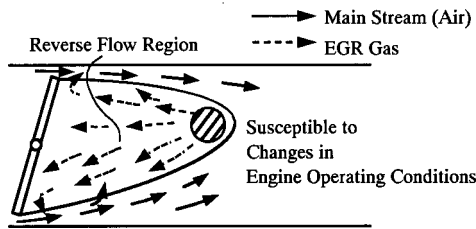


Fig. 16 Schematic gas flow pattern (EGR introduced in reverse flow region)

results explain why the EGR rate variance in each cylinder and its tendency vary depending on the engine operating conditions as shown in Fig. 2. Conventional EGR systems are thus not robust enough. It is difficult to achieve a uniform EGR distribution under a wide range of engine operating conditions where heavy EGR is applied, because the degree of mixing is greatly dependent on the reverse flow region.

New Exhaust Gas Recirculation (EGR) System for Uniform EGR Distribution

Lower Side Blow-Type EGR System. New EGR systems were investigated based on the foregoing analytical results. The key factor was to develop an EGR system that would not be susceptible to the reverse flow region even though the EGR gas was still introduced downstream of the throttle body. A lower side blow-type EGR system has been developed by applying the knowledge obtained about the gas flow in the throttle body. Figure 17 shows the location of the EGR introduction ports and schematic gas flow pattern. The EGR gas is introduced on the lower side of the throttle body (upstream edge side of the throttle valve), not in the center. As indicated in the figure, two EGR introduction ports are facing each other. As shown in Fig. 14, the main stream of the fresh air coming from the upstream edge of the throttle valve progresses toward the upper side. The lower side blow-type EGR system makes effective use of this upward stream. The EGR gas coming from both sides of an EGR introduction port uses the momentum of the upward main stream to create a twin-vortex flow. This twin-vortex flow enhances the mixing of the EGR gas and fresh air to achieve a uniform EGR distribution even when heavy EGR is applied.

Figure 18 shows the EGR rate in each cylinder with the lower side blow-type EGR system. Both the calculated and experimental results are shown. The EGR rate variance in each cylinder was much smaller than with the conventional EGR system (Fig. 3), especially when the EGR rate was increased to about 30%. With the lower side blow-type EGR system, a uniform EGR distribution was obtained under most of the engine operating conditions

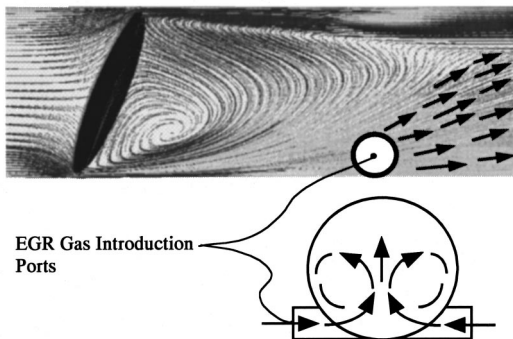


Fig. 17 EGR gas introduction ports and gas flow pattern of lower side blow-type EGR system

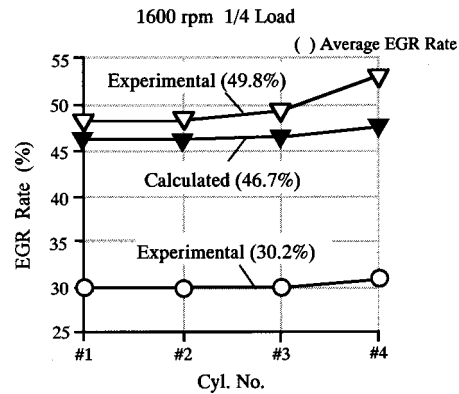


Fig. 18 EGR rates with lower side blow-type EGR system

with a small EGR rate. However, the EGR rate variance in each cylinder became as large as 5% when a large EGR rate such as 50% was applied. It is assumed that the direction of the upward flow due to the main streams of the fresh air was still slightly influenced by the throttle valve opening angle.

There is still room to improve the lower side blow-type EGR system by optimizing the location and size of the EGR introduction ports. However, one disadvantage of this EGR system is that the momentum of the main gas flow coming from the downstream side free edge of the throttle valve is not used for mixing energy. It is concluded that it is possible to achieve a uniform EGR distribution with a small EGR rate but difficult to do so under heavy EGR conditions with this lower side blow-type EGR system.

Spiral Blow-Type EGR System. As explained above, EGR distribution characteristics are substantially influenced by the reverse flow region generated downstream of the throttle valve. Based on the analytical data presented here, it is concluded that the requirements for achieving a uniform EGR distribution under a wide range of engine operating condition are as follows:

- to avoid interference with the reverse flow region (enhance robustness),
- to increase the travel time of the EGR gas from its introduction port to the intake manifold (enhance the mixing effect), and
- to mix the EGR gas with both main streams of fresh air (make effective use of the momentum and turbulence of the main streams).

One practical way to meet these requirements is to adopt a spiral blow-type EGR system like that outlined in Fig. 19. One EGR gas introduction port each is located just at the rear of the downstream and upstream side free ends of the throttle valve. The two introduction ports are opened in a cross-flow (or counter-flow) manner in opposite directions. Each port is connected to the throttle body tangentially and EGR gas flows into the passage in a spiral manner. The cross-sectional shape of each port is elongated along the direction of the main streams of fresh air to avoid interference with the reverse flow region. The mixing of the EGR gas and fresh air is thus enhanced by creating a spiral flow.

The EGR gas flows into both main streams of fresh air in a tangential manner, creating a strong spiral flow in the downstream direction by using the momentum of the main streams. Each introduction port is inclined downstream so as to form a predetermined angle θ (lead angle with respect to the fresh air flow direction). The optimum lead angle θ depends on the intake system configuration and it is generally between 5–15°. The port is extended along a line tangent to the circular cross section of the throttle body. This extended pipe serves as a guide for the main stream of the gas, causing it to flow in a spiral manner. Both the lead angle and extended port design strengthen the spiral flow. The EGR gas mixes with the fresh air using this spiral flow gen-

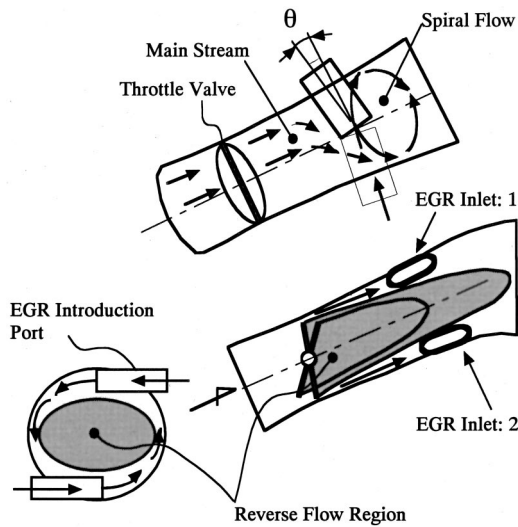


Fig. 19 Schematic diagram of spiral blow-type EGR system

erated intentionally. In addition to that, the EGR gas travels a greater distance along the cylindrical wall surface toward the collector than in a conventional EGR system. This longer distance allows more time for the EGR gas to mix with the fresh air. The EGR gas diffuses from the wall surface toward the center of the collector, achieving a uniform EGR distribution by the time the gas goes into the collector. As a result, the EGR rate in each cylinder becomes equal. Figure 20 shows the trace lines of the EGR gas flow. It is clearly seen that the EGR gas flows into the collector in a spiral manner.

Figure 21 shows the EGR rate in each cylinder with this spiral blow-type EGR system. Both the calculated and experimental results are shown. The EGR rate difference was much smaller than

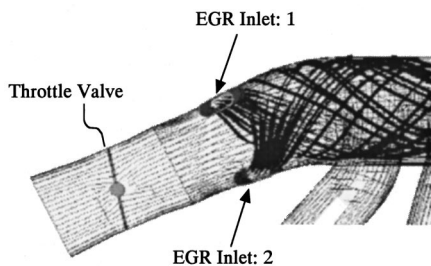


Fig. 20 Trace lines of EGR gas flow with spiral blow-type EGR system

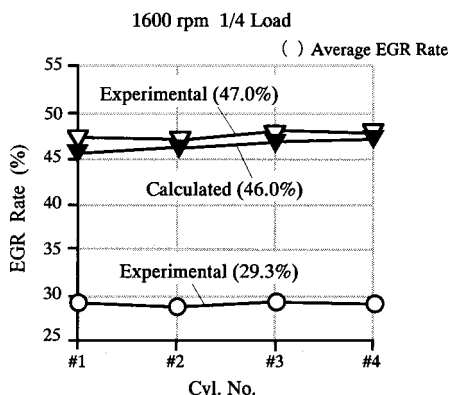


Fig. 21 EGR rates with spiral blow-type EGR system

| | Guide | Inlet Shape | Cross-Sectional View |
|--------|---------------|--------------|---------------------------|
| Base | with Guide | 15mm 10mm | |
| Case 1 | without Guide | | EGR Gas Introduction Port |
| Case 2 | without Guide | 12mm 8mm | |

Fig. 22 Shapes of EGR gas introduction ports

that seen for the conventional EGR system (Fig. 3), especially when the EGR rate was increased. With the spiral blow-type EGR system, a uniform EGR distribution is obtained under a wide range of engine operating conditions even when a large EGR rate is applied.

Application of Spiral Blow-Type Exhaust Gas Recirculation (EGR) System to Nissan QR Engine

As seen in the preceding section, the spiral blow-type EGR system makes it possible to achieve a uniform EGR distribution for a wide range of engine operating conditions, even when heavy EGR is applied. As the next step, this EGR system was modified for application to the Nissan QR engine. There were two engineering tasks involved in that application. One was to improve the discharge coefficient of the intake system and the other was to reduce the production cost.

As shown in Fig. 19, in the spiral blow-type EGR system, the ports for introducing EGR gas are extended into the throttle body to intensify the spiral flow. These extended ports generate pressure loss in the throttle body and reduce the discharge coefficient. That would cause volumetric efficiency to decline, thereby reducing engine power. Therefore, the discharge coefficient must be improved. One simple way would be to remove the guide of the EGR gas introduction ports. However, without a port guide, it is assumed that the spiral flow would become weak and the mixing effect would be smaller. It is necessary to enhance the spiral flow without using a port guide. Therefore, the cross-sectional area of the EGR introduction port was reduced to increase the gas flow velocity.

Figure 22 shows the shapes of the EGR gas introduction ports that were examined. Two modified types without a port guide were compared with the original type with the port guide. Case 1 had the same sectional area and the guide was removed. In case 2, the sectional area was reduced. Figure 23 shows the calculated EGR rates. As expected, with case 1, the EGR rate variance was increased compared with the base type, since the mixing effect was smaller. However, with case 2, the level of EGR rate variance was similar to that of the original type. These results confirmed that it is possible to achieve a uniform EGR distribution with the spiral flow-type EGR system without port guides, if the size and shape of the port cross section is optimized.

The possibility of reducing the production cost was then investigated. As shown in Fig. 1, conventional EGR systems have only one EGR introduction port. By contrast, the spiral blow-type EGR system requires two ports, one each on the upper and lower sides, as shown in Fig. 19. The use of two ports would increase the production cost. In addition to that, there are layout limitations around the throttle body and it would be difficult to install two ports in some engine types. To reduce the production cost, the number of ports should be reduced to one.

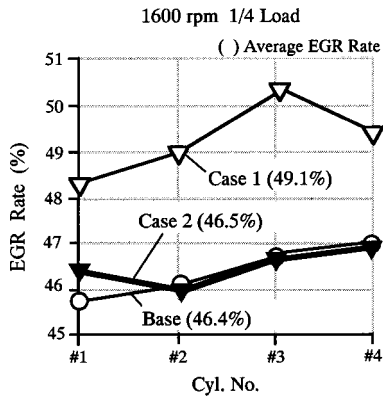


Fig. 23 Effect of EGR gas introduction port shape on EGR rate (calculated)

Therefore, the effect of the location of the EGR gas introduction port was examined. Figure 24 shows the port locations that were investigated. Both upper and lower side locations were analyzed. In the case of one port, the port location and the lead angle θ (Fig. 19) were optimized. Figure 25 shows the calculated EGR rates. With an upper side port location, the EGR rate variance increased compared with the base type. As shown in Fig. 10, the cross-sectional area where the upper main flow of air passes is smaller than that of the lower side. The velocity of the main air flow on the upper side is larger than that on the lower side. Therefore, the spiral flow generated by the EGR gas flow weakens, reducing the mixing effect. For that reason, the EGR rate variance increased. On the other hand, with the lower side port location, the EGR rate variance was at the same level as that of the base type,

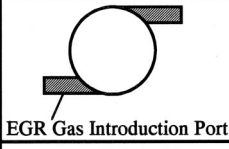

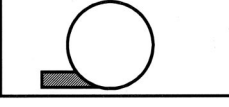
| | Inlet Port | Cross-Sectional View |
|-------|-----------------|---|
| Base | Upper and Lower |  |
| Upper | Upper |  |
| Lower | Lower |  |

Fig. 24 Location of EGR gas introduction port

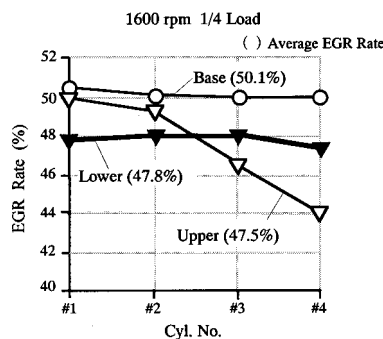


Fig. 25 Effect of EGR gas introduction port location on EGR rate (calculated)

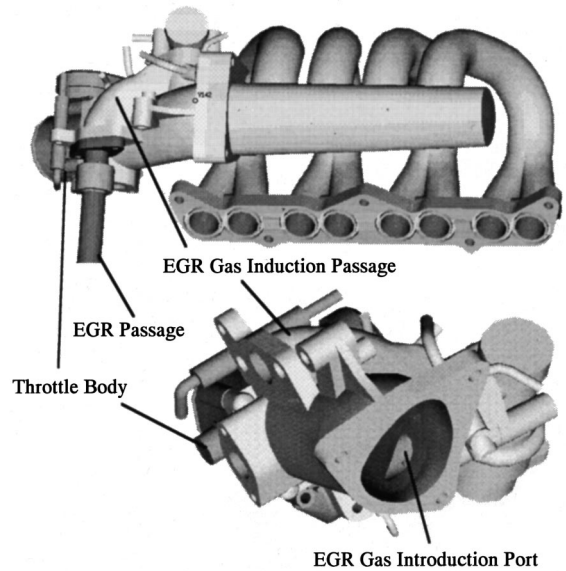


Fig. 26 Spiral blow-type EGR system applied to Nissan QR engine

though the EGR rate in the #4 cylinder was a little smaller than that of the other cylinders. As explained above, the velocity of the main air flow on the lower side is smaller than that on the upper side. It is possible to generate sufficient spiral flow with just one EGR gas introduction port. These results confirmed a uniform EGR distribution can be achieved with the spiral flow-type EGR system having only one EGR gas introduction port, if the port location and lead angle θ (Fig. 19) are optimized.

Figure 26 shows the spiral blow-type EGR system applied to the Nissan QR Engine. The EGR gas introduction passage is attached to the throttle body. The single EGR introduction port is connected to the lower side of the throttle body tangentially. Therefore, the EGR gas flows into the throttle body in a spiral manner.

Figure 27 shows the EGR rate variance obtained experimentally with this system under different engine operating conditions. The EGR rate variance indicates the difference between the maximum and minimum EGR rates among the four cylinders. The variance was less than three percentage points under all engine operating conditions with the application of heavy EGR. This result demonstrates that the spiral blow-type EGR system makes it possible to

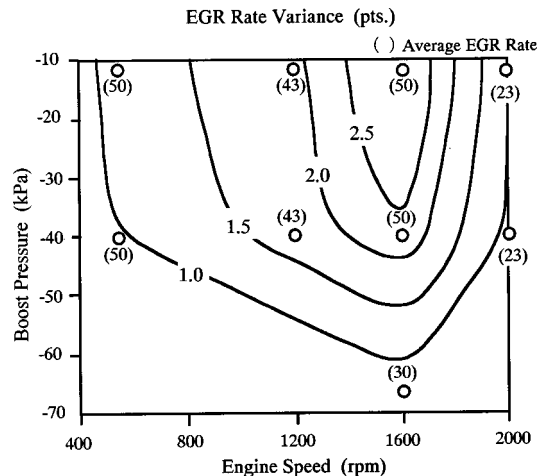


Fig. 27 EGR rate variance (experimental)

achieve a uniform EGR distribution regardless of the engine operating conditions even when heavy EGR is applied.

This spiral blow-type EGR system is robust against the size and shape of the intake system. Therefore, it is possible to apply this technology to many types of engine with little optimization work required. As one example, this spiral blow-type EGR system has been applied to small diesel engines. Variations of this spiral blow-type EGR system for application to different engines are now under development.

Moreover, it is now possible to predict the EGR distribution with the pulsation flow simulation method that combines a one-dimensional gas exchange calculation and a three-dimensional gas flow calculation. Much of the development work for EGR systems can now be done by simulation, thereby greatly reducing the development lead time and cost.

In this study, pulsation flow simulation was used to analyze the EGR gas flow. It is also possible to apply this pulsation flow simulation method to an analysis of other gas flows, such as blow-by gas from the cylinder and purge gas from the canister. Either gas must be distributed uniformly in the intake system. This method is an effective tool for analyzing this type of intake gas flow. In future work, it will be applied for analyzing these other intake gas flows.

Conclusion

A pulsation flow simulation method that combines a one-dimensional gas exchange calculation and a three-dimensional gas flow simulation was used to investigate the EGR gas flow in the intake system. This analysis was done with the aim of improving the EGR distribution and the following results were obtained in this study.

1. With this analysis method, the EGR rate in each cylinder was accurately predicated to within 3–5%.
2. When the EGR gas was introduced downstream of the throttle valve, the distribution was significantly influenced by the engine operating conditions. This was due to the influence of the reverse flow region that formed downstream of the throttle valve.
3. Simulation and experimental results confirmed that the EGR distribution was improved by a newly developed mixing system that uses a spiral flow to mix the fresh air and EGR gas. As a result of adopting this system, a uniform EGR distribution is obtained, regardless of the engine operating conditions.
4. This spiral blow-type EGR system has been applied to a low-emission vehicle (LEV) put on the Japanese market.

Acknowledgments

The author would like to thank all of the people who contributed to the development of the new EGR system and to the writing of this paper.

Nomenclature

| | |
|-----------------------------|--|
| C_{EGR} | = EGR gas concentration |
| D | = throttle body diameter |
| EGRR | = EGR rate |
| EGRR_{mea} | = measured EGR rate |
| EGRR_{pre} | = predicted EGR rate |
| $\text{ERROR}_{\text{EGR}}$ | = calculation error of EGR rate |
| M_{air} | = air mass flow rate |
| M_{EGR} | = EGR gas mass flow rate |
| M_{gas} | = total gas mass flow rate ($M_{\text{air}} + M_{\text{EGR}}$) |
| θ | = lead angle of EGR introduction port |

References

- [1] Kimura, S., Muranaka, S., and Aoki, O., 1999, "Possibility of Attaining High-Efficiency, Ultra-Clean Diesel Engines With Low-Temperature Premixed Combustion," *Journal of JSAE*, **53**(4), pp. 17–23 (in Japanese with English abstract).
- [2] Takagi, Y., Itoh, T., Muranaka, S., Iiyama, A., Iwakiri, Y., Urushihara, T., and Naitoh, K., 1998, "Simultaneous Attainment of Low Fuel Consumption, High Output Power and Low Exhaust Emissions in Direct Injection SI Engines," SAE Paper 980149.
- [3] Mamiya, N., and Chuubachi, M., 1997, "Application of Three-Dimensional CAD System to Engine Development," *Journal of JSAE*, **51**(12), pp. 50–56 (in Japanese with English abstract).
- [4] Yoshizawa, K., Takeyama, S., Sakai, E., and Tanzawa, K., 1997, "Numerical Analysis of Exhaust Gas Flow during the Gas Exchange Process and Design Optimization," *Proceedings of the JSAE Annual Autumn Meeting*, **975**, pp. 129–132 (in Japanese with English abstract).
- [5] Yoshizawa, K., Mori, K., Arai, K., and Iiyama, A., 1999, "Numerical Analysis of Exhaust Gas Flow and Its Application for Lambda Control Improvement," *Proceedings of the ASME Technical Conference*, ICE-Vol. 33-3, pp. 151–159.
- [6] Ahn, H., Cho, K., and Choi, J., 1999, "Analysis of EGR Distribution Characteristics in Intake Manifolds and Plenum Chamber With 1-D and 3-D Hybrid Calculations," JSAE and KSAE ICE Symposium.
- [7] Bolton, B., Takenaka, Y., Aoyagi, Y., and Joko, I., 1993, "Analysis of Intake Manifold Flow in an Inline 6-Cylinder DI Diesel Engine," *Proceedings of the JSAE Annual Spring Meeting*, **933**, pp. 159–162 (in Japanese with English abstract).
- [8] Takeyama, S., Ishizawa, S., Yoshikawa, Y., and Takagi, Y., 1987, "Gas Exchange Simulation Model for Improving Charging Efficiency of 4-Valve Internal Combustion Engine," *I.M.E. The First Conference of Computers in Engine Technology*, pp. 123–129.
- [9] Kimura, S., and Yokoyama, T., 1994, "Reduction of Intake Pulsation Noise by Reducing Noise Sources," *Proceedings of the JSAE Annual Autumn Meeting* (in Japanese with English abstract).
- [10] STAR-CD Version 3.05 Manual, 1998.

Energy and Exergy Analyses of the Pulse Detonation Engine

T. E. Hutchins

M. Metghalchi

e-mail: metghal@coe.neu.edu

Mechanical, Industrial and Manufacturing
Engineering Department,
Northeastern University,
Boston, MA 02115

Energy and exergy analyses have been performed on a pulse detonation engine. A pulse detonation engine is a promising new engine, which uses a detonation wave instead of a deflagration wave for the combustion process. The high-speed supersonic combustion wave reduces overall combustion duration resulting in an nearly constant volume energy release process compared to the constant pressure process of gas turbine engines. Gas mixture in a pulse detonation engine has been modeled to execute the Humphrey cycle. The cycle includes four processes: isentropic compression, constant volume combustion, isentropic expansion, and isobaric compression. Working fluid is a fuel-air mixture for unburned gases and products of combustion for burned gases. Different fuels such as methane and JP10 have been used. It is assumed that burned gases are in chemical equilibrium states. Both thermal efficiency and effectiveness (exergetic efficiency) have been calculated for the pulse detonation engine and simple gas turbine engine. Comparison shows that for the same pressure ratio pulse detonation engine has better efficiency and effectiveness than the gas turbine system. [DOI: 10.1115/1.1610015]

Introduction

Pulse Detonation Engines (PDEs) have been predicted to be more efficient than current aeronautical propulsion systems. They potentially represent a revolutionary propulsion technology that offers advantages in hardware simplicity, operations, and reliability, [1]. PDE's show performance advantages in both the subsonic and supersonic flight regimes, [2]. PDE's are unsteady propulsion devices. They use detonation waves, which allow the chemical energy of the fuel used to be released in a far more rapid manner, [3]. The combustion chamber is filled with a fuel/air mixture and detonated. A detonation wave propagates through the chamber creating high pressures that produce thrust. Products of combustion are exhausted and the cycle starts again. Either running this cycle at high frequencies or coordinating multiple combustion chambers can produce quasi-steady thrust, [4].

PDE's have been sought out by many different organizations. The Navy has shown great interest in the engine. The Multi-disciplinary, Multi-University Research Initiation (MURI), which is sponsored by the Office of Naval Research, has completed research on many of the issues facing the PDE, [4]. The Air Force has also shown interest in the engine. A recent paper summarized their progress towards developing a kerosene-based PDE, [5].

Many design challenges lie ahead for researchers in the PDE area. Four major areas need design considerations for the PDE to be a success, [1]. The first design challenge is an air intake that will perform well over the engine's full range of Mach numbers. A mixing chamber must be designed to provide the fuel/air mixture to the combustion chamber under conditions favorable to detonation. A third consideration is an inlet and injection system that provides reproducible detonations in multiple chambers. Finally, a nozzle must be designed to optimize the thrust provided from the unsteady engine.

Another major hurdle, which needs to be crossed by PDE researchers, is to show that 75–100 Hz required to perform well at Mach 1.2 to 3 can be achieved. Experimental data showing 100 Hz has been recorded. However, the experiment did not always produce a detonation wave causing the shock tube to become hot and suspend the test, [3].

Previous Pulse Detonation Engine (PDE) Research. A gen-

eral introduction to PDEs can be found in Bussing and Pappas's [6] article in the AIAA journal. They give a description of the basic ideas behind both PDEs and detonation waves. A constant specific heat efficiency model was used to show that the Humphrey cycle has an advantage over the Brayton cycle. The Humphrey cycle is used to model the constant volume combustion process present in PDE's. Finally, a computational fluid dynamics (CFD) model was constructed to study the unsteady operation PDEs.

An initial experiment, involving prototype PDEs, was conducted by Bussing et al. [7] Results including wall pressure history, thrust force histories, detonation wave velocities, and deflagration to detonation transition (DDT) distances. DDT is the distance necessary for transition from deflagration to detonation combustion wave. This parameter is dependant on many different characteristics of the shock tube including tube diameter and wall texture.

Multiple combustion tubes may be a viable way to balance out the unsteady thrust produced by PDE combustion chambers. The basic idea behind using multiple tubes is to isolate the steady-state operation of the air intake and mixing chamber from the unsteady operation of the combustion chamber. Tubes are bundled together and fired in an alternating manner. Bussing [8] has addressed one possible method of coupling multiple combustion tubes. Some of the benefits of his design are high-cycle frequency and lower inlet loss.

Bratkovich and Bussing [9] developed a PDE performance model. They used detail calculations to analyze all the components necessary for a PDE. A comparison was made to CFD calculations as well as experiment results. They were able to predict the wall pressure history within a reasonable amount in comparison to the experimental results.

For detonation to occur at all, the detonation properties of hydrocarbon fuels must be understood. Ting et al. [10] conducted experiments on the detonation abilities of propane. Parameters such as wave velocity, pressure wall history, and deflagration to detonation transition (DDT) distances were measured. Shchelkin spirals were used in the tubes to help induce detonation. This metal coil helps create a turbulent flow through the tube, which helps to create a detonation wave. They found that using obstacles such as Shchelkin spirals helped to create shorter DDT. In addition, the article shows that small tube diameter leads to shorter DDT. Another important result was that a mixture of propane and

Contributed by the Fuels and Combustion Division of THE AMERICAN SOCIETY OF MECHANICAL ENGINEERS for publication in the ASME JOURNAL OF ENGINEERING FOR GAS TURBINES AND POWER. Manuscript received by the F&C Division May 2002; final revision received Aug. 2002. Associate Editor: S. Gollahalli.

oxygen is capable of detonating a mixture of propane and air. This means that using a driver of fuel/oxygen would work to accomplish shorter DDT.

Williams et al. [11] studied the initiation of detonation waves. In particular, JP10 ($C_{10}H_{16}$) fuel was analyzed in detail with respect to PDEs. JP10 is widely used in volume-limited combustion chambers. The authors concluded that JP10 breaks down to 176 reactions of 36 different species. A chemical-kinetic model was developed in order to predict ignition times for PDEs. JP10 ignition is a process of decomposition to smaller hydrocarbons following by ignition of the resulting products.

One of the major design issues is the frequency capability of the engine. Bussing et al. [12] determined the basic parameters that govern the cycle time. The fill time was shown to be the longest portion of the cycle. This highlighted the need for an efficient valve system to keep the fill time at a minimum. They also determined the theoretical frequency scaling laws that go along with the PDE.

Rockets have also been considered as an application for PDEs. The simple mechanics of the PDE offer many advantages over propulsion systems currently used. Bratkovich et al. [13] have written an introductory article regarding the pulse detonation rocket engines (PDRE). Many of the basic components are similar to that of standard PDEs. The major difference is requirement of on board oxidizer. The cycle involved in PDREs is identical to that of a standard PDE.

A discussion of detonation waves and their applications in propulsion have been provided by Kailasanath [3]. A general review of detonation waves was conducted including standing normal detonations, pulse detonations, rotating detonations, and oblique shock-induced detonations. This paper includes an extremely in-depth and complete history of research on PDEs and their components. The author also gave two important points regarding PDEs. First, he suggested that PDE's operating on multiphase mixtures should be explored. In addition, the exhausting of the products of combustion needs to be better understood so that the products do not interfere with the next detonation cycle.

One component missing from the overall understanding of PDEs is a full understanding of how much is gained by using PDEs. The purpose of this paper is to complete both an energy and exergy analyses of PDEs. Previous work has developed the constant specific heat model for the Humphrey cycle, [6]. A complete thermodynamic analysis based on combustion has not been completed. The purpose of this paper is to develop this analysis. The Humphrey cycle is used to model the PDE. A major characteristic of the Humphrey cycle is the constant volume combustion process. For comparison, the Brayton cycle is also analyzed. The Brayton cycle represents a standard gas turbine engine, which is widely used in aeronautics. A pressure versus volume diagram of the Brayton Cycle is shown in Fig. 1.

A detailed combustion analysis has been used to determine the efficiency and effectiveness of the Humphrey and Brayton cycles. Using the Stanjan™ [14] Chemical Equilibrium software, the efficiency and effectiveness of both cycles is calculated using both methane and JP10 as the fuel.

Pulse Detonation Engines (PDEs)

Pulse detonation engines are characterized by a supersonic combustion wave. Supersonic flame propagation is known as a detonation wave. In contrast, gas engines use a deflagration wave (subsonic flame propagation). A detonation wave will increase the pressure and density of the unburned fuel/air mixture ahead of the wave increasing its temperature, [6].

A basic PDE consists of a shock tube, a system designed to deliver the fuel air mixture and a device to initiate the detonation waves. The shock tube is closed at one end and open to atmospheric air at the other end. The location of the detonation device has produced considerable attention. Two possibilities exist. The detonation wave can be initiated from either the closed end, or the

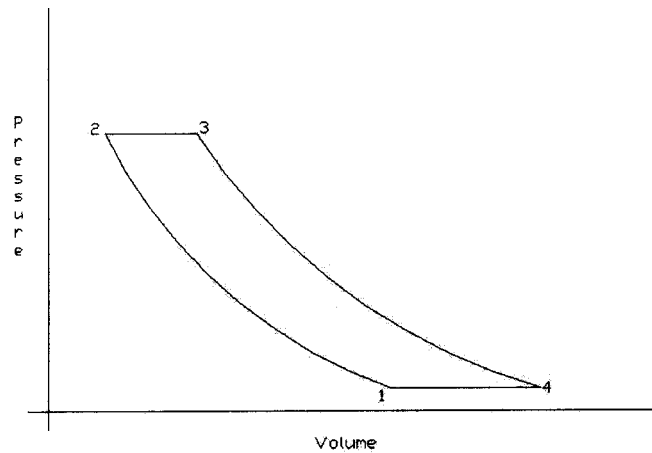


Fig. 1 Brayton cycle

open end. These are the basics involved in a pulse detonation engine. Other components, including fuel and air mixing chambers, nozzles and diffusers, need to be considered for a working model, [15].

The full PDE process is illustrated in Fig. 2. The fuel/air mixture enters the shock tube. The detonation is initiated either directly or through deflagration to detonation transition. Direct ini-

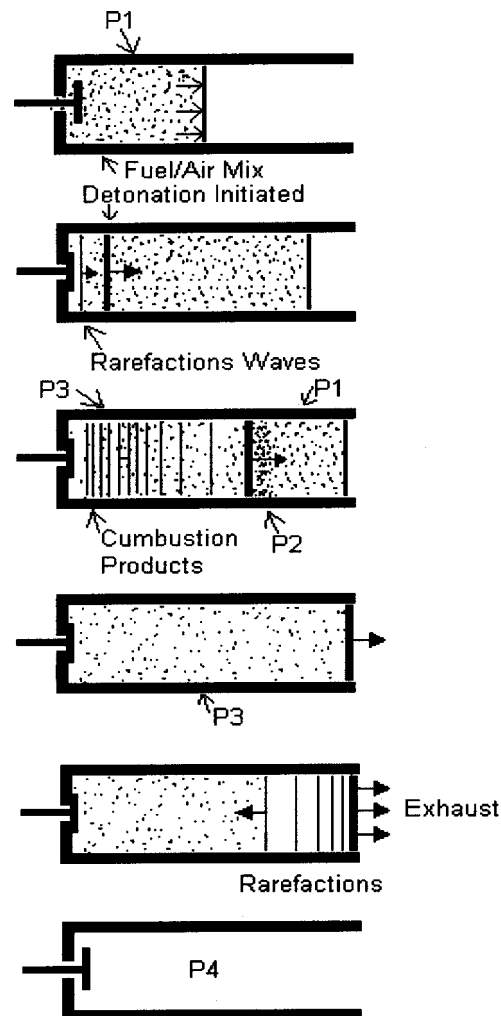


Fig. 2 PDE combustion cycle

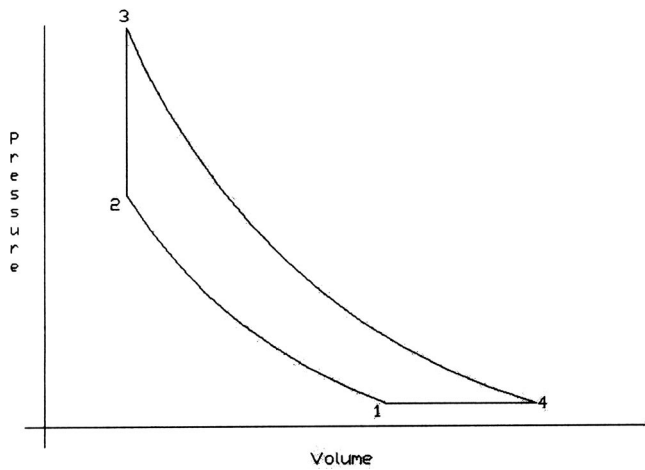


Fig. 3 Humphrey cycle

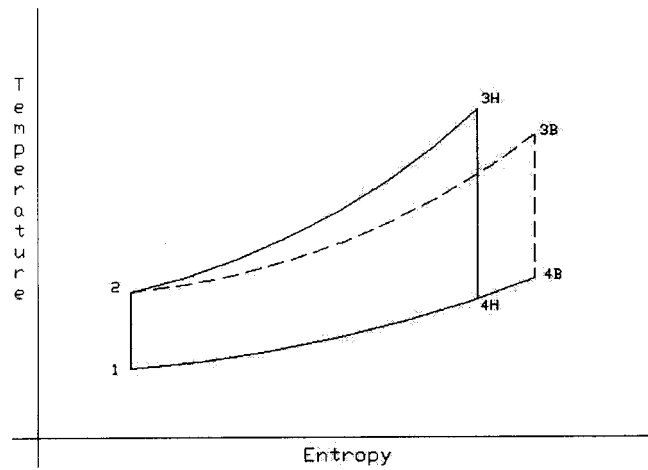


Fig. 4 T-s diagram

tion requires a considerable amount of energy to start detonation. Using deflagration and transitioning to detonation takes less energy to initiate. However, there is a distance required to transition to a detonation wave. This distance is known as deflagration to detonation transition (DDT) distance, [10].

Rarefaction waves follow the detonation wave. As the wave propagates through the chamber, the fuel/air mixture ahead is compressed. High pressure and temperature is reached creating engine thrust. As the detonation exits the shock tube, the rarefaction waves start back into the tube, exhausting the products of the combustion. This brings the chamber back to the initial pressure where the process can begin again. The engine is mechanically simple requiring few moving parts. This offers many advantages in reliability, [6].

Processes in pulse detonation engines are very complicated employing subsonic and supersonic combustion waves propagation. To analyze the processes involved in this device requires complete computational fluid dynamic analysis with detail chemical kinetic modeling, which is beyond the scope of this investigation. Jacob cycle, [16], has been used to model the detonation process while, historically Humphrey cycle has been used to represent the process in the pulse detonation engine. While the model is a simplification of the processes that gas mixtures experience, it provides information that can be used to compare this engine to the gas turbine system.

The Humphrey Cycle. In order to evaluate thermodynamic characteristics of PDEs, a cycle must be chosen to model the engine. The detonation wave allows the combustion to be modeled as constant volume. The Humphrey cycle is chosen as the model.

The Humphrey cycle consists of four processes. The first process is an isentropic compression. This compression occurs ahead of the detonation wave in PDEs. Compression is followed by constant volume combustion. Another isentropic process expands the combustion products back to atmospheric pressure. In the PDE, the rarefaction waves cause this expansion process. Finally, an isobaric process brings the cycle back the start. Figure 3 shows this process on a p-v diagram.

A T-s diagram is shown in Fig. 4 comparing the Humphrey and Brayton cycles.

Energy and Exergy Analyses

In order to quantify the expected gains, which a pulse detonation engine will offer in comparison to current methods of combustion, an energy and exergy model must be established for both characteristic cycles.

The Brayton cycle, which includes a compressor, a combustor and a turbine, uses a constant pressure combustion process. From the p-v diagram shown in Fig. 1, the net work produced by the system is determined by

$$w_{\text{net}} = (h_3 - h_4) - (h_2 - h_1). \quad (1)$$

For the Humphrey cycle, the combustion process occurs with constant volume. From the p-v diagram shown in Fig. 2, the net work produced for the closed system is

$$w_{\text{net}} = (u_1 - u_2) + (u_3 - u_4) + R(T_1 - T_4). \quad (2)$$

To determine the thermal efficiency, the net work is divided by the high heating value (HHV) of the fuel.

$$\eta = \frac{w_{\text{net}}}{\text{HHV}} \quad (3)$$

For the effectiveness or exergetic efficiency, the net work is divided by the chemical availability of the fuel.

$$\varepsilon = \frac{w_{\text{net}}}{\text{ach}_{\text{fuel}}} \quad (4)$$

Determining Thermodynamic Properties. The Chemkin™ [17] system was used to determine the thermodynamic properties required for this analysis. Chemkin™ provides coefficients for a polynomial fit for specific heat, enthalpy and entropy of different species. The three equations necessary are

$$c_p^o = R(a_1 + a_2T + a_3T^2 + a_4T^3 + a_5T^4) \quad (5)$$

$$h^o = RT \left(a_1 + \frac{a_2}{2}T + \frac{a_3}{3}T^2 + \frac{a_4}{4}T^3 + \frac{a_5}{5}T^4 + \frac{a_6}{T} \right) \quad (6)$$

$$s^o = R \left(a_1 \ln T + a_2T + \frac{a_3}{2}T^2 + \frac{a_4}{3}T^3 + \frac{a_5}{4}T^4 + a_7 \right) \quad (7)$$

The values for a_1 through a_7 were found in a data file used for the Chemkin code, which will be discussed later.

Compression Process. The compression process was assumed isentropic. Enthalpy is determined under the initial conditions based on a temperature of 300 K. In the case of the Humphrey cycle, the initial internal energy is also determined from the following expression:

$$u^o = h^o - RT. \quad (8)$$

The pressure ratio, r , is used to find the pressure just prior to combustion assuming the initial pressure is 1 atm. Initial entropy

is found based on a stoichiometric fuel and air mixture. (Air is assumed to be 79% N₂ and 21% O₂.) The temperature prior to combustion is determined by solving Eq. (7) by the Newton-Raphson method. Enthalpy is then evaluated from this temperature. Again, for the case of the Humphrey cycle, internal energy is also found.

Combustion Process. Stanjan™ chemical equilibrium software is used to find properties after combustion. In order to find the major contributing species in the combustion products, a list was generated of possible compounds that can be created from carbon, hydrogen, oxygen, and nitrogen atoms. The species considered were

N₂ O₂ N O CH O+ O- H+ H-
H₂O CO₂ CO H HO₂ HO H₂O₂ H₂ NO
NO₂ CH₃ CH₂O C₂H₆ CH₄ CH₂ NH NH₂ NH₃
NNH

The chemical equilibrium was found using Stanjan™ based on these species being the products of combustion. For the purpose of a combustion analysis, only the species that have a mole fraction greater than 10⁻³ have been considered in the combustion calculations. The eight most dominant species are

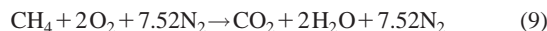
N₂ H₂O CO CO₂ O₂ OH H₂ NO

This result was found to be the same for both fuels used in this analysis.

In order to validate the assumption that eight species characterizes the chemical reaction sufficiently, the Humphrey cycle was analyzed based on 20 most dominant species. The following were used:

N₂ H₂O CO₂ CO O₂ OH H₂ NO H
O NO₂ H₂O₂ N NH₃ NH NNH NH₂ CH₃
CH₄ CH₂

Methane Combustion. Methane was used as a simple fuel to determine the thermodynamic performance of PDEs. The balanced stoichiometric chemical reaction for methane combustion with air is



The high heating value and the chemical availability for methane were found to be, [18],

$$\text{HHV}_{\text{CH}_4} = 93,522 \frac{\text{kJ}}{\text{kmol}_{\text{CH}_4}} \quad \text{ach}_{\text{CH}_4} = 86,642 \frac{\text{kJ}}{\text{kmol}_{\text{CH}_4}}$$

JP10 Combustion. A jet fuel, JP10, was used as the second fuel since the Navy has expressed interest in using JP10. The average chemical formula for JP10 is C₁₀H₁₆, [19]. The balanced chemical reaction for C₁₀H₁₆ combustion with air is



The high heating values and chemical availability for C₁₀H₁₆ were calculated. The heating value was calculated by the following:

$$\text{HHV}_{\text{C}_{10}\text{H}_{16}} = 10h_f^{\circ}|_{\text{CO}_2} + 8h_f^{\circ}|_{\text{H}_2\text{O}(l)} - h_f^{\circ}|_{\text{C}_{10}\text{H}_{16}} \quad (11)$$

where

$$h_f^{\circ}|_{\text{C}_{10}\text{H}_{16}} = h^{\circ}(300 \text{ K}).$$

The high heating value was found to be

$$\text{HHV}_{\text{C}_{10}\text{H}_{16}} = 94,224 \frac{\text{kJ}}{\text{kmol}_{\text{C}_{10}\text{H}_{16}}}$$

For the chemical availability, the following equation was used:

$$\text{ach}_{\text{C}_{10}\text{H}_{16}} = g_{\text{C}_{10}\text{H}_{16}} + 14g_{\text{O}_2} - 10g_{\text{CO}_2} - 8g_{\text{H}_2\text{O}(l)} + 10\text{ach}_{\text{CO}_2} + 8\text{ach}_{\text{H}_2\text{O}} - 14\text{ach}_{\text{O}_2} \quad (12)$$

The Gibbs function was found by the following:

$$g^{\circ} = h^{\circ} - Ts^{\circ} \quad (13)$$

The chemical availability was found to be

$$\text{ach}_{\text{C}_{10}\text{H}_{16}} = 93,700 \frac{\text{kJ}}{\text{kmol}_{\text{C}_{10}\text{H}_{16}}}$$

Brayton Cycle. Stanjan™ was used to determine chemical equilibrium of the products of combustion. Stanjan™ requires two constant properties to perform the equilibrium calculations. For the case of the Brayton cycle, constant pressure and constant enthalpy was chosen. The code calculates all properties after combustion.

Humphrey Cycle. The properties of the combustion products are found in the same manner as with the Brayton cycle. The Humphrey cycle is characterized by a constant volume combustion process. For the Stanjan™ program, constant volume and constant internal energy was chosen to conduct the chemical equilibrium calculations. Temperature and pressure of the burned gases were determined by Stanjan™.

Expansion Process. The expansion process was assumed isentropic. Using the entropy found for the burned gases Eq. (7) was solved for the temperature after the expansion.

The temperature found after expansion is only valid for frozen chemistry. However, for this cycle, the chemistry of the products cannot be assumed frozen. Stanjan™ was again employed to find the chemical equilibrium mixture. The inputs include the chemical molar concentrations of the products, the frozen chemistry temperature at state four and atmospheric pressure. The two property constants required to run the program were pressure and entropy.

Temperature and chemical concentrations at chemical equilibrium were determined by Stanjan™. Enthalpy was then determined for the expanded products. In the case of the Humphrey cycle, the internal energy was found from the enthalpy.

Results and Discussion

Methane was the first fuel analyzed for use in pulsed detonation engines. A range of compression ratios was used to compare the thermal efficiency and effectiveness of the Humphrey and Brayton cycles. Figure 5 shows the Humphrey cycle to have an advantage over the Brayton cycle with respect to thermal efficiency.

Similar results are seen in the effectiveness. Figure 6 shows the advantage held by the Humphrey cycle with respect to effectiveness.

A more probable fuel to be used for pulsed detonation engines would be JP10 jet fuel. For this reason, Figs. 7 and 8 confirm the same advantage will be present when using JP10 fuel as when methane is used.

These results show a significant advantage in using the Humphrey cycle over the Brayton cycle. An increase of 4 to 12% in thermal efficiency and effectiveness can be expected over the Brayton cycle based on methane. Similar results are shown when using JP10 fuel.

Figure 9 compares the thermal efficiency between methane and JP10 based on the Humphrey cycle. There is an insignificant dif-

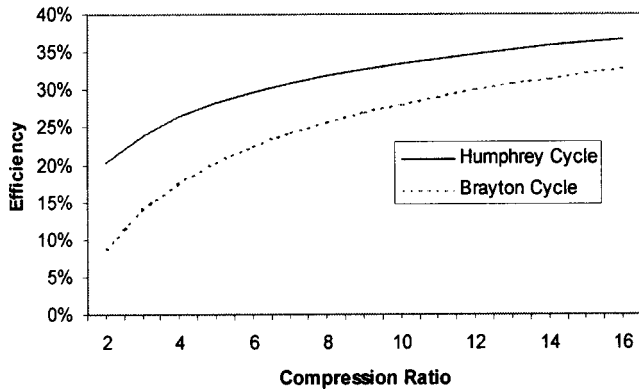


Fig. 5 Thermal efficiency of the Humphrey and Brayton cycles using methane as the fuel

ference between the two fuels. There is, however, a slight difference between methane and JP10 based on effectiveness. Figure 10 shows methane to have slightly higher effectiveness than JP10.

Figure 11 compares efficiency of the Humphrey cycle based on 8 species and 20 species. The analysis is conducted using methane as the fuel. In order to compare these two models, the assumption was made that chemistry is frozen during the expansion portion of the cycle. There is not a significant difference between the results of the two models. Similarly, Fig. 12 shows the same comparison based on effectiveness. Again, there is not a significant difference.

Future Considerations. The pulse detonation engine works on an unsteady basis. In order to make the PDE a viable jet propulsion engine, a frequency must be achieved to produce the

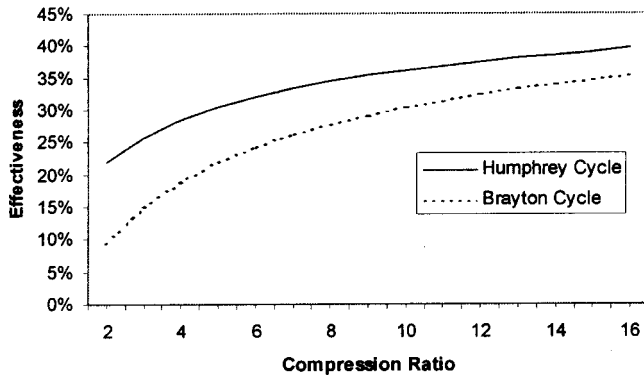


Fig. 6 Effectiveness of the Humphrey and Brayton cycles using methane as the fuel

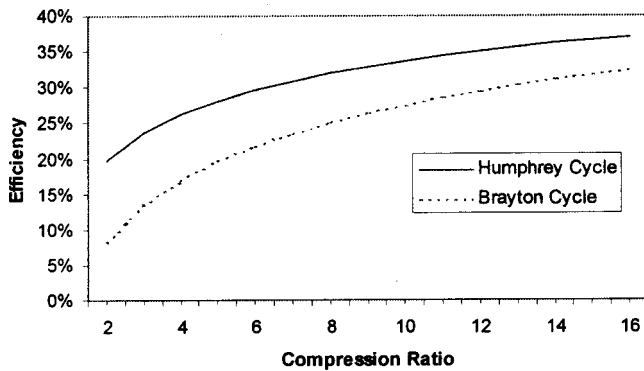


Fig. 7 Thermal efficiency of the Humphrey and Brayton cycles using JP10 as the fuel

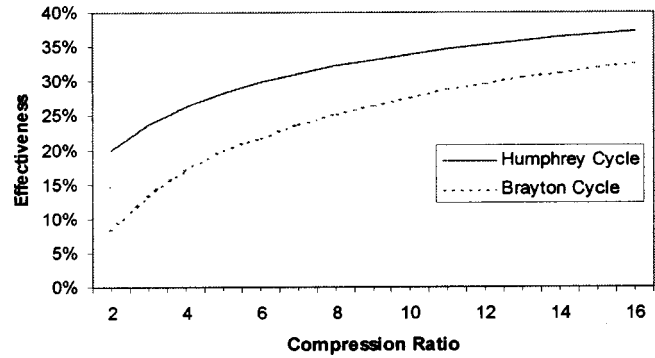


Fig. 8 Effectiveness of the Humphrey and Brayton cycles based on a combustion analysis using JP10

equivalent power that a comparable gas turbine engine produces. Each cycle of combustion produces a set amount of energy based on fuel used per cycle. Frequency is directly proportional to the power produced. Further experimentation and research is necessary to determine a frequency that will produce the equivalent power produced by gas turbine engines.

Conclusions

The pulse detonation engine has been shown to have significant thermodynamic performance advantages over current air-breathing jet engines. These performance advantages are seen to be similar for both fuels studied. The greatest advantage was seen at lower compression ratios.

PDEs have many advantages that may make them the choice for propulsion in the future. Along with performance advantages,

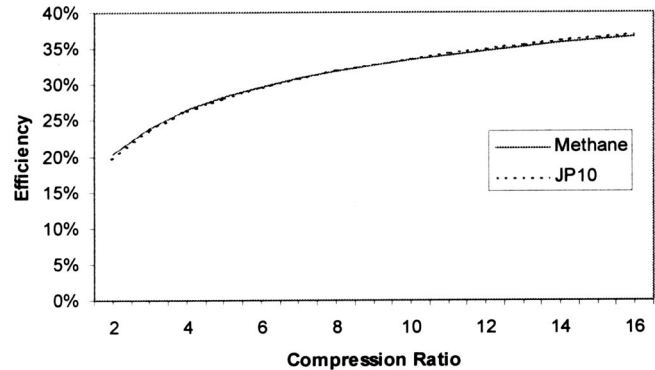


Fig. 9 Efficiency of methane and JP10 based on the Humphrey cycle

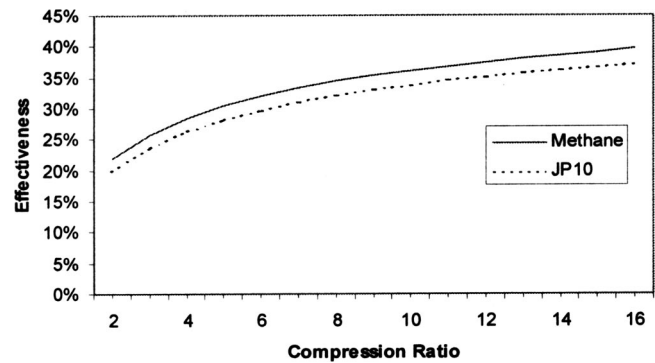


Fig. 10 Effectiveness of methane and JP10 based on the Humphrey cycle

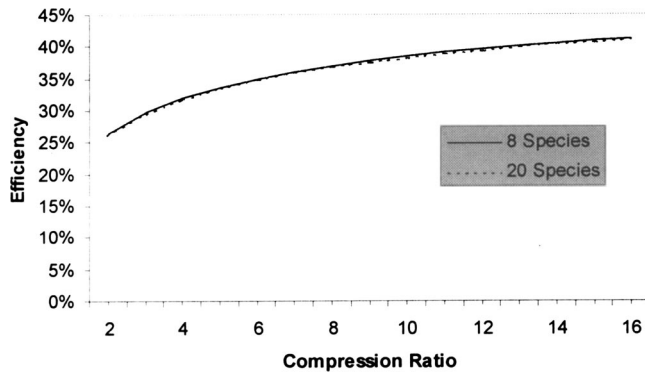


Fig. 11 Thermal efficiency of the Humphrey cycle using 8 and 20 species based on methane

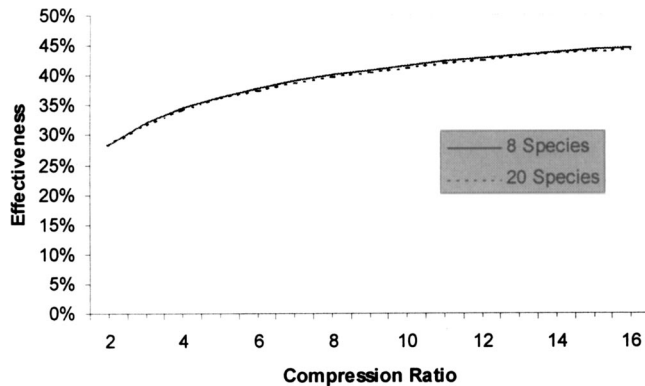


Fig. 12 Effectiveness of the Humphrey cycle using 8 and 20 species based on methane

PDEs have a potential mechanically simple design with far less moving parts than other air-breathing engines.

Nomenclature

a = Chemkin
 ach = Chemical availability
 c_p = specific heat
 g = Gibbs free energy
 h = enthalpy
 h_f = enthalpy of formation
 HHV = high heating
 R = universal gas constant
 s = entropy

T = temperature
 u = internal Energy
 w = work

Superscripts

o = standard state

Greek

ε = effectiveness
 η = thermal efficiency

References

- [1] Santoro, R. J., Yang, V., Law, C. K., and Shepard, J. E., 1999, "Multidisciplinary study of Pulsed Detonation Engine Propulsion," ONR Contract N99914-1-0744.
- [2] Pegg, R. J., Couch, B. D., and Hunter, L. G., 1998, "Pulsed Detonation Engine Air Induction System Analysis," NASA Langley Research Center and Lockheed Martin Tactical Aircraft Systems.
- [3] Kailasanath, K., 1999, "Review of Propulsion Applications of Detonation Waves," AIAA Paper No. 99-1067.
- [4] "Pulsed Detonation Engines," Caltech University, 2000, <http://web.galci.caltech.edu/EDL/projects/pde/pde.html> (Apr. 18, 2001).
- [5] Anthenian, R. A., Schauer, F. R., Stutrid, J. S., Frayne, C. W., Bradley, R. P., Chen, L. P., and Katta, V. R., 1999, "Development of a Pulse Detonation Research Engine," Air Force Research Laboratory and Innovative Scientific Solutions, Inc.
- [6] Bussing, T., and Pappas, G., 1994, "An Introduction to Pulsed Detonation Engines," AIAA Paper No. 94-0263.
- [7] Hinkey, J. B., Bussing, T. R. A., and Kaye, L., 1995, "Shock Tube Experiments for the Development of a Hydrogen-Fueled Pulse Detonation Engine," AIAA Paper No. 95-2578.
- [8] Bussing, T. R. A., 1995, "Rotary Valve Multiple Pulse Detonation Engine (RVMPDE)," AIAA Paper No. 95-2577.
- [9] Bratkovich, T. E., and Bussing, T. R. A., 1995, "A Pulsed Detonation Engine Performance Model," AIAA Paper No. 95-3155.
- [10] Ting, J. M., Bussing, T. R. A., and Hinkey, J. B., 1995, "Experimental Characterization of the Detonation Properties of Hydrocarbon Fuels for the Development of Pulse Detonation Engine," AIAA Paper No. 95-3154.
- [11] Williams, F. A., and Varatharajan, B., 2000, "Theory of Initiation of Detonation in Pulse Detonation Engines: Chemical Kinetics and Mechanisms," ONR Contract N00014-99-1-0745.
- [12] Bussing, T. R. A., Bratkovich, T. E., and Hinkey, Jr., J. B., 1997, "Practical Implementation of Pulse Detonation Engines," AIAA Paper No. 97-2748.
- [13] Bratkovich, T. E., Aarnio, M. J., Williams, J. T., and Bussing, T. R. A., 1997, "An Introduction to Pulse Detonation Rocket Engines (PDREs)," AIAA Paper No. 97-2742.
- [14] Reynolds, W. C., 1986, Stanford University Report, ME 270, No 7.
- [15] Bussing, T. R. A., Hinkey, J. B., and Kaye, L., 1994, "Pulse Detonation Engine Preliminary Design Considerations," AIAA Paper No. 94-3220.
- [16] Fickett, W., and Davis, W. C., 2000, *Detonation Theory and Experiment*, Dover, New York.
- [17] Kee, R. J., Rupley, F. M., Meeks, E., and Miller, J. A., 1996, "Chemkin III: A Fortran Chemical Kinetics Package for the Analysis of Gas Phase Chemical and Plasma Kinetics," Sandia National Laboratories, http://nathan.ca.sandia.gov/chemkin/docs/CHEMkin_III.pdf (Feb. 20, 2001).
- [18] Moran, M. J., and Shapiro, H. N., 1996, *Fundamentals of Engineering Thermodynamics*, John Wiley and Sons, New York.
- [19] Li, S. C., Varatharajan, B., and Williams, F. A., 2001, "The Chemistry of JP-10 Ignition," AIAA J., **39**(12).

Numerical Investigation of the Effects of Axial Cylinder Bore Profiles on Piston Ring Radial Dynamics

Y. Piao
S. D. Gulwadi

Ricardo, Inc.,
7850 Grant Street,
Burr Ridge, IL 60527

The role of cylinder bore shapes in engine performance has been the subject of several studies in recent years. In particular, the influence of bore distortion on oil consumption under high speed conditions has generated significant interest. In this paper, the effect of an axial bore profile on radial dynamics of a ring is investigated. Radial ring motions within grooves due to the axial bore profile can generate significant inertial effects and also have an impact on ring end-gap sizes and lubrication conditions at the ring-liner interfaces. The magnitude of such effects is dependent on the ring-pack configuration, engine operating conditions (speed and load) and axial bore profile details. These issues are investigated in this study due to their implication on engine oil consumption, friction and blow-by. The authors have developed an analytical expression to account for the effects of radial ring inertia due to an axial bore profile for implementation in a piston ring-pack simulation tool RINGPAK. Simulation results from a gasoline engine study are presented to illustrate the effects of engine speeds, ring tensions, and characteristics of axial bore profiles on ring radial dynamics and ring-liner lubrication. Relevant qualitative comparisons are made to experimental measurements available in the literature.

[DOI: 10.1115/1.1610016]

Introduction

A desirable piston ring-pack set is one that provides good sealing performance (i.e., minimal gas blow-by) with low lubricating oil consumption and friction loss. This is a challenging task due to the nature of the phenomena and interactions associated with piston rings. For example, increasing the installed ring tension which is a method to control oil consumption also tends to increase ring friction, [1]. Hence, any attempt to optimize ring-pack performance output parameters requires a good understanding of the dynamics of cylinder-kit components (e.g., piston, rings, liner) and lubrication at the interfaces (e.g., ring-liner, ring-groove, skirt-liner) for various operating conditions. To this effect, cylinder bores have been the subjects of several investigations. There have been extensive studies, [2–5], on the effects of bore surface finish, bore out-of-roundness and bore distortion on lubricating oil consumption. The topic addressed in this paper is the effect of axial bore profiles on radial ring dynamics. Axial bore profiles occur due to various reasons (e.g., thermal gradients, liner supports). A particular phenomenon associated with axially profiled bores is that piston rings tend to move away from the bore in the radial direction as they slide over the heavily distorted portions of the cylinder bore, especially at high engine speeds. This has been observed experimentally by M. Basaki et al. [6], who also reported that this ring separation from the bore contributes to increased oil consumption at high engine speeds. The ability of piston rings to slide along an axially profiled cylinder wall and to conform to a circumferentially distorted cylinder bore is a critical factor in determining the oil consumption associated with that ring-pack set. Hence, these effects are important and need to be considered when simulating and/or analyzing ring-pack behavior.

This study places the focus on radial ring motion in an axially profiled bore only with no circumferential distortions (i.e., only

bore diameter values are different at various axial locations along the cylinder). The mathematical model used to simulate the radial dynamics of the ring within the groove, [7], has been extended to include the inertial effects arising from the piston ring sliding over an axial profiled bore. Besides modeling details, simulation results are also presented for response of piston ring motions to an axially profiled bore in a gasoline engine at various speeds. The simulation studies have been carried out using a piston ring-pack simulation code RINGPAK, [8]. Qualitative comparisons are made with experimental results from the literature, [6], that are shown in the Appendix.

Mathematical Model

In an operating engine, piston rings are subjected to forces and moments arising from several sources such as ring-liner hydrodynamic lubrication, ring-liner boundary lubrication, ring tension, inter-ring gas pressures, etc. Figure 1 depicts the various force components acting on a ring in the radial direction under any operating condition.

Radial Ring Dynamics. The radial force balance on a piston ring, as depicted in Fig. 1, may be expressed as

$$F_{oil} + F_{asp} + F_{gas} - F_{gro} - F_{ten} - F_{ine} - F_{frc} = 0, \quad (1)$$

where F_{oil} is force due to oil film pressures at ring-liner interface, F_{asp} is force due to contact pressures at ring-liner interface, F_{gas} is force from land gas pressures at ring-liner interface, F_{gro} is force due to groove gas pressure at back of the ring, F_{ten} is force due to installed ring tension, F_{ine} is inertia force on the ring due to its radial motion, and F_{frc} is friction force at the ring-groove interface.

At the ring-liner conjunction, based on operating conditions, several types of lubrication modes are possible. In general, piston rings tend to operate in the mixed lubrication regime but there are some instances such as “ring lift” where the ring is gas lubricated or “starved conditions” when the ring operates in the boundary lubrication regime. In order to capture these phenomena, a mass-

Contributed by the Internal Combustion Engine Division of THE AMERICAN SOCIETY OF MECHANICAL ENGINEERS for publication in the ASME JOURNAL OF ENGINEERING FOR GAS TURBINES AND POWER. Manuscript received by the ICE Division, June 2002; final revision received Oct. 2002. Associate Editor: D. Assanis.

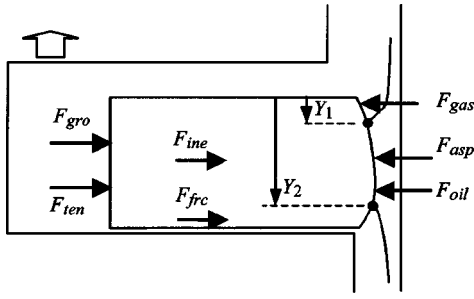


Fig. 1 Forces acting on a ring in the radial direction

conserving mixed lubrication model is employed. Details of this model are provided in Ref. [7] and only a brief overview is given in this paper.

The oil film pressure distribution $p(y)$ at the ring-liner interface is obtained on solving the Reynolds equation

$$\frac{\partial}{\partial y} \left(\frac{h(y)^3}{12\mu} \frac{\partial p}{\partial y} \right) = \frac{V_y}{2} \frac{\partial h(y)}{\partial y} + \frac{\partial h(y)}{\partial t}, \quad (2)$$

where $h(y)$ is the clearance profile at the ring face-liner conjunction defined along the axial coordinate y , V_y is the piston ring axial velocity, and μ is the lubricant viscosity. The oil film lubrication extents Y_1 and Y_2 are determined by the coupled mass-conserving lubrication model and the oil transport model described in Ref. [7].

From the oil film pressures, the force due to oil pressures F_{oil} is computed using

$$F_{oil} = \left(\int p(y) dy \right) \pi D, \quad (3)$$

where D is the nominal bore diameter. During boundary lubrication at the ring-liner interface, local contact pressures p_{asp} are calculated using the Greenwood-Tripp model, [9],

$$p_{asp} = \frac{16\sqrt{2}}{15} \pi (\sigma\beta\eta)^2 E \frac{\sqrt{\sigma}}{\sqrt{\beta}} G \left(\frac{h(y)}{\sigma} \right), \quad (4a)$$

where

$$G(x) = \frac{1}{\sqrt{2}\pi} \int_0^\infty (s-x)^{2.5} \exp\left(-\frac{s^2}{2}\right) ds. \quad (4b)$$

σ , β , and η are surface roughness parameters which represent the mean r.m.s. height, radius of curvature, and density of the surface asperities, respectively, and E is the composite elastic modulus of the contacting materials. Consequently, the contact force F_{asp} is calculated using

$$F_{asp} = \left(\int p_{asp}(y) dy \right) \pi D. \quad (5)$$

Gas pressures in the groove and land volumes surrounding the ring are needed to calculate F_{gro} and F_{gas} . Additionally, land pressures are also used as boundary conditions in solving the Reynolds Equation given by Eq. (2). As a result, a gas dynamics model is employed to compute inter-ring pressures (i.e., pressures in a labyrinth of land and groove subvolumes which make up the ring-pack region). Flow paths exist between these subvolumes, for example, gas flows between adjacent land subvolumes through the ring end-gap and ring-liner nonconforming areas whereas gas flows between the land and groove subvolumes through the ring-groove side clearances. Hence, to compute these instantaneous inter-ring pressures ideal gas law in conjunction with mass conservation is applied to each subvolume, such that

$$\frac{dm_i}{dt} = \sum \dot{m} \quad \text{and} \quad m_i = \frac{p_i V_i}{RT_i}, \quad (6)$$

where m_i is mass of gas in the subvolume i , \dot{m} is the gas mass flow rate across the boundaries of the subvolume, R is the gas constant, and p_i and T_i are the gas pressure and temperature in the subvolume V_i .

Gas mass flow-rates between adjacent lands through the ring end-gap and ring-liner nonconforming areas are calculated using the isentropic orifice flow equation

$$\dot{m} = \frac{C_d A p_u}{\sqrt{RT_u}} \left(\frac{2\gamma}{\gamma-1} \right)^{1/2} \left(\frac{p_d}{p_u} \right)^{1/\gamma} \left(1 - \left(\frac{p_d}{p_u} \right)^{\gamma-1/\gamma} \right)^{1/2}$$

or

$$\dot{m} = \frac{C_d A p_u \gamma^{1/2}}{\sqrt{RT_u}} \left(\frac{2}{\gamma+1} \right)^{\gamma+1/2(\gamma-1)} \quad \text{if} \quad \frac{p_d}{p_u} \leq \left(\frac{2}{\gamma+1} \right)^{\gamma/\gamma-1}, \quad (7)$$

where C_d and A are the discharge flow coefficient and flow area associated with the orifice, T_u is the upstream gas temperature, p_u and p_d are the upstream and downstream pressures, and γ is the polytropic exponent.

On the other hand, flow between lands and grooves through the ring-groove side clearances is treated as an isothermal compressible flow through a narrow channel, such that

$$\dot{m} = \frac{(p_u^2 - p_d^2)}{24\mu_{mix}RT} \left(\int \frac{dx}{h(x)^3} \right)^{-1} \pi (D - L_{ring}), \quad (8)$$

where $h(x)$ is the ring-groove side clearance profile along the radial coordinate x , T is the average temperature of this volume, μ_{mix} is the oil-gas mixture viscosity, and L_{ring} is radial thickness of the ring.

Thus, on calculating the groove and land pressures, the radial force components F_{gro} and F_{gas} are expressed as

$$F_{gro} = p_{gro} B \pi (D - 2L_{ring}), \quad (9)$$

$$F_{gas} = [p_{ul} Y_1 + p_{ll} (B - Y_2)] \pi D, \quad (10)$$

where p_{gro} , p_{ul} , and p_{ll} are gas pressures in the groove, upper land and lower land surrounding each ring, respectively, B is the ring axial width, Y_1 and Y_2 are locations on the y -axis along the ring face which define the boundaries of the oil lubricated zones at the leading and trailing edges, respectively.

The force component F_{ten} is based on design information available from the drawings while the force component F_{frc} is based on calculation of oil film pressures and contact pressures at the ring-groove interfaces, similar to those shown in Eqs. (2), (4a), and (4b). Since the radial inertial force component F_{ine} is an important aspect of this study, it is treated in detail in the next section.

Using the approach described above, the instantaneous radial location of a piston ring within its groove is computed over the engine cycle. Although a brief summary of the interaction between the various phenomena is given here, more information on coupling between the various phenomenological models is given in Ref. [8].

The study undertaken in this paper focuses on the effect of an axial bore profile on the radial motion of a piston ring. An axial bore shape alters the instantaneous ring-liner clearance profiles as the rings slide within the cylinder bore. In addition to its impact on the radial inertia term F_{ine} , the axial bore profile has a significant influence in determining the lubricating conditions at the ring-liner interfaces (i.e., full lubrication, partial lubrication or starved). As a result, calculations of the force components F_{oil} , F_{asp} , and F_{gas} are affected along with the radial ring motion within the groove.

Radial Inertia. Figure 2 shows the schematic of an axially profiled bore and the coordinate system used in the analysis. The

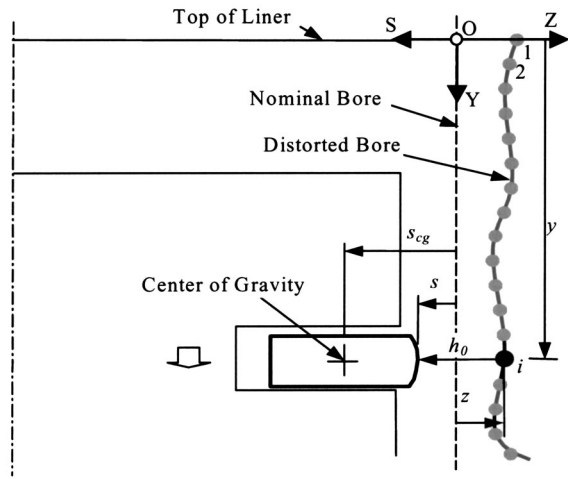


Fig. 2 Schematic layout of a ring in an axially profiled bore

axial bore profile is based on bore diameter values calculated at different axial locations along the cylinder wall. In this study, the nominal bore diameter is used as the reference diameter. The variation in value of the bore radius at each axial location along the cylinder wall is then represented by $z(y)$ about the nominal bore. The dots in Fig. 2 represent the resulting axial bore profile.

At any given axial location of the ring y , h_0 is the minimum ring-liner oil film thickness, s_{cg} and s are the radial distances of the ring center of gravity and ring face (minimum clearance location) from the nominal bore, respectively. Using the nominal bore diameter as a reference, the inertial term in Eq. (1) can be written as

$$F_{\text{ine}} = -m_{\text{ring}} a_r, \quad (11a)$$

where the acceleration term is given by

$$a_r = \frac{d^2 s_{cg}}{dt^2} = \frac{d^2 s}{dt^2} + \frac{d^2 (s_{cg} - s)}{dt^2}. \quad (11b)$$

m_{ring} is mass of the ring, and $(s_{cg} - s)$ is the radial distance between center of gravity of the ring and minima of the ring face profile, which is dependent on instantaneous values of ring toroidal twist. However, due to the relatively small magnitude of the twist angle and its rate of change, this term may be neglected in Eq. (11b). Thus, the acceleration term reduces to

$$a_r = \frac{d^2 s}{dt^2}. \quad (12)$$

Since $s = h_0 - z$, Eq. (12) can be rewritten as

$$a_r = \frac{d^2 h_0}{dt^2} - \frac{d^2 z}{dt^2}. \quad (13)$$

Further, the term $d^2 z/dt^2$ can be expanded as

$$\frac{d^2 z}{dt^2} = \left(\frac{d^2 z}{dy^2} \right) \left(\frac{dy}{dt} \right)^2 + \left(\frac{dz}{dy} \right) \left(\frac{d^2 y}{dt^2} \right), \quad (14)$$

where $dy/dt = V_y$ and $d^2 y/dt^2 = a_y$ are the velocity and acceleration of a ring in the axial direction. Therefore, Eq. (14) reduces to

$$\frac{d^2 z}{dt^2} = \left(\frac{d^2 z}{dy^2} \right) V_y^2 + \left(\frac{dz}{dy} \right) a_y. \quad (15)$$

In this formulation, a_y and V_y can be expressed analytically in terms of engine speed and configuration (based on ideal crank-slider motion) by neglecting the relative axial motion of the ring

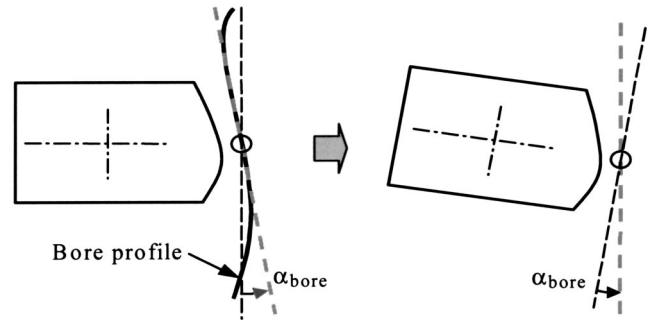


Fig. 3 Effect of axial bore profile on ring-liner clearance

within the piston groove. The terms dz/dy and $d^2 z/dy^2$ are the first and second derivatives of the bore profile. In order to obtain continuous dz/dy and $d^2 z/dy^2$, cubic splines (cubic spline curve-fitting) are used to represent the bore profile based on the input "points" of the bore profile. Hence an analytical expression is developed to completely represent the term $d^2 z/dt^2$ as described in Eq. (15).

Ring-Liner Clearance Profile. The users input the ring face profiles along with the axial bore profile and the simulation program computes the clearance shape for ring-liner lubrication at each time-step. The instantaneous clearance profile is dependent on ring radial motion and toroidal twist within the groove, piston secondary motion, and bore shape. The general procedure for including effects of an axial bore shape on the ring-liner clearance profile is given here. Axial length of the bore is roughly two orders of magnitude more than the axial width of a ring. Additionally, the axial bore profile is generated on a coarser mesh compared to the ring-face. Therefore, calculation of the instantaneous ring-liner clearance profile uses a representation of the liner as a line that's tangential to the local bore profile (i.e., at a location along the cylinder bore corresponding to the axial location of the ring). Figure 3 illustrates the effect of an axial bore profile on ring-liner clearance.

The angle α_{bore} in Fig. 3 is calculated from $\alpha_{\text{bore}} = \arctan(dz/dy)$. This angle is used in the calculation of the ring-liner clearance profile in a manner similar to the inclusion of ring toroidal twist or piston tilt as described in Ref. [10].

Simulation Results and Discussions

Engine and Ring-Pack Configuration. Simulations are conducted on an automotive gasoline engine with an 84.8-mm bore diameter and 88.0-mm stroke length. The piston ring-pack consists of a standard set of three rings: a barrel faced top ring with a rectangular cross section, a taper faced second ring with a rectangular cross section, and a twin-rail oil ring.

Results are presented in this investigation from parametric studies involving (a) engine speeds, (b) ring tensions, and (c) axial bore profiles. For simplicity, the same cylinder pressure and temperature values (typical for a medium load and medium speed condition) versus crank angle are used for various configurations and engine speeds. In addition, focus is placed on radial ring dynamics during the intake and exhaust strokes. During these portions of the engine cycle which have relatively low gas pressures, ring motions within the grooves are more dependent on engine speed and bore profile.

Baseline Case. A baseline model with an axial bore profile is set up as shown in Fig. 4. The discrete user-input points and the calculated spline-fitted curve used to represent the axial bore profile are shown in Fig. 4. For reference purposes, ring locations at

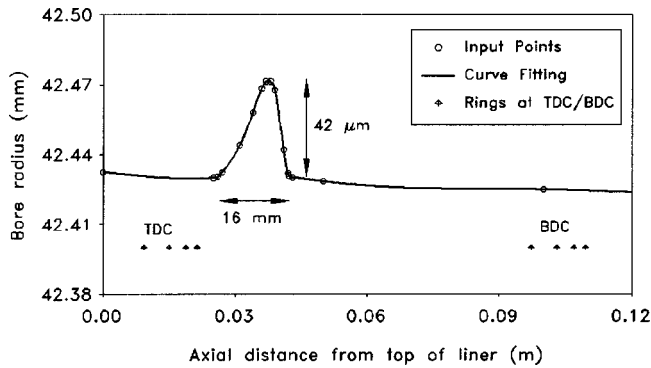


Fig. 4 Baseline axial bore profile

TDC and BDC reversal positions are included in Fig. 4. It should be noted that the two rails of the oil ring are shown along with the upper compression rings.

In a relevant experimental study, [6], a similar axial bore profile (including a deformed segment or “depression” of 32-mm axial extent and 0.076-mm radial depth) is used in a gasoline engine of 95-mm bore diameter and 86-mm stroke length. The axial bore profile used in that study is shown in Fig. 21 in the Appendix. This can be compared to the current bore profile with the deformed portion or “depression” of 16-mm axial extent and 0.042-mm radial depth, as shown in Fig. 4. The engine and ring-pack model in the present study is “similar” to the setup of the aforementioned experimental investigation. This enables some qualitative comparisons to be made between the current study and reported experimental work, [6].

An important parameter in ring-liner lubrication is the minimum oil film thickness (MOFT), which is also a measure of ring radial motion relative to the cylinder bore. The MOFT calculation for a ring is based on the radial force balance given by Eq. (1). Figure 5 shows the values of MOFT from simulations of all three rings at an engine speed of 4000 rpm.

The differences in MOFT values between the three rings can be attributed to many factors such as groove pressures, ring tensions, ring face profiles, oil availability, etc. Relevant to this study, the axial bore profile and axial spacing between rings also play an important role in the calculation of MOFT. For example, consider the “depression” on the bore shown in Fig. 4; each ring passes over it at a different instant of the engine cycle when values of piston velocity and acceleration are different. As seen in Fig. 5, during up-strokes, the top ring slides over the “depression” first followed by the second ring evidenced by the sequence of sudden rise and fall in their MOFT values. This is the reverse of down-strokes, when the second ring first passes over the “depression” followed by the top ring. The oil ring motion does not show much

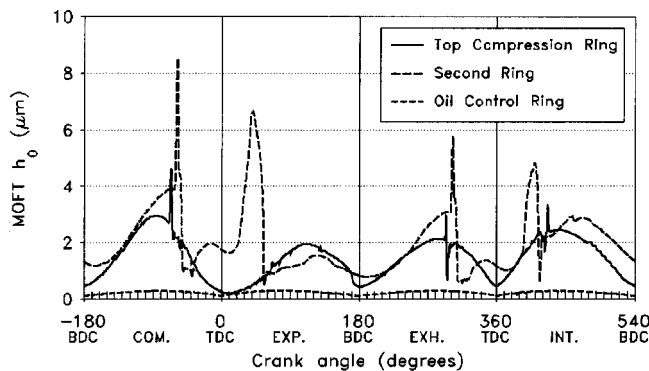


Fig. 5 MOFT values for the ring-pack at 4000 rpm

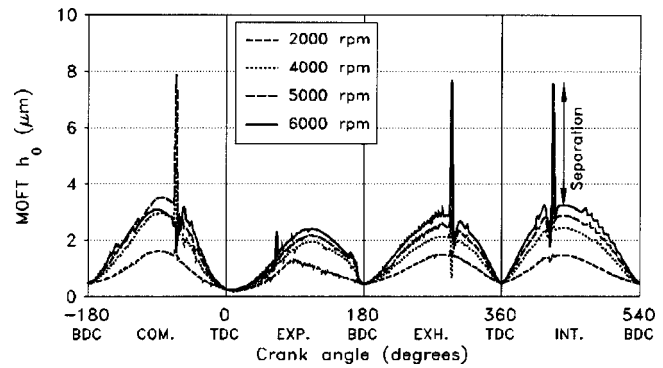


Fig. 6 Top ring MOFT at different engine speeds

sensitivity to the bore profile due to the large tension of the ring. During the power stroke, top ring radial motion is also insensitive to the bore shape due to high gas pressures.

In particular, the top ring behavior is of significant interest since oil flowing past this ring towards the combustion chamber contributes to oil consumption. Thus, the analysis presented here will focus on the top ring for parametric studies involving engine speeds, ring tensions, and axial bore shapes.

Effect of Engine Speed. Keeping other input of the ring pack model unchanged, simulations are carried out for engine speeds of 1000, 2000, 3000, 4000, 5000, and 6000 rpm. Figure 6 shows minimum oil film thickness (MOFT) values of the top ring at different engine speeds.

In Fig. 6, the sharp gradients in MOFT values occur when the top ring passes over the “depression.” It is seen that as the speeds increase, these gradients in MOFT values also increase. The “jump” in MOFT value is defined as the “ring separation distance” from the bore, as shown in Fig. 6. The variable “ring separation distance,” during the intake stroke, is plotted as a function of engine speed in Fig. 7.

The “ring separation” from the bore is based on radial inertial force due to the combined effects of ring radial dynamics, piston axial motion and an axial bore profile as described in Eqs. (1), (11a), (13), and (15). The contribution to ring radial inertia due to piston/ring axial motion in an axially profiled bore is represented by Eq. (15). Here, the terms for axial piston ring velocity and acceleration are proportional to engine speed N and square of the engine speed N^2 , respectively. As a result, this radial inertia contribution due to an axial bore profile is a function of N^2 and the variable “ring separation distance” versus engine speed in Fig. 7 shows this trend. A similar behavior is also observed in the measurements, [6], of “ring separation distance” versus engine speeds and these are shown in Fig. 23 in the Appendix.

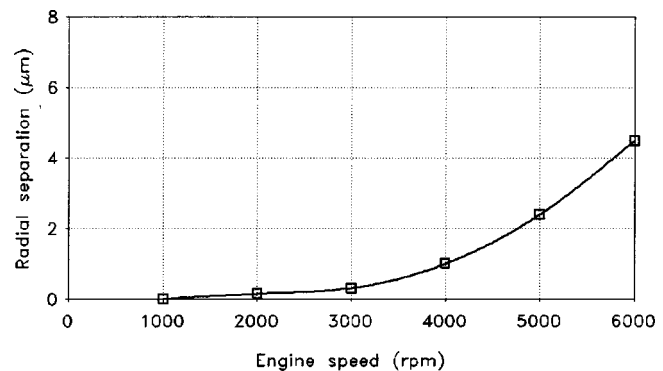


Fig. 7 Ring separation distance versus engine speed

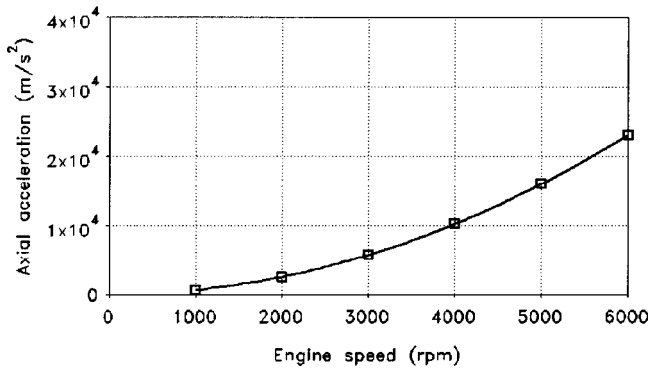


Fig. 8 Peak values of piston acceleration versus engine speed

Figure 8 shows a plot of peak piston acceleration as a function of engine speed and the similar trends observed between Figs. 7 and 8 are consistent with the above discussions.

Although Fig. 7 provides a trend of peak ring radial inertia effects during intake over engine speeds, more information can be obtained by resolving the “ring separation” event at a crank angle level for a fixed engine speed. In other words, ring radial motion as it slides over the “depression” on the liner would provide more insight into the phenomenon. Figure 9 shows the top ring radial motion in the crank angle interval spanning from 400 through 440 deg (i.e., early part of the intake stroke). For comparative purposes, Fig. 9 shows the MOFT of the top ring in this crank angle interval for an axially profiled bore as well as a straight bore at a speed of 6000 rpm. The MOFT values for a top ring moving in an axially profiled bore behave in a manner consistent with instantaneous ring-liner clearance profiles. To demonstrate this aspect, Fig. 9 also shows the instantaneous axial location of the top ring inside the profiled bore in this crank angle interval. In particular, around 425 crank angle deg, as the piston/ring assembly accelerates towards the bottom of the liner, the top ring moves out of the “depression” and radially accelerates away from the bore leading to “ring separation.” As seen from Fig. 9, the top ring eventually returns to the bore around 430 crank deg.

In the duration of “ring separation” (from 425 to 430 crank deg), oil flow rate past the ring face and gas flow rate through the end gap also show a corresponding response to the radial ring motion. Figure 10 shows the oil flow rate below the top ring face and gas flow rate through the end gap for the same period as in Fig. 9.

As shown in Fig. 10, there is increased oil flow under the top ring face towards the combustion chamber creating the potential for higher oil consumption. The implications of the “depression” in the bore profile relevant to the gas dynamics model are (1)

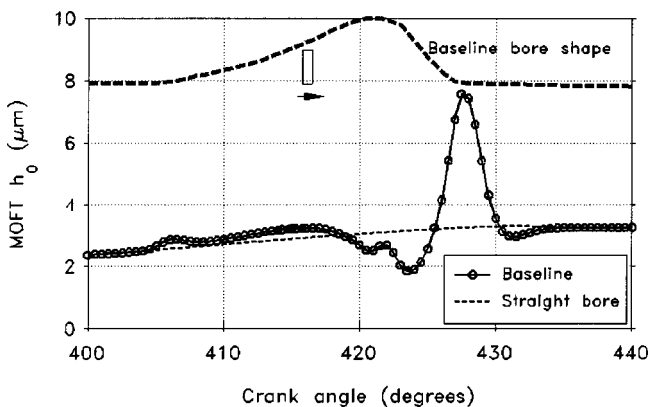


Fig. 9 MOFT of top ring in the intake stroke at 6000 rpm

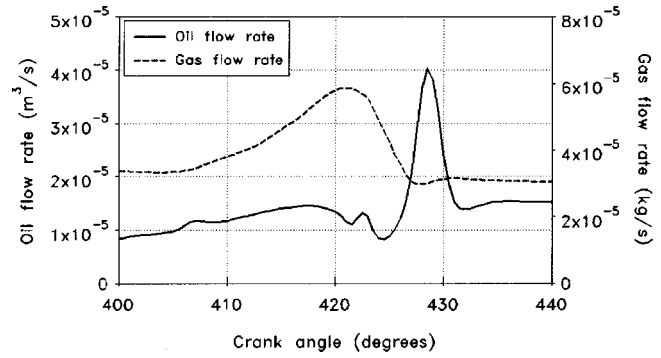


Fig. 10 Oil flow rate below the ring face and gas flow rate through end gap of the top ring in the intake stroke at 6000 rpm

increase in land volume between the rings as this region passes over the “depression” and (2) increase in the ring end gap area for gas flow. As shown in Fig. 10, gas flow rate changes in a manner similar to the change in axial bore profile since the end gap area is directly related to the shape of bore (effect of the oil film thickness on the end gap area is generally relatively small). Due to the influence on oil consumption and gas dynamics, analysis of this type of ring motion merits a detailed investigation.

Figures 6 and 9 show plots of top ring minimum film thickness (MOFT), which are measured from the liner. An alternative method of analyzing ring radial motion is by tracking the radial location of the top ring measured from the cylinder axis. To this effect, Fig. 11 shows radial location of the top ring versus axial location along the liner when the ring slides over the “depression” during the intake stroke for increasing engine speeds. At higher speeds, increasing inertial effects lead to “ring separation” which is clearly visible and highlighted as the top ring emerges from the “depression” (located at a distance of 0.0425 m from top of the liner).

The “ring separation” seen in Fig. 11 at high engine speeds (e.g., 6000 rpm) occurs during the downward motion of the piston/ring assembly in the early part of the intake stroke. During up-strokes (e.g., exhaust), the signs of velocity and acceleration of the piston/ring assembly in Eq. (15) changes compared to the intake stroke for the same axial location. Thus, Fig. 12 shows the differences in values of radial location of the top ring between the intake and exhaust strokes when the top ring slides over the “depression” at an engine speed of 6000 rpm.

An initial inspection of Fig. 12 seems to suggest that the top ring separates from the bore only during the intake stroke and not during the exhaust stroke. However, this is not the case as noted from a closer look at the ring radial motion provided in Fig. 13. Figure 13 shows that during the exhaust stroke “ring separation”

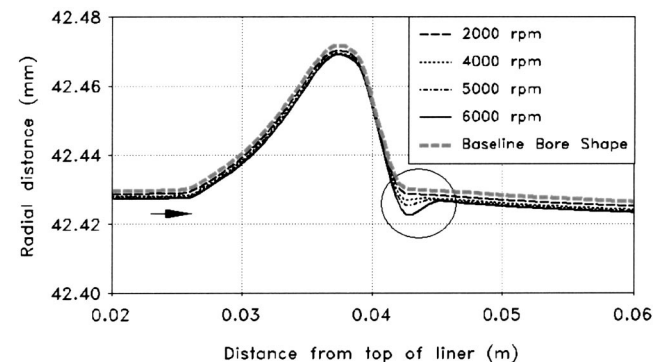


Fig. 11 Radial location of top ring face measured from the cylinder axis at different engine speeds during intake stroke

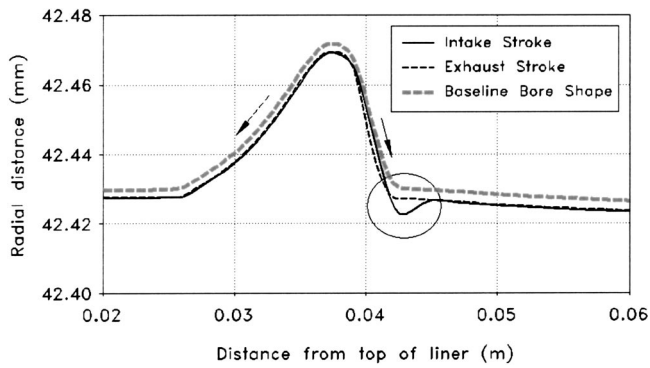


Fig. 12 Radial location of top ring face measured from the cylinder axis during intake and exhaust strokes at 6000 rpm

occurs just after the top ring enters the “depression” (at a location approximately 0.04 m measured from top of the liner). On the other hand, Fig. 13 also shows “ring separation” during early part of the intake stroke when the ring emerges from the “depression” in the bore profile.

Effect of Ring Tension. Ring tension plays a key role in the conformance of a ring to a distorted bore. Hence, it has been selected as one of the variables in the parametric study undertaken here. In particular, the installed tension of the top ring and its effect on radial ring motion in an axially profiled bore are of interest. For purposes of this study, three values of the top ring tension (tangential) are used; a baseline tension of 9.39 N, a high tension value of 12.21 N and a low tension value of 6.58 N.

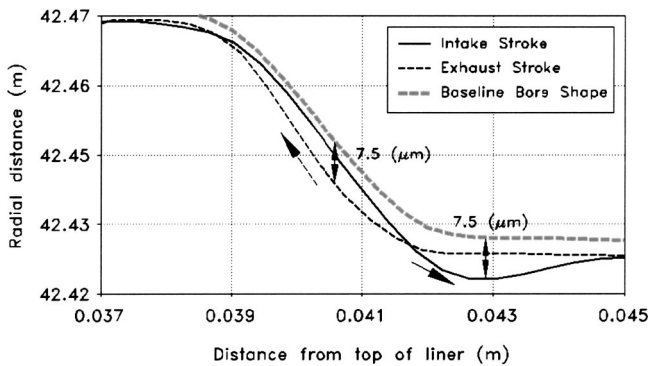


Fig. 13 Enlarged view of highlighted region in Fig. 12

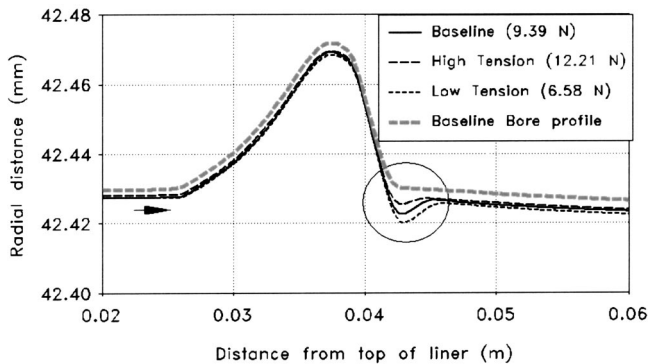
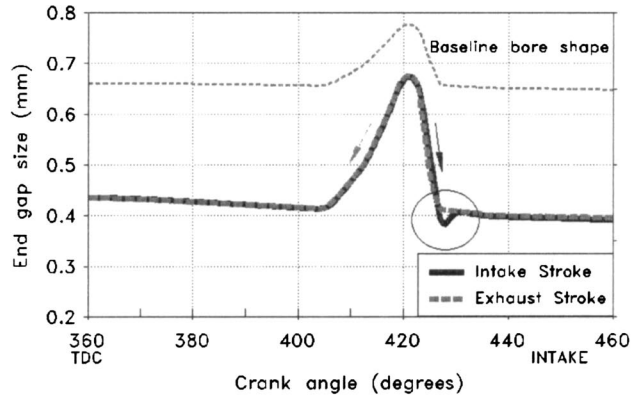


Fig. 14 Effect of ring tension on radial location of top ring face during the intake stroke at 6000 rpm

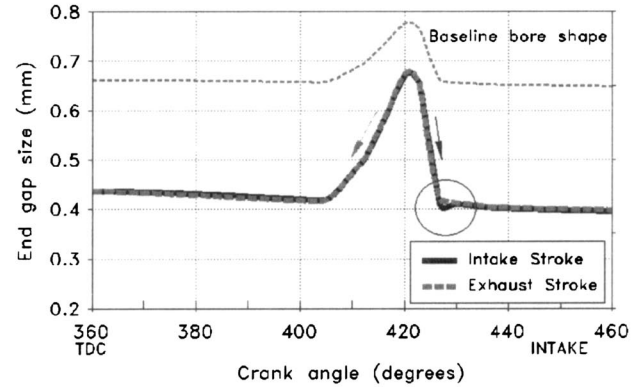
Simulations have been carried out for the baseline axial bore profile depicted in Fig. 4 at a fixed engine speed of 6000 rpm.

Figure 14 displays the top ring radial motion during the intake stroke when it slides over the “depression” for different ring tension values. As expected, with increasing tension, the ring conforms more to the profiled bore and shows lower tendency to “separate” from the bore.

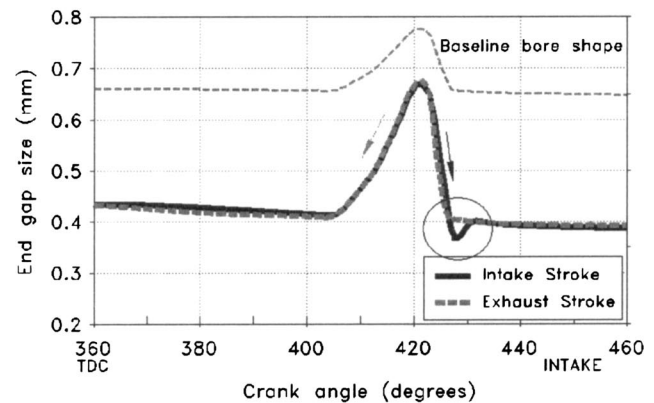
In the experimental work conducted by M. Basaki et al. [6], instantaneous end gap sizes were measured for various ring tension values. The simulated results carried out in this study are



(a) Baseline tension (9.39 N)



(b) High tension (12.21 N)



(c) Low tension (6.58 N)

Fig. 15 Top ring end gap sizes during intake and exhaust strokes for different tensions; (a) 9.39 N, (b) 12.21 N, and (c) 6.58 N at 6000 rpm

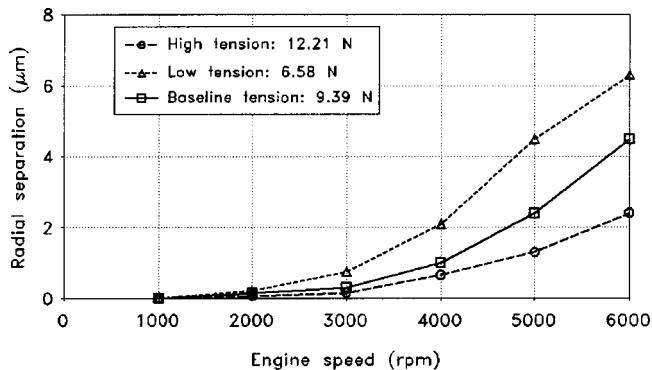


Fig. 16 "Ring separation distance" versus engine speeds for different values of top ring tension

presented for comparison purpose. Figure 15 shows the simulated top ring end-gap behavior during the intake and exhaust strokes, for different tension values, when the top ring is moving over the "depression" in the bore profile.

The changes in end-gap size as the ring slides over the "depression" was also measured in [6] and the results from that study are shown in Fig. 22 in the Appendix. From Fig. 15 it is noted that, during "ring separation," there are smaller changes in the end-gap size between the intake and exhaust strokes with increasing ring tension values. The instantaneous response of ring end-gaps to a bore profile is critical to gas blow-by, blow-back, and oil consumption in engines. The computed results show good qualitative comparison with the measurements and underscore the need for such effects to be incorporated in ring-pack models.

Figures 16 and 17 show the combined effects of engine speed and ring tension on the variable "ring separation distance." As expected, for a fixed engine speed and decreasing ring tension, the top ring has a higher tendency to move away or "separate" from the liner as it slides across the "depression" in the bore profile. For a given ring tension and with increasing engine speeds the top ring shows the appropriate influence of higher inertial effects as discussed in the prior section. The predicted radial motion of the top ring in response to the axial bore profile and varying values of engine speed and ring tension compares favorably with the measured trends reported in [6] and shown in Figs. 23 and 24 in the Appendix.

Effect of Axial Bore Profiles. In order to study the influence of axial bore profiles on top ring radial dynamics; three different axial bore shapes are used in the simulation. The intent of this

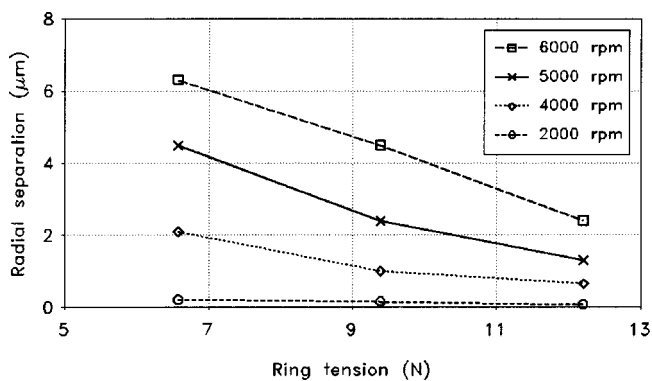


Fig. 17 "Ring separation distance" versus top ring tension values for different engine speeds

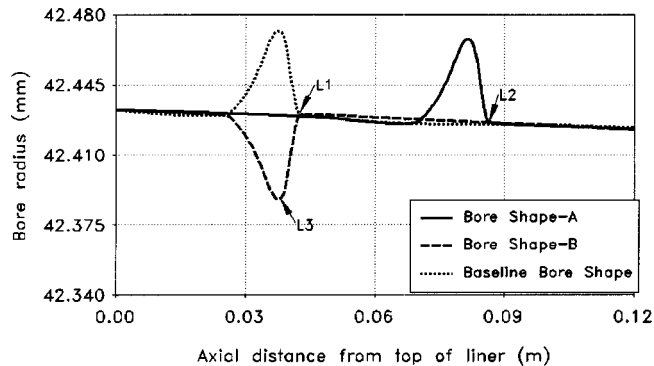


Fig. 18 Various axial bore profiles used in this study

section is to illustrate how the shape of the "depression" and its location on the liner affects the radial dynamics of the top ring. Figure 18 shows the three axial bore profiles used (a) baseline profile with the "depression" located in the upper part of the cylinder (also shown in Fig. 4), (b) bore profile designated "A" with the identical "depression" but located in the lower portion of the cylinder, and (c) a bore profile designated "B" with a "bump" instead of a "depression" with identical geometry and at the same axial location of the baseline case in the cylinder.

Figure 19 shows the top ring radial motion when it slides over the "depression" associated with bore profile A during the exhaust and intake strokes at 6000 rpm. Comparisons in top ring radial motions between the baseline bore profile and bore profile A during the intake stroke can be made from Figs. 12 and 19. In particular, the "ring separation" event during the intake stroke, observed with the baseline bore profile, is not seen with profile A, from Fig. 19. Also, "ring separation" during the exhaust stroke in Fig. 13 is not seen in Fig. 19. The differences in ring radial motions at locations L1 and L2 shown in Fig. 18, arise due to different values of piston/ring velocity and acceleration at those locations on the cylinder bore. Such analysis is useful in determining/evaluating the limits of bore distortion so that they do not adversely affect the ring-pack performance.

Figure 20 shows the top ring radial motion when sliding in a bore with profile B that has a "bump" instead of a "depression." Comparing Figs. 12 and 20 shows the main difference; the radial location of the top ring measured from the cylinder axis decreases when the ring moves over the "bump" compared to the increase in radial location when moving over the "depression" (i.e., motion at locations L1 and L3).

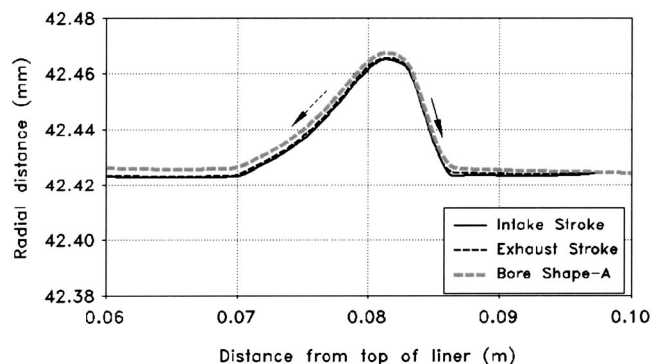


Fig. 19 Radial location of top ring face during the intake and exhaust strokes while sliding over the "depression" in bore profile A at 6000 rpm

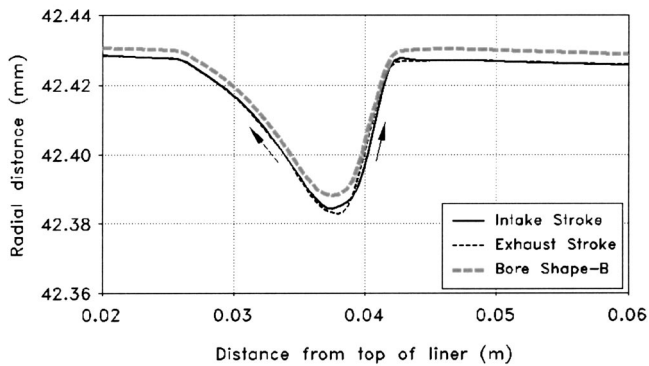


Fig. 20 Radial location of top ring face during the intake and exhaust strokes while sliding over the "bump" in bore profile B at 6000 rpm

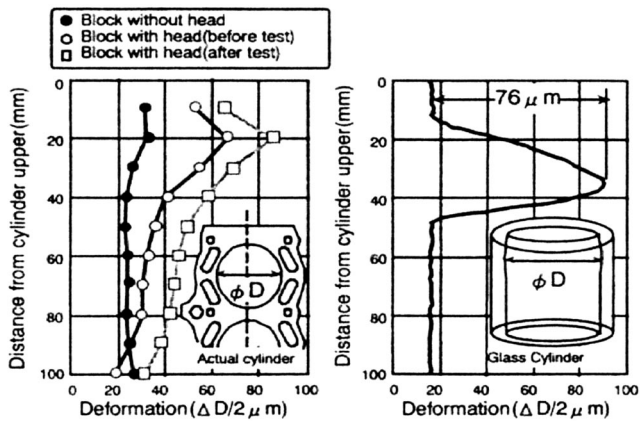


Fig. 21 Measured cylinder bore deformation

Conclusions

The effect of an axial bore profile on ring radial dynamics has been accounted in the ring-pack phenomenological models and numerically investigated. The predictions from simulations show good qualitative comparisons with experimental results on a similar engine. Some conclusions can be drawn from this study which are listed below:

1. Radial ring motion is significantly influenced by axial bore profiles. An analytical expression has been developed to represent the radial inertia of a ring due to an axial bore profile, which provides an insight to the phenomena. There can be situations of "ring separation" from the bore dependent on (a) bore profile geometry, (b) engine speed, (c) ring tension, and (d) gas loads.

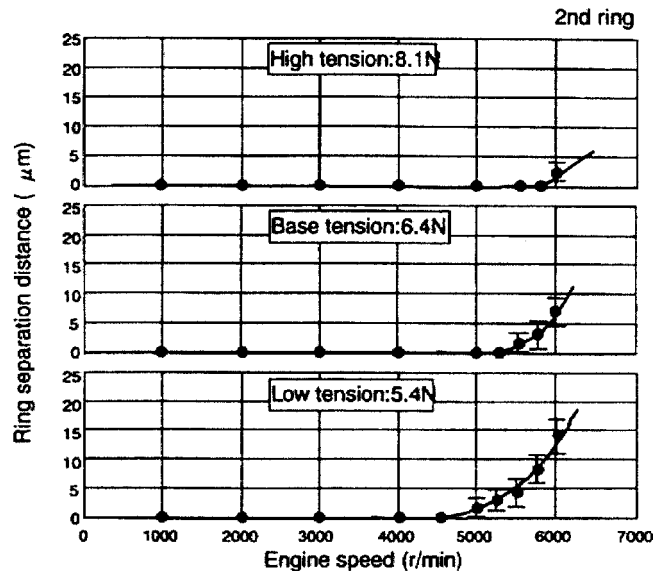


Fig. 23 Ring separation from bore versus engine speed

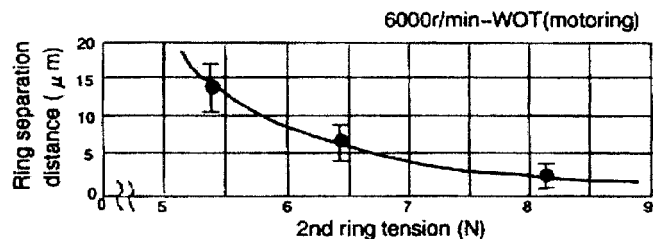


Fig. 24 Ring separation from bore versus ring tension

2. The "ring separation distance" can be substantial so as to allow oil to flow past the ring towards the chamber, potentially leading to higher oil consumption. Large predicted values of ring minimum oil film thickness (MOFT) during "ring separation" are accompanied by substantial oil flow rates below the ring-face during this event.

3. The ring end-gap sizes change continuously as the rings slide in an axially profiled bore. This has an impact on inter-ring gas dynamics, blow-by, and blow-back. Additionally, since oil is entrained in the blow-back gases, this oil consumption contribution mode may also be affected.

4. The influence of axial bore profiles on ring radial dynamics has been demonstrated in this investigation. These effects should be taken into consideration in ring-pack analysis due to their im-

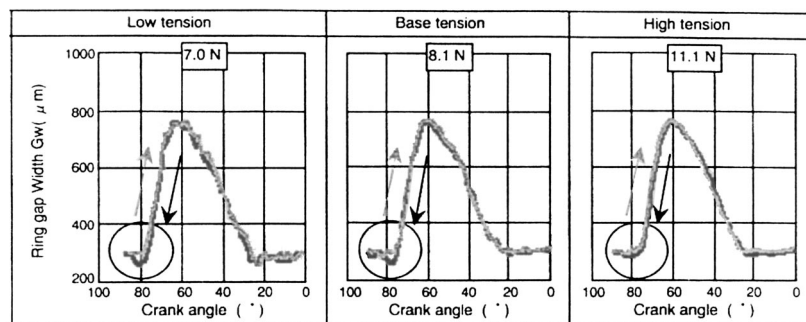


Fig. 22 Measured ring end gap at 6000 rpm

plication on the performance parameters such as oil consumption, friction and blow-by. Such analysis helps to (a) evaluate/determine limits for acceptable bore distortion, (b) optimize location of liner supports without adverse effects on ring-pack behavior.

Acknowledgments

The authors acknowledge the support and permission of Ricardo, Inc. for publishing this paper.

Nomenclature

| | |
|------------|---|
| A | = flow area of orifice (m^2) |
| a_r | = ring radial acceleration (m/s^2) |
| a_y | = ring axial acceleration (m/s^2) |
| B | = axial ring width (m) |
| C_d | = discharge flow coefficient of an orifice |
| D | = nominal bore diameter (m) |
| E | = composite elastic modulus of contacting materials (N/m^2) |
| F_{asp} | = force due to asperity contact pressures at ring-liner interface (N) |
| F_{frc} | = friction force at the ring-groove interface (N) |
| F_{gas} | = force from land gas pressures at ring-liner interface (N) |
| F_{gro} | = force due to groove gas pressure at back of the ring (N) |
| F_{ine} | = force on the ring due to its radial inertia (N) |
| F_{oil} | = force due to oil pressures at ring-liner interface (N) |
| F_{ten} | = force due to installed ring tension (N) |
| $h(x)$ | = ring-groove side clearance (m) |
| $h(y)$ | = clearance at the ring face-liner conjunction (m) |
| h_0 | = minimum radial distance from ring face to liner (m) |
| L_{ring} | = ring radial thickness (m) |
| \dot{m} | = gas mass flow rate across boundaries of a subvolume (kg/s) |
| m_i | = mass of gas in the subvolume i (kg) |
| m_{ring} | = ring mass (kg) |
| N | = engine speed (rpm) |
| p | = oil film pressure at ring-liner interface (Pa) |
| p_{asp} | = asperity contact pressure at ring-liner interface (Pa) |
| p_d | = downstream pressure of an orifice (Pa) |
| p_{gro} | = gas pressure in a ring groove (Pa) |
| p_i | = gas pressure in subvolume i (Pa) |
| p_{ll} | = gas pressure in the lower land of a ring (Pa) |
| p_{ul} | = gas pressure in the upper land of a ring (Pa) |
| p_u | = upstream pressure of an orifice (Pa) |
| R | = gas constant ($J/kg \cdot K$) |
| s | = radial distance the minima of ring face profile (m) |
| s_{cg} | = radial distance of center of gravity of a ring (m) |
| t | = time (s) |
| T_i | = gas temperature in subvolume i (K) |
| T_u | = upstream gas temperature of an orifice (K) |
| V_y | = piston ring axial velocity (m/s) |

| | |
|-----------------|---|
| V_i | = volume of subvolume i (m^3) |
| x | = radial coordinate (m) |
| y | = axial coordinate (m) |
| z | = radial deformation of cylinder bore (m) |
| Y_1 | = axial location of leading edge of ring oil lubricated zone (m) |
| Y_2 | = axial location of trailing edge of ring oil lubricated zone (m) |
| α_{bore} | = slope of axial bore profile |
| β | = radius of curvature at the peak of surface asperities (m) |
| γ | = polytropic exponent |
| η | = density of the surface asperities (l/m^2) |
| μ | = lubricant dynamic viscosity ($Pa \cdot s$) |
| μ_{mix} | = dynamic viscosity of oil-gas mixture ($Pa \cdot s$) |
| σ | = mean r.m.s. height of surface asperities (m) |

Appendix

Figures 21 to 24 in this Appendix are selectively extracted from an experimental study on a similar engine by M. Basaki, K. Saito, T. Nakashima, and T. Suzuki [6] in order to make relevant qualitative comparisons with the current numerical investigation. This experimental work was conducted on a gasoline engine of 95-mm bore diameter and 86-mm stroke length with a three-ring ring pack set. In their study, instantaneous end gap size was measured by a visualization method. Using the relation between radial movement and change in end gap size of a ring, "ring separation" from the bore was calculated as shown in Figs. 23 and 24.

References

- [1] Takiguchi, M., Watanabe K., Kato, T., Sato, M., and Ueno, H., 1999, "Effects of Piston Ring Tension on Oil Consumption and Piston Friction in Diesel Engines," ASME ICE Spring Technical Conference, Vol. 32-3, Paper No. 99-ICE-199.
- [2] Hill, S. H., Kantola, T. C., Brown, J. R., and Hamelink, J. C., 1995, "An Experimental Study of the Effect of Cylinder Bore Finish on Engine Oil Consumption," SAE Paper No. 950938.
- [3] Schneider, E. W., Blossfeld, D. H., Lechman, D. C., Hill, R. F., Reising, R. F., and Brevick, J. E., 1993, "Effect of Cylinder Bore Out-of-Roundness on Piston Ring Rotation and Engine Oil Consumption," SAE Paper No. 93796.
- [4] Hitosugi, H. et al., 1996, "Study on Mechanism of Lubricating Oil Consumption Caused by Cylinder Bore Deformation," SAE Paper No. 960305.
- [5] Goto, T., Arai, T., Goto, T., and Hamai, K., 1989, "Influence of Cylinder Bore Distortion on Engine Performances (Part I: Static Mode Analysis of Bore Distortion for Amount of Oil Consumption)," JSAE Paper No. 891010.
- [6] Basaki, M., Saito, K., Nakashima, T., and Suzuki, T., 2000, "Analysis of Oil Consumption at High Engine Speed by Visualization of the Piston Ring Behaviors," SAE Paper No. 2000-01-2877.
- [7] Gulwadi, S. D., 1998, "A Mixed Lubrication and Oil Transport Model for Piston Rings Using a Mass-Conserving Algorithm," ASME J. Eng. Gas Turbines Power, **120**, pp. 199–208.
- [8] Gulwadi, S. D., 2000, "Analysis of Tribological Performance of a Piston Ring Pack," Tribol. Trans., **43-2**, pp. 151–162.
- [9] Greenwood, J. A., and Tripp, J. H., 1971, "The Contact of Two Nominally Flat Rough Surfaces," Proc. Inst. Mech. Eng., **185**, pp. 625–633.
- [10] Piao, Y., and Gulwadi, S. D., 2000, "Effect of Piston Secondary Motion on the Numerical Modeling of Ring Pack Performance," ASME-ICE Fall Technical Conference, ICE-Vol. 35-3, Paper No. 2000-342.

Erratum: “Effect of Biodiesel Utilization of Wear of Vital Parts in Compression Ignition Engine” (ASME J. Appl. Mech., 2003, 70, pp. 604–611)

A. K. Agarwal, J. Bijwe, and L. M. Das

The title of this paper should read “Effect of Biodiesel Utilization on Wear of Vital Parts in Compression Ignition Engine” (“Effect of Biodiesel Utilization on Wear . . . ” instead of “Effect of Biodiesel Utilization of Wear . . . ”).